UCRL 53868-99

FY 99

Engineering Research, Development and Technology

Acknowledgments

Scientific Editing
Andrea L. Baron
Robert T. Langland
Camille Minichino

Composition
Andrea L. Baron

Graphic Design
Pamela A. Allen

Cover Design
Jeffrey B. Bonivert

Art Production/Layout
Jeffrey B. Bonivert
Dennis Chan
Irene J. Chan
Lucy C. Dobson
Linda Moore

Publication Services
Cynthia Tinoco

Available to the public from the
National Technical Information Service
U.S. Department of Commerce
5285 Port Royal Rd.
Springfield, VA 22161

DISCLAIMER

This document was prepared as an account of work sponsored by an agency of the United States Government. Neither the United States Government nor the University of California nor any of their employees makes any warranty, express or implied, or assumes any legal liability or responsibility for the accuracy, completeness, or usefulness of any information, apparatus, product, or process disclosed, or represents that its use would not infringe privately owned rights. Reference herein to any specific commercial products, process, or service by trade name, trademark, manufacturer, or otherwise, does not necessarily constitute or imply its endorsement, recommendation, or favoring by the United States Government or the University of California. The views and opinions of authors expressed herein do not necessarily state or reflect those of the United States Government or the University of California and shall not be used for advertising or product endorsement purposes.

Work performed under the auspices of the U.S. Department of Energy by Lawrence Livermore National Laboratory under Contract W–7405–Eng–48.

UCRL 53868-99

FY 99

Engineering Research, Development and Technology

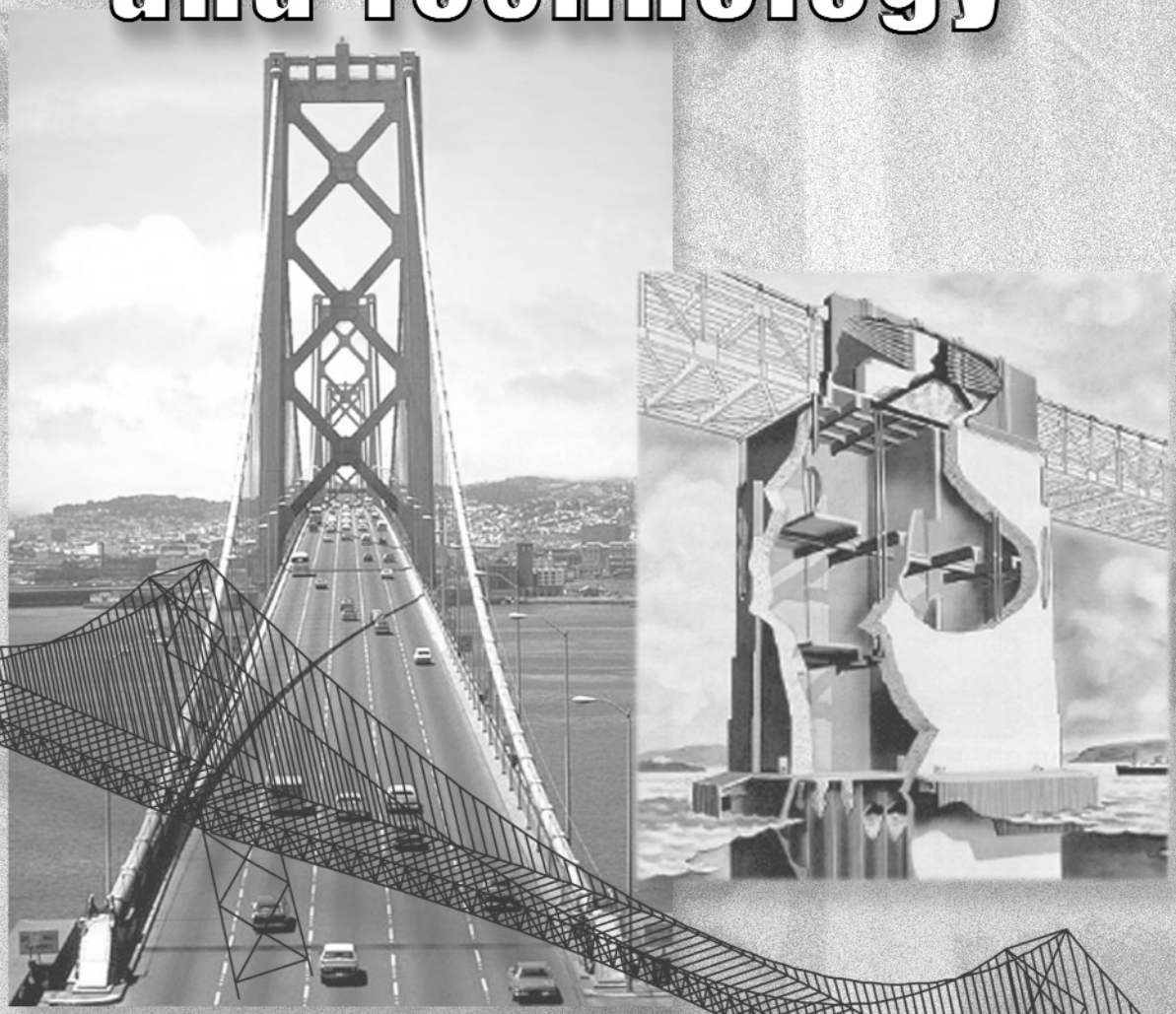

Manuscript Date February 2000
Distribution Category UC-706

Introduction

Spiros Dimolitsas, Associate Director for Engineering

1. Center for Complex Distributed Systems

Overview
David B. McCallen, Center Director

A Reduced-Order Model for Nonlinear Suspension Bridge Analysis
David B. McCallen, Abolhassan Astaneh-Asl 1-1

Seismic Studies of the San Franciso-Oakland Bay Bridge
David B. McCallen, Shawn C. Larsen, Abolhassan Astaneh-Asl 1-25

Signal Processing for Evaluation and Update of Simulation Models in Structural Analysis
Gregory C. Burnett, Gregory A. Clark, David B. McCallen, and Charles R. Noble 1-33

Controlled Biological Systems for Sensor Platforms
Dino R. Ciarlo, Jonathan Simon, and Matt Harren 1-41

An Instrumentation System for Remote Monitoring of Large Structures
Mathew S. Hoehler, Charles R. Noble, David B. McCallen, and Jon P. Lewis 1-43

Underground Facilities Characterization
Rexford M. Morey, Michael H. Buettner, and William D. Daily 1-51

2. Center for Microtechnology

Overview
Raymond P. Mariella, Jr., Center Director

Exploration of Novel Fabrication Methods for Microfluidics/Microelectromechanical Systems Devices
Harold D. Ackler, Julie Hamilton, William J. Benett, and Thomas E. Shell 2-1

Microtechnology for High-Explosive Testing
Dino R. Ciarlo, Kirk P. Seward, Mehdi Balooch, and Scott E. Groves 2-3

Improved Microgripper Process
Dino R. Ciarlo, Abraham P. Lee, Dawn L. Hilken, and Jimmy C. Trevino 2-7

Miniature Sample Collector/Concentrator for Biological Weapons Agent Detectors
Jonathan Simon 2-9

Microfabricated Deformable Mirrors for Adaptive Optics Applications
June Yu, James A. Folta, Peter Krulevitch, Harold D. Ackler, Scot S.Olivier, and William D. Cowan 2-11

High-Voltage Photovoltaics
Jeffrey D. Morse, Gregory A. Cooper, and Karla G. Hagans 2-15

Microfabricated Flow Cell for DNA Analysis
Peter Krulevitch and Laurence R. Brewer 2-19

Microvalves for Microcatheters
Kirk P. Seward, Amy W. Wang, and Abraham P. Lee 2-21

Microelectromechanical-System-Based Fuel Cell for Microscale Energy
Jeffrey D. Morse and Alan F. Jankowski. 2-23

Custom Silicon Etching
Jeffrey D. Morse, Leslie M. Jones, and Robert T. Graff 2-27

Micromechanical Characterization Tools for Highly-Filled Polymers
Scott E. Groves, Steve J. DeTeresa, Bruce J. Cunningham, Dino R. Ciarlo, David Allen, K. Clayton, and C. Yoon 2-31

Advanced Imaging Catheter
Amy W. Wang, Abraham P. Lee, Daniel L. Schumann, Luiz Da Silva, Matthew J. Everett, Billy W. Colston, Jr., Steve B. Brown, Dale L. James, Richard A. London, and Peter Amendt 2-41

Intelligent Wavefront Reconstructors for Adaptive Optics
Chi Yung Fu, George F. Chapline, Scot S. Olivier, and Loren I. Petrich 2-45

Lambda Connect: Multiwavelength Technologies for Ultrascale Computing
Michael C. Larson, Steven W. Bond, Michael D. Pocha, Mark A. Emanuel, and Mark E. Lowry 2-49

Low Power Wireless Modem Technology
Charles F. McConaghy and Charles Chien 2-57

Wireless Micropower RF Components
Charles F. McConaghy 2-59

Acoustically-Driven Microfluidic Systems
Amy W. Wang, William J. Benett, Christopher D. Fuller, and Richard G. Couch 2-63

3. Center for Precision Engineering

Overview
Kenneth L. Blaedel, Acting Center Director

Atmospheric Pressure Plasma Processing for Damage-Free Optics and Surfaces
Jeffrey W. Carr 3-1

Design of an Ultra Precision Machining Facility: ULTRA350
Keith Carlisle and Stanley L. Edson 3-11

Intermittent Single-Point Machining of Brittle Materials
Mark A. Piscotty 3-17

A Spatial-Frequency-Domain Approach to Designing Precision Machine Tools
Debra Krulewich Born 3-21

Power Spectral Density Measurements of Machined Surfaces over an Extended Range of Spatial Frequencies
Jon M. Baldwin 3-25

Dimensional Metrology of Non-Rigid Objects
Kenneth L. Blaedel and David W. Swift 3-29

4. Center for Computational Engineering

Overview
Kyran D. Mish, Center Director

High-Precision Droplet-Based Net-Form Manufacturing
Arthur B. Shapiro and Melissa Orme 4-1

Improved Implicit Structural Finite Element Algorithms
Michael A. Puso 4-5

Post-Processing and Data Management Software Development for Computational Mechanics
Douglas E. Speck 4-11

Linear Equation Solvers for Parallel Computational Mechanics
Robert M. Ferencz and Chandrika Kamath 4-17

EIGER Preprocessor and User Interface
Robert M. Sharpe, Nathan J. Champagne, and Andrew J. Poggio 4-23

Strength and Reliability of Brittle Materials
Robert A. Riddle, Chol K. Syn, Michael J. O'Brien, Steve Duffy, Joe Palko, and Eric Baker 4-27

Lattice Boltzmann Modeling of Spherical Solutes in Confined Domains
David S. Clague 4-35

Modeling of Anisotropic Inelastic Behavior
Daniel J. Nikkel, Jr., Deepak S. Nath, Arthur A. Brown, and James Casey 4-39

Development of Laser-Driven Photocathode Injector and Femtosecond-Scale Laser Electron Synchronization for Next Generation Light Sources
Gregory P. Le Sage, Thomas E. Cowan, Todd R. Ditmire, and J. Rosenzweig 4-47

A Segment-to-Segment Sliding Interface Algorithm for DYNA3D
Jerry I. Lin 4-49

Usability Enhancements for TIGER
David J. Steich, Gerald J. Burke, Jeffery S. Kallman, S Terry Brugger, and Daniel A. White 4-53

Enhanced Fluid Dynamics Capability and Multidisciplinary Coupling in ALE3D
Rose C. McCallen, Timothy A. Dunn, John S. Dolaghan, and Richard G. Couch 4-63

5. Center for Nondestructive Characterizaiton

Overview
Harry E. Martz, Jr., Center Director

The Optically Parallel Ultrasound Sensor (OPUS)
Jeffrey S. Kallman, A. Elaine Ashby, Graham H. Thomas, and Dino R. Ciarlo 5-1

Speckle Reduction for LIDAR Using Optical Phase Conjugation
Mark W. Bowers 5-5

Evaluation of an Amorphous-Silicon Array for Industrial X-Ray Imaging
Kenneth W. Dolan, Clinton M. Logan, Jerry J. Haskins, R. Derrill Rikard, and Daniel J. Schneberk 5-11

High-Frequency Laser-Based Ultrasound for NDC Applications
Robert D. Huber, Graham H. Thomas, Howard Lee, Christopher Richardson, and Professor James Spicer . . 5-25

New Developments in RECON
Jessie A. Jackson 5-31

Component Gap Detection by Infrared Imaging
Charles S. Landram, Richard W. Martin, Nancy K. Delgrande, and Philip F. Durbin 5-37

Quantitative Tomography Simulations and Reconstruction Algorithms
Harry E. Martz, Jr., Dennis M. Goodman, Jessie A. Jackson, Clinton M. Logan,
Maurice B. Aufderheide, III, Alexis Schach von Wittenau, James M. Hall, and Dale M. Sloan 5-47

Ultra-Wideband Phased Array
Rexford M. Morey 5-71

Photonic Velocimetry System Optimization
Paul D. Sargis, Nicole E. Molau, Jeffrey B. Cooke, Oliver T. Strand, and Mark E. Lowry 5-77

Selected Engineering Publications

Selected Engineering Publications *PB-1*

Author Index

Author Index *AI-1*

Spiros Dimolitsas, Associate Director for Engineering

Engineers often study turbulence and its effects, but in 1999, we spent most of our time experiencing it. Lawrence Livermore National Laboratory (LLNL) was featured in headlines coast-to-coast this past year, and our operating requirements from the Department of Energy, particularly on security and safety, became much more rigorous. However, despite overwhelming distractions and competing priorities, we in Engineering have kept focused on our mission and our milestones.

Whether using computational engineering to predict how giant structures like suspension bridges will respond to massive earthquakes or devising a suitcase-sized microtool to detect chemical and biological agents used by terrorists, we have made solid technical progress. This report summarizes our technical R&D objectives, methods and key results for the past year—as structured through our technology centers.

Each Center is responsible for the vitality and growth of the core technologies it represents. The five Centers focus and guide longer-term investments within Engineering, as well as impact all of LLNL. My goal is that each Center will be recognized on an international scale for solving compelling national problems requiring breakthrough innovation.

1999 highlights

We attracted national attention with our Center for Microtechnology work in chemical/biological nonproliferation, featured in the April issue of *Science* magazine. We achieved the fastest polymerase-chain-reaction detection time for chemical and biological agents of warfare. Other microtechnology achievements include a substantial joint venture with industry in extreme ultraviolet technology to produce the world's smallest computer chip, as well as collaborations with the University of California at Los Angeles on wireless sensors.

Within the Center for Complex Distributed Systems (CCDS,) we are working with the University of California at Berkeley on massive simulation models for large structures. Our CCDS employees have written model-based signal processing algorithms that provide a much improved methodology for validating and updating computational models. They have also developed wireless data acquisition systems to better monitor optical support structures within large systems like the National Ignition Facility (NIF), one of the largest high-tech construction projects in the country.

In the area of nondestructive characterization (NDC) science and measurement, we are advancing our core competencies and technologies in quantitative NDC and fast nanoscale imaging. The Center for Nondestructive Characterization has performed breakthrough work in applying NDC at the beginning of the lifecycle of fabricating finished parts. This saves time and money by finding flaws in the part or process in the early stages, when change is easier to make.

The Center for Computational Engineering (CCE) is integrating the common technical aspects of mechanical and electronics engineering within the scope of computational engineering. Mechanical engineering research has centered on fundamental work on the responses of various materials, such as brittleness and inelasticity, as well as improvements to algorithms in two popular LLNL-designed software codes: NIKE3D and DYNA3D. In electronics engineering CCE has pioneered advances in Lattice-Boltzmann simulations for chemical engineering and microfluidics.

Within the Center for Precision Engineering, we are pursuing a breadth of technologies—from machine tool design to manufacturing process engineering. Much of our work centers on the ability to design, manufacture, and characterize field experiments in NIF. Here we must be able to build millimeter-size structures from exotic materials to precise tolerances in extremely clean environments.

Leveraging our work

In a sense, our Centers serve as the internal venture capitalists for our programs. They provide the mechanism by which Engineering can help LLNL's programs attract funding, while pioneering the technologies that will sustain long-term investment.

Engineering must continually work to build LLNL's competitive advantage; we must continue to create things that are technically one-of-a-kind. Our new centers do this by fusing the best of mechanical and electronics engineering, creating a synergy that most organizations cannot. Our future depends on how we find innovative but cost-effective engineering solutions to emerging technical problems that lead to solutions on a national scale.

Introduction

David B. McCallen, Center Director

The growth of computer power and connectivity, together with advances in wireless sensing and communication technologies, is transforming the field of complex distributed systems. The ability to deploy large numbers of sensors with a rapid, broadband communication system will enable high-fidelity, near real-time monitoring of complex systems. These technological developments will provide unprecedented insight into the actual performance of engineered and natural environment systems, enable the evolution of many new types of engineered systems for monitoring and detection, and enhance our ability to perform improved and validated large-scale simulations of complex systems.

One of the challenges facing engineering is to develop methodologies to exploit the emerging information technologies. Particularly important will be the ability to assimilate measured data into the simulation process in a way which is much more sophisticated than current, primarily *ad hoc* procedures.

The reports contained in this section on the Center for Complex Distributed Systems describe activities related to the integrated engineering of large complex systems. The first three papers describe recent developments for each link of the integrated engineering process for large structural systems. These include 1) the development of model-based signal processing algorithms which will formalize the process of coupling measurements and simulation and provide a rigorous methodology for validation and update of computational models; 2) collaborative efforts with faculty at the University of California at Berkeley on the development of massive simulation models for the earth and large bridge structures; and 3) the development of wireless data acquisition systems which provide a practical means of monitoring large systems like the National Ignition Facility (NIF) optical support structures.

These successful developments are coming to a confluence in the next year with applications to NIF structural characterizations and analysis of large bridge structures for the State of California. Initial feasibility investigations into the development of monitoring and detection systems are described in the papers on imaging of underground structures with ground-penetrating radar, and the use of live insects as sensor platforms. These efforts are establishing the basic performance characteristics essential to the decision process for future development of sensor arrays for information gathering related to national security.

Center for Complex Distributed Systems

1

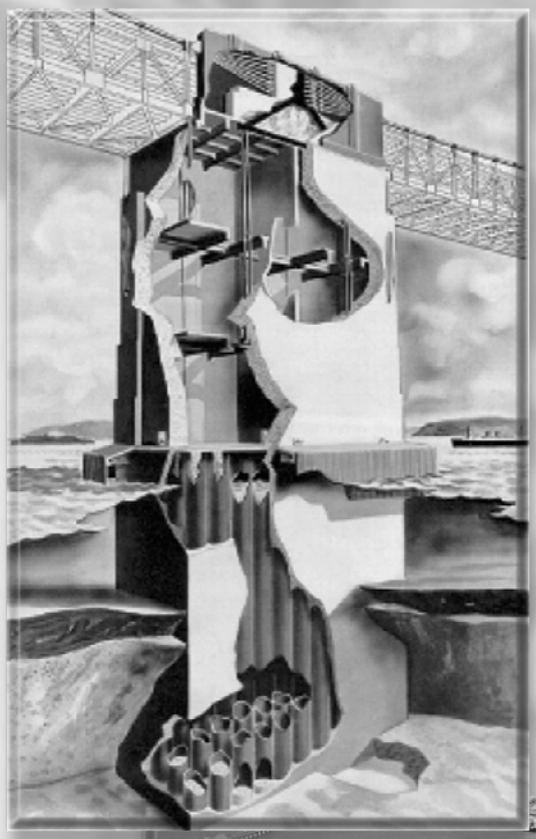

1. Center for Complex Distributed Systems

Overview
David B. McCallen, Center Director

A Reduced-Order Model for Nonlinear Suspension Bridge Analysis
David B. McCallen, Abolhassan Astaneh-Asl 1-1

Seismic Studies of the San Franciso-Oakland Bay Bridge
David B. McCallen, Shawn C. Larsen, Abolhassan Astaneh-Asl 1-25

Signal Processing for Evaluation and Update of Simulation Models in Structural Analysis
Gregory C. Burnett, Gregory A. Clark, David B. McCallen, and Charles R. Noble 1-33

Controlled Biological Systems for Sensor Platforms
Dino R. Ciarlo, Jonathan Simon, and Matt Harren 1-41

An Instrumentation System for Remote Monitoring of Large Structures
Mathew S. Hoehler, Charles R. Noble, David B. McCallen, and Jon P. Lewis 1-43

Underground Facilities Characterization
Rexford M. Morey, Michael H. Buettner, and William D. Daily 1-51

A Reduced-Order Model for Nonlinear Suspension Bridge Analysis

David B. McCallen
Center for Complex Distributed Systems

Abolhassan Astaneh-Asl
Department of Civil and Environmental Engineering
University of California
Berkeley, California

With the proliferation of commercially available software tools for structural mechanics and powerful compute engines, computational simulation of long-span cable-supported bridges is experiencing rapid growth. However, due to the physical size and large number of individual members in these structures, the application of general purpose computational mechanics software may not represent the optimal solution, particularly for computationally intensive nonlinear analyses and parametric studies where multiple simulations are required. We have developed a numerical simulation tool specific to the nonlinear, transient, dynamic analysis of cable-supported bridges. The methodology is predicated on special element technologies which allow a significant reduction in the number of global equations in the bridge system model. The solution of the equations of motion is based on a hybrid implicit/explicit procedure in which the bridge gravity configuration is determined with an implicit solution, and the transient time-stepping solution is based on explicit integration of the equations of motion.

Introduction

In recent years, the design and analysis of large, distributed structural systems has become increasingly reliant on large-scale computational simulation. Linear simulations have been the mainstay of design computations. However, as performance-based design procedures become more prevalent, there will be increased demand for accurate numerical models capable of simulating nonlinear response and ultimate structural collapse.

The computational requirements for nonlinear analyses, which include changes in the global model geometry, impact between adjacent bridge segments, and material inelasticity, can be prohibitive if general purpose finite-element programs are used. This fact begs for efficient nonlinear computational models which allow parametric studies essential to developing a clear understanding of the dynamic bridge response.

In addition to computational difficulties, there continue to be phenomenological issues in the analyses of these important structures. The effects of spatially varying earthquake ground motions; near-field earthquake ground motions containing long-period ground displacement pulses and permanent ground displacements; and fluid-structure interaction between a bridge and the turbulent atmosphere, are topics for which scientific and engineering understanding are incomplete. Appropriate characterization of damping mechanisms in a long-span cable bridge remains an area of great uncertainty.

A rigorous understanding of the mechanics of cable bridge damping, which discriminates between complex aerodynamic and mechanical damping mechanisms, has yet to be developed, and it remains necessary to rely on simple spectral representations of damping. Spectral damping representations are complicated by the fact that cable bridge dynamics can be very broad-band with long wavelength modes of a flexible deck system on the order of 10- to 15-s periods, and modes of stiff towers on the order of 0.1- to 0.2-s periods.

There have been extensive analytical and numerical studies of the vibrational characteristics of cable-supported bridges undergoing small amplitude, linear vibrations. The early work of Abdel-Ghaffar[1-3] was important in developing

basic understanding of the linear vibratory dynamics of suspension bridges. Abdel-Ghaffar's work developed analytical models for the natural vibrations of suspension bridges and provided insight on the vibrational interactions between towers, cables, and deck systems. As part of a combined simulation and field observation study, Dumanoglu, Brownjohn, and Severn[4] used 2- and 3-D linear computational models to investigate the natural vibrations of the Fatih Sultan Mehmet suspension bridge (Turkey) and extracted a large number of modes for the structure.

Long-span cable bridges are complex and distributed dynamic systems and model validation and parameter calibration (such as selection of appropriate damping forms) must rely on experimentally obtained observational data. The only database currently available for suspension bridges consists of low amplitude, linear vibrations.[5-9]

The cited experimental and computational studies have generally demonstrated the ability of computational models to adequately represent the lower natural modes associated with small amplitude, linear dynamics of a suspension bridge vibrating about the gravity configuration of the system. Due to the complexities and computational difficulties of large-scale nonlinear analyses, and a lack of measured response data in the nonlinear regime, the effect of nonlinearities on cable bridge response has been investigated to a lesser extent.

Abdel-Ghaffar and Rubin[10,11] demonstrated the nonlinearity associated with modal coupling in amplitude-dependent free vibrations of suspension bridges with applications for the Golden Gate and Vincent Thomas Bridges. Computational studies by Nazmy and Abdel-Ghaffar[12,13] have indicated the importance of geometric nonlinearities in cable-stayed bridges with long spans and reinforced the importance of considering the spatial variation of earthquake ground motions.

In addition to research studies, consideration of nonlinearities in cable-supported bridges is beginning to infiltrate into engineering practice. Ingham, Rodriguez and Nadar[14] have described practical design application of nonlinear analysis in the seismic retrofit studies of the Vincent Thomas Bridge.

Further study is necessary to develop a clear understanding of the nonlinear response of long-span bridges to strong ground motions, particularly when the bridge is located in the near-field of a causative earthquake fault where ground motions may contain both high-frequency and significant long-period motions due to near-field effects. There is no existing observational database for this response regime, and nonlinear computational simulations must play a central role in developing improved understanding.

The objective of our work was the development of a simple and robust computational model for 3-D, nonlinear transient analysis of suspension bridges. The resulting finite-element model accounts for nonlinearities due to finite displacements, material nonlinearities in the bridge members, impact between adjacent bridge segments, and potential rocking and uplift of large caisson foundations.

Unique features of the model include the element technologies, which are tailored to the construction of a reduced-order model with a significant reduction in the global degrees of freedom; and the use of an explicit time-integration scheme for dynamic analyses. The explicit scheme provides a simple and highly reliable nonlinear solution framework for transient nonlinear analyses, particularly when considering the sudden events associated with impact between adjacent bridge segments, sudden tensioning of slack cables, or collapse of bridge components.

The model incorporates an implicit based, automated procedure for nonlinear gravity initialization of the bridge model, which computes the correct bridge geometry and the correct initial stress field in the cable and deck trusses for gravity loading.

The nonlinear model we have developed can be particularly useful for parametric studies aimed at understanding the complex transient response of long-span bridges and the relationship between bridge response and ground motion characteristics. Because of the importance of validating special numerical models, particular attention was paid to comparison of the reduced order model with both experimental data and higher order detailed models.

Progress

Computational Bridge System Model

The research study which motivated development of the computational model consisted of a multidisciplinary seismological and engineering study of the San Francisco-Oakland Bay Bridge (**Fig. 1**). With approximately 280,000 vehicles per day, the Bay Bridge carries the highest traffic volume of any bridge in the United States. The bridge is a critical transportation link and a seismically interesting structure by virtue of its close proximity to major active earthquake faults.

Two new computational tools for numerical simulation of seismic ground motions and structural

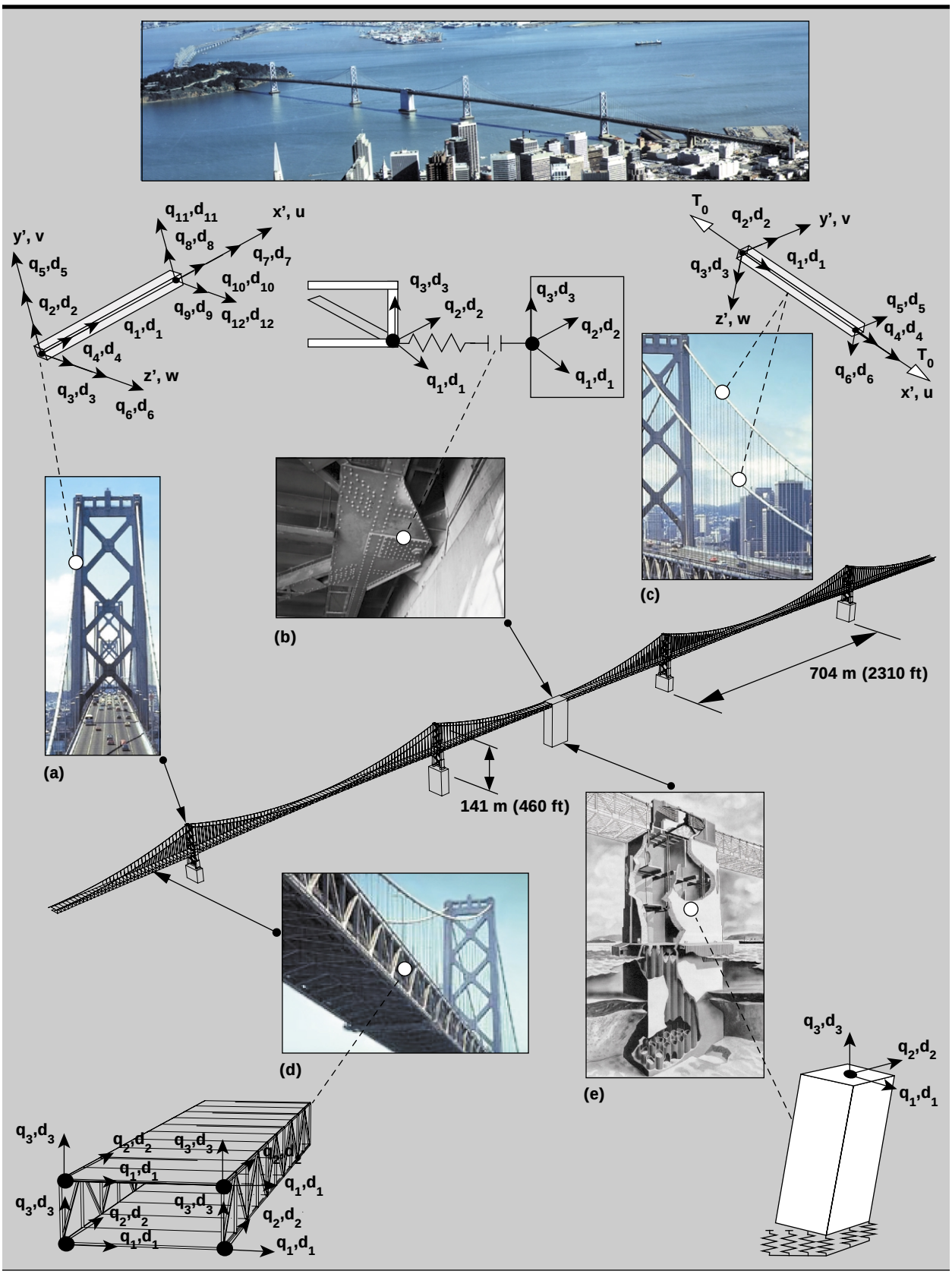

Figure 1. The five elements of the bridge system model. (a) Finite rotation fiber flexure element for the bridge towers; (b) penalty node-to-node contact for deck impact; (c) tension-only two-force member with initial stress for cables; (d) composite membrane, truss, and sway stiffness deck model; (e) caisson block with uplift.

response were developed for this study. A massively parallel, geophysics based finite-difference program has been constructed to model seismic wave propagation.[15,16] The geophysics model, which is described in a companion paper, provides ground motion estimates, including the effects of near-field phenomena such as long-period ground displacement pulses, and coseismic, permanent ground displacements associated with tectonic plate movements.

The second computational tool, and the subject of this paper, consists of the special-purpose finite-element program for nonlinear bridge analysis. The description references the Bay Bridge system. However, the solution algorithms and element technologies described can have broader applicability to other suspension and cable-stayed bridges with appropriate changes in element properties.

The model consists of five major elements, as shown in **Fig. 1**. A finite-rotation, fiber bending element is used to represent the bridge towers. A tension-only cable element with user-defined initial stress represents the bridge cable system. A reduced-order deck model, consisting of a composite combination of truss, membrane, and sway stiffness elements, represents the deck and stiffening truss system. A penalty-based node-to-node contact element captures potential contact and impact between the deck system and towers, and a rocking foundation element represents the large caisson foundations with potential uplift.

Our philosophy was to maintain the greatest possible simplicity in the element formulations and solution algorithms, and to provide a robust algorithm which could handle a multiplicity of strong nonlinearities. An explicit time integration algorithm provided the robustness for strongly nonlinear dynamic problems. Since explicit integration schemes are conditionally stable with the time step size governed by the highest frequency of the simulation model, explicit schemes are typically too costly for long duration dynamic loads such as earthquakes with existing general-purpose finite-element programs. However, the potential advantages of explicit integration are well known for highly nonlinear problems. These advantages include the basic simplicity and reliability of the algorithm when compared with the most efficient quasi-Newton implicit schemes.

Explicit integration provides accuracy and high reliability for large nonlinear structures when strong nonlinearities occur and can readily handle softening systems or contact intensive problems which defy or hamper convergence of implicit integration schemes. Explicit integration is computationally feasible for long duration problems if the element technologies and physical element sizes in the discretized model do not result in prohibitively small time steps. The simple elements developed in this study lead to manageable time steps and thus enable the use of explicit integration. The nonlinear computational elements and algorithms developed have been incorporated into the special purpose finite-element program SUSPNDRS. The methodologies are described briefly in this paper. A complete description, including detailed evaluations of element and software performance, is given elsewhere.[17]

Nonlinear Solution Framework

In the numerical simulation of cable-supported bridge systems subjected to dynamic loads, two distinct steps must be undertaken to obtain the transient solution. The first step is performance of an appropriate static, nonlinear gravity load initialization of the computational model such that the model emulates the correct geometric shape of the bridge with the appropriate forces in the individual bridge deck members, towers, and cable system.

This initialization must take into account the design objectives and construction sequence of the bridge, since the construction procedure can significantly influence gravity-induced forces and the final overall geometrical shape of the bridge. Once the appropriate gravity configuration is achieved, the solution can proceed to a transient dynamic analysis with the static configuration (member forces and model geometry) serving as the initial condition state for the dynamic analysis. The total nonlinear solution must adequately handle both the nonlinear-static and the nonlinear-dynamic solution phases.

Implicit Static Solution. In the computational bridge model, the deformation of the structure is defined by the vector of global displacement components $\{D\}$. For a given set of statically applied external loads on the structure $\{P\}$, the structure is in a state of equilibrium if the external loads equilibrate the internal resisting forces of the structure, denoted $\{Q(\{D\})\}$, and the forces generated by any contact across disjoint parts of the structure (such as expansion joints), denoted $\{\Gamma(\{D\})\}$. In a nonlinear system, the internal and contact forces are nonlinear functions of the system displacements.

Defining a residual vector $\{R(\{D\})\}$ as the difference between the various force components in the direction of each degree of freedom of the model,

$$\{R(\{D\})\} = \{\{Q(\{D\})\} - \{P\} - \{\Gamma(\{D\})\}\} \tag{1}$$

then an equilibrium configuration of the structure, denoted $\{D^*\}$, results in a null residual vector, such

as R{D*} = 0. If {D*} is the kth approximation to {D*}, then a Taylor series expansion of the residual vector about $\{D^k\}$ yields,

$$\{R(\{D^*\})\} = \{R(\{D^k\})\} + \left[\frac{\partial\{R(\{D^k\})\}}{\partial D}\right]\{\Delta D\} + o\left\langle\{\Delta D\}^2\right\rangle \quad (2)$$

where,

$$\left[\frac{\partial R}{\partial D}\right] = \begin{bmatrix} \frac{\partial Q_1}{\partial D_1} \cdots \frac{\partial Q_1}{\partial D_n} \\ \cdots \cdots \cdots \\ \frac{\partial Q_n}{\partial D_1} \cdots \frac{\partial Q_n}{\partial D_n} \end{bmatrix} - \begin{bmatrix} \frac{\partial \Gamma_1}{\partial D_1} \cdots \frac{\partial \Gamma_1}{\partial D_n} \\ \cdots \cdots \cdots \\ \frac{\partial \Gamma_n}{\partial D_1} \cdots \frac{\partial \Gamma_n}{\partial D_n} \end{bmatrix} . \quad (3)$$

Neglecting higher order terms in **Eq. 2**, and invoking the fact that {R({D*})} = 0, the incremental displacements are given by,

$$\left[\frac{\partial\{R\left\langle\{D^k\}\right\rangle\}}{\partial D}\right]\{\Delta D\} = -\{R\left\langle\{D^k\}\right\rangle\} . \quad (4)$$

The instantaneous stiffness matrix is defined as the immediate rate of change of the internal resisting forces and contact forces with respect to system displacements, thus,

$$\left[K_I(\{D^k\})\right] = \left[\frac{\partial\{R(\{D^k\})\}}{\partial D}\right] \quad (5)$$

and the individual terms of this matrix are given by **Eq. 3**. The first matrix in **Eq. 3** represents the stiffness contribution from the structural elements in the bridge model; the second represents the effective stiffness contribution from the penalty-based contact elements activated during contact between disjoint parts. In the absence of contact, the contact stiffness matrix vanishes. The incremental relationship given by **Eq. 4** provides the basis for equilibrium iterations which yield incremental displacements for updating the displacement vector until the nodal force residuals and incremental displacements become acceptably small. In the static solution algorithm implemented in this study, the instantaneous stiffness is completely reformed for each equilibrium iteration, leading to a full Newton-Raphson procedure for equilibrium iterations. Equilibrium iterations proceed until the Euclidean norms of the residual and incremental displacement vectors become acceptably small. In the SUSPNDRS program, the implicit solution is used for gravity initialization of the bridge system, for other nonlinear static analyses such as push-over tests for a bridge or bridge components, and as a diagnostic tool when implementing new nonlinear elements.

Explicit Dynamic Solution. The transient bridge solution is based on an explicit integration scheme which readily admits arbitrary multiple support earthquake ground motions. The earthquake ground motions are defined by ground displacement time histories at the bridge base support locations referenced to an identical time frame to preserve phasing information across the bridge structure. The coupled equations of motion for the bridge system, constructed from the assembly of element matrices, are given by,

$$[M]\{\ddot{D}(t)\} + [[C_{fsi}]\{\dot{D}(t)\} + [C_{mech}]\{\dot{D}_r(t)\}] + \{Q(\{D(t)\})\} + \{\Gamma(\{D(t)\})\} = \{P_{Boundary}(\{D_{g_i}(t)\})\} \quad (6)$$

where conceptually, $[C_{fsi}]$ defines the damping due to fluid-structure interaction and $[C_{mech}]$ defines the mechanical damping. The vector {Q({D})} represents the internal resisting forces of the model elements, vector {Γ({D})} represents the nodal forces due to contact of disjoint bridge segments, and $\{P_{Boundary}(\{D_{g_i}(t)\})\}$ contains the support point forces generated by applied ground displacements. In **Eq. 6**, the fluid-structure interaction damping forces are assumed proportional to the absolute velocity $\{\dot{D}_r(t)\}$ of the structure and the mechanical damping forces are assumed proportional to the relative velocity $\{\dot{D}_r(t)\}$ of the structure.

The specific form assumed for the bridge energy dissipation, as characterized by the viscous terms in **Eq. 6**, has significant implications for the numerical implementation of the explicit integration procedure for the equations of motion. An appropriate damping form must be inferred from experimentally identified structural damping values. The results of the modal damping observations from several studies[6-9] are constructed in graphical form in **Fig. 2**. In each plot, the experimentally observed damping values are shown as a function of frequency. The experimental data consistently exhibits an inverse relationship between modal damping and modal frequency, the only major difference between the various bridges being the specific amplitude of the damping values. In addition to the experimental values, a solid line is included for each dataset indicating the frequency dependency of damping which would be obtained with an assumption of mass-proportional spectral damping (that is, [C] = β[M]).

For three of the cases (Golden Gate, Newport, and William Preston), the mass proportional

damping was anchored at the fundamental mode; for the Fatih Sultan Mehmet data, there was a wider scatter and an anchor damping value somewhat lower than the damping of the fundamental mode proved to yield a better fit. For all of the small amplitude vibration data, mass-proportional damping provides a good representation of the observed frequency dependency of damping. While this reveals a general trend in the frequency dependency of the data for these broad-band

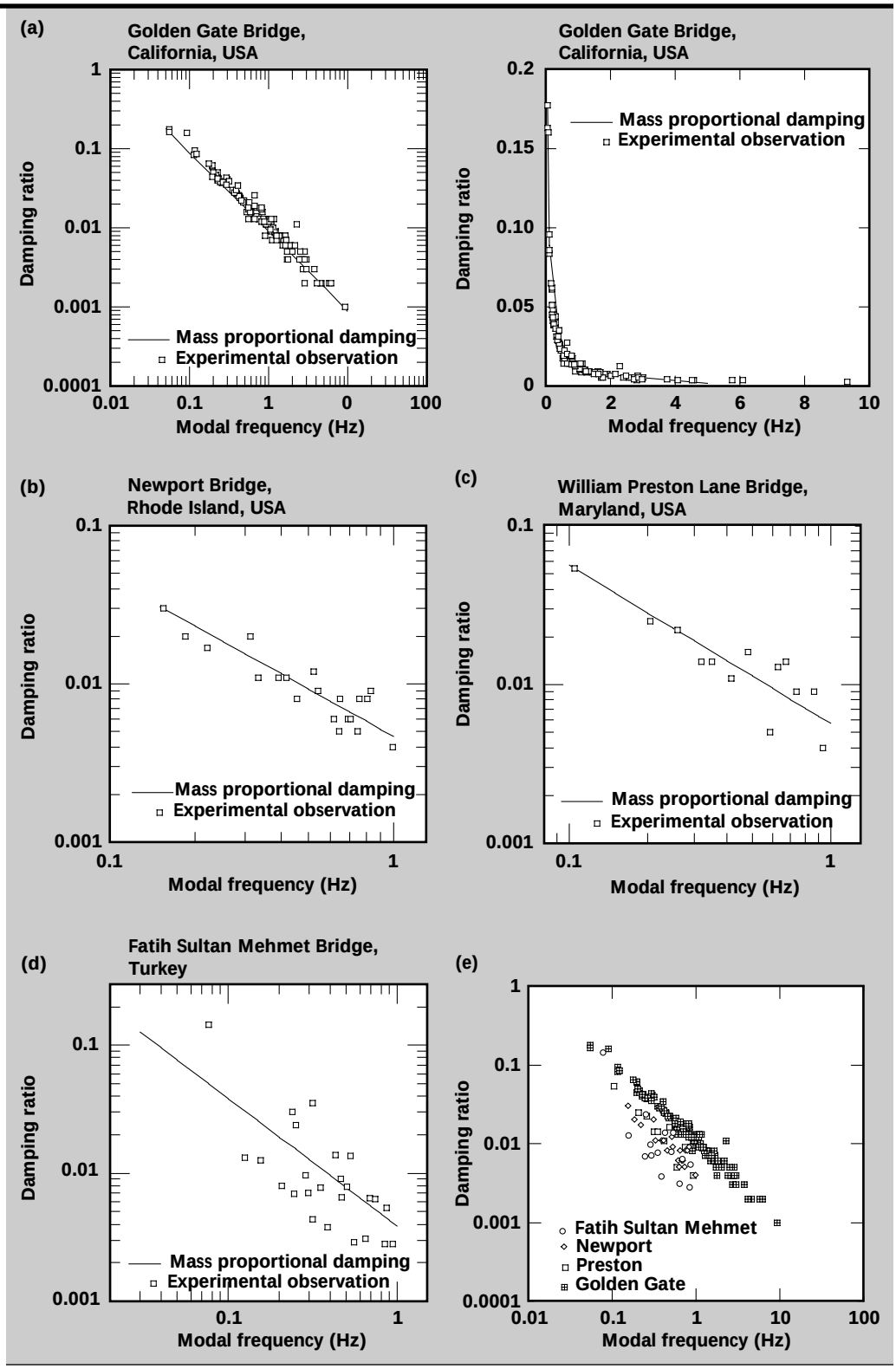

Figure 2. Experimentally observed damping in suspension bridges. (a) Golden Gate Bridge (length = 2738 m); (b) Newport Bridge (length = 907 m); (c) William Preston Lane Memorial Bridge (length = 890 m); (d) Fatih Sultan Mehmet Bridge (length = 1510 m); (e) damping overlay for all four bridges.

structures, it must be kept in mind that the damping values were obtained from small amplitude vibrational data. In practice, it is necessary to augment the mass proportional damping with some stiffness-proportional damping to ensure high-frequency modes are appropriately damped. This issue is particularly important for explicit time integration schemes where the higher frequency modes are resolved in the model.

For mathematical expediency, and lacking more specific information about the mechanical and aerodynamic partitioning of the damping in cable bridges, an assumption of viscous, absolute velocity-dependent damping was assumed in the computational model. Thus, **Eq. 6** simplifies to,

$$[M]\{\ddot{D}(t)\}+[C]\{\dot{D}(t)\}+\{Q(\{D\})\} \\ +\{\Gamma(\{D\})\}=\{P_{Boundary}(\{D_{g_i}(t)\})\} \quad . \tag{7}$$

Traditional central difference formulas provide expressions for the velocity and acceleration,

$$\{\dot{D}\}_n=\frac{1}{2\Delta t}[\{D\}_{n+1}-\{D\}_{n-1}] \tag{8}$$

$$\{\ddot{D}\}_n=\frac{1}{(\Delta t)^2}[\{D\}_{n+1}-2\{D\}_n+\{D\}_{n-1}] \tag{9}$$

where n refers to the nth time step. However, if a stiffness-proportional term is included in the damping matrix,

$$[C] = \alpha[M] + \beta[K] \tag{10}$$

the damping matrix is non-diagonal and the finite-difference expressions in **Eq. 8** and **Eq. 9** will result in a matrix inversion for each time step of the explicit integration scheme. To avoid matrix inversions, and thus preserve the economy of the explicit integration scheme, an approximation to the velocity is used in place of **Eq. 8**,

$$\{\dot{D}\}_n=\frac{1}{\Delta t}[\{D\}_n-\{D\}_{n-1}] \, . \tag{11}$$

This expression will result in some accuracy loss in the integration scheme, which is generally insignificant for these structures due to the short time step of the explicit integration scheme.

Combining **Eq. 7**, **Eq. 9**, and **Eq. 11**, yields the recursion relationship for displacement,

$$\frac{1}{\Delta t^2}[M]\{D\}_{n+1}=\left\{P_{Boundary}\left(D_{g_i}(t)\right)_{n+1}\right\} \\ -\{Q(\{D\}_n)\}-\{\Gamma(\{D\}_n)\}+\frac{1}{\Delta t}\left[\frac{2}{\Delta t}[M]-\alpha[M]-\beta[K]\right]\{D\}_n \\ +\frac{1}{\Delta t}\left[\alpha[M]+\beta[K]-\frac{1}{\Delta t}[M]\right]\{D\}_{n-1} \quad . \tag{12}$$

The application of seismic excitation is most easily introduced in these equations by specification of the displacements at the base support points of the structure. Specified displacements are introduced by assigning identity equations for each specified support displacement in **Eq. 12**, yielding,

$$\frac{1}{\Delta t^2}[M]\{D\}_{n+1}=\Delta t^2[M]^{-1}\{D_g\}_{n+1}-\{Q(\{D\}_n)\} \\ -\{\Gamma(\{D\}_n)\}+\frac{1}{\Delta t}\left[\frac{2}{\Delta t}[M]-\alpha[M]-\beta[K]\right]\{D\}_n \\ +\frac{1}{\Delta t}\left[\alpha[M]+\beta[K]-\frac{1}{\Delta t}[M]\right]\{D\}_{n-1} \tag{13}$$

where vector $\{D_g\}$ contains the earthquake ground motion displacement time histories of the bridge supports, the terms of which are zero except at the structure support locations. For the Bay Bridge evaluation, the structure is founded directly on bedrock and the support displacement time histories were obtained directly from a massively parallel finite-difference model.[16]

The equations expressed in **Eq. 13** provide the explicit recursion relationships for update of the structural model displacements at time step n+1, based on the displacement vectors at previous time steps n and n–1. Because of the velocity approximation which has been invoked, and the fact that the model mass matrix is always a diagonal due to lumped mass assumptions, no matrix inversions are required for the solution of $\{D\}_{n+1}$. This explicit integration is conditionally stable, with the maximum time step permitted being governed by the Courant limit for the discretization of the particular bridge model at hand. The approximation invoked in **Eq. 11** does effect the integration stability time step, which must be accounted for in the selection of the integration time step.[18]

For earthquake ground motions, there are two fundamental differences between the explicit algorithm defined in **Eq. 13** and traditional seismic analyses methods. In the explicit formulation, ground motion is defined in terms of ground displacement time histories rather than acceleration time histories, and the computed displacement quantities are absolute displacements rather than displacements relative to the ground reference frame.

Element Technologies

With careful construction and appropriate validation, it is often possible to develop an accurate reduced-order model of a bridge system which captures the salient features of the dynamics of the system, yet

results in a significant reduction of the global degrees of freedom relative to a classical discretization from a general-purpose finite-element program.

The element technologies developed were aimed at significantly reducing the number of equations in the global bridge model. The Courant time step limit for stability of the explicit integration scheme depends on the transit time of a stress wave through the smallest elements in the bridge model, and is thus a function of the physical dimensions of the elements in the computational model. To maximize the integration time step, an additional objective was to construct element technologies which resulted in physically large element dimensions.

Tower Flexural Fiber Model. A fiber flexural element was developed for characterization of the bridge towers. The element can also be used for other bridge members which may require a flexural bending element characterization. The element incorporates both geometric and material nonlinearities. The framework for tracking geometry changes and initial stress inclusion are common to the bridge deck truss and cable elements described in a subsequent section.

For 3-D bending with finite (large) rotations, rotations are nonvectorial and must be incrementally updated. The flexure element uses three local element coordinate systems to track both the finite displacements and the finite rotations of the beam segments. Two local coordinate systems rotate and translate with the principal axes of the beam element at each end (the x″, y″, z″ and x‴, y‴ and z‴ axes in **Fig. 3**), and the third updated Lagrangian system (x′, y′, z′) extends between the element end nodes and tracks the overall displacement and rotation of the element.

A fundamental assumption of the element is that incremental rotations occurring between equilibrium iterations in the implicit solution procedure or between time steps in the explicit dynamic solution, are small and can be transformed vectorially between the local coordinate systems. This assumption is easily met for practical problems, particularly with explicit integration where the time steps are quite small. The element also assumes the deformational rotations, for example, the rotations between the x′, y′, and z′ axes and the x″, y″, and z″ axes, are small.

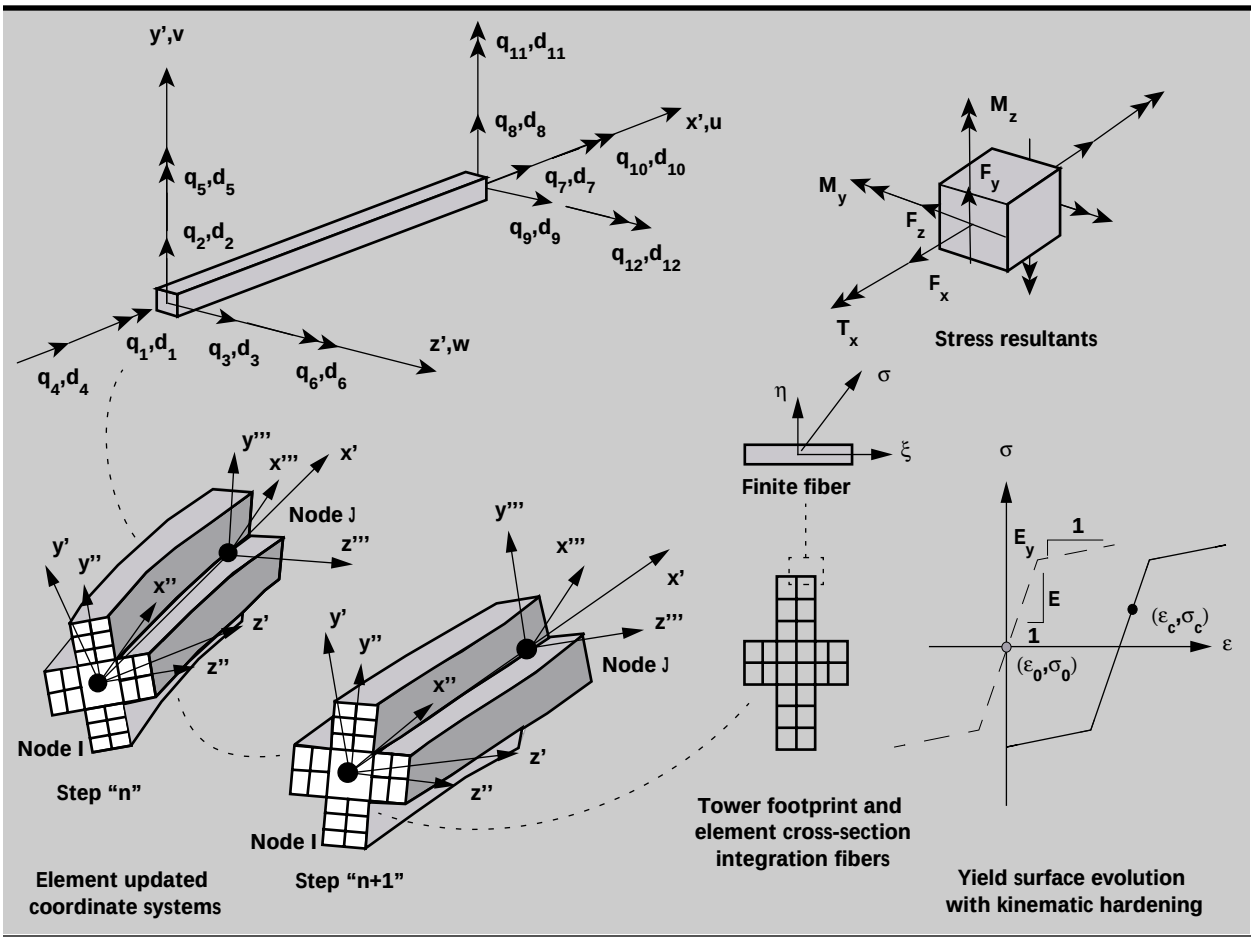

Figure 3. Finite rotation tower fiber flexure element.

Gross rigid-body rotations and translations are removed via the updated coordinate systems. However, to include the initial stress (geometric stiffness) contributions for the flexural element, which is required for initiating the bridge model, it is necessary to include all nonlinear terms in the strain-displacement relationships. To ensure efficiency of the element for linear as well as nonlinear problems, a cubic displacement field approximation is used for the transverse displacements of the flexural element.

Inelasticity in the flexure element is accounted for by division of the cross-section into a number of fiber zones with uniaxial plasticity defining the normal stress-strain relationship for each fiber zone, as indicated in **Fig. 3**. The element stress resultants are determined by integration of the fiber zone stresses over the cross section of the flexural element. The evolution of the yield surface is monitored by tracking the center of the yield region, and a stress update algorithm was implemented to allow accurate integration of the stress-stress constitutive law for large strain increments, including full load reversals.

To ensure path independence of the solution, the implementation of the plasticity model for the implicit Newton-Raphson equilibrium iterations uses a path-independent procedure whereby the element stresses are always updated from the last fully converged equilibrium state. The transformation between element local and global coordinates is accomplished through a vector transformation of element forces and displacements in which the transformation matrix consists of the direction cosines of the current updated element coordinate system. The flexural element matrices in natural coordinates are given by,[17]

$$\{Q_{Flexure}\} = [T]^T \int_{-1}^{1} [B]^T \{F\} J d\xi \tag{14}$$

$$[K_{Flexure}] = [T]^T \times \left(\int_{-1}^{1} [B]^T \left[\frac{\partial F}{\partial \varepsilon}\right] [B] J d\xi + \int_{-1}^{1} \left[\left[\frac{\partial}{\partial d_k} B_G(\{d\})\right]^T \{F\} \right]_{k=1,12} J d\xi \right) [T] \tag{15}$$

where [T] is the transformation matrix of direction cosines for the x′, y′, and z′ coordinate system, [B] is the linear strain-displacement matrix, $[B_G(\{d\})]$ is the displacement-dependent strain-displacement matrix resulting from the nonlinear strain terms, {F} is the element stress resultants, and $\left[\frac{\partial F}{\partial \varepsilon}\right]$ is the element constitutive matrix.

The second term of **Eq. 15** represents the initial stress contribution to the element stiffness, and with appropriate mathematical manipulation,[17] this matrix can be written as a function of the current axial force in the member.

For earthquake simulations, the element stiffness is only necessary for the implicit iterations required for the model gravity initiation. After gravity initiation, the element internal resisting forces are computed from **Eq. 14** for the explicit integration of the equations of motion.

The fiber element representation of the cellular Bay Bridge tower structure was assessed by comparison with detailed shell-element-based models of the Bay Bridge towers. For this comparison, a detailed shell- and beam-element model was constructed for the general purpose finite-element program NIKE3D,[19] and a reduced-order fiber model was constructed for a selected bridge tower, as shown in **Fig. 4**.

The detailed model used shell and beam elements to represent the massive laced members which constitute the tower diagonals and struts. The shell model completely discretized the internal cellular structure of the tower and included the transverse stiffening diaphragms. The fiber model uses one fiber zone for each cell segment in the tower, for example, the element uses 62 zones at the base of the tower, as shown in **Fig. 4**. The reduced-order tower model contains 126 active global degrees of freedom.

The first six natural modeshapes of the tower, as computed with detailed and reduced-order models, are shown in **Fig. 4**. The tower frequencies observed by Carder in 1936 are also shown in **Fig. 4**. Carder performed vibrational measurements of the Bay Bridge towers when the tower construction was completed prior to spinning of the main cables, thus experimental frequencies were obtained for all four of the stand-alone towers of the bridge. Carder identified the first longitudinal and first transverse mode for each tower.

The reduced-order model provides good estimates of the tower dynamics, and in light of the potential errors in the measured response, there is also good agreement between both of the numerical models and the experimental data of Carder. The modeshapes shown in **Fig. 4** exhibit excellent agreement and the modal periods also exhibit good correlation.

Reduced-Order Deck Model. A truss bridge deck system can demand an enormous number of elements with brute force modeling based on shell and beam elements; an effective reduced-order model can dramatically reduce computational effort. The representation of a 3-D discrete lattice truss structure by an equivalent continuum has seen wide use in the development of reduced-order models.[3,20,21] For certain bridge deck configurations, beam-like continua models can adequately characterize the stiffening truss system in the mid-deck region of the structure.

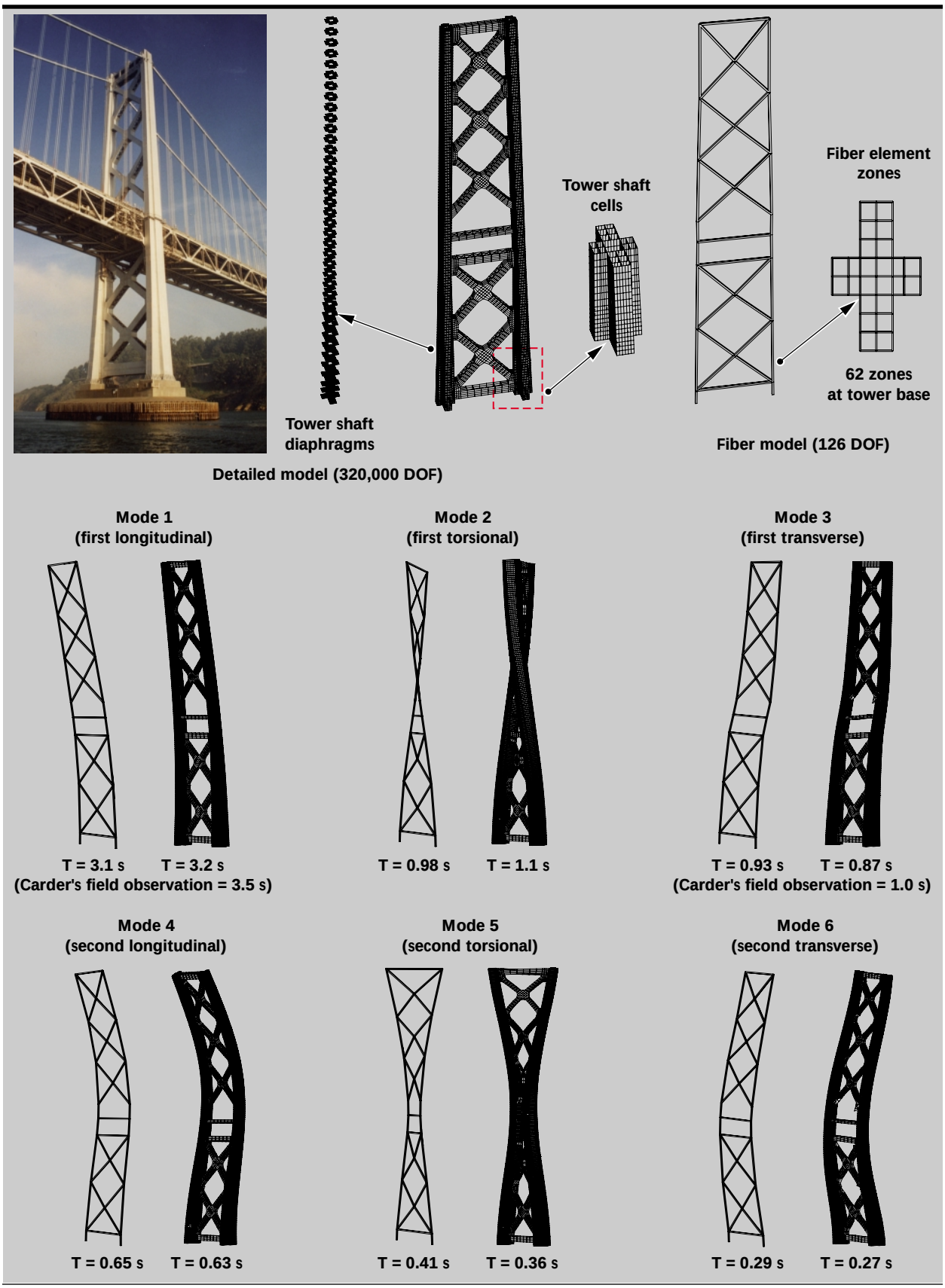

Figure 4. Detailed shell- and beam-element and reduced-order fiber bending element tower models and computed modeshapes (experimental values shown parenthetically).

However, the ability of continuum-based models to capture the effects of complex articulations at the ends of the stiffening trusses is highly suspect, especially where individual member forces can vary significantly depending on the specific connectivity between the truss joints and the towers and abutments. Accurate continuum representations also become problematic when the bridge deck system lacks transverse sway bracing, and the deck is subjected to severe warping deformation. Complex warping deformations defy attempts to represent the deformations with simple beam-like kinematics. Because of the limitations of continuum-based representations, a more detailed discrete model for bridge deck systems was developed. The resulting model represents a compromise between a highly efficient but questionably accurate continuum model of the deck system and a prohibitively expensive, highly detailed, brute force discrete shell- and beam-element model of the deck system.

The configuration and connection details in the two-level deck system of the Bay Bridge made appropriate reduced-order model construction particularly challenging. Lacking any transverse sway bracing between the upper and lower decks (**Fig. 5**), forces generated between the upper and lower part of this structure must be transferred through bending of the stiffening truss elements in an inter-deck sway deformation. In the longitudinal direction, the deck slab-to-stiffening truss connection occurs through weak axis bending of the deck beams (**Fig. 6**), providing an extremely flexible connection between the deck slabs and the stiffening trusses. The deck slab systems, consisting of the concrete slab, deck beams, and stringers, are consequently weakly coupled to the deck stiffening truss in the longitudinal direction of the bridge, and the full membrane stiffnesses of the deck slabs are not activated by deformation of the stiffening trusses in the vertical plane. The complex kinematic characteristics associated with deck cross-section warping of this particular deck system do not readily lend this system to accurate characterization with beam-like continua.

The reduced-order model is based on special discrete elements for the deck system components. The deck model constituents consist of simple truss elements for the stiffening truss members, an orthotropic plane stress element for the deck slab and girder system, and a sway-stiffness element to account for the transverse bending of the lateral frames composed of the deck beams and stiffening truss vertical posts, as shown in **Fig. 5**. The active

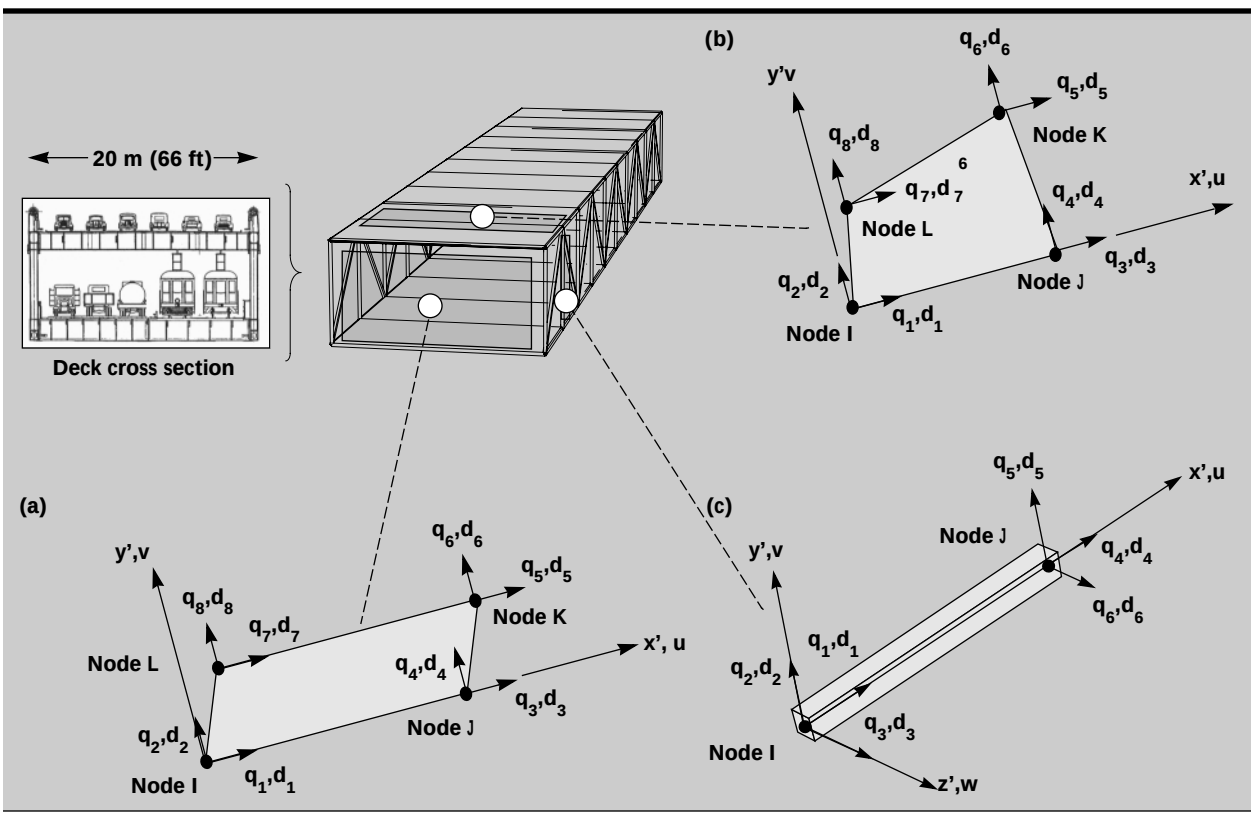

Figure 5. Reduced-order model of the deck system. (a) Sway stiffness element; (b) slab membrane; (c) stiffening truss element. All elements are shown in local element updated Lagrangian coordinate systems.

global degrees of freedom consist of three translations at each joint of the deck system. The sway-stiffness element was implemented to eliminate the need for any rotational degrees of freedom in the deck model. The capability of the deck system model to accommodate geometric nonlinearities associated with arbitrarily large displacements was included in the model to accurately capture the effects of potential large displacements occurring in a long bridge during earthquake ground motions.

Depending on the bridge system and the method by which the model is initialized to achieve the appropriate gravity configuration, gross model geometry changes and large model displacements can also occur during gravity initialization of the bridge model; and inclusion of geometric nonlinearities is necessary for the model initialization process.

The deck truss element shares common features with the flexural fiber tower model element in terms of the methodology for including geometric nonlinearities, displacement tracking, and material inelasticity. Similar to the tower flexure element, the member motions are tracked with a local element updated Lagrangian coordinate system which translates and rotates through space with the element. For the static initialization sequence, it is necessary to include the geometric component of element stiffness for some of the truss elements to create a nonsingular initial global stiffness matrix which allows equilibrium iterations to initiate. To include the initial geometric stiffness, the user must provide as input an initial axial tension in selected members of the deck stiffening truss system. For

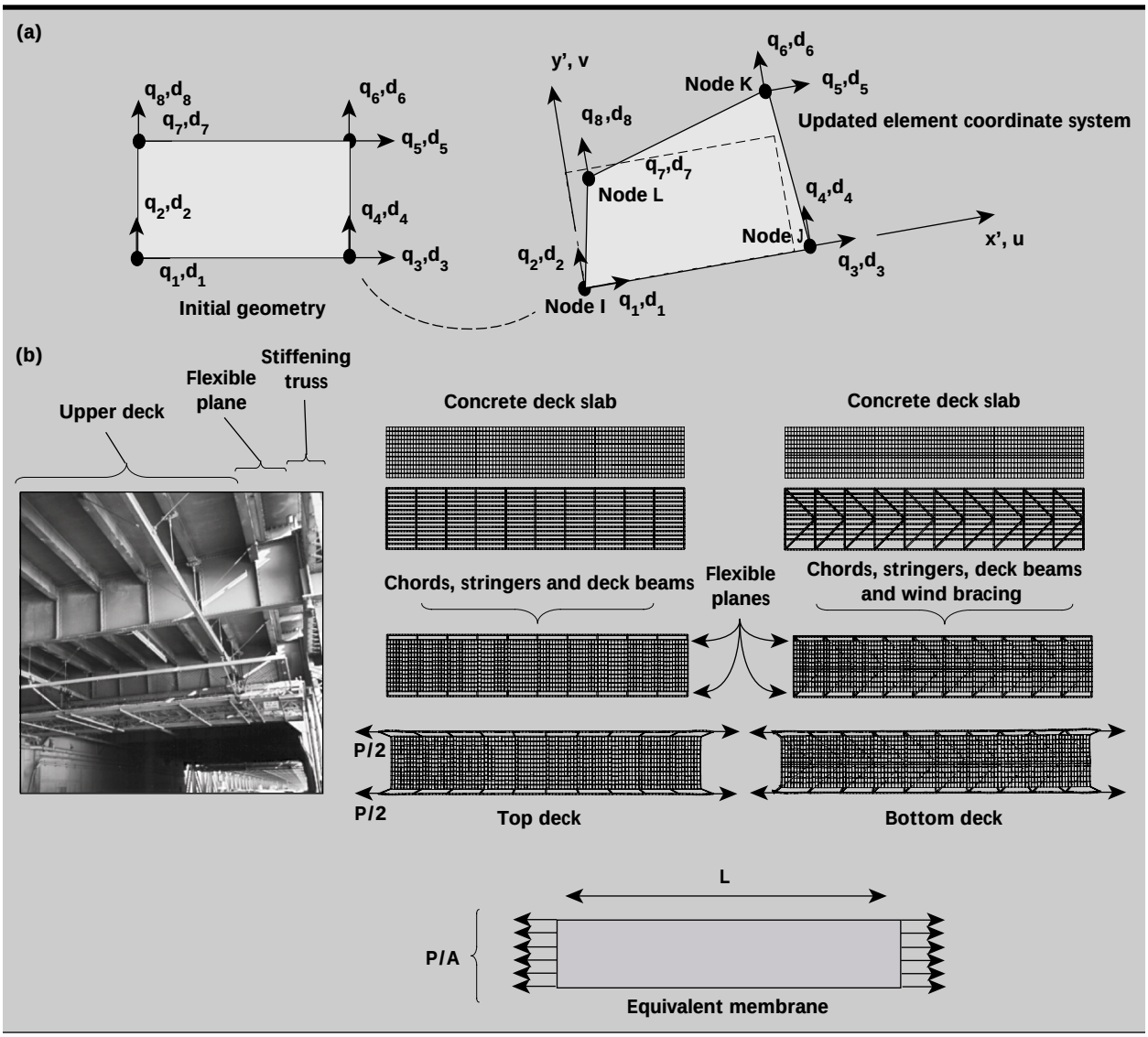

Figure 6. Deck membrane element. (a) Element degrees of freedom and updated Lagrangian coordinate system; (b) upper and lower deck in-plane models and equivalent membrane.

the Bay Bridge configuration, for example, an initial tension must be input for all of the vertical posts of the deck trusses.

For some vintage truss members, such as steel laced members, recent research[22] indicated the inelastic behavior can be controlled by inelastic buckling of the member or buckling of the plate connections at the end of the members, and can be quite complex. For these members, a simple elasto-plastic model is not an accurate representation of the complex inelastic buckling behavior. However, idealized elasto-plastic representation can be appropriate for modern bridge members where elements consist of rolled sections, and connections are based on sound inelastic design methods. The incorporation of complex inelastic buckling of vintage laced members and their connections will be addressed in future SUSPNDRS developments.

The deck membrane element, which represents the deck slab, beams, stringers, and any existing in-plane sway bracing, consists of a four-node, isoparametric, orthotropic plane stress element. The potentially large rigid-body displacements of the element are accounted for with an updated coordinate system which tracks with the element through space, as indicated in **Fig. 6**. The element matrices are based on a classical four node isoparametric formulation.

Selection of appropriate membrane properties was a nontrivial problem in the development of the reduced-order deck model for the Bay Bridge deck system. Because of the flexible connection between the deck system and the stiffening trusses (**Fig. 6**), there is weak longitudinal coupling between the deck slab system and the stiffening truss. This significantly reduces the composite action of the deck slabs and stiffening trusses. The deck membrane element requires elastic constants which will characterize the stress-strain behavior of the deck system.

Because of the complex coupling in the Bay Bridge deck system, the effective membrane properties cannot be easily obtained analytically from consideration of first principles. Because of the complex deformations, the equivalent membrane elastic properties were determined numerically by selective loading of detailed models of deck segments (**Fig. 6**). The detailed deck models shown in **Fig. 6** were constructed to include the weak connection between the deck system and the stiffening truss chords. The effective membrane properties are obtained from the detailed model analysis. For example, the longitudinal membrane effective elastic modulus is given by,

$$E_{Effective} = \frac{\frac{PL}{\Delta_1} - 2(EA_{Chords})}{A_{membrane}} \tag{16}$$

where Δ_1 is the stretch of the deck system for an applied load of P. After determining the appropriate elastic constants, the membrane element contribution to the element internal resisting forces and instantaneous stiffness are given by,[17]

$$\{Q_{Membrane}\} = \left[\int_{-1}^{1} \int_{-1}^{1} [B]^T [E][B] t Det J d\xi d\eta \right] \{d\} \tag{17}$$

$$[K_{Membrane}] = \int_{-1}^{1} \int_{-1}^{1} [B]^T [E][B] t Det J d\xi d\eta \tag{18}$$

where [E] contains the effective material constants obtained from the detailed deck segment models. Classical four-point Gaussian quadrature integration is used for the natural coordinate integration of the matrices.

The sway-stiffness element accounts for the lateral sway deformation between the upper and lower decks which results from flexure of the frame consisting of the deck beams and stiffening truss vertical posts. In the deck model the sway stiffness element is an 8×8 stiffness matrix which relates nodal forces to a measure of the lateral sway deformation of the frame. The sway and truss elements are shown in **Fig. 7**. The sway deformation between the decks is approximated by the summation of angles γ_1 and γ_2,

$$\gamma_{sway} = \gamma_1 + \gamma_2 \tag{19}$$

where,

$$\gamma_1 = \left(\left(\frac{d_4 + d_6}{2} \right) - \left(\frac{d_8 + d_2}{2} \right) \right) / W \tag{20}$$

$$\gamma_2 = \left(\left(\frac{d_5 + d_7}{2} \right) - \left(\frac{d_3 + d_1}{2} \right) \right) / H. \tag{21}$$

The nodal forces associated with sway deformation can be obtained either analytically or numerically by analysis of the cross-section frame with the loading and boundary conditions shown in **Fig. 7**.

For elastic behavior of the frame, the nodal forces associated with sway are given by,

$$\begin{bmatrix} F_H \\ F_V \end{bmatrix} = \begin{bmatrix} k_h \\ k_v \end{bmatrix} \gamma_{sway} \quad . \tag{22}$$

Combining **Eq. 19** through **Eq. 22**, and using overall equilibrium relationships between the nodal forces in **Fig. 7**, the sway element stiffness matrix is given by,

$$\begin{bmatrix} q_1 \\ q_2 \\ q_3 \\ q_4 \\ q_5 \\ q_6 \\ q_7 \\ q_8 \end{bmatrix} = \frac{k_h}{2D} \begin{bmatrix} 1 & \eta & 1 & -\eta & -1 & -\eta & -1 & \eta \\ \eta & \eta^2 & \eta & -\eta^2 & -\eta & -\eta^2 & -\eta & \eta^2 \\ 1 & \eta & 1 & -\eta & -1 & -\eta & -1 & \eta \\ -\eta & -\eta^2 & -\eta & \eta^2 & \eta & \eta^2 & \eta & -\eta^2 \\ -1 & -\eta & -1 & \eta & 1 & \eta & 1 & -\eta \\ -\eta & -\eta^2 & -\eta & \eta^2 & \eta & \eta^2 & \eta & -\eta^2 \\ -1 & -\eta & -1 & \eta & 1 & \eta & 1 & -\eta \\ \eta & \eta^2 & \eta & -\eta^2 & -\eta & -\eta^2 & -\eta & \eta^2 \end{bmatrix} \begin{bmatrix} d_1 \\ d_2 \\ d_3 \\ d_4 \\ d_5 \\ d_6 \\ d_7 \\ d_8 \end{bmatrix} \tag{23}$$

or,

$$\{q\} = [k_s]\{d\} \tag{24}$$

where $\eta = \frac{H}{W}$. **Equation 23** provides the sway element nodal forces in terms of the nodal displacement quantities. The element matrices in global coordinates are provided by the transformation between the element instantaneous updated Lagrangian system and the global system coordinates,

$$\left[Q_{sway}\right] = [T(\{d\})]^T [k_s]\{d\} \tag{25}$$

$$\left[T_{sway}\right] = [T(\{d\})]^T [k_s][T(\{d\})] \quad . \tag{26}$$

To evaluate the adequacy of the deck model, a number of comparisons were made between the reduced-order deck model and a detailed beam- and shell-element model of the Bay Bridge deck system. The first five natural modes of a simply-supported twenty-bay segment of the Bay Bridge deck, as computed from detailed and reduced-order models, are shown in **Fig. 8**. The mode shapes computed with the two models exhibit excellent correlation, and the frequencies are within approximately 10% for all of the first five modes. The simulations of the deck segment verified the reduced-order deck model can adequately capture the deck deformational modes, and the reduced-order model only necessitates a one-element discretization across the width of the deck.

This simple example provides a challenging problem for the reduced-order model because the discrete boundary conditions applied at the base of the deck segment result in modes which exhibit severe racking and warping of the deck (see mode 5, for example). In a deck with distributed support, such as the suspended deck of the bridge, the important deck modes will be of significantly longer wavelengths, and the effect of the discrete boundary

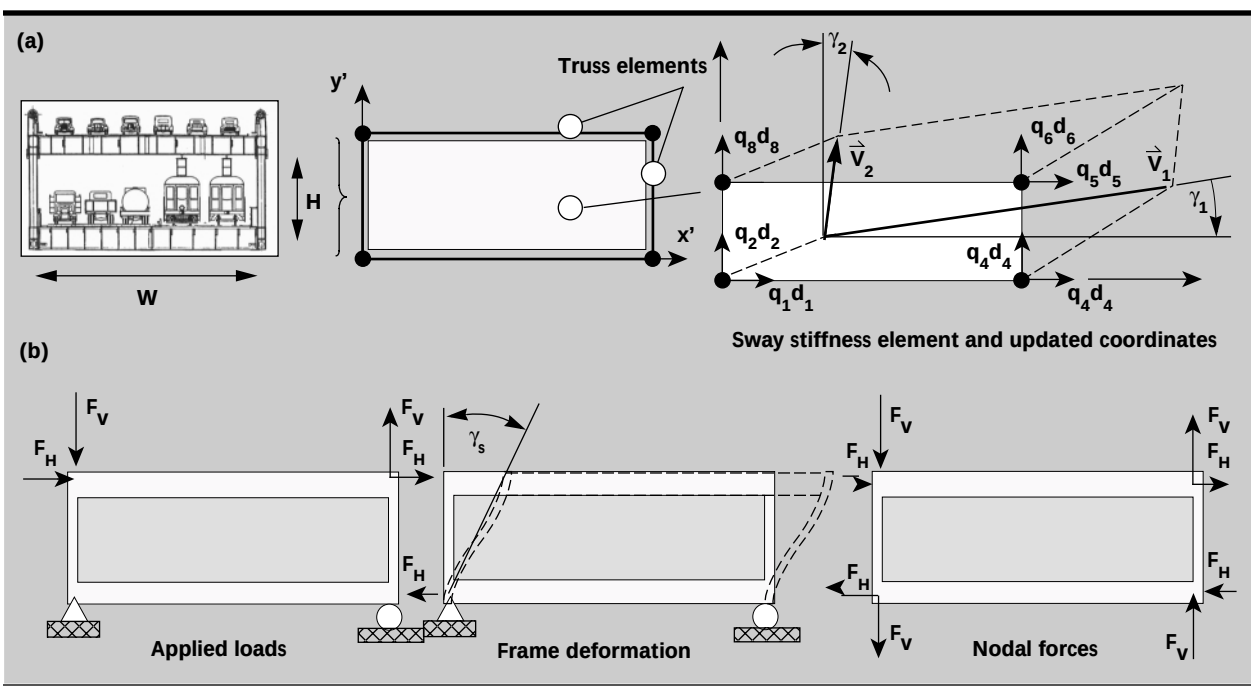

Figure 7. Sway stiffness element providing lateral sway resistance. (a) Sway and truss elements; (b) determination of sway element nodal forces for a sway displacement.

conditions will be more localized rather than propagating throughout the entire deck system, as is the case with the twenty-bay segment.

Bridge Cable Model. The bridge cables are modeled with a simple tension-only two-force member. The cable element is essentially identical to the deck truss element with the exception that the element coding does not permit compression to develop in any of the cable elements. If the cable element attempts to compress, the element stiffness and residual contributions are neglected in the implicit solution and the element forces are neglected in the explicit solution. An initial stress contribution to the element instantaneous stiffness is included to render the initial global tangent stiffness matrix of the bridge system nonsingular during gravity initialization. All of the bridge cable elements require an initial estimate of the cable tension as user input; a gross estimate of cable tension proved to be adequate to initialize the implicit static solution.

The procedure developed to define the initial geometry of the cables is based on constraining the cables by the initial unstretched cable length and allowing the Newton-Raphson equilibrium iterations to determine the natural sag geometry and tension of the cables. With the initial unstretched cable length of each cable serving as the constraint for the cable system model, the initial definition of the cable geometry in the finite-element model can be quite arbitrary and only affects the number of equilibrium iterations required to achieve the natural sag.

A SUSPNDRS program simulation of a simple sagging cable based on this approach is illustrated in **Fig. 9**. The initial geometry in the finite element model is crudely represented with two prescribed initially linear segments of cable elements, the total length of which exactly equals the total unstretched length of the actual cable. A uniform initial tension guess is applied as user input to each cable element for initialization of the initial stress contribution, and once gravity is applied, full Newton-Raphson equilibrium iterations achieve the appropriate cable geometry rapidly within five equilibrium iterations. The individual cable elements displace through large rigid-body displacements, and the overall geometry rapidly progresses to the appropriate hanging cable geometry. The numerical simulation results precisely match experimental data for the hanging cable obtained by Irvine and Sinclair.[23] Application of a point load was also considered after gravity initialization, and the simulation model accurately computed the deformed shape under gravity plus point loading, as shown in **Fig. 9**.

In the case of the Bay Bridge, the design and construction objectives included achieving a stress state in which the chords and diagonals of the stiffening truss were essentially stress free under full gravity dead load. The vertical posts of the truss

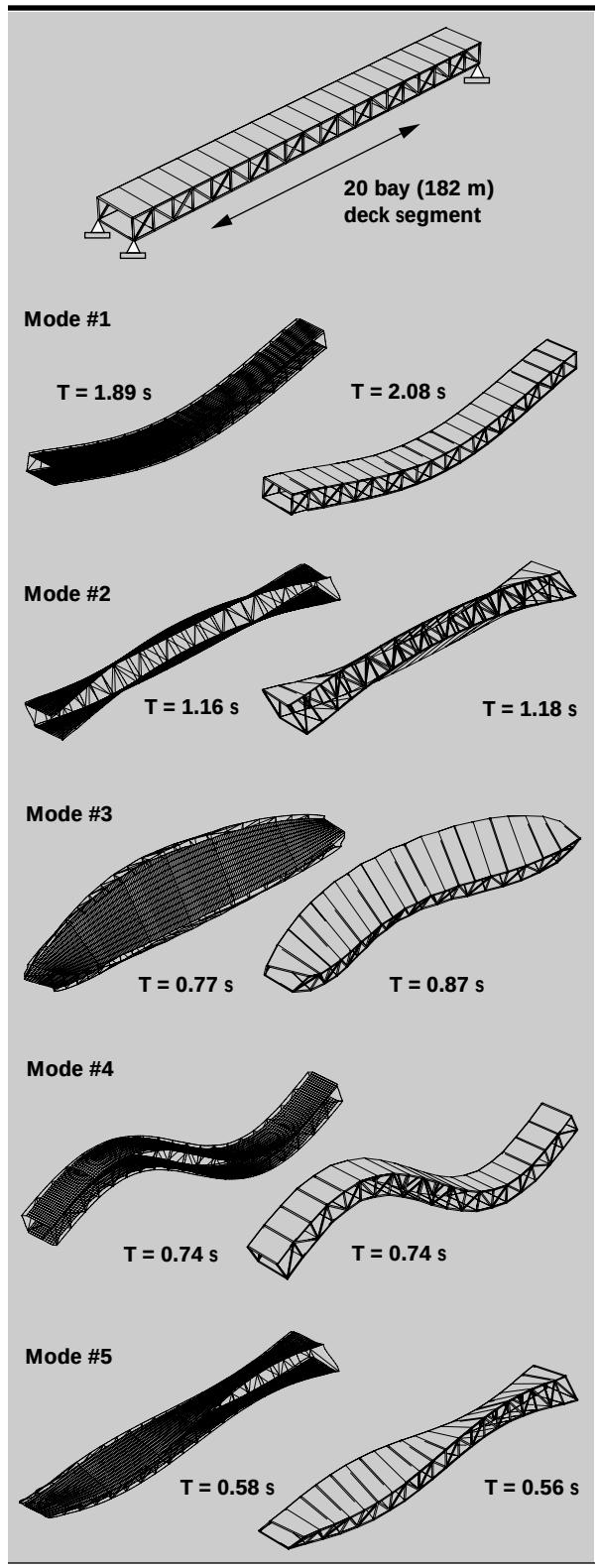

Figure 8. Natural modeshapes of a twenty-bay deck segment from detailed and reduced-order models.

were thus assumed to be the only gravity stressed members in the deck truss. This condition was obtained in field construction by allowing the truss joints to remain loosely tied together with construction pins until the deck was entirely supported from the vertical suspenders, with final riveting of the joints after the entire deck was suspended.

As a result of this construction sequence, the deck stiffening truss did not resist the bridge's gravity load as a composite structure. This design objective is common for many lattice deck suspension bridges. On the Bay Bridge, hydraulic jacking was also used between the main cables and the cable saddles atop the towers prior to application of the deck system to ensure the towers would be straight, vertical, and free of large shear forces at the completion of the construction sequence.

The computational procedure for model initialization must emulate this construction sequence. To initialize the bridge model to the appropriate gravity configuration, an automated procedure was developed. The procedure (**Fig. 10**) first analyzes the main cables and towers under full bridge dead load to determine the final main cable elevations under full gravity load (**Fig. 10b-c**).

In practice, the arbitrary geometry shown in **Fig. 10** is not used. Because of the availability of powerful mesh generators, once the initial unstretched cable lengths are determined, a subroutine mesh generator produces an initial bridge model based on a parabolic approximation of the main cable geometry. For most bridges, the parabolic approximation provides a geometry close to the correct shape. Use of a parabolic geometry is only used for computational expediency; any initial geometry could actually be used, the only computational difference being the computational effort required to achieve the final geometry. The achievement of the final bridge configuration, starting with two entirely different initial geometries, is shown in **Fig. 11**. The only difference between the

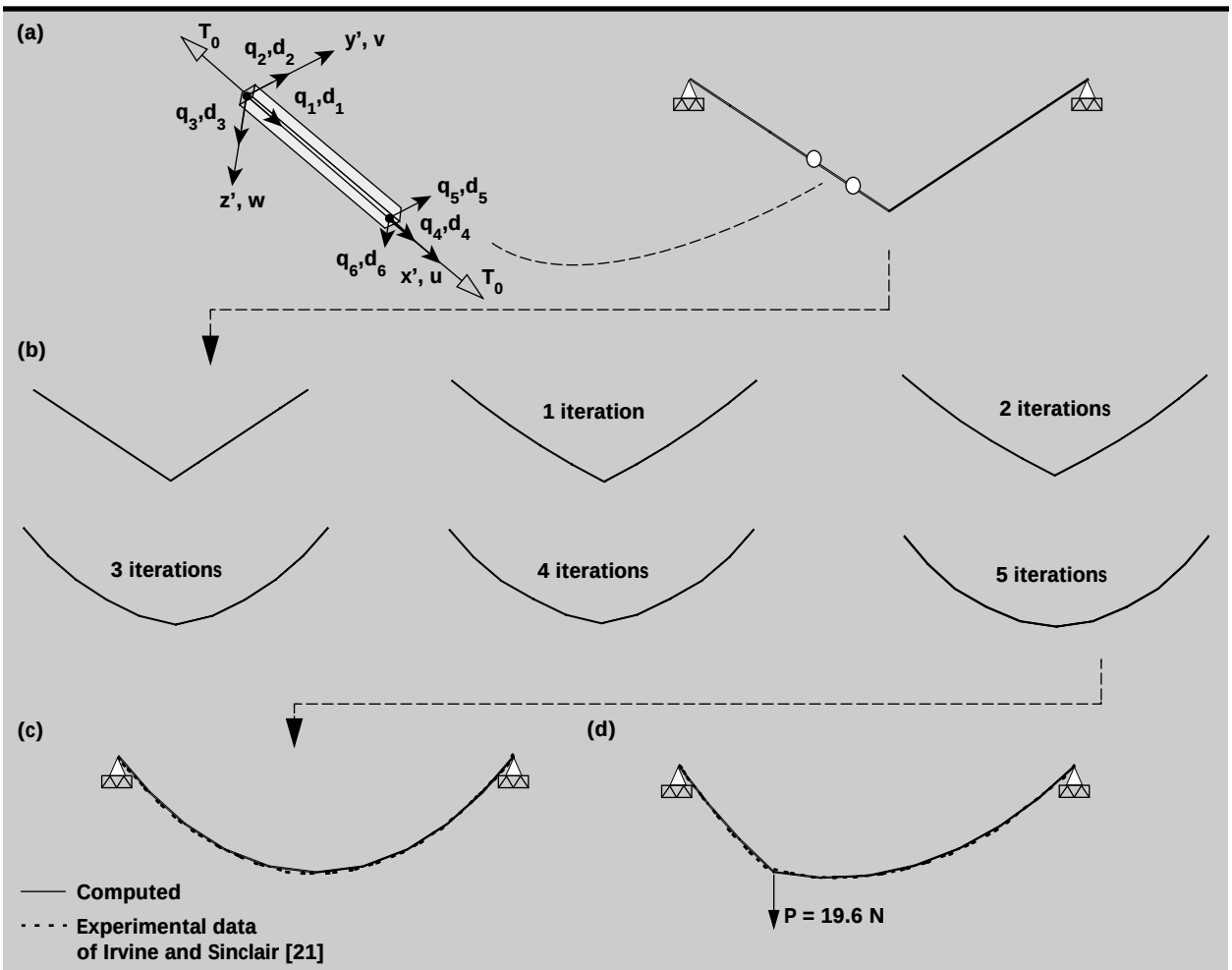

Figure 9. Analysis of a hanging cable. (a) Ten-element cable model with initial tension and constrained length; (b) deformed shape at each equilibrium iteration; (c) computed and observed cable geometry under gravity load; (d) computed and observed cable geometry under gravity and point load.

models is the required number of equilibrium iterations to achieve the final gravity-loaded model.

The parabolic shape is computed such that the main cables have the appropriate length, and the initial locations of the deck nodes are determined by dropping to an elevation corresponding to the unstretched length of the vertical suspenders. The chord and diagonal elements of the truss are inactivated for the gravity initialization, therefore the deck truss will not contribute stiffness to the model during gravity initialization. In addition, the main cables are allowed to slip horizontally relative to the tops of the towers, in order that the towers will be straight and subjected to pure axial load at the end of gravity initialization.

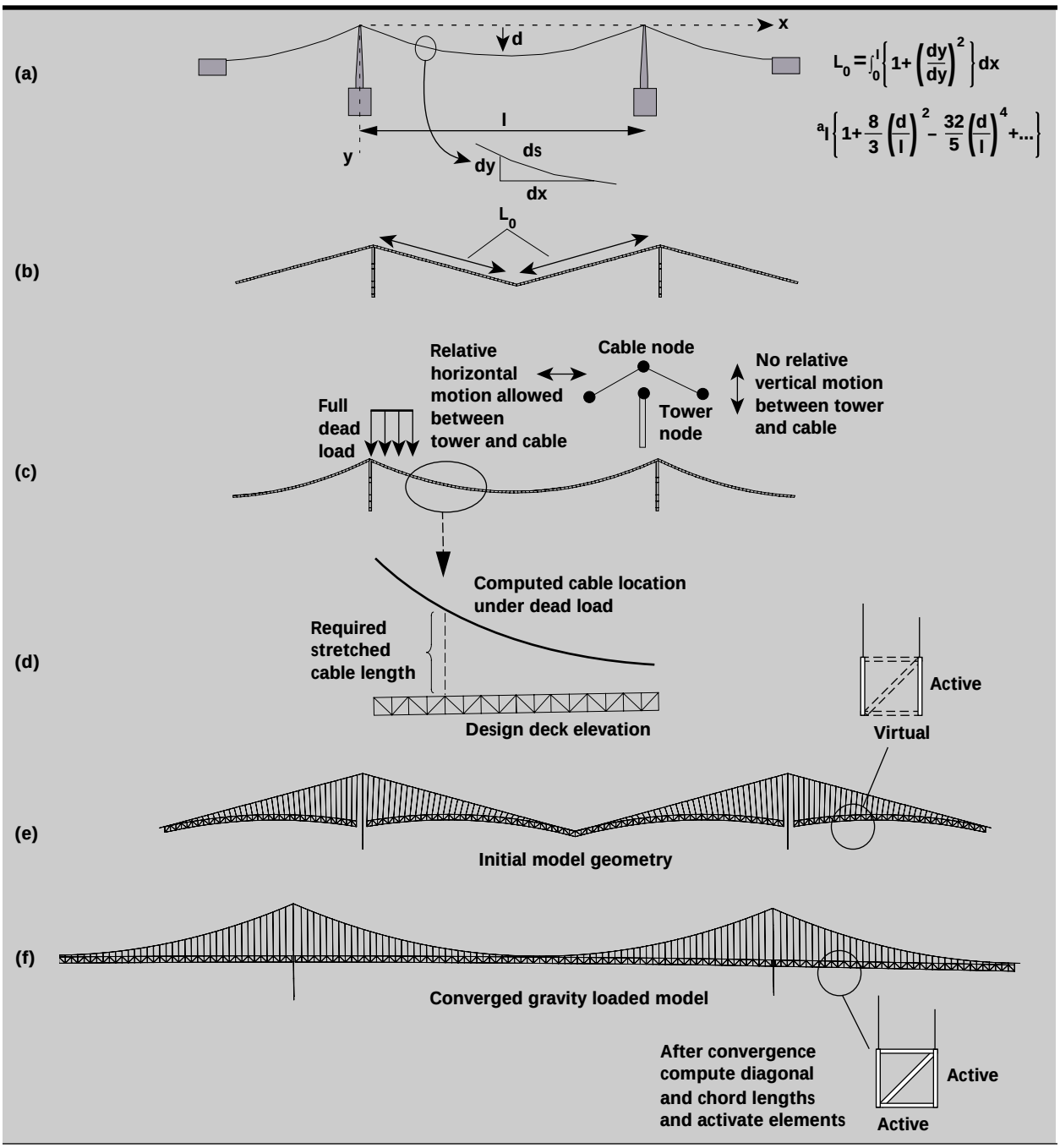

Figure 10. Development of a model with appropriate gravity shape and forces. (a) Estimate unstretched length of main cables based on bridge design and cable field survey data; (b) generate simple model geometry with appropriate unstretched lengths; (c) perform static load analysis of main cables with full dead load of deck system; (d) based on computed main cable geometry and design deck elevations, determine stretched lengths of suspenders under gravity load; (e) generate a model with arbitrary geometry constrained by unstretched cable lengths; (f) perform implicit Newton-Raphson equilibrium iterations for gravity loads until convergence.

Once the gravity load equilibrium iterations are complete, precise new element lengths are computed internally by the SUSPNDRS program and stored for the chord and diagonal members, so that they will be exactly unstressed at the gravity load geometry when the dynamic analysis is initiated. The gravity deformed shape and tension stress fields obtained from the static analysis become the initial condition state for the transient earthquake computation. Once the appropriate gravity load configuration is achieved, the main cables, which were allowed to slip relative to the towers under gravity initialization to keep the towers vertical and absent of longitudinal shear loads, are slaved to the top of the towers to provide cable-to-tower connectivity for the transient response analysis.

The model developed for half of the Bay Bridge geometry, based on this procedure, is shown in **Fig. 11**. This model initialization procedure ensures that the bridge computational model will have the correct as-built bridge geometry.

Deck and Caisson Contact Models. Bridge deck systems typically contain a number of structural discontinuities at interior expansion joints and at abutments to accommodate thermal deformations. These discontinuities can have a pronounced influence on the dynamic response of the bridge system and can result in significant dynamic impact between disjoint bridge segments. Observational measurements of the earthquake response of bridges have indicated the occurrence of large accelerations and inter-segment forces as a result of impact of adjacent bridge segments.[24]

In addition to deck segment impact, during seismic motions, bridge foundations can potentially be subjected to rocking and uplift, with multiple occurrences of impact. For the Bay Bridge, the towers are placed on large caissons which rest on bedrock, the caissons are unanchored to the bedrock, and the potential exists for rocking and uplift of the caissons under strong ground motion. Foundation rocking can significantly affect the superstructure response to earthquake ground motions[21] and should be accounted for in an accurate numerical simulation.

To simulate deck impact and foundation rocking, a simple node-to-node contact element was developed for the SUSPNDRS program which allows two nodes to close within a specified stand-off distance before node-to-node contact occurs. The element also admits tensile forces to develop between the nodes as the nodes separate to allow representation of displacement-limiting structural details which can prohibit large separation of two bridge segments. For the Bay Bridge, the main suspended spans are connected to the towers and central anchorage caisson with a slip joint that couples the deck to the tower or caisson in the transverse direction, but allows limited longitudinal motion once static friction of the joint is overcome, as shown in **Fig. 12**. This construction detail can be compressive when the deck moves into the caisson or tensile when the deck pulls away from the caisson.

In the node-to-node contact element, the nodal force contributions are generated vectorially and translated into the global bridge geometry based on

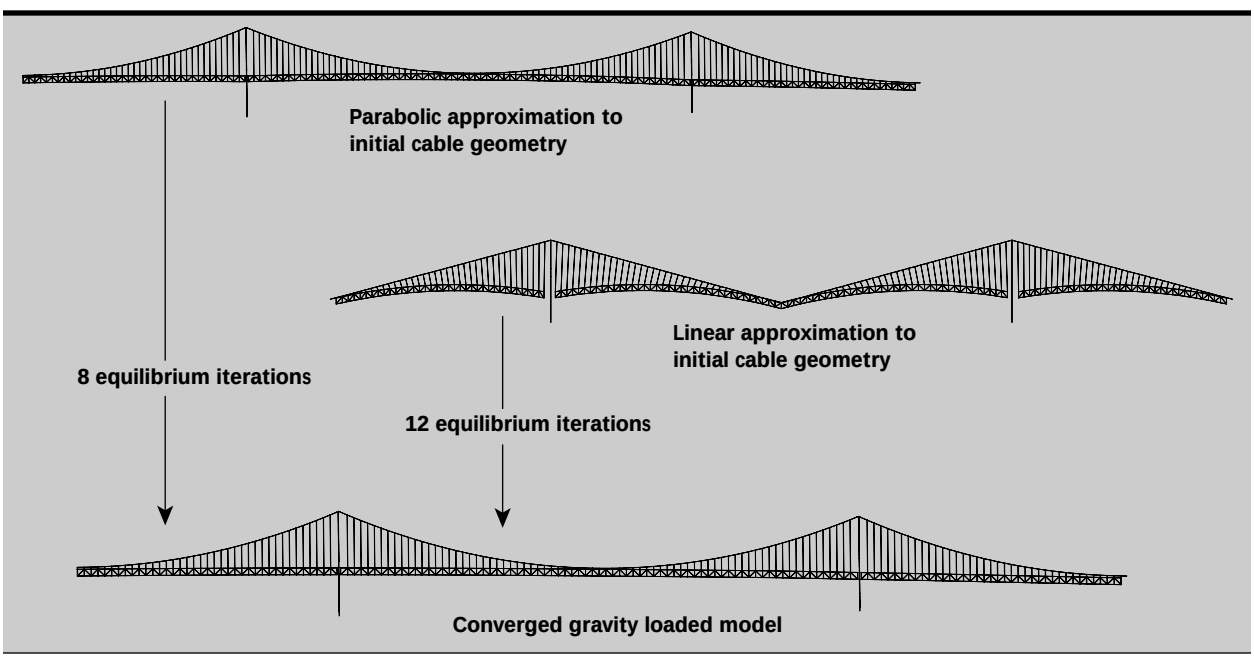

Figure 11. Gravity initialization of the model with different initial model geometries.

the current deformed shape of the bridge system. The contact forces are given by,

$$\begin{bmatrix}\Gamma_1\\ \Gamma_2\end{bmatrix} = K_C\left[\begin{bmatrix}1 & -1\\ -1 & 1\end{bmatrix}\begin{bmatrix}d_1\\ d_2\end{bmatrix} + \begin{bmatrix}-1\\ 1\end{bmatrix}\delta_C\right]\left(\psi_C\left(d_2, d_1, \delta_C\right)\right) + K_T \times \left[\begin{bmatrix}1 & -1\\ -1 & 1\end{bmatrix}\begin{bmatrix}d_1\\ d_2\end{bmatrix} + \begin{bmatrix}1\\ -1\end{bmatrix}\delta_T\right]\left(\psi_T\left(d_2, d_1, \delta_T\right)\right) \quad (27)$$

where,

$\psi_C(d_2, d_1, \delta_C) \equiv 1.0$ when $((d_1 - d_2) - \delta_C) > 0$ and $\psi_C(d_2, d_1, \delta_C) \equiv 0$ when $((d_1 - d_2) - \delta_C) \leq 0$, $\psi_T(d_2, d_1, \delta_T) \equiv 1.0$ when $((d_2 - d_1) - \delta_T) > 0$ and $\psi_T(d_2, d_1, \delta_T) \equiv 0$ when $((d_2 - d_1) - \delta_T) \leq 0$.

The nodal contact forces are assumed directed collinear along the line defined by the two contact nodes (Node I and Node J in **Fig. 12**) and can be transformed to global coordinates based on the direction cosines of the line segment.

With explicit time integration, the numerical values of the effective contact stiffnesses K_T and K_C must be selected in a way which does not result in a reduction of the Courant time step, or alternatively, the Courant time step must be decreased to reflect the added stiffness to the system when contact occurs. Numerical experimentation has indicated that if the contact stiffnesses are selected such that they are of the same order as the stiffness of the structural elements which couple to the point of contact, the interface stiffness will not adversely affect the integration time step. Based on this, upper-bound limiting values for the interface stiffnesses have been used in the SUSPN-DRS contact elements.

Impact between bridge segments or foundation rocking with impact can result in sudden large nonlinearities in the bridge system model. Rigorous representation of impact phenomena presents a computationally difficult problem, and based on the authors' experience with implicit time-integration finite-element programs, the seismic analysis of bridges with multiple impacting segments can be quite difficult with many equilibrium iterations and potential converge failure for each severe impact event. At best, multiple impacts significantly detract from the efficiency of implicit time-integration schemes.

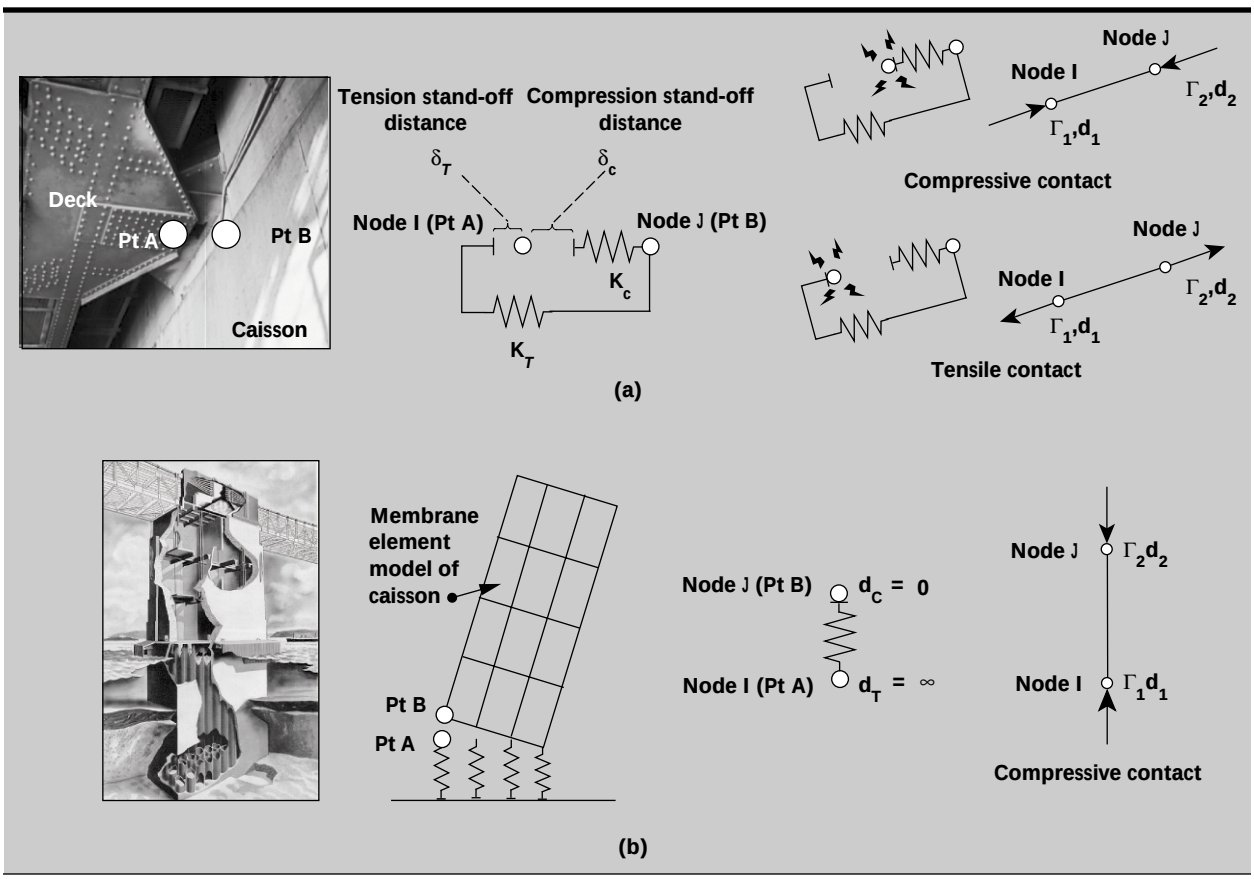

Figure 12. Nodal contact in the bridge model. (a) Contact at the deck-to-tower and deck-to-caisson connection; (b) contact at the base of a caisson.

Explicit time-integration, on the other hand, is particularly adept at accurately tracking impact events, with essentially no detriment to the algorithm efficiency when impact occurs. This was one of the primary motivators for including explicit integration in the SUSPNDRS program.

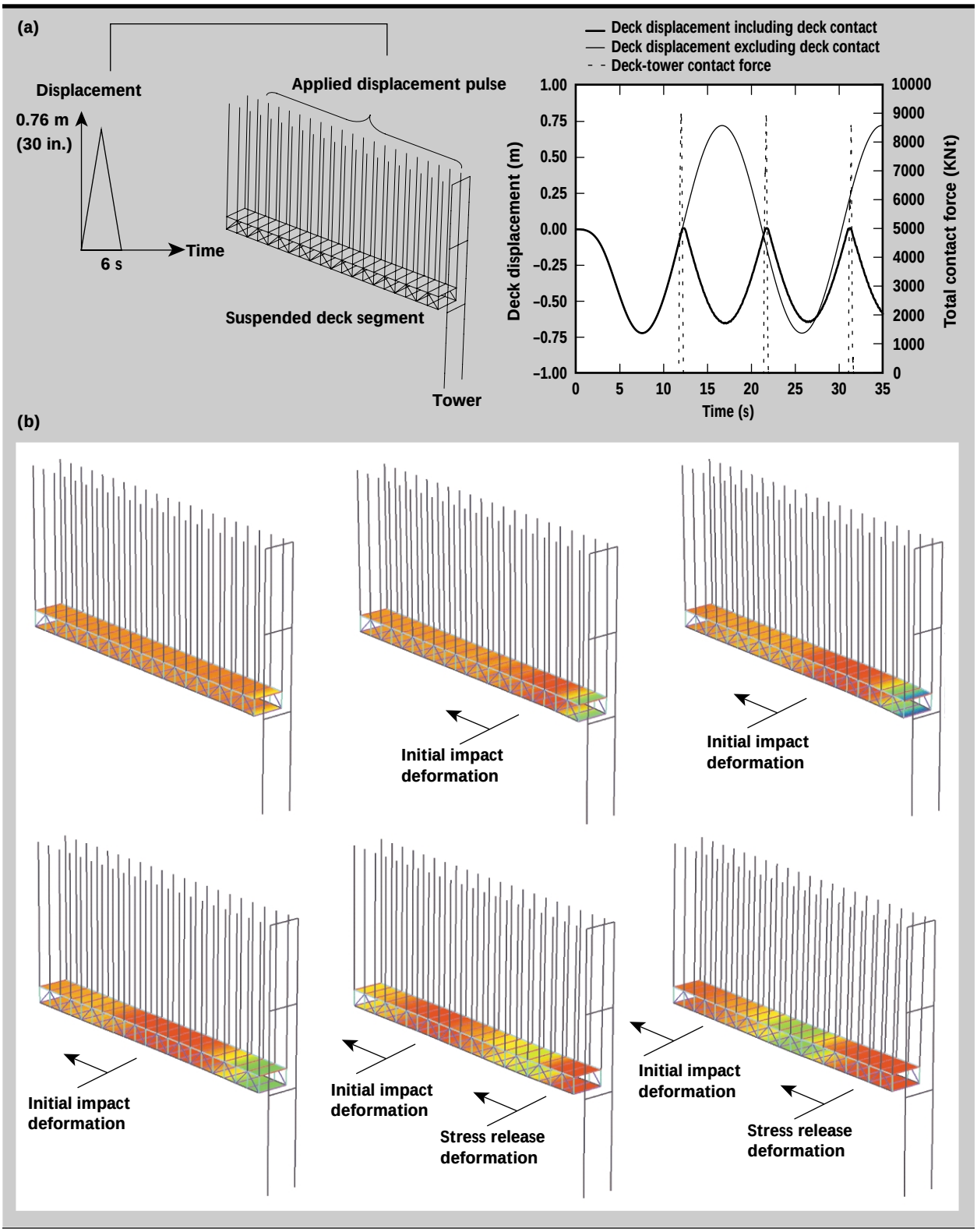

Figure 13. Impact of a deck segment with a tower. (a) Deck displacement and contact forces; (b) impact and relief stress wave propagating in the deck.

An example of computed deck-tower impact with the SUSPNDRS program is shown in **Fig. 13**. A twenty-segment length of bridge deck is given an initial applied displacement pulse by moving the top of the suspension cables with a prescribed 0.75-m displacement over 6 s. This support motion imparts an initial swinging motion into the deck segment. The deck segment is moved away from the tower, and as the segment swings back freely toward the tower, impact occurs between the deck segment and the tower. A stand-off distance is included in the contact element which represents the physical width of the tower at the location of the bridge deck, so the model will initiate impact at the correct physical location in space.

When the deck segment impacts the tower, large compressive forces are developed in the deck and stiffening truss elements, and a compressive wave propagates down the deck system. During the impact, the relatively flexible deck is in contact with the tower for a finite length of time, generating large contact forces, and when the deck swings back away from the tower, a propagating release wave is generated as the stresses in the deck slab and stiffening truss system are suddenly relieved. The simulation shown in **Fig. 13** was carried out through three successive impacts as the deck swung back and forth. The significance of the impact phenomenon on the deck dynamics can be seen by comparing the deck displacements for the cases in which impact is included and neglected, respectively (**Fig. 13a**). The impacts significantly change the displacements of the deck segment as the flexible deck system essentially bounces off of the stiff tower three times.

The simulation was performed for an undamped system, and the explicit integration algorithm accurately tracked the impacts and the impact-generated waves. Computer animations of the impact sequences indicated that the waves generated with each impact continued to travel back and forth across the deck without dissipation for as long as the simulation was continued.

The explicit time integration scheme implemented in the SUSPNDRS program has no difficulties tracking the sequence of impacts and modeling the wave propagation up and down the deck segment.

Global Model Dynamics and Transient Earthquake Response

Once the bridge model geometry is appropriately initialized under gravity loading, eigenvalue analyses can be performed to determine the natural mode-shapes and the transient response to earthquake ground motion can be computed. For one span of the San Francisco-Oakland Bay Bridge, selected computed natural modes are shown in **Fig. 14a**. The fundamental mode of the model consists of transverse motion of the main span and this concurs with the fundamental mode observation made by Carder in 1936. The computed modal period also agrees well with the observation of Carder.

The range of period values from the computed model reflect different assumptions of connectivity between the deck and tower with the lower period corresponding to an assumption of a locked expansion connection at the deck-tower interface and the higher value corresponding to a completely free connection.

A major objective of the research was to develop understanding of the response of long-span bridges to near-field ground motions. The companion paper discusses in some detail the relationship between the near-field ground motions and transient bridge response.[16]

As an example of the potential effects of near field motions, the response of the bridge segment to 80 s of earthquake ground motion is shown in **Fig. 14b**. The ground motions indicated included a large long-period displacement pulse and permanent ground displacement which result at the Bay Bridge site due to a M = 7 Hayward fault earthquake (see **Fig. 1**). The exaggerated bridge displacements indicate that when the large displacement pulse occurs, the flexible deck cannot react as fast as the stiff towers and lags behind, as the towers begin to return in the opposite direction, the deck has finally begun to respond and essentially flings through the towers in the opposite direction. This type of motion can impart tremendous energy into the bridge system right at the initiation of the earthquake motions, and is not unlike the near field phenomenon described for buildings by Hall *et al.*[25,26]

Conclusions

A new nonlinear computational tool has been developed for numerically simulating the earthquake response of suspension bridges. The resulting finite-element model incorporates geometric nonlinearities due to large displacements, potential contact and impact between disjoint bridge segments, rocking foundation uplift, and material nonlinearities due to steel plasticity.

The system solution algorithms use a combination implicit-explicit solution scheme to achieve appropriate nonlinear static initialization and nonlinear transient analysis of the bridge system. The model relies on reduced-order characterizations

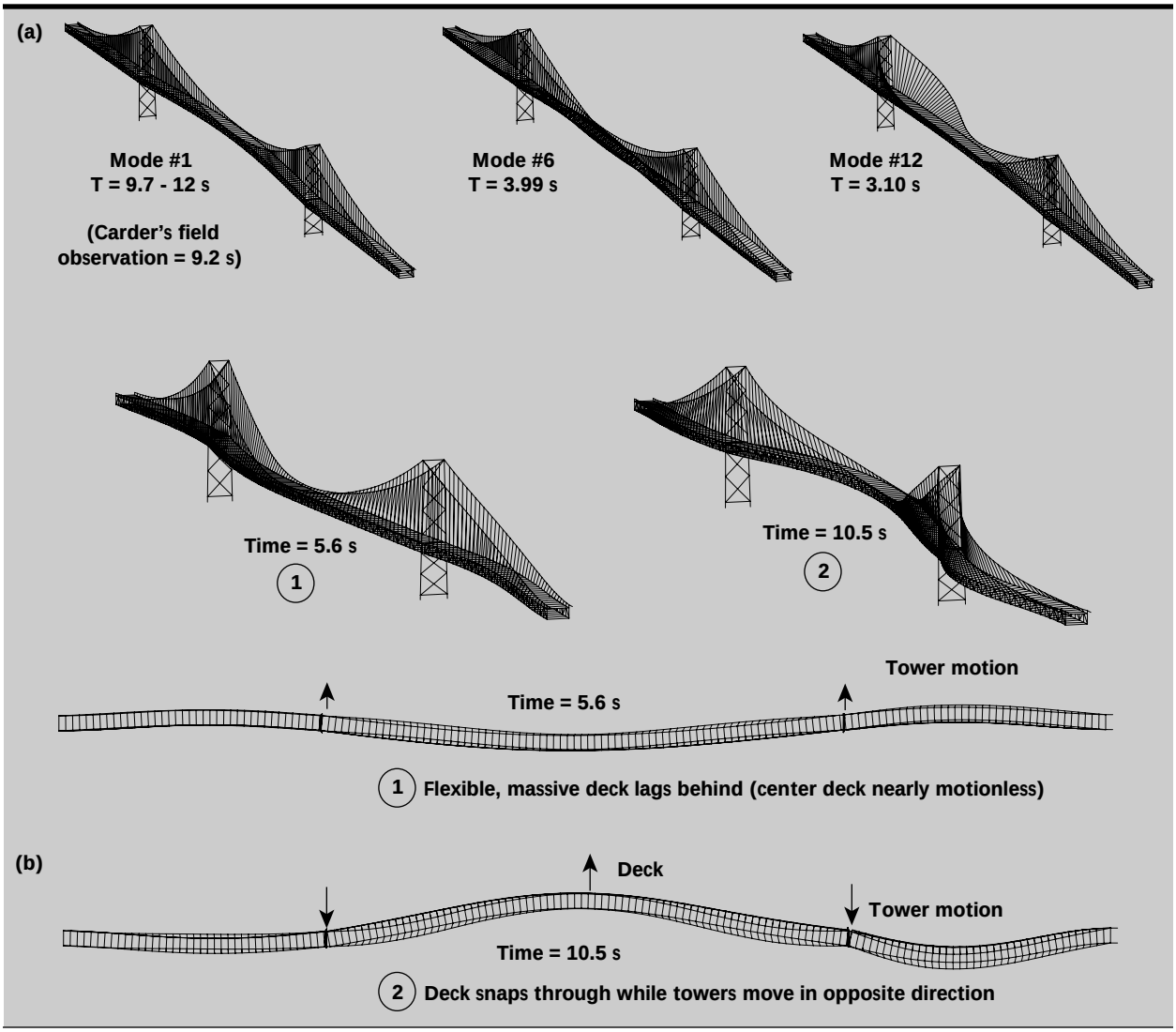

Figure 14. Global response of a Bay Bridge span. (a) Computed modeshapes (experimental values shown parenthetically); (b) transient response due to near-field motions.

of the bridge components to minimize the number of equations in the bridge system model and to ensure element physical dimensions will be large, thus maximizing the time step for the conditionally stable explicit solution algorithm.

The robust nature of the explicit time-integration scheme provides a numerical solution framework ideally suited to the transient analysis of a system with severe nonlinearities and to ultimate collapse simulations. This framework will readily accommodate and exploit new characterizations of complex individual member nonlinearities (such as laced members and structural joint nonlinearities and joint failures) as the information becomes available from experimental research.

Acknowledgments

The authors would like to thank Drs. C. Max and P. Kasameyer of Lawrence Livermore National Laboratory for their continued support.

This work was funded by the University of California Research & Development fund.

References

1. A. M. Abdel-Ghaffar (1978), "Free lateral vibrations of suspension bridges," *J. of the Structural Division*, ASCE, Vol. **104**, No. 3, pp. 503–525.

2. A. M. Abdel-Ghaffar (1979), "Free torsional vibrations of suspension bridges," *J. of the Structural Division*, ASCE, Vol. **105**, No. 4, pp. 767–788.

3. A. M. Abdel-Ghaffar (1982), "Suspension bridge vibration: continuum formulation," *J. of Engineering Mechanics*, ASCE, Vol. **108**, No. 6, pp. 1215–1231.

4. A. A. Dumanoglu, J. M. W. Brownjohn, and R. T. Severn (1992), "Seismic analysis of the Fatih Sultan Mehmet (second Bosporus) Suspension Bridge," *Earthquake Engineering and Structural Dynamics*, Vol. **21**, pp. 881–906.

5. D. S. Carder (1937), "Observed vibrations of bridges," *Bulletin of the Seismological Society of America*, Vol. **29**, No. 4, pp. 267–303.

6. A. M. Abdel-Ghaffar and R. H. Scanlan (1985), "Ambient vibration studies of Golden Gate Bridge: suspended structure," *J. of Engineering Mechanics*, ASCE, Vol. **111**, No. 4, pp. 463–482.

7. A. M. Abdel-Ghaffar and R. H. Scanlan (1985), "Ambient vibration studies of Golden Gate Bridge: suspended structure," *J. of Engineering Mechanics*, ASCE, Vol. **111**, No. 4, pp. 483–499.

8. J. M. W. Brownjohn, A. A. Dumanoglu, and R. T. Severn (1992), "Ambient vibration survey of the Fatih Sultan Mehmet (second Bosporus) Suspension Bridge," *Earthquake Engineering and Structural Dynamics*, Vol. **21**, pp. 907–924.

9. V. R. McLamore, G. C. Hart, and I. R. Stubbs (1971), "Ambient vibration of two suspension bridges," *J. of the Structural Division*, ASCE, Vol. **97**, No. 10, pp. 2567–2582.

10. A. M. Abdel-Ghaffar and L. I. Rubin (1983), "Nonlinear free vibrations of suspension bridges: theory," *J. of Engineering Mechanics*, ASCE, Vol. **109**, No. 1, pp. 313–329.

11. A. M. Abdel-Ghaffar and L. I. Rubin (1983), "Nonlinear free vibrations of suspension bridge: application," *J. of Engineering Mechanics*, ASCE, Vol. **109**, No. 1, pp. 330–345.

12. A. S. Nazmy and A. M. Abdel-Ghaffar (1990), "Nonlinear earthquake response of long-span cable-stayed bridges: theory," *Earthquake Engineering and Structural Dynamics*, Vol. **19**, pp. 45–62.

13 A. S. Nazmy and A. M. Abdel-Ghaffar (1990), "Nonlinear earthquake response of long-span cable-stayed bridges: application," *Earthquake Engineering and Structural Dynamics*, Vol. **19**, pp. 63–76.

14. T. J. Ingham, S. Rodriguez, and M. Nader (1997), "Nonlinear analysis of the Vincent Thomas Bridge for seismic retrofit," *Computers and Structures*, Vol. **64**, No. 5/6, pp. 1221–1238.

15. S. C. Larsen and C. A. Schultz (1995), "ELAS3D: 2D/3D elastic finite difference wave propagation code," Lawrence Livermore National Laboratory, Livermore, California (UCRL-MA-121729).

16. D. B. McCallen, and A. Astaneh-Asl (1999), "A reduced order model for nonlinear suspension bridge analysis," *Computers and Structures*, (in review).

17. D. B. McCallen and A. Astaneh-Asl (1997), "SUSPNDRS: a numerical simulation tool for the nonlinear transient analysis of cable supported bridge structures, part I: theoretical development," Lawrence Livermore National Laboratory, Livermore, California (UCRL-ID-127626).

18. R. D. Cook, D. S. Malkus, and M. E. Plesha (1989), "Concepts and applications of finite elements," John Wiley & Sons.

19. B. N. Maker (1995), "NIKE3D - a nonlinear, implicit three-dimensional finite element code for solid and structural mechanics," Lawrence Livermore National Laboratory, Livermore, California (UCRL-MA-105268 Rev. 1).

20. D. B. McCallen and K. M. Romstad (1990), "A continuum model for lattice structures with geometric and material nonlinearities," *Computers and Structures*, Vol. **37**, No. 5, pp. 795–822.

21. D. B. McCallen and K. M. Romstad (1994), "Nonlinear model for building-soil systems," *J. of Engineering Mechanics*, ASCE, Vol. **120**, No. 5, pp. 1129–1152.

22. A. Astaneh-Asl, S. W. Cho, C. M. Bowen, and M. Blondet (1993), "Post-buckling ductility of critical members of the Golden Gate Bridge," University of California at Berkeley, Report UCB/CE-Steel-93/01.

23. H. M. Irvine and G. B. Sinclair (1976), "The suspended elastic cable under the action of concentrated vertical loads," *Int. J. of Solids and Structures*, Vol. **12**, pp. 309–317.

24. P. K. Malhotra, M. J. Huang, and A. F. Shakal, "Seismic interaction at separation joints of an instrumented concrete bridge," *Earthquake Engineering and Structural Dynamics*, Vol. **24**, pp. 1055–1067.

25. J. F. Hall, T. H. Heaton, M. W. Halling and D. J. Wald (1995), "Near-source ground motion and its effects on flexible buildings," *EERI Earthquake Spectra*, Vol. **11**.

26. T. H. Heaton, J. F. Hall, D. J. Wald, and M. W. Halling (1995), "Response of high-rise and base-isolated buildings to a hypothetical M = 7.0 blind thrust earthquake," *Science*, Vol. **267**.

Seismic Studies of the San Francisco-Oakland Bay Bridge

David B. McCallen
Center for Complex Distributed Systems

Shawn C. Larsen
Computer Systems and Applications
Computation Directorate

Abolhassan Astaneh-Asl
Department of Civil and Environmental Engineering
University of California at Berkeley
Berkeley, California

We have developed new methodologies and computational tools for simulating earthquake ground motions and the seismic response of cable-supported bridges. The simulation tools are described and an example application for an important long-span suspension bridge is demonstrated. The application portion of the study has particular focus on the potential damaging effects of long period displacement pulses and permanent ground displacements which can occur when a bridge is located in the near-field of a major earthquake fault.

Introduction

Realistic and accurate simulation of the seismic response of long-span bridges presents a significant technical challenge. The generation of broad-band, spatially varying ground motion is a difficult seismological and geotechnical problem, particularly for bridges located near a causative fault where long-period near-field effects may dominate the ground motion hazard for flexible structures. Accurate simulation of the transient dynamic response of large bridges also presents the structural engineer with a significant challenge. Nonlinear response simulations are computationally intensive for long-span bridges due to the size of the structural systems. If significant nonlinearities are prevalent in the structural system, such as geometric nonlinearities associated with large displacements, material nonlinearities due to members yielding or buckling or strong nonlinearities due to impact at expansion connections or rocking foundations, the computational requirements for general purpose finite-element codes may be prohibitive.

A multidisciplinary research and development project conducted by the University of California at Berkeley and the Lawrence Livermore National Laboratory is investigating both earthquake ground motion and structural response issues for long-span bridges. The research is developing a new massively parallel linear finite-difference computer program for modeling earthquake wave propagation in bedrock on a regional basis.[1] A special purpose finite-element program has also been developed for simulating the nonlinear response of cable-supported bridges.[2] This program exploits the special characteristics of cable-supported bridges to arrive at an efficient and economical simulation model for nonlinear time history analyses.

These tools are being applied in a case study to an important bridge on the West Coast of the US. The San Francisco-Oakland Bay Bridge is located in California, crossing the San Francisco Bay and connecting the cities of San Francisco and Oakland (**Fig. 1**). The bridge was completed and opened to traffic in 1936. Currently, the bridge carries an average of more than 280,000 vehicles per day and is one of the busiest major bridges in the US. The bridge consists of two steel suspension bridges in tandem on the western crossing of the bridge, and a series of cantilever and simply-supported truss spans on the eastern crossing. The bridge has two decks, each deck with five car lanes. During the 1989 Loma

Prieta earthquake, a 15-m-long segment of the eastern crossing bridge deck collapsed, causing closure of the bridge for one month. Since the Loma Prieta earthquake, this bridge system has been the subject of a number of research and design studies supported by the California Department of Transportation. This bridge was selected for the current study because the bridge and surrounding seismic setting embody all of the important issues related to long-span bridge response. The bridge is also a key transportation link for the San Francisco Bay Area and additional insight into the seismic response adds information to the knowledge base for this critical structure.

Progress

Ground Motion Modeling

Ground motion synthetics for long-span bridges must include waveform information across a frequency range which encompasses the characteristic frequencies of the structure. In long-span cable bridge structures, this can represent a very broad frequency range since the long wavelength modes of the deck system can exhibit very low frequencies (0.1 to 0.05 Hz) relative to the vibrational frequencies of the bridge towers (5 to 8 Hz). Historically, very long period motions have not been accounted for in seismic hazard characterizations because of a lack of understanding of ground motion phenomenology and the unknown existence of long-period ground motion pulses. In the last few years, with additional insight gained by a handful of near-field ground motion measurements, the importance of long-period motions have become clear. Analytical and numerical studies of wave radiation patterns have confirmed the potential for large, long-period ground displacement pulses and significant permanent ground displacements in the near field. Ground motion observations obtained from the 1992 Landers, California earthquake in particular have provided insight into these important issues, with observations of large, long-period displacement pulses near the fault.[3] However, the paucity of near-field strong motion measurements leaves significant uncertainty regarding the precise waveforms of near-field motions. Seismologists must rely on analytical and numerical methods to provide engineers with estimates of the near-field wave forms.

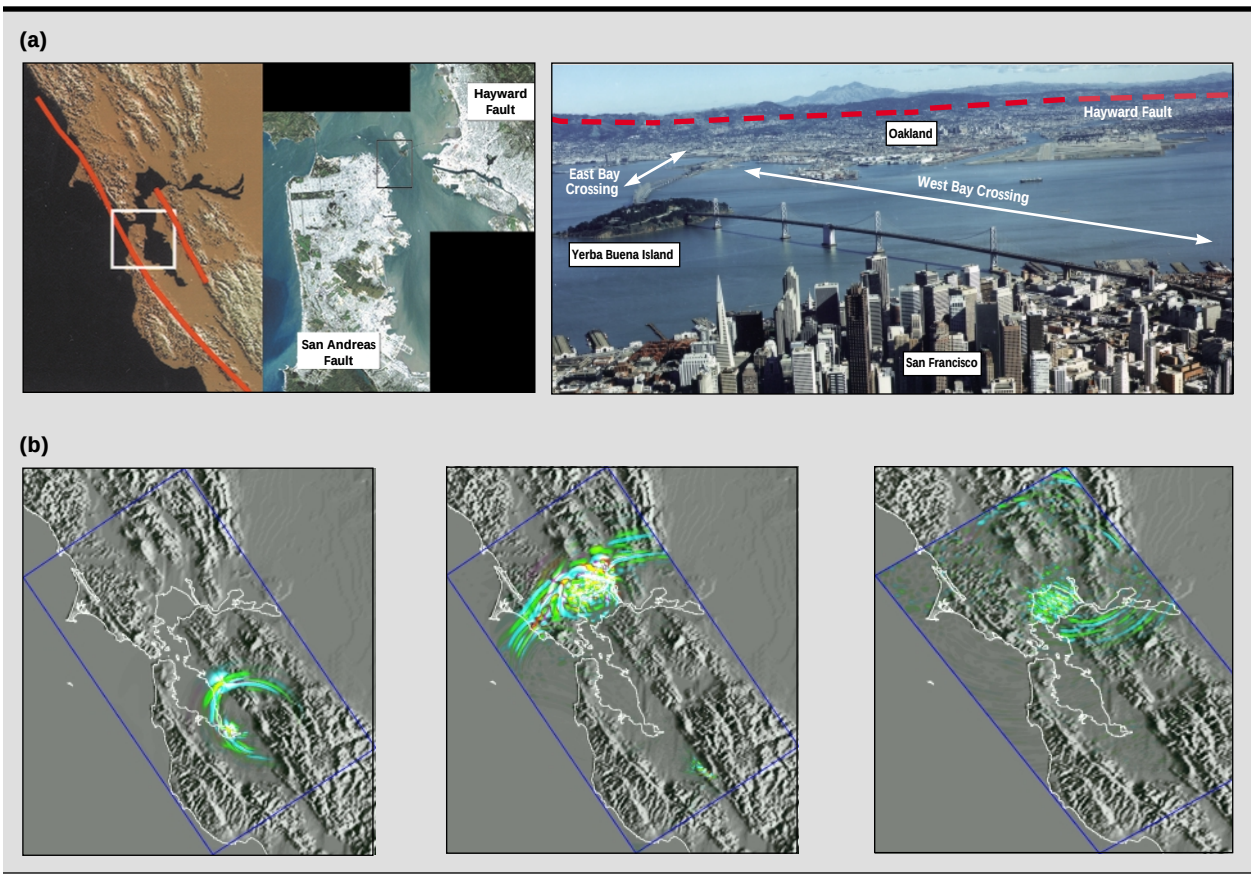

Figure 1. The San Francisco-Oakland Bay Bridge and local faulting. (a) Eastern and western crossings and fault locations; (b) computed regional wave propagation for an M = 7 Hayward fault earthquake.

The ground motion estimates completed for this study were generated using forward computations with physics-based models. To capture the required broad-band motion two approaches were used. The high-frequency components of motion were determined based on a Green's function approach in which small micro-earthquakes occurring along the Hayward fault were measured over a period of time with sensitive seismic sensors in bedrock (**Fig. 2a**) at the Bay Bridge site. The small earthquakes serve as empirical Green's functions which incorporate information about the complex path and site response characteristics as seismic waves emanate from a "patch" on the fault to the site of the structure in question.

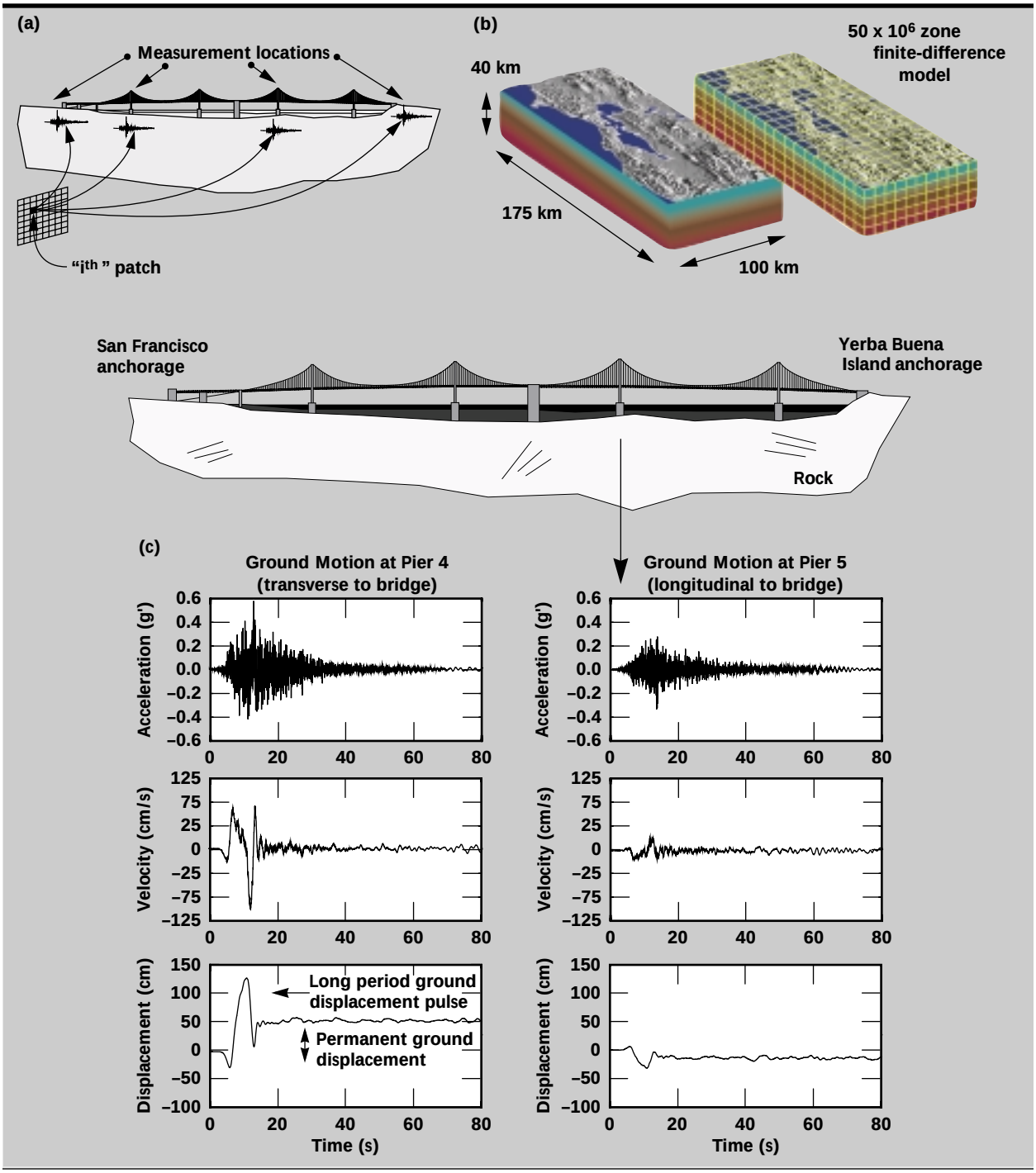

Figure 2. Broad-band synthetic ground motion generation. (a) Measured small micro-earthquake motions at the bridge site serve as empirical Green's functions for high-frequency motions; (b) regional massively parallel finite-difference model for low-frequency motions; (c) bedrock motions for one idealized fault rupture scenario for an M = 7 Hayward fault earthquake.

By appropriately summing up the sources for the entire fault region through a convolution process, the site motion for a large earthquake can be estimated.[4,5] The small micro-earthquakes which are recorded to construct the empirical Green's functions are deficient in long-period information because the small events do not generate significant energy at long wavelengths. Research studies have indicated that the Green's functions can resolve motions down to approximately 1 Hz, with lower frequency motions being in the signal noise.

To develop understanding of the long-period motions which could occur at the bridge site, and to augment the high-frequency motions from the Green's function method, a massively parallel finite-difference model was constructed for the Bay Area region. This model consisted of 50×10^6 regular finite-difference zones of 1/4 km dimensions. The existing geologic database does not provide sufficient spatial detail on the inhomogeneities in the earth to warrant any finer discretization of the geology.

This lack of geology definition on a fine scale results in a frequency limitation in the simulation as higher frequency wave components of motion are scattered by the inhomogeneities which cannot be characterized in the model. As a result, the numerical simulations provide information at frequencies of approximately 1 Hz and lower. The complete synthetic broadband characterization of site ground motions is obtained by a frequency domain merging of the high-frequency motions obtained from the empirical Green's functions method with the low-frequency motions obtained from the massively parallel simulations.

The specific manner in which the fault rupture evolves during an earthquake has a large effect on the ground motions at a specific site. Since the precise manner in which the fault ruptures is not known *a priori*, a number of potential fault rupture scenarios must be investigated when developing the hazard for a particular site. Recent research indicates that on the order of 25 to 30 rupture scenarios should be examined to capture the variability of the fault rupture process. **Figure 2** shows example synthetic ground motions at the Bay Bridge site for one particular rupture scenario for an M = 7 Hayward fault earthquake. This particular rupture scenario, which corresponds to a bilateral rupture propagation on the Hayward fault with rupture initiating adjacent to the Bay Bridge, results in a particularly large ground displacement pulse at the bridge site.

Structural Modeling

The San Francisco-Oakland Bay Bridge consists of two segments: the West Bay Crossing, which is the subject of this study, connecting the city of San Francisco with Yerba Buena Island, and the East Bay Crossing, which connects Yerba Buena Island with the city of Oakland (**Fig. 1**). The West Bay Crossing consists of twin suspension bridges in tandem connected to a central anchorage pier. The central anchorage pier was specially designed to resist the unbalanced live load of the suspension cables of the two suspension bridges. The foundation system chosen for the bridge was open caissons, which include the central anchorage caisson and the caissons which support each tower. The caissons were placed directly on bedrock and rely entirely on self weight to maintain contact with the bedrock. There is no positive anchorage system to resist uplift of the caissons. The San Francisco anchorage consists of a concrete block supported on bedrock and the Yerba Buena anchorage consists of a cable bent and eye-bar chains buried in two reinforced concrete filled tunnels.

The steel towers are attached to the piers by 40 anchor bolts connected to steel girders deep in the concrete piers. The suspension bridge towers consist of two multi-cell legs braced to each other with diagonal elements and struts. The tower legs are silicon high-strength steel while the diagonals and struts are mild carbon steel. Each of the main cables are attached to the tower tops with a single cast steel saddle. The main cables consist of 37 strands with each strand having 472 wires, each wire having a diameter of 5 mm. The deck stiffening trusses are Warren type trusses with the individual truss members constructed with laced steel members. The ends of the stiffening trusses are supported on rocker posts. The rocker posts provide transverse restraint but permit longitudinal movement of the stiffening trusses to accommodate thermal expansion and contraction. Expansion joint connections limit longitudinal motion of the trusses to approximately 36 cm outward and 25 cm inward.

In this research, a special purpose nonlinear finite-element program, SUSPNDRS, has been developed for the transient nonlinear analysis of cable bridge structures. The program uses special element technologies which were developed to significantly reduce the number of degrees of freedom required to accurately characterize a cable bridge system. The program includes capabilities for both geometric and material nonlinearities. The program accounts for finite displacements in the

bridge system and uses an updated Lagrangian framework for each structural element in which a local element coordinate system tracks with the element through space and time to remove gross rigid body displacements.

The five major components of the bridge model are illustrated in **Fig. 3**, and the details of the bridge model element technologies are provided in the referenced report.[2]

One of the objectives of the simulation model development was the construction of a transient solution framework which could handle a multiplicity of strong nonlinearities, including the abrupt and strong nonlinearities associated with impact and contact in the bridge system. The solution algorithm which was developed consists of a hybrid implicit-explicit algorithm whereby the initial static state of the bridge under gravity load is determined based on an implicit solution with Newton equilibrium iterations. A static load initialization procedure has been developed which allows the SUSPNDRS program to compute the correct static geometry and element forces starting with any arbitrary initial geometry definition of the bridge cables and deck.[2] Once the appropriate gravity configuration is achieved, transient earthquake analysis is carried out with an explicit, central difference-based time-integration scheme. The explicit scheme is particularly powerful, and has significant advantages over implicit time-integration schemes traditionally used in earthquake computations, when modeling the impact and contact associated with caisson rocking or deck-to-tower or deck-to-caisson impacts. Rigorous modeling of contact phenomenon can lead to significantly increased computational effort, or complete lack of appropriate convergence in implicit integration schemes, whereas the efficiency of explicit schemes is not adversely effected by contact.

In the explicit scheme, the bridge equations of motion are formulated in terms of absolute displacements rather than the displacements relative to the ground and the specification of multiple support input motions is trivially simple.

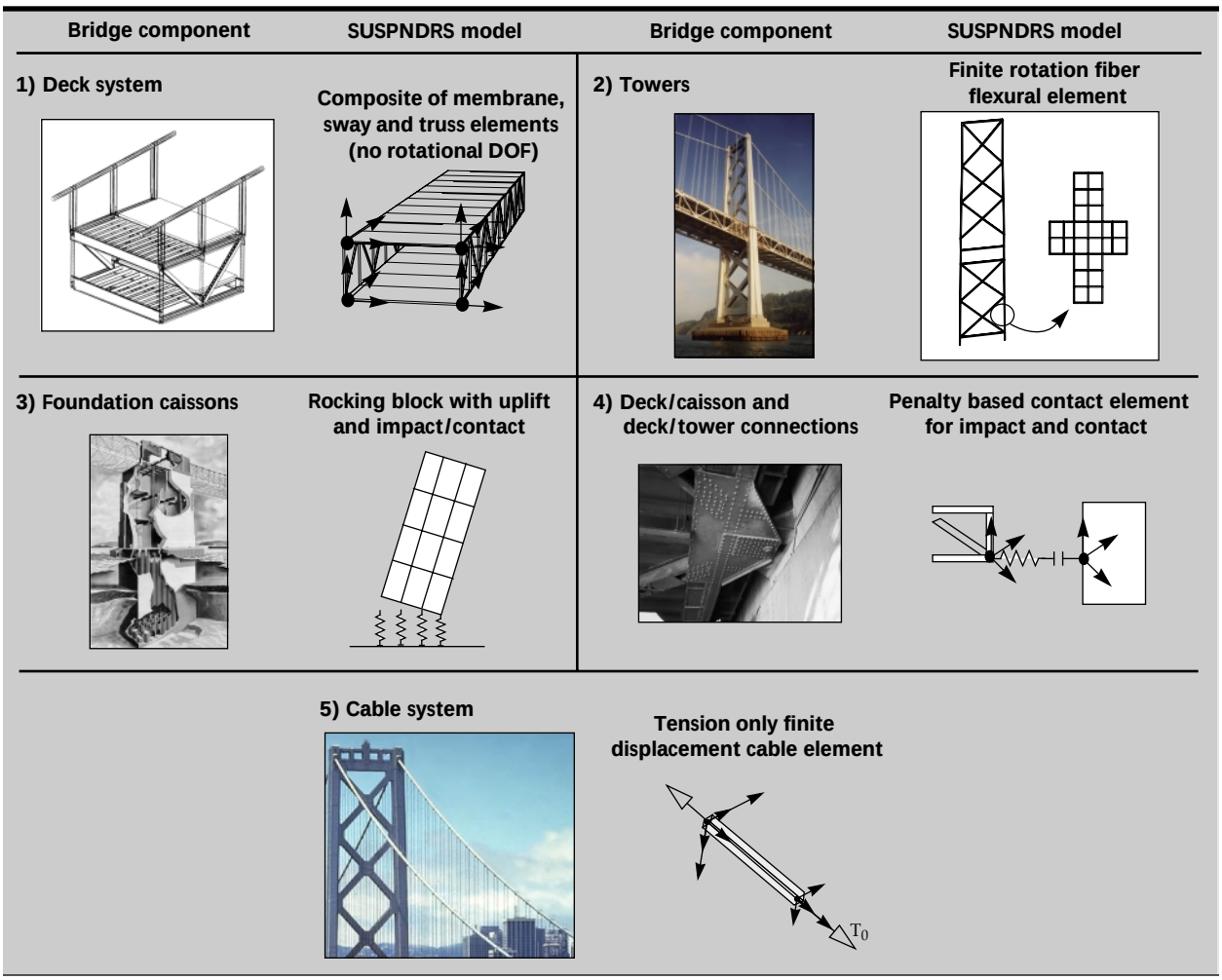

Figure 3. Components of the bridge system model.

Simulated Earthquake Response

The large ground displacement pulse in the synthetic earthquake records (**Fig. 2**) has a total time duration on the order of 5 s. For stiff structures, which exhibit natural periods of vibration significantly shorter than 5 s, the structure would have minimal dynamic response to this long duration pulse and would move essentially as a rigid body with the ground motion. For long-period flexible structures, on the other hand, this long-period pulse can significantly excite the lower frequency modes of vibration, providing a significant dynamic impulse to the structure.

The fundamental vibrational mode of one of the Bay Bridge suspension segments consists of

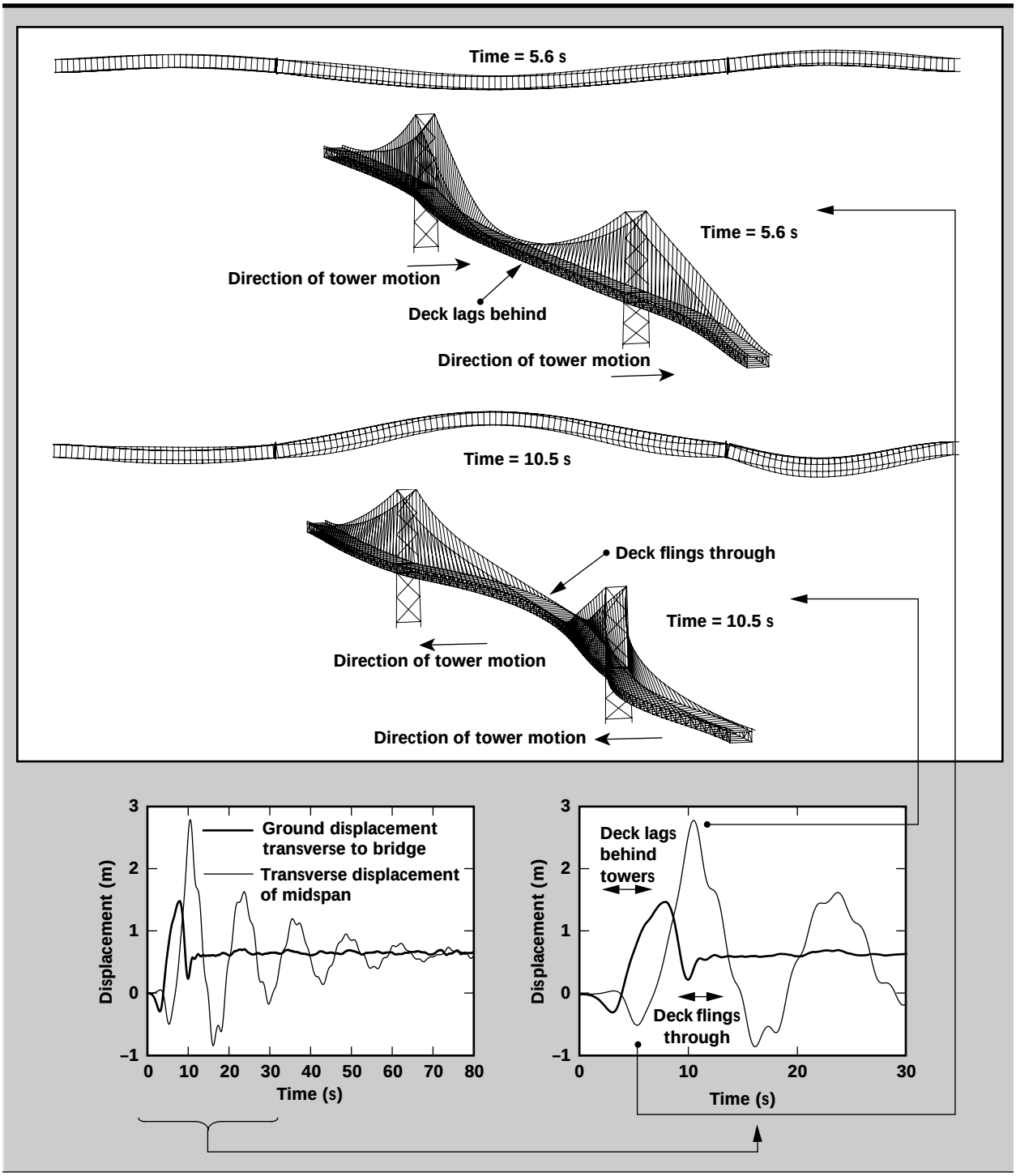

Figure 4. Displacements of bridge system due to near-field motions containing a large displacement pulse.

transverse vibration of the main span. Based on field measurements completed in 1936, and natural mode computations from the current study, the fundamental mode has a period of approximately 9 to 10 s. Thus the ground motion pulse duration is almost exactly one-half the natural period of the bridge. The result is that the ground displacement pulse imparts tremendous energy to the Bay Bridge system at the start of the earthquake motions. Animation of the bridge response indicates that the towers of the bridge move with the ground, while the mainspan deck can't respond fast enough due to its large mass and flexibility and it essentially lags behind the towers. As the deck finally starts to move to catch up with the displaced towers, the tower motion has reversed direction and started to move with the ground displacement pulse in the opposite direction (**Fig. 4**). The result is that the main span deck is essentially flung between the towers in sling shot fashion, with a large transverse displacement and corresponding high stresses in the deck system.

An assessment of the member forces for this earthquake loading indicated that a large number of main load-bearing members would be significantly overstressed. The deck beams, which connect the deck slabs to the stiffening trusses, would be particularly susceptible to damage from the deformations associated with the deck fling.

Conclusions

Two new computational tools have been developed for simulating earthquake ground motions and the response of long-span cable bridges. These tools are shedding light on the nature of near-field ground motions, including long-period and permanent displacements which can occur in the near-field, and the damaging effects these motions can have on flexible, long period structures.

References

1. S. C. Larsen and C. A. Schultz (1995), "ELAS3D:2D/3D elastic finite difference wave propagation code," Lawrence Livermore National Laboratory, Livermore, California (UCRL-MA-121792).

2. D. B. McCallen and A. Astaneh-Asl (1997), "SUSPN-DRS: A numerical simulation tool for the nonlinear transient analysis of cable supported bridge structures," Lawrence Livermore National Laboratory, Livermore, California (UCRL-ID-127626).

3. W. D. Iwan and X. Chen (1995), "Important near-field ground motion data from the Landers earthquake," *Proc. 10th Eur. Conf. on Earthquake Eng.*, A. A. Balkema, Vol. **1**, pp. 229–234.

4. L. J. Hutchings (1991), "Prediction of strong ground motion for the 1989 Loma Prieta earthquake using empirical Green's functions," *Bull. Seis. Soc. of Am.*, Vol. **81**, pp. 88–121.

5. L. J. Hutchings (1988), "Modeling strong earthquake ground motion with an earthquake simulation program EMPSYN that utilizes empirical Green's functions," Lawrence Livermore National Laboratory, Livermore, California (UCRL-ID-105890).

Signal Processing for Evaluation and Update of Simulation Models in Structural Analysis

Gregory C. Burnett and Gregory A. Clark
Defense Sciences Engineering Division
Electronics Engineering

David B. McCallen
Center for Complex Distributed Systems

Charles R. Noble
New Technologies Engineering Division
Mechanical Engineering

We are developing a methodology that uses model-based signal processing to compare simulations of structural responses with measured data. The work completed to date indicates that the model-based signal processing can readily identify significant differences between a simulation model and an actual measured structure. The signal processing algorithms can also be used to detect changes in a structure associated with damage in the system. The appropriate placement of sensors in under-observed systems is critical and sensor locations should be based on as much structural insight as possible.

Introduction

The design of engineering systems has traditionally resulted from a mix of theory, empiricism, and experience based on historical performance. With the advent of high-performance computers and massively parallel computations, the hope is that simulations based on first principles will play an even more commanding role in the engineering process. However, for this to come about, it is essential that large-scale simulation models yield demonstrably accurate results for the particular problem type under study. The ability to validate computational models, based on a rigorous comparison between the actual measured system response and the simulated response, is a requisite to building confidence toward a simulation-dominated engineering process.

Progress

Objectives

Our project is concerned with the evaluation and validation of computational structural models. The methodology under development relies on model-based signal processing to compare simulations with measured structural response. The signal processing algorithms are intended to determine the degree to which the simulation model represents the actual behavior of the structure, and to provide guidance on how the simulation model could be improved. In addition, the signal processing can sense changes in the structural system, which offers the potential for establishing an approach for damage detection in large structural systems.

There are important programmatic applications which could immediately benefit from the ability to reconcile simulation models with actual measured structural response. These applications span a range of structural types and loading regimes including the rather violent vibrational response of reentry vehicles in missile flight tests, the small amplitude ambient vibrations of optical components and structures for the National Ignition Facility (NIF), and the vibrations and transient response of large transportation structures to earthquake ground motions (**Fig. 1**).

In year one of this study, the framework for model-based signal processing has been established and the ability of the signal processing to sense differences between a simulated and a measured structure has been studied parametrically. We have also investigated the degree to which model-based signal processing can identify the regions of the

structural model which are deficient and the ability of the signal processing to provide guidance on how to update the computational model to enhance accuracy. The important questions of observability and how many sensors are required to provide adequate measurements have also been addressed.

Model-Based Signal Processing

The signal processing methodology under development follows the procedure outlined in **Fig. 2**. The essential inputs to the signal processing include the matrices which result from the finite-element structural simulation model, including mass [*M*], damping [*C*], and stiffness [*K*] matrices, and the measured response of the structure for a given loading. Ideally, the structure should be subjected to carefully controlled white noise type of excitation for the initial model identification process so that the input forcing function is precisely known and a wide range of vibrational modes are excited.

The model-based signal processor uses the finite-element-generated system matrices as a starting point and constructs a simulator of the system based on a state-space first-order equation system characterization of the second-order finite-element equations of motion. A Kalman filter-based residual whiteness test is used to detect any divergence between the simulation model and the actual structure response. A Gauss-Newton search routine minimizes

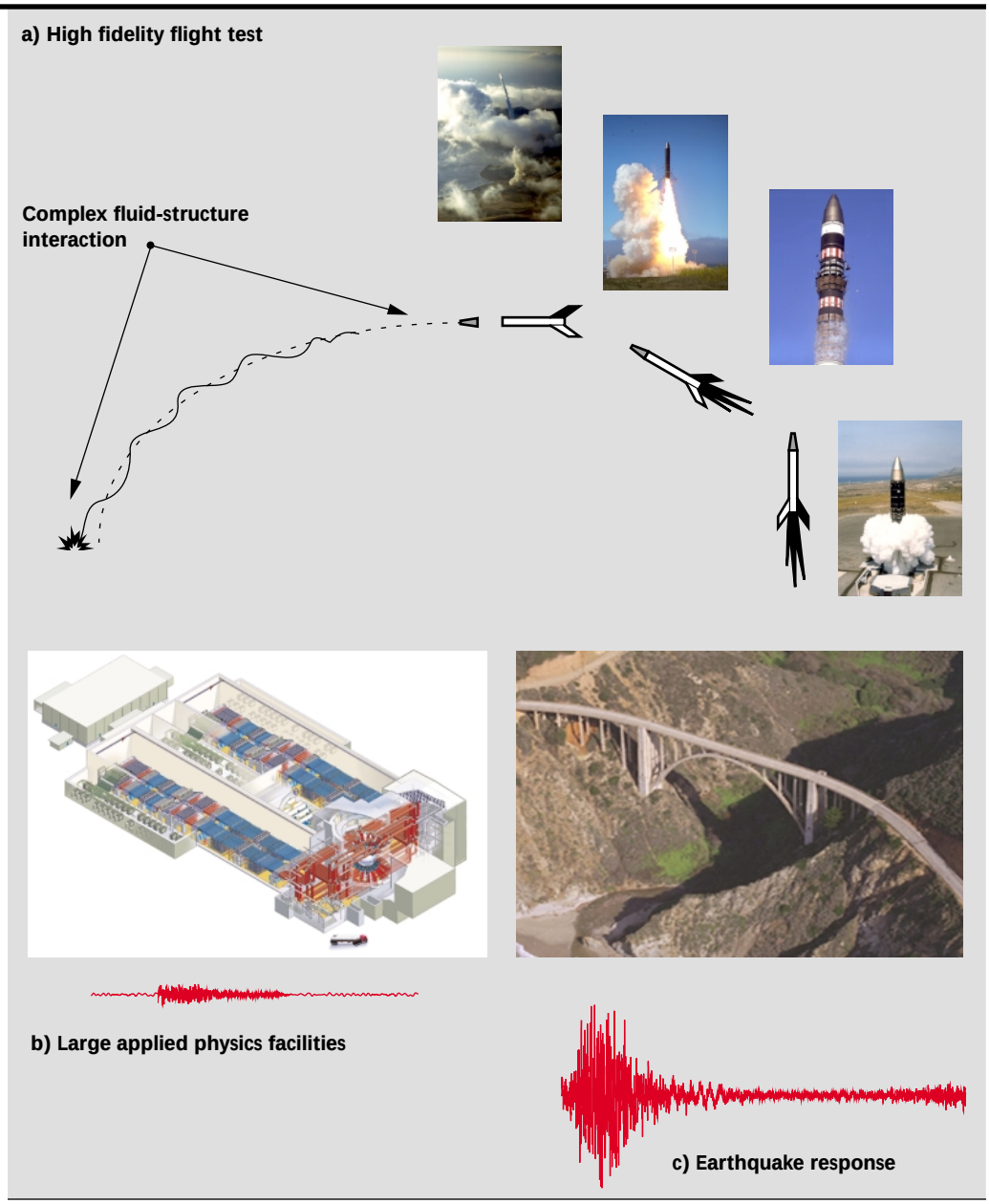

Figure 1. Applications of model-based signal processing. (a) Understanding complex fluid-structure iteration in flight dynamics, including model validation and appropriate data reduction; (b) validating design model simulations and understanding ambient vibrations for NIF; (c) validating simulation models for massive transportation structures and developing damage detection capabilities.

the differences between the simulation model and the measured structure in a least squares sense. The minimization process results in system identification in which optimal structural model parameters are identified. These optimal parameters (indicated by the updated system matrices in **Fig. 2**), can be passed back to the finite-element model for parameter update. The signal processing also provides a methodology for damage detection in that changes in the structure which are associated with damage can be sensed once the virgin, undamaged structure is appropriately identified.

The signal processing procedure which has been developed has been studied parametrically by extensive investigation of a simple dynamic structural system, a five-story building model, as shown in **Fig. 3**. The utility of this example is that with appropriate idealization of the member section properties, the number of degrees of freedom in the model can be easily varied from as low as 5, to as high as 500, with maintenance of the same basic system dynamics. The equations of motion can also be readily written down analytically as shown in **Fig. 3**. This allows issues of observability and scaling of the signal processor to be readily investigated.

This simple example was used in paper studies to evaluate the ability of the signal processing to detect divergence between simulated and real structures and to identify appropriate model parameter modifications. To achieve this, a finite-element model was constructed for the structure, and a perturbed finite-element model was constructed to represent the "real" structure. For example, one perturbation might consist of modifying all stiffnesses of the structure by a significant margin. Another might consist of modifying selected segments of the structure in a local fashion. The signal processing algorithm was then called upon to identify differences between

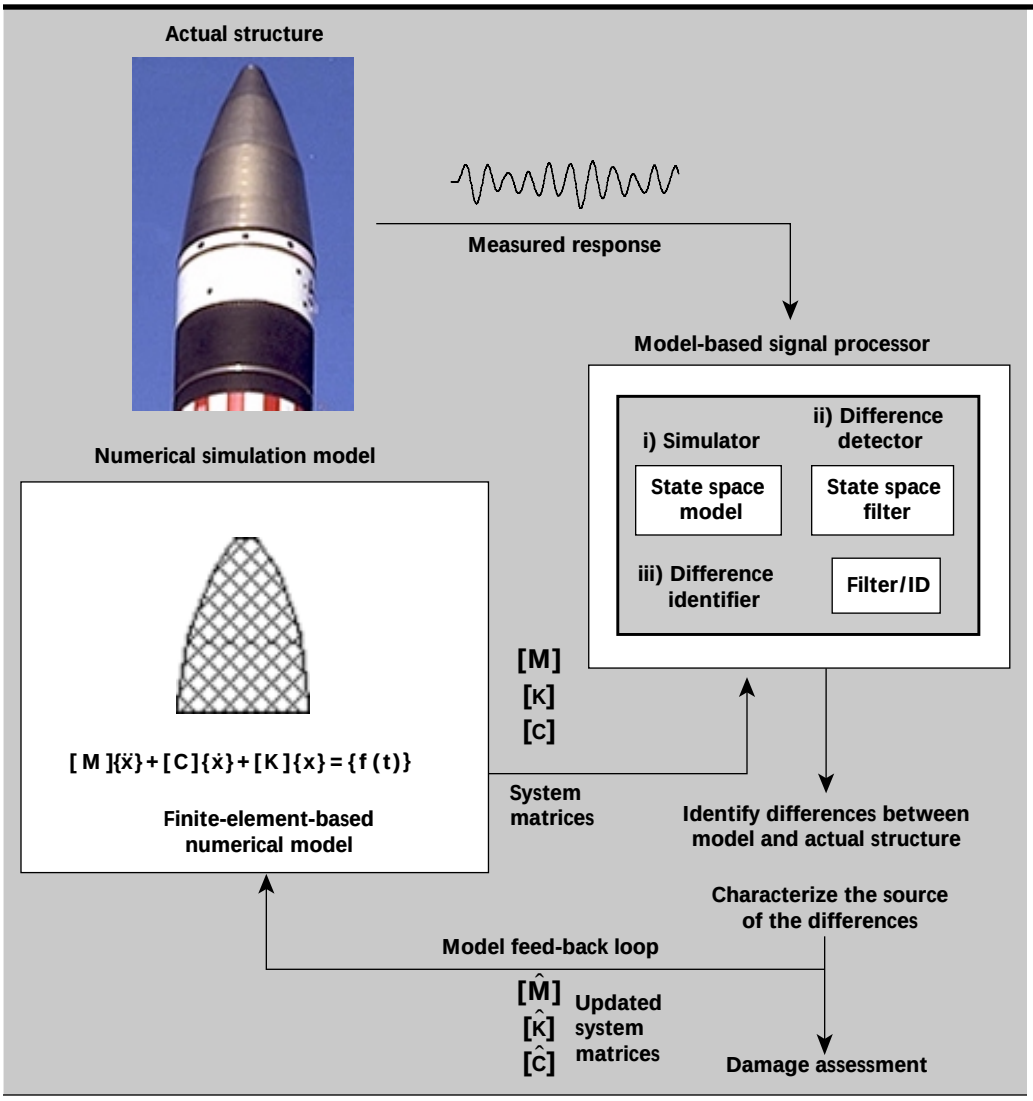

Figure 2. Model-based signal processing for evaluation and update of simulation models.

the simulated and "real" structures and to identify structural parameter updates for the simulation model.

These studies were carried out in blind fashion, whereby the mechanical engineering team members constructed the simulated model and the data from the measured "real" structure and passed this information to the electrical engineers responsible for the signal processing. Thus the signal processors were dealing with two sets of information with no prior knowledge of the structural perturbations.

For the simple baseline system with 5 degrees of freedom fully observed, the signal processing algorithms readily identified the differences between the simulated and "real" structure, and provided the appropriate parameters for the model update, as illustrated with a subset of examples in **Fig. 4**. For this analysis the response of the model was simulated for a white noise forcing function applied at the top of the structure, and the "measured" response of the "real" structure was also computed with a perturbed model for the same white noise forcing function.

For a fully observable system (for example, the acceleration response of all five floors was assumed measured), the signal processing was found to be very robust, and could accurately ascertain that the

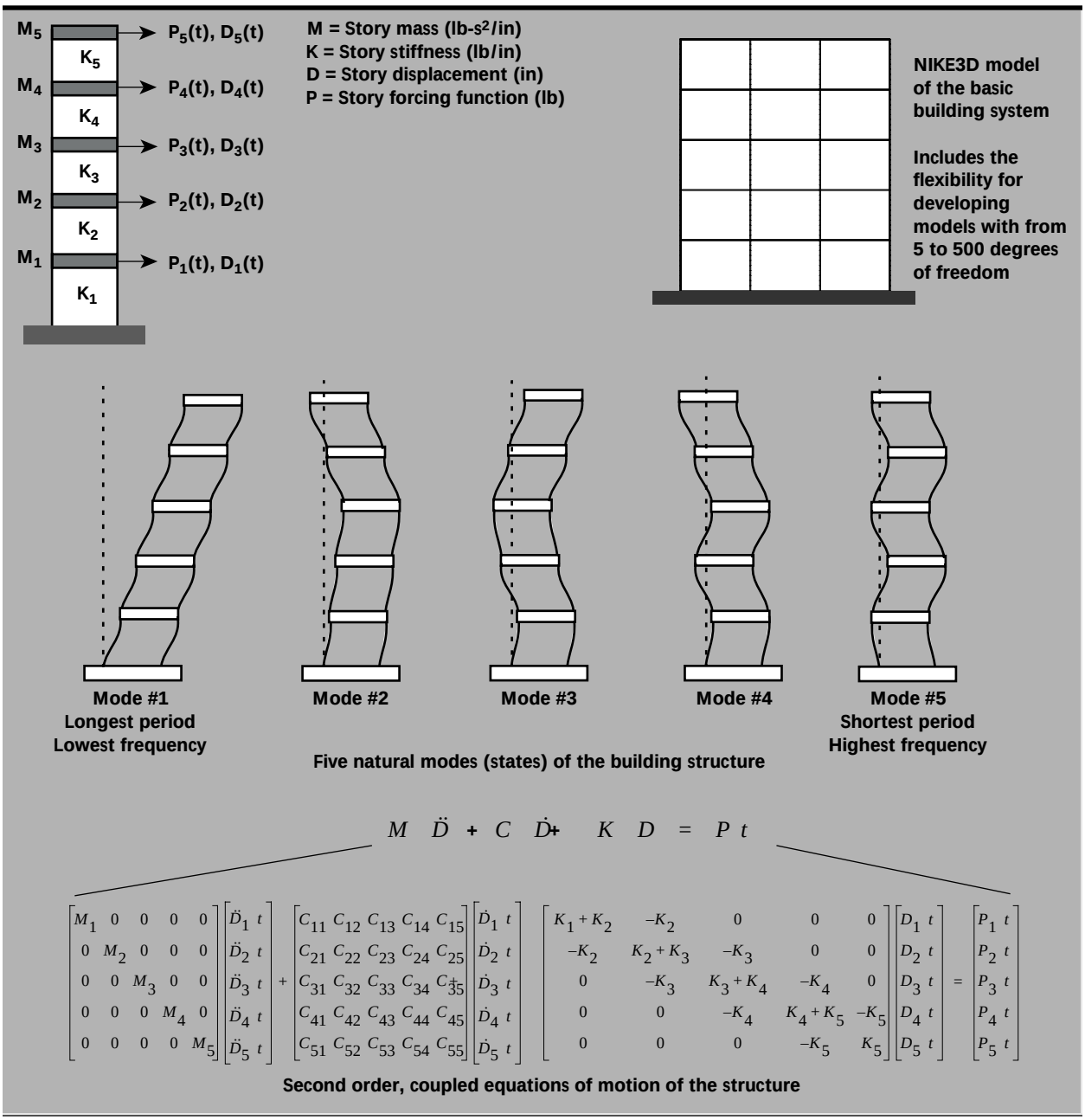

Figure 3. Simple dynamic system consisting of a five-story shear building.

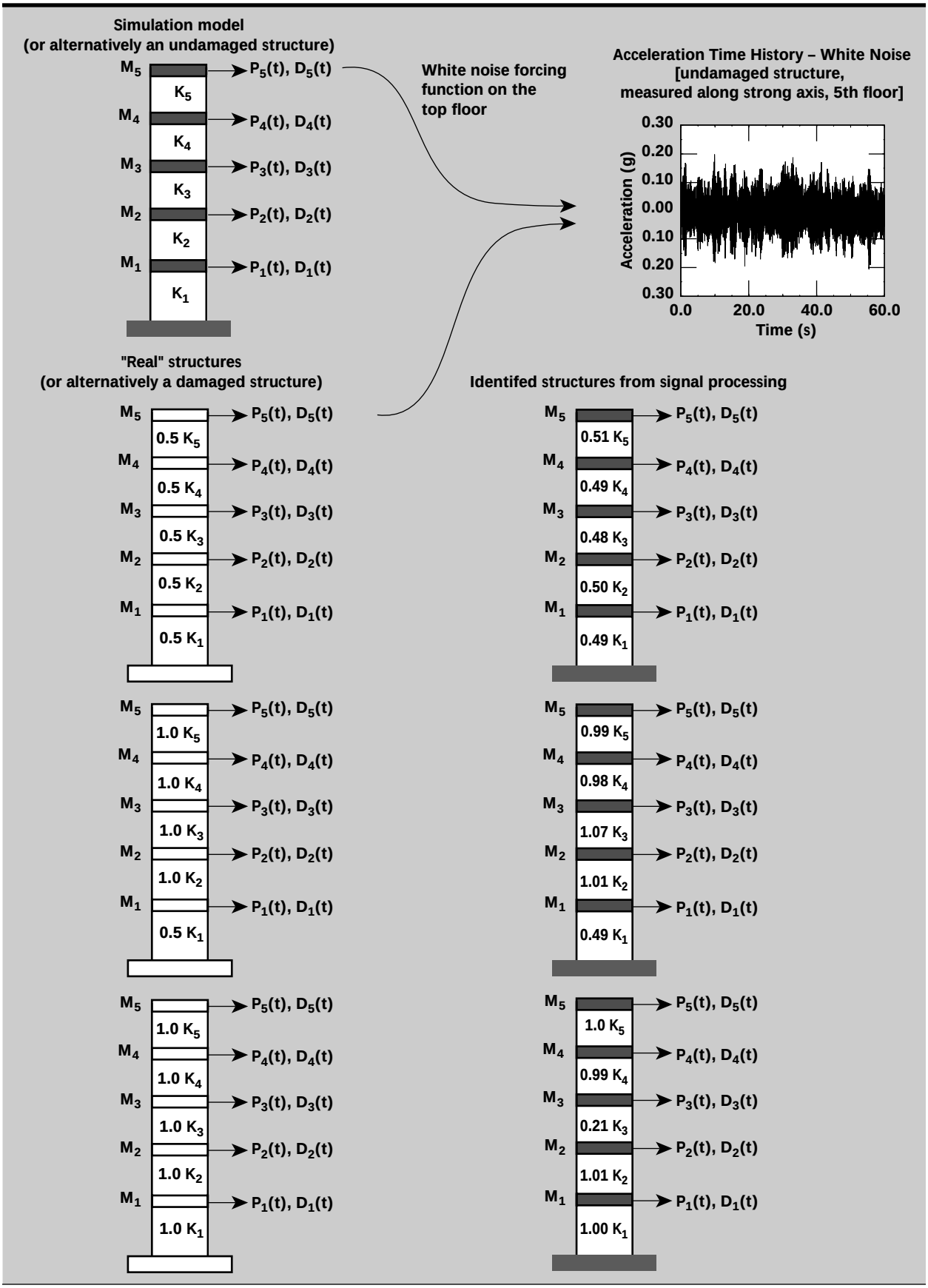

Figure 4. Identification of structural properties from the model-based signal processor.

model and "real" structure were different, as well as identify the correct distribution of the stiffness in the "real" structure.

It should be noted that the differences between the simulated and "real" structure in **Fig. 4** could equally well be interpreted as the differences between an undamaged structure (the modeled structure) and a damaged structure (the "real" structure). Thus, if one can ascertain that two structures are different and how they are different, damage detection is enabled.

In actual large structures, full observability (for example, every point in the actual structure corresponding to a degree of freedom in the finite-element model is measured), is a condition which will rarely if ever be achieved. Because of typical limitations in the number of sensors and the amount of data which can be measured practically, almost any real system will be significantly under-observed.

The potential impact of low observability has also been investigated with the simple shear building model. For this investigation, the dimension of the model was increased to 10 degrees of freedom with appropriate master-slaving of the active degrees of freedom. The ability of the signal processing algorithm to correctly identify the structure with a reduced set of observations was investigated for a number of different observation schemes. For this analysis the perturbation to provide the "real" structure was as indicated in **Fig. 5**. This perturbation represented a significant and complex change from the original structure. With all 10 degrees of freedom observed the mean error in the identified stiffness parameters was $1.2 \times 10^{-9}\%$, which verifies that precise identification is achieved for a fully observed system. The mean error in the system identification for various under-observed scenarios is summarized in **Fig. 5**.

In **Fig. 5** the cross-hatched box indicates a floor at which translation was "measured" and a hollow box indicates a floor at which translation was not measured. These results indicate that the accuracy of the signal processing identification tends to be significantly lower if measurements are not made for the top two stories of the building. This is correlated to the fact that the fourth and fifth stories have the most significant change in stiffness and, if there is not a local sensor measurement to capture the dynamics of this softening region, the system identification can miss these significant changes.

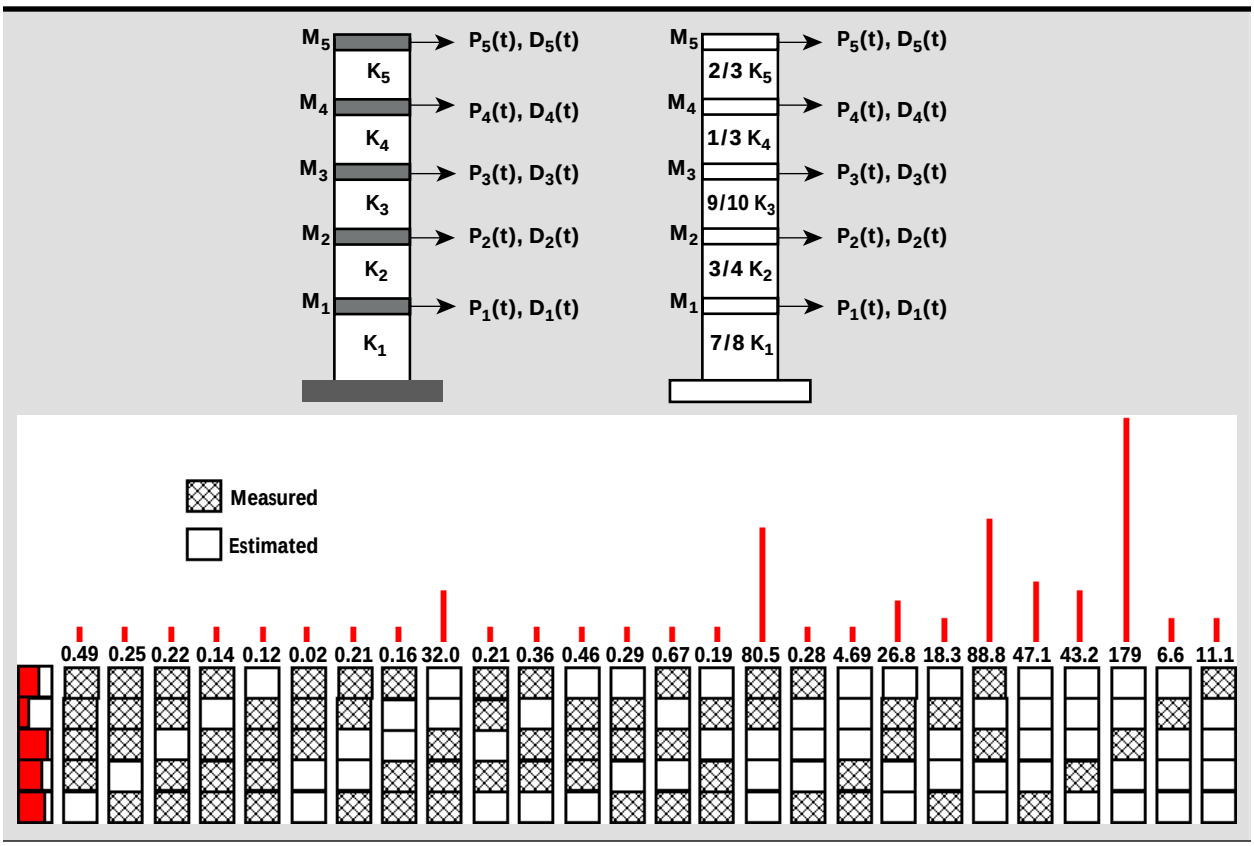

Figure 5. Accuracy of signal processing system identification if reduced observations are made.

Perhaps just as significant is the observation that if the top floor alone is measured (such as with only one observation), the system identification still does a reasonable job of parameter estimation. These observations underscore the need to have adequate measurements in the regions of the structure for which a high degree of uncertainty is anticipated or, alternatively, regions where damage to the structure might be anticipated.

Future Work

The second year of this project will investigate applications for some real structures, in which real-world issues associated with noisy data come into play. The focus will also include scaling up the existing signal processing algorithms to attack much larger structures.

Controlled Biological Systems for Sensor Platforms

Dino R. Ciarlo
Electronics Engineering Technologies Division
Electronics Engineering

Jonathan Simon
New Technologies Engineering Division
Mechanical Engineering

Matt Harren
Cornell University
Ithaca, New York

We have been developing wireless circuits for the control of the Madagascan Hissing Cockroach with the intention of using them as distributed sensors or possibly in search and rescue missions.

Introduction

During the past several years there has been research into the controllability of various insects by external stimuli such as electrical pulses to their antennae area. Prof. I. Shimoyama started the work at the Tokyo University in Japan. In the U.S., Prof. S. Crary, a physicist at the University of Michigan, conducted pioneering work. More recently there have been over 30 projects of this type funded by the Defense Sciences Office of DARPA. The scope of the DARPA projects includes: the response of the animals to stimuli, animal experiments, animal models and the development of low power, light weight controlling circuits and sensors. For the past year, we have been developing wireless circuits for the control of the Madagascan Hissing Cockroach with the intention of using them as distributed sensors or possibly in search and rescue missions.

Progress

We decided to experiment with the Madagascan Hissing Cockroach following the advice of Prof. Crary of the University of Michigan and Dr. M. Willis, an entomologist at the Arizona Research Laboratory, Division of Neurobiology, University of Arizona. Both Crary and Willis are being funded by DARPA to study the neural control of flight steering in the *Manduca sexta* moth.

The Madagascan cockroach is a robust animal, easy to work with. These animals are often used as displays in grammar and high school biology classes. The name hissing comes from the hissing noise they make when annoyed. They generate the noise by expelling air from their abdomens. The Carolina Biological Supply Co. in North Carolina sells them but they cannot be shipped into California. We found cockroach colonies at the University of California at Davis and at the Clorox Co. in Oakland; the managers of these facilities were ready to give us animals to experiment with. Instead, we purchased three adult female cockroaches from a pet store for $5 each. We kept them in a suitable container and fed them dried dog food, bread, lettuce and water. They remain quite active even after six months of experiments.

In our experiments, we attempted to steer the Madagascan cockroach by the use of two LED light sources mounted on either side of the cockroach's head. **Fig. 1** is a photograph of the electronics components. The larger circuit board on the left contains the left and right button and the transmitter electronics. The smaller circuit board on the right contains the receiver circuit and is mounted on the animal's back. We used transmitters/receivers from RF Monolithics and microcontrollers from Microchip Technology to remotely activate one or the other of the LEDs. The transmitter/receiver operates at a frequency of 916.5 MHz. The circuit was designed so that if a 1-kHz signal was received by the receiver

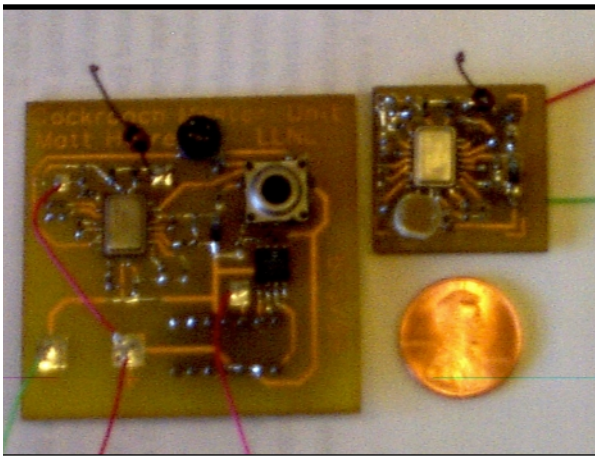

Figure 1. Photograph of electronics system used to steer cockroach.

on the animal's back, the left LED would light, but if a 3-kHz signal was received the right LED would light. The entire backpack on the animal, including the 3-V battery weighs 5 g. The cockroach weighs 7 g and is capable of carrying over 100 g. **Fig. 2** is a photograph of this configuration of a cockroach with the installed electronic backpack and two LEDs. These animals are nocturnal and the thought was that they have an aversion to light and would turn in a direction away from any light source.

In actual tests, we did see a tendency for the animal to turn away from the light source. However, this was observed once the animal was in forward motion. Often we had to resort to extra effort to get the animal moving (such as a slight nudge from behind). In addition, the turns in response to the light signals tended to be rather gradual. We did not see any right angle turns. Also, of the three animals we had in captivity, one was especially responsive while the other two showed little interest in our experiments.

Future Work

We demonstrated the ability of the Madagascan cockroach to carry wireless, battery powered circuits on their backs. They certainly have enough carrying capacity to add an environmental sensor to the transmitter/receiver package we used. The cost of this electronics is not high, just a few dollars. We concluded from our work that best scenario would be to outfit hundreds of these animals with such electronic backpacks and then let them wander on their own, sending back information on the environment, without attempting to steer them.

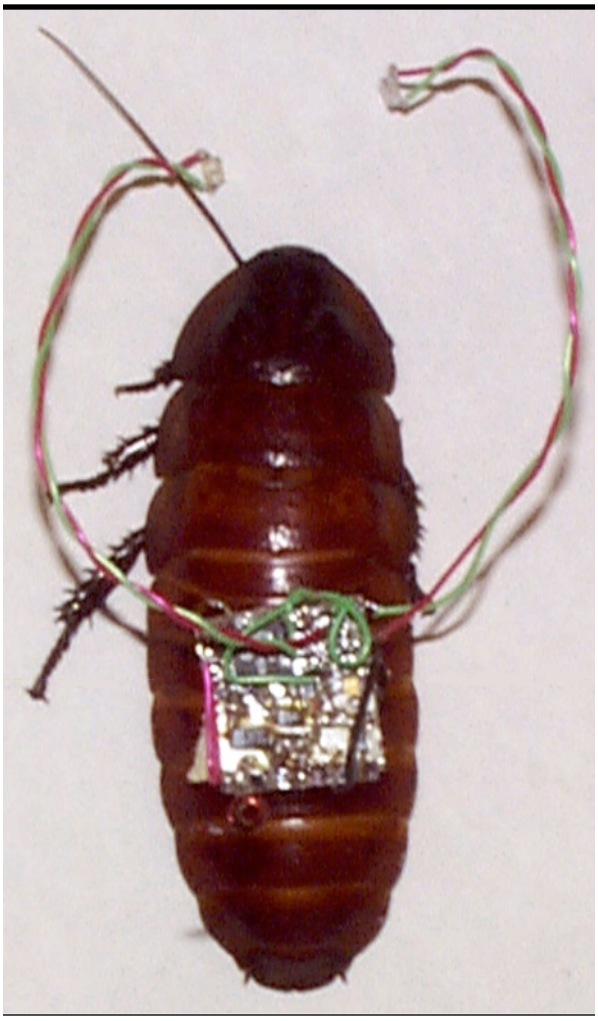

Figure 2. Photograph of cockroach with installed electronic backpack and two LEDs.

An Instrumentation System for Remote Monitoring of Large Structures

Mathew S. Hoehler, and Charles R. Noble
New Technologies Engineering Division
Mechanical Engineering

David B. McCallen
Center for Complex Distributed Systems

Jon P. Lewis
Defense Sciences Engineering Division
Electronics Engineering

We have developed a new instrumentation system for the remote monitoring of structures. A key element of the system, which enables practical application to large structures, is a wireless communication capability, allowing remote contacting of the system to provide commands and to retrieve measured data. The application of this system to vibration monitoring has demonstrated the utility of such a system and has provided the opportunity for optimization and fine tuning of the system design.

Introduction

The design and analysis of large structural systems has become increasingly reliant on computational simulation. As the speed of computational engines increases, computer memories grow, and massively parallel simulations become commonplace, the trend toward reliance on simulations will continue and likely become even more pervasive. With the increase in fidelity of simulation models, there are great expectations that simulations will provide improved understanding and insight into the way in which structures respond to various loading conditions. However, in many respects our ability to discretize and compute has significantly outpaced our ability to test and verify our computational models. There is a pressing need to ensure that the ever larger models which are being constructed are actually representative of the structure being simulated.

There are two topical areas which necessitate research and development attention to address the growing model validation deficit.

The first area deals with the need for expedient collection of response data from large, distributed structures. Traditional wired sensor and data acquisition systems are not capable of practical monitoring for very large structures. Recent experience with wired system monitoring of large structures (**Fig. 1**) has shown that the placement and continuous data collection tasks will be intractable for structures like a large applied physics facility on the scale of the National Ignition Facility (NIF) at Lawrence Livermore National Laboratory (LLNL) or a transportation structure of the size of the Bay Bridge (**Fig. 2**). For example, LLNL engineers recently performed field experimental testing of the famous Bixby Creek Bridge near Carmel, California (**Fig. 1**), and that experience was found to stretch the application of wired data acquisition systems to the limit.

The second topical area deals with the processing of measured response data once the data is obtained. There is an immediate need to develop robust algorithms which rigorously compare simulated system response and actual measured system response, quantify limitations and shortcomings of the simulation model, and prescribe appropriate perturbations to the simulation model.

The project described here dealt with the problem of monitoring large structural systems. A companion article in this report deals with the second issue of data processing and model update.

Progress

Our focus was the development of a wireless instrumentation system which can be used to monitor very large structural systems. The overall

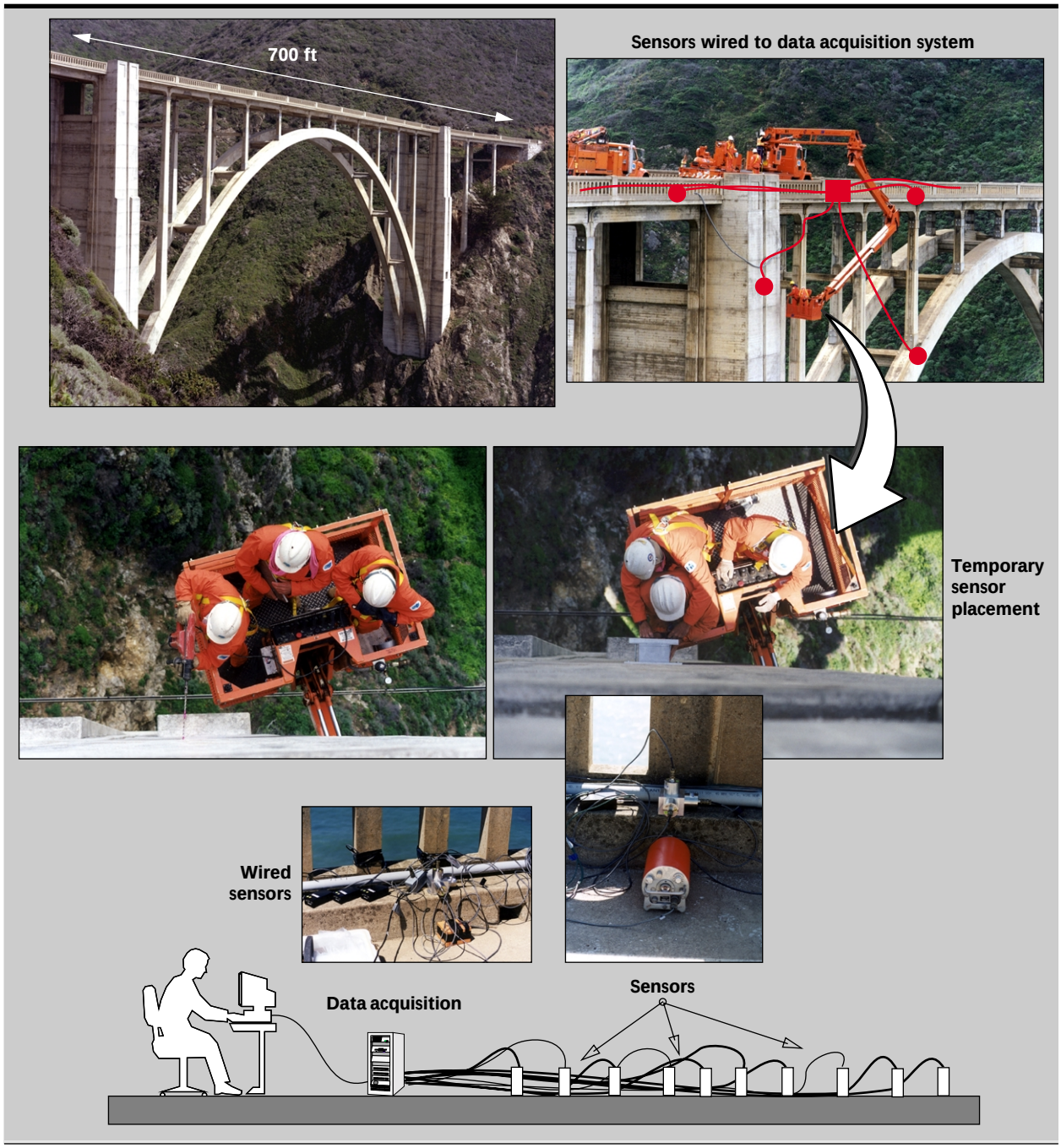

Figure 1. Traditional structural monitoring with a wired system. LLNL study of Bixby Creek Bridge is shown.

strategy was to construct the most economical system with readily available, commercial off-the-shelf components. The specifications for this system included:

1. capability for remote access to allow adjustment and setting of system parameters and downloading of data;
2. incorporation of sensors, amplifiers and sampling rate which would allow selectable data acquisition over a large amplitude range (such as ambient vibrations to strong earthquake motions) and a broad frequency band (from 15-Hz modal vibrations typical of stiff NIF structures, to 0.1 to 0.2 Hz vibrations of a long-span bridge); and
3. capability for accurate time keeping so that all measurements can be referenced to a precise time scale.

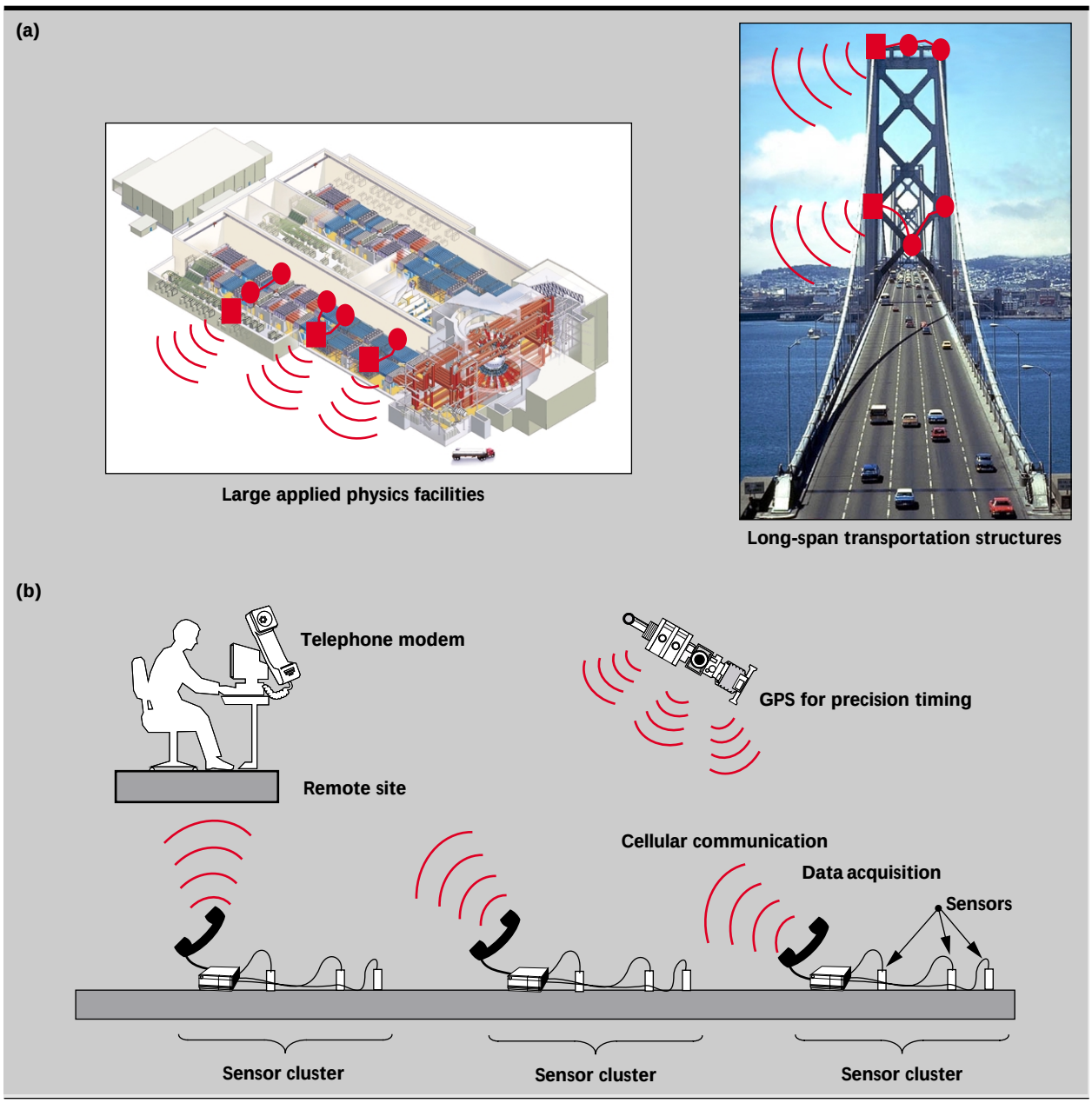

Figure 2. Structural monitoring of large distributed systems with remote data transmission. (a) Example structures which would benefit from distributed monitoring; (b) distributed individual sensor clusters.

In addition to these basic functions, the intent was to develop a modular system so that the various options could be mixed and matched to most economically suit a specific application. The project included the design of the overall system, construction and testing of a prototype system and a field application of the prototype system at the NIF construction site. A corollary objective was to provide data for validation of the NIF vibrational design criteria.

The ultimate objective of the instrumentation system is to allow placement of an array of sensor clusters around a distributed structure, such that the local sensor clusters are wired to individual data acquisition systems and each data acquisition system can be remotely accessed for data download, as indicated in **Fig. 2**. This pattern of instrumentation was selected after careful review of the maturity of communication technologies and consideration of system costs and reliability. For example, wireless communication between individual sensors and the data acquisition system would be very desirable, but was judged too expensive and potentially problematic with regard to reliability within the context of cost-effective 1999 technology.

Monitoring System

The monitoring system, shown schematically in **Fig. 3**, was developed to provide the required funtionality. All of the system components, with the exception of the sensor housing, were commercially purchased. The system sensors consist of heavy seismographic accelerometers, housed in a stiff aluminum container designed and built at LLNL. The massive accelerometers provide good signal-to-noise performance in the low frequency regime. The sensor housing was designed to ensure strong coupling through rigid mounting and to mitigate potential vibrations of the housing which could affect sensor measurements. Commercial signal amplifiers were used, and the digital recorder was constructed to LLNL specifications by a commercial vendor. Each digital recorder has a companion GPS unit for accurate positioning and precision timing, and a cellular-phone-based communication transmitter/receiver for remote communication with the system. The system can be contacted via a laptop computer with a phone modem. The system can be powered with AC hook-up or a solar panel. A battery power option was included for immediate applications in the NIF construction area.

In the course of the development, it was found that the cellular communication system was a major source of power consumption in the instrumentation system. To assist in minimizing power usage, a pager system was implemented which allowed the system to be "beeped," thus powering up and turning

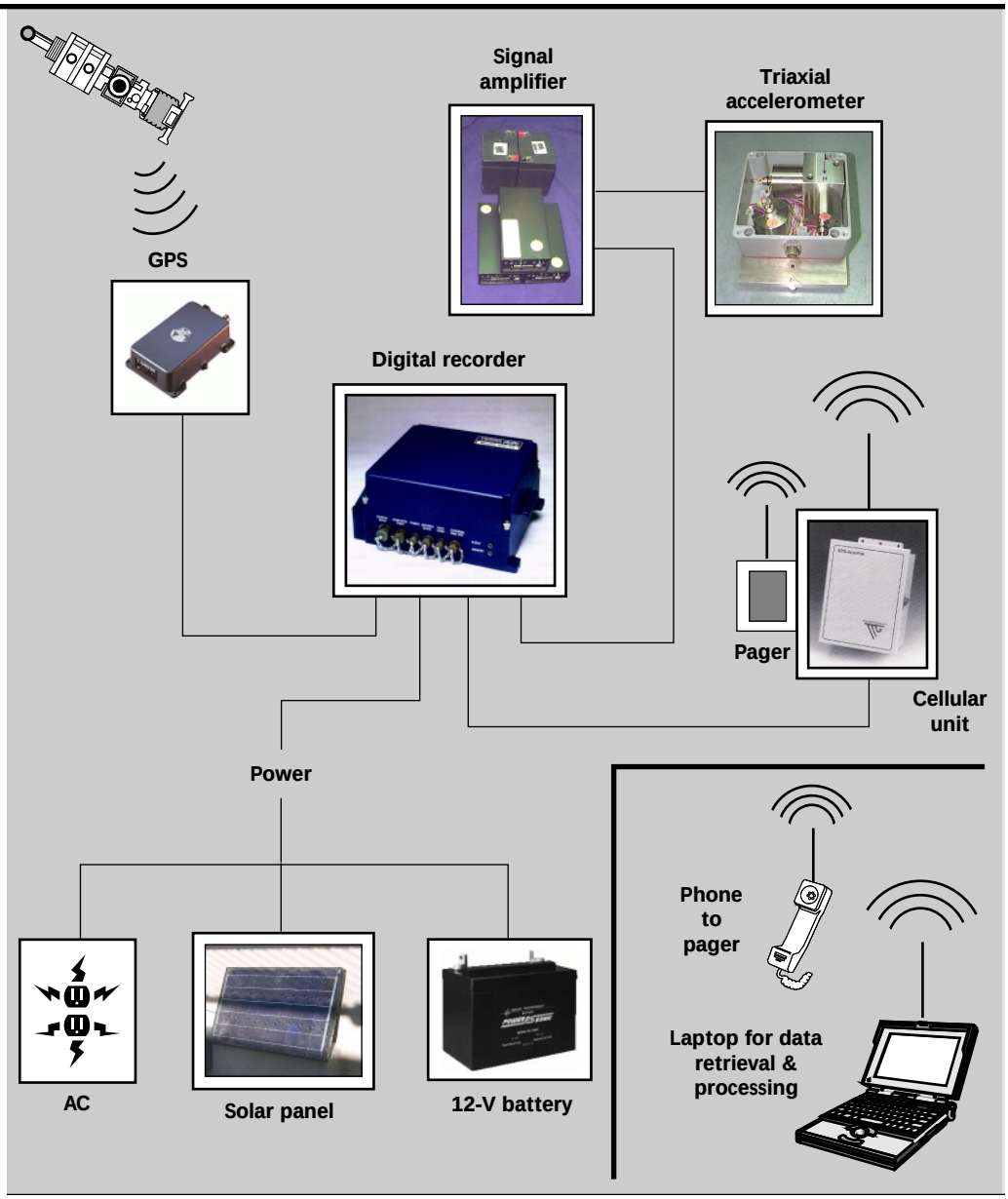

Figure 3. Instrumentation for sensing, data recording and storage, precision timing, and communications.

on the cellular communication package. The cellular package can then be powered down after information is relayed or data is retrieved.

An essential element of the development of any data acquisition system is the establishment of the accuracy of the measured data. This is particularly important when a number of different electronic components are being interfaced together. The accuracy of data obtained with remote monitoring instrumentation system was thoroughly evaluated by careful comparison with existing high performance data acquisition systems (**Fig. 4).** A series of experiments were conducted for a number of different types of dynamic loadings and the performance characteristics of the system were established by comparison of the new remote monitoring system with a system which has had long-term use and multiple validations for LLNL seismological applications.

After validating the first prototype of the remote monitoring system, the system was deployed at the NIF construction site to monitor ambient ground motions over an extended period. Such a deployment provided for evaluation of system performance, including communications, power usage, and data

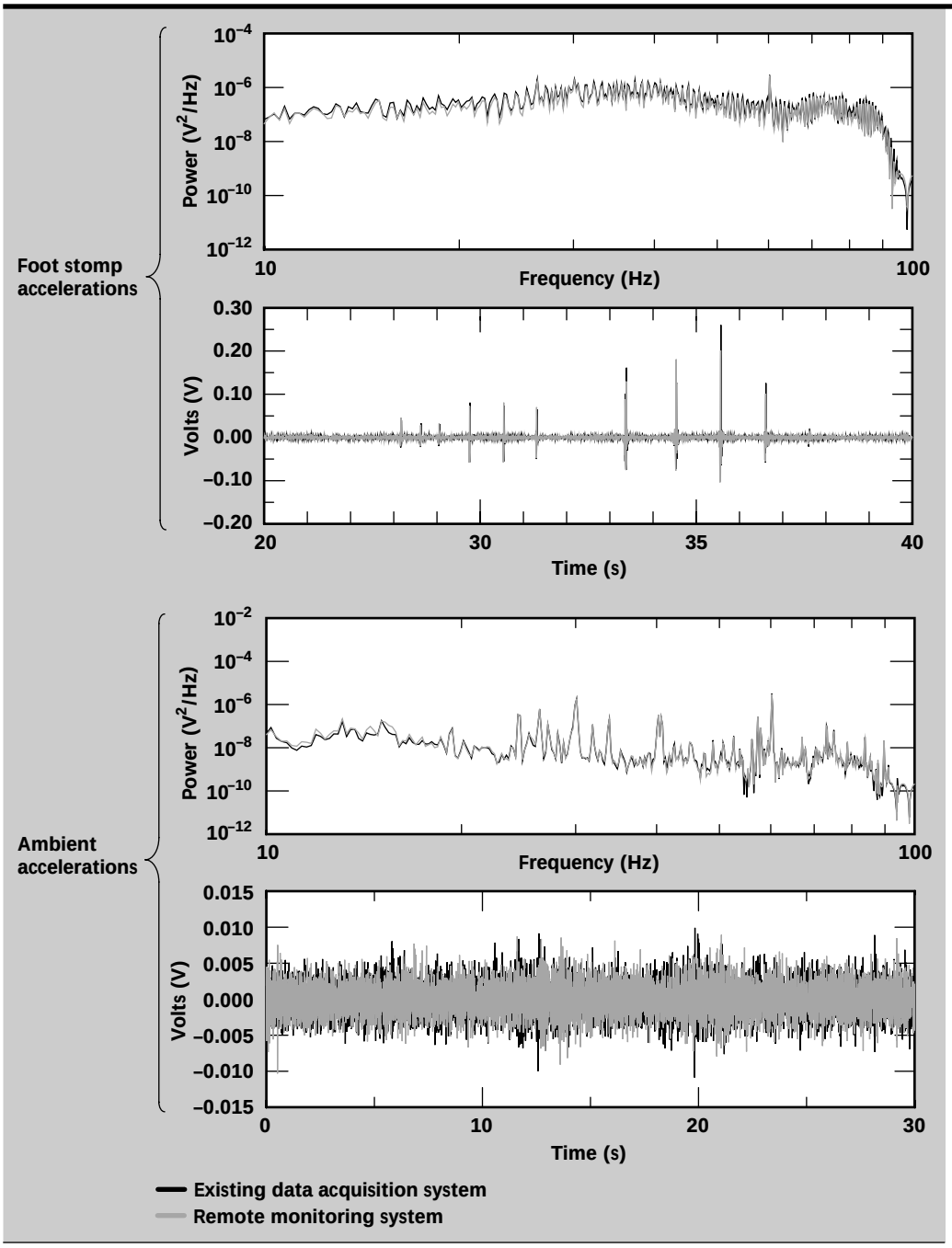

Figure 4. Power spectral density functions and time histories of existing data acquisition system and remote monitoring system for various loadings.

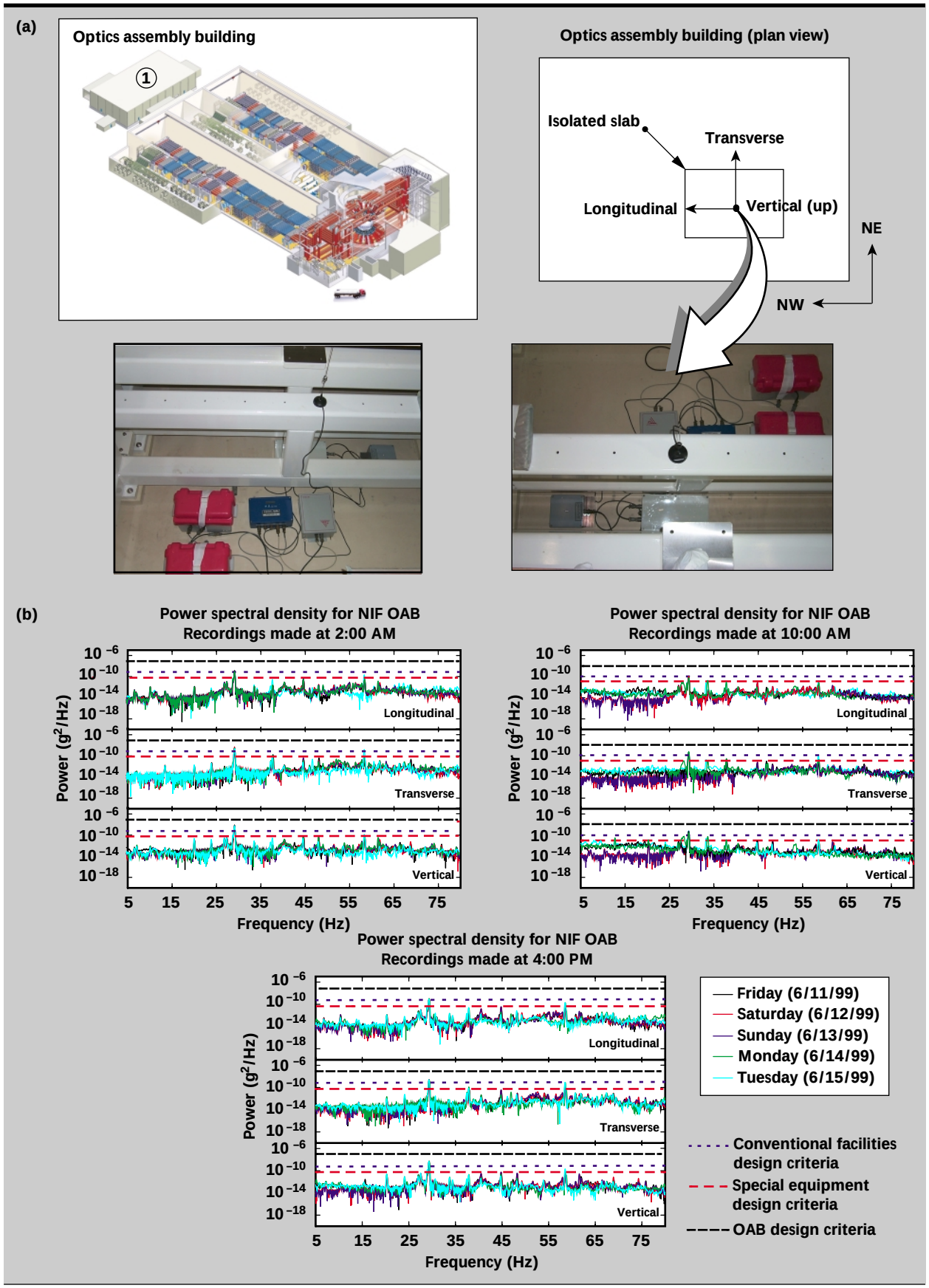

Figure 5. Measurements of ambient vibrations at LLNL's NIF. (a) Instrument locations; (b) measured vibrations at different times of the day.

transfer rates, and also provided important site specific data for validation of the NIF ambient vibration design criteria. The monitoring system was located in the Optics Assembly Building (**Fig. 5**), where the facility was at cleanroom Protocol 2 during the measurements and the access was limited. In addition, AC power was unavailable, so battery operation of the monitoring system was essential. The capability to remotely contact the system, to set recording starting and stopping times, and to download measured data, was essential for this application.

The ambient vibration measurements indicated that the site vibrations were generally within the NIF design specifications (**Fig. 5**). There were spikes in the power spectral density plots at 30 Hz and 60 Hz which were indicative of vibrations due to running equipment. As NIF construction progresses, ground vibration monitoring will continue and particular attention will be paid to the equipment frequency ranges.

Conclusion

An effective wireless system has been developed for monitoring large structural systems. This system provides a tool for practical acquisition of vibration data essential to understanding system response and validation of system computational models.

Underground Facilities Characterization

Rexford M. Morey
Laser Engineering Division
Electronics Engineering

Michael H. Buettner and William D. Daily
Electronics Engineering Technologies Division
Electronics Engineering

Neutralization of underground facilities (UGFs) is identified by the US military as a high priority because underground facilities may be used for the manufacturing and storage of weapons of mass destruction (WMD) or for other purposes of military importance. Effective neutralization and battle-damage assessment, especially in a hostile environment, requires the deployment of unattended sensor systems for detecting and/or imaging subsurface conditions. For the past several years geophysical techniques have been evaluated for solving this problem. However, seismic methods cannot provide the level of detail the military needs on the internal structure of UGFs.

Ground penetrating radar (GPR) has been used to investigate shallow subsurface situations. In many soil conditions the penetration depth of a single GPR unit is limited. Theoretical considerations and preliminary experiments indicate that a large array of simultaneously excited radar transmitters will substantially increase the depth of penetration (on the order of tens to hundreds of meters). To our knowledge, the design and deployment of a multi-element GPR array has not been done because of the cost, complexity and data-handling requirements. Several preliminary experiments were performed at tunnel sites at the Nevada Test Site (NTS) to evaluate the efficacy of GPR arrays to characterize underground structures. These tests included measuring the bulk conductivity of the rock and soil over UGFs, profiling a tunnel with a 25-MHz GPR system, deploying a small array of two synchronized GPR transmitters, and performing an electrical resistivity topography (ERT) survey over the same tunnel.

Introduction

Electromagnetic (EM) propagation through dispersive, inhomogeneous, and conductive materials, such as soil, rock, and biological tissue, is of continuing interest, especially when the goal is to "see" deeper targets with greater clarity. Currently, single-channel instruments, such as GPR, have a limited range of investigation in lossy media due to a limited equipment dynamic range or performance factor. However, new simulation and experimental evidence suggests that arrays of radar sensors could increase characterization depths of subsurface targets. The array would be composed of multiple, synchronized transmitters and/or receivers.

This report presents the initial steps of a new program to develop a core technology in high power arrays for 3-D image formation and visualization in dense media, such as the subsurface of the earth. The program is built on the extensive body of work at Lawrence Livermore National Laboratory (LLNL) in geophysics,[1–5] GPR imaging,[6–8] and laboratory measurements of EM properties of materials.[9] To determine the utility of high power ultra-wideband (UWB) arrays, "proof-of principle" experiments were performed. These experiments included EM measurements over tunnels at NTS.

Applications of high power arrays include characterizing UGFs, battle-damage assessment of targeted UGFs, detection and mapping of unexploded ordnance (UXO), and geophysical surveys, such as earthquake assessment and monitoring fluid flow. The deployment of a sparse multi-element UWB array, which includes multiple time-synchronized transmitters, has not been done before.

Progress

Electrical conductivity of soil and rock determines the depth of penetration of EM signals in these materials. High conductivity means limited penetration, low conductivity leads to greater penetration. Therefore, field measurements were made to get estimates of the bulk electrical conductivity of the rock at four sites at NTS. With this information estimates of the RF attenuation in the rock are calculated, and thus estimate the penetration depth of GPR at these sites.

Four areas at NTS were investigated: (1) the BEEF facility in area 4, (2) U-tunnel in area 12, (3) tunnel 16-A, and (4) tunnel 16-B. To measure the bulk conductivity we used a standard two-loop induction survey with a Geonics EM-34 tool. This system is designed to be used in the vertical dipole mode (coil lying on the ground surface) or the horizontal dipole mode (coils normal to the surface and coplanar). The instrument is designed to work with fixed loop spacings of 10, 20, and 40 m, and conductivity is read directly on a panel meter in mS/m. **Figure 1** shows the Geonics EM-34 being used at the BEEF facility.

Table 1 lists the measurement results at the four locations along with the estimated depth of penetration for a GPR operating at 25 MHz. **Figure 2** is a plot of maximum radar range as a function of electrical conductivity showing ranges to the tunnel sites. Available single-channel GPR systems have an advertised performance factor (Q) of about –110 dB. Improvements in Q, such as with multiple transmitters or signal processing, will increase depth of penetration.

Since Tunnel 16-B is an "active" tunnel being used as a test site by a number of investigators, and since reasonable penetration is predicted, GPR and ERT experiments were performed over this tunnel in September 1999. The GPR work used equipment rented from Sensors and Software, Inc. and was operated at 25 MHz. The ERT data acquisition system was developed at LLNL over a period of many years, and has been used successfully for a wide variety of imaging applications. Survey lines were established on the ground surface (**Fig. 3**), normal to the tunnel axis at overburden thicknesses of approximately 10, 12.5 and 20 m. The survey line at 12.5 m was used for ERT data collection.

The GPR equipment was assembled, set up, and tested. Profiles were collected along the 10- and 20-m lines, in the constant offset mode. That is, the transmitter and receiver were kept at a constant spacing (4 m) from each other, and the pair was moved in steps of 1 m along the survey line from 50 m on the east side of the tunnel to 50 m on the west

Figure 1. Electrical conductivity measurements at the BEEF facility, NTS.

Table 1. Results of electrical conductivity measurements at NTS.

Location	Rock	Conductivity (mS/m)	Estimated radar detection range* (m)
U-Tunnel	Dolomite	1.0 to 1.5	20 to 26
Tunnel 16-A	Ash-fall tuff	9 to 15	3.7 to 5
Tunnel 16-B	Limestone	2 to 2.4	14 to 16
BEEF	Gravel/soil	30 to 35	2.2 to 2.4

*Assumptions for GPR: 110 dB effective dynamic range, 25 MHz, metal mesh in roof.

side. At each survey point, the transmitter was fired many times, and the received signals were stacked (improves S/N) to produce a plot of received signal versus two-way travel time.

The resulting display is a series of these plots (one per survey point) slightly displaced from each other as one moves from left to right. When gain is applied to the data, the characteristic hyperbolic signature of a target (such as a tunnel) appears at about the right lateral position and depth, as shown in **Fig. 4**. The assumed dielectric constant for converting the time-scale to a depth-scale is 6, which is a reasonable value for moist rock. Our interpretation of **Fig. 4** is that the reflector at 10 m is from the top of the tunnel, while the reflectors above 10 m are moisture filled joints in the rock, joints created during tunnel construction. (There was a heavy rain about a week before this experiment.) Other reflectors appear in the data as well. A tunnel signature does not appear in the 20-m overburden profile, **Fig. 5**. These results are consistent with the predictions in **Fig. 2** for Q= –110 dB.

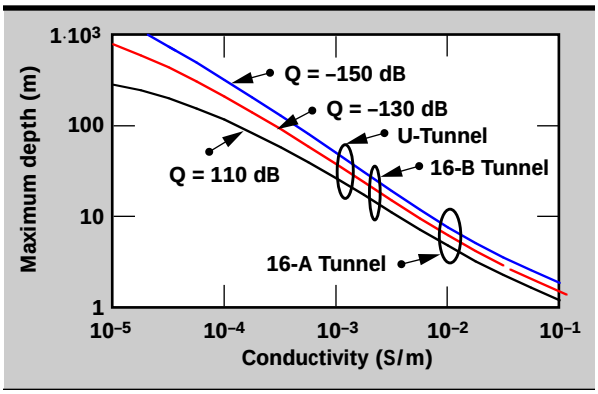

Figure 2. Calculated maximum depth as a function of electrical conductivity and performance factor.

Figure 3. GPR and ERT survey area over Tunnel 16-B, NTS.

The final GPR work used two transmitters instead of one as described above. The reasoning is that two transmitters will increase the returned radar signal from the tunnel. The initial experiment to verify this used a receiver placed over the tunnel axis with a transmitter 4 m to the west and another 4 m to the

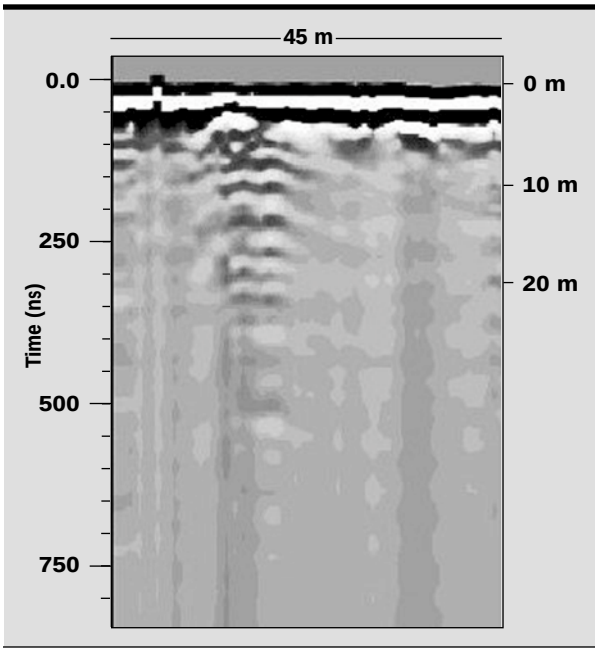

Figure 4. GPR profile at ~10-m overburden.

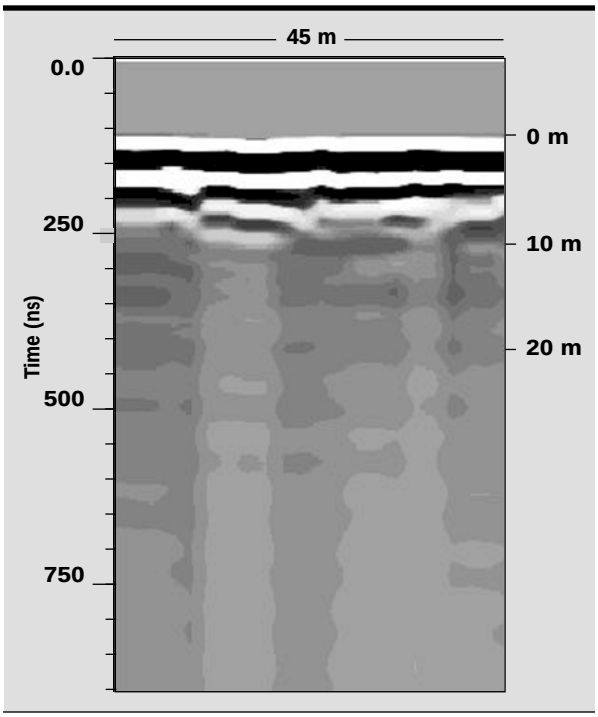

Figure 5. GPR profile at ~20-m overburden.

east of the receiver, as in **Figs. 6** and **7**. A special trigger circuit enabled control of the trigger delay between the two transmitters. This is necessary because the paths from the two transmitters to the receivers are not exactly identical in terms of velocity. Thus to get the tunnel-reflected pulses from the two transmitters to arrive at the receiver at the same time, one needs to adjust the trigger delay between the two transmitters.

The final measurement used a receiver placed over the tunnel axis with two transmitters 4 m to the east (next to each other or collocated) of the receiver, as diagrammed in **Fig. 8**. If our hypothesis about superposing the returns from two transmitters is correct, this experiment should have essentially the same result as that described in the previous paragraph.

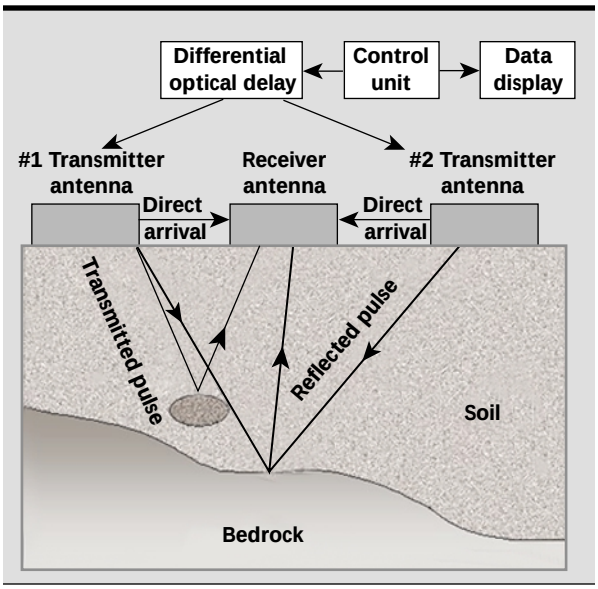

Figure 6. GPR setup using two transmitters.

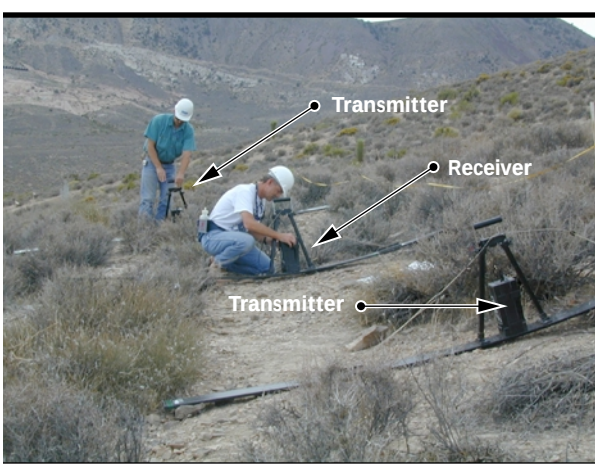

Figure 7. Photograph of three GPR antennas, two transmitters and one receiver.

The total variation in the differential trigger delay between the transmitters is about 30 ns. During the two-transmitter experiments, the differential trigger delay was incremented in 10 steps. For each delay-step, each transmitter was turned on and then off sequentially, then both transmitters were turned on together. **Figure 9** shows examples of the data for the two collocated transmitters over the tunnel. The upper panel displays the sequence of measurements for the 10 delay settings.

Interpretation involved looking for the strongest signal at a range of about 10 m, as shown in the lower left panel, where the tunnel reflections aligned in time for the three transmitter conditions, T × 1 on only, T × 2 on only, and then both on. The lower right panel shows the received GPR waveforms for these three transmitter conditions, plus the mathematical summation of T × 1 on and T × 2 on. Note that summing the two separate transmitter responses gives very similar results to having both transmitters on and time-synchronized at the target region.

The ERT survey was performed along the 12.5 m line. ERT data were collected using a 30-electrode array that extended from 145 ft (44.2 m) to the east of the tunnel axis to 145 ft. west of the tunnel axis. Data were also collected in the EOM mode in which the steel mesh and rock bolts in the tunnel are excited to some value of potential and the resulting potentials measured using the electrode array. **Figure 10** displays the two ERT inversions perpendicular to the tunnel axis.

The top image in **Fig. 10** is from data collected using only the 30 surface electrodes. The surface

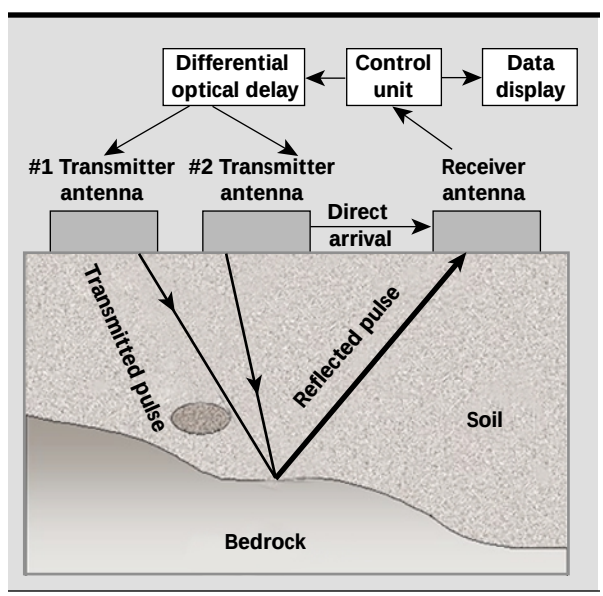

Figure 8. Diagram of two transmitters collocated.

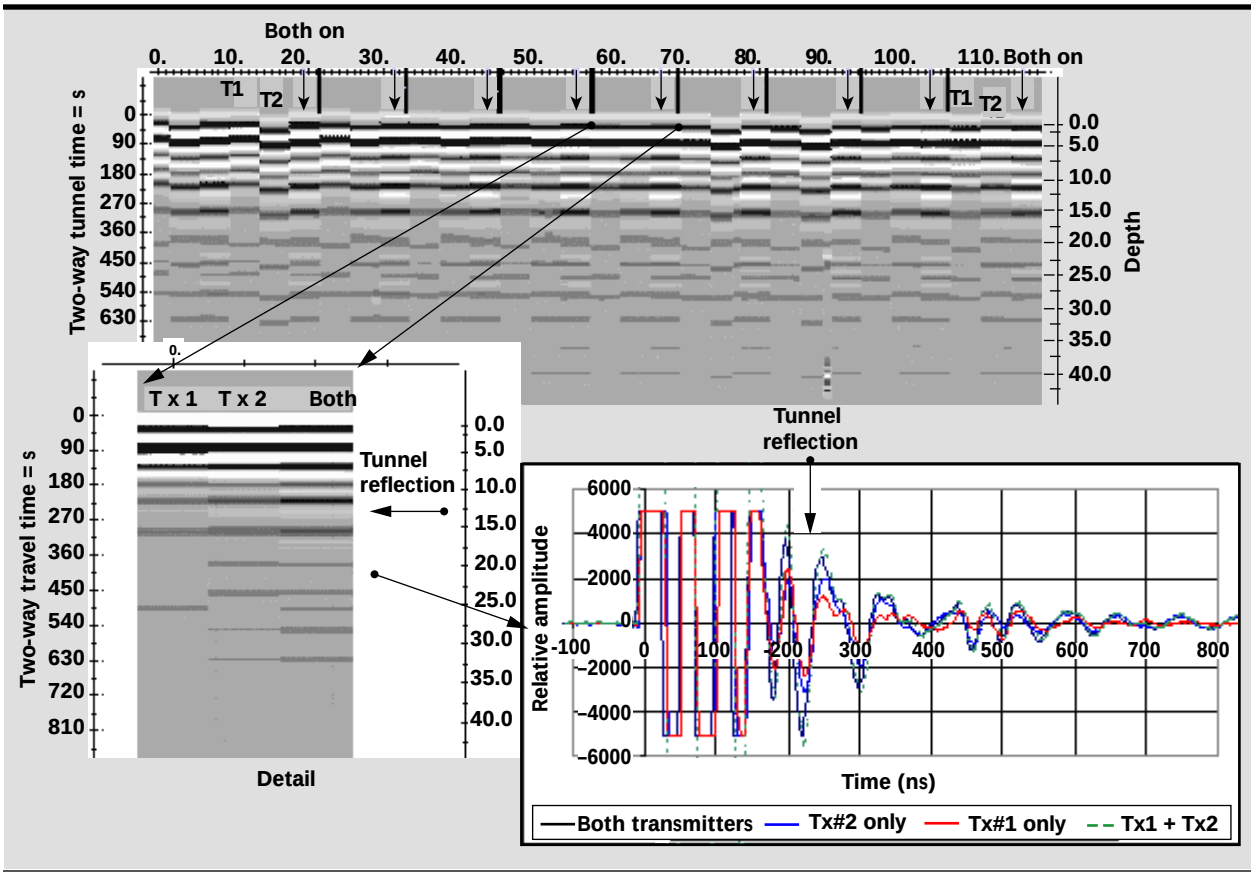

Figure 9. Examples of GPR data for the collocated transmitter experiments.

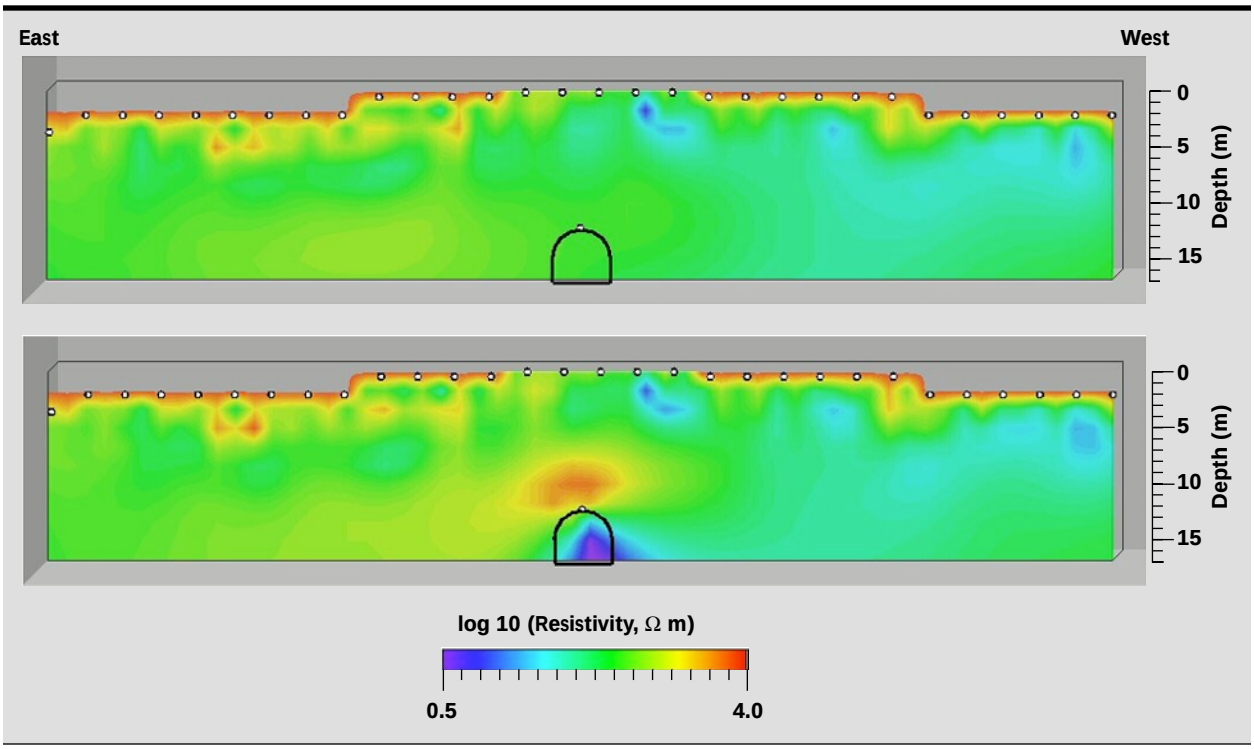

Figure 10. ERT profiles over Tunnel 16-B, NTS.

topography is approximated by the discrete steps formed by the mesh blocks in the top row. The approximate outline of the tunnel section is superimposed. The formation resistivity varies between about 50 to 3000 Ω m with the most resistive part in the dry surface material. We do not know what geological feature causes the prominent conductive anomaly above and to the right of the tunnel. In this image the greatest sensitivity is near the surface and decreases rapidly with depth. At the tunnel depth the sensitivity is obviously too small to detect any effect of the void or the metal on the walls.

The lower image was inverted from data collected using the 30 surface electrodes and the single electrode in the tunnel. This data was collected only to see what additional information could be generated in the image using the additional electrode. Notice that the reconstruction is essentially identical to the top image except near the tunnel. The additional information added by the tunnel electrode, although distorted by the lack of spatial coverage, does give some additional information. The resistive region above the tunnel is likely the dehydration of the rock mass (loss of water results in increased resistivity) as a result of the tunnel ventilation. This region extends all the way around the tunnel but only the upper part is imaged here because of the way the electrode array is arranged. The conductive region below the electrode is likely the distorted image (again because of the electrode arrangement) of the wire mesh in the tunnel.

Summary

The GPR data indicate that (1) the tunnel was detectable at 10 m depth of overburden, but not at 20 m depth, and (2) two transmitters can be triggered properly so that additional energy can be put on target as indicated by a larger radar return. Without the additional electrode in the tunnel, the ERT survey did not detect any effect of the tunnel void or the metal in the tunnel.

Future Work

Groups both inside and outside LLNL are showing interest in multi-element UWB arrays. As an example, a presentation was made to DARPA on using UWB arrays for UGF characterization. Present day GPR will not reliably detect deep UGFs. Experimental studies indicate that a large GPR array will increase radar range to a level that will interest DARPA and also DTRA. These programs and others will be pursued.

References

1. R. J. Lytle and D. L. Lager (1972), "Electromagnetic propagation, transmission, reflection, and refraction: equations and numerical results," Lawrence Livermore National Laboratory, Livermore, California (UCRL-51245).

2. R. J. Lytle, E. F. Laine, D. L. Lager, and D. T. Davis (1979), "Cross-borehole electromagnetic probing to locate high-contrast anomalies," *Geophysics*, Vol. **44**, No. 10, October.

3. W. Daily, A. Ramirez, D. LaBrecque, and J. Nitao (1992), "Electrical resistivity tomography of vadose water movement," *Water Resource Research*, Vol. **28**, pp. 1429–1442.

4. S. D. Nelson and E. Johansson (1995), "Single pass surface-to-borehole reconstruction," Lawrence Livermore National Laboratory, Livermore, California (UCRL-53868-95).

5. A. Ramirez, W. Daily, M. Butner, and D. LaBrecque (1997), "Electrical resistivity monitoring of the thermomechanical heater teat in Yucca Mountain," *Proc. of the Symp. on the Appl. of Geophysics to Eng. and Environmental Problems*, Reno, Nevada, Vol. **1**, pp. 11–20.

6. S. D. Nelson (1994), "Electromagnetic modeling for ground penetrating radar using finite difference time domain modeling codes," *Proc. on Advanced Microwave and Millimeter Wave Detectors, SPIE Proceedings*, Vol. **2275**, July.

7. J. E. Mast and E. M. Johansson (1994), "Three-dimensional ground penetrating radar imaging using multi-frequency diffraction tomography," *Proc. on Advanced Microwave and Millimeter Wave Detectors, SPIE Proceedings*, Vol. **2275**, July.

8. E. M. Johansson *et al.*, "Three-dimensional ground penetrating radar imaging using synthetic aperture time domain focusing," *Proc. on Advanced Microwave and Millimeter Wave Detectors, SPIE Proceedings*, Vol. **2275**, July.

9. J. J. Roberts, E. Carlberg, and W. Lin, " Electrical properties of tuff from the ESF as a function of water saturation and temperature," Lawrence Livermore National Laboratory, Livermore, California (UCRL-ID-129594).

Raymond P. Mariella, Jr., Center Director

The mission of the Center for Microtechnology is to invent, develop, and apply microtechnologies with the Lawrence Livermore National Laboratory (LLNL) programs in global security, global ecology, and bioscience.

Our capabilities cover materials, fabrication, devices, instruments, or systems which require microfabricated components, including microelectromechanical systems (MEMS), electronics, photonics, microstructures, and microactuators. Much of our microtechnology work revolves around our microfabrication facility. We also rely upon LLNL's precision manufacturing and characterization facilities in plastics and glass. Moreover, we incorporate modeling to assist the design of our instruments. An example of this is the report on the experimental testing and theoretical modeling of highly-filled polymers.

Our work is driven principally by the applications of LLNL programs, and, to a lesser extent, by external applications. For both of these we must have multidisciplinary teams to deliver complete solutions to the problems. The Center for Microtechnology includes more than 60 people, who have training in electronics engineering, mechanical engineering, chemical engineering, chemistry, physics, and the biosciences. Our recent successes in analytical instrumentation reflect our broad, multidisciplinary base.

We continue to show a very high rate of return on investment with a total budget of roughly $17M, including $0.55M of Tech-Base projects. We have successfully performed collaborations with industry, and we have achieved considerable national recognition for the successes we have demonstrated in our Chem-Bio Nonproliferation (CBNP) Program instrumentation, supported by the DOE and the Defense Intelligence Agency. In April of 1999, we published a highlighted article in *Science* on the fastest polymerase-chain-reaction (PCR) detection, starting with 1000 bacterial cells—seven minutes for automated detection. (The technology for this PCR instrument was invented under Engineering TechBase funds.)

The support for our work on detection instruments for the CBNP program has grown significantly for FY-00. As the applications for microtechnology continue to grow, we continue to perform activities to fulfill the needs of our LLNL and external partners and stay in a leadership position, both nationally and world-wide.

The small, previous TechBase investments in Microtechnology have paid off this year:

1) highlighted article in *Science* on the performance of the LLNL PCR instrument;
2) article in *Science* on Protein-DNA interactions in the flow cell built and operated by Microtechnology personnel;
3) laboratory success in DARPA-funded dielectrophoresis technology for blood cells;
4) optical interconnects in partnership with the Photonics Program–significant demonstration of multiple-wavelengths carried per fiber;
5) a large CRADA with semiconductor houses for EUV lithography—we have expanded our facilities to accommodate this work, and the semiconductor industry has selected EUVL as the follow-on technology on their roadmap;
6) collaboration with UCLA on wireless sensors.

Articles in this report are: 1) Exploration of Novel Fabrication Methods for Microfuidics/ Microelectromechanical Systems Devices; 2) Microtechnology for High-Explosive Testing; 3) Improved Microgripper Process; 4) Miniature Sample Collector/Concentrator for Biological Weapons Agent Detectors; 5) Microfabricated Deformable Mirrors for Adaptive Optics Applications; 6) High-Voltage Photovoltaics; 7) Microfabricated Flow Cell for DNA Analysis; 8) Microvalves for Microcatheters; 9) Microelectromechanical-Systems-Based Fuel Cell for Microscale Energy; 10) Custom Silicon Etching; 11) Micromechanical Characterization Tools for Highly-Filled Polymers; 12) Advanced Imaging Catheter; 13) Intelligent Wavefront Reconstructors for Adaptive Optics; 14) Lambda Connect: Multiwavelength Technologies for Ultrascale Computing; 15) Low Power Wireless Modem Technology; 16) Wireless Micropower RF Components; and 17) Acoustically-Driven Microfluidic Systems.

Center for Microtechnology

2

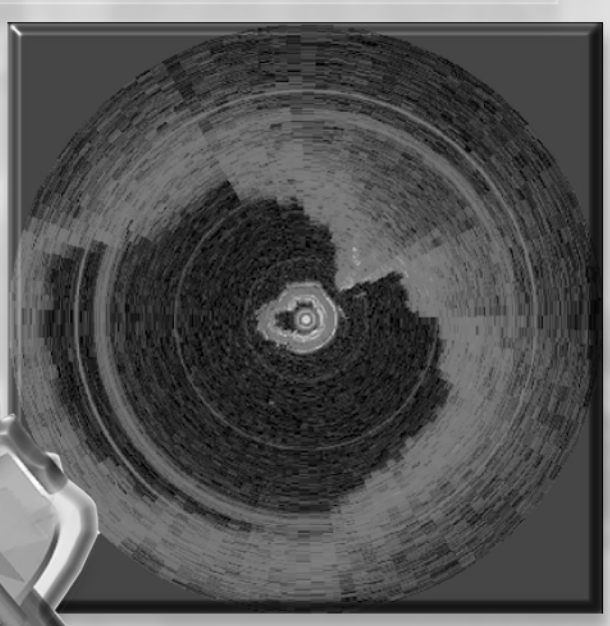

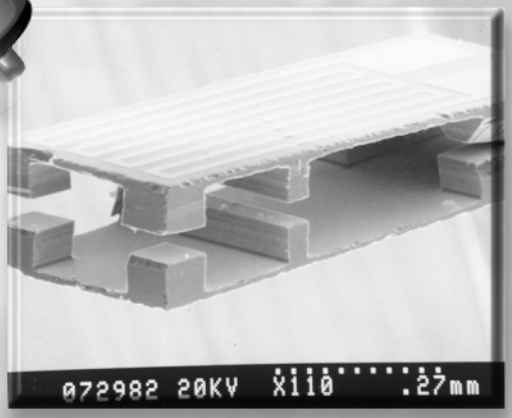

2. Center for Microtechnology

Overview
Raymond P. Mariella, Jr., Center Director

Exploration of Novel Fabrication Methods for Microfluidics/Microelectromechanical Systems Devices
Harold D. Ackler, Julie Hamilton, William J. Benett, and Thomas E. Shell 2-1

Microtechnology for High-Explosive Testing
Dino R. Ciarlo, Kirk P. Seward, Mehdi Balooch, and Scott E. Groves 2-3

Improved Microgripper Process
Dino R. Ciarlo, Abraham P. Lee, Dawn L. Hilken, and Jimmy C. Trevino 2-7

Miniature Sample Collector/Concentrator for Biological Weapons Agent Detectors
Jonathan Simon 2-9

Microfabricated Deformable Mirrors for Adaptive Optics Applications
June Yu, James A. Folta, Peter Krulevitch, Harold D. Ackler, Scot S.Olivier, and William D. Cowan 2-11

High-Voltage Photovoltaics
Jeffrey D. Morse, Gregory A. Cooper, and Karla G. Hagans 2-15

Microfabricated Flow Cell for DNA Analysis
Peter Krulevitch and Laurence R. Brewer 2-19

Microvalves for Microcatheters
Kirk P. Seward, Amy W. Wang, and Abraham P. Lee 2-21

Microelectromechanical-System-Based Fuel Cell for Microscale Energy
Jeffrey D. Morse and Alan F. Jankowski 2-23

Custom Silicon Etching
Jeffrey D. Morse, Leslie M. Jones, and Robert T. Graff 2-27

Micromechanical Characterization Tools for Highly-Filled Polymers
Scott E. Groves, Steve J. DeTeresa, Bruce J. Cunningham, Dino R. Ciarlo, David Allen, K. Clayton, and C. Yoon . 2-31

Advanced Imaging Catheter
Amy W. Wang, Abraham P. Lee, Daniel L. Schumann, Luiz Da Silva, Matthew J. Everett,
Billy W. Colston, Jr., Steve B. Brown, Dale L. James, Richard A. London, and Peter Amendt 2-41

Intelligent Wavefront Reconstructors for Adaptive Optics
Chi Yung Fu, George F. Chapline, Scot S. Olivier, and Loren I. Petrich 2-45

Lambda Connect: Multiwavelength Technologies for Ultrascale Computing
Michael C. Larson, Steven W. Bond, Michael D. Pocha, Mark A. Emanuel, and Mark E. Lowry 2-49

Low Power Wireless Modem Technology
Charles F. McConaghy and Charles Chien 2-57

Wireless Micropower RF Components
Charles F. McConaghy 2-59

Acoustically-Driven Microfluidic Systems
Amy W. Wang, William J. Benett, Christopher D. Fuller, and Richard G. Couch 2-63

Exploration of Novel Fabrication Methods for Microfluidics/Microelectromechanical Systems Devices

Harold D. Ackler and Julie Hamilton
Electronics Engineering Technologies Division
Electronics Engineering

William J. Benett
New Technologies Engineering Division
Mechanical Engineering

Thomas E. Shell
Materials Science and Technology Division
Chemistry and Materials Science

We have developed a preliminary capability for fabricating microdevices from different glass and ceramic material systems. This project provided more flexible fabrication routes to expand the number of device designs accessible by the Center for Microtechnology staff and customers at Lawrence Livermore National Laboratory (LLNL).

Introduction

We investigated potential uses of commercial materials technologies, used in the fabrication of microelectronic packages and planar waveguides for photonic devices, for microfluidics and microelectromechanical systems (MEMS) fabrication. General processes addressed include the fabrication of channels with or without electrodes and bonding the materials together. Materials to be studied are thick glass films and multilayers deposited on alumina substrates via dip-coating of glass slurries, which are then densified and channels etched therein, multilayer ceramics fabricated from ceramic tapes with channels and vias which may include screen-printed metal conductors, and the photostructurable glass Foturan™. The point is to explore how the selection of materials and sequencing of process steps may enable the fabrication of devices with as-yet unimagined functionality. Some materials may enable certain aspects of device packaging, for example fluidic and electronic interconnects, to be integrated into the device.

If LLNL's Center for Microtechnology were able to develop a suite of device fabrication methods that offered adequate flexibility to essentially make whatever an engineer wanted, then the initial emphasis in device and system development would shift from "what can we make?" to "what do we want?" By conducting this exploratory work with a team of materials researchers oriented to the needs of the Center for Microtechnology staff, not only may materials solutions to current limitations be discovered, but also new uses for "old" materials technology may arise.

Progress

Deliverables for this project included the following: (1) an evaluation of the viability of the above materials (microelectronic packaging materials, glasses other than Pyrex™) for microfluidic device fabrication; (2) process to fabricate multilayer ceramics, with channels and holes, from ceramic tapes; (3) process to bond the above materials. Measures of success: a new process that enables the fabrication of more functional devices, or current devices with reduced difficulty.

Dip-Coated Glass Films

Glass films have been deposited by dip-coating a glass slurry onto alumina substrates with patterned metal electrodes, then firing to densify the slurry coat. Channels were then etched into the glass film, their thickness determined by the film thickness as expected. The film thickness was only 5 µm for a single dip-coat. A means of producing thicker dip-coated glass layers on substrates was developed by patterning a thick layer of SU-8 photopatternable epoxy onto a substrate (patterned with metal) where channels are to be. The substrate is coated with an excess of glass slurry and the excess "squeegeed" off above the SU-8 features. The SU-8 thus acts like a mold, and is burned off during firing of the glass layer to leave the desired channels in the glass layer. However, more sophistication is required to produce glass films of very uniform thickness.

Photopatternable Metal and Dielectric Pastes

Photopatternable dielectric paste and gold paste (Fodel™ from DuPont) were screen printed and dried (by offsite vendor) on alumina substrates. Those coated with dielectric were prepatterned with metal electrodes. Pastes were photolithographically patterned and developed to form electrodes in the gold film, and channels in the dielectric film whose depth was determined by the dielectric layer thickness (25 µm) with the prepatterned electrodes in the channel bottom. The dielectric films were fired to densify the ceramic material. Screen printed, photopatternable conductor paste was successfully patterned and fired on commercial alumina substrates. The minimum resolvable feature size appears to be in the 30 to 50 µm range.

Green Tape

Channels and vias have been hand cut in ceramic green tapes. More precise features were formed by laser cutting green tape. Multilayer channel structures have been formed in laminated ceramic green tape and fired. Layers of tape have also been laminated to 0317 glass and fired. However, the moderate mismatch in thermal expansion (2 to 3 ppm/°C) is enough to cause deformation and/or cracking of the glass. A potential means of incorporating electrical connectors into a multilayer device formed from green tape has been designed. An initial attempt was made to fabricate such a structure, but deformation during firing of the multilayer tape structure rendered the part useless. The structure may be constrained during firing to prevent this, but it has not been tried.

Bonding

The bonding of Corning code 0317 glass to the commercial alumina substrates patterned with screen printed, photopatternable dielectric paste has been determined to be a nonviable process. While it is possible to achieve adherence of the glass to the dielectric layer, the moderate mismatch in thermal expansion (2 to 3 ppm/°C) between the glass and alumina substrate is enough to cause either spallation of the dielectric layer from the alumina or severe cracking of the glass. Substrates (glasses, ceramics) may be bonded at 600 to 650 ºC if a thin layer of dip-coated glass (VIOX Corp. no. 12922) is between them. However, coefficient of thermal expansion mismatches must be very small. This process works very well for bonding code 0317 glass to Foturan™.

Smoothing Foturan™ Surfaces

A thin layer of dip-coated glass, when fired, was observed to smooth the roughness of etched Foturan™ significantly. However, the magnitude of the remaining roughness was not quantified.

Future Work

No actual devices were fabricated during this project. Many of these processes are well suited to the fabrication of microfluidic devices, so the next stage of this work is to develop the details of routes to fabricate working devices with these materials.

Microtechnology for High-Explosive Testing

Dino R. Ciarlo and Kirk P. Seward
Electronics Engineering Technologies Division
Electronics Engineering

Mehdi Balooch
Materials Science and Technology Division
Chemistry and Materials Science

Scott E. Groves
Manufacturing and Materials Engineering Division
Mechanical Engineering

We have used a high aspect ratio probe in an atomic force microscope to obtain images of the surface morphology of mock high explosives. This probe has a diameter of 0.2 µm and a length of 2 µm, which allows it to fit between the individual crystals of the material. In addition, a silicon force transducer for determining the viscoelastic properties of binder material has been built and tested.

Introduction

To better understand the material properties of composite materials it is necessary to measure the individual properties of the constituents as well as the adhesive forces between them. As an example, in the high-explosive (HE)—binder system, one would like to know the properties of the binder and the individual HE crystals as well as the adhesive forces between these two components. Groves *et al.*[1] discusses how this information can be used to develop models to predict the behavior and aging of such composites.

A relatively new technique uses atomic force microscopy (AFM) and nano-indentation to measure the modulus and the viscoelastic properties of a material on a microscale. Unfortunately most of the available probes for this work have large cone angles (60° to 90°), making it difficult to probe material that is thinly sandwiched between taller structures. In addition, the probes are designed to apply micronewtons (µN) of force instead of nanonewtons (nN). Microfabrication techniques can be used to provide these special probes and force transducers.

Progress

Plastic bonded explosives are composed of approximately 95% HE crystals and 5% binder. The crystal sizes tend to be in the 10- to 50-µm range and the space between crystals can be in the 2- to 5-µm range. To get a true representation of the surface morphology using an AFM, the probe must be capable of extending down in between the HE crystals. Standard AFM probes have very sharp tips, but they have large cone angles, as shown in **Fig. 1**. This prevents them from reaching down in between the HE crystals.

Recently, high aspect probes became available from Digital Instruments. They are called FISpike Probes and are fabricated using a focused ion beam to obtain the high aspect ratio. **Figure 2** is an SEM of one of these probes showing a shaft diameter of 0.2 µm and a length of 2 µm. We used this to probe the binder material in between the crystals in mock HE material (cyanuric acid). **Figures 3** and **4** show two images taken of this mock HE. The **Fig. 3** scan is with a standard AFM probe; **Fig. 4** is taken with the high aspect ratio probe, at a much higher resolution.

Ultimately the plan is to find an area of binder material between HE crystals and to measure the viscoelastic properties of this binder by recording the displacement versus time for a constant applied force. To do this, the force in the nN range needs to be measured and displacements of tenths of a micron need to be recorded. This is a challenge for most commercially available force transducers.

Figure 5 is a photograph of a silicon force transducer we built and tested. Four silicon cantilever beams hold the central 3-mm-×-3-mm silicon platform. Each beam is 500 µm wide, 3.4 mm long and 0.1 mm thick. The force versus distance for this transducer was measured using a differential variable-reluctance transducer (DVRT) made by MicroStrain. The results are

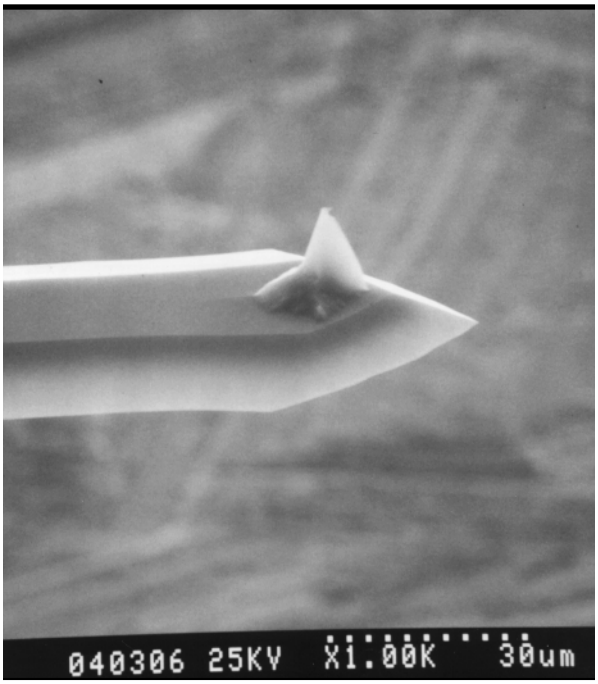

Figure 1. SEM of a standard AFM probe with a large cone angle.

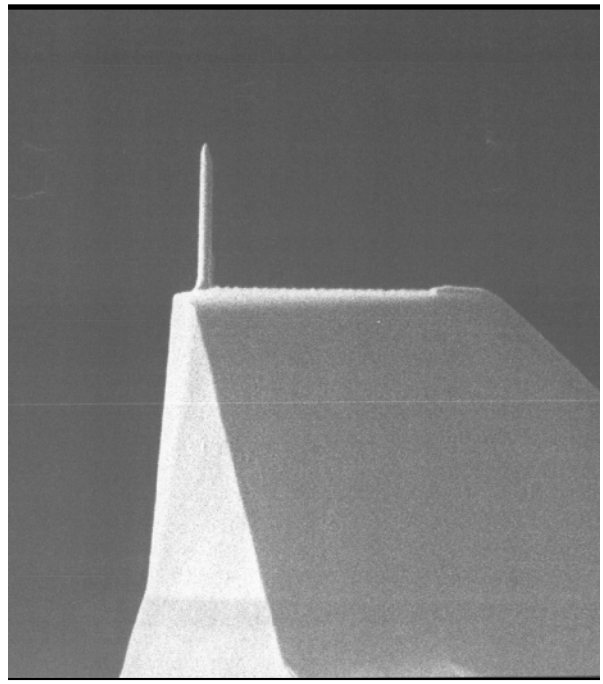

Figure 2. SEM of a high aspect ratio AFM probe. The diameter of the probe is 0.2 µm and the length is 2 µm.

Figure 3. SEM scan of mock HE taken with the standard AFM probe shown in Fig. 1.

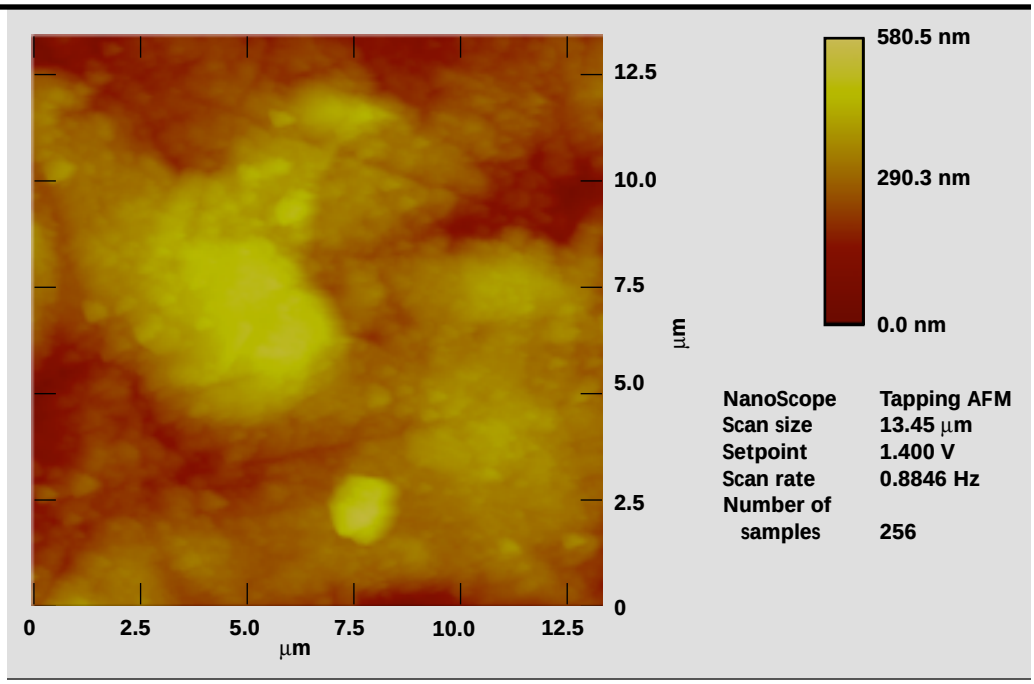

shown in **Fig. 6**. The advantage of this type of silicon transducer is that the motion of the 3-mm-×-3-mm silicon plate is piston-like, without tilt. The motion of this plate can be measured by sensing the change in capacitance between the moving plate and a reference ground. The equation governing the deflection of the cantilevers is:

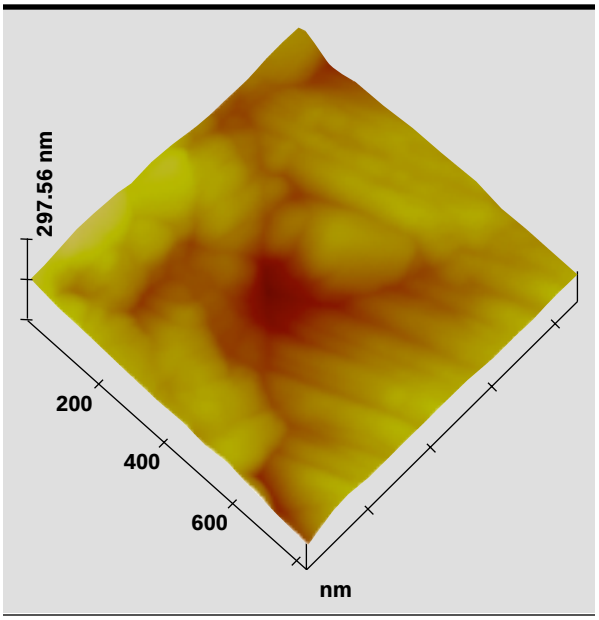

Figure 4. SEM scan of mock HE taken with the high aspect ratio probe shown in Fig. 2.

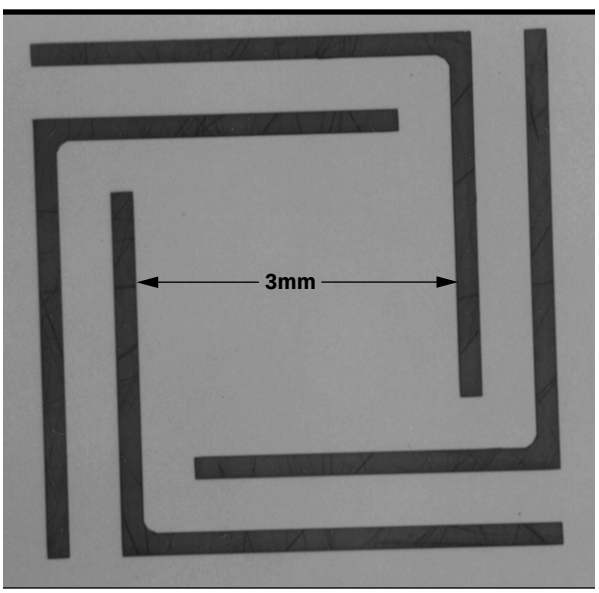

Figure 5. Planar view of a silicon force transducer consisting of a 3-mm-×-3-mm silicon plate supported by four silicon cantilever beams.

$$F = \frac{EB}{4}\left(\frac{H}{L}\right)^3 X, \qquad (1)$$

where

F = force at the cantilever end (N)
X = cantilever deflection (mm)
E = silicon modulus (1.8×10^5 N/mm^2)
B = cantilever width (0.5 mm)
H = cantilever thickness (0.1 mm)
L = cantilever length (3.4 mm)

In **Eq. 1**, the spring constant for the force transducer can be considered to be:

$$\frac{EB}{4}\left(\frac{H}{L}\right)^3. \qquad (2)$$

For the values listed, **Eq. 1** reduces to:

$$F = 0.6\,X. \qquad (3)$$

Since there are four of these cantilevers supporting the central 3-mm plate, the relation between the force on this plate and its displacement is:

$$F_T = 2.4\,X. \qquad (4)$$

The data taken in **Fig. 6** shows a spring constant of 1.4 as opposed to 2.4 in **Eq. 4**. The difference, less than a factor of two, can be accounted for by errors in the true dimensions of the fabricated transducer.

For the transducer design shown in **Fig. 5**, a force of 100 µN will cause a deflection of 71 nm. To get a nanometer deflection with a nanonewton force, the spring constant needs to be lowered by a factor of 100. This can be easily accomplished by halving the value of the thickness (H) and the width (B) and by lengthening the cantilevers by 50%.

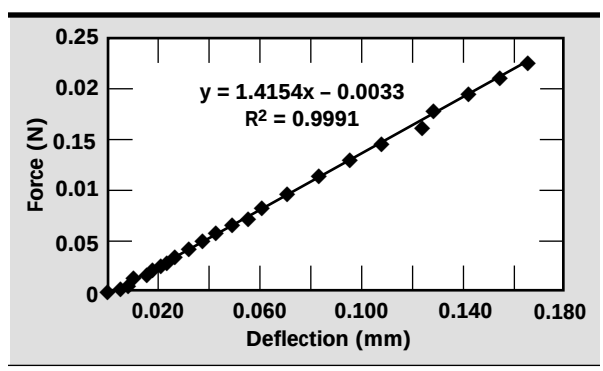

Figure 6. Force versus deflection measurements of the force transducer shown in Fig. 5.

Future Work

The next logical task is to build the nanonewton force transducer and combine it with the commercially available high aspect ratio probes. The viscoelastic properties of composite materials can then be measured.

Reference

1. S. Groves, S. DeTeresa, B. Cunningham, D. Ciarlo, D. Allen, K. Clayton, and C. Yoon (1999), "Micromechanical characterization tools for highly-filled polymers," *Engineering Research, Development and Technology*, Lawrence Livermore National Laboratory, Livermore, California (UCRL-53868-99).

Improved Microgripper Process

Dino R. Ciarlo, Abraham P. Lee, Dawn L. Hilken, and Jimmy C. Trevino
Electronics Engineering Technologies Division
Electronic Engineering

A deep etch RIE silicon process has been used to simplify the fabrication of a silicon microgripper. The microgripper is 1 mm long, 0.2 mm wide and can grip objects as big as 110 µm with a force of 13 mN.

Introduction

Several years ago, a silicon-based microgripper[1] was developed at Lawrence Livermore National Laboratory (LLNL). This microgripper had many uses, including the delivery of coils for the treatment of aneurysms and the manipulation of very small parts. The overall size of the microgripper is 0.2 mm × 1.0 mm, with a gripper opening of 100 µm. The gripper action is actuated by shaped-memory-alloy (SMA) films, deposited on silicon cantilever beams. The original microgripper was fabricated using silicon etch-stop technology to define the thickness of the gripping cantilevers. This report describes a simplified microgripper fabrication process.

Progress

Following the installation of the STS deep silicon etcher in LLNL's Microfabrication Laboratory, it was evident that the fabrication of the Lee microgripper could be simplified. **Figure 1** is a cross-sectional view of the simplified fabrication procedure. The simplification comes in the step shown in **Fig. 1b** where the thickness of the gripping cantilever is defined by a controlled STS etch instead of the more complicated wet-etch-stop procedure. The etch rate for silicon using the STS etcher is 5 µm/min, so the cantilever thickness can be controlled by etching 100-µm-thick wafers for 18 min. Following the cantilever formation, the two halves of the microgripper are bonded together using a gold eutectic. The final microgrippers are then defined by a sawing operating which establishes the length and width of the microgripper. **Figure 2** shows three SEM views of an assembled microgripper.

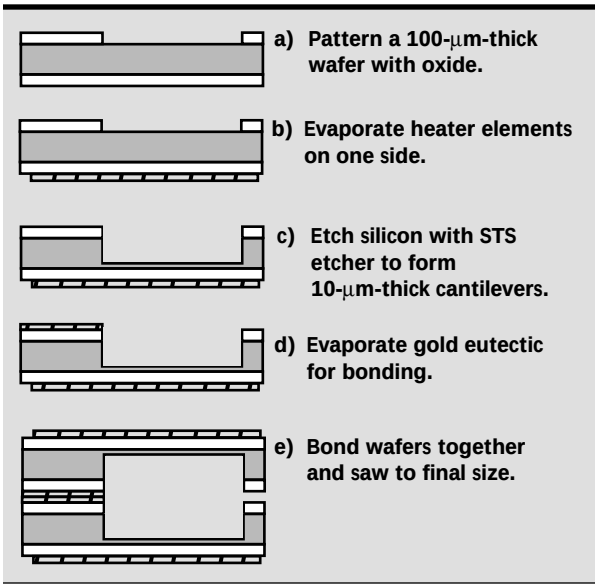

Figure 1. Cross-sectional view of the improved microgripper process.

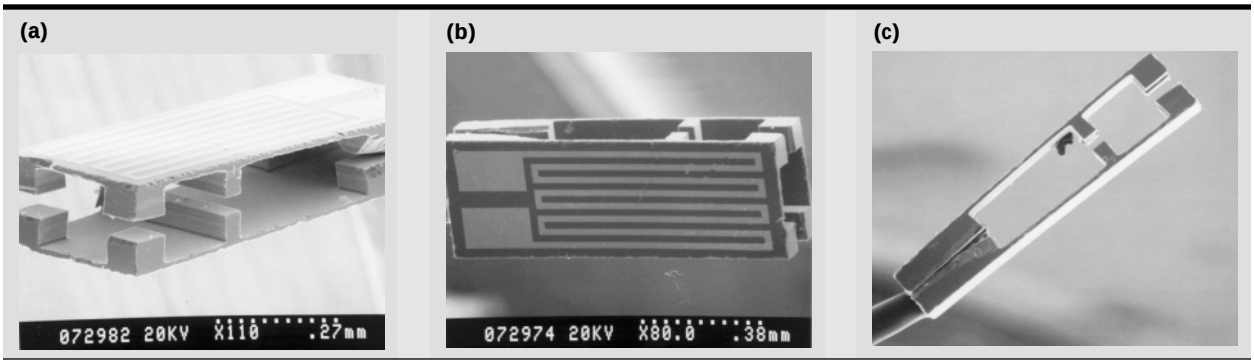

Figure 2. Three SEM views of a completed microgripper, 1 mm long by 0.2 mm wide. The serpentine gold pattern is used to heat the shaped memory alloy actuator.

Future Work

To save time, the above process did not include the SMA films, since the purpose was to demonstrate the timed etch in the STS deep etcher. To fabricate a fully-functional microgripper, this SMA actuator needed to be applied to the silicon cantilevers.

Reference

1. A. P. Lee, D. R. Ciarlo, P. A. Krulevitch, S. Lehew, J. Trevino, and A. M. Northrup (1996), "A practical microgripper by fine alignment, eutectic bonding and SMA actuation," *Sensors and Actuators A* **54**, pp. 755–759.

Miniature Sample Collector/Concentrator for Biological Weapons Agent Detectors

Jonathan Simon
Center for Microtechnology

Miniature aerosol samplers are desired by the nonproliferation community to detect the use of biological weapons consisting of aerosolized pathogens such as bacterial spores. A prototype miniature collector has been developed which decouples the sampling time from the final sample volume, allowing for greater concentration of trace pathogens. The device would be used at the front end of a portable biological weapons agent detection system.

Introduction

As the threat of biological weapons (BW) increases, both in military theaters and on civilian populations, the need for portable systems for the rapid analysis of pathogenic organisms becomes increasingly important. At the front of any system for the detection and characterization of biological agents is a sample collector. This can take the simple form of a swab for solid surfaces, or as in the case of airborne pathogens, an aerosol sample collector used to collect and concentrate particles into a liquid sample volume for subsequent analysis. An aerosol sampler is most appropriate for continuous monitoring scenarios, where repeated swabbing of settled particles is impractical.

The agents to be sampled are in the form of respirable particles with sizes in the range of 1 to 10 µm. Commercial sample collectors now available for field use are large, power-hungry, and typically produce sample volumes of many milliliters. Prototypical portable fieldable systems use assays that analyze much smaller sample volumes, typically <100 µL. Collector technology, however, has not entirely kept pace with this trend towards miniaturization, and present milliliter samples must be subsampled, reducing sensitivity, or preconcentrated, increasing complexity and the probability of breakdown.

Several commercial collectors use a thin film of liquid to capture target particles. Current designs generally have a lower limit to their sample collection volume because they send captured particles to a reservoir in a continuous stream. In the case of a low concentration sample, this leads to a large sample volume since the sampling time must increase to capture enough particles to be detected. Typical sample collectors provide for concentration factors of 104 to 106. That is, one particle per liter of air yields 103 particles per milliliter of solution, after a set time for collection. Subsampling for a miniature detector can reduce the number of organisms available for analysis by a factor of 10 or more.

Progress

During FY-99, we developed a prototype low power, miniature sample collector which concentrates the sample into a volume <100 µL. Its major advantages over existing samplers are: (1) decoupling of sample volume and sample time, making it very attractive for low (air) concentration samples; (2) miniature size and low weight, making it easily portable; (3) low power consumption, also adding to portability and ease of deployment; and (4) low noise operation. The prototype device is very quiet.

Our design (patent pending[1]) uses a two-step process to capture respirable particles in a way that decouples sample concentration from final sample volume. An illustration of the concept of the device is shown in **Fig. 1**. The heart of the system is the capillary surface, which consists of a cylinder of material with an array of vertical slits. These slits are connected to a supply reservoir, and fill with water by capillary action. This provides a wetted surface of prescribed volume which captures particles present in the air, and makes the sample volume independent of sample time.

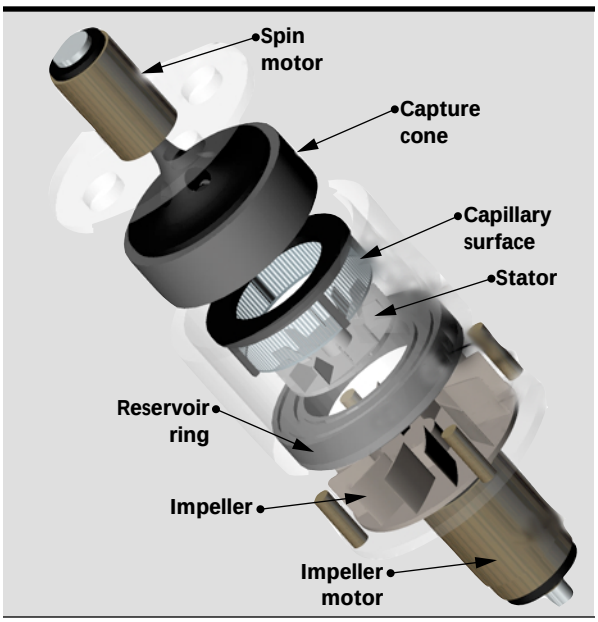

Figure 1. Illustration of the concept of the miniature aerosol sample collector.

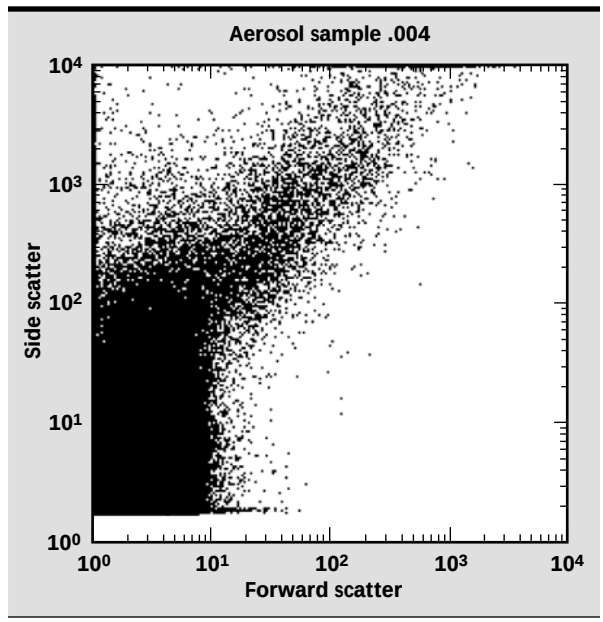

Figure 2. Flow Cytometer scattering plot of sample, indicating 300,000 particles in sub-micron to several micron size range.

In the first step of operation (inspiration), which may last for several minutes, an impeller draws turbulent air (>200 L/min at 2 W of power consumption) through the device and over the capillary surface, collecting and concentrating particles present in the air. An optional stator turns the flow towards the surface to increase likelihood of capture at the expense of throughput. The capillary channels are connected to a central reservoir which also replenishes the capillary fluid as it evaporates. The channels arranged around the perimeter yield a total volume <100 µL with a wettable area of several cm^2.

In the second step (spin), the upper portion of the device consisting of the capillary surface and the capture cone is spun, and the sample volume is forced out of the capillary channels by centrifugal force. The liquid impinges on the non-wetting surface of the capture cone, and is deflected to the bottom of the device where it is finally collected in the capture portion of the reservoir ring.

In a short smoke test consisting of particles ranging from sub-micron to several microns in size, the device captured over 300,000 particles in a 50 µL volume (2×10^{11} particles/ft^3), demonstrating the working principle of the device **(Fig. 2)**. Further characterization with known aerosol concentration is needed to determine collector efficiency and concentration factors for longer sample times.

Future Work

The device and associated final sample volume are an order of magnitude smaller than existing collectors, providing for a truly portable, high quality aerosol sample collector.

Future works include iterative refinement of the device, supported by detailed experimental analysis and quantitative testing to measure capture efficiency and other flow properties. Integration of a separately developed microfabricated fractionator to removed particles outside of the target size range (1 to 10 µm) is also planned.

This sample collector could be used in a system both as a monitor, or in a response deployed situation. Any organizations responsible for BW incident response (National Guard, FBI, CDC, USAMRIID) are potential customers, as well as the Chem-Bio Nonproliferation Program at DOE. While we are targeting the BW application, the collector could also be used for gathering forensic evidence, and as such it would be useful to the FBI and local law enforcement.

Reference

1. Lawrence Livermore National Laboratory, ROI IL-10401.

Microfabricated Deformable Mirrors for Adaptive Optics Applications

June Yu, James A. Folta, Peter Krulevitch, and Harold D. Ackler
Electronics Engineering Technologies Division
Electronics Engineering

Scot S. Olivier
Information Science and Technology
Laser Programs

William D. Cowan
Air Force Research Laboratory
Wright-Patterson Air Force Base

We have designed a high-stroke actuator suitable for adaptive optics (AO) applications. The advantage of this new actuator design are its simplicity of fabrication (only four lithography steps), and low susceptibility to lateral actuation forces which would cause contact and binding during displacement. Microelectromechanical systems-fabricated deformable mirrors based on this actuator will allow for broadband AO applications. Preliminary bonding experiments performed show great promise of the Au-to-Au compression technique for transferring mirror structures to foundry fabricated microactuator arrays.

Introduction

Adaptive optics (AO) technology is critical for many current and developing applications at Lawrence Livermore National Laboratory (LLNL). In particular, most large laser systems, including those being developed for inertial confinement fusion and laser isotope separation, require AO to correct for internal aberrations. In addition, AO can provide capability for both high-resolution imaging and beam propagation through the atmosphere. Requirements for laser systems, imaging, and propagation applications are currently driving wavefront control technology toward increased spatial and temporal frequency capacity, as well as reduced system costs.

Three classes of wavefront control devices can be considered for AO applications: standard deformable mirror (DM) technology using ceramic (for example, piezoelectric) actuators, liquid crystal (LC) spatial light modulators (SLMs), and microelectromechanical systems (MEMS) DMs.

Some disadvantages of standard DM technology are limitations on the number of controllable degrees of freedom, large separation between active elements, significant power requirements, weight, and expense. The large physical size of conventional DMs also leads to large optical components, making the entire AO system more cumbersome and costly. LC SLMs have the advantage of providing capability for high spatial frequency control applications. However, commercially available LC SLMs have the disadvantage of slow operating speeds, limited stroke, and low damage thresholds in comparison to conventional DMs.

The use of MEMS techniques to fabricate DMs for AO represents a nearly ideal match of technology and applications. These devices have the advantage of low power consumption, fast response, and high spatial density. Using MEMS fabrication techniques, the cost of DMs for AO can be reduced by a factor of 1000 from that of standard DM technology. Proper design and coating of the MEMS DM arrays will extend the operation of these devices to high average and peak power conditions. On-chip integration of electronic control circuits and batch fabrication will lead to reduced complexity and cost of AO systems. Taken together, the advantages of MEMS DM technology have the potential to revolutionize the field of AO.

For MEMS DM devices, several important technical issues must be resolved before they can be routinely used for wavefront control applications. Optical surface quality remains a principal challenge. Improvements of a factor of ~5 are needed over the current state of the art in the surface quality. Stroke (in and out of plane movement) is limited to ~1 µm for existing MEMS DMs. Scaling to large arrays also presents a technical challenge, mostly limited by the ability to address individual pixels.

In addition, further studies on high reflectivity, low-stress coatings for MEMS DMs and the optical damage characteristics of MEMS DMs remain to be carried out. Despite the unresolved issues, MEMS DMs offer tremendous potential for greatly expanding the use of AO in both laser and imaging system applications. It is our expectation that activities over the next few years will lay the technical groundwork for incorporation of these devices into laser and imaging systems.

Progress

In this first year, we accomplished the following:

1. Designed a high-stroke actuator. MEMS DMs based on this high-stroke actuator can offer vertical strokes up to tens of microns with kHz response time.
2. Identified a technical approach to improve the mirror surface quality and optical fill-factor of existing MEMS DM prototypes. Technologies developed will also be applied to the high stroke device.

High-Stroke Actuator Design

Existing MEMS DM designs suitable for AO applications are based on the parallel-plate electrostatic actuation principle. These devices have the advantage of low power dissipation, fast response time, and compatibility with standard MEMS fabrication process. Actuation ranges of these devices are limited to ~1 µm with reasonable actuation voltages. These devices are therefore best suited for single wavelength or low-stroke AO applications. In some cases, a hybrid AO system architecture with a low-order standard DM coupled with a high spatial resolution MEMS DM could extend the dynamic range. Another approach to extend the dynamic range is to design MEMS DM devices based on a high-stroke actuator (greater than 4 µm).

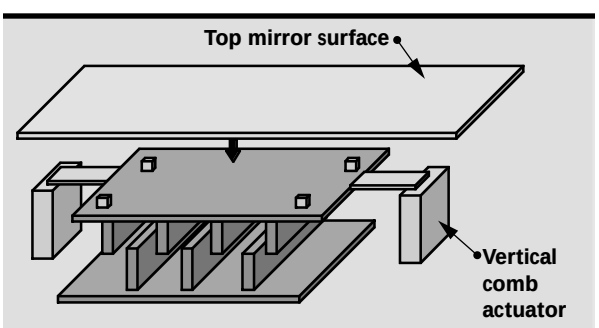

Figure 1. Conceptual picture of a vertical comb actuator. Details of our design are not shown here.

We have analyzed a variety of actuation concepts to achieve high stroke. Actuator concepts analyzed included piezoelectric (bulk-, fiber-, and thin film-based), electromagnetic, and capacitive. We have selected a design based on the vertical comb capacitive actuator (**Fig. 1**) from among the various designs analyzed. Vertical comb actuators have the potential of allowing up to tens of microns stroke with very low power consumption.

Fabrication of these actuators has been made possible by the recent acquisition of an STS deep silicon etcher at LLNL. The simple four lithography step fabrication process we have developed for this design solves long-standing challenges in microfabrication and addresses deleterious lateral actuation forces. Mechanical and electrostatic calculations show large actuation can be achieved with reasonable voltage. **Figure 2a** shows the pull-in force as a function of voltage for a vertical comb with geometry shown in **Fig. 2b**. For 50 V, the force is approximately 0.01 µN/µm. To determine the total force, this number must be multiplied by the total length of drive fingers. For example, if there are ten 200-µm-long fingers, then the force is (0.01)(10)(200) = 20 µN. This is enough force to achieve a 4-µm stroke for our existing design. Further optimization of our suspension design will increase the stroke. For comparison, the gravitational force on a solid piece of silicon 50 µm × 50 µm × 5 µm is 0.3 nN. Risk reduction experiments addressing a potentially difficult Si-etching step in the STS etcher were successful.

Au-to-Au Compression Bonding of Mirror Membranes

The two most critical issues limiting the application of current prototype MEMS DMs are surface quality and the fill factor. There are currently no available devices that meet minimum requirements for LLNL AO applications. Even for the most advanced MEMS DM prototypes, significant

improvements are needed to make them useful for LLNL AO applications. Our goal is to accelerate MEMS DM development in collaboration with external groups to produce a working device for evaluation in the LLNL advanced AO test-bed. We have established collaboration with Major Cowan at the Air Force Research Laboratory at Wright-Patterson Air Force Base. The Cowan MEMS DMs are the most advanced in terms of quality, reliability, and availability.

We are improving MEMS DM surface quality by performing post-processing on Cowan devices by adding a final mirror surface to the foundry fabricated actuator array. **Figure 3** shows a 12-×-12 array Cowan microactuator with a 203-µm period. These actuators have up to 0.7 µm vertical stroke. The 90-µm circular post in the middle of each actuator is designed to accept the bonding of a continuous or pixilated mirror facesheet.

The technique we are using for bonding our mirror facesheet is an Au-to-Au compression bonding technique developed at BSAC for micro-component transfer processes. This bonding technique is superior to other micro-component transfer processes in a number of ways: (1) it is a room temperature process; (2) it does not require atomically clean or smooth interfaces; and (3) it does not require large bond bumps as does solder bump technology. This last advantage makes the technique suitable for fabrication of MEMS structures with small features. The ability to develop the technique with single die (chips) greatly reduces the cost and lowers the development risk by maximizing the number of experiments that can be performed at reasonable cost.

We have selected a multilayer stack to serve as our mirror facesheet. Experimental data show we can accurately tune the stress of this multilayer during and post deposition, thus allowing us to precisely control the mirror flatness. Since the mirror facesheet is fabricated in a separate process, what we do with them (such as high temperature anneal) will not affect the properties of the actuator and circuitry structures. Some of the fabrication challenges included electroplating uniform arrays of

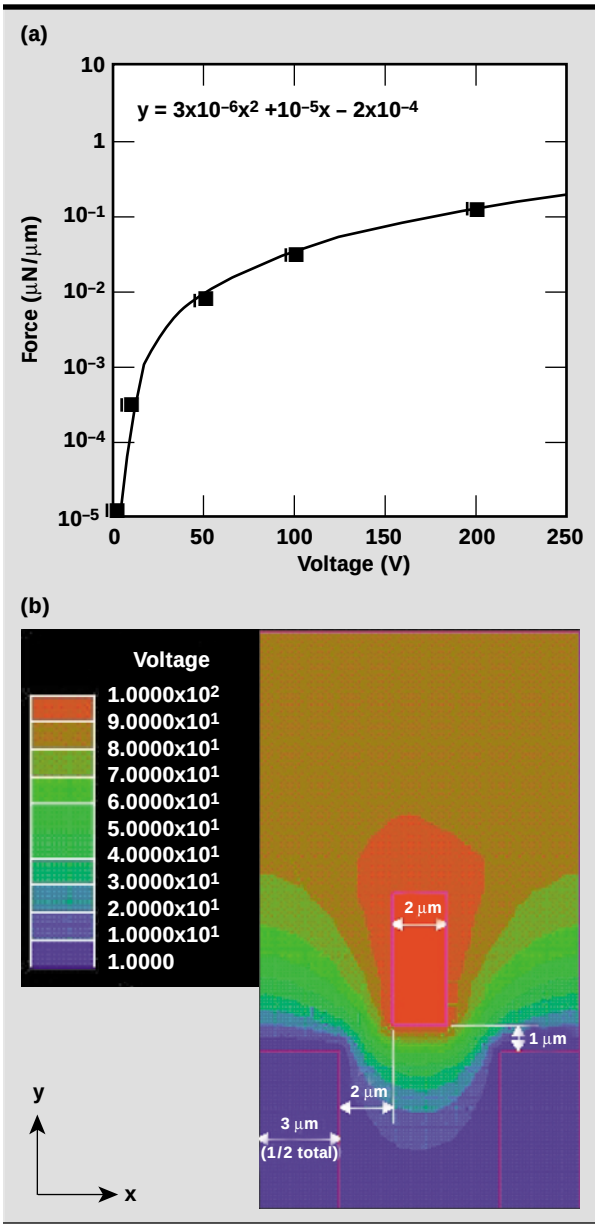

Figure 2. (a) Pull-in force as a function of voltage for the vertical comb actuator shown in (b). (b) The geometry and pull-in force field line for the vertical comb actuator.

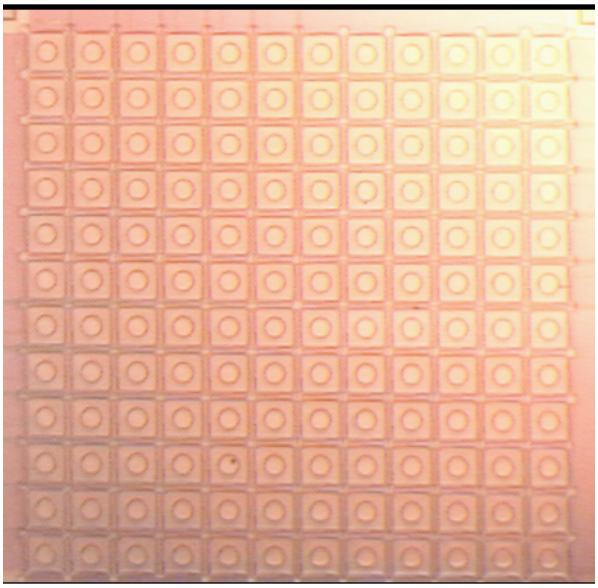

Figure 3. Photograph of a 12-×-12 Cowan microactuator array designed and fabricated for mirror facesheet bonding experiments.

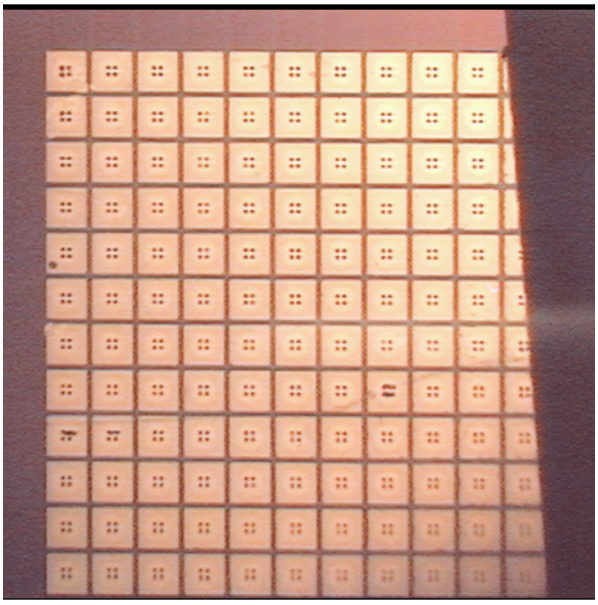

Figure 4. Photograph of a 12-×-12 array of 11-µm-tall electroplated Au bumps sitting on a continuous mirror facesheet.

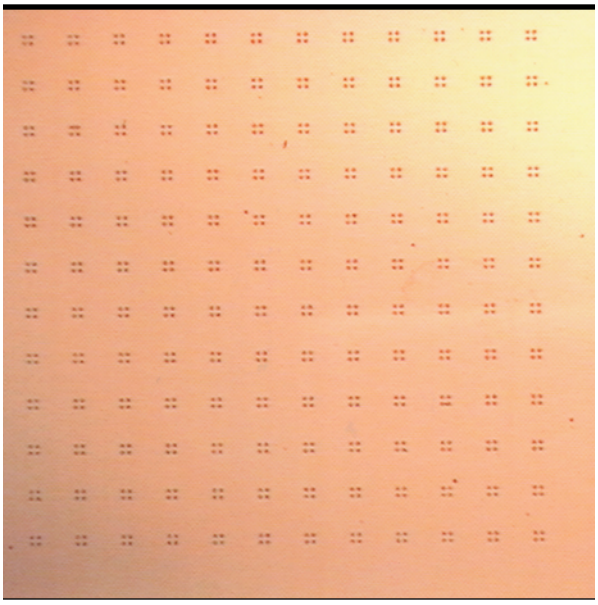

Figure 5. Photograph of a portion of a continuous multilayer facesheet that has been pixilated to a 12-×-12-µm mirror array. A group of four 11-µm-tall Au bumps used to bond are located in the center of each mirror element.

high-aspect ratio Au bumps for bonding process. **Figure 4** shows a uniform array of 11-µm-tall Au bumps that were electroplated onto a continuous mirror facesheet.

In **Fig. 5**, the 1.38-µm mirror facesheet has been pixilated, resulting in a 12-×-12 mirror array. The gap between each mirror element will be reduced in the future by using our high-resolution projection aligner to do the lithography. We have successfully bonded mirror facesheets to Au-coated Si wafers. The bond has greater than 9 MPa tensile strength (we have not tested the bond to failure) and endured greater than 6 h of hydrofluoric acid release bath without failure. We are currently working on the release process.

High-Voltage Photovoltaics

Jeffrey D. Morse and Gregory A. Cooper
Electronics Engineering Technologies Division
Electronics Engineering

Karla G. Hagans
Defense Sciences Engineering Division
Electronics Engineering

We have generated high-voltage power directly with an array of low-voltage photocells. The concept is to optically illuminate an array of photocells in parallel. While the low-voltage power generation of approximately 6 V has been previously demonstrated with commercial photocells using this approach, many program applications at Lawrence Livermore National Laboratory (LLNL) require the generation of significantly higher voltages (hundreds to thousands). Previous efforts have shown the generation of 1200 V using discrete arrays of GaAs diodes. A limitation in voltage scaleup and forming a compact, integrated photocell is excessive leakage current due to parasitic electric fields as arrays of series diodes are placed in parallel to minimize footprint. The result is a collapse of the voltage across each component of the array, thereby degrading the overall voltage generated by the entire photocell. To demonstrate an integrated photocell array, we are developing a current isolating buffer layer integrated with the diode array.

Introduction

High-voltage photovoltaic arrays are being developed as a means to provide power via fiber optics for a variety of applications. **Figure 1** shows an example of high-voltage arrays which have been previously fabricated and tested. The limitation has been a collapse of the voltage across each component of the array, thereby degrading the overall voltage generated by the entire photocell. This collapse is believed to be due to excess leakage current being generated between the rows of the diode array having opposite polarity as the rows are placed in parallel (**Fig. 2a**), which results in a maximum voltage difference of 180 V at the unconnected ends of adjacent diode array rows (1 V/diode × 90 diodes/row = 90 V differential/row).

Thus, with a distance of 300 µm between adjacent rows, the field strength between certain portions of each row is high enough to inject current into the substrate, resulting in a leakage

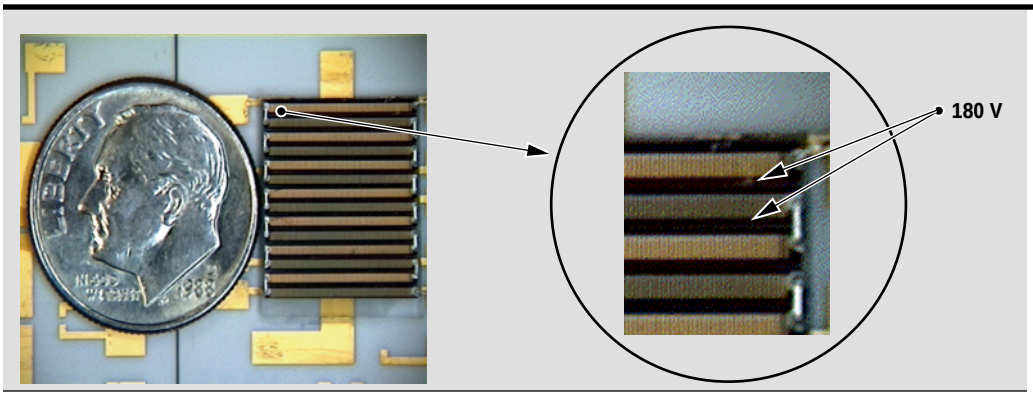

Figure 1. Photocell. High-voltage array developed to provide power via fiber optics.

current path between adjacent rows. The problem can be solved by physically separating adjacent rows and connecting the leads at each end by a wire, thus isolating the substrates electrically, as illustrated in **Fig. 2b**. However, this approach is not consistent with increasing the overall voltage of the array and reducing the footprint. An array having current isolating buffer layers between the diode structures and the substrate provides an integrated solution to the problem.

Progress

To reduce or eliminate the leakage current between adjacent rows, a current isolating buffer layer is required. Since the photocell array is fabricated using the gallium arsenide (GaAs) materials system grown by metallorganic chemical vapor deposition (MOCVD), the natural approach to reduce substrate leakage current is to incorporate a layer between the substrate and diode structure which acts as a barrier to current flow. For this work, the growth of aluminum arsenide (AlAs) epitaxial layers on the substrate provides an offset in the conduction and valence bands at the GaAs-AlAs interface, as illustrated in **Fig. 3a**. As the voltage across the structure increases, causing the bands to bend, the path of flow of electrons is impeded by this band offset, until the effective distance across the barrier becomes small enough such that the electrons can tunnel through the barrier (**Fig. 3b**), at which point the current has an exponential dependence on voltage. Intuitively, the thicker the barrier layer, the higher the voltage at which the electrons begin to conduct current.

Test structures were grown on semi-insulating GaAs substrates by MOCVD. An AlAs film was grown first, varying in thickness from 200 Å to 2 µm, followed by 5000 Å N+ GaAs to provide an electrical contact.

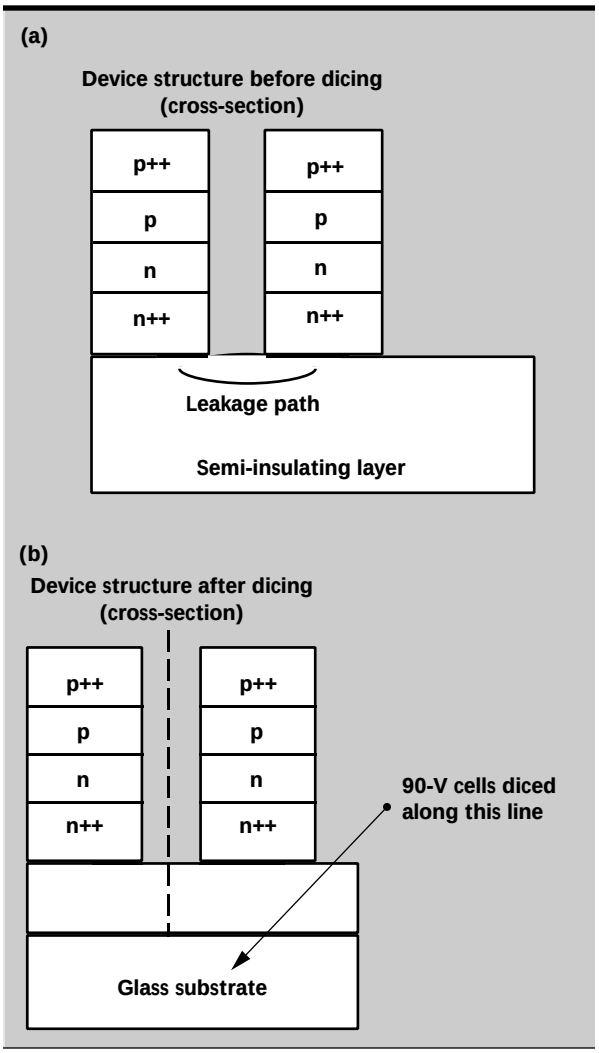

Figure 2. Device structure before (a) and after (b) dicing.

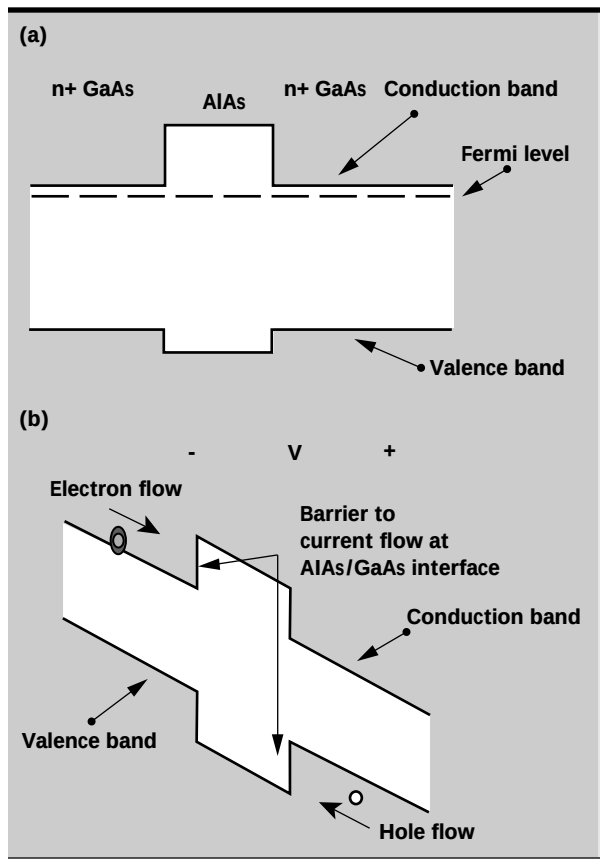

Figure 3. (a) Illustration of band diagram for N = GaAs/AlAs/n + GaAs structure at equilibrium.
(b) Band diagrams with applied voltages showing barriers to current flow at AlAs/GaAs interface.

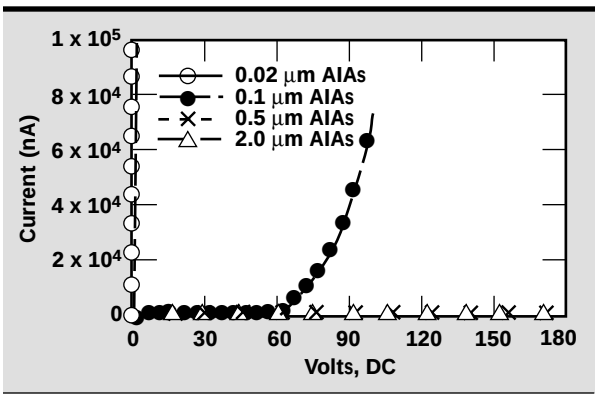

Figure 4. Leakage currents for 200-µm electrode spacing.

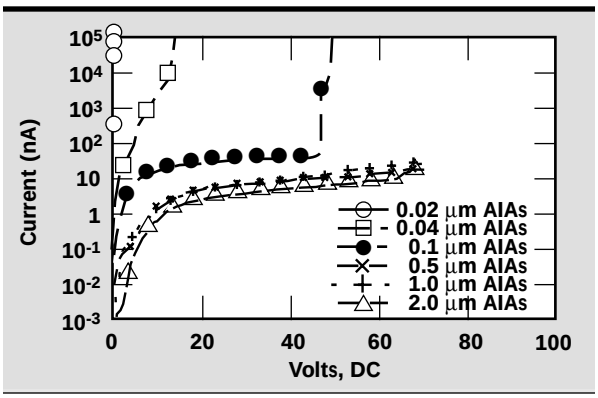

Figure 5. Leakage currents for 20-µm electrode spacing.

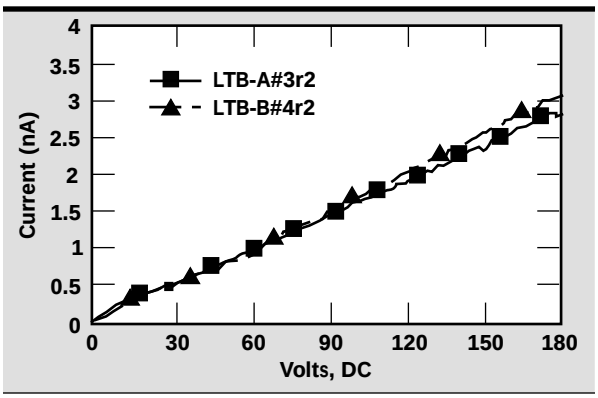

Figure 6. Leakage currents for 1-µm-thick low-temperature buffer.

Test devices were fabricated by forming a mesa ridge structure on which a contact metal pad was patterned. The current vs. voltage characteristics were then measured as a function of distance between the electrodes. These results are shown in **Fig. 4**.

From the data, it can be seen that the voltage or electric field at which the current begins to conduct significantly increases as a function of AlAs layer thickness. A similar comparison presented on a log-I plot (**Fig. 5**) shows the leakage current is reduced by 3 to 5 orders of magnitude as the buffer layer thickness increases.

Additional buffer layers based on the low temperature growth of GaAs (LTB-GaAs) by molecular beam epitaxy (MBE) was investigated. The LTB-GaAs has the property that the crystal lattice of the MBE layer has a significant level of naturally occurring defects which act to trap any charge which is injected into it, yet retains adequate crystalline properties such that high quality layers can be grown on top of it. Similar structures were fabricated in 1-µm-thick LTB-GaAs layers. The resulting current/voltage characteristics are shown in **Fig. 6** where a current of only a few nanoamps is exhibited at 200-V bias, thus the current is essentially eliminated.

Future Work

We are proceeding to the fabrication and testing of the entire high-voltage photovoltaic array with integrated buffer layers as discussed above. Both AlAs and LTB-GaAs layers are being investigated, and will likely provide an integrated solution to next generation high-voltage photocells for applications at LLNL.

Microfabricated Flow Cell for DNA Analysis

Peter Krulevitch and Laurence R. Brewer
Electronics Engineering Technologies Division
Electronics Engineering

We have microfabricated a flow cell for investigating the interaction of various proteins with DNA molecules. The cell proved to be superior to previous designs, with improved optical clarity and low background fluorescence.

Introduction

We have microfabricated a flow cell for investigating the interaction of various proteins with DNA molecules. The objective was to produce a flow cell with microchannels such that two fluid streams could be made to converge under laminar flow conditions, with mixing occurring only by diffusion across the interface between the two fluids. The top surface of the cell was required to be thin (0.007 in.) to enable visualization within the channel using a confocal microscope. An additional specification called for the cell to be made of a material with low background fluorescence. The challenge was to devise a fabrication scheme that did not introduce a fluorescing or optically-diffusing layer in the illumination or viewing path.

Progress

A new process was developed to fabricate flow cells having high optical clarity, with the channels formed in such a way as to produce a smooth surface which does not scatter the illuminating laser beam. The original plan was to investigate quartz as a material for the flow cell. However, Lawrence Livermore National Laboratory has considerable expertise in etching smooth microchannels in borosilicate glass substrates (20 to 40 nm roughness for 20-µm-deep channels), and the glass was found to have low autofluorescence at the desired wavelength.

Figure 1 illustrates the fabrication process. Twenty-micron-deep flow channels were photolithographically patterned in 1.1-mm-thick borosilicate glass substrates. Holes were wet-etched through 0.007-in. cover slips for fluid ports. These two substrates were placed in contact, and a low viscosity UV-curable epoxy was introduced along the edge. The epoxy wicked in between the substrates under capillary forces, but stopped at a moat that surrounded the flow channels. Using this approach, no epoxy layer was present in the optical pathway. The sandwich was then exposed to UV radiation to cure the epoxy. Finally, HPLC tubing connectors were bonded to the fluid ports using Ablestick sheet adhesive.

The flow cell was connected to a syringe pump and tested under pressure, and no leakage was observed. The cell proved to be superior to previous designs, with improved optical clarity and low background fluorescence.

High-resolution images of DNA condensing with this flow cell were recorded.

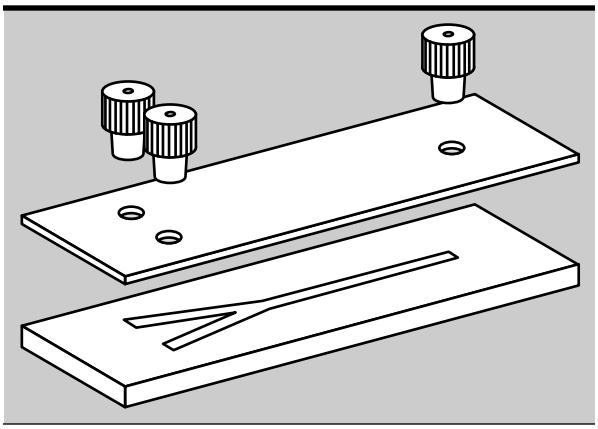

Figure 1. DNA flow cell fabrication process.

Microvalves for Microcatheters

Kirk P. Seward
New Technologies Engineering Division
Mechanical Engineering

Amy W. Wang and Abraham P. Lee
Electronics Engineering Technologies Division
Electronics Engineering

We have invented and are developing microvalves compatible with microcatheters for interventional neuroradiology applications. The main goal was to control the flow rate of fluid injection into the brain arteries with inner diameters as small as 1 mm. The applications are for the deposition of therapeutic material to close off arteriovenous malformations (AVMs) or for localized drug delivery. This technology is aligned with core competencies in microfluidics and advanced packaging at Lawrence Livermore National Laboratory (LLNL)'s Microtechnology Center (MTC). The project has also supported LLNL's Medical Technology Program (MTP).

Introduction

Beginning in 1995, LLNL began to focus on stroke as an area where its expertise in lasers, optics, computer modeling, and micromechanical systems could be used to develop treatments where few options were available. The MTC and MTP have invented several microtools that fit through microcatheters (0.5-mm inner diameter) including microgrippers, microcauterizers, micro-biopsy devices and microsensors.

A mechanical release mechanism to deposit coils into brain aneurysms resulted in a major cooperative research and development agreement (CRADA) and to date the animal tests have been 100% successful.

Microfluidics has also been a core competency at LLNL. Several microvalves have been developed over the last five years. The integration of microvalves onto microcatheters would be a natural evolution of this technology. A manager at Boston Scientific made the request to implement a microvalve at the tip of their microcatheters for depositing therapeutic fluids into brain AVMs. Current methods use an external shut-off valve that leaves undesirable residual traces. As we develop a proof-of-concept prototype, a collaborative effort is likely.

Another application of microvalves on microcatheters is to position and steer the distal tip of microcatheters within the blood vessels.

Progress

Several design options were considered for a microvalve to attach to the distal tip of a microcatheter. One of the designs that was tested was a one-shot valve consisting of a shape memory polymer (SMP) tube that is initially set to a closed position by heating it above its glass transition temperature T_g, crimping it shut, and allowing it to cool and form to the closed shape. Actuation of this tube is accomplished by optically heating the pigment-dyed polymer with a laser via an optical fiber. A SMP tube with 460-µm outer diameter and 50-µm wall thickness was extruded and tested to determine the opening force against a spring-loaded transducer. Tests confirmed the validity of a SMP microtube valve as the tube produced ~20 mN of radial opening force from a fully closed loading condition. After opening and allowing the tube to cool below its glass transition temperature, it could withstand >160 mN of radial force before crushing to half of its original diameter. The behavior of these tubes is illustrated in **Fig. 1**, and the data from the experiments is displayed in **Fig. 2**.

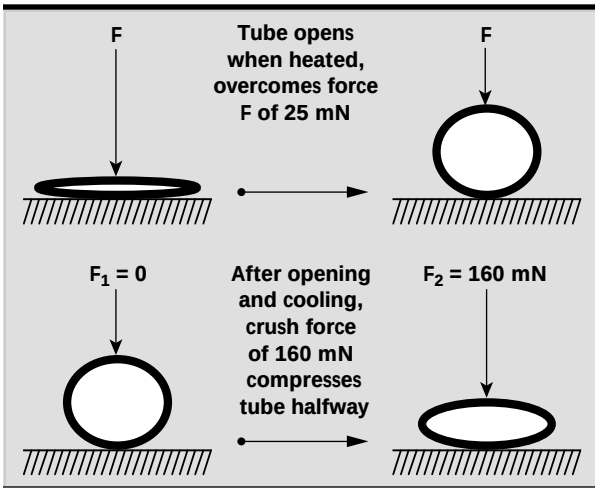

Figure 1. Behavior of SMP tubes during loading and heating (tube diameter = 460 μm, wall thickness = 50 μm).

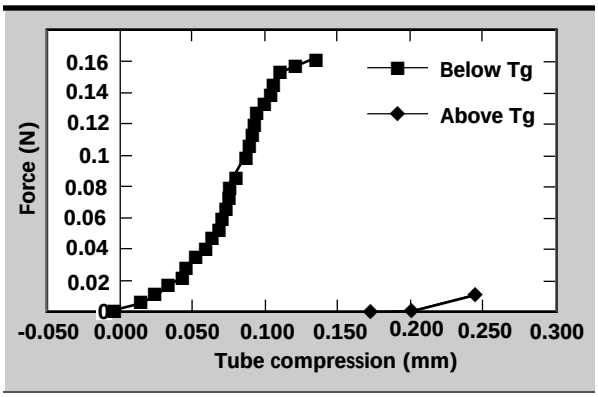

Figure 2. Experimental data, illustrating increased stiffness in tube below glass transition temperature, and 18 mN of force produced by the tube at full compression above the glass transition temperature.

A second valve design using molded SMP was also investigated. This design draws from typical micromachining capabilities to create mold cavities in silicon and glass wafers and then to use these molds, male and female, to create intricate polymer shapes with high repeatability and extremely tight tolerance. The valve, illustrated by the axial cross-section seen in **Fig. 3**, looks much like a micro-sombrero with the top of the hat cut off to allow fluid flow. It has therefore been dubbed the "sombrero-valve."

The valve is operated by optical heating and fluidic pressure changes. While at ambient temperature, the valve has 200× the stiffness as when it is heated above the glass transition temperature by the optical fiber laser. Fluid flow is therefore not inhibited because the valve retains its stiffness. Upon heating, however, a high enough pressure difference across the orifice of the valve will close or open it, depending on the direction of the pressure drop. This

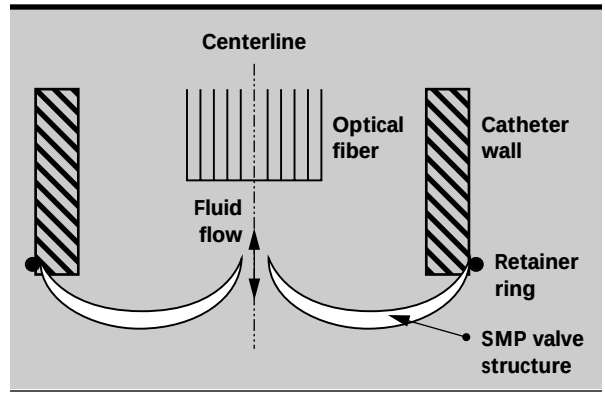

Figure 3. Cross-sectional view of sombrero valve attached to the distal end of a catheter. The diameter of the entire structure is <1 mm.

design for a bistable valve that can be used to precisely control the flow of fluids through the distal end of a microcatheter has not yet reached proof-of-concept, but the molds are nearly completed, at which time the valves can be created and tested.

Summary

Through our effort on this project, we have met the following milestones:

1. Two new bio-compatible microvalve technologies have been conceived that use the properties of SMPs to create molded or extruded valves to be fit onto catheter tips. The extruded valves have been reduced to proof-of-concept, while the molded valves are being processed.
2. One record of invention (IL-10569) has been filed for the sombrero valve and a second record of invention is being written for the one-shot tube valve.
3. An NIH proposal has been submitted with the collaboration of SUNY-Buffalo to design additional SMP BioMEMS devices for catheter-based surgery.
4. Processing knowledge to extrude and mold SMP and to create silicon and glass "micromolds" was gained and mold cavities are near completion.

We are currently taking steps to develop proof-of-concept devices so that patents can be more avidly pursued and collaborations can be realized with medical device companies.

Acknowledgments

The authors gratefully acknowledge D. Schumann and J. Moore for their plastics expertise and D. Maitland and M. Triggs for effectively conveying their knowledge of the behavior of SMPs.

Microelectromechanical-System-Based Fuel Cell for Microscale Energy

Jeffrey D. Morse
Electronics Engineering Technologies Division
Electronics Engineering

Alan F. Jankowski
Materials Science and Technology Division
Chemistry and Materials Science

We have investigated a novel approach to a miniature fuel cell power source by combining thin-film solid-oxide or proton-exchange-membrane electrolyte-electrode materials with microelectromechanical system (MEMS) techniques to integrate a fuel-cell stack monolithically on a manifolded host structure. This will enable a scalable, portable fuel cell power source system for a broad range of applications having requirements in the <1 W to >10 W regime. The MEMS approach offers a direct means to integrate the fuel cell stack with required manifolding and fuel delivery system, while providing the means to control the performance of the power source for specific applications. Results describing our progress in the fabrication, integration, and testing of MEMS-based fuel cells are presented below.

Introduction

Miniature fuel cells are receiving renewed interest for applications in portable power generation. Fuel cells store energy as fuel rather than as an integrated part of the system, which is the case with batteries. Therefore, fuel cells can potentially exhibit significantly higher energy densities in comparison to other energy storage devices.

While this power source has been demonstrated in bulk for higher power portable applications (50 to 500 W), effective scaling of fuel cell systems has not been demonstrated for low-power applications (<1 to 20 W). Present applications in portable power include the full range of consumer electronics, such as cell phones, laptop computers, video camcorders, and radios. New applications in portable power span the range of power consumption from micro, as in long duration sensors and remote communication devices, to macro, as in light-weight packages for use in the field.

Present requirements for autonomous remote sensors and communications devices for the intelligence community and the military are for power sources having extremely long shelf life and operating times, which are not presently available from battery technologies. The demonstration of a novel, high-performance power source will provide a mission-enabling technology that will expand the range of applications for electronic sensors and communication devices in intelligence gathering, military, and commercial applications. Furthermore, demonstration of the viability of this technology will accelerate the prototype system development time cycle, thereby expediting the deployment for realistic applications.

Progress

Technical Concept

The MEMS-based fuel cell is conceptually illustrated in **Fig. 1**, with an expanded detailed schematic

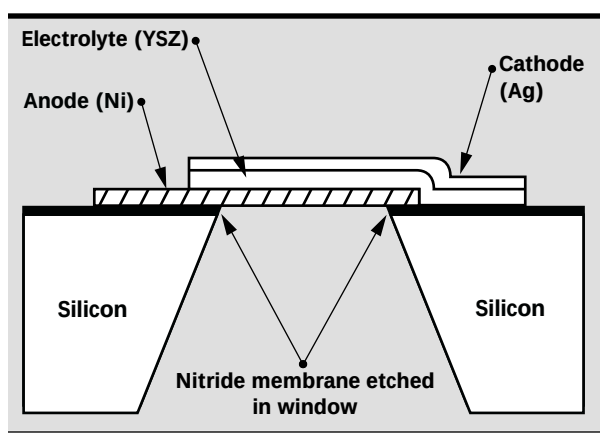

Figure 1. Schematic illustration of MEMS-based fuel cell concept.

of the thin film assembly approach in **Fig. 2**. This approach represents a completely new method for fuel-cell technology, potentially circumventing several problems traditionally associated with fuel cells, while further opening up a new range of applications for fuel cells as portable power sources. The MEMS-based fuel cell offers advantages in terms of manufacturability, fuel flexibility, reduced temperature of operation, and higher specific energy in comparison to other fuel-cell and battery technologies.

A further advantage of a thin modular design is the direct stacking of individual fuel cell modules, as shown in **Fig. 3**, enabling applicability to a wide range of power requirements.

The impact of the proposed effort is that a new, miniature power source will be established which provides an alternative to battery technologies, providing lighter weight, longer life, and potentially lower cost of portable power. This provides new functionality for use of sensor systems under development at Lawrence Livermore National Laboratory (LLNL) and the military for autonomous and manual use in the field. This technology will ultimately find its way into the commercial sector for portable electronics, and will open new markets for US manufacturers.

Experimental Results

Our efforts during the past year[1–5] were to determine the viability of thin-film MEMS-based fuel-cell technologies. These efforts have demonstrated the fabrication and initial operation of both solid-oxide and proton-exchange-membrane (PEM) electrolytes in fuel cells, monolithically integrated on silicon chips having micromachined manifold systems.

In developing the fabrication process we have addressed several issues associated with the integration and performance of a fuel-cell stack, micromachined fuel manifold, and flow field structure. This was accomplished by creating a thin-film porous-anode structure using photolithographic and etching techniques, combined with micromachining of silicon to form a free-standing fuel-cell membrane.

Photographs of these structures are shown in **Figs. 4** and **5**. Similar structures have been formed in the cathode layer by a comparable method. This allows the rapid diffusion of fuel and oxidant through the electrode structures to the electrolyte interface, as well as the exhaust of reaction byproducts (water).

A test fixture, illustrated in **Fig. 6**, was constructed to enable manifolding of fuel and oxygen to the anode and cathode respectively while the entire assembly was positioned in a furnace. Thus, the fuel-cell structure on the micromachined silicon chip was mechanically stabilized as the temperature was increased.

The fuel cell performance was measured by sweeping the voltage applied across the electrodes and measuring the current drawn from the power supply. The current-voltage characteristics for both

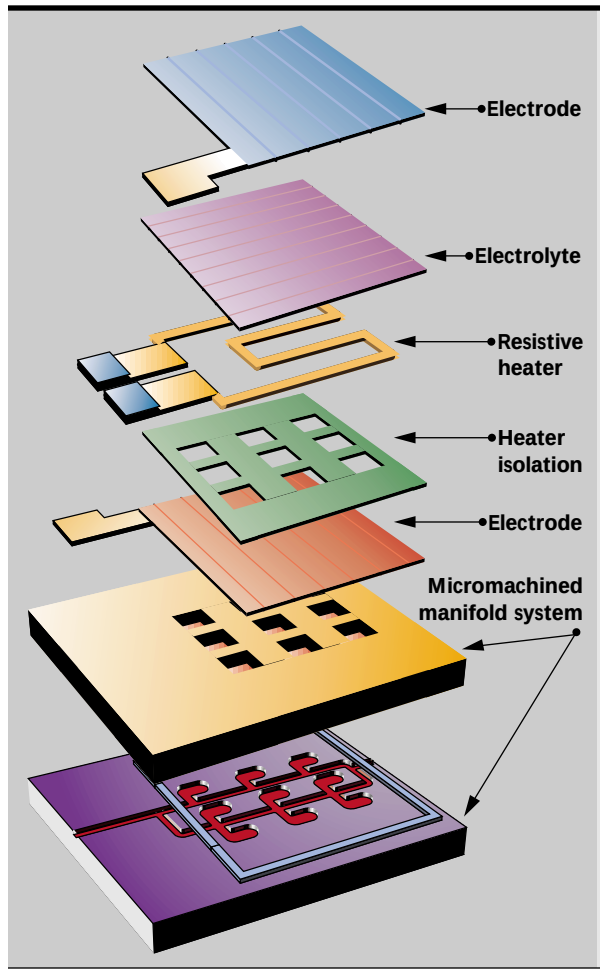

Figure 2. Schematic illustration of MEMS-based fuel cell thin film assembly.

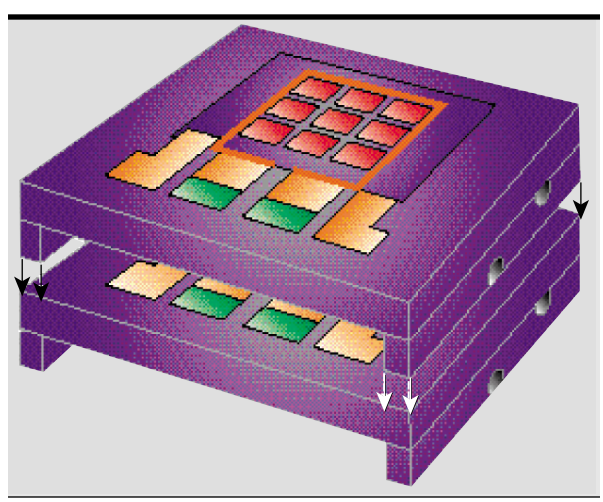

Figure 3. Power scaling by stacking of fuel cell modules.

the PEM and solid-oxide fuel cells (SOFC) at various temperatures of operation are shown in **Figs. 7** and **8**, respectively. From a technical standpoint, there are several key points to be drawn from these data. First, the PEM thin-film fuel cell operates over the temperature range from 50 to 90 °C, with a cell overpotential exhibited at room temperature. The fuel used for these tests was dilute hydrogen (4%) in argon, for safety reasons. For the PEM device, steam was added to the fuel feed, since the electrolytes require water to be retained in the membrane for adequate proton conduction.

Perhaps more compelling is operation of the solid-oxide thin film fuel cell over the temperature range 250 to 320 °C. The SOFC used a porous nickel anode, yttria-stabilized-zirconia electrolyte, with a silver cathode, all deposited using vacuum sputter-deposition techniques. The free standing SOFC membrane was tested using dilute (4%) hydrogen fuel, with the resulting current voltage characteristics plotted in **Fig. 8**. This is the lowest temperature of operation reported to date for a SOFC, the advantage offered by using thin-film components for the electrode and electrolyte.

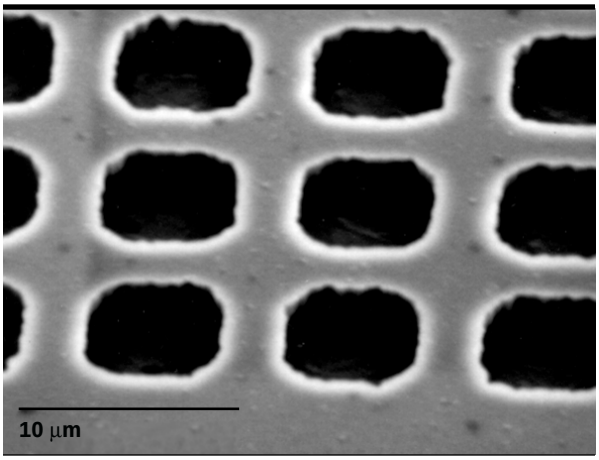

Figure 4. Top view of 0.5-μm thick Ni anode layer, imaged using scanning electron microscopy at higher magnification.

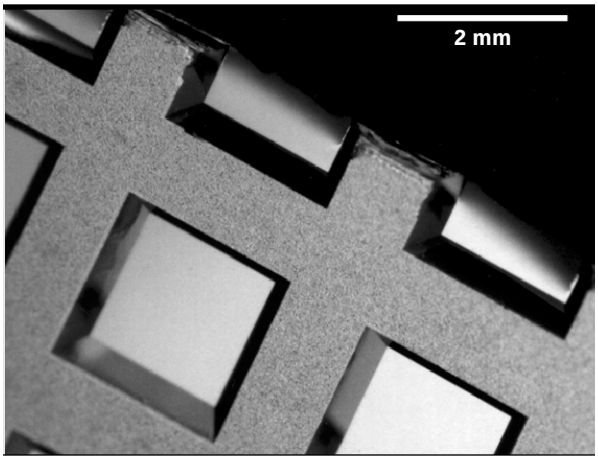

Figure 5. Bottom view of Ni anode layer deposited on the substrate platform, imaged using scanning electron microscopy.

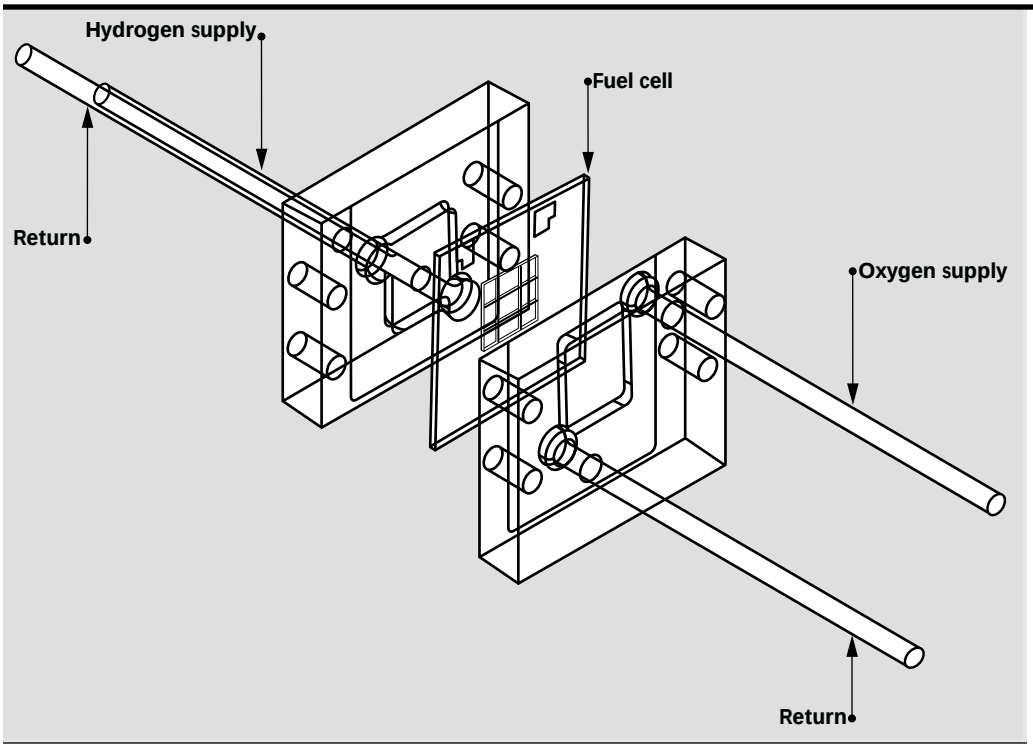

Figure 6. Schematic illustration of test fixture design.

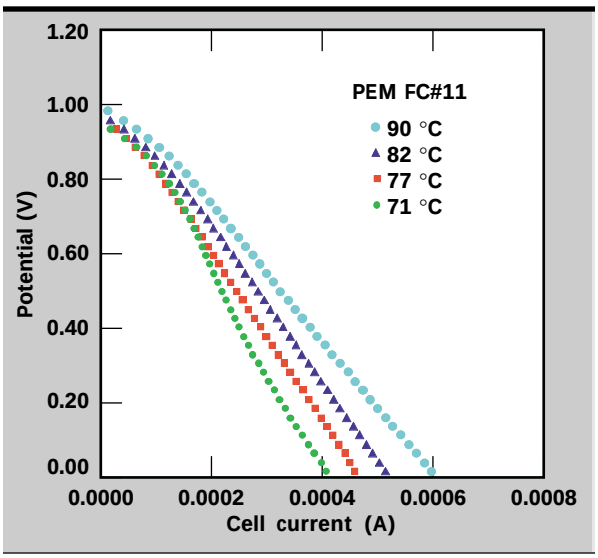

Figure 7. Current-voltage characteristics of MEMS-based PEM fuel cell (Pt/Nafion™) with 4% dilute hydrogen fuel.

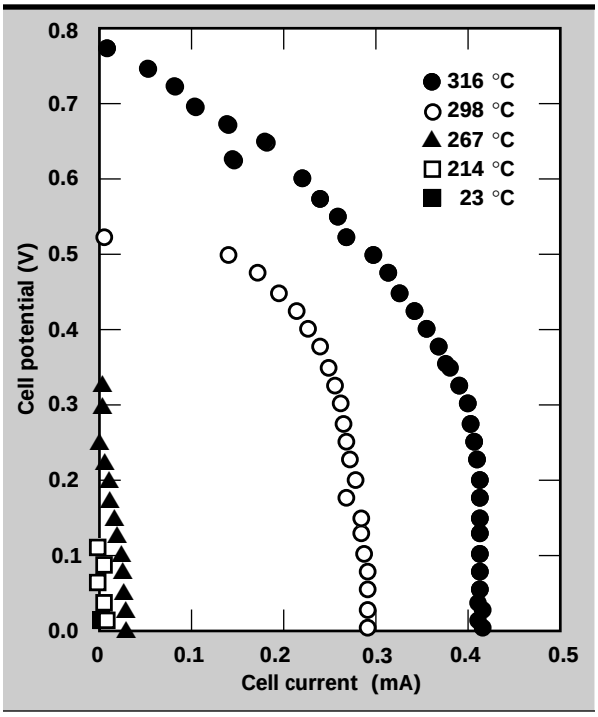

Figure 8. Current-voltage characteristics of MEMS-based solid oxide (Ni/YSZ/Ag) fuel cell with 4% dilute hydrogen fuel.

Future Work

Our efforts continue to optimize the process integration of the electrode/electrolyte material and structure for both the PEM and SOFCs. We are testing at fully-concentrated hydrogen fuel, and developing a computational modeling capability that will enable optimal design and thermal isolation approaches for the fuel cell. This is of particular importance now having demonstrated the operation of SOFC technology in the 250 to 320 °C range, which is thermally compatible with a wider range of materials for packaging, wafer bonding, stacking, and fuel delivery and control. We will begin the design and test of integrated resistive heaters based on the thermal modeling results. The primary focus, entering FY00, will be the integration, packaging, and stacking of several fuel-cell modules to demonstrate a power source at nominal voltage and current output of 3 V and 300 mA. Additional investigations will look at the use of hydrocarbon fuel and the fuel-cell design optimized for overall power efficiency.

References

1. J. D. Morse, R. T. Graff, J. P. Hayes, and A. F. Jankowski (1999), "Porous thin-film anode materials for solid-oxide fuel cells," submitted to *Mat. Res. Soc. Symp. Proc.* **575**, April.

2. A. F. Jankowski and J. D. Morse, "A MEMS-based thin film fuel cell," patent pending.

3. A. F. Jankowski and J. D. Morse (1998), "Thin film synthesis of novel electrode materials for solid oxide fuel cells," *Mat. Res. Soc. Proc.* **496**, 155–158.

4. J. D. Morse, A. F. Jankowski, J. P. Hayes, and R. T. Graff (1999), "A novel thin-film solid-oxide fuel cell for microscale energy conversion," submitted to ASME Symp. on Microscale Energy Conversion, November.

5. A. F. Jankowski, R. T. Graff, J. P. Hayes, and J. D. Morse (1999), "Testing of thin-film SOFCs for micro to macro power generation," accepted for publication in *Electrochem. Soc. Proc.*, SOFC-VI, October.

Custom Silicon Etching

Jeffrey D. Morse and Leslie M. Jones
Electronics Engineering Technologies Division
Electronics Engineering

Robert T. Graff
New Technologies Engineering Division
Mechanical Engineering

We have developed new, customized silicon etch processes to fabricate deep, anisotropic microstructures in support of present and future microelectromechanical systems (MEMS) projects at Lawrence Livermore National Laboratory (LLNL). The processes were established in the STS Plasma Etch system which uses sequential etch and passivation steps to achieve high etch rates for silicon, selectivity in etching silicon over silicon dioxide or photoresist masking materials, and highly anisotropic, high-aspect-ratio features.

Introduction

Present MEMS projects at LLNL require the capability to etch high-aspect-ratio, anisotropic structures in bulk silicon, which is critical for continued development of silicon MEMS-based technologies. This need has been addressed with the acquisition of an STS Plasma Etch system. While the system has validated processes for a specified set of structures and mask selectivities, we expect requests for numerous custom designs. Each design will require time and effort to optimize the process to achieve the desired results. In other words, the etch processes are not simple turn-key approaches, and each custom design will require variations in the operating parameters of the system.

The basis for the deep anisotropic etch capability of the STS Plasma Etch System is an iterative cycle of plasma etch and passivation layer deposition steps. A masking layer is formed from either a thick photoresist or a silicon-dioxide layer (3 to 6 µm) on a silicon wafer, and is subsequently patterned using photolithographic and etching techniques to expose the silicon surface pattern to be etched.

The actual silicon etch process in the STS system begins with a brief etch step in which the silicon is etched on the order of 1 to 2 µm, followed by a passivation step. During this step in the cycle, the gas composition and power levels are adjusted such that a Teflon™-like polymer is actually deposited, and no silicon is etched. With appropriate power and pressure during this portion of the cycle, the sidewalls of the etched structure will be coated with a thicker passivation layer than the bottom. As the cycle iterates to the etch step, the silicon is etched preferentially downward because the sidewall passivation prevents lateral etching. The key is to iterate the etch and passivation steps, each with specific durations, such that the desired relative profile is achieved.

Competing requirements include etch rate, selectivity of etching silicon over mask material, critical dimensions and aspect ratio of the features being etched, and effective area of silicon being etched. Thus, small variations in a given design can significantly complicate the etch procedures.

Progress

For initial process development, three specific project requirements were selected, each having different critical requirements to be achieved from the deep anisotropic etch capability. The first is a new impedance sensor fabrication process for the dielectrophoresis project, which used our STS deep-trench etcher to etch 20-µm channels with vertical walls in a silicon substrate. The first step was to back-etch the silicon with the STS etcher to make the fluid input and output ports and electrical contact openings, followed by the growth of 0.2 µm

of thermal oxide on the silicon for electrical insulation. Subsequently, electrodes are formed down the sidewall of the etched channel; thus, it is critical to achieve a uniform, smooth sidewall surface.

The initial process used a standard etch procedure to form the channels with nominally vertical sidewalls.

Upon further inspection, the sidewalls were heavily scalloped, as shown in **Fig. 1**. To solve this problem and create a smoother sidewall surface, the etch and passivation steps were reduced to where the etch step only proceeded to the point at which the sidewall passivation was removed. While this had the overall effect of reducing the etch rate, it eliminated lateral etching, which resulted in the scalloped profile. **Figure 2** illustrates the final structure with sidewall metallization down into the channel.

The second process investigated the fabrication of a test structure for a high-sensitivity accelerometer for the wireless sensor project. The critical need

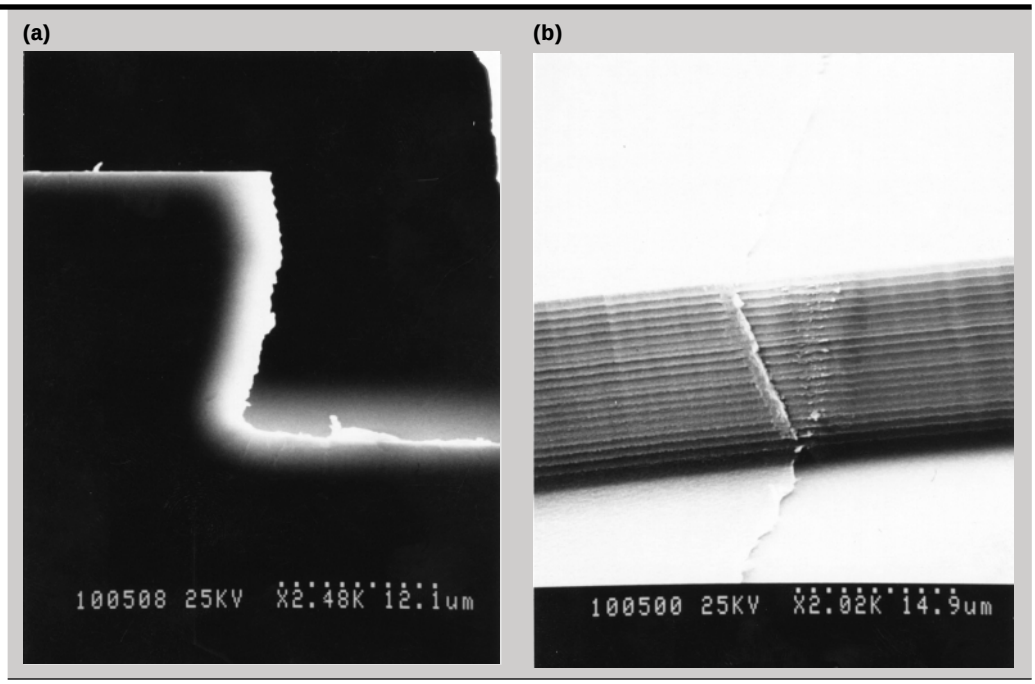

Figure 1. Channels formed with standard etch procedure. Note the heavily scalloped sidewalls.

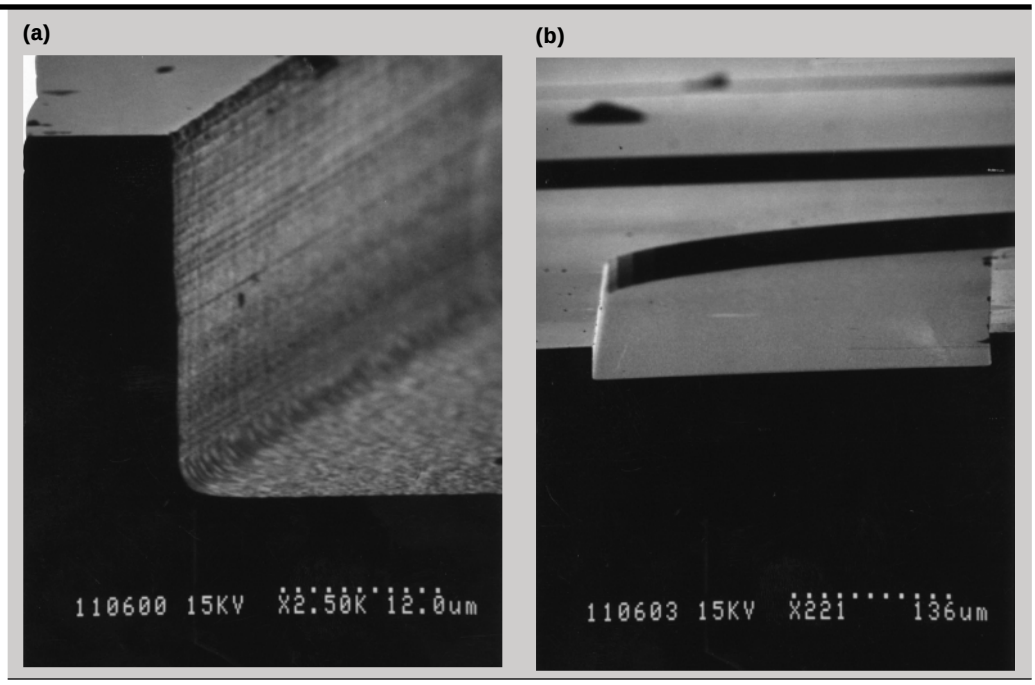

Figure 2. Final structure, with sidewall metallization into the channel.

for this device is an interdigitated finger structure, as illustrated in **Fig. 3a**, in which the fingers are perfectly straight structures through the entire silicon wafer. The critical dimension shown in the blown-up illustration in **Fig. 3b** is 14 µm. The initial process that we used was limited as the depth approached ≥250 µm because the trench would become significantly narrower towards the bottom.

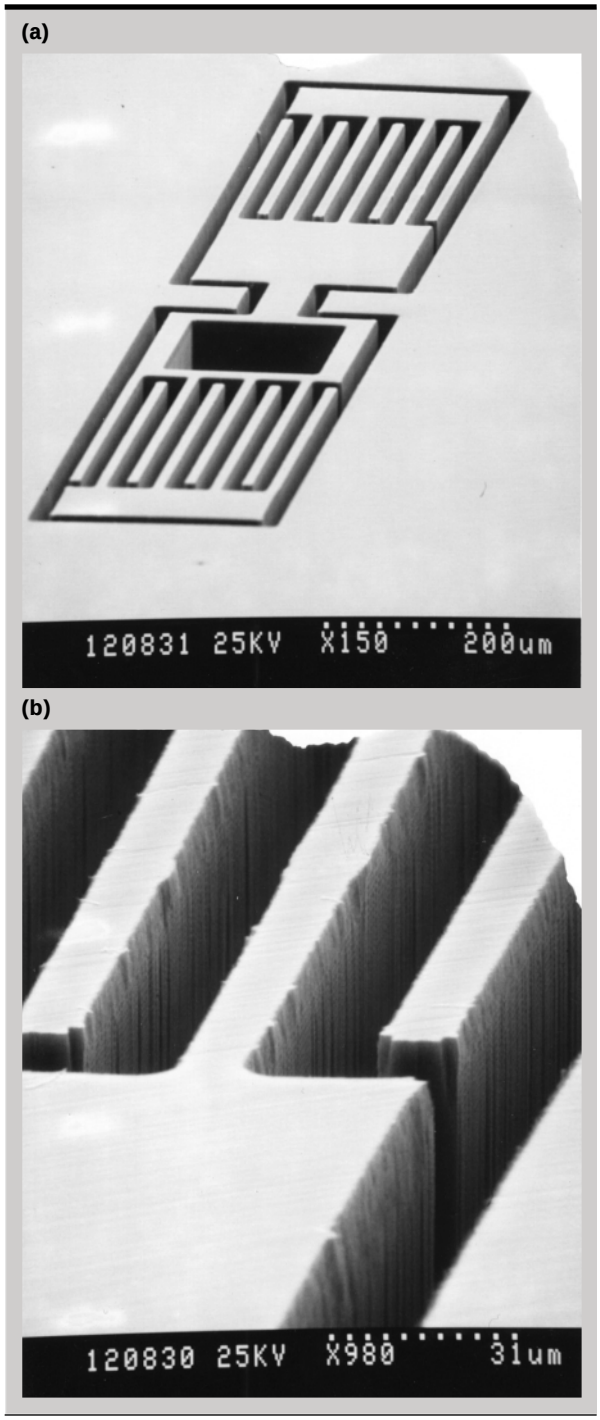

Figure 3. (a) Interdigitated finger structure. (b) Enlargement of (a), with critical dimension 14 µm.

To improve this, the passivation step time was reduced, and the process pressure was increased as the trench depth approached this range. These changes enabled the process to achieve straight sidewall trenches to a depth of 280 µm (14:1 aspect ratio), as shown in **Fig. 4**, but fell short of the required 380 µm of the full silicon wafer. Thus, a hard limitation in aspect ratio was determined, and in this case the structure had to be redesigned with larger critical dimensions (20 µm).

The final process investigates the opposite situation in which a larger trench or via of silicon is etched while leaving a narrow, high-aspect-ratio wall remaining. In this case, a large (1-in. square) array of 100-µm-×-100-µm vias having 20-µm separations was etched (**Fig. 5**). The initial processes resulted in undercutting of the wall structures at fairly shallow depths, leaving a grid structure suspended over a large well. By increasing the passivation step time, the lateral etching was eliminated, and the wall profile was completely vertical. **Figure 6** illustrates the cross section of a wall structure remaining between two etched cavities. The trench is etched to approximately 300 µm in this case, and features are presently being etched through entire silicon wafers (500 µm). Problems still remain in achieving a smooth bottom to the etched cavity as the entire wafer is etched, likely as a result of scattering of the ions off the oxide layer on the back of the silicon wafer, resulting in lateral etching of the trench.

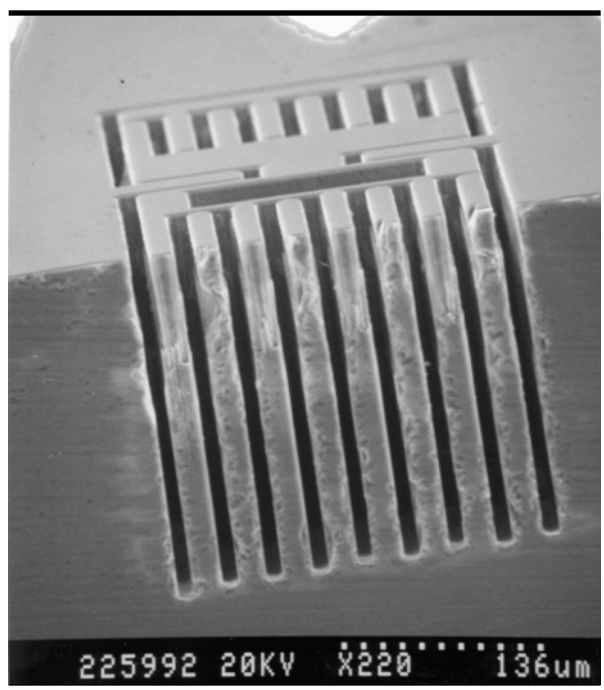

Figure 4. Channels with straight sidewall trenches to a depth of 280 µm (14:1 aspect ratio).

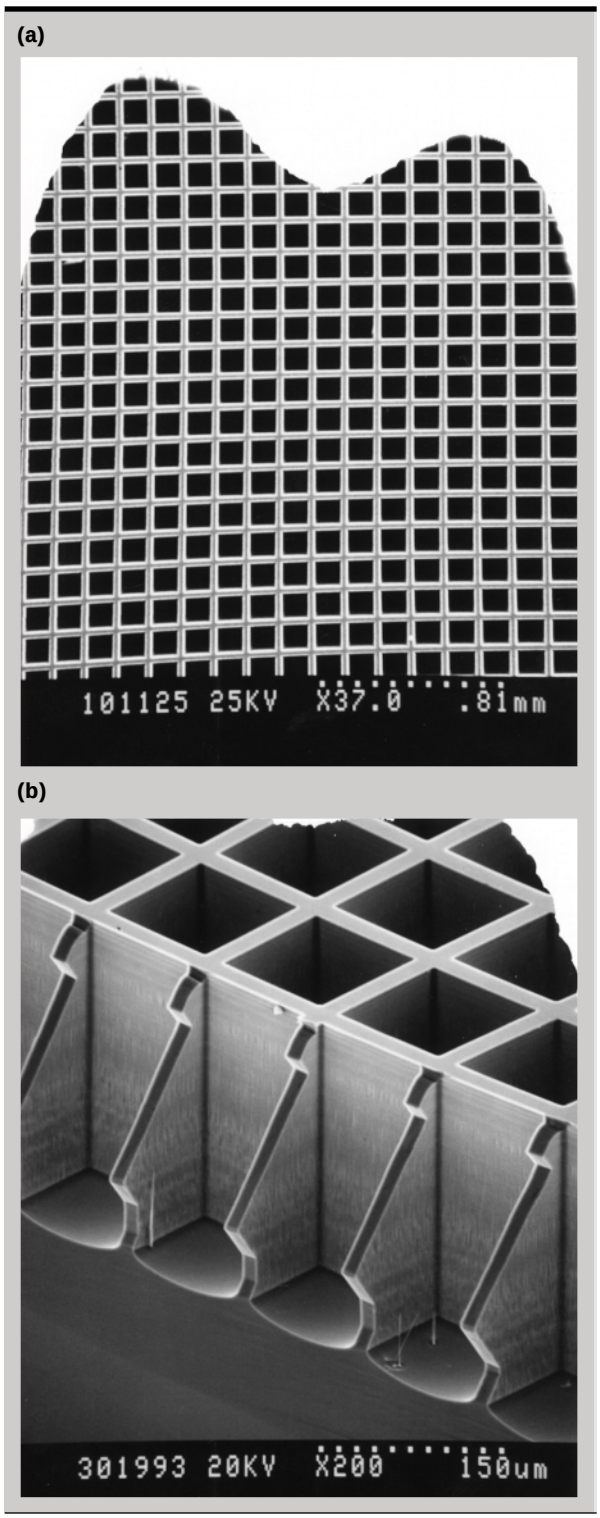

Figure 5. Etching of silicon trench: 1-in. square array of 100-μm-×-100-μm via with 20-μm separations.

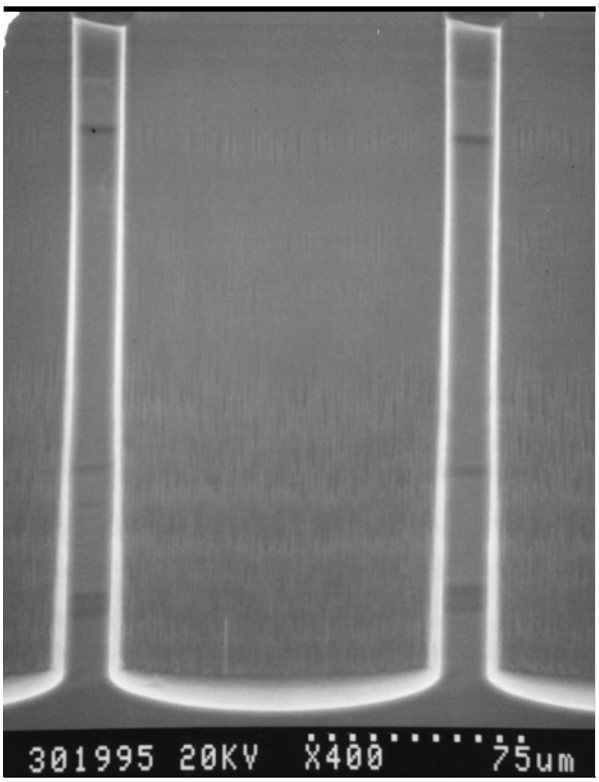

Figure 6. Cross-section of wall structure between two etched cavities.

Future Work

Several processes have been established for the STS Plasma Etch system which enable deep, anisotropic etching of silicon structures for MEMS applications. Our understanding has improved as to which subtle changes in parameters affect the final etch profile and structure. While several key issues remain to be resolved, this effort has provided an important database which will reduce the process design cycle for MEMS projects requiring this capability, and further provide critical design rules and methodologies for future projects.

Micromechanical Characterization Tools for Highly-Filled Polymers

Scott E. Groves and Steve J. DeTeresa
Manufacturing and Materials Engineering Division
Mechanical Engineering

Bruce J. Cunningham
Chemistry and Materials Science
Chemistry

Dino R. Ciarlo
Engineering Research Division
Electronics Engineering

David Allen, K. Clayton, and C. Yoon
Texas A&M University

We are attempting to characterize and model the micromechanical response of highly-filled polymers. In this class of materials, the continuous plastic binder used to bond the highly-filled material dominates the observed viscoelastic response. As a result, realistic lifetime analysis of these materials will require a thorough understanding of the contribution of the plastic binder. In support of our activities we have explored numerous techniques to characterize the microstructure of these materials.

We have made progress in developing an appropriate micromechanical constitutive modeling framework, based on a finite-element method incorporating a cohesive zone model to represent the binder contribution within a Voronoi tesselation mesh structure for plastic bonded explosive (PBX) grains. A second modeling approach was used to incorporate analytical micromechanics (generalized self-consistent schemes). However, preliminary theoretical analysis strongly suggested that this approach would be invalid for extremely high-filled systems like PBX.

Introduction

The mechanical properties of highly-filled polymers (HFPs) are generally dominated by the properties of the binder, because the binder is still a continuous phase, even at low concentrations. An example of this effect is shown in **Fig. 1**. Here, the mechanical properties of a representative PBX are shown to be highly dependent on relatively small changes in temperature. This particular system is composed of 95% high explosive (HE) crystals and 5% binder. Over the temperature range shown, the HE crystals experience no significant change in properties, whereas the binder experiences significant mechanical property changes. This is in large part because the binder has a glass transition temperature that falls within the range of operation.

In general, HFPs are highly time-dependent and nonlinear, with typical applications at Lawrence Livermore National Laboratory (LLNL) requiring more than 30 years of expected service. Long-term modeling will require accurate thermo-visco-elastic/plastic material models with the ability to capture microstructural/*in-situ* properties of the constituents. Developing material models that can relate constituent properties to macroscopic composite properties has considerable benefits, especially in the case of energetic materials. Characterizing the polymer binder independently is simpler and with PBX, poses no safety concern. These tools would also facilitate the incorporation in models of any identifiable chemical or physical aging mechanisms, thus forming a solid foundation for conducting accelerated aging studies on these materials. Furthermore, this suite of tools and models

will enhance the prediction of the mechanical response of new HFP formulations, which in turn, could reduce the qualification time for the replacement of material components.

This paper will discuss our efforts to characterize the local microstructure, to measure *in-situ* properties of the local volume, to measure binder constituent properties, and to perform micromechanical modeling.

Progress

Microscopic Characterization of the Local Volume

This task is associated with developing tools for determining the local microstructure of HFPs. In extremely high-volume filled polymers like PBX, it has been difficult to distinguish the location of the binder phase. Traditional surface microscopy has not been very useful. The example shown in **Fig. 2** represents a Los Alamos National Laboratory (LANL)-developed polarized light microscopy image of a very thin wafer of PBX (which required considerable effort to produce).

Micro-computed x-ray tomography has been explored, but proved to lack the resolution necessary to clearly identify the binder. The best resolutions available are 3 to 5 μm, which falls short of the requirement by better than an order of magnitude.

Atomic force microscopy (AFM) was also explored, but suffered from having incompatible tip designs for probing and identifying soft binder between the grains of HE crystals.

To improve our ability to characterize the local microstructure of PBX, this project applied the majority of its funding to purchase a new type of scanning electron microscope (SEM) that can image organic materials without the need to apply a thin layer of conductive coating such as gold. With regard to coating, our concern has been that the conductive coating would mask some of the microstructural features of interest. The SEM purchased was an LEO 438 Variable Pressure System (**Fig. 3**). LEO is the new name of Cambridge Instruments (developer of the first commercial SEM). This facility has only recently been approved for HE work. Some of the images that we have obtained with this system are shown in **Fig. 4a–f**.

Figure 4c represents our first attempt at imaging a polish surface of LX17. This surface was hand-lapped in an ice water bath to improve KELF polishing. We believe that the lighter material is the KELF binder. It appears light in this image due to electron charging.

To further enhance our imaging capabilities we are exploring stereo image capture and rerendering within the SEM. Modern software and tools developed for the computer gaming industry have made it very user friendly within the PC environment. Our preliminary work with 3-D imaging on filled organics and mock explosives reveals significantly greater depth of field information.

We also intend to explore tagging the binder with a stain or a higher density element during processing to enhance its contrast relative to the filler.

In-situ Property Characterization

A relatively new technique, "Atomic Force Microscopy with Nano-Indentation," was explored to investigate the *in-situ* response (that is, to measure force deflection behavior) on mock HE. It became apparent quickly that current probe

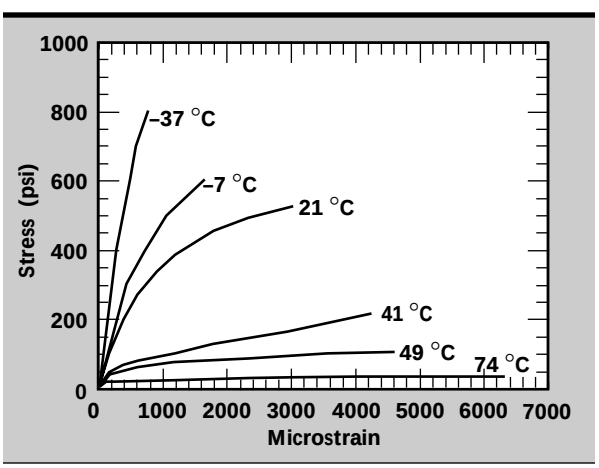

Figure 1. Temperature dependence of tensile properties of PBX-LX14.

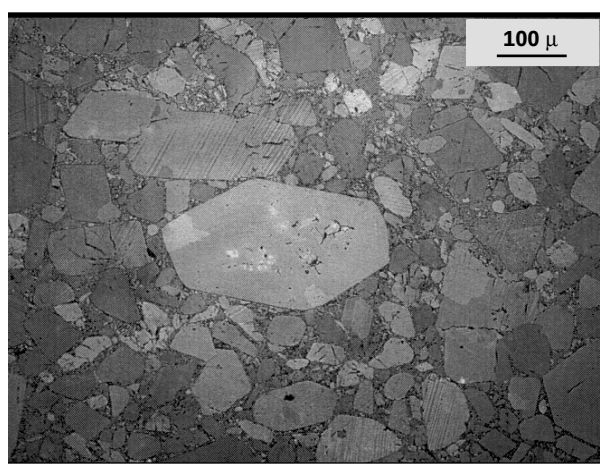

Figure 2. Polarized light microscopy image for PBX from LANL.

designs are grossly inadequate to determine the required *in-situ* properties. What is needed is to reduce the size of the probe diameter while at the same time increasing the probe length. Concurrently, we must also reduce applied forces from micronewtons to nanonewtons.

An effort was initiated to develop our own nano-indentation system around a newly designed, high-aspect-ratio probe tip. Hardware was purchased for what was expected to be our base system foundation, including three stages of nanometer motion control as well as hardware to develop a stereo microscopic viewing system for positioning the nano-indentation probe on the material.

Initially, we planned to measure the viscoelastic properties of the binder material in its position surrounding the HE. To do this, a special probe was needed to apply a constant force on the binder material and measure the displacement as a function of time. It is expected that the material will yield plastically as well as creep. We will also apply a constant strain to the material and monitor the relaxation in force required to maintain this strain. The forces, displacements, and time constants resulting from these measurements will be used in developing micromechanics models.

With limited funding, we have made some progress in the development of the tool set. In some sense, commercial technology has passed us by, with the newly available nano-indentation systems.

We continued development of the high-aspect-ratio tip. For our applications, we need a probe with a circular contact area having a diameter of 0.1 µm and a shaft length of 2 µm. Silicon micromachining

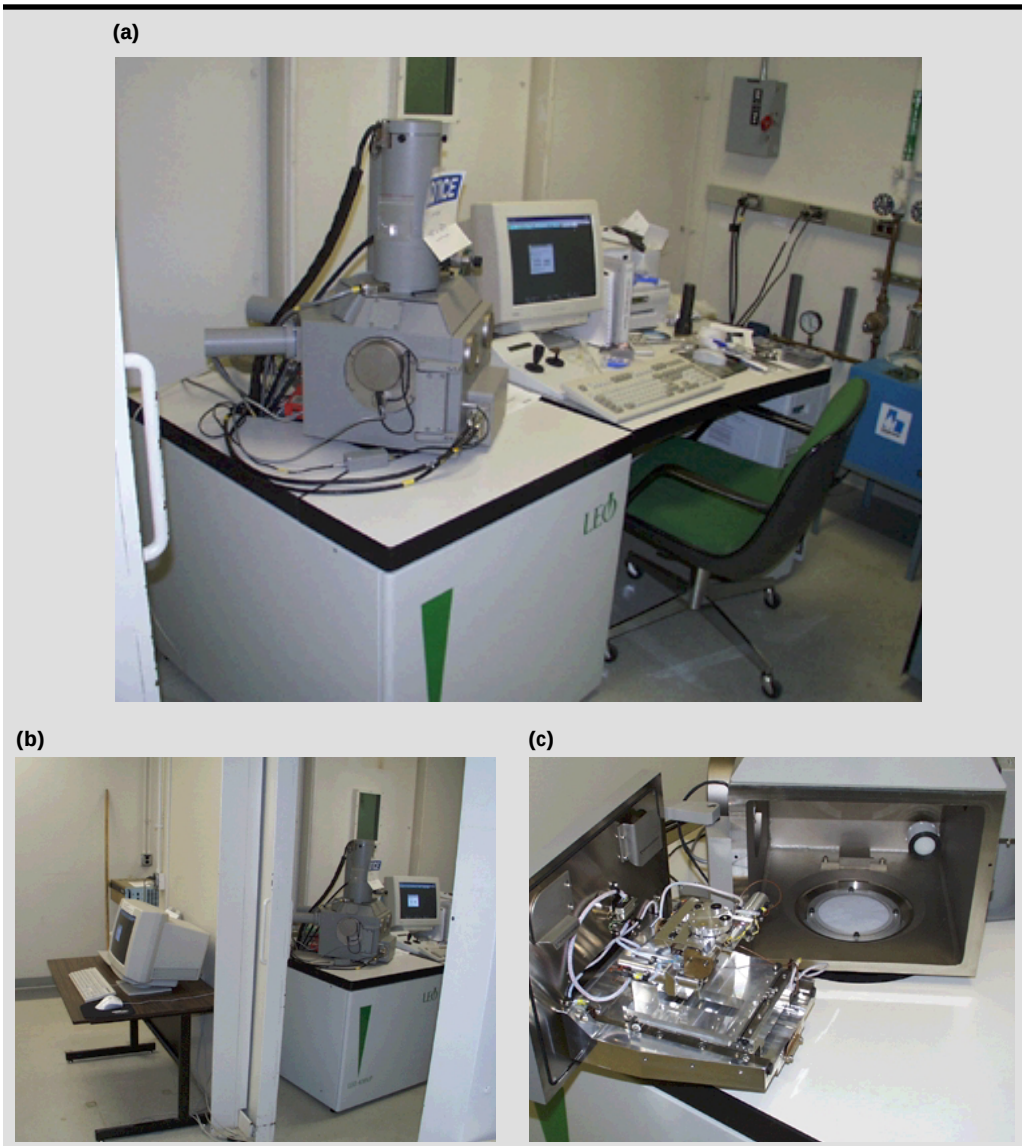

Figure 3. (a) LEO 438 Variable Pressure Scanning Electron Microscope; (b) configured in remote operation for high explosives; (c) scanning chamber open, revealing high explosive filters on turbo pump.

was used to fabricate this probe. The tip has a radius of ~1.5 nm. Just recently this new nano-tip was installed in a traditional AFM. Our recent scans on mock HE have been very encouraging, with the results shown in **Fig. 5**. In these results, shading is used to denote surface height.

Additional progress has included demonstration of stereo microscopic imaging tools, as well as

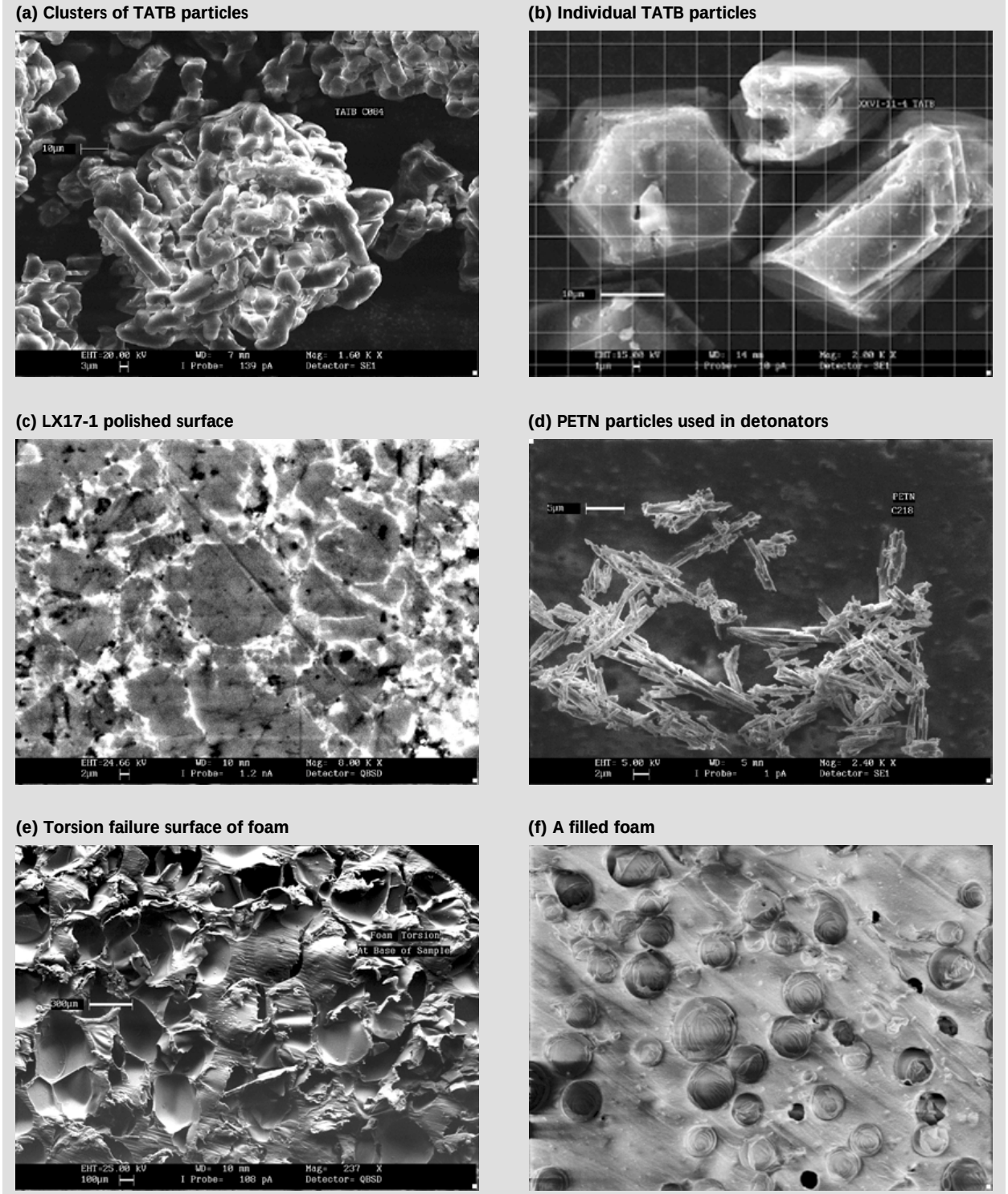

Figure 4. SEM images obtained with LEO 438 Variable Pressure Scanning Electron Microscope. All of the pictures shown were obtained without conductive coatings.

development of a baseline labview control system for the nano-mover stages.

Characterization of Binder Constituent Properties

The objective of this task was to determine the mechanical properties of the individual constituents for the selected material systems. For the case of PBX, our focus was on characterizing the response of the KELF binder used in LX17. Other groups are attempting to characterize the elastic properties of the explosive crystals. Characterizing the mechanical response of binders is not a trivial task. These materials are very soft and require self-supporting grips to prevent premature deformation or bending of the specimen. Furthermore, since the glass transition temperature is spanned by the operating

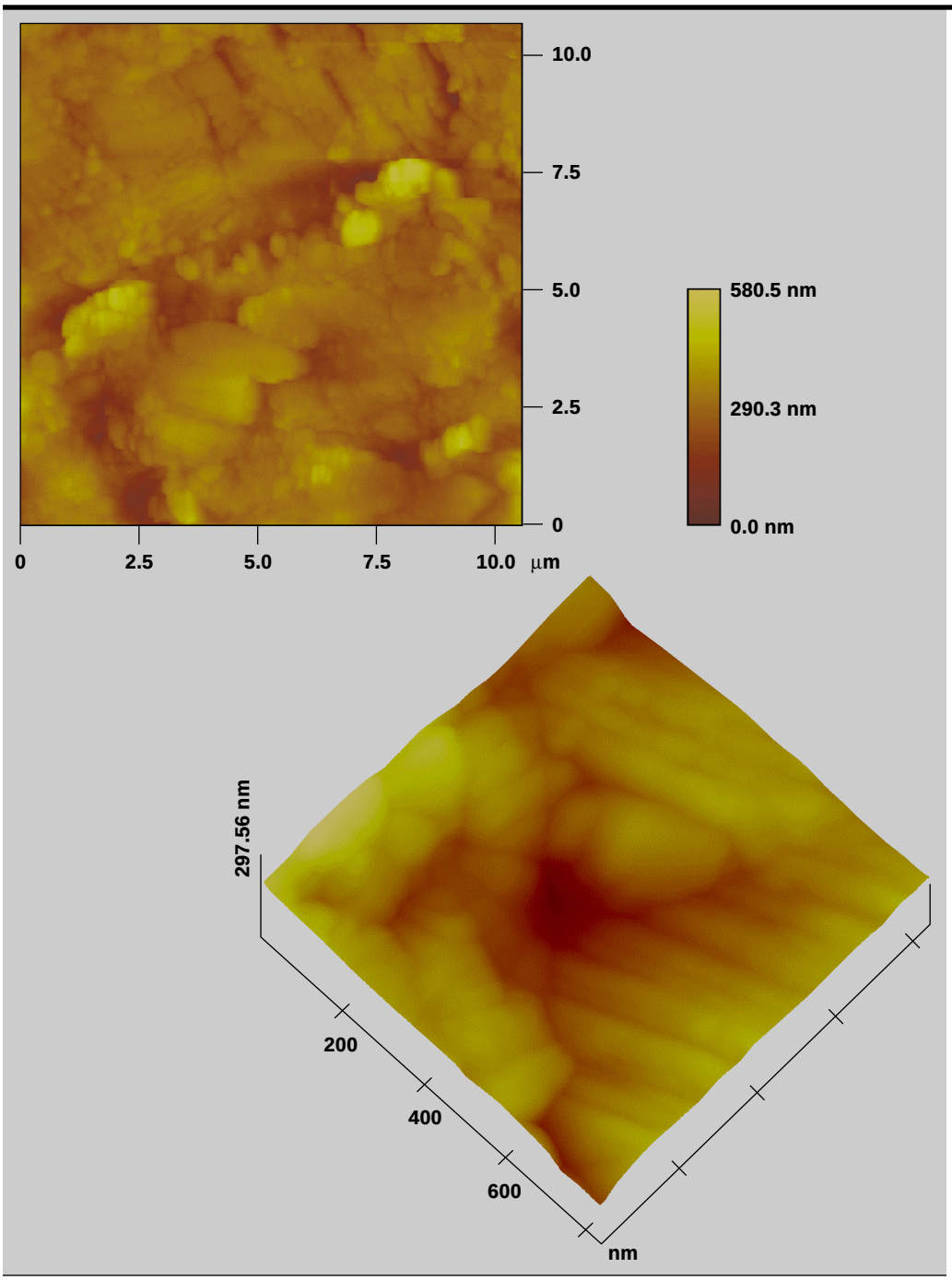

Figure 5. Atomic Force Microscope scans using the recently developed nano-tip probe.

temperature of this system, temperature control during testing is very critical. This has required the installation of water bath temperature controls for maintaining temperature stability, especially at any temperatures near and below 22 °C.

A suite of thermal creep data has been generated on the KELF binder. These results are shown in **Figs. 6** and **7**. This data was converted into compliance data as shown in **Fig. 8**.

For use in finite-element material modeling codes, compliance data must be recast into relaxation modulus data using the following inversely proportional relationship:

$$\tilde{E}(s) = \frac{1}{\tilde{D}(s)}$$

where *D(s)* is the creep compliance in Laplace space, *E(s)* is the relaxation modulus in Laplace space, and the ~ indicates the Carson transform. The inverse Laplace transform (ILT) was taken of *E(s)* to get the relaxation modulus as a function of time. The ILT was performed two different ways—analytically, and using Schapery's Direct method.[1] The different curve fits and different ILT methods were used to make comparisons and thereby decide which method would be the best. The predicted relaxation moduli are shown in **Fig. 9**.

Since the values of the relaxation moduli at the different temperatures differ so greatly, the higher temperatures do not show up well on **Fig. 9**. However, this graph shows the potential for making the master curve of the binder. By using a shift factor and a time scaling factor for the relaxation moduli at different temperatures, the master curve can be obtained for the binder. The shift factor is typically calculated using different methods for above and below the glass transition temperature (T_g).[2, 3] Below T_g, the Arrhenius relation can often be used:

$$\log a_T = \frac{\Delta F}{2.303R}\left(\frac{1}{T} - \frac{1}{T_M}\right)$$

where a_T is the shift factor, ΔF is a constant activation energy per gram mole when R = 1.987 (cal/g-mole K) and T_M is the reference temperature. Above T_g, the WLF form is often used:

$$\log a_r = \frac{-C_1(T - T_M)}{C_2 + T - T_M}$$

where C_1 and C_2 are constants. T_g of this material is around 25 °C, so all except the 35 °C data will be shifted using the Arrhenius form.

Figure 6. KELF binder tensile creep at 15 °C.

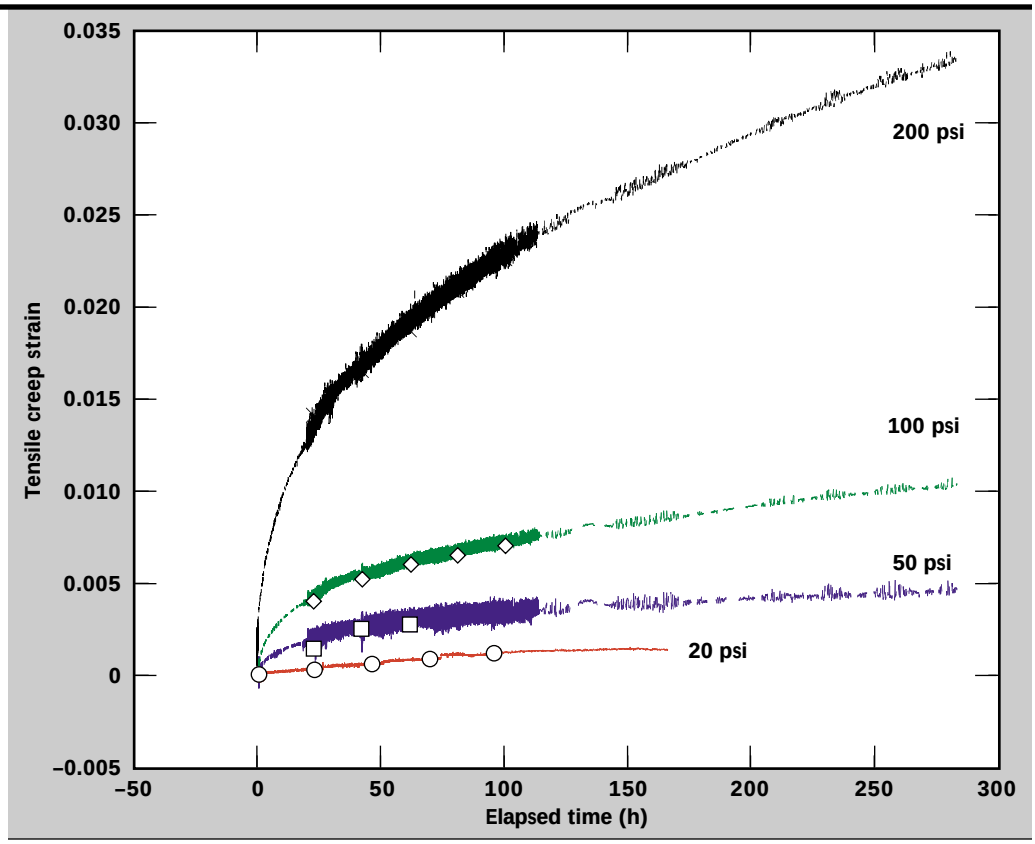

These transformations are made to model the thermorheologically simple thermoviscoelastic material properties of the PBX.

Micromechanical Modeling

In our micromechanical modeling effort we are assessing the merits of two different approaches: analytical micromechanics (a composite spheres model) and finite-element analysis. Common in all methods is the desire to develop a representative local volume element of material. Theoretical analysis of the former analytical approach suggests that method would be inappropriate for modeling extremely highly-filled systems like PBX. The discussion of this is given below.

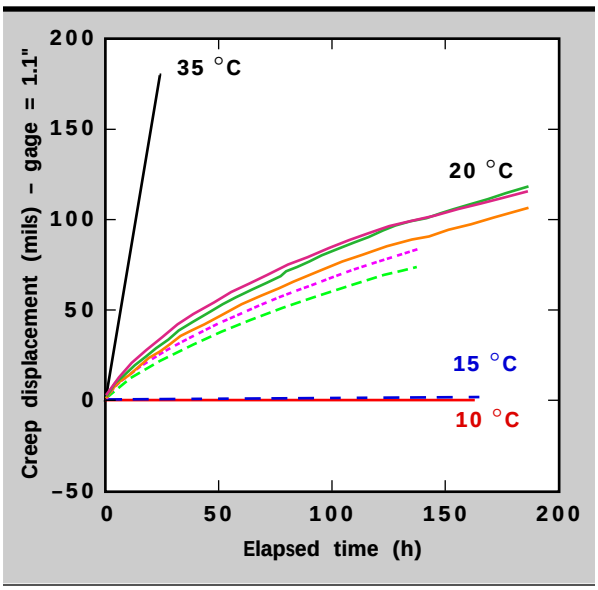

Figure 7. Variation in the thermal tensile creep response of KELF at 20 psi.

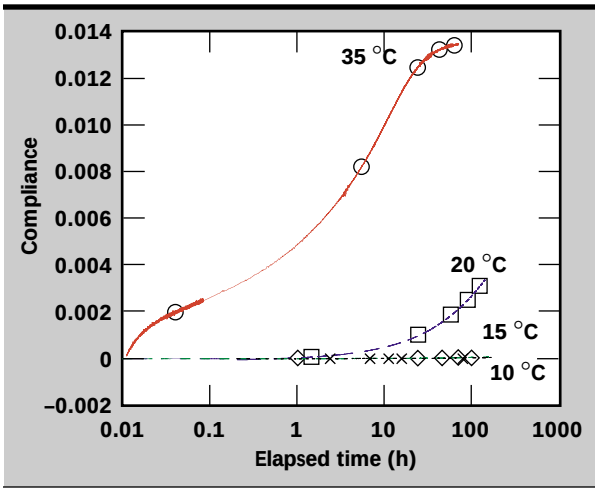

Figure 8. KELF creep compliance data.

Inefficiency of Analytical Micromechanics (Composite Sphere Model) for Material System with Inclusions of High Volume Concentration. A very small or large volume concentration formula for heterogeneous material can be validly obtained from the analytic solutions of classical micromechanics by truncating the higher order terms of volume fraction of the inclusion or that of the matrix. However, it has been assumed in the theoretical micromechanics analysis that the contact length between particles (called 'contiguity') is always zero for all concentrations, no matter what the configuration of the inclusion is. Clearly, this assumption cannot be expected to hold for the case of PBX. A citation from a well-known work in the field of theoretical micromechanics reads:

"A fundamental assumption made in this work is that of zero contiguity. Obviously, this cannot be true for a real material. The contiguity is an increasing function of the fractional volume of inclusions and can be expected to be very small only in the case of small concentration. When the concentration is close to unity it would appear more reasonable to assign the role of matrix to the inclusion material and that of inclusions to the matrix."[4]

The suggestion about switching the roles of inclusions and matrix does not seem to be reasonable even when no damage is introduced, since the inclusions (explosive particles) have elastic material behavior whereas the binder material (matrix) behaves viscoelastically. Once damage evolves and cracks propagate in the

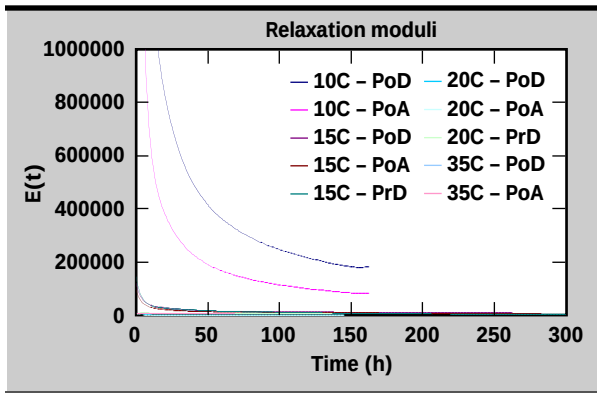

Figure 9. Predicted relaxation moduli for KELF binder.

matrix, this proposed role reversal continues to be unrealistic.

Aside from the contiguity problem, there are other difficulties in using analytic estimation to obtain the effective moduli. It is commonly believed that whenever the difference in moduli between inclusions and matrix materials is not too large, the upper and lower bounds will be close together. However, in such an extreme case as PBX, the bounds are not close enough to provide a good estimation of an effective moduli of the composite.

Analytic theory has another discrepancy. The composite spheres model cannot account for the size deviation effect and irregular shape effect that play critical roles in estimating the effective material properties. Inclusion particle sizes in PBX show large scatter. In addition, it has been shown that the inclusion particles in PBX have various irregular shapes and most of them are of sharp configuration. Wherever the explosive particles have sharp corners or acute angled edges, a stress concentration is expected. These stress concentrations will make damage evolve in the binder material, and the damage evolution consequently leads to more stress concentrations. With the composite spheres model these effects are not accounted for, so that the subsequent prediction of damage evolution will necessarily be erroneous. For these reasons, finite-element methods are being studied in this research with the expectation that they will better predict damage-dependent, effectively averaged properties for PBX.

Finite-Element Approach. In our finite-element material modeling effort we are using Voronoi tessellation mesh structures[5–7] to simulate the distribution of the highly-filled component and a cohesive zone model[8, 9] between each component. The fundamental idea in this approach is to reduce the effects of the extremely low volume material to that of a line function in the finite-element mesh, thus avoiding the tremendous memory penalty for modeling both grains and binder.

The later method of modeling both grains and binder from a pure continuum sense within the finite-element algorithm will be explored in the future. It is essential to have correct material properties for the line function. (This approach might be considered similar to having a tied slide line, as in NIKE, except the line will have constitutive properties). The advantage of the cohesive zone model, which contains double nodes at each point, is in the facilitation of simulated damage (fracture between the grains) in our representative local volume. Homogenization of the boundary response (with or without damage) leads to a set of representative properties.

For our particular case the highly-filled component is the explosive grains, and the low concentration material is the viscoelastic binder, KELF.

Two meshes, shown in **Fig. 10**, will initially be used to model the material. They are double-noded meshes with 30 grains and 100 grains, respectively. Since the material has such a high volume fraction (~92%), a refined mesh with a finite space between grains is difficult to generate. Therefore, we are using these meshes with a cohesive zone model and zero opening dimension in the undeformed configuration along the grain boundaries to model the binder. The relaxation moduli obtained through the method described previously are fitted using a Prony series that is used in the cohesive zone model. The characteristic length scale of the cohesive zone and the Young's modulus of the particles (grains) are still unknown but are necessary if we hope to achieve an accuracy in our finite-element models. Preliminary

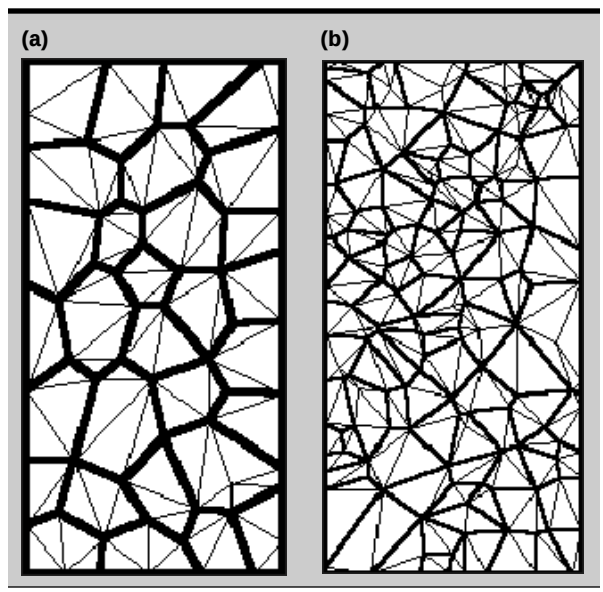

Figure 10. Preliminary Voronoi finite-element mesh structures for PBX. Mesh (a) is a 30-grain and 97-element model. Mesh (b) is a 100-grain and 292-element model. One of our goals is to determine the convergence of mesh refinement.

properties for the elastic behavior of the explosive grains will have to be initially estimated by extrapolation from measured PBX global properties.

Summary

This project has served to further the development of those tools necessary to characterize HFPs. When further developed and linked together with the viscoelastic modeling tools, this methodology will provide a basis for estimating the useful lifetime and identifying any age-related problems for these materials.

References

1. R. A. Schapery (1967), ”Stress analysis of viscoelastic composite materials,” *J. of Comp. Mat.*, Vol. **1**, pp. 228–267.

2. L. C. E. Struik (1978), ”Physical aging in amorphous polymers and other materials,” Eksevier Scientific Publishing Co.

3. R. M. Christensen (1962), ”Theory of viscoelasticity,” Academic Press, New York, New York.

4. Z. Hashin (1962), “The elastic moduli of heterogeneous materials,” *J. of Appl. Mech.*, pp.143–150.

5. G. J. Rodin (1995), “Stress transmission in polycrystals with frictionless grain boundaries,” *J. of Appl. Mech.*, March, Vol. **61**/2.

6. M. W. D. Van Der Burg and E. Van Der Giessen (1994), “ Delaunay-network modelling of creep failure in regular polycrystalline aggregates by grain boundary cavitation,” *Int. J. of Damage*, Vol. **3**, April.

7. M. O. Starzewski and C. Wang (1989), “Linear elasticity of planar Deluanay networks: random field characterization of effective moduli,” *Acta Mechanica*, Vol. **80**, pp. 61–80.

8. C. Yoon and D. H. Allen, “Damage dependent constitutive behavior and energy release rate for a cohesive zone in a thermoviscoelastic solid,” submitted to *Int. J. of Fracture*.

9. F. Costanzo and D. H. Allen (1993), “A continuum mechanics approach to some problems in subcritical crack propagation,” *Int. J. of Fracture*, Vol. **63**, pp. 27–57.

Advanced Imaging Catheter

Amy W. Wang and Abraham P. Lee
Electronics Engineering Technologies Division, Center for Microtechnology
Electronics Engineering

Daniel L. Schumann
Manufacturing and Materials Engineering Division
Mechanical Engineering

Luiz Da Silva, Matthew J. Everett, Billy W. Colston, Jr.,
Steve B. Brown, and Dale L. James
Medical Technologies Program

Richard A. London and Peter Amendt
Defense and Nuclear Technology

Optical coherence tomography (OCT) imaging of arterial vessels has been previously demonstrated using a single fiber rotated in the central lumen of a catheter. OCT images have been shown to provide improved resolution (<10 μm) over ultrasound images. We have fabricated a prototype catheter that uses embedded optical fibers in the inter-wall lumens of a catheter tube for OCT imaging. Using inter-wall lumens of the catheter keeps the central lumen open for insertion of surgical instruments during minimally invasive procedures, while permitting continuous on-board imaging. We have also explored actuation techniques for articulating the tip of the catheter for steering through arterial vessels during catheter positioning.

Introduction

Minimally invasive surgery (MIS) is an approach whereby procedures conventionally performed with large and potentially traumatic incisions are replaced by several tiny incisions through which specialized instruments are inserted. The key advantage of this technique is that recovery time can be reduced from months to a matter of days. Early MIS, often called laparoscopic surgery, used video cameras and laparoscopes to visualize and control surgical devices. The difficulty is that the images produced using these techniques are 2-D projections of a 3-D network. The surgeon, as a consequence, is often uncertain which direction to navigate the catheter. Toxicity issues, moreover, limit the continuous use of contrast agents, so often the surgeon is unable to visualize any component of the arterial network.

Catheter-based minimally invasive procedures are a rapidly-growing sector of all surgical procedures. These include balloon angioplasty, now performed on an outpatient basis, aneurysm treatment, and laser thrombolysis. In the U.S. over one million catheter procedures are performed annually, representing a market of over $500 million. An example of a catheter-based procedure is one in which a catheter is navigated into the neck of an aneurysm, and then embolizing coils coated with thrombolytic (clotting) agents are inserted into the aneurysm to initiate thrombus. This is a very difficult procedure that can often take hours of manipulation to accurately position the catheter within the neck of the aneurysm. At times, the procedure cannot be performed, simply because the catheter cannot be positioned.

Practicing clinician contacts have repeatedly mentioned the frustration at not being able to navigate and image at the catheter tip. The difficulty can be appreciated when you consider that catheters are hollow polymer tubes that can be as long as 2 m and taper down to outside diameters of 800 μm and working channel diameters of 500 μm. They are made soft and pliable to reduce the possibilities of perforating

arteries or damaging the arterial wall. This makes the control problem similar to pushing on a string. Both the navigation and artery damage problems could be solved if we could produce a compact catheter that offers imaging and active control capabilities to guide and position the distal end (the end in the body). Clinicians have emphasized that if we could produce such a device it would be a tremendous breakthrough.

Previous work[1] demonstrated imaging through the use of optical coherence tomography (OCT), a non-invasive, non-contact optical technique for imaging through highly scattering media.[2–4] Although analogous to ultrasound imaging in many ways, OCT offers superior depth (<20 µm) and lateral spatial resolution (<10 µm). In addition to providing improved resolution over current "snap-shot" imaging systems, the use of OCT will also significantly reduce the amount of x-ray dosage to patients and physicians and allow procedures to be completed without the need of cumbersome lead vests. The ultimate benefit of the advancement of catheter and surgical technology is a critical path for improving patient survival and clinical success.

Progress

To date we have demonstrated an OCT imaging system that is ten times faster than our previous system. This gives us the ability to acquire eight fiber images at 10 Hz, which is adequate for a practical medical device. In addition, we have developed a compact (18-in. × 18-in. × 3-in.) fiber optic system replacing large rack-mounted instruments and improving reproducibility. The design of the optics at the distal ends of the fibers has been greatly improved, making 150-µm-diameter probes feasible while significantly reducing manufacturing cost and enhancing robustness. An *in vivo* image of a pig artery taken with the OCT system using a 250-µm-diameter probe is shown in **Fig. 1**.

A prototype catheter (**Fig. 2**) has been built in which optical fibers are threaded through internal lumens in the catheter wall (**Fig. 3**). An imaging prototype is being fabricated that integrates two single-mode optical fibers in the 250-µm-diameter inter-wall lumens of a 1.5-mm-diameter catheter tubing with a 900-µm-diameter center lumen. This fiber optic probe has the capability of imaging the tissue through the side walls of the catheter, while leaving the central lumen of the catheter available for a medical device.

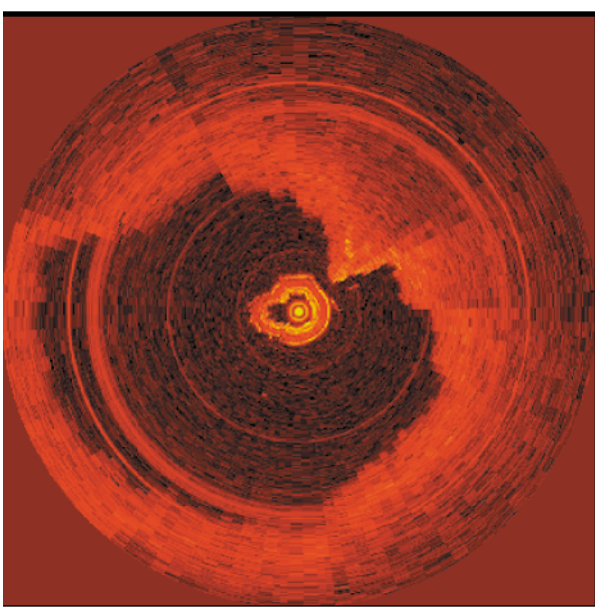

Figure 1. In vivo image of a pig artery using the OCT system.

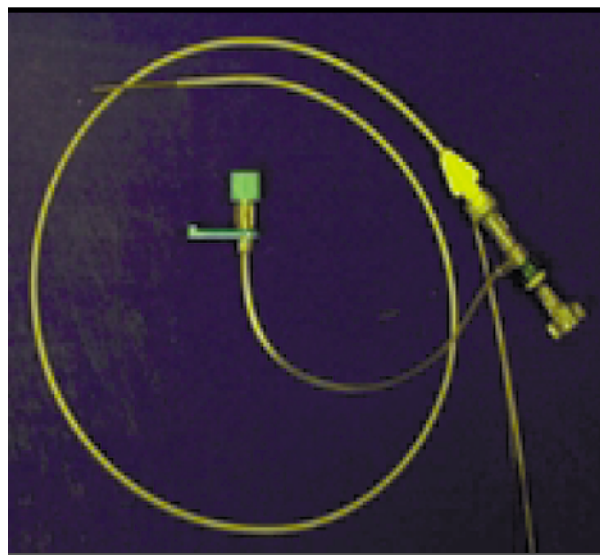

Figure 2. Multi-lumen catheter prototype.

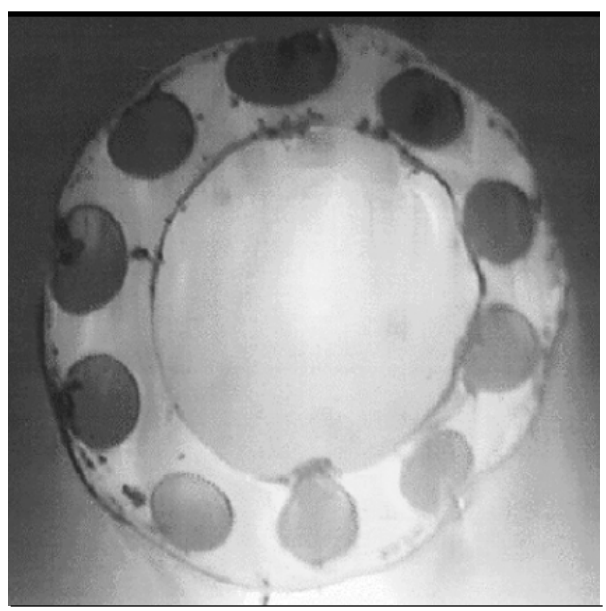

Figure 3. Example of multi-lumen catheter tubing with inner-wall lumens for optical fiber and actuator integration.

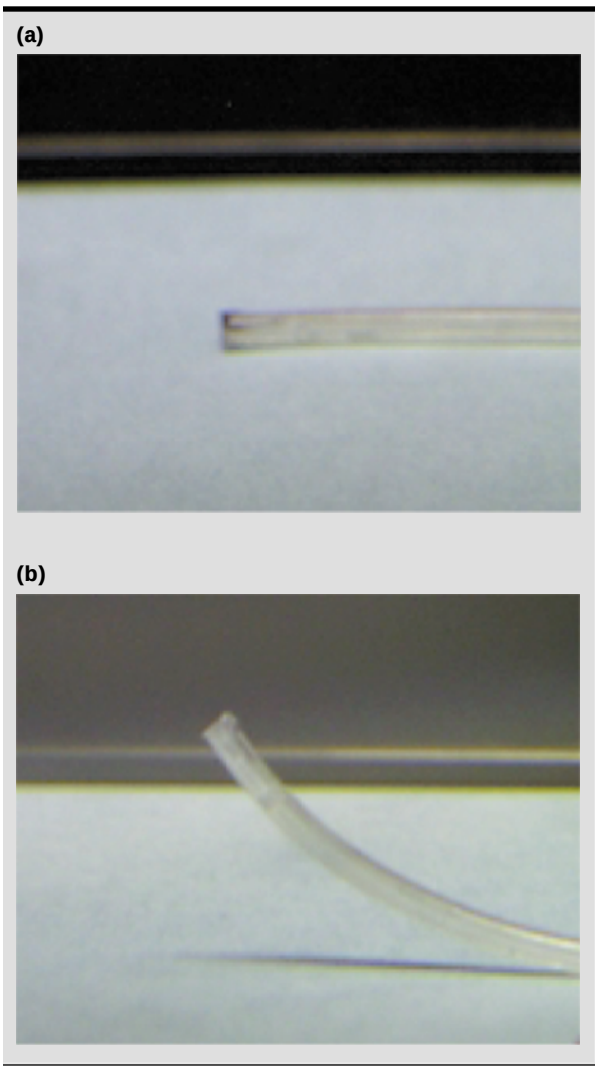

Figure 4. Catheter tip articulation actuated by heating of SMA wire threaded along catheter wall lumens.

Catheter tip actuation has been tested using a shape memory alloy (SMA). SMAs undergo a reversible temperature-dependent transformation between a low-temperature martensite phase and a high-temperature austenite phase. These materials are able to recover large amounts of mechanical deformation (strain) upon heating. In a technique similar to Takizawa *et al.*[4], nickel titanium (NiTi) wire was mechanically stretched in length then threaded up and down two adjacent catheter wall lumens. The wire was resistively heated, shrinking the NiTi wire to its original length, causing the catheter tip to bend (**Fig. 4**).

We have also developed the capability to model OCT imaging. Specifically, we modified existing Monte Carlo photon transport codes to track the phase and path length of photons propagating through biological tissue and an OCT imaging system. In **Fig. 5** we show the predicted OCT signal from a single imaging fiber in an artery filled with blood. The results show the

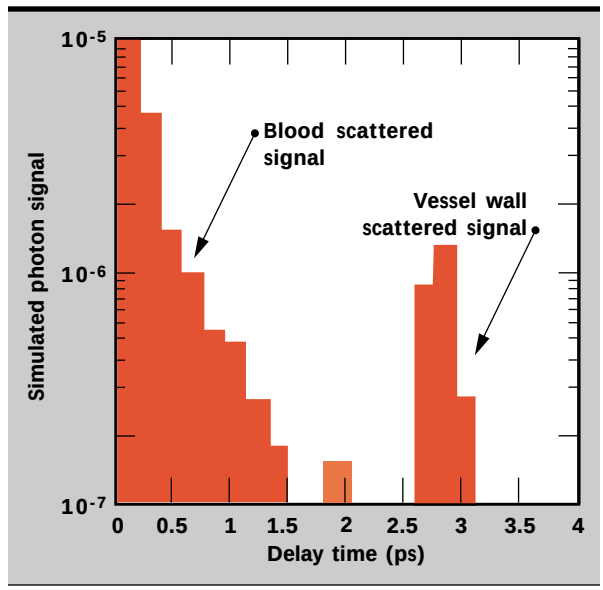

Figure 5. Predicted OCT signal from a single imaging fiber in blood-filled artery.

rapid decay in photon signal as you move away from the fiber surface due to the high scattering coefficient of blood. The artery wall is identified by a jump in the observed signal attributable to increased scattering. The results are in good agreement with the data collected in previous experiments.

Future Work

We have demonstrated a prototype catheter with on-board imaging capability with an open central lumen for introducing surgical instruments during a procedure. We have also tested an initial tip articulation using SMA-based actuation. In the future we will pursue alternative designs for catheter tip articulation.

References

1. B. W. Colston, Jr., M. J. Everett, L. B. Da Silva, L. L. Otis, P. Stroeve, and H. Nathel (1998), "Imaging of hard and soft tissue structure in the oral cavity by optical coherence tomography," *Appl. Opt.*, **37**(16), 3582.

2. D. Huang *et al.* (1991), "Optical Coherence Tomography," *Science* **254**, 1178.

3. G. J. Tearney, S. A. Boppart, B. E. Bouma, M. E. Brezinski, N. J. Weissman, J. F. Southern, and J. G. Fuijimoto (1996), "Scanning single-mode fiber optic catheter-endoscope for optical coherence tomographys," *Opt. Lett.*, **21**, 541.

4. H. Takizawa, H. Tosaka, R. Ohta, S. Kaneko, and Y. Ueda (1999), "Development of a microfine active bending catheter equipped with MIF tactile sensors," *Proc. Twelfth IEEE Ann. Conf. on MEMS*, Orlando, Florida, 412.

Intelligent Wavefront Reconstructors for Adaptive Optics

Chi Yung Fu
Electronics Engineering Technologies Division
Electronics Engineering

George F. Chapline
Physics Directorate

Scot S. Olivier
Information Science and Technology Program
Laser Programs

Loren I. Petrich
University of California at Berkeley
Berkeley, California

We have successfully demonstrated our algorithm for wavefront reconstruction from gradients in one dimension. We have achieved both of our goals: a great reduction in computational load within an error of less than 2%.

Introduction

Developing different paradigms for adaptive and intelligent control systems for adaptive optics (AO) will provide state-of-the-art control technology for many Lawrence Livermore National Laboratory (LLNL) programs.

For example, many current and future high-priority programs, such as the National Ignition Facility (NIF) and Laser Guide Star (LGS) for the Lick and Keck Observatories, are critically dependent on their capabilities in advanced wavefront control for their success. Unless this problem is solved, it may impact the delivery of these systems at a reasonable cost. The economic implications for just two of the many important applications—the development of programs for DOD laser weapons with potential values of $10 to 100M, and the extreme UV lithography programs worth over $100M—provide strong motivation for this project.

This project directly aligns with LLNL's core competency areas and also impacts areas such as national defense and nonproliferation, advanced sensors and instrumentation, atmospheric sciences and geosciences, and computational engineering.

Scope

The central problem in AO is reconstructing the distorted wavefront of incoming light so that one can then adjust a deformable mirror to compensate for its distortion. Using traditional technology, these calculations require solving a system of linear equations resulting in a computational complexity of N^2, where N is the degree of freedom or the number of actuators for the deformable mirror.

The goal of this project is to develop different paradigms for adaptive and intelligent AO control that would be scalable for systems with a few hundreds of degrees of freedom, up to tens of thousands or even hundreds of thousands of degrees of freedom.

The specific problems we are trying to solve here are the performance and cost issues that arise for adaptive wavefront control when we scale the number of degrees of freedom up to tens or hundreds of thousands. Our first goal is to demonstrate that in 1-D, the computational requirement of our proposed new paradigm will scale with N, rather than N^2. This new scaling implies that desirable performance and reasonable cost will be attainable

even if N is very large, thus getting to the heart of this problem. Our second goal is to demonstrate that the error in adopting our paradigm will be acceptable (less than 2%).

Solutions and Architecture

Broadly speaking, there are two very different approaches to solving the problem. One would be to replace the current sensors with more sophisticated ones. An example is the use of interferometers to directly measure phase rather than the phase gradient and thus eliminate the need for wavefront reconstructors. This new approach, however, faces uncertainty in terms of cost, noise, and other factors. The other approach would be to improve wavefront reconstruction by using existing or future sensors. By speeding up the wavefront reconstruction at a lower cost, one could essentially solve the problem.

Up to now the existing technology has been adequate for addressing the requirements of most AO as long as the number of degrees of freedom is limited. However, for many new applications that require a multiple-order-of-magnitude scale-up in the number of mirror segments, or equivalently, the number of pistons that control the mirror's shape, and also an increase in system speed to accomplish wavefront control in real time, the traditional approach is neither efficient nor economical.

Thus for applications that need corrections not only at local and global levels but at all the levels in between, we have investigated a multi-level, multi-resolution solution. Using an iterative method, we work towards an approximate solution instead of an exact one and thus a substantial amount of computational time can be eliminated.

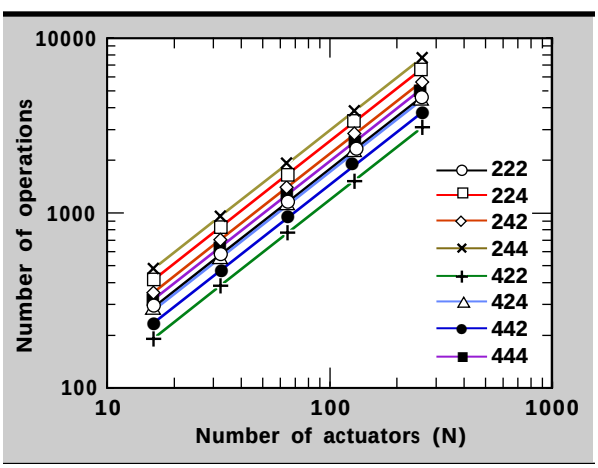

Figure 1. Number of operations as a function of number of actuators and local configuration.

Computational Performance–Cost Analysis and Results

Through 1-D simulation we have worked out the number of calculations needed for various configurations. These are shown in **Fig. 1**. The parameter values are shown in the legend, and are, in order, the averaging factor, the number of outputs, and the pad size. As we can see within this range of parameters, for 256 degrees of freedom the number of operations is between 3840 and 7680, instead of 65536 in the case of traditional methodology. Using our algorithm, the range of computational load also allows us to trade off computational complexity with accuracy.

Error Analysis and Results

Though we have demonstrated an approach that reduces the computational complexity, there is the serious question of whether it is possible to get the error down to an acceptable level with the number of operations much less than N^2. For Fourier transforms, the answer seems simple: the translational symmetry of the problem makes the solution of the problem a simple O(N) calculation in the Fourier domain, though there is the complication of boundary conditions.

For our algorithm, there is no such exploitable symmetry, but the expected behavior of the turbulence provides an answer. Atmospheric turbulence follows Kolmogorov's law, with the turbulent energy being proportional to $k^{-11/3}$. This translates into a turbulent amplitude that is proportional to $k^{-4/3}$, and our system made use of this feature to achieve acceptable errors, as can be seen in **Fig. 2**, which shows the error achieved for each level in the multi-level structure.

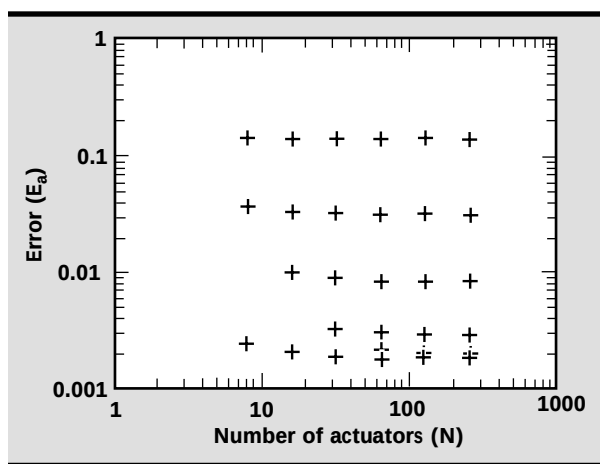

Figure 2. Error per level.

Acknowledgments

We would like to acknowledge the support of the Engineering Department and the Laser Directorate for this work. We are especially indebted to Drs. R. Deri, J. Brase, G. Suski, and R. Langland for their encouragement and their faith in this project.

Lambda Connect: Multiwavelength Technologies for Ultrascale Computing

Michael C. Larson, Steven W. Bond, and Michael D. Pocha
Electronics Engineering Technologies Division
Electronics Engineering

Mark A. Emanuel
Laser Science and Technology Program
Lasers

Mark E. Lowry
Information Science and Technology Program
Lasers

Byte-wide, multiwavelength optical interconnects can substantially improve the performance of the system interconnects used in ultrascale computing platforms ("supercomputers"), leading to substantial improvements in overall system performance for applications that require global communications within the supercomputer. Optical hardware required for such interconnects includes byte-wide multiwavelength transmitters and wavelength routing and filtering modules. This year, we have fabricated and characterized a byte-wide four-wavelength transmitter and developed the technology to increase wavelength count to eight and beyond. In addition, we have dramatically increased the wavelength range available for large-wavelength count systems by demonstrating long-wavelength emitters. Finally, we have developed a photon-conserving wavelength routing module to more efficiently connect multiple transmitter and receiver modules.

Introduction

Ultrascale computing—the integration of large numbers of processors into a single, highly capable multiprocessor system—is currently of great interest in several DOE and other government programs. These systems contain 100s to upwards of 1000 CPUs, to attain computing capabilities from 100 GFLOPS to 100 TFLOPS and beyond. The provision of fast data communications within such systems poses a significant challenge. Effective communication is currently hampered by the bandwidth, latency, and congestion characteristics of the electronic fabric used to interconnect the many system processing and memory elements. This communications bottleneck can substantially degrade computational performance, significantly complicate programmability, and cause inefficient use of costly memory resources.

The recent emergence of byte-wide optical interconnects, which use linear arrays of multimode optical fibers in a ribbon cable assembly, has substantially improved the cost and performance of Gbyte/s point-to-point communications. To fully leverage this technology, however, the latency and congestion issues with distributed electronic switching must be overcome. We have recently proposed to perform source-routed switching in the optical domain using a wavelength-switching mechanism, and shown that this approach can yield highly capable switches that support 100s of Gbyte/s ports and yield minimal internal congestion and latency. Instruction-level simulation has demonstrated the advantages of this approach.[1]

To implement this multiwavelength optical interconnect requires the addition of multiwavelength capability to the existing byte-wide optical interconnect. The required components, which include optical transmitters capable of fast wavelength tuning and fixed optical filters, differ substantially from existing telecommunications fiber optics. All components must be compatible with existing multimode fiber ribbon cables, and provide compact form factors suitable for populating electronics boards. This project aims at developing prototypes of these

components, to investigate the feasibility of implementing byte-wide, multiwavelength optical interconnects for ultrascale computers.

Progress

Multiwavelength Transmitters

We have fabricated and characterized prototype modules with the capability of transmitting on any of four selectable wavelengths. The module wavelength is selected by directing current into different lasers, each laser emitting at a different wavelength, so that current switching is used to provide fast wavelength switching on a timescale of the laser modulation bandwidth (1 to 2 ns switch time). Each module contains one linear array of 10 laser diodes for each wavelength, with a moderate channel separation (8 to 10 nm) that minimizes issues associated with wavelength registration, uniformity, and drift between different photonic components within the interconnect. Each array element can be independently addressed (modulated) by a current drive, so that the module can transmit 10 independent data streams comprising the 8 bits in an electronic data word of 1 byte capacity, plus clock and framing.

Our modules use arrays of vertical cavity surface-emitting lasers (VCSELs), which we have fabricated from GaAs/InGaAs/AlGaAs semiconductor layers grown by molecular beam epitaxy. Our VCSEL design uses an oxidized AlAs layer to control the "active region" of the laser which is pumped by the applied current drive, to achieve lasing thresholds of less than 2 mA for devices of 7 to10 µm oxide aperture. The VCSELs are sized to emit in multiple transverse modes (1.5 nm spectral extent), to minimize speckle noise during multimode fiber transmission. These devices provide milliwatts of optical power when pumped with <10 mA at voltages ≤3 V, conditions compatible with conventional complementary metal oxide semiconductor (CMOS) electronic drive electronics.

This year, we fabricated and fully characterized a byte-wide four-wavelength transmitter module under high speed modulation. We used a combination of direct fiber coupling and broad-band add/drop filtering to demonstrate a four-wavelength by 10-fiber VCSEL-based transmitter in a pin grid array (PGA) package with mechanical transfer (MT)-connectorized optical output.[2]

A schematic diagram and photograph of the four-wavelength parallel fiber transmitter are shown in **Fig. 1**. It consists of four single-wavelength VCSEL arrays fabricated from separately-processed wafers, emitting near 825, 845, 977, or 988 nm, fastened to a silicon optical bench submount. VCSEL chips are cleaved such that the ~8-µm-diameter emitter active area is centered within 15 µm of the chip edge, so that two arrays can be placed back-to-back to directly couple to the 62.5-µm core diameter and 250-µm pitch of the fiber ribbon.

Dual-wavelength optical signals are separately collected in bands near either 830 nm or 980 nm. These two bands are then multiplexed using a fiber-guided add/drop filter, which is a parallel-fiber three-port device consisting of an AlGaAs/AlAs Bragg mirror embedded at 45° within a fiber ribbon rigidly encased in an MT ferule.[3] Vertical emission at the 830-nm band is reflected horizontally by the Bragg mirror and combined with 980-nm band light transmitted through the filter in the horizontal direction. A (nonmultiplexing) gold turning mirror, packaged in a similar fashion to the Bragg mirror, directs the vertical 980-nm band emission to the horizontal input of the add/drop filter. Together these turning and multiplexing optics form a fiber-guided superstrate with the four-wavelength output terminated in a MT connector.

Spectra for each of the ten output fibers of the fiber ribbon are plotted on a logarithmic scale in **Fig. 2**; VCSELs at all four wavelengths were simultaneously biased at 3 mA. Due to wire bonding difficulties, not all wavelengths were demonstrated for

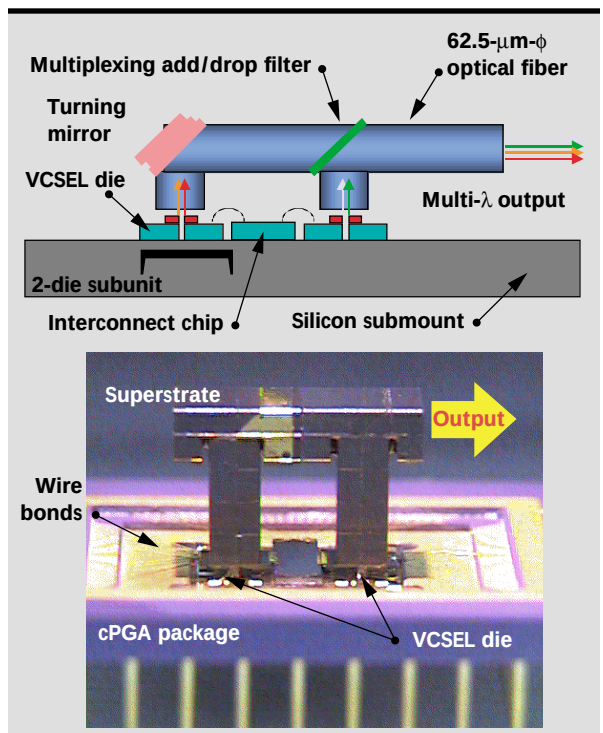

Figure 1. (top) Cross-sectional schematic diagram of the four-wavelength transmitter. This structure is repeated on a 250-µm pitch for each of the ten fibers comprising the fiber ribbon; (bottom) photograph of the completed module.

all fibers. Coupled output power as high as –2 dBm is achieved; the lower than expected power for the 977-nm emitter is likely due to misalignment. An eye diagram showing digital modulation at 1.25 Gbit/s under a 2^{23}-1 pseudo-random bit stream (channel #3, 988 nm) is plotted in **Fig. 3**.

Cross-talk between wavelengths and between fiber channels was studied using bit error rate testing. The bit error rate was measured as a function of signal power over a link consisting of the multiwavelength transmitter modulated with a pseudo-random bit sequence at 1 Gbit/s and connected by fiber ribbon successively through a variable attenuator and a wavelength filter[3] to a commercial receiver. **Figure 4** shows the error rate on a particular fiber of the 825-nm channel with and without modulation of a 990-nm channel. Essentially, no cross-talk penalty is seen within experimental measurement limits. Furthermore, the lack of a power-independent noise floor indicates the absence of speckle noise. Similar results are observed for adjacent fiber-to-fiber cross-talk.

To achieve higher wavelength counts in a compact form factor requires the monolithic fabrication of multiple wavelengths per VCSEL chip to complement the hybrid packaging scheme described above. This leads to a total wavelength count equal to the product of the number of hybridly-multiplexed VCSEL chips and the number of wavelengths per chip. This year, we have developed several different approaches that selectively shift the lasing wavelength by altering the VCSEL's effective cavity length. A major challenge is satisfying the requirements of (1) a tightly-spaced multiple-wavelength cluster

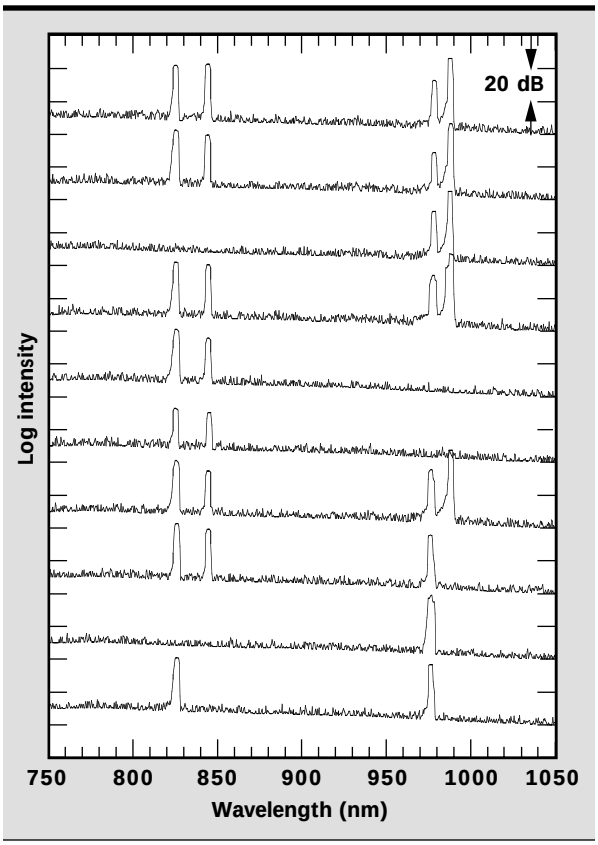

Figure 2. Output spectra for each fiber with VCSELs simultaneously biased at 3 mA each. Note that the spectrum is displayed on a logarithmic (decibel) scale.

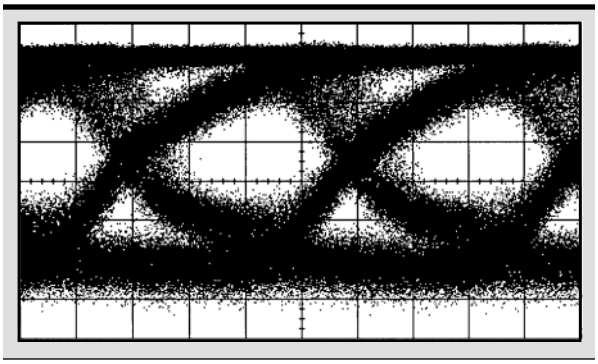

Figure 3. Eye diagram at 1.25 Gbit/s of fiber channel #3, 988 nm. The vertical axis is signal level and the horizontal scale is 200 ps/div.

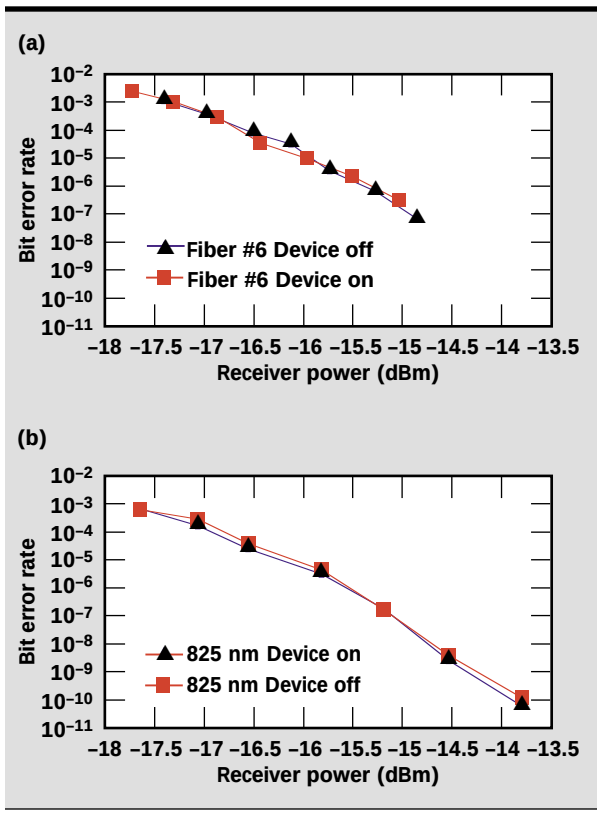

Figure 4. (a) Wavelength-to-wavelength (single fiber) and (b) fiber-to-fiber (single wavelength) bit error rate measurements vs. received optical power. The deviation between curves is within experimental error.

such that all emitters in the cluster can be efficiently coupled to one multimode fiber, (2) repeating this structure for each fiber in the ribbon, and (3) a controllable, manufacturable fabrication process.

Figure 5 shows our first results using a technique whereby the physical cavity length is etched before deposition of the top mirror. Lasing spectra were obtained for two emitters—one of which had its cavity layer etched—spaced apart by a center-to-center distance of only 27 µm, allowing for straightforward coupling of both devices to the 62.5-µm fiber core diameter. Each of these two-wavelength clusters was furthermore repeated on a 250-µm pitch for direct coupling to byte-wide multimode fiber ribbon cable. A wavelength shift between emitters of 8.9 nm was demonstrated, within our targeted wavelength separation of 8 to 10 nm required for ease of system tolerancing. The degraded lasing efficiency shown on the left of **Fig. 5** is attributed to the non-optimized device geometry. Subsequent devices are expected to show better efficiency.

We have also explored a proprietary technique for adjusting the VCSEL cavity length after a single-step growth process. This development can vastly simplify the demanding thickness control requirements otherwise needed when these arrays are fabricated with

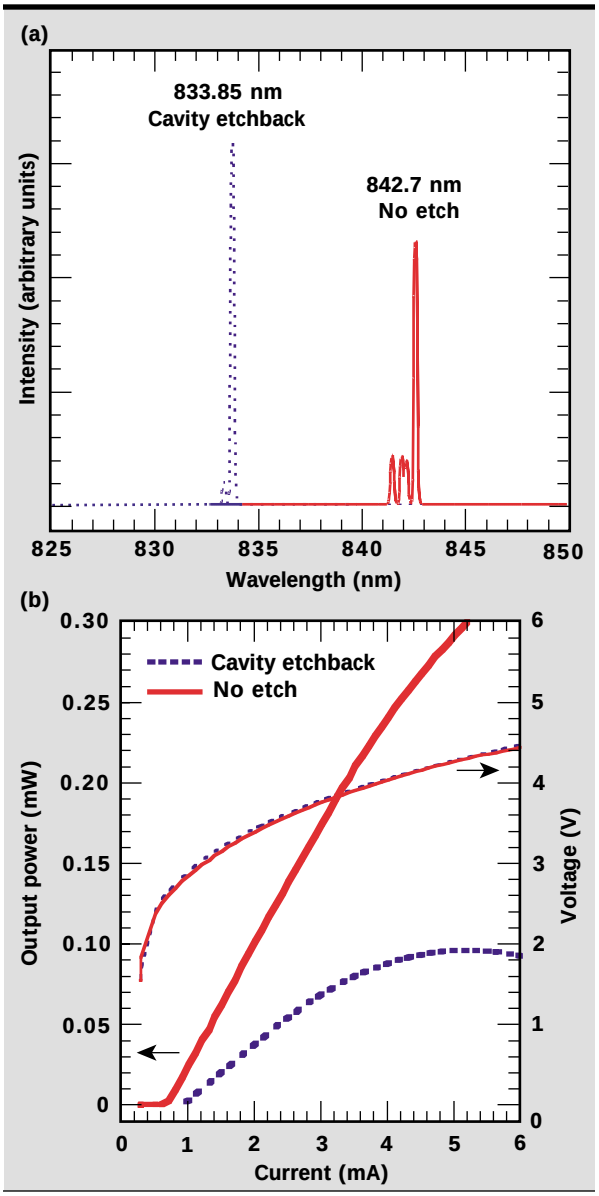

Figure 5. (a) Spectral and (b) output characteristics of first-generation monolithic WDM VCSELs using cavity etchback and multistep growth. Notice that the spectrum is plotted on a linear scale.

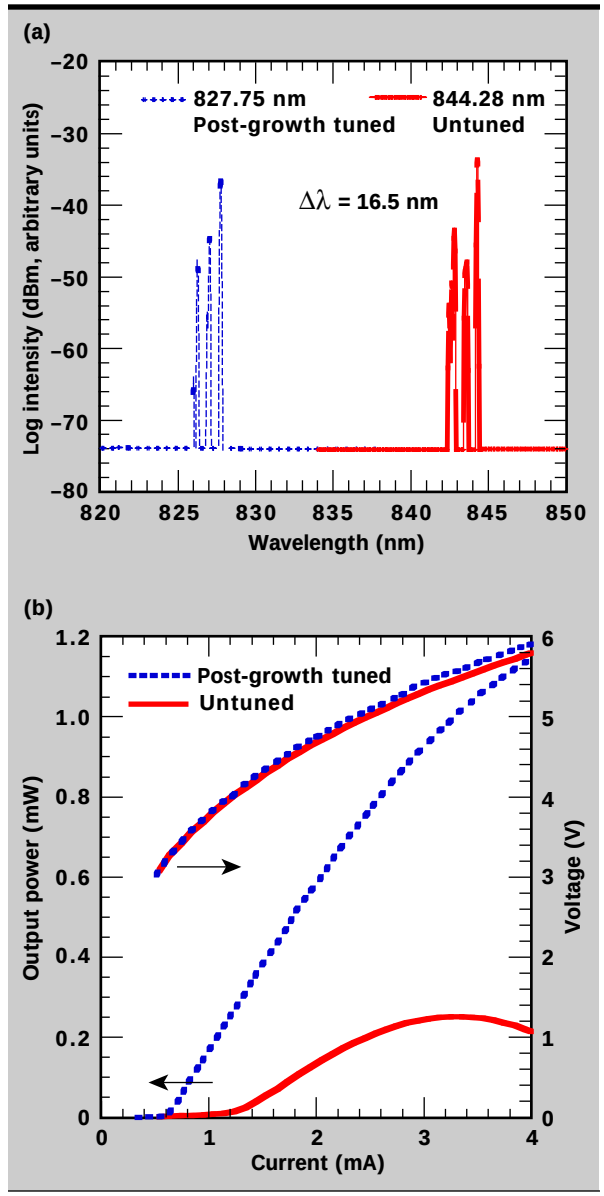

Figure 6. (a) Spectral and (b) output characteristics of first-generation monolithic WDM two-emitter VCSEL cluster using single-step growth followed by post-growth tuning of one of the devices. Notice that the spectrum is plotted on a decibel scale.

two separate growths. Initial characteristics for arrays fabricated with a similar layout as described above are shown in **Fig. 6**. A wavelength shift of 16.5 nm is considerably larger than the required 8 to 10 nm, indicating the potential of this approach for wide wavelength spacing. Current work is underway to extend these monolithic approaches to yield four wavelengths per single-fiber cluster with uniform characteristics across wavelengths.

Long-Wavelength VCSELs

Our transmitter modules have spanned the near IR spectrum with wavelengths ranging from approximately 800 to 1000 nm. For an 8 to 10 nm channel spacing, this yields a maximum possible channel count of 21 to 26 wavelengths, assuming no gaps and even spacing. To scale beyond this, we need to either choose a smaller channel spacing, which can negatively impact system robustness as discussed earlier, or use a larger portion of the spectrum. Extending to longer wavelengths is especially attractive because of improved performance of silica optical fiber, particularly at 1300 nm and beyond. Unfortunately, InGaAs/GaAs-based VCSELs are limited by strain in the active layer to a lasing wavelength of at most ~1100 nm. However, although edge-emitting lasers with InGaAsP/InP-based active layers are commonly used for 1300- and 1550-nm telecommunications applications, this material system is not suitable for fabricating the high-performance mirrors required by VCSELs. Therefore, we are exploring the GaInNAs material system for use as a long-wavelength active layer that can be directly integrated with GaAs/AlGaAs-based mirrors. Since it is a direct extension of technology proven for 850-nm and 980-nm devices, it holds great promise for viable long-wavelength emitters.

This year we fabricated simple broad-area (50-µm-square, no-oxide aperture) GaInNAs VCSELs and demonstrated room-temperature pulsed operation. As shown in **Fig. 7**, devices emitting at 1200 nm exhibited threshold currents as low as 68 mA (current density 2.7 kA/cm^2), slope efficiency above 0.06 W/A, and peak power above 17 mW. Although threshold current density is still approximately a factor of 3 higher than comparable shorter-wavelength InGaAs designs, these results represent the best yet reported for GaInNAs. Improved material crystallinity, mirror design, and use of advanced oxide-apertured geometry should yield small-area devices with considerably lower threshold currents.

Wavelength Router Development

Our original system concept used a simple broadcast element and wavelength bandpass filtering to achieve the multi-bus or crossbar implementation of the LambdaBus architecture, through a “broadcast and select” approach. A potential problem with this approach is that optical signal is wasted. With N ports and optical power at the transmitter of P, any given receiver will only receive P/N optical power. Recently, however, we conceived a power efficient wavelength routing fabric which routes a particular input port and wavelength to one particular output port rather than broadcasting to all output ports simultaneously. The multimode nature of our fiber

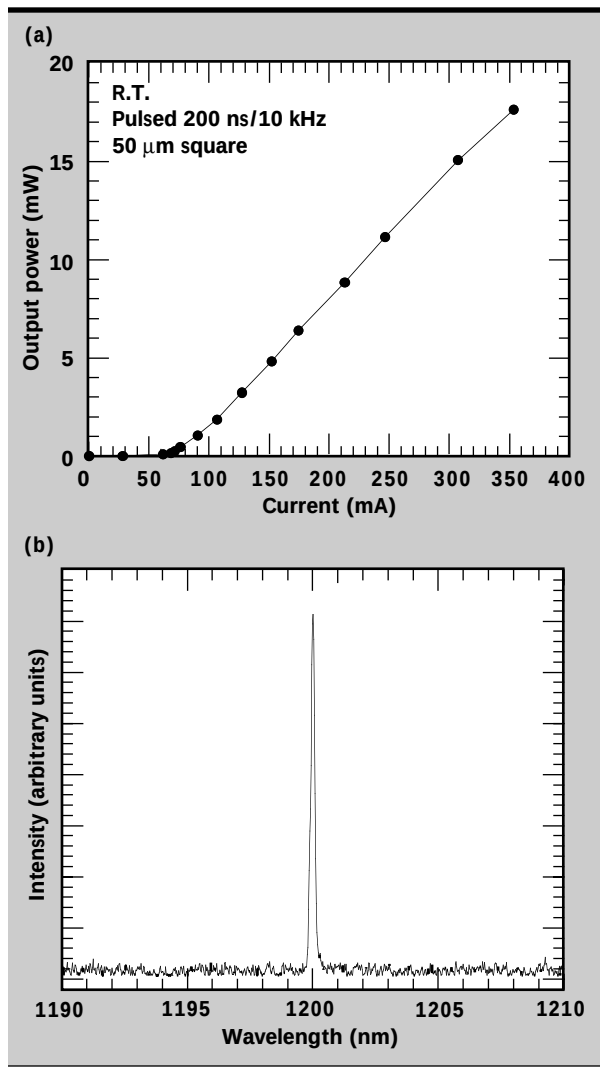

Figure 7. (a) Output power vs. injection current and (b) lasing spectrum near threshold for a GaInNAs long-wavelength VCSEL.

transmission medium prevents the use of existing arrayed waveguide grating router technology, which for single-mode fiber provides passive wavelength routing, with spectral channels being used more than once in the routing table to achieve full N-×-N interconnection with only N wavelengths.

This year, we have developed a wavelength router (N-×-N-wavelength multiplexer) for use in multimode fiber based optical networks. The device uses a blazed diffraction grating and broadband add/drop filters to provide wavelength re-use thus enabling fully non-blocking N-×-N interconnection with only N wavelengths. First, we demonstrated[4] a single-bit wavelength router with three spectral channels, resulting in a 3-×-3 fully non-blocking crossbar switch. However, to make use of wavelength routing for parallel optical interconnects a byte-wide wavelength router is required. Therefore, we also demonstrated a bit-parallel wavelength router by building upon the single-bit 3-×-3 wavelength router. Using a ferrule with two parallel arrays of 12 fibers each, we have demonstrated a 3-input by 3-output wavelength router where each input/output channel is two bits wide. The device provides fully non-blocking interconnection between all inputs and outputs and shows virtually no bit-to-bit cross-talk.

Figure 8 shows the Routing Table for both bit-lines of the router. As seen in the figure, each output port receives all three spectral channels; however, each spectral channel comes from a different input port. (The letters next to each spectral channel on the plots indicate input ports labeled A, B, and C, or outputs labeled X, Y, and Z.) Bit-to-bit cross-talk was measurement limited at below -30 dB.

Future Work

The results described above demonstrate the required building blocks for high-performance, byte-wide, multiwavelength optical interconnects. We

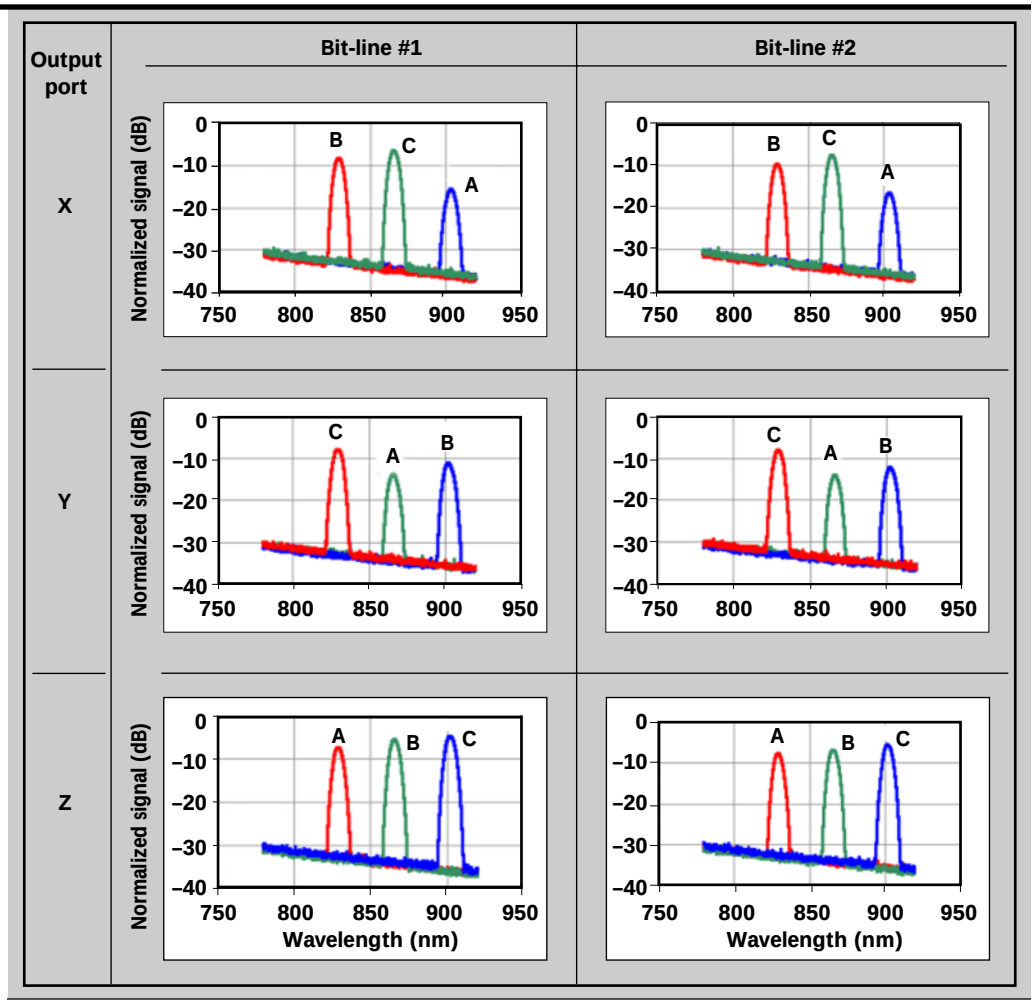

Figure 8. Bit-parallel wavelength routing demonstrated with our initial 3-×-3-port prototype.

have shown low cross-talk in four-wavelength transmitters fabricated by hybrid integration, as well as demonstrating monolithic processes for achieving multiwavelength emitter arrays on a single chip. In addition, we have realized a bit-parallel wavelength router for a more efficient connection architecture.

Our goal for next year is to demonstrate manufacturable components enabling systems with higher wavelength count by combining our hybrid and monolithic integration approaches. Earlier simulations showed that eight system wavelengths are required for several interesting multiprocessing applications.[1] We also intend to extend our wavelength router to eight parallel bit-lines for a byte-wide interconnect, and to eight or more spectral channels.

Acknowledgments

This project has benefitted substantially from the efforts of H. Garrett, W. Goward, R. Patel, and H. Petersen (LLNL), R. Deri (formerly of LLNL), and C. Coldren and Prof. J. Harris (Stanford University).

References

1. A. J. DeGroot and R. J. Deri, *et al.* (1996), *IEEE Proc. Third Intl. Conf. Massively Parallel Processing using Opt. Interconnections*, October.

2. M. C. Larson, M. D. Pocha, H. E. Garrett, H. E. Petersen, S. W. Bond, R. F. Drayton, R. R. Patel, M. A. Emanuel, R. J. Deri, and M. E. Lowry (1999), "Multiwavelength VCSEL transmitter for WDM parallel optical fiber interconnects," *IEEE Lasers and Electro-Opt. Soc. Ann. Meeting*, San Francisco, California, November.

3. R. R. Patel, H. E. Garrett, M. A. Emanuel, M. C. Larson, M. D. Pocha, D. M. Krol, R. J. Deri, and M. E. Lowry (1999), "Compact, low-crosstalk, WDM filter elements for multimode ribbon fiber data links," *Forty-Ninth Elec. Comp. and Tech. Conf.*, San Diego, California, June.

4. R. R. Patel, S. W. Bond, M. C. Larson, M. D. Pocha, H. E. Garrett, and M. E. Lowry, "Multi-mode fiber coarse WDM grating router using broadband add/drop filters for wavelength re-use," *IEEE Lasers and Electro-Opt. Soc. Ann. Meeting*, San Francisco, California, November.

Low Power Wireless Modem Technology

Charles F. McConaghy
Electronics Engineering Technologies Division
Electronics Engineering

Charles Chien
University of California at Los Angeles
Los Angeles, California

A key component in spread spectrum RF systems is the modulator/demodulator (modem). We have developed a modem based on a state-of-the-art field-programmable gate array which is customized for wireless sensor applications.

Introduction

To reduce the size and power of RF communication systems for wireless sensor networks, a custom direct sequence spread spectrum transceiver was built.[1] The total RF system consists of an RF section which up-converts transmitted signals and down-converts received signals, and a modem which processes these signals. The modem takes an incoming data stream and mixes it with a pseudo-random sequence. This complex signal then phase-modulates the transmitter. On receive, or demodulation, a reciprocal process is used. However, additional complexity is required during demodulation since the phase relationship between the transmit and receive pseudo-random codes is not known and varies with signal propagation.

Part of the modem circuitry locks on a header and then stays locked via a control loop for the duration of the transmitted data packet. Such modems can be built as a custom applications-specific integrated circuit (ASIC) chip or in a field programmable gate array (FPGA). The latter has the option that design iterations can be made with no change in the hardware. Although ASICs have ultimately the smallest size and lowest power, recent advances in FPGA are yielding near comparable performance to ASICs with the advantage that such devices are re-programmable.

Progress

Initial work focused on development and reiteration of modem designs with hardware developed during FY-98. This is largely a software effort with the designs downloaded to the FPGA from a PC. After debugging, the software was transferred to an on-board boot PROM. The initial design was developed around a Xilinx XC4062XL FPGA. This 240-pin, 62,000-gate device comes in a package that is 35 × 35 mm. The modem was designed for a processing gain of 127 with a chip rate of 1 MHz. This results in a data rate of 7.8 kbits/s, which was sufficient for our wireless sensor needs.

The FPGA ability to quickly reiterate the modem design was an important aspect of this development. In the initial design the FPGA also took care of non-modem tasks such as reading an A/D converter, buffering data, and transmitting packet headers. This modem was interfaced to a 900-MHz RF board. Performance was demonstrated by transmitting accelerometer sensor data from a 2-in.-×-2-in.-×-2-in. module to a host computer where the data was displayed with Labview.

In FY-99 a second design was begun which used a smaller 10,000-gate FPGA. This design makes use of Xilinx XCS20XL 100-pin device which is in a package 14 × 14 mm. The use of the smaller package

allowed us to build the next generation wireless sensor module which uses boards that are 30 × 50 mm. The new modem design is expected to use one fifth of the power of the initial design. The higher level functions such as A/D conversion and packet formation have been moved from the FPGA and relegated to another controller within the wireless sensor module, allowing more versatility in the programming of the overall module. Although similar in design to the original modem, more finesse was required to make use of the smaller FPGA. An additional feature of the newer modem is the ability to program the processing gain with bit rates from 7.8 to 90 kbits/s Yet an additional feature of the new modem is the ability to power down the FPGA without having to reboot on power-up. This latter feature is being incorporated into the overall power management within the module.

Future Work

We are in the evaluation stage of the new modem design. We are making tests of power consumption as well as data transmission reliability. On-the-air tests will be made with the modem board interfaced to two custom designed boards, a dual conversion 900-MHz RF board and a controller-signal processing board which reads the sensor.

In the coming year we will further evaluate the current design and port the design from FPGA to a custom ASIC.

Reference

1. A. P. Lee, C. F. McConaghy, and J. N. Simon, “Wireless microsensor modules for distributed network sensing,” Lawrence Livermore National Laboratory, Livermore, California (UCRL-LR-113717-98), pp. 1–10.

Wireless Micropower RF Components

Charles F. McConaghy
Electronics Engineering Technologies
Electronics Engineering

Battery size is the main limitation to producing small volume RF systems such as those used by the wireless sensor project[1]. This work has focused on power reduction techniques in receiver architectures as well as RF components such as oscillators and mixers, to enable the use of small size batteries.

Introduction

The RF section of modern spread spectrum transceivers uses a number of building blocks such as mixers, low noise amplifiers, phase locked loops, and oscillators. All of these components consume current. Generally receivers are more complex than transmitters but in many applications, transmitters dissipate more electrical power, with most of this power dissipated in the power amplifier used to amplify RF signals to the 1 W power regime. However, in low power applications where transmit power is on the order of a milliwatt and in networks which transmit with a low duty cycle, the receiver becomes the dominate electrical drain.

Table 1 shows the current requirements for two 3.3-V, 900-MHz RF transceivers. This data was obtained from specifications of state-of-the-art oscillators, mixers, and phase lock loops (PLL) as well as a single chip transceiver built in RF complementary metal oxide semiconductors (CMOS).[2] The important thing to note from the table is that the total receiver current drain (73 mA and 66 mA) is similar in both implementations. Even though the single chip solution is a physically smaller implementation both require the same battery which dominates the physical size of the overall package.

In addition, receivers that use more complex modulation schemes such as binary or quaternary phase shift keying (BPSK or QPSK) have more parts and subsystems than simpler modulation techniques such as frequency shift keying (FSK) or on-off keying (OOK). The more advanced modulation techniques are more robust but usually come at the price of higher current consumption and additional parts. Most direct sequence spread spectrum transceivers use some form of phase modulation for modulating the RF carrier. It was one of the goals of this work to still make use of phase modulation but to reduce the complexity and power required in these receivers.

Progress

BPSK is accomplished by changing the phase of the RF signal by 180° for a logical one and leaving the phase unchanged at 0° for a logical zero. This is fairly easily accomplished on the transmit side with a single component such as a balanced mixer.

Table 1. Comparison of current* requirements for single chip RF CMOS vs. multi-chip transceivers.

	LNA	Divider	VCO	PLL	Mixer	PA	IF Amp	Misc.	RX/TX Total
RF CMOS	15 RX	14 RX	13 RX/TX	14 RX/TX	8 RX/TX	28 TX	7 RX	2 RX	73/63
RF COTS	8 RX	NA	9.5 RX/TX	7 RX/TX	23 RX/TX	35 TX	8.5 RX	10 RX	66/74.5

*Current in milliamps

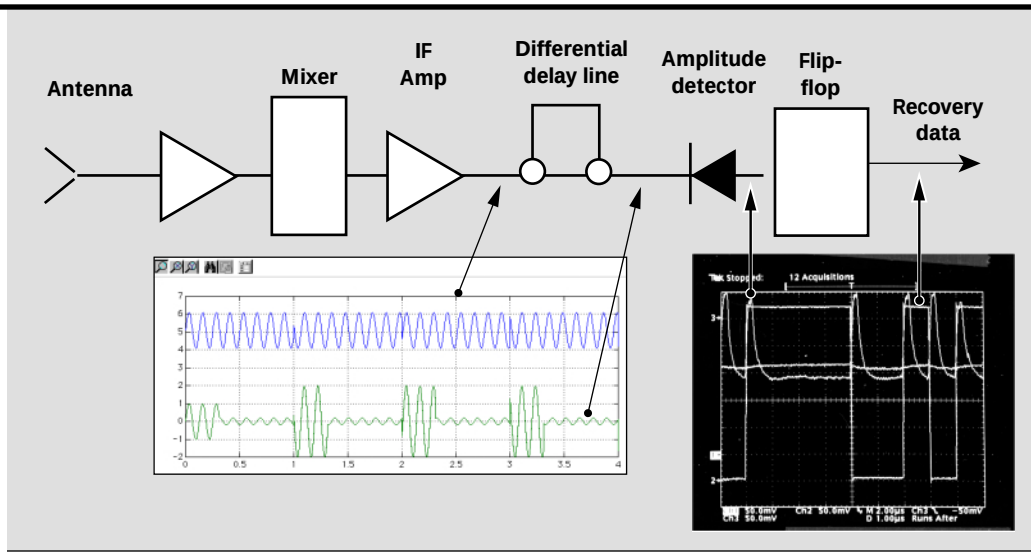

Figure 1. Block diagram of BPSK receiver with differential delay line. Waveforms are shown at several places within the receiver.

However, the typical demodulation technique on the receiver side usually requires mixing a reference source with the modulated received signal. The output of this mixer is the recovered data. The reference oscillator generally needs a control loop which adds to the complexity and current consumption of the overall receiver.

One of the accomplishments of this year's work has been a simpler receiver architecture for a BPSK receiver. **Figure 1** shows a block diagram for this receiver. The key feature of this design is the absence of a reference oscillator. Instead, a differential delay line is used to pick up the edge transitions of each phase change. The delay line is adjusted to give a 180° phase change and when summed with the direct path yields no output. However, due to the delay, a phase transition causes the output to be non-zero for a short time. Therefore, each phase transition results in a pulse output. These pulses, when used to edge trigger a flip-flop, yield a regenerated data stream. A nice feature of this technique is some frequency offset between the transmitter and receiver can be tolerated. This means high-stability oscillators are not a requirement and lower power oscillators can be used.

Although **Fig. 1** shows the differential delay line being used at an intermediate frequency, it is possible to directly use the delay line at the RF frequency, which allows for very simple receivers. We demonstrated such a receiver which used four stages of RF amplifiers and a differential delay line implemented with a surface acoustic wave (SAW) filter as the delay element. Although this receiver was not as sensitive as one which uses an intermediate frequency amplifier, it did perform well enough for short range applications. The receiver was quite simple as it avoided the use of both oscillators and mixers.

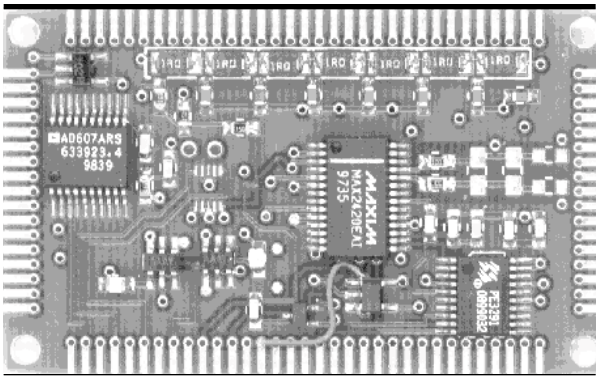

Figure 2. BPSK transceiver implemented on a 30-mm-×-50-mm board.

Figure 2 shows a more sensitive intermediate frequency amplifier receiver we built that was based on an L/C delay line. This receiver occupies a 30-mm-×-50-mm board and also contains transmitter circuits. The power requirements are 3.3 V at 60 mA. Further power reduction is anticipated from duty cycling as the receiver has a power down mode, which reduces current drain to under 10 mA.

Future Work

To further reduce power we have designed a system which has the main receiver powered down and has a parallel very low current receiver (2 mA) which just detects the presence or absence of RF. This parallel receiver would then be used to switch on the main receiver only when needed. It is anticipated that this type of power reduction can provide a factor of ten improvement in battery life. We hope to test this idea experimentally in the near future.

References

1. A. P. Lee, C. F. McConaghy, and J. N. Simon (1998), "Wireless microsensor modules for distributed network sensing," Lawrence Livermore National Laboratory, Livermore, California (UCRL-LR-113717-98).

2. H. Samueli, A. Abidi, G. J. Pottie, and Y. Rhamat-Samii, "Hardware technologies for robust personal communications transceivers," *http://www.icsl.ucla.edu/aagroup/PDF_files/900MHz.pdf*.

Acoustically-Driven Microfluidic Systems

Amy W. Wang, William J. Benett, and Christopher D. Fuller
Electronics Engineering Technologies Division
Electronics Engineering

Richard G. Couch
Defense and Nuclear Technology

We have demonstrated a non-contact method of concentrating and mixing particles in a microfluidic chamber using acoustic radiation pressure. A flow-cell package has also been designed that integrates liquid sample interconnects, electrical contacts and a removable sample chamber. Experiments were performed on 3-, 6-, and 10-µm polystyrene beads. In addition, finite element modeling has been used to predict pressure profiles in fabricated chambers. Flow cell designs to maximize acoustic energy coupling into the chamber and generate standing acoustic waves have been fabricated and tested.

Introduction

The threat of chemical and biological warfare agents has made apparent the need for autonomous, portable, and fast pathogen detection systems. Sample pre-treatment is one of the most critical aspects in the development of autonomous systems, yet it remains largely an unsolved problem. Sample handling is also of key interest in private industry. The global market for microelectromechanical systems (MEMS) is currently estimated at $10 billion, with biological and medical MEMS representing the most rapidly growing sector. The medical arena brings the additional challenges of disposability and low cost. Emerging MEMS-based companies are targeting miniaturized microfluidic systems that are able to perform a complete bioassay on what is loosely defined as a "chip." A necessary goal of these systems is to obviate manual handling of samples, which is slow, requires trained personnel, and is not cost-effective. Integrated sample preparation requires a high degree of functionality to truly permit biological or chemical analysis to be performed in a miniaturized system, yet the danger of sample-to-sample contamination dictates inexpensive, disposable parts. Typically the cost of a part increases with its functionality.

Acoustic forces can be used for concentrating, mixing, sorting, and transporting particles in disposable sample chambers. The use of remotely-coupled acoustic energy into a micromachined chamber combines high functionality with an inexpensive, disposable sample chamber. A bulk PZT transducer can be used multiple times as the source of acoustic energy, while the sample chamber can be inexpensively processed and thrown away after one use. In addition, acoustic forces act over a volume, are not media-dependent, allow the manipulation of uncharged and opaque particles, and do not require integrated electrodes or magnetic beads. Thus, acoustic actuation provides features that are not met by electroosmotic, electrophoretic, dielectrophoretic, electrohydrodynamic, magnetic, or optical techniques.

Acoustic radiation pressure exerts a force on a particle. Radiation pressure generated in the presence of a standing wave induces a pressure field that forces particles to collect in the nodes or anti-nodes of the standing wave. The acoustic force exerted on a particle can be expressed as,

$$F_{ac} = -4\pi/3\ R^3 kEA \sin(2kx),$$

where R denotes the particle radius, k is the wave number, and E is the acoustic energy density.[1–5] The compressidensity factor, A, reflects the relative density and compressibility of the particle with respect to the ambient medium, and the sign of A determines whether the particles concentrate in the nodes or the anti-nodes of the standing wave. It follows that acoustic radiation pressure can be used to differentiate particles based on their size and their material attributes.

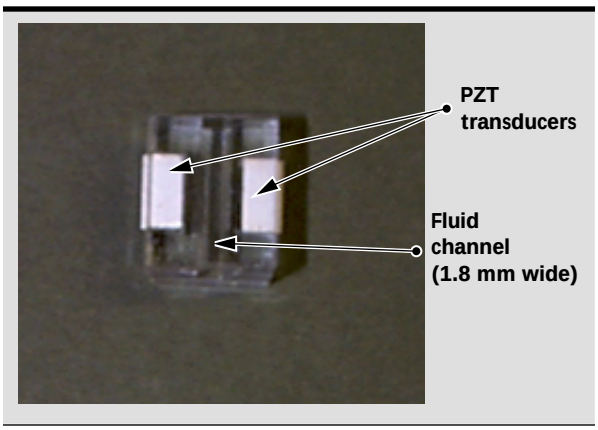

Figure 1. Photograph of prototype device for acoustic particle manipulation.

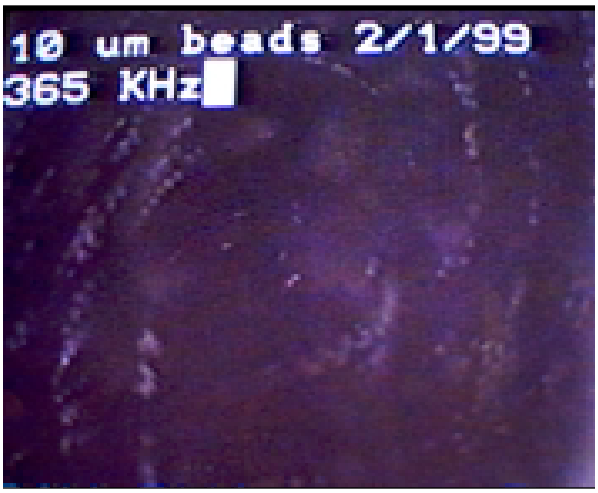

Figure 2. Evidence of bead mixing.

Progress

We have tested a prototype device for acoustic-based particle manipulation. The device consisted of a single half-wavelength width fluid channel (**Fig. 1**).

Mixing (**Fig. 2**) and concentration (**Fig. 3**) of polystyrene beads were observed in water. PZT transducers were driven at 20 Vpp. Degassing of the water was not required. **Figure 3** shows concentration of 10-µm polystyrene beads at the center of the fluid channel, an expected pressure node of the standing wave. Also shown in **Fig. 3** is separation of particles based on size. The larger beads collect at the central node of the channel, while smaller, 3-µm beads remain dispersed in solution. Bead concentration times were on the order of minutes.

To better understand the observed mixing phenomenon, we performed finite element modeling of the fluid channel geometry. One-dimensional models verified generation of a standing pressure wave given the geometry of the chamber. Three-dimensional models showed a distribution of pressure

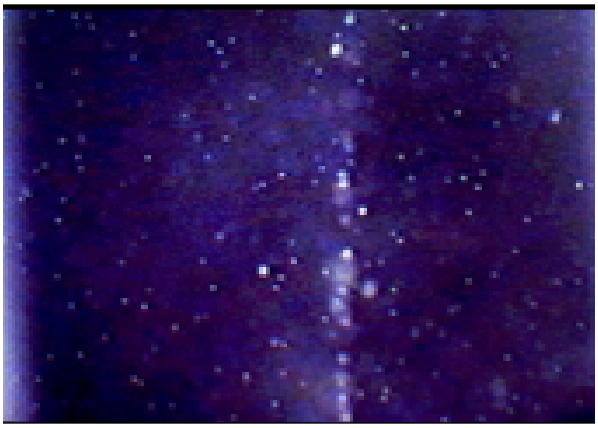

Figure 3. Evidence of size-preferential bead concentration.

across the length of the fluid channel, specifically, a higher pressure profile at the center of the wall, with decreasing energy radiating towards the channel ends. We believe this is due to the mechanical clamping at the ends of the chamber wall, which appears to cause a circular mixing motion at the clamped wall interface.

Summary

Mixing and concentration of particles in fluids have been shown in a microfabricated sample chamber with a flow cell package. We have tested prototype designs that indicate preferential geometry for mixing versus concentrating functions.

Acknowledgments

The authors gratefully acknowledge J. Butler and W. Jensen for their expertise, and K. Fisher for frequent acoustics discussions.

References

1. L. V. King (1934), *Proc. Roy. Soc., A*, **147**(212).

2. K. Yosioka and Y. Kawasima (1955), "Acoustic radiation pressure on a compressible sphere," *Acustica*, **5**, 167–173.

3. K. Yasuda, K. Takeda, and S. Umemura (1996), "Studies on particle separation by acoustic radiation force and electrostatic force," *Jpn. J. Appl. Phys.*, **35**, 3295–3299.

4. M. Whitworth, A. Grundy, and W. T. Coakley (1991), "Transport and harvesting of suspended particles using modulated ultrasound," *Ultrasonics*, **29**, 439–444.

5. W. H. Benett and P. Krulevitch (1999), "Flexible packaging and interconnect scheme for microfluidic systems," *Proc. Micro- and Nanofabricated Structures and Devices for Biomedical Environmental Applications*, San Jose, California, 111–118.

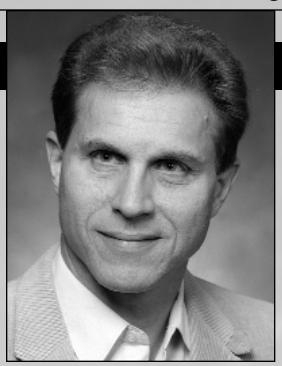

Kenneth L. Blaedel, Acting Center Director

The projects described in the following articles demonstrate the breadth of interest, from machine tool design to manufacturing process engineering, that has traditionally defined the Center for Precision Engineering at Lawrence Livermore National Laboratory (LLNL). In addition, a new set of programmatic requirements has been articulated that will challenge the Center far into the future.

The first article describes a project whose goal is to devise and prove a method of dimensional metrology for non-rigid components, for example, those that can deform during the inspection process. No such methodology exists to the precision that will be required for the weapons program in the future.

The second article summarizes a new approach to designing a precision machine tool where its performance is characterized in the spatial-frequency domain instead of the spatial domain alone, which is the basis for classical design.

The third article describes how we combined data sets from three metrology instruments to achieve a broader characterization of surface quality than could be done by any one of the instruments alone.

The fourth article describes a fabrication process that holds promise for predictably removing material down to the molecular level.

The fifth article discusses a machining process whose goal is to radically reduce the wear of a diamond tool, thus enabling us to machine difficult materials to higher precision than is currently possible.

We will continue to pursue some of these ideas through the next year.

In looking to the future of Precision Engineering, we have recently defined a new challenge that will provide a focus for our R&D resources. This focus is the manufacturing and characterization of "meso-scale devices" for LLNL's National Ignition Facility (NIF). The science-based Stockpile Stewardship Program will conduct weapons physics experiments in NIF in much the same way it used to conduct experiments at the Nevada Test Site (NTS). The major difference between the NTS experiments and those on NIF will be one of scale. Future weapons physics experiments will be of the order of millimeters in the NIF, which is 100 to 1000 times smaller than those conducted at the NTS. These millimeter-scale physics experiments or "meso-scale devices" will provide data about shock physics, equation of state, opacity, and other essential measurements of weapons physics.

This program faces many new challenges, not the least of which is the ability to design, manufacture, characterize, and field the experiments in the NIF chamber. These experiments will involve millimeter-size structures fabricated from exotic materials and to precise tolerances down to 0.1 μm or less. In addition, cleanliness will be an extremely important requirement since particulate even at the sub-micrometer level could ruin an experiment. Diagnostics must interface with the meso-scale device at precise locations and will include miniaturized fiber optic technology, x-ray optics, digital cameras, and radiation detectors. These experimental systems must be aligned in the NIF chamber to a precision of micrometers over distances of meters. And finally, all of this must be done at minimum cost and expenditure of time since there will be hundreds of experiments performed per year if NIF is to be a cost-effective facility and fulfill its promise of science-based stockpile stewardship.

Virtually all of the engineering and manufacturing problems faced by the early weapons program must be rethought, redefined, and resolved. The problem of small, precise devices, including diagnostics, requires a systems engineering approach to meet the challenges of precision, cost, and throughput. The challenge to engineering in general and to the precision engineering community in particular is clear.

Center for Precision Engineering

3

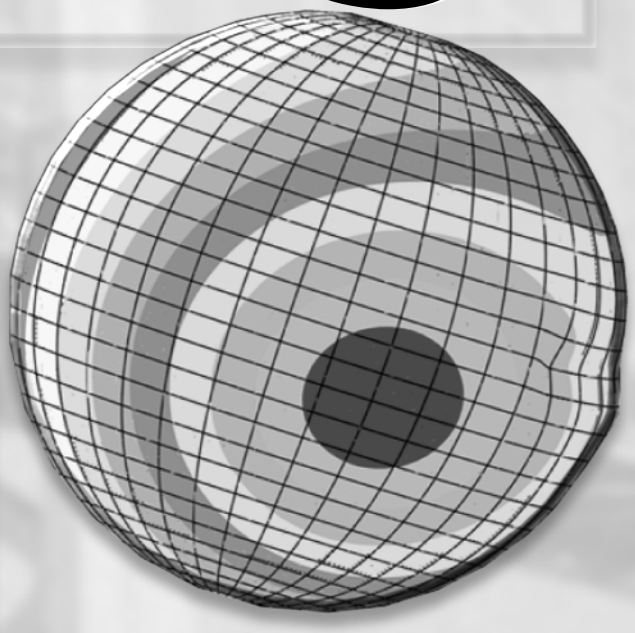

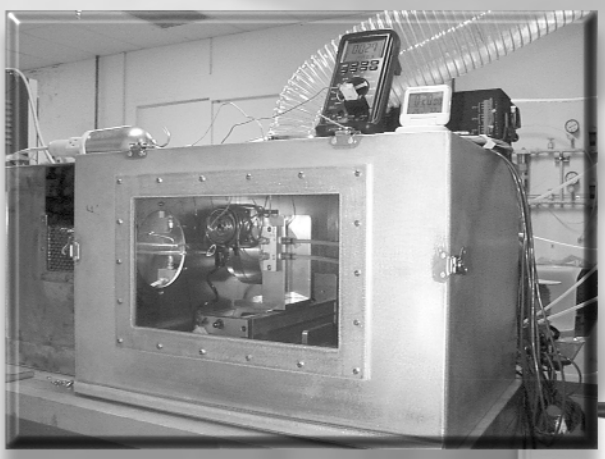

3. Center for Precision Engineering

Overview
Kenneth L. Blaedel, Acting Center Director

Atmospheric Pressure Plasma Processing for Damage-Free Optics and Surfaces
Jeffrey W. Carr 3-1

Design of an Ultra Precision Machining Facility: ULTRA350
Keith Carlisle and Stanley L. Edson 3-11

Intermittent Single-Point Machining of Brittle Materials
Mark A. Piscotty 3-17

A Spatial-Frequency-Domain Approach to Designing Precision Machine Tools
Debra Krulewich Born 3-21

Power Spectral Density Measurements of Machined Surfaces over an Extended Range of Spatial Frequencies
Jon M. Baldwin 3-25

Dimensional Metrology of Non-Rigid Objects
Kenneth L. Blaedel and David W. Swift 3-29

Atmospheric Pressure Plasma Processing for Damage-Free Optics and Surfaces

Jeffrey W. Carr
Manufacturing and Materials Engineering Division
Mechanical Engineering

The goal of this project is to develop a fabrication technology capable of shaping and finishing difficult materials with minimal subsurface damage. The technique developed uses an atmospheric pressure mixed gas plasma discharge as a sub-aperture polisher of fused silica and single crystal silicon. Workpiece material is removed at the atomic level through reaction with fluorine atoms. These reactive species are produced by a noble gas plasma from trace constituent fluorocarbons or other fluorine containing gases added to the host argon matrix. The products of the reaction are gas phase compounds that flow from the surface of the workpiece, exposing fresh material to the etchant. An initial system has been built and tested. Preliminary etch rates have been measured on fused silica and silicon.

Introduction

Modern materials present a number of formidable challenges to the fabricators of optics and precision components. In many Lawrence Livermore National Laboratory (LLNL) programs there is a general need for spherical and non-spherical surfaces fabricated from a variety of media that are able to handle high fluences. Traditional finishing and final figuring techniques, still largely a black art, fall far short of today's requirements. Unfortunately, any form of contract figuring or polishing introduces a degree of distortion into the workpiece. Present finishing technologies produce significant levels of surface and subsurface damage and are difficult to apply to non-spherical shapes. In many applications, mechanically inferior or more costly materials are used because the material of first choice (in terms of performance) is too difficult to fabricate. Reactive atom plasma polishing presents an opportunity to significantly improve the capabilities of our precision manufacturing technology.

The thrust of this effort is to develop a final procedure that can remove damage introduced by previous process steps, figure highly aspheric optics or precision components and reduce high-frequency surface roughness. In its final stage, this technology functions as a shaping and a finishing operation in both the subtractive and the additive mode. Subsurface damage in the form of cracks and plastically deformed materials are removed in an atmospheric pressure, dry etch process. Removal rates in an optimized system are expected to be high, and large workpieces will be configured in a relatively short time.

The final shaping of optics and precision surfaces is executed by exposing the workpiece to reactive atoms generated by an atmospheric pressure, inert gas plasma. Reactants are created from trace gases introduced into the discharge and are chosen to fit the chemistry of the workpiece. Interaction of reactants with the workpiece is almost entirely chemical, resulting in the removal of the existing damaged layer without distorting the underlying material. The plasma footprint is highly reproducible, resulting in predictable removal rates. By translating the plasma across the workpiece, a symmetric or highly asymmetric damage-free surface can be created.

Background

In demanding applications the success of any manufactured precision component depends on the surface and near-surface quality. Damage, present in crystalline or amorphous substrates as cracks, voids or plastically deformed material can lower the damage threshold for high fluence use or increase the chemical activity of the surface (corrosion). Any shaping and finishing process that involves surface contact will introduce damage to some degree. In addition, for silica glass optics, high quality final finishing is accomplished through complex solution phase chemistry that tends to deposit contaminants

in a gel-like layer on the surface of the component. While an extremely smooth part can be produced, the top layer often hides an extensive damage zone below. An optimum approach to final surface generation would involve a non-contact system that removes material chemically without residual contamination. A number of attempts at non-contact material removal have been reported.

Plasma etching at reduced pressure is used extensively in the semiconductor industry for processing a wide variety of materials including semiconductors, metals and glasses.[1] Removal mechanisms and removal rates have been studied in detail and are reasonably well understood. With pressures in the 10 to 20 mtorr range, ion and electron densities are on the order of 10^9 to 10^{10} cm^{-3}. These reactive ions are believed responsible for the majority of material removal. Consequently, the technique is known as reactive ion etch (RIE). With electron energies in the 3 to 30 eV range, material removal tends to be largely chemical in nature. Below 50 eV, physical sputtering is negligible and subsurface damage is non-existent. Above 50 eV, the induced damage will affect device performance. In the absence of sputtering, reaction products must be volatile or the process is self-terminating after the formation of the first product layer.

Considerable effort has been put into developing plasmas with uniform etch rates over the entire discharge, making RIE unsuitable for the production of figured precision components. Shaped discharges are possible, but usually have a Gaussian shape over the width of the reaction chamber. If removal of the damage layer from a pre-shaped part were the only task, RIE would be usable for smaller optics. However, the technique would fail when non-uniform material removal is required. RIE etch rates are also quite low and not suitable for removing large amounts of material.

An additional practical drawback to the technique for precision finishing would be the requirement of a vacuum. Translating either the source or workpiece with precision in a complicated pattern inside a vacuum chamber would be challenging, especially in the case of large optics. *In-situ* metrology would also be awkward. Fortunately for the development of this process, the chemistry that occurs in RIE systems is similar to that of higher pressure systems. The main difference is the population shift between atom and ion species. In the tail of the high-pressure discharge, the part that interacts with a workpiece, the population of ions would be low. There, atoms produced by ion-electron recombination reactions predominate. However, reactive gas mixtures that are used in RIE will also work for atmospheric pressure systems. In the atmospheric plasma it is the chemical potential of the atoms rather than the ions that is responsible for the removal of material.

A modified RIE for polishing at reduced pressure has been built using a capacitively coupled discharge.[2–5] Named "Plasma Assisted Chemical Machining" (PACE), the system has been successful in shaping and polishing fused silica. In the first application of PACE, Bollinger *et al.*[2] noted that a 1-in. discharge controlled material removal to better than 1% with removal rates from 0 to 10 μm/min. The footprint and the rates could be varied during the process by changing plasma parameters such as power and reactive gas flow. In subsequent analysis, the parts showed no evidence of subsurface damage, no surface contamination and no distortion at the edge of the optic (roll-off). Material removal could be predicted from a linear superposition of the static footprint. Control algorithms were developed to permit fabrication of a spherical optic from knowledge of static behavior.[3]

An updated low pressure system with a 13-mm capacitively-coupled discharge was built to shape and polish single crystal silicon and silicon over silicon carbide.[5] While the results for subsurface damage were similar to previous studies[2–4] the authors also considered the evolution of surface roughness and its relationship to previous process steps. Not surprisingly, they found that greater subsurface damage results in an increase in roughness.

A major limitation of the capacitively-coupled discharge is the requirement that the workpiece be either conductive or <10 mm thick. In addition, etch rates were noted to be dependent on part thickness, decreasing by a factor of ten when thickness changed from 2 to 10 mm. Above 10 mm the rates were too low to be of much use for shaping, but could find some application in damage layer removal (20 nm/min).[4] Optics up to 188 mm in diameter with 30° slope were polished under mild vacuum. If metrology is needed in an iterative procedure, the chamber must be vented, the part removed and measured, replaced in the chamber and then pumped down for the next etch step. The convergence rate for PACE is typically low, resulting in a long and arduous (expensive) process. *In-situ* real-time metrology becomes difficult if the equipment is not dedicated to a single type of workpiece. While extension to larger workpieces is certainly possible, the difficulty in handling large parts is clear.

Ion beam sputtering or neutral ion beam milling remove material from the workpiece by kinetic interaction of ions with atoms or molecules of the surface. The technique has been around for quite a while[6] and the main application has been optical

polishing for fused silica optics.[7,8] Earliest sources used beams with energies that were a large fraction of 1 MeV, while most recent systems use Kaufman sources with energies of 1500 eV to provide the optimum sputter yield. Researchers claim several advantages for ion milling. Chief among them are: no surface contact, no weight on the optic, no edge effects, high removal rate, and efficient correction of long spatial wavelength errors. The removal rates for a 1-A beam on fused silica are about 0.35 $cm^{3/}h$; unfortunately, such high currents are rarely used. A more typical value is 30 mA providing a removal rate nearer to 0.01 $cm^{3/}h$. Zerodur, a proprietary form of low-expansion glass, was a factor of two slower. Ten hours were required for correcting (not figuring) a 30-cm optic.

As with any sub-aperture tool, the footprint must be stable and predictable. The Kaufman source, which typically produces Gaussian beams 3 to 15 cm in diameter, meets these needs quite well. The size of the beam can usually be reduced with an aperture. Configuring algorithms for the production of aspheric or non-rotationally symmetric workpieces have been extensively developed.[9]

Observed disadvantages include high surface temperatures, an increase in surface roughness, and the need for a vacuum (and to do translation in that vacuum). The temperature is dependent on beam current so an increase in etch rate assumes an increase in temperature, often surpassing several hundred degrees Centigrade. An increase in roughness on undamaged material occurs primarily from redeposition, although later efforts suggest that any amount of subsurface damage in the workpiece will increase roughness and degrade surface quality.[10] Typically, a 50% roughness increase for shallow etched parts can be expected.[11] The difficulty in working under vacuum is only a practical consideration, especially for large optics. Clearly this doesn't concern the engineers at Kodak who have built an ion beam figuring chamber capable of handling a workpiece that is 2.5 m × 2.5 m × 0.6 m in size.[8]

One investigator has used a direct current plasma (DCP) at atmospheric pressure to build a device capable of thinning wafers.[12] The system, called a "plasma jet," uses argon as the plasma gas with a trace amount of fluorine or chlorine for reactive atom production. The main intent of the device is to do backside thinning of processed silicon wafers for smart card and other consumer applications. The industry requirement of a 200-mm wafer with a thickness <50 μm cannot be met with any current commercially viable polishing process. The defects and microcracks introduced by abrasive systems create a damage layer that is a large fraction of the desired 50-μm thickness. Thin wafers produced by polishing are prone to fracture even with delicate handling. Wafers are thinned in a batch mode by placing them on a platen and using planetary type motion to move the sub-aperture plasma in a pseudo-random fashion across the surface. Irregularity from fluctuation in the plasma jet is removed by this randomization. The discharge is about 1 in. in diameter and the removal rate is 0 to 20 μm/min for a 200-mm wafer with a uniformity of <5%. Total material removal comes to about 30 cm^3/hr.

A number of analytical methods were used to assess surface quality. Scanning electron microscopy did not show defects or scratches on either side of the wafer. X-ray photoelectron spectroscopy, used to measure surface contamination, showed no evidence of elements other than silicon. The chemistry of the plasma is quite specific. As a result, metal or carbon contamination (fingerprints) present before etching were not removed. Transmission electron microscopy did not reveal any subsurface defects in the silicon crystal, supporting the supposition that the plasma is nearly 100% chemical in nature. A number of other studies, including optical microscopy and adhesion tests, did not reveal any additional defects.

In its current configuration, the DC plasma is not well suited for aspheric generation or material deposition. The trace reactants are introduced along with the bulk gas and, as a consequence, are widely distributed throughout the discharge, substantially increasing the footprint and the minimum feature size. Electrodes that are used to establish the arc are eroded by the reactants and add particulates to the atom stream. Electrode erosion also causes fluctuations in the plasma and accounts for the reduced uniformity compared to RIE systems. Detrimental electrode reactions also preclude the use of oxygen and many other potentially useful plasma gases. Finally, the discharge is not as hot as an inductively-coupled plasma (ICP) and, as a result, the production of reactant atoms is reduced.

A radio frequency (RF) plasma has been used to slice silicon and as a sub-aperture tool to polish optics.[13–15] The plasma is generated around a wire or blade electrode immersed in a noble gas atmosphere that contains a trace of reactive components. The plasma converts the reactive precursors to radical atoms that react chemically with the workpiece, removing material one atom at a time. Referred to as chemical vapor machining (CVM), the electrode is brought to within 200 μm of the workpiece wherever material is to be eroded. Analysis has shown the resulting surfaces to be damage free and the process is considered to be entirely chemical in nature. A comparison of damage in silicon for

polishing, sputtering, CVM and chemical etching is reported in the literature.[13] Both mechanical polishing and argon sputtering induced significant damage into the silicon surface. The damage for CVM and wet chemical etching was similar and near to the intrinsic damage typically found in silicon used in the semiconductor industry.

Unfortunately, the non-rotationally symmetric nature of the CVM footprint makes the process difficult to model and control. In the case of a blade, the footprint takes the shape of a high aspect ratio rectangle with rounded corners. Process rates are limited by the ability of the plasma to decompose reactive precursor into radical atoms. While no vacuum is required, the workpiece must be enclosed in a vessel to contain the plasma atmosphere.

The ICP discharge in its most familiar commercial form was originally developed to grow crystals.[16,17] In a configuration remarkably similar to the excitation source used in current analytical spectrometers, a powder of the crystal to be synthesized was aspirated into the center of the discharge. Reed was able to grow boules from 5 to 15 mm in diameter and as long as 30 to 90 mm with a growth rate of 20 to 50 mm/hr. No mention was made of crystal quality. This approach to crystal growth seemed dormant until the early part of this decade when it was used to produce crystalline films of a number of oxides (MgO, ZrO_2, NiO, SnO_2, TiO_2, $ZnCr_2O_4$, Cr_2O_3, $CoCr_2O_4$, $NiCr_2O_4$, and several rare earth oxides).[18,19] X-ray diffraction was used to confirm the crystalline nature of the films. Superconducting thin films of Bi-Pb-Sr-Ca-Cu-O were also fabricated with plasma spray methods.[20] Between the two efforts, an ICP was used on several occasions to produce ultrafine particles by desolvating droplets aspirated into the discharge.[21]

The conditions of the ICP make it an ideal source for reactive atoms needed for shaping damage-free surfaces. In his initial work Reed surmised that the high electrical conductivity of partially ionized gases (for argon, 120 Ω/cm at 15,000 K) contributed to the ease of plasma formation at high pressures. There are no electrodes and a number of gases can be used as the host matrix, although argon is usually the principle component. A typical discharge is characterized by high current (100 to 1000 A) and a relatively low voltage (10 to 100 V). The flowing plasma is not in complete thermodynamic equilibrium; however, ion and excited state atom populations are within 10% of equilibrium values. Electron densities are high ($>10^{15}$ cm^{-3} is typical) suggesting equilibrium temperatures >9000 K.[22–24] Reed calculated a peak temperature of 10,000 K from the ratio of emission intensities for a set of argon lines, again assuming equilibrium, making the ICP an efficient source for the generation reactive atoms.

Figure 1 shows a standard plasma torch used as an emission source for analytical spectroscopy. The current from a 27.12-MHz RF generator flows through a three-turn copper load coil around the top of the torch. The energy is coupled into the plasma through a cylindrical skin region that is located on the outer edge of the discharge nearest the load coil. The plasma is supported in a quartz tube by the plasma gas that is introduced tangentially to form a stabilizing vortex. In analytical spectroscopy, trace elements are introduced into the plasma as an aerosol through the central tube. The plasma skin is thin in this region and the sample easily penetrates the discharge. As the sample travels upward it

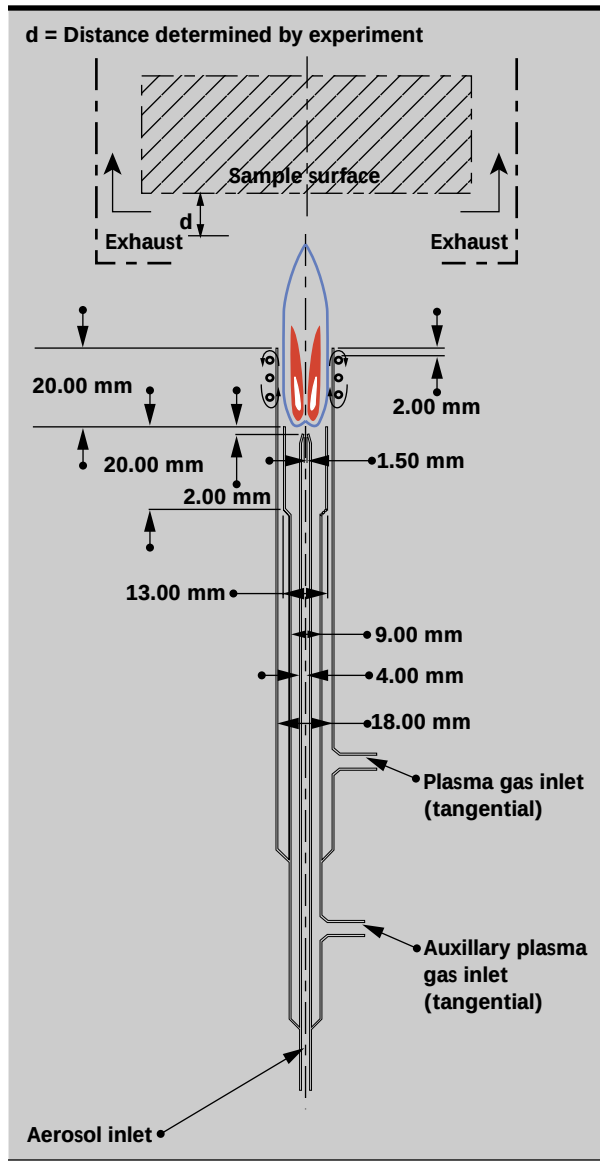

Figure 1. ICP torch showing the three types of gas flow and the location of the plasma relative to the load coil.

becomes progressively desolvated, atomized, excited and ionized. The relative distribution of ions and atoms in the discharge is represented in **Fig. 2**. Spatial profiles for five plasma regions indicate that the ion population decays before that of the excited atoms. The maximum atomic emission occurs several millimeters above the load coil near the visible tip of the discharge (zones 3 and 4). Recombination and radiative decay in this region are used to spectroscopically determine the concentration of the sample in the injected solution. Since the main thrust of ICP research has revolved around its use as an excitation source, information on the unexcited neutral atom population throughout the discharge is limited.

The characteristics of several shaping and finishing technologies are summarized in **Table 1**. Typically, all of the approaches have one or more areas where they excel. In the case of low-end consumer optics where cost is always an issue, traditional methods such as lapping and polishing will be used for many years. For some applications, including high fluence optics, the categories of subsurface damage, contamination and figure control would be emphasized. Unfortunately, none of the current techniques is adequate for demanding applications. It is in these critical areas that reactive atom plasma polishing (RAPP) will be very effective. No other method has the potential to produce damage-free, non-contaminated surfaces with high removal rates and good figure control over a large range of materials.

Progress

An initial system has been designed and built using commercial equipment as well as home-built components. The unusual application of the RF generator and impedance-matching network made initial operation difficult. Several modifications to the load coils and plasma chamber were necessary to achieve a stable discharge. The range of gas flow rates necessary to achieve a stable plasma was studied. Temperature shifts at the workpiece surface were measured over a period designed to simulate the figuring of a highly aspheric optic. Etch rates were measured for silicon.

Design and Construction

A commercial plasma generator from Advanced Energy, developed for use as a low-pressure etching system for use in the semiconductor industry, has been modified to produce reactive atoms in a flowing argon stream. The plasma chamber, containing the torch and load coils (**Fig. 1**) was built from copper and attached directly to the impedance-matching network. Initially, a four-turn coil was used to couple energy into the discharge. The energy from the RF generator was shunted directly through the water-cooled coil, constructed from 3-mm copper tubing. Unless the plasma is ignited, there is very little resistance to the energy flow. The 5 kW from the generator either reflects back to the source or flows to ground. After ignition the power is inductively

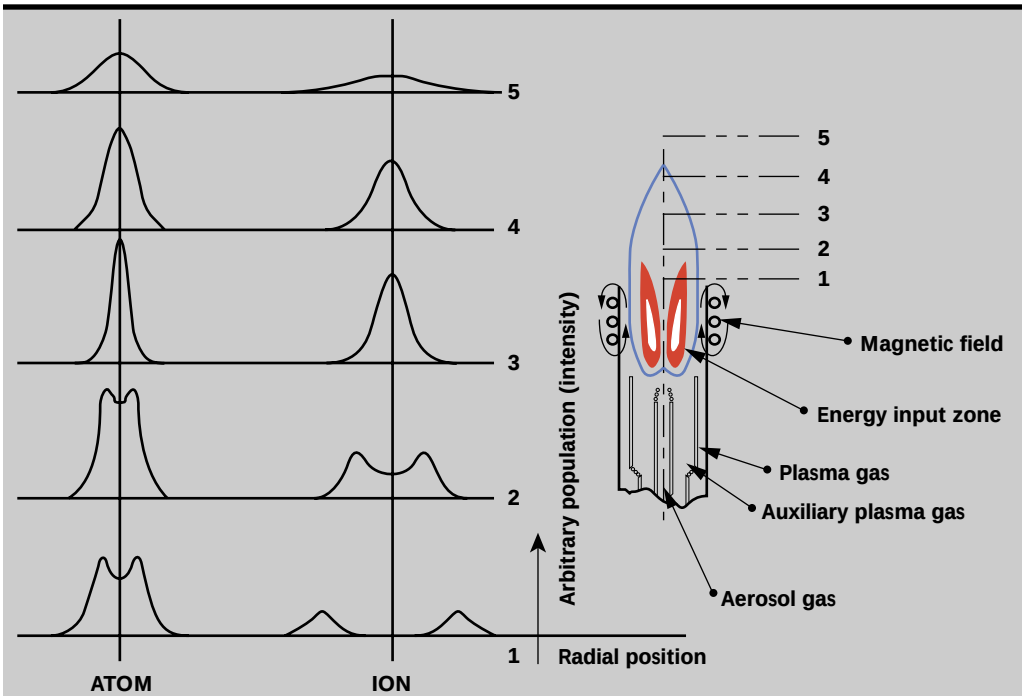

Figure 2. Atom and ion distribution in the ICP.

Table 1. Comparison of finishing and shaping methods.

	Material set	Figure control	Removal rates	Sub-surface damage	Surface rough-ness	Contam-ination	Foot-print	Vacuum required
Diamond machining	Moderate	Very good	Very high	High	Good	None	1 to 100 µm	No
Lapping and grinding	Large	Very good	Moderate to high	Very high	Moderate	Moderate	25 mm to full aperture	No
Chemical etch	Large	None	High	None	Good	Low	Full aperture	No
Traditional polishing	Small	Poor	Low	High	Excellent	High	25 mm to full aperture	No
RIE	Moderate	Good	Moderate	Low	Good	Low	Full aperture	Yes
PACE	Small	Good to very good	Moderate	Low	Good to very good	Low	25 mm to full aperture	Yes
Ion milling	Large	Good	Moderate	Moderate	Good	Low to moderate	100 nm to 50 mm	Yes
Plasma jet	Small	Good	High	None	Good	Possible	10 mm to 25 mm	No
Plasma CVM	Moderate to large	Moderate	Moderate	None	Good to very good	None	Long and narrow	No
RAPP	Moderate to large	Good to very good	Very high	None	Good to very good	None	1 mm to 50 mm	No

coupled into the plasma; very little power is either reflected or lost to ground. Under normal operating condition, the discharge generates large amounts of stray RF energy that must be confined to the plasma chamber. The design must take these two operating extremes into account.

The plasma chamber was constructed from a single sheet of 0.125-in. copper, folded into the proper shape. The use of folds rather than seams reduces the amount of RF leakage that invariably occurs at the joined edges. Where connection was necessary, the bond was created by braising the pieces together, minimizing RF leakage. An inside view of the copper box (**Fig. 3**) shows a later model torch mounted in place of the earlier solid version. A two-turn coil also replaced the original four-turn design. The lower copper block on the rear wall is the hot end of the coil and is isolated from the plasma chamber. The ground side can clearly be seen, firmly attached to the inside of the box. In the configuration pictured here, a long outer torch tube has been added to the torch to prevent quenching of active species via entrained atmospheric gasses. The torch extends into the sample chamber (**Fig. 4**).

The discharge occurs in the region of the coils (**Fig. 5**). The shadows of the two turns of the load coil can be seen through the netting of the observation window. They are located just to the left of the bright portion of the plasma. The hot gases are contained entirely within the quartz outer tube of the

torch. The color of the plasma is modified by the trace elements used to form the reactive atoms. In this photograph, only the argon host gas is being excited. Nearly all of the energy (1.5 kW) used to generate this discharge is radiated in the visible and near ultraviolet region of the spectrum. The light is produced through relaxation of excited states of argon as well as ion/electron recombination of the ionized host gas. Only a small portion of the energy is diverted to kinetic energy and to dissociation of the reactive atom precursors.

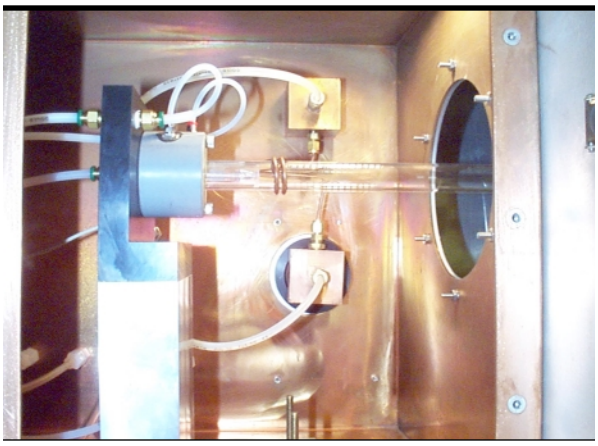

Figure 3. View inside the plasma chamber showing the demountable torch with a long outer tube.

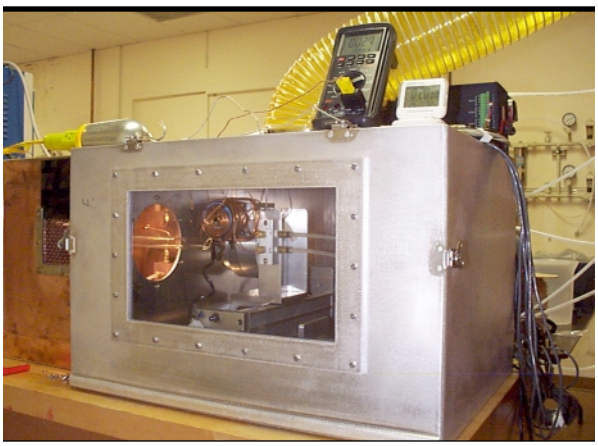

Figure 4. The sample chamber. The three-axis translation stage can be seen through the observation window. The plasma chamber is to the left.

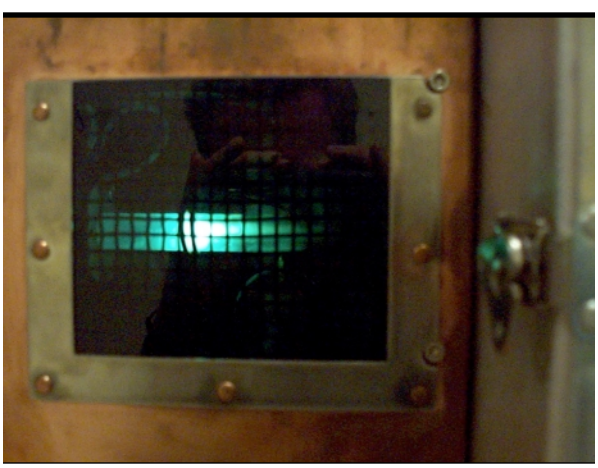

Figure 5. The discharge seen through a dark filter glass.

Reactive atoms from the plasma are delivered to a workpiece that is mounted on translation stages in the sample chamber. In its present configuration, a crossed X-Y slide and a rotary stage allow the fabrication of rotationally symmetric workpieces up to 200 mm in diameter. Repositioning both the torch and the sample mount within their respective chambers can increase the range of the stages. A large range was necessary to investigate conditions for material deposition in the additive configuration of the reactive atom system. A large ventilation duct removes reaction products and the host argon gas along with any unreacted chemicals from the sample chamber.

Initial Operation and System Modifications

The plasma was initially tuned on argon gas only. Before any trace gases were added, the plasma was stable over a wide range of tuning and operating conditions. The auto tuning function supplied with the system for low-pressure operation was able to compensate for any shifts in impedance when power settings or gas flows were altered. The system was tuned to operate under minimum reflected power. When run at 1.5 kW, a typical operating condition, the reflected power was below 15 W.

The first gas used to generate fluorine atoms was a mixture of sulfur hexafluoride (SF_6) in a nitrogen host. Unfortunately, the nitrogen seemed to promote quenching of the reactive atoms, lowering the etch rate to nearly zero and complicating plasma tuning. The precursor was switched to pure SF_6 reducing quenching and improving tuning sensitivity. After a prolonged period of use, SF_6 appeared to deposit sulfur on the surface of the plasma chamber as well as the sample box and the ventilation system. Energy in the radio frequency range tends to propagate along the surface of a metal. Adding a dielectric to the surface in the form of a sulfur compound substantially altered the system tuning characteristics.

To adjust to the new tuning conditions, it was necessary to reduce the number of turns in the load coil and to shift the spacing between the coils. Even after a considerable investment of time, the system never regained its wide stability range. The auto tune function is now unable to compensate for shifts during operations. It is now necessary to tune

manually for minimum reflected power. When a suitable tuning point is found, reflected power again stays below 15 W; however, the adjustment range of the tuning capacitors is very narrow (that is, a narrow range of stability).

During early operation of the reactive atom plasma, the exterior of the plasma chamber and sample box was measured for RF leakage. The detection system was calibrated by placing it inside the plasma box without igniting the plasma. The generator was then operated over a range of power from 0.1 to 1.0 kW to estimate the sensitivity of the detector. We were then able to measure power levels outside the plasma chamber and sample box as well as inside the sample box over the entire range of operating conditions with and without plasma ignition. Not surprisingly, radiation was detected in the workpiece area, although the energy levels were very low when the plasma was ignited. Outside the plasma chamber and sample box, it was not possible to detect any RF signal.

To limit reactive atom quenching, the length of the outer torch tube was increased in several steps until it nearly touched the workpiece. For this experiment, a demountable torch was used. The demountable system permits a change in the tube length without dismantling of the entire torch assembly. It is also useful on those rare occasions when something goes amiss and the outer tube is transformed into a glowing pile of quartz slag. While reaction rates at the surface of the workpiece did increase, suggesting an increase in the reactive atom population, surface temperatures also increased. Thermocouples were placed at several locations in the sample box; one above the sample, one between the thin silicon wafer sample and the rotary stage and two others at probable hot spots in the chamber. The maximum temperature of the workpiece (measured from the rear of a silicon wafer) increased from 70 ^{o}C with the short torch to 225 ^{o}C with the longest torch. The temperature is reached quickly, a matter of a few minutes, and stays there for the duration of the experiment, as long as 60 min in some cases. At this time, the major concern with the temperature increase is resistance of the stage motor. To prevent overheating, the rotary stage and motor were covered with a cooling coil.

Silicon Etch Rates

A silicon wafer with a known mass was exposed to a flow of fluorine atoms from the reactive atom plasma. The fluorine atoms were created from the dissociation of SF_6 delivered to the plasma at a flow rate of 30 ml/min. In 20 min the silicon wafer was reduced in mass by 0.372 g. In a balanced reaction, two molecules of SF_6 react with three atoms of silicon to produce three molecules of SiF_4 and two atoms of silicon:

$$2SF_6 + 3Si = 3SiF_4 + 2S$$

If the reaction were 100% efficient a total of 1.143 g of silicon would have been consumed. Under the operating parameters used in this experiment, silicon reacted with an efficiency rate of 32.6%. The reduction in rate could be from a number of factors. The two most probable are quenching or the inability of the reactants to reach the surface of the workpiece. Quenching of the reactive gases in the plasma can come from at least two sources: either from entrained atmospheric nitrogen or from recombination of the fragmented precursor. At the surface of the workpiece, boundary layer conditions may prevent the fluorine atoms from reacting. Two other experiments were performed under similar conditions, the only change being small changes in flow rate of the reactive gas and a small increase in the plasma power.

Initial studies using an optical interferometer have shown the footprint to be roughly Gaussian in shape. The material is removed in a symmetric fashion across the discharge. As expected, there is little evidence of redeposition. In addition, preferential etching, caused by dirt or other debris on the surface seems not to be an issue in early tests.

Future Work

In the initial experiments, the reactive precursor was added to the plasma, giving the reactive atoms the broadest distribution possible. The concentration of reactive species was also kept on the low side. The combination of a wide footprint and a low reactant concentration should minimize the boundary layer effect. On the surface, the 30% efficiency suggests that quenching in the plasma was responsible for a reduction in active species leading to the lower than expected consumption of silicon.

To confirm this statement, the proficiency of the reaction over a wide range of concentration will be measured. The distribution of reactants throughout the discharge will also be altered. Confining the reactants to the central channel of the plasma will decrease quenching of the active species. The addition of a second downstream load coil can also serve to redissociate the fluorine if recombination is an issue. Besides increasing understanding of the

reduction in reaction rate, this study will determine the range over which the reaction is linear, an important parameter in fabrication of precise optical profiles. The etching pattern caused by a translated discharge will also be studied.

The shape and symmetry of the static footprint will be measured as a function of plasma conditions (power, shape of load coils), primary gas mixture, primary gas flow rate, reactive gas type and concentration, discharge size, distance from the plasma and dwell time. The effect of crystal orientation on the etch rate of silicon will also be investigated. The footprint shape, surface roughness and removal rates will be measured with a Fizeau-type interferometer and an atomic force microscope. If necessary, etch rates and materials removal mechanisms will be determined *in situ* by emission or absorption spectroscopy. Once the stability and shape of the footprint is determined, convolution algorithms can be developed to generate specific surface shapes. The program would determine a path of motion for the discharge over the surface of the workpiece. A long term objective is to develop a well understood technology that can be tuned to produce a highly asymmetric surface in a single operation from a data file.

References

1. G. S. Oehrlein (1994), "Reactive ion etching," Handbook of Plasma Processing Technology, Vol. **196**.

2. L. D. Bollinger and C. B. Zarowin (1988), Part 1, *Proc. SPIE*, Vol. **966**, p. 82.

3. L. D. Bollinger and C. B. Zarowin (1988), Part 2, *Proc. SPIE*, Vol. **966**, p. 91.

4. S. J. Hoskins and B. Scott (1995), *Proc. SPIE*, Vol. **2542**, p. 220.

5. S. J. Hoskins and B. Scott (1995), *Proc. SPIE*, Vol. **2542**, p. 235.

6. A. Meinel, S. Bashkin, and D. Loomis (1965), *Appl. Opt.*, Vol. **4**, p. 1674.

7. S. R. Wilson, D. W. Reicher, and J. R. McNeil (1988), *SPIE*, Vol. **966**, p. 74.

8. L. N. Allen and R. E. Keim (1989), *SPIE*, Vol. **1168**, p. 33.

9. T. W. Drueding, T. G. Bifano, and S. C. Fawcett (1995), *Prec. Eng.*, Vol. **17**, p. 10.

10. S. R. Wilson and J. R. McNeil (1987), *SPIE*, Vol. **818**, p. 320.

11. S. C. Fawcett, T. W. Drueding, and T. G. Bifano (1994), *Opt. Eng.*, Vol. **33**, p. 967.

12. O. Siniaguine (1996), *Int. Symp. Plasma Process-Induced Damage*, Vol. **151**.

13. Y. Mori, K. Yamamura, K. Yamauchi, K. Yoshii, T. Kataoka, K. Endo, K. Inagaki, and H. Kakiuchi (1993), *Nanotechnology*, Vol. **4**, p. 225.

14. Y. Mori, K. Yamamura, K. Yamauchi, and Y. Sano (1996), *The Japan - China Bilateral Symp. on Adv. Manuf. Eng.*, Hayama, Kanagawa, Japan.

15. Y. Mori, K. Yamamura, K. Yamauchi, K. Yoshii, T. Kataoka, K. Endo, K. Inagaki, and H. Kakiuchi (1993), Technology Reports of Osaka University, Vol. **43**, No. 2156, pp. 261–266.

16. T. B. Reed (1961), *J. Appl. Phys.*, Vol. **32**, p. 821.

17. T. B. Reed (1961), *J. Appl. Phys.*, Vol. **32**, p. 2534.

18. M. Suzuki, M. Kagawa, Y. Syono, and T. Hirai (1990), *J. Crystal Growth*, Vol. **99**, p. 611.

19. M. Suzuki, M. Kagawa, Y. Syono, and T. Hirai (1991), *J. Crystal Growth*, Vol. **112**, p. 621.

20. M. Suzuki, M. Kagawa, Y. Syono, T. Hirai, and K. Watanbe (1991), *J. Mat. Sci.*, Vol. **26**, p. 5929.

21. M. Kagawa, M. Kikuchi, R. Ohno, and T. Nagae (1981), *J. Am. Ceram. Soc*, **Vol. 64**, p. C7.

22. "Inductively Coupled Plasma Emission Spectroscopy, Part I: Methodology, Instrumentation and Performance, in Chemical Analysis" (1987), Vol. **90**, P. W. J. Boumans, ed., John Wiley & Sons, New York, New York.

23. "Inductively Coupled Plasma Emission Spectroscopy, Part II: Applications and Fundamentals in Chemical Analysis" (1987), Vol. **90**, P. W. J. Boumans, ed., John Wiley & Sons, New York, New York.

24. *ASPE Spring Topical Meeting on Prec. Eng.* (1998), Carmel, California, April.

Design of an Ultra Precision Machining Facility: ULTRA 350

Keith Carlisle and Stanley L. Edson
Manufacturing and Materials Engineering Division
Mechanical Engineering

This report describes the advanced machine tool technology used in the design of an Ultra Precision Machining Facility, the ULTRA 350 at Lawrence Livermore National Laboratory (LLNL). It outlines the collaborative research undertaken in key technology areas to ensure we maintain our world leadership in precision machine technology. It also describes the new enhanced manufacturing process capabilities the machine brings to LLNL's precision manufacturing group.

Introduction

The drive for miniaturization and higher precision across a widening range of manufacturing activities is increasing, placing demands on engineering for new capabilities for machining, positional control, and measurement to nanometer tolerances. It also calls for improved understanding of materials and processes at the molecular or atomic level.

NASA recently reported that one of the principal missions for the International Space Station (ISS) is material science in microgravity, stating that "manufacturing is 17% ($1.2 trillion) of the US gross domestic product." This means that even the modest improvements in materials and their production can have a great impact on the US economy. The 1998 Metal Casting Industry Roadmap lists lack of knowledge of interactions among process, microstructure, chemistry, and material properties as one of the major technology barriers in materials.

It is critical to the ongoing success of LLNL and the US economy that we have the right engineering tools that will lead to improvements in our manufacturing techniques and the development of new products and processes. Our objective is to establish a national world-class research and manufacturing facility to take us confidently into the twenty-first century.

Progress

The ULTRA 350 machine concept design is now complete and the final detail design will commence in the next fiscal year.

The machine configuration is illustrated in **Figs. 1** and **2**. **Figure 1** shows the machine as it would be used in a single-point diamond turning mode and **Fig. 2** shows the machine in its grinding mode.

This four-axis diamond turning and grinding machine uses a 'L'-bed base construction, which supports the 'X' axis tool carriage slide and the 'Z' axis work slide. Both carriages run on pressurized hydrostatic oil guide-ways. The 'Z' work carriage carries the 'C' axis work-head spindle, which has hydrostatic bearings. The 'X' tool carriage carries the integral 'A' axis rotary table which also has hydrostatic bearings. This rotary table supports a tool-post for diamond turning or metrology equipment for workpiece inspection. A good feature of

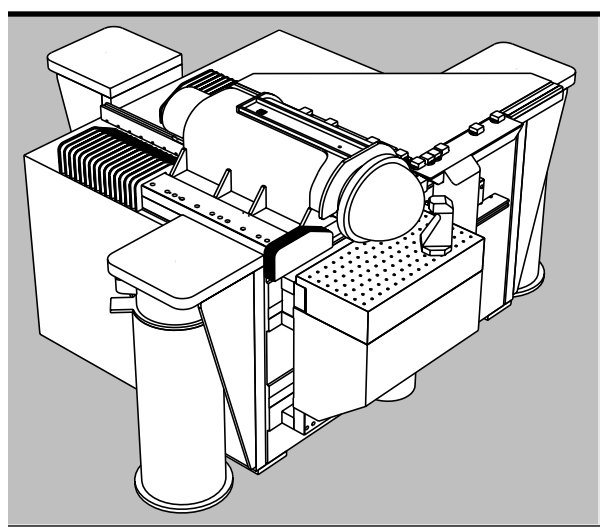

Figure 1. Schematic illustration of ULTRA 350 in single-point diamond turning mode.

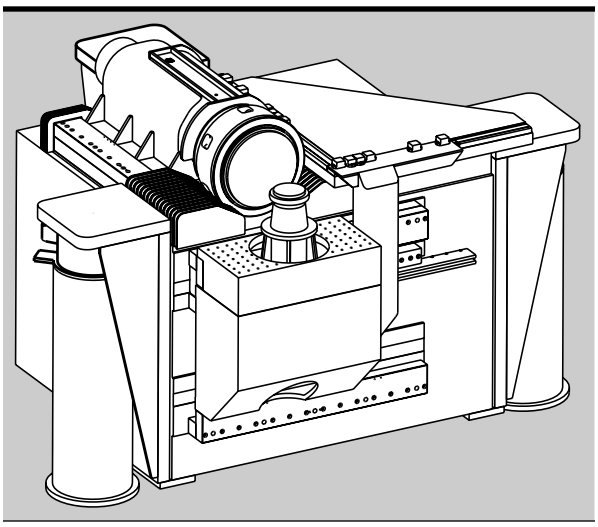

Figure 2. Schematic illustration of ULTRA 350 in grinding mode.

this rotary table is that it can be removed from the machine to accommodate a grinding spindle.

The work capacity of the machine is 350 mm in diameter and 225 mm in length. Each slide has a maximum travel of 350 mm with a positional resolution of 1 nm. The target performance for the machine is 25 nm (p-v) contouring accuracy and 4 nm rms surface finish.

The machine base is to be constructed from steel, chosen because of its high modulus of elasticity, giving high specific stiffness. Finite element analysis will be used to determine the final design, which may include the selective addition of synthetic granite to achieve high internal damping. Subjecting the base fabrication to thermal stress relief will ensure long-term dimensional stability. Seismic vibrations will be reduced by supporting the base on a three-point, self-leveling pneumatic isolation system, which may have to stand on a damped, large-mass concrete foundation. This will depend on the final site conditions.

Oil hydrostatic bearings have been selected for their attainable high stiffness and load carrying capacity. They also provide smooth motion and good damping with freedom from slip-stick, all essential requirements when servo-positioning slides down to 1 nm during contouring operations. Oil also has the added advantage of being temperature controllable to within 0.01 °C or better to ensure thermal stability of the machine.

The work slide uses an opposed bearing pad design for both vertical and horizontal bearings. Designing the slide motion to be parallel to the work spindle axis ensures that any out-of-balance forces generated by the rotary motion will be absorbed by the slide bearings and not seen directly by the linear drive system.

The tool slide uses the same bearing design as the work slide. Mounting the bearings to a vertical face gives better operational access. It also enables the 'A' axis rotary table to be embedded within the carriage and permits greater slide bearing separation, which was an important design consideration when trying to reduce carriage roll effects. Carriage roll is seen as a departure from straightness at tool travel height in the 'Z' direction. With a 2:1 ratio between bearing separation and bearing-to-tool position, it is possible to control straightness of carriage motion through bearing adjustment. Another design feature of the machine is the ability to exchange the rotary table with a motorized grinding spindle.

The work spindle is integrated into the work carriage for maximum stiffness and uses oil hydrostatic bearings designed to give high stiffness, high load carrying capacity, good damping and low error motion.

Thermal stability is to be maintained by careful selection of the materials used for its construction: the bearing is designed for low 'Δt' and temperature control of the oil to better than ±0.001 °C. All these design factors have been optimized to achieve the highest standards in single-point turning and enable full exploitation of ductile regime grinding of brittle materials.

The spindle is to be driven through a non-influencing drive coupling by a high-performance brushless DC motor, supported by an air bearing. The drive motor has its own temperature control system. A rotary encoder is built into the spindle to provide commutation for the servodrive and positional information for a "fast-tool-servo" (FTS) axis.

Additional facilities built into the spindle include provision for two-plane dynamic balancing and vacuum work holding.

The 'B' axis rotary table gives great flexibility to the range of work that can be carried out on the machine. Unlike most other machines, there is no loss in workpiece swing diameter when using the rotary table. This is because of the unique design of the rotary table, which is embedded within the tool slide. The rotary table uses the same hydrostatic bearing design as the work spindle to ensure high stiffness and load carrying capacity. The drive system consists of a direct drive frameless DC torque motor and tacho-generator mounted directly onto the spindle. The measuring system comprises a rotary encoder. The whole assembly is temperature controlled by the oil to better than ±0.001 °C.

Brushless linear drive motors are used to drive both carriages. The particular non-contact linear servomotor selected for this application possesses

clear advantages over conventional drive train technologies in applications requiring high resolution and high-accuracy positioning. Because linear motors consist of only two non-contacting parts, a moving coil and rare earth magnet track, they eliminate backlash, windup, wear and maintenance issues associated with ball screws. They can also outperform the tried and tested capstan drive system.

The moving coil assembly of this motor design uses a compact, reinforced ceramic epoxy structure without metal support for the coils in the magnetic field. This feature eliminates eddy current losses, cogging and magnetic attraction.

The unique magnet spacing in the magnet track minimizes force ripple and allows for excellent velocity control. This highly rigid, low inertia assembly achieves outstanding motion smoothness by sinusoidal commutation, with or without Hall Effects sensors. The very highest positional resolution and accuracies are possible.

A Heidenhain incremental linear encoder, with measuring steps of 1 nm, was selected to measure linear displacement for each axis. Collaboration with Heidenhain has already led to the development of a new encoder system that can measure in two orthogonal directions so that linear displacement and departure from straightness of carriage motion can be determined simultaneously. This is now the subject of an LLNL patent application.

The machine uses two of these linear encoder systems, which are mounted orthogonal to each other on a super invar metrology frame. Each system uses three reading heads.

One head measures displacement in the direction of the carriage travel and the other two heads measure the orthogonal effects of carriage roll and yaw to determine straightness and tilt. Care has been taken to position the scales at the operational height of the machine to avoid pitch errors. From these measurements, an actual position of tool-to-workpiece can be determined.

Particular attention has been given to the work head where, in addition to the design features described, capacitance sensors are positioned within the metrology frame measuring loop-to-monitor any axial or tilt movement of the face plate. These measurements are to be used for automatic compensation made through the machine computer numerical control (CNC) system.

The optical tool setting facility is a non-contacting device used to measure the tool profile and its relative position to the machine coordinate system to an accuracy of 25 nm. This device enables tool errors to be eliminated from the part profile automatically through the CNC system, resulting in higher accuracy of the part profile.

The FTS device is an additional servo-controlled axis mounted to the tool slide carriage to provide tool motion that is synchronized to the work spindle rotation. A piezoelectric (PZT) mechanism provides tool motion up to a 500-µm maximum travel with a bandwidth of 600 Hz. The PZT is driven by the machine digital signal processor (DSP)-based controller, synchronized to the spindle by an encoder, which provides a master time based in an electronic cam configuration.

This device will be used to improve the intrinsic accuracy of the work spindle, which should be of the order of 25 to 50 nm. By recording the systematic errors of the work spindle in a lookup table, it is possible to servo the FTS in a controlled manner to achieve true nanometric accuracy.

The FTS will also be used to enhance the machine manufacturing capability by enabling non-rotational symmetric components such as correcting secondary mirrors, anamorphic optics, off-axis conic sections, turned on-axes and generated surfaces.

The grinding facility for this machine has been designed for maximum loop stiffness. Unlike many other machines, where the grinding spindle is treated as an attachment that can be somewhat limited in dynamic performance by its support system, the objective for this machine is to design a fully integrated facility.

The air-bearing grinding spindle is designed to use existing Westwind spindle bearing components, and will be driven by a direct drive three-phase motor, which is temperature controlled. The system is mounted rigidly to the tool slide, as can be seen in **Fig. 3**.

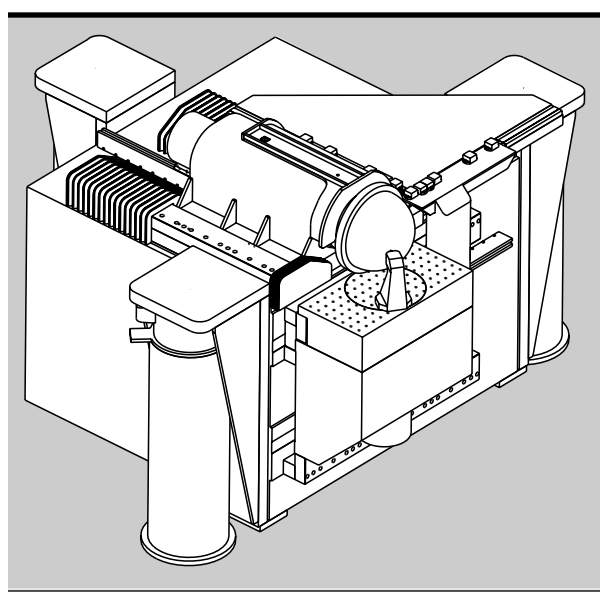

Figure 3. Schematic illustration of ULTRA 350, with air-bearing grinding system and tool slide.

Great importance is given to the method of mounting the spindle to achieve a stiff and well-damped support system. The flange mounting interface and ribbed column support to the wheel spindle ensure this.

An essential feature of any grinding facility is the ability to true the wheel to run concentric to the spindle axis. It is also necessary to be able to contour the wheel profile to give clearance to the wheel when grinding concave shapes. The on-machine truing facility uses an air-bearing spindle, which is attached to a servo-driven vertical 'Y' axis carriage. Wheel profiles are to be programmable through the machine CNC system.

Thermal stability of the machine is essential for maintaining geometric and dimensional accuracy.

Hydrostatic oil from the linear and rotary bearings are to be temperature controlled to within ± 0.01 °C accuracy using a control resolution of ± 0.001 °C. Temperature sensors are designed into the machine to monitor both the oil feed and exhaust temperatures to ensure thermal stability of the machine. After exhausting from the machine bearings, the oil is to be deliberately run over the machine surfaces before running back to the collection tank.

All drive motors are to be temperature controlled to the same level. Unlike the bearing oil, the cooling oil from these motors does not come into contact with the machine structure but will be taken back to the collection tank via lagged pipes.

A process coolant facility will be provided for both single-point machining and grinding. The coolant is prevented from contacting the machine structure to avoid thermal transients that may be present due to process heating or chilling effects caused by latent heat of evaporation of the coolant.

Self-supporting machine containment will be used to protect the machine from environmental effects. This also protects the machine from inadvertent collisions or loading from the operator. Acoustic damping material may be added to the containment panels to reduce airborne effects that may induce structural vibration of the machine elements.

The containment also supports an oil shower thermal control system for the machine structure. A laminar flow of oil, controlled to ± 0.01 °C, will be directed over the structure in a manner that will provide good operator working conditions. The oil will be gravity collected in a tray beneath the machine, thus providing insulation from any ground thermal effects.

A Delta Tau, Programmable Multi-Axis Controller (PMAC) CNC controller system has been selected for the machine. Using an open architecture design with standardized PC components, this unit combines a network-ready Pentium-based PC, a multi-axis motion control board and Windows-based operator software.

At the heart of the system is the Turbo PMAC motion control board, which is a high-performance Motorola DSP chip. The feature offers high-speed computational capability for more axes of control, more sophisticated control on each axis, or both. The additional axes can be used as true physical axes or as "virtual axes" for inverse kinematics, superimposed moves, or hybrid force/position loops for grinding operations. The Turbo also offers a special dynamic look ahead/look back buffer that permits acceleration control anticipated over 100 blocks ahead, and reversal through hundreds or even thousands of blocks. This is very desirable for obtaining high accuracy of complex shapes especially when using the FTS axis for non-axis symmetrical shapes.

Future Work

The ULTRA 350 is targeted both for continuing multi-program support and also for enabling program development.

First, this machine will allow us to improve support to our current customers. For example, because of its FTS and increased accuracy, it will allow us to fabricate meso-scale device components that we currently cannot produce. One case is sine-wave interfaces where the pattern of the sinusoidal surface requires a fast-moving axis. In the short term, this machine will provide this improved capability and will more generally allow physicists wider choice of experimental configurations for fielding on LLNL's Omega and NIF projects. In the long term, the ULTRA 350 will lead to the specific upgrade of capability in manufacturing high-precision devices.

Second, this machine will lead to new program development. For example, it will allow certain classes of optical surfaces to be turned that cannot now be turned. One category is an off-axis conic surface where the distance that the surface falls from its optical axis is greater than the swing of the machine. A second category is a surface that is both reflective and diffractive, particularly on an aspheric surface with changing blaze angle. This has value to

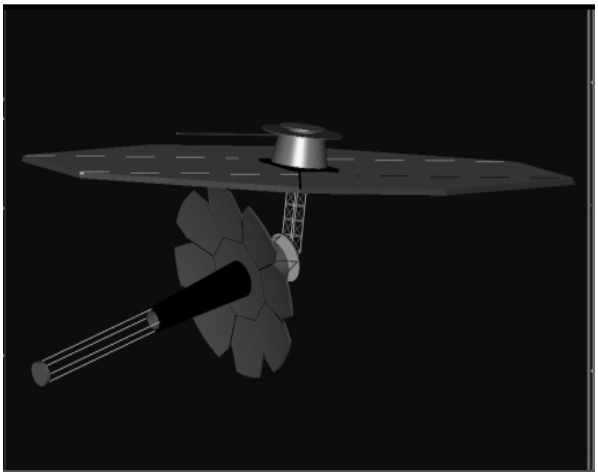

Figure 4. Illustration from NASA's Next Generation Space telescope.

internal programs dealing with novel optical designs as well as external agencies such as NASA which require a 6-m–aperture telescope for their Next Generation Space Telescope (NGST) (**Fig. 4**). LLNL has put forward a manufacturing proposal to machine the 2.1-m-long segments for the telescope, which will require new machining technology to be developed, the third category of anamorphic surface, made possible by the FTS.

Third, this machine will become the platform for the further development of precision machining processes. One example is the machining of brittle materials to complex shapes. Using the highest quality platform is a requirement for such projects to provide the highest probability of success. The Air Force has a continuing work program with LLNL to manufacture optics for the Space Based Laser Program.

Fourth, this machine will evolve to an integral part of our continuing mission to produce the larger weapons components because of its integrated rotary tool axis.

Finally, this machine is a vehicle that allows us to import external, newly developed technologies to LLNL. In a related role, we have assembled a team in anticipation of future projects for programs, such as the upgrade of our facility to manufacture meso-scale devices for NIF.

Intermittent Single-Point Machining of Brittle Materials

Mark A. Piscotty
Manufacturing and Materials Engineering Division
Mechanical Engineering

Single-point diamond turning is generally considered ill-suited to machine brittle materials, largely due to excessive tool wear resulting in poor part quality. The goal of this project is to investigate observed reduced tool wear by applying a controllable intermittent cutting duty cycle to the diamond turning process of brittle materials. Two methods are evaluated where the cutting edge of the tool is periodically separated from the part surface. It is hypothesized that the tool edge may wear less due to resulting lower temperatures of the diamond. The first method uses piezoelectric (PZT) ceramic elements to induce an elliptical motion of the diamond tool at frequencies ranging from 2 to 30 kHz. The elliptical motion of the tool is used to enhance a typical cylindrical turning operation. A second method investigated is diamond tool fly cutting of flat surfaces also using the concept of intermittent machining, but at a much lower frequency than the ultrasonically assisted turning. Repeatable, low tool wear in currently non-diamond turnable materials holds significant benefits to national defense programs and industry.

Introduction

The demand for innovative fabrication methods compatible with brittle materials is largely driven by organizations such as Lawrence Livermore National Laboratory (LLNL)'s Weapons and Lasers Programs, DOD, and private industry. Single-point diamond machining is an attractive process due to the vast experience and knowledge base available, combined with process efficiency and accuracy. However, these attractive characteristics are typically present only when machining ductile materials such as aluminum, copper or electroless nickel. The goal of this project is to extend the database of important engineering materials that may be diamond turned in an efficient and repeatable manner.

The approach taken here is to vary the cutting dynamics of the material removal process by varying the interaction between the diamond tool edge and the workpiece material. One method of accomplishing this is to vibrate the diamond tool so that it moves in an elliptical motion in the direction of cut, as shown in **Fig. 1**. The amplitude and frequency of the vibration are two parameters that are used to modify the cutting process.

Another method of introducing dynamics modification to the cutting process is to arrange the workpiece and tool in a fly cutting arrangement. In this case the workpiece is typically stationary and the diamond tool moves in a circular planar path relative to the face of the workpiece. The material removal process in this arrangement is intermittent with the on/off contact time determined by the angular speed of the tool, the relative sizes of the workpiece and the circular path of the tool.

Both of these techniques offer potential to modify the standard diamond turning process dynamics to accommodate traditionally non-turnable materials

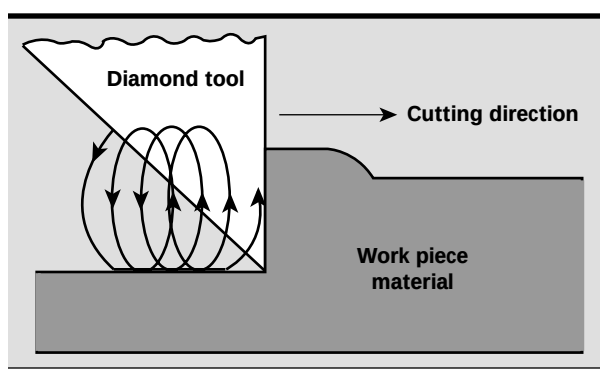

Figure 1. Schematic of elliptical vibration-assisted diamond turning.

such as brittle materials[1–2] and steels.[3] A leading hypothesis generated to explain the observed reduction of tool wear using these techniques centers about the thermal interaction between the diamond tool edge and the workpiece surface. Specifically, it is hypothesized that catastrophic tool wear can be mitigated by modifying the material removal process such that the diamond tool edge temperature is maintained below a critical temperature at which edge breakdown occurs.

The two methods described above are used in this project in an effort to verify this hypothesis and to develop processes needed to single-point diamond machine materials outside the current range of those used in typical single-point diamond turning.

Elliptical Vibration–Assisted Diamond Turning

A method of PZT-induced vibration at the interface between the diamond tool edge and workpiece surface was developed at LLNL, leveraging both internal ultrasonic and diamond turning expertise, as well as external, international research efforts.[2,4] The hardware developed for this project includes a stainless steel 'resonator' that holds the diamond tool for the turning application. **Figure 2** shows a photograph of the actual resonator hardware. The resonator is driven by a pair of PZT crystals mounted in pockets on the large diameter portion of the resonator. The pockets are located on 90º faces of the resonator. Expanding and contracting the PZT crystals along the length of the resonator by applying bipolar voltages causes the resonator to flex in the first bending mode in two perpendicular directions. By manipulating the relative phase between the driving signals of the two PZT crystals, the motion of the tool can be varied from almost linear to elliptical.

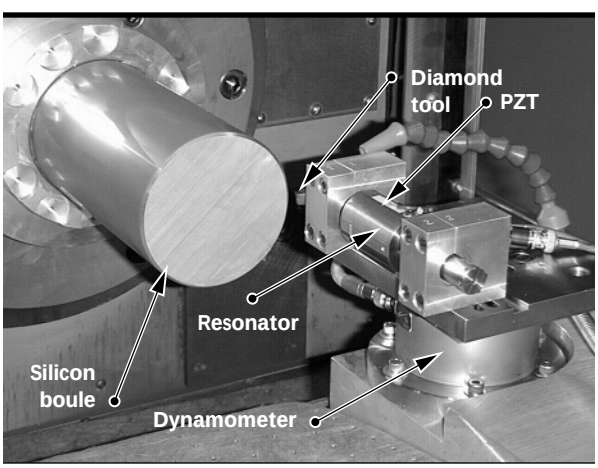

Figure 2. LLNL's diamond tool resonator.

The magnitude of the displacement of the tool tip is a function of the driving PZT frequencies and phase. A Michelson interferometer was used to measure the peak-to-peak motion amplitude of a tool in a single direction. Data were obtained by varying the PZT frequency and measuring the peak-to-peak displacement. **Figure 3a** shows the displacement data as a function of driving frequency and **Fig. 3b** is the same data, but from 0 to 10 kHz. The largest displacements are more than 45 nm and occur at about 2.5 kHz and 4.0 kHz. Note that these

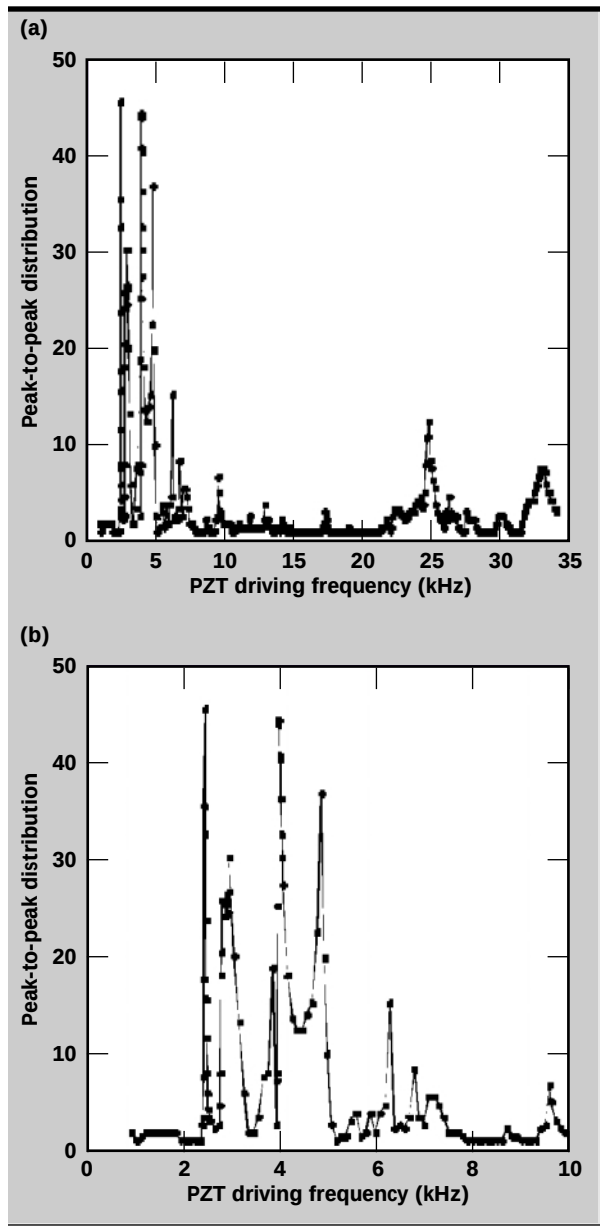

Figure 3. Single direction, peak-to-peak tool displacement data.

frequencies are below the ultrasonic frequencies. Further analysis and testing is being conducted to investigate the reason these frequencies generate the largest displacements in the resonator.

Figures 4a and **4b** are Wyko white-light surface interferograms of a copper workpiece diamond-turned to examine the effect of applying elliptical tool vibration (2.54 kHz) to the diamond tool. **Figure 4a** is a diamond-turned surface without tool vibration. The striations from the tool path are clearly seen. The copper surface topography changes dramatically in **Fig. 4b** when the tool vibration is introduced. Both surfaces used identical process parameters (0.76 m/s, 5.08 μm depth of cut), except that the surface in **Fig. 4b** used the tool vibration. As expected, the surface roughness with the vibrating tool is higher than without the tool vibration.

Experimental Diamond Fly Cutting

Fly cutting is a popular machining technique that can be used to generate precision flat surfaces using single-point diamond tooling. A specialized, precision fly cutting apparatus was developed at Pennsylvania State University (PSU) under Prof. E. Marsh to investigate possible improved tool wear using this form of intermittent contact machining with brittle material workpieces. **Figure 5** shows the precision machining hardware that consists of two air-bearing spindles mounted on a Moore No. 3 Jig-Grinder machine base.

The single-point diamond tool is mounted in a fixture on the face of one of the spindles while the other spindle is used to hold the workpiece (in this case, a silicon workpiece). The workpiece spindle is held stationary with the silicon part mounted on the face, while the tool spindle rotates the diamond tool. Fine in-feed motion control is generated by increasing the air pressure in the air bearing of the workpiece spindle, which produces 11 nm of axial growth per kPa of increased air pressure. This fine in-feed capability provides the ability to fly cut with submicron depths of cut.

Figure 6 shows an example silicon workpiece that has been fly cut with a single-point diamond tool. The overall workpiece surface roughness is about 17 nm rms, with smaller sections having roughness values of less than 2 nm rms. Note that these data are from

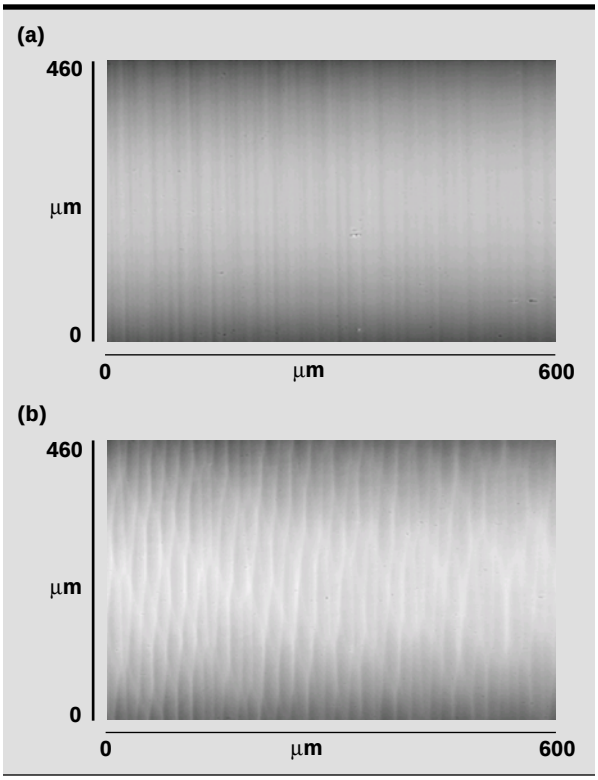

Figure 4. Wyko white-light surface interferograms of a copper workpiece. (a) Vibration off, roughness 6.1 nm rms; (b) vibration on, roughness 12.1 nm rms.

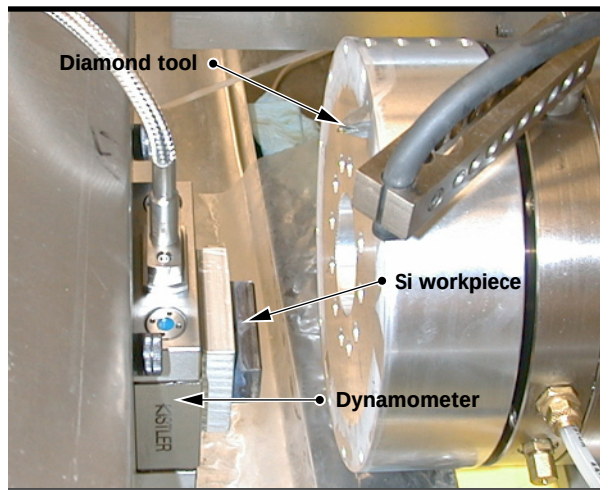

Figure 5. Dual spindle diamond fly cutting set-up.

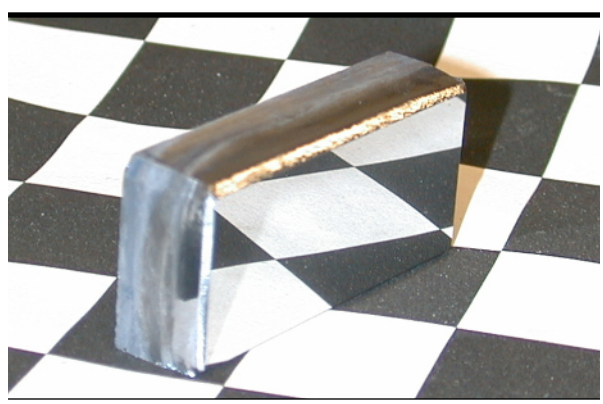

Figure 6. Fly cut silicon workpiece.

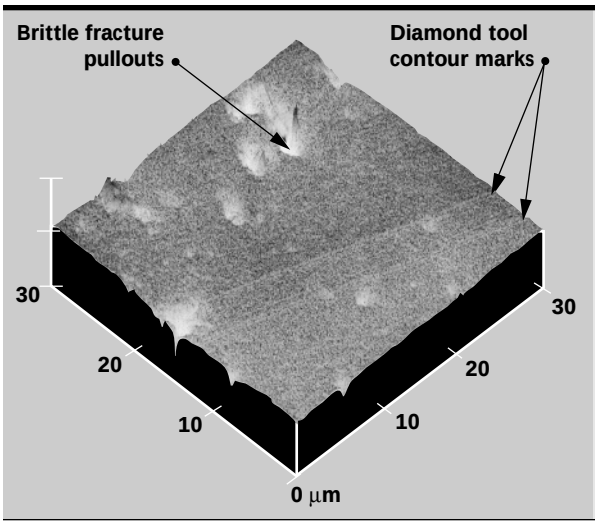

Figure 7. Atomic force microscope image of a fly cut silicon workpiece.

demonstration runs and the process continues to be optimized. **Figure 7** is an atomic force microscope image of a silicon fly cut surface from this process. There are areas that appear to be machined in a ductile mode and areas that exhibit characteristics of brittle fracture mode machining with material pull outs. Also present are streaks that are left by imperfections of the diamond tool. A goal of this project is to machine a surface that is free of brittle fractures and machine tool marks, while maintaining tool wear within acceptable levels.

Future Work

The anticipated future work for this project includes continued exploration of both the vibration-assisted single-point diamond turning and diamond tool fly cutting at PSU. Among the areas of investigation for the vibration-assisted diamond turning are optimizing the PZT ceramic driving frequencies and phases, mapping tool wear and testing materials in addition to silicon. Future work for the fly cutting experimentation at PSU will include diamond tool wear mapping, surface and subsurface damage analysis and process optimization. The results of both experimental projects will be used to support the hypothesis for reduced tool wear due to lower temperatures generated at the tool and workpiece interface.

References

1. E. Marsh (1998), "Preliminary results from flycutting of BK-7 glass," work in progress.

2. Y. Takeuchi, K. Sawada, and T. Sata (1996), "Ultraprecision 3D micromachining of glass," *CIRP Ann. Manufacturing Technology*, Vol. **45**, No. 1, January.

3. E. Shamoto and T. Moriwaki (1999), "Ultraprecision diamond cutting of hardened steel by applying elliptical vibration cutting," *CIRP Ann. Manufacturing Technology*, Vol. **48**, January.

4. T. Moriwaki and E. Shamoto (1995), "Ultrasonic elliptical vibration cutting," *CIRP Ann. Manufacturing Technology*, Vol. **44**, January.

A Spatial-Frequency-Domain Approach to Designing Precision Machine Tools

Debra Krulewich Born
Manufacturing and Materials Engineering Division
Mechanical Engineering

We have developed an error budgeting methodology for the design of machines used to manufacture parts with spatial-frequency-based specifications.

Introduction

The aim of this project is to develop a methodology to design machines for the manufacture of parts with spatial-frequency-based specifications.

One of our responsibilities is to design machine tools that can produce advanced optical and weapons systems. Recently, many of the component tolerances have been specified in terms of the spatial frequency content of surface profile, waviness, and finish errors.

During the design of a new machine tool, we use an error budget as a sensitivity analysis tool to ensure that the parts will meet the specified tolerances. Error budgets provide the formalism whereby we account for all sources of uncertainty in a process and sum them to arrive at a net prediction of how "precisely" a manufactured component will likely meet a target specification. Using the error budget, we are able to minimize risk during the design stage by ensuring that the machine will produce components that meet specifications before the machine is actually built.

Minimizing the risk while maintaining accuracy is a key manufacturing goal for programs that cannot tolerate yield factors less than 100%, such as in fabricating components for the nuclear weapons program. However, the current error budgeting procedure provides no formal mechanism for designing machines that will be required to produce parts with spatial-frequency-based specifications. We have received specifications for advanced optical and weapons systems that are posed in terms of the continuous spatial frequency spectrum of the surface errors of the machined part.[1] Based on these requirements, it is no longer acceptable to specify tolerances in terms of a single number that spans all temporal and spatial frequencies. During this fiscal year, we have developed a new error budgeting methodology to aid in the design of new machines used to manufacture parts with spatial-frequency-based specifications.

Progress

Technical Approach

Figure 1 shows flowcharts for both the conventional and the new error budget procedures. The upper portion of **Fig. 1** shows Donaldson's flowchart[2] and illustrates the mapping of error sources onto part geometry. The first step of the conventional error budget is to identify the physical influences that generate the dimensional errors that propagate through the machine tool. These include effects such as thermal gradients and temperature variability, bearing noise, fluid turbulence in cooling passages, and geometry errors such as linear bearing non-straightness.

The next step is to determine how each source couples to the machine. A coupling mechanism converts these physical influences into tool or part displacements (errors). An example of a coupling mechanism is the thermal expansion that may transform a time-varying heat source into a machine axis distortion. These displacements represent dimensional changes in the system. A single peak-to-valley number is usually used to quantify the dimensional changes, not differentiating between the spatial frequency content of the error. The next step is to sum all the contributing errors using an appropriate combinatorial algorithm.[3] The last step in the error budgeting procedure is to transform these errors into the workpiece coordinate system.

To convert these machine displacements into the errors on the workpiece surface in the directions of

interest, we must consider the tool path (for example, feed rates and spindle speeds). The output from this procedure is a single number predicting the net error on a machined workpiece. We then compare this number to the part specifications. If the prediction does not meet specifications, we evaluate methods to improve this design by observing which sources are the dominating error contributors. In this way we can evaluate the cost versus accuracy improvement of different candidate designs.

If improvements can be made to an existing design, the error budget can be used to predict the effect on part accuracy. If modifications are not practical, we then consider an entirely new design or possibly reevaluate the specifications.

The lower portion of **Fig. 1** shows the new error budget approach. The first two steps, identifying the sources and how they couple to the machine, are identical and are explained in the previous paragraph. However, the new approach differs in the next step, where the elemental errors are converted into the frequency domain.

The next step is to combine the errors in the frequency domain. The combinatorial rule is a new algorithm with a statistical foundation. The combined errors then go through a material removal transfer function that accounts for the dynamics of the material removal process and machine tool.

The material removal process creates cutting forces. The ratio between the cutting force and amount of material removed is the material removal transfer function. These cutting forces combine with forces induced by the machine kinematic errors. The machine structure responds to these forces with dynamic tool-to-part relative displacements that ultimately result in additional errors on the machined part. The last step is to transform the errors into the part coordinate system. The output from this process is the continuous spectrum of errors at all spatial frequencies on the part. Details on the technical approach appear elsewhere.[4]

Experimental Results

To verify the procedure, we machined copper and aluminum parts on a T-base lathe and measured the spatial frequency content of the resulting surfaces. We machined disks in a facing operation. During the facing operation, the tool shank is parallel to the axis of rotation of the spindle and feeds inward toward the centerline of the part as the spindle rotates. The final part is a disk with a nominal flat surface perpendicular to the spindle axis of rotation.

We then identified six main contributing errors: (1) spindle axial errors, (2) x-axis straightness in the z-direction; (3) squareness of the x-axis to the spindle axis of rotation; (4) spindle thermal growth; (5) thermal growth due to cycling of the environmental controller; and (6) diurnal cycles due to temperature changes during the day.

We measured the machine tool-to-part displacement errors individually and converted them to the frequency domain. We then used the combinatorial rule and mapped the errors to the surface to produce a prediction of the frequency content of the resulting surface. We compared this prediction to the measured surface along a radial trace across the part.

Results are reported for the following machining conditions:

Material: copper
Spindle speed: 180 RPM
Feed rate: 0.08 in./min
Tool radius: 0.03 in.

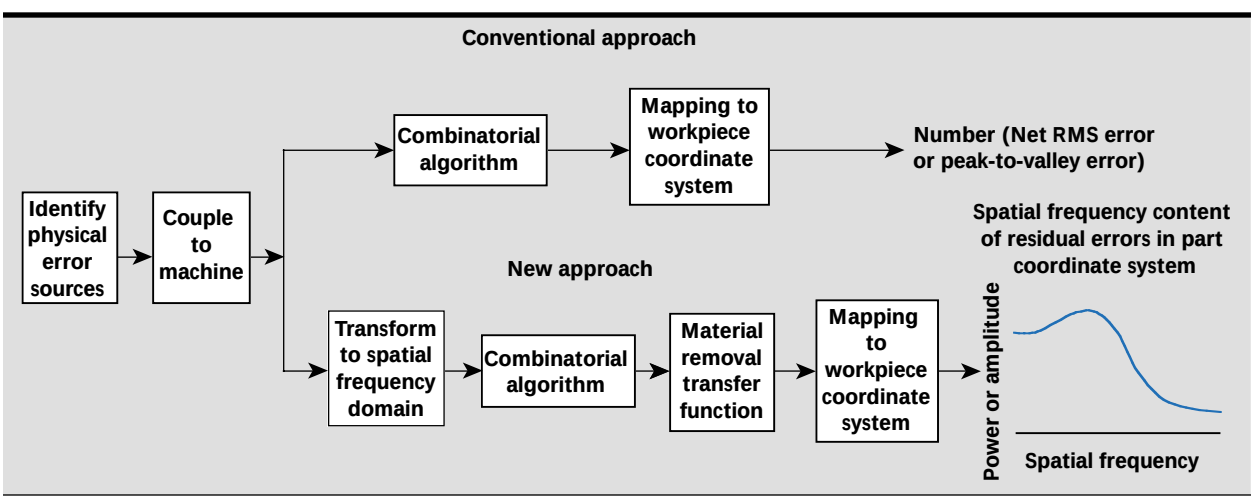

Figure 1. Flowcharts for both the conventional and the new error budget procedures.

The conventional error budget predictions of errors along a radial trace are shown in **Table 1**.

The total error across the entire part while machining copper at 180 RPM and a feed of 0.08 in./min was measured to be 13.36×10^{-6} in. This value falls within the RMS and algebraic sum as reported in **Table 1**. However, this value provides no information about the frequency content of this total error.

The results of the new error budget procedure are plotted in **Figs. 2** and **3**. **Figure 2** shows the dominant errors that occurred at relatively low frequencies. The expected errors and 95% confidence limit are arrived at through the statistically based combinatorial rule and error budget procedure. We measured errors on the machined part using a profilometer. The measured errors stayed below the upper limit with the exception of one point at approximately 1 cycle/in. This may be due to a thermal condition that existed during either the machining process or the measurement process that was not accounted for. It may also be due to some simplifications that were made while mapping the tool geometry onto the part.

Table 1. Conventional error budget results.

Parameter	Predicted error (in.)
Spindle growth	27.26×10^{-6}
Environmental control	14.00×10^{-6}
Straightness	4.50×10^{-6}
Squareness	9.70×10^{-6}
Spindle axial errors	0.51×10^{-6}
Tool marks	0.41×10^{-6}
Algebraic sum	56.38×10^{-6}
RMS	9.38×10^{-6}
Mean	32.88×10^{-6}

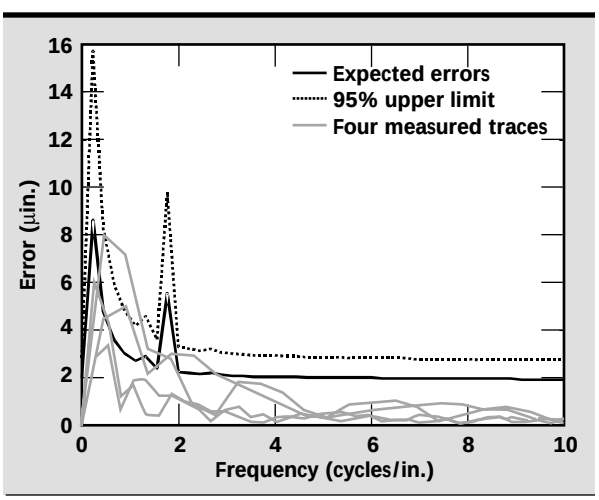

Figure 2. Low-frequency errors.

We also predicted a peak at around 2 cycles/in. that we didn't significantly observe on the measured part. This peak is due to the cycling of the environmental control. While machining, we used cutting lubricant that likely supplied thermal control at the tool/part interface, minimizing the thermal growth due to environmental cycling.

The high-frequency errors are dominated by the tool marks. During this project we did not evaluate the surface of a sharp tool or the surface of a worn tool. However, we observed that a sharp tool leaves behind not only the nominal shape of the tool, but higher frequency errors that can be approximated by a white noise of amplitude 0.01×10^{-6} in. at all frequencies. This accounts for the upper bound in **Fig. 2**. We measured errors on the machined part using an atomic force microscope (AFM). The measured errors stayed below the upper bound. Note that to predict the effect of a worn tool, the expected tool edge geometry would have to be put into the model.

Future Work

Further work needs to be performed to better measure surfaces in the frequency domain. As we see more parts specified in the frequency domain, this characterization will become more important whether or not this error budgeting procedure is used. Currently we have a variety of measurement instruments, each of which has a specific resolution, range, and frequency response, and it is not clear how to combine each of these instruments to yield a continuous profile measurement over a broad frequency band.

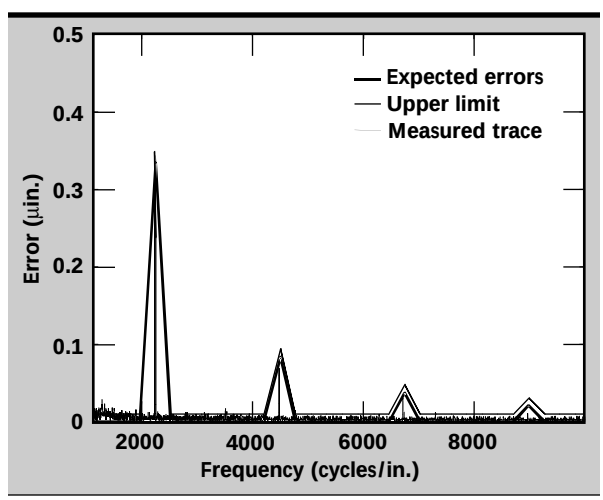

Figure 3. High-frequency errors.

For example, the AFM can only measure the high-frequency content of a surface due to its limited range of motion, while a profilometer has the ability to measure only lower frequency components. However, the output is filtered mechanically by the shape of the stylus and cannot measure very high frequency components. A procedure that can accurately combine these measurements over a broad frequency band would be extremely useful. Without this, we have no way of verifying the accuracy of parts that have been specified in the spatial frequency domain.

For this procedure to work, we must have a method of estimating the expected errors in the frequency domain associated with each machine component. It is not practical to perform detailed tests on every machine as we did in our test study. Furthermore, in some cases, the machine may not yet exist.

Using the current error budgeting procedure, where possible analysis is performed to determine a single peak-to-valley or RMS number, at times it is possible to use the manufacturers' specifications. Where analysis is not possible and no manufacturer's data exists, we rely on prior experience and data as well as expert opinions. This task is much more complex when we must predict the function of these errors over the frequency domain rather than predicting a single number as in the conventional approach. In some cases, we may be able to perform appropriate analysis, such as predicting the machine's dynamic characteristics. It is very unlikely that manufacturers will provide useful information since the component errors are not typically expressed in this way. Furthermore, most experts will not be familiar with characterizing errors in the frequency domain, so we cannot rely on expert advice. As more machines are characterized in this way, we hope to develop an archive of typical error types. This archive can then be referenced during the error budgeting procedure.

References

1. D. M. Aikens, C. R. Wolfe, and J. K. Lawson (1999), "The use of power spectral density (PSD) functions in specifying optics for the National Ignition Facility," *SPIE*, Vol. **2576**, pp. 281–292.

2. R. R. Donaldson (1980), "Error budgets," in *Machine Tool Accuracy*, Vol. **5** of *Technology of Machine Tools: A Survey of the State of the Art by the Machine Tool Task Force*, R. Hocken, ed., ch. 9.

3. Y. L. Shen and N. A. Duffie (1993), "Comparison of combinatorial rules for machine error budgets," *Ann. CIRP*, Vol. **42** (No. 1), pp. 619–621.

4. D. A. Krulewich (1998), "A spatial-frequency-domain approach to designing precision machine tools," *Engineering Research, Development and Technology*, Lawrence Livermore National Laboratory, Livermore, California (UCRL 53868-98), pp. 3-3–3-6.

Power Spectral Density Measurements of Machined Surfaces over an Extended Range of Spatial Frequencies

Jon M. Baldwin
Materials and Manufacturing Engineering Division
Mechanical Engineering

We have measured the surface error of a workpiece using several instruments, then combined the data into one set. We have resolved problems concerning normalization of the data among the instruments, transfer functions of the instruments, and other power spectral density issues.

Introduction

It is becoming increasingly common to specify the quality of precision-machined surfaces, particularly those intended for optical applications, by the power spectral density (PSD) function of the dimensional error of the surface. The PSD is useful in such applications because, when captured over a suitable range of spatial frequency, it efficiently encapsulates a great deal of information about the performance of the surface.

The goal of this project is to measure the surface error of a workpiece and display its PSD over a wide spectrum of spatial frequency. This requires measuring the workpiece on several instruments and combining the data into a single set. Among the problems are: normalizing the instruments with respect to each other, assessing and incorporating the transfer function or the bandwidth of the instruments, dealing with the loss of signal to noise at high spatial frequency, and assessing the PSD confidence interval across the multiple instruments.

Use of the 1-D PSD is fairly well understood. The 2-D PSD, however, is more powerful in these instances. Integration of the 2-D PSD over a suitable range of spatial frequencies yields, directly, the RMS roughness. The 2-D PSD has been used in optical component evaluation by a number of researchers[1,2] who have applied it to specification of components for the National Ignition Facility (NIF), and have been concerned with fabrication of optics for extreme ultraviolet lithography (EUVL). For optical components, a spatial frequency range from 1/(clear aperture) to 50 μm^{-1} is of interest.[2] The metrology instruments used in this study span the approximate spatial frequency range from 0.01 mm^{-1} to 10 μm^{-1}.

Some issues remain unsettled for 2-D PSDs as tools for evaluation of machined surfaces. The primary concern has been with surfaces produced by methods that are expected to generate spatially isotropic PSDs. Here, we are concerned with general surfaces including those manufactured by diamond turning, that is, surfaces with obvious lay.

The available publications provide little information about the details of data collection, data analysis, and normalization of data taken with several instruments over a wide range of spatial frequency. An example of an average radial 2-D PSD of a polished surface with reasonable continuity over six orders of magnitude of spatial frequency has been demonstrated, but with no description of steps involved, with evidence that the 2-D PSD inherently captures information regarding lay. This topic was not developed.

Progress

The purpose of our work is to reduce the PSD technique to routine practice for diamond turned surfaces, to evaluate, and, if possible, to resolve problems associated with combining data from several instruments. The specific instruments addressed here are: a Digital Instruments Nanoscope atomic force microscope (AFM), a Wyko NT2000 interferometric microscope, and a Zygo Mark GPI 4-in. interferometer. These instruments together can cover a spatial frequency range of more than six orders of magnitude, with substantial frequency overlap between instruments.

All of the above instruments are provided with software systems that provide significant data analysis power. In all cases, the details of the embedded

algorithms are unavailable. To eliminate unknown processing operations and algorithms as a source of uncertainty, only the unprocessed data from each instrument were recorded. The only operations performed with software provided by the instrument manufacturer were those necessary for conversion of data file and disk formats to be compatible with the Windows NT environment. MATLAB routines were written to read the raw data files produced by each instrument and to convert them to a common format. From this point on, all data sets were processed identically by appropriate MATLAB programs.

For each instrument/artifact/resolution combination, multiple data sets (~20) are required to (1) improve the statistical uncertainty in the PSD estimate, and (2) give a valid representation of the surface which is, at best, sampled over a small percentage of its total area by the higher resolution instruments. Each instrument must be applied at two or three resolution settings to get adequate overlap across the six-order-of-magnitude frequency range. For each measurement (except the full aperture measurements with the 4-in. interferometer) the specimen was oriented so that the x-axis was parallel to the direction of the tool feed. Each data sample was treated separately by first subtracting the least-squares plane and computing the 2-D PSD by the periodogram method, with appropriate scaling. All the PSDs for each set of conditions were averaged and a variety of display methods was used to view the individual and combined results.

A 3-D plot of the PSD works well for displaying results from a single instrument and resolution setting. A typical example, obtained with the AFM, is shown in **Fig. 1**. The x scan direction is nominally parallel to the tool feed direction, and the nature of the lay is evident. The average radial PSD used elsewhere works well for anisotropic surfaces and is a useful intermediate in getting RMS roughness numbers, but suppresses data about lay and does not seem particularly useful in visualizing anisotropic surfaces.

For this application, two separate 2-D plots of the PSD seem useful, sectioned parallel to or across the lay direction, with the section chosen to give the maximum area under the PSD. This gives, in a sense, a worst-case estimate of the surface and preserves lay information (see **Fig. 2**). Plots thus taken show, on average, agreement between instruments and resolutions within about an order of magnitude, and are fairly linear on a log-log scale over the frequency range. An example, showing data from all three instruments at two resolution settings for each, is presented in **Fig. 2**. Agreement between instruments and instrument resolution settings needs to be improved.

A model for the instrument transfer function (ITF) of the Wyko exists[3] and appears to slightly improve agreement between different resolutions of that instrument[4] and between it and the AFM. It fails visibly and predictably, though, at frequencies greater than half the Nyquist frequency since the correction term, which appears as a divisor to the PSD, goes to zero too rapidly. Compensation for the ITF is an area that needs further and careful study. Either additional, better models should be developed, or the ITF in each case measured.

The Zygo may be particularly challenging in this respect. Zygo has both modeled and measured the ITF of a similar instrument and, while their results do not apply directly to the present situation, their methods may apply.

The other major area that needs further work is development of reasonable estimates of uncertainty of the PSD. Current estimates consider only the

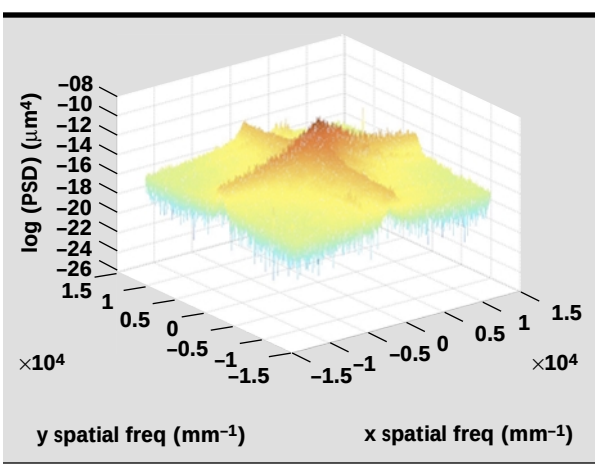

Figure 1. Three-dimensional plot of power spectral density for single instrument.

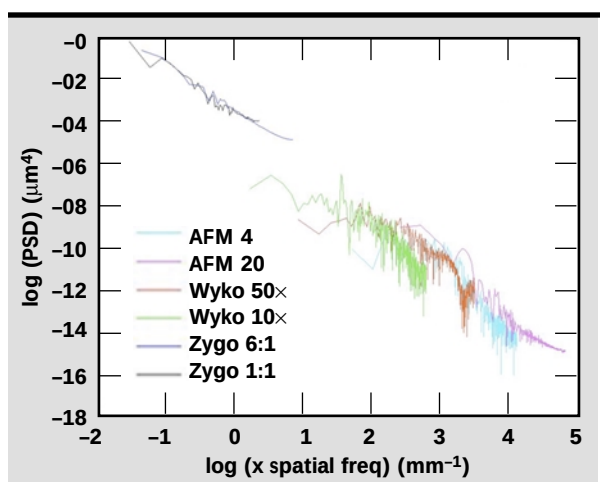

Figure 2. Two-dimensional plots of power spectral density for several instruments.

statistical properties of the PSD, under somewhat unreasonable assumptions. When applied to the data of the current study, they produce estimates that, clearly, are overly optimistic.

Additional measurements are under way at lower resolution for both the interferometric microscope and the AFM. In the former case, the objective is to increase overlap with the high frequency end of the 4-in. interferometer data. In the latter case, overlap is already adequate, but it is hoped that we will be able to resolve some questions about the ITF model for the Wyko.

Finally, the user interface for the MATLAB data analysis routines needs to be improved. The current version uses a DOS-style command line interface, presently appropriate in view of the developmental status of the work. When the analysis has been reduced to routine practice, a Windows-style interface should be considered.

References

1. J. K. Lawson, C. R. Wolfe, K. R. Manes, J. B. Trenholme, D. M. Aikens, and R. E. English, Jr. (1995), "Specification of optical components using the power spectral density function," *SPIE Proceedings*, Vol. **2536**, pp. 38–50.

2. J. S. Taylor, G. E. Sommargren, D. W. Sweeney, R. M. Hudyma, and E. M. Gullikson (1998), "The fabrication and testing of optics for EUV projection lithography," Lawrence Livermore National Laboratory, Livermore, California (UCRL-JC-128290).

3. E. L. Church, T. V. Vorburger, and J. C. Wyant (1985), "Direct comparison of mechanical and optical measurements of the finish of precision machined optical surfaces," *Opt. Eng.*, Vol. **24**(3), pp. 388–395.

4. J. A. Soobitsky, L. Deck, J. Biegen, J. Kramer, K. Khalsa, T. L. Miles, and F. Demarest (1997), "Zygo engineering report: NIF high resolution large aperture interferometer," June 23.

Dimensional Metrology of Non-Rigid Objects

Kenneth L. Blaedel and David W. Swift
Manufacturing and Materials Engineering Division
Mechanical Engineering

We have developed a method of measuring non-rigid objects for inspecting component parts. Our method of metrology also allows prediction of the shape of an assembly of non-rigid parts.

Introduction

The goal of this project is to devise and prove a method of dimensionally measuring non-rigid objects for inspecting component parts, which will further allow predicting the shape of an assembly of multiple non-rigid components. This is beyond the ability of conventional dimensional metrology, which assumes the artifact to be measured is rigid. The approach we developed is to perform a measurement while the non-rigid body is constrained under well-defined conditions. Through simulation, the effect of the constraints is then "backed out" to reveal information about the non-rigid part only. Then, the part can be constrained by a "virtual" fixture that is embodied in software to determine whether the object meets its specification.

The virtual fixture must be designed to reveal those aspects of the part that are functionally important to its end use. While using this approach may appear to be a straightforward analysis problem, it is subject to many sources of error that must be quantified and reduced to apply such analysis with high precision.

No method of dimensional metrology exists that adequately characterizes non-rigid parts to high accuracy. Inspections are often made by constraining a non-rigid part in a rigid fixture that controls the low-order, compliant modes of the part and then the part is measured as though it were rigid. Hence, the measurements inseparably confound the effects of the part itself and the effects of the fixture.

This year's task was to devise a method that would allow the separation of the effects of the fixture, which could then lead to a decision to accept or reject a non-rigid part.

The method to determine the acceptability of a non-rigid part that resulted requires two transformations of the measurement data, as shown schematically in **Fig. 1**.

The first step in the process is to inspect the non-rigid part, for example, on a coordinate measuring machine. The data that result reflect both errors of the part and deformations of the part that are caused by the fixture that holds the part during inspection.

The second step is to perform a structural analysis to calculate the shape of the part, as though it were free from external constraints and external forces such as gravity. The predicted shape is referred to as the "free" state of the part and is not usually physically realizable. The importance of

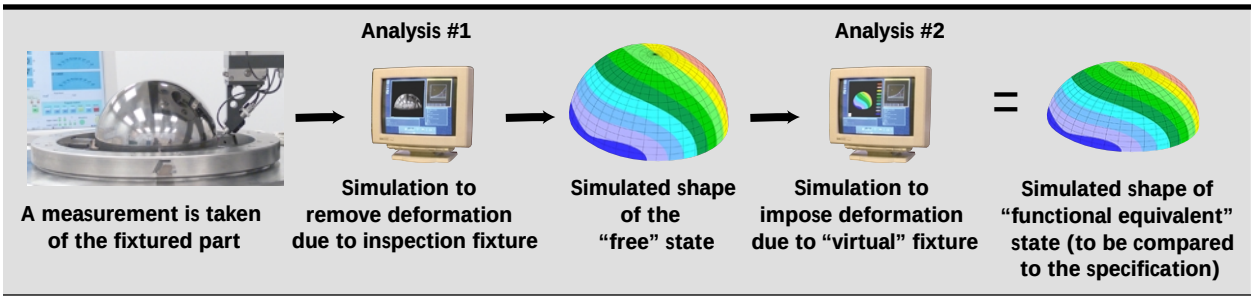

Figure 1. Methodology for dimensional inspection of a non-rigid component.

this state is that it reflects only errors in the part itself and does not include deformation induced by the fixture. This state is ordinarily not comparable to the specification of the part because for non-rigid parts, the low-order deformations, which are associated with the most compliant modes, are not the more important to the function of the part. Hence, the specification of the part often allows significant error in the low-order, compliant modes. The exercise is often to measure the higher order modes in the presence of significant low-order modes.

Therefore, before the free state can be compared to the drawing that specifies the part, the free state must have the low-order, compliant mode(s) removed. This is the purpose of the third step, which is shown in **Fig. 1** as the imposition of a "virtual" fixture. The virtual fixture is one that preserves characteristics that are important to the function of the part and removes the characteristics that are less important. Its general purpose is to simulate the functional state of the part, and results in the "functional-equivalent" state shown in **Fig. 1**.

In the fourth step, this state is directly compared to the drawing that specifies the part to determine the acceptability of the part.

In addition to enabling a method of inspection for non-rigid parts, the method of metrology proposed above also allows the prediction of the shape of an assembly of non-rigid parts. As shown in **Fig. 2**, the simulation of the assembly of two non-rigid parts, each in its free state, is performed by imposing a common boundary between them. Because current metrology methods confound deformation arising from the fixture and the part, the inspection data do not allow accurate prediction of the distortion that will occur when two non-rigid components are assembled.

Progress

Three particular tasks require further development to make this lengthy method of metrology successful. First, the uncertainty introduced in the measurement from the finite-element analysis (FEA) needs to be assessed. Second, fixturing needs to be devised that particularly allows its effect on the deformation of the part to be accurately modeled. Third, virtual fixturing needs to be conceptualized that enables the evaluation of important properties of the part and "filters out" those properties that are not. Of these, the assessment of uncertainty in performing an FEA is being pursued first.

Dimensional Uncertainty Introduced by Structural Analysis

Modern dimensional metrology requires that a statement of uncertainty accompany all dimensional measurements.[1] The basis for assessing the overall uncertainty is a comprehensive error budget which identifies each potential source of error, quantifies its probable magnitude, assigns the error to a workpiece category, and then combines the individual workpiece errors to estimate the total uncertainty associated with the measurement.

For the integration of dimensional measurement and analytical modeling, a simulated deformation that is caused by the fixturing constraints of a non-rigid part is one component of the best estimate of its real geometry (such as its dimensions). The error associated with analytical prediction is unusual to the practice of dimensional metrology and its uncertainty must be assessed to make a statement about the overall dimensional uncertainty.

The uncertainty of a simulated deformation is also established through an uncertainty budget and

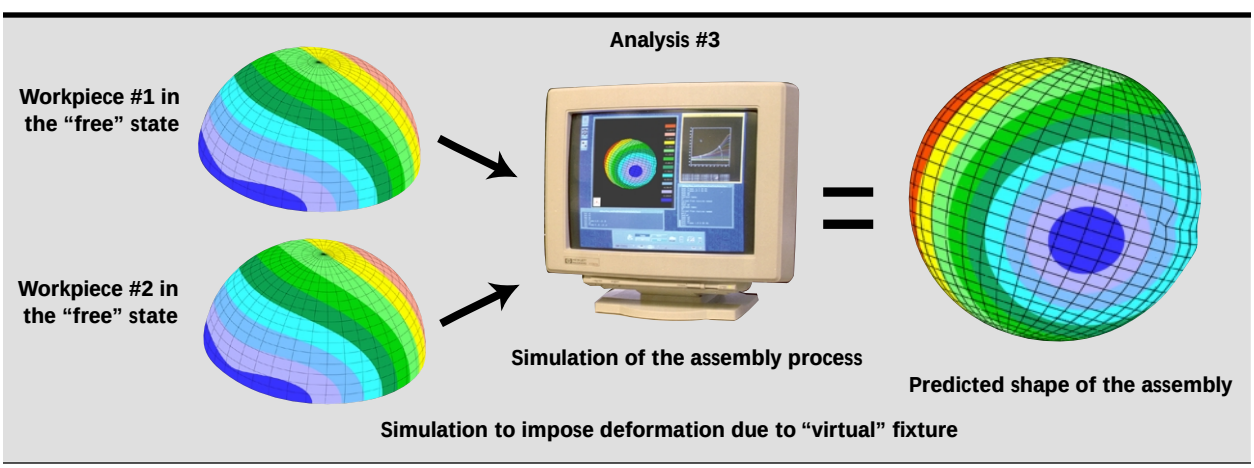

Figure 2. Methodology for simulating the assembly of two non-rigid bodies.

is corroborated by comparing the deformation calculated from simulation to that measured in a "verification" experiment. The verification geometry chosen for the initial experiment is a thin right-circular cylinder because its analysis is straightforward and easy to measure interferometrically. The initial method of simulation will be a linear finite-element method because of its generality. There are three general categories of errors to quantify.

The first category of error *(validation)* is associated with the overall accuracy of the simulation and how quickly it converges to the correct solution for the given boundary conditions. This will be assessed by conventional methods, such as comparing the difference in calculated deformation as a function of discretization error, element kinematics and material inhomogeneity. Also, for the geometry of the verification experiments, the accuracy of the simulations will be compared to an analytical solution.

The second category of error *(verification)* concerns the difference between the deformation predicted by the simulation and the deformation measured in a verification experiment. A dominant source of error in this category is the modeling of the material and determining its properties. Because material properties given in handbooks can easily be in error, the important properties, such as the elastic moduli and Poisson ratios, will have to be measured for the actual material used in the experiment.

In addition, the homogeneity of the material may have to be quantified for the actual experiment. Other material properties such as creep and plasticity will be assessed but will not likely be required in the simulation. These effects will be minimized in the validation experiment by selecting a material known to be elastic.

A second significant error in corroborating calculation with experiment is in the modeling of constraints, for example, the "contact algorithms." It is not known in advance whether this will be a significant error contributor, so the validation experiments will yield the first estimates of the error. Some iteration on the contact algorithms may be required to determine the best contact algorithms to use for thin shells.

The initial verification experiments are devised to check exactly this category of error. They will focus on a thin cylindrical shell where deformation can be calculated by closed-form analytic solution. A cylinder is also easy to mesh and inexpensive to measure.

The third category of error *(application to a real problem)* is to estimate how well the simulation will perform under different, real conditions beyond those of the verification experiment, and in particular, for a different geometry. This category of error is somewhat less studied than the first two categories.

Verification Experiment

The geometry for the verification experiment is a thin cylinder whose wall thickness-to-radius ratio is about 1:100 and governs how "non-rigid" the part is. Its length-to-radius ratio is 1:1 so that radial deformation at one end of the cylinder is quite different from the deformation imposed by a constraint at the opposite end of the cylinder.

This geometry was chosen because it is well suited to validation and verification. Easy validation arises because the deformation of a cylinder can be calculated by closed-form analytic solution, against which the results of the finite-element code can be directly compared. Easy verification arises because the deformation of the cylinder can be quickly and accurately measured for comparison to the analyses.

The status of the verification experiment is that the cylinder is being fabricated as a free-standing, electro-formed nickel shell. The electro-formed material is known to be quite homogeneous. The residual stresses induced by the electro-forming process, however, will cause the shell to be non-round, which is the desired effect. The measurement will be performed with a cylindrical, grazing-incidence interferometer,[2] which gives a very quick characterization of the deformation of the entire cylindrical surface.

Figure 3 shows the structural analysis of the verification cylinder supported by three wires, that is, three constraints that are each very compliant in five degrees of freedom and very stiff in the sixth degree of freedom. This may not be the best method of fixing the cylinder during measurement. The analysis calculates deformation for a radial load that is diametrically imposed on the end of the cylinder opposite from the three constraints. The verification experiment involves taking measurements of the unloaded cylinder, which provides the measurement data in **Fig. 1** and then imposing the radial load to compare the measured deformation directly to the analysis. The actual material properties of the electro-formed shell will be measured by conventional methods.

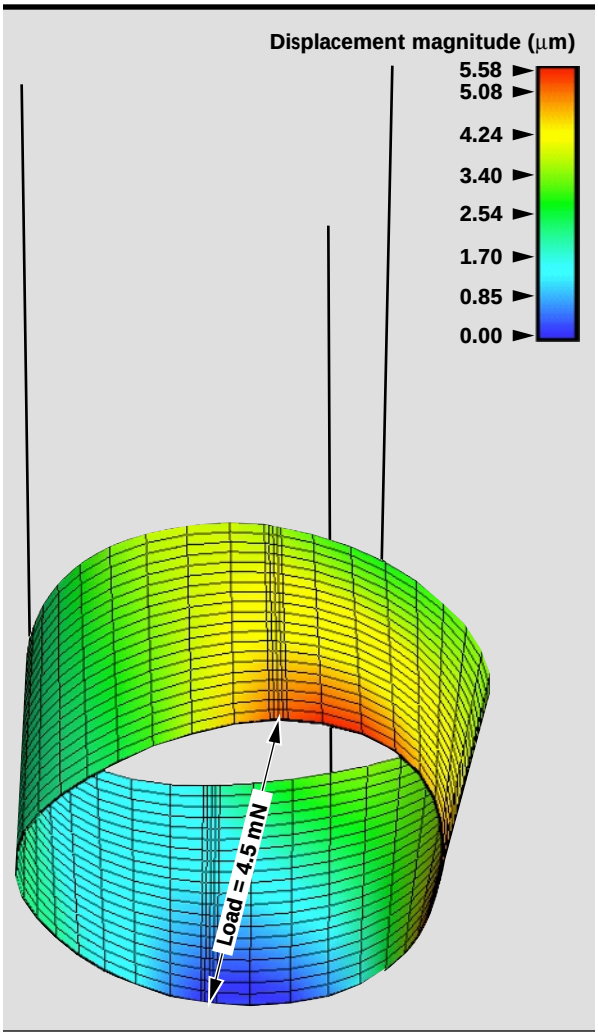

Figure 3. Structural analysis of verification cylinder. A radial load imposes a complex pattern of deformation on a thin cylindrical shell.

Future Work

This past year's work was the formulation of a method of metrology for non-rigid parts. Next year's tasks are to actually qualify, by the method described above, the use of a structural analysis code by quantifying the uncertainty with which it predicts the deformation.

Also for next year is to determine how to fixture non-rigid components for inspection that particularly allows its effect on the deformation of the part to be accurately modeled.

Current metrology methods inspect non-rigid components under over-constrained and often ill-defined conditions. Such inspections suffer from two shortcomings. First, they are not traceable from one institution to another unless the two institutions agree to the use of identical inspection fixtures. Second, such data do not allow accurate prediction of the distortion that will occur when two non-rigid components are assembled. The approach to this problem is to develop classes of restraints/fixturing for components during inspection that fall into the category of "exact-constraint" and that allow the accurate simulation of their effect on the deformation of the object.

Beyond next year, we will develop the concept of virtual fixturing, which allows the evaluation of important properties of the part and "filters out" those properties that are not. Specific application will be for thin cylindrical and spherical shells. This problem is largely unexplored.

References

1. "Geometrical Product Specification (GPS)—Inspection by measurement of workpieces and measuring equipment," (ISO 14253:1997).

2. Tropel "CylinderMaster 25" available from Carl Zeiss, 7008 Northland Drive, Minneapolis, MN 55428.

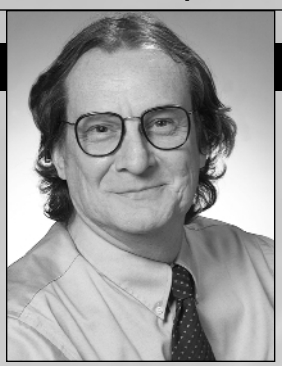

Kyran D. Mish, Center Director

The work presented here represents a transition period in computational engineering at Lawrence Livermore National Laboratory (LLNL). This year's effort marks the emergence of an integrated administrative structure designed to recognize the common aspects of mechanical and electrical engineering as well as their fundamental differences. This administrative organization is the Center for Computational Engineering, integrating the former mechanical and electrical engineering thrust areas into a more coherent unit, with a clear focus on the development and use of engineering simulation software as an enabling technology for LLNL.

Our FY-99 research portfolio still reflects the natural divisions present in the engineering directorate, though some of the projects demonstrate the cross-cutting multidisciplinary nature of computational engineering. A fine example of such an effort is the droplet-based net-form manufacturing work, which couples mechanical and thermal response into a simulation code capable of guiding experimentation into the emerging field of droplet-based manufacturing techniques. Three other examples of multiple-use technology are the development of finite-element preprocessors for the EIGER electromagnetics suite, the investigation into data-management software for computational mechanics, and the research into scalable solver technology for the NIKE3D mechanics code.

Each of these research efforts is oriented toward one branch of engineering, but has substantial potential benefits to other engineering disciplines at LLNL.

Mechanical engineering research includes fundamental work on material response, such as the reliability analyses of brittle materials and the simulation of anisotropic inelasticity, as well as developmental research on mathematics and computation, such as the improvements in implicit temporal integration algorithms for structural response in NIKE3D, or the slidesurface interface efforts developed for the DYNA3D code.

Electrical engineering enterprises include the development of femtosecond-resolution laser/RF/x-ray pulses for accelerator technology improvements, and software usability efforts developed for the TIGER time-domain electromagnetics code. Finally, the emerging discipline of automata methods in engineering is aptly demonstrated by our pioneering work in Lattice-Boltzmann simulations for chemical engineering and microfluidics.

This nascent computational engineering organization at LLNL will continue to grow in the future, and will both cement the areas of commonality in engineering and reinforce the natural differences. The mission of the center is to build a community of software engineers who are both broad and deep in their understanding of engineering computation.

Center for Computational Engineering

4

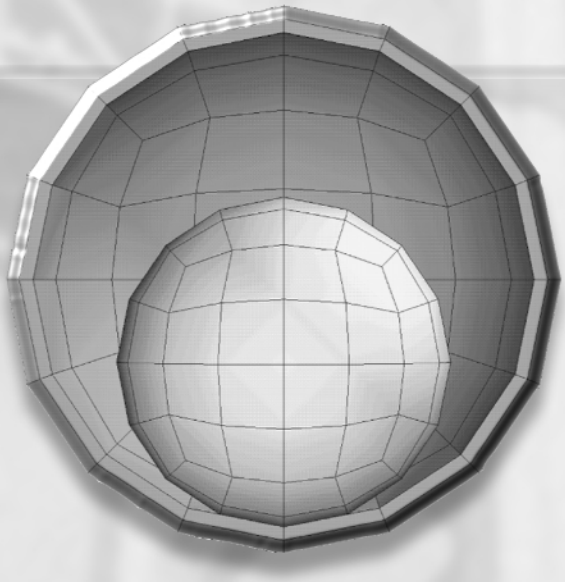

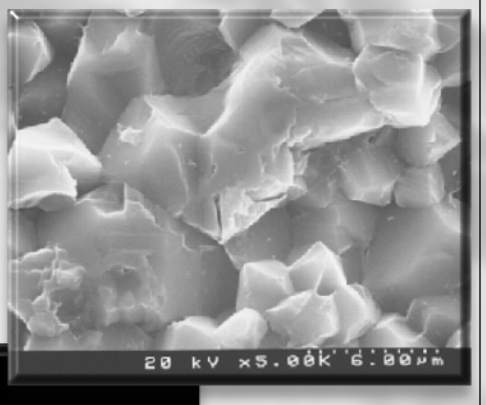

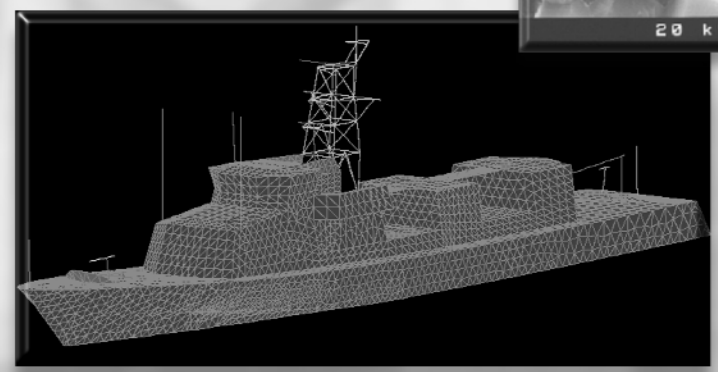

4. Center for Computational Engineering

Overview
Kyran D. Mish, Center Director

High-Precision Droplet-Based Net-Form Manufacturing
Arthur B. Shapiro and Melissa Orme 4-1

Improved Implicit Structural Finite Element Algorithms
Michael A. Puso 4-5

Post-Processing and Data Management Software Development for Computational Mechanics
Douglas E. Speck 4-11

Linear Equation Solvers for Parallel Computational Mechanics
Robert M. Ferencz and Chandrika Kamath 4-17

EIGER Preprocessor and User Interface
Robert M. Sharpe, Nathan J. Champagne, and Andrew J. Poggio 4-23

Strength and Reliability of Brittle Materials
Robert A. Riddle, Chol K. Syn, Michael J. O'Brien, Steve Duffy, Joe Palko, and Eric Baker. 4-27

Lattice Boltzmann Modeling of Spherical Solutes in Confined Domains
David S. Clague 4-35

Modeling of Anisotropic Inelastic Behavior
Daniel J. Nikkel, Jr., Deepak S. Nath, Arthur A. Brown, and James Casey 4-39

Development of Laser-Driven Photocathode Injector and Femtosecond-Scale Laser Electron Synchronization for Next Generation Light Sources
Gregory P. Le Sage, Thomas E. Cowan, Todd R. Ditmire, and J. Rosenzweig 4-47

A Segment-to-Segment Sliding Interface Algorithm for DYNA3D
Jerry I. Lin 4-49

Usability Enhancements for TIGER
David J. Steich, Gerald J. Burke, Jeffery S. Kallman, S Terry Brugger, and Daniel A. White. 4-53

Enhanced Fluid Dynamics Capability and Multidisciplinary Coupling in ALE3D
Rose C. McCallen, Timothy A. Dunn, John S. Dolaghan, and Richard G. Couch. 4-63

High-Precision Droplet-Based Net-Form Manufacturing

Arthur B. Shapiro
New Technologies Engineering
Mechanical Engineering

Melissa Orme
University of California at Irvine
Irvine, California

In collaboration with the University of California at Irvine (UCI), we are working on a new technology that relies on the precise deposition of nanoliter molten-metal droplets that are targeted onto a substrate by electrostatic charging and deflection. In this way, 3-D structural materials can be manufactured microlayer by microlayer. Because the volume of the droplets is small, they rapidly solidify on impact, bringing forth a material component with fine grain structures which lead to enhanced material properties such as strength. Lawrence Livermore National Laboratory (LLNL), with its unique expertise in computational modeling and large-scale computer resources, modeled the system to gain insight into manufacturing process control. UCI, with its state-of-the-art experimental facility, provided computer model validation and demonstrated manufacturing feasibility.

Introduction

This new manufacturing process has the potential to fabricate parts with complex geometry, using novel alloys, and possessing improved strength. The very rapid solidification of nanoliter-sized metal droplets leads to finer grains which results in a part possessing higher strength than achievable by conventional casting processes. New and novel alloys can be created by co-jetting droplet streams using metals of different droplet size and deposition rates. Additionally, the microstructure can be varied at different locations in the fabricated part by our ability to control the droplet size, deposition rate, and temperature.

Using multiple nozzles with droplet deposition rates of 40,000 droplets/s would provide a means for rapid prototyping metal parts. Currently, there are several manufacturing techniques using plastic, but no adequate methods exist for rapid prototyping parts using metal. This capability will benefit LLNL's design engineers building one-of-a-kind metal parts or small production quantities.

Progress

Figure 1 is a schematic of the droplet manufacturing facility at UCI. A crucible at the top of the apparatus contains liquid metal which flows through an orifice forming a capillary stream into the lower vacuum chamber. A method for generating deterministic droplet patterns from capillary stream breakup has been developed by Orme. By applying specific amplitude-modulated disturbances with an

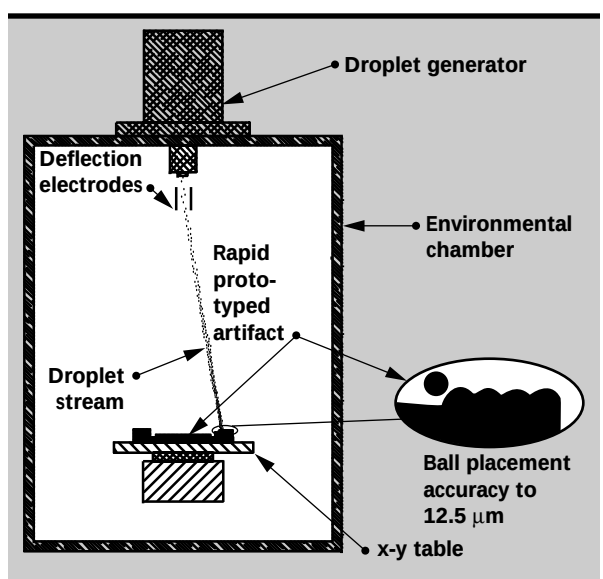

Figure 1. Schematic depicting the High Precision Droplet-Based Net-Shape Manufacturing facility at UCI.

arbitrary modulation to a viscous capillary stream, predictable and flexibly controlled patterns of droplets can be obtained. The disturbance is created by a piezoelectric transducer above the orifice. The metal droplets are charged and their trajectory is controlled by deflection electrodes. The substrate itself can be moved by a controllable x-y positioning table for fabricating planar 3-D parts, or the substrate rotated to fabricate axisymmetric parts as shown in **Fig. 2**.

The parts in **Fig. 2** were fabricated from a former prototype facility using 200-μm solder droplets. The scope of this work is to push the technology so that higher melting point metals such as aluminum can be used and smaller droplet sizes (5 to 50 μm) can be formed to fabricate thin walled parts of interest to LLNL.

During 1998, UCI began moving the technology forward from solder droplets to more interesting materials with higher melting points, such as aluminum. A new facility came on-line in August 1998. By the end of the year, metallurgical investigations of sectioned aluminum-droplet-on-substrate samples from initial shake-down runs had revealed that the grain structure was equiaxed, the grain size ranged from 120 to 150 μm, the average porosity was about 3%, and oxides and other impurities were present. Tensile tests were promising: the measured yield stresses (8900 psi) were greater than both the yield stress for the starting aluminum ingot (6816 psi) and published handbook values for aluminum (6800 psi).

A significant fabrication challenge this year was to overcome the inclusion of oxides and other contaminants in the droplet stream, which would result in defective parts. **Figure 3** shows a droplet formed "stalagmite" (on the right) with a significant presence of oxides indicated by the dark mottled exterior. A filter pack was designed to fit at the bottom of the liquid metal crucible. After four design iterations, we successfully filtered the metal stream and reduced the oxides, as shown by the shiny stalagmite on the left in **Fig. 3**.

During the shake-down runs, we also noted a loss of control on the deposited location of the droplets. This was caused by electrostatic interaction between the closely spaced charged droplets. The solution was to charge alternate droplets in the stream and capture the uncharged droplets following a straight trajectory by a "gutter" to prevent them from striking the substrate. The charged droplets, with a curved trajectory, avoid capture by the gutter. We have perfected the operating procedure for creating a uniform stream of droplets. We are concentrating now on making components. We have made three cylinders from three different runs but haven't honed in on the correct temperature or speed conditions. We have some really porous or really "globby" cylinders depending on our conditions. The poor quality of these cylinders is a good illustration of the need for precise operating conditions, and shows the importance of the modeling effort to guide the experiments.

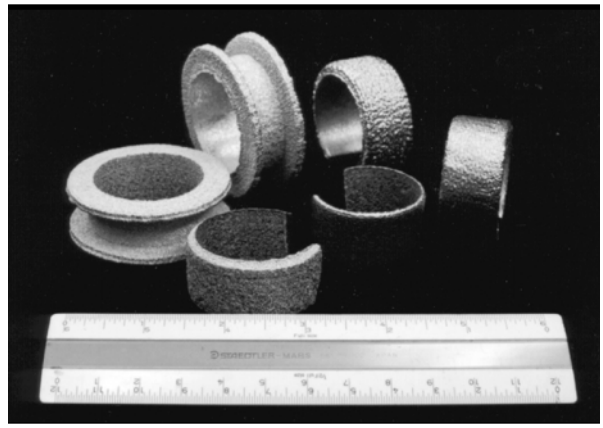

Figure 2. Axisymmetric parts fabricated from a prototype facility using 200-μm solder droplets.

Figure 3. Aluminum stalagmites fabricated by directing a stream of aluminum droplets downward onto a substrate. The stalagmite on the right shows the presence of oxides indicated by the dark mottled exterior. A significant challenge was to design a filter to reduce the oxides and other contaminants. This was successfully accomplished as demonstrated by the shiny stalagmite on the left.

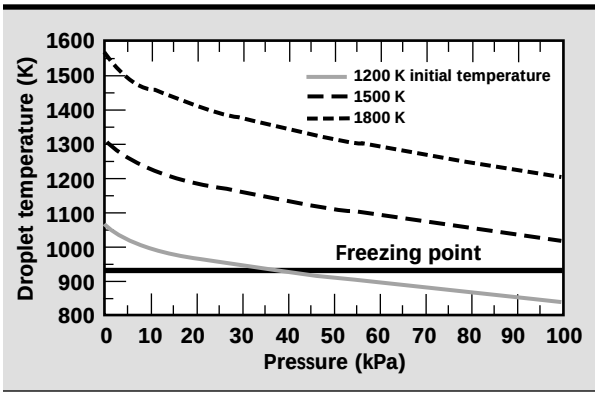

Figure 4. Temperature drop of a 189-μm aluminum droplet with an initial velocity of 9 m/s in nitrogen as a function of chamber pressure. Such curves helped define the process parameters of crucible temperature and chamber pressure that would result in a liquid droplet with a specified superheat when striking the substrate.

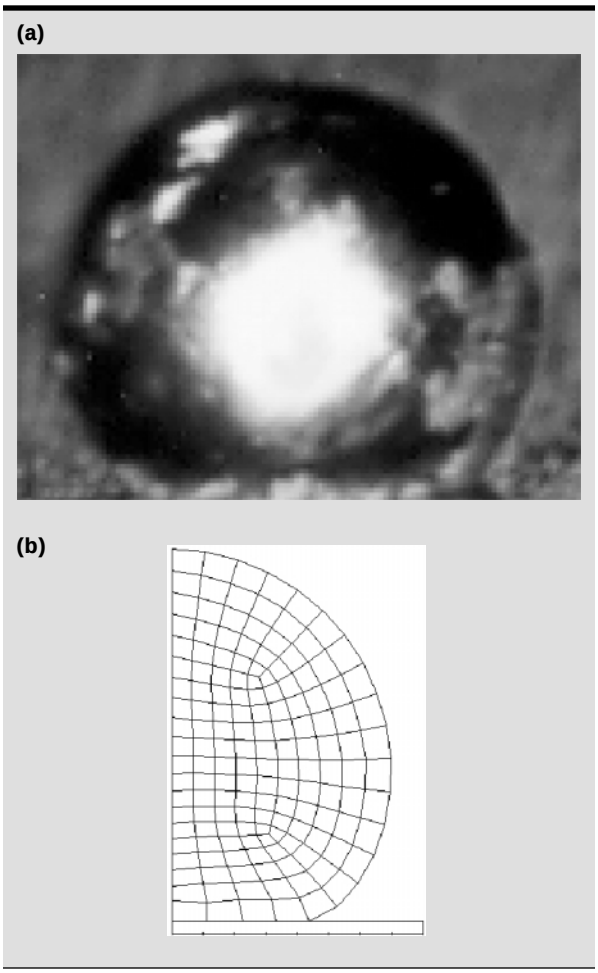

Figure 5. Experimental sessile drop (a) used to determine the material properties for liquid aluminum for our finite element model shown in (b).

During the last year, LLNL pursued process modeling both on the micro-scale of an individual droplet striking a substrate and on the larger system scale to predict velocity and temperature drop during time of flight. We also investigated material constitutive models that would capture the low strength of the metal in the liquid state and transition to the higher strength solid.

Empirical equations were found in the literature to predict the temperature and velocity drop during time of flight. These equations also include the effect of the wake of one droplet on a trailing droplet. Salvador Aceves developed the MELISSA code to solve these equations, which was further developed by Wayne Miller into the code HOTDROP.[1] **Figure 4** shows the temperature drop of a 189-μm aluminum droplet with an initial velocity of 9 m/s in nitrogen as a function of chamber pressure. The bottom curve shows that a droplet with an initial temperature of 1200 K will solidify before striking the substrate at chamber pressures above 40 kPa. Such curves helped define the process parameters of crucible temperature and chamber pressure that would result in a liquid droplet with a specified superheat when striking the substrate.

Our next step is to incorporate these empirical equations into our finite element heat transfer code TOPAZ. This will allow us to do system process modeling. Our approach is to "birth" finite elements (but without modeling the impact process—see next paragraph) at the droplet arrival time defined by its velocity and at the arrival temperature. These elements will then lose energy to the environment, previously deposited material, and the substrate. In this way we can predict the cooling rate of the deposited material and gain insight into the microstructure.

On the microscale, we faced a challenge in predicting the shape of a droplet upon impact. The difficulty existed because of our attempt to model a liquid with an elastic-plastic constitutive model. Such a model would be applicable after the droplet solidified. After many failed simulation attempts with ALE3D and DYNA3D to model the impact, we tried to model a stationary liquid drop deforming under gravity (a sessile drop as shown in **Fig. 5**).

The material constants, such as Young's modulus, that resulted in the best fit between the analysis and experiment will be used to model the liquid. These properties will be modified for the solid phase according to a temperature dependent function found in the literature for aluminum. We plan to re-investigate the use of ALE3D and DYNA3D in predicting the deformation of a droplet on impact.

Our greatest modeling challenge is to predict the coupled thermal-mechanical response of a droplet impact. We have coupled the solid mechanics code DYNA3D with TOPAZ3D. The hardest part was developing a thermal-mechanical contact algorithm. The algorithm developed has been verified by modeling the heat transfer between two sliding blocks. Our next step is to model droplet impact. Also, other features still need to be implemented, such as, conversion of plastic work to heat.

Validation is critical to our success. The literature is rich in papers investigating the splat of a liquid droplet without solidification.[2] We found one paper describing an energy balance method that predicted the maximum splat diameter. We had good success in using this equation to predict the results in other papers. This theoretical equation was modified to include solidification[3] and predicted a 15% greater spread diameter than measured in an experiment. We will use this equation for validation of our constitutive model under development and results from the coupled DYNA-TOPAZ code effort.

Future Work

We plan to concentrate on manufacturing simple geometric shapes, such as cylinders, and improve the process to decrease defects such as porosity. We will use the system modeling code to determine process parameters.

References

1. W. O. Miller (1999), "HOTDROP Operation Guidelines," Lawrence Livermore National Laboratory, Livermore, California (UCRL-CODE-99040), July.

2. S. M. Aceves, A. B. Shapiro, and V. Sahai (1999), "An accuracy evaluation for the Madejski splat quench solidification model," Lawrence Livermore National Laboratory, Livermore, California (UCRL-JC-133757), March.

3. N. Hadjiconstantinou (1999), "Estimating the maximum splat diameter of a solidifying droplet," Lawrence Livermore National Laboratory, Livermore, California (UCRL-JC-133712), March.

Improved Implicit Structural Finite Element Algorithms

Michael A. Puso
Defense Technologies Engineering
Mechanical Engineering

We developed new algorithms for contact and implicit dynamics. These algorithms were implemented into the structural mechanics finite element code NIKE3D. The new algorithms provided a more robust and efficient code and improved accuracy. A cursory description of the algorithms along with representative numerical examples are presented here.

Introduction

Implicit nonlinear structural analysis has been used for many years. Nevertheless, it can still be difficult to perform on many problems due to a variety of numerical issues. Implicit finite element analysis has been used most often for determining quasistatic response of structural models, whereas explicit finite element codes have typically been used for nonlinear dynamics problems. Many structural dynamics problems occur over time spans that are quite long for explicit analysis due to the Courant time step limitation, but are too nonlinear or big for implicit dynamic analysis. Seismic analysis, reentry vehicles and transportation container vibration analysis are examples of problems in the "gray area," that is, highly nonlinear, long term dynamics problems.

Progress

Our work solves some of the numerical problems inherent to the implicit method.

The three fundamental difficulties for implicit analysis are as follows:

1. Problem size: Implicit analysis requires the solution to a large system of linear equations which is both memory- and computation-intensive.
2. Nonlinearity: Convergence of the nonlinear solution algorithm is severely impacted by the presence of contact surface unilateral constraints.
3. Stability: For nonlinear problems, Newmark's method is not, in general, unconditionally stable.

New parallel linear solvers have been implemented into NIKE3D and others are in the works for dealing with the large linear systems that are to be handled. Furthermore, a new line of enhanced strain elements was implemented into NIKE3D this year which provides coarse mesh accuracy. These are *fully* integrated elements based on extensions of our work in *single-point* elements last year.[1] With these elements, an analyst can use a much smaller mesh for the same amount of accuracy as a fine mesh with the older element technology. In this report, we highlight the new developments we have made in the areas of *convergence* and *stability*.

Convergence

The primary culprits for convergence difficulties are the nonlinearities from contact surface interactions due to the non-smooth nature of the contact surfaces. The finite element contact surface comprises bilinear patches or facets. This discretization causes jumps in contact forces at facet edges and vertices making it very difficult for global convergence of the Newton nonlinear solution algorithms.

To alleviate this problem, we have used 3-D bilinear Hermitian surfaces to interpolate the bilinear surface mesh, providing C1 continuity between facets. A 2-D representation of this is shown in **Fig. 1**. This provided a vast improvement in convergence of the contact algorithm.

For example, a solid sphere is contained within a hollow sphere and pressed against the bottom by a vertical pressure (**Fig. 2**). With the new smoothing algorithm we get superior convergence compared to the old method as demonstrated by the residual energy norm produced during the nonlinear iteration loop, as shown in **Table 1** for a given time step. The smoothed representation of the finite element mesh model for the sphere is shown in **Fig. 3**. The smoothed mesh shown in **Fig. 3b** was produced

using Mathematica.[2] The grid lines are just the level of discretization used for visualization (the true mesh is totally smooth).

In the next example, a single block element is pushed down and then dragged along a surface (**Fig. 4**). This problem particularly illustrates the improved performance when slave nodes encounter new facets during sliding. With the old algorithm, contact forces experience a significant jump when a node changes facets during sliding due to the new normal direction of the facet. The smoothed surface for the configuration in **Fig. 4b** is shown in **Fig. 4c**. The new algorithm provides quadratic convergence as demonstrated by the energy norm results during nonlinear iterations shown in **Table 2**.

Stability

Using Newmark's method for example, the implicit structural dynamics method can be shown to be unconditionally stable for small deformation analysis. For general nonlinear dynamic analysis, the implicit method can become numerically unstable and often does in the presence of large rigid body rotations or severe contact impact. This is a pathological result of the discrete time integration scheme and is not to be confused with a mechanical instability.

With linear analysis, the spectral method is typically used for stability analysis. This is performed by calculating the eigenvalues of the amplitude matrix formed by the recursive integration algorithm. In

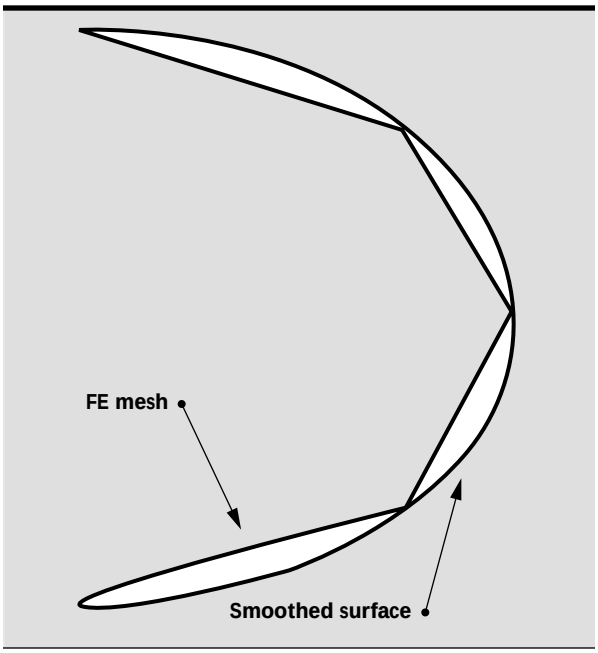

Figure 1. Finite element faceted surface and interpolated smooth surface.

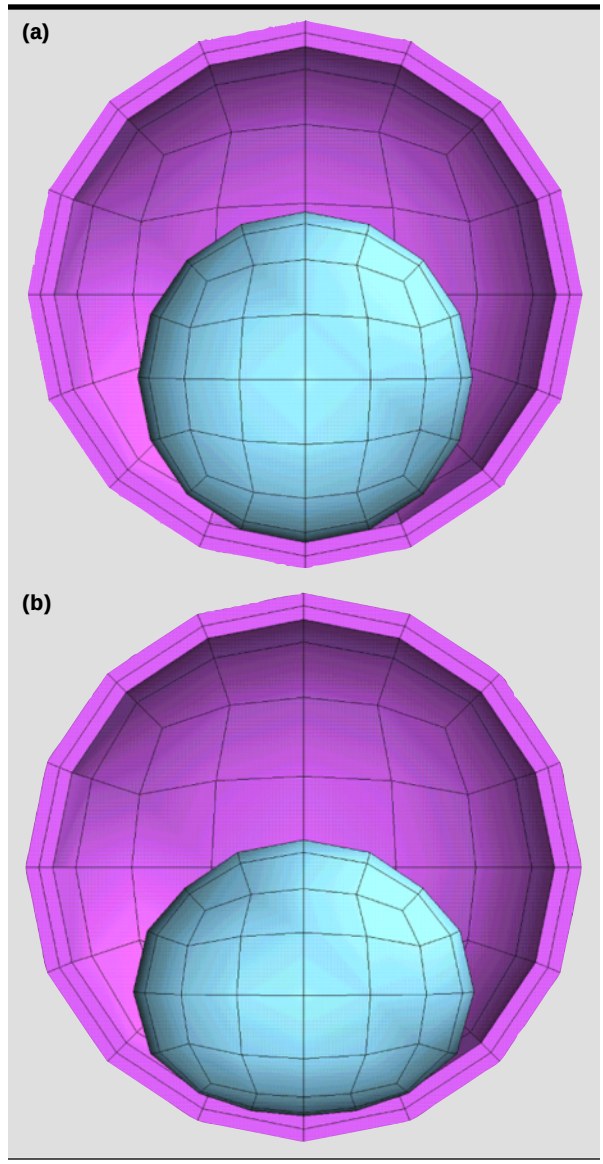

Figure 2. Solid sphere pushed against bottom of hollow sphere.

Table 1. Energy norm results for spheres.

Iteration #	New method	Old method
1	1.3394×10^{2}	1.3862×10^{2}
2	1.0054×10^{-1}	1.0287×10^{2}
3	2.4924×10^{-11}	8.7395×10^{-2}
4	4.9348×10^{-17}	9.2101×10^{-7}
5		9.0672×10^{-7}
6		2.9843×10^{-7}
7		6.0875×10^{-7}
8		5.2122×10^{-7}
9		6.1894×10^{-7}
10		1.1556×10^{-6} (diverged)

nonlinear implicit analysis, an amplitude matrix is not available, so another method is necessary. In particular, the stability in the energy sense can be ensured when the appropriate algorithmic adjustments are made. This was shown by Simo and Tarnow[3] for nonlinear elasticity, such that the "algorithmic energy" is conserved when the constitutive (material) evaluation is made appropriately. This algorithmic energy balance is in terms of the discretized nodal velocities and displacements. For a closed mechanical system

$$\boldsymbol{v}_{n+1}\, \boldsymbol{M}\boldsymbol{v}_{n+1} + U(\boldsymbol{u}_{n+1}) - \boldsymbol{v}_n\, \boldsymbol{M}\boldsymbol{v}_n - U(\boldsymbol{u}_n) = 0 \qquad (1)$$

where $\boldsymbol{v}_n$ is the vector of nodal velocities at time t_n, $\boldsymbol{u}_n$ is the vector of nodal displacements at time t_n, $\boldsymbol{M}$ is the system mass matrix and U is some given strain energy function. **Equation 1** balances the energy at time t_n and t_{n+1} such that velocity and

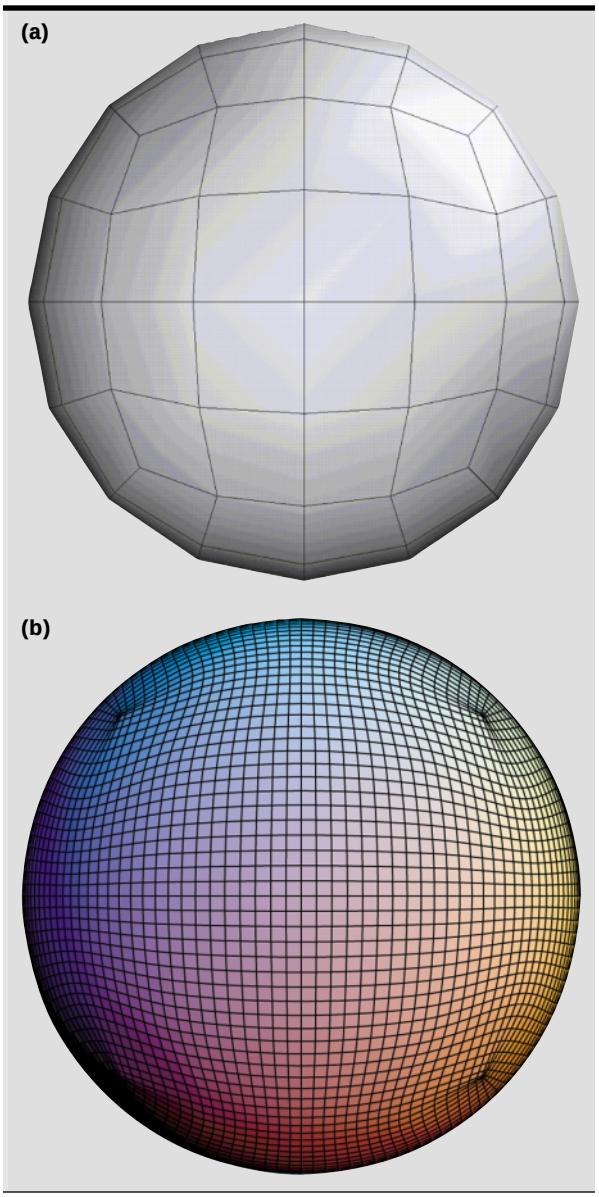

Figure 3. (a) Finite element model of sphere. (b) Smoothed version of faceted finite element mesh shown in (a).

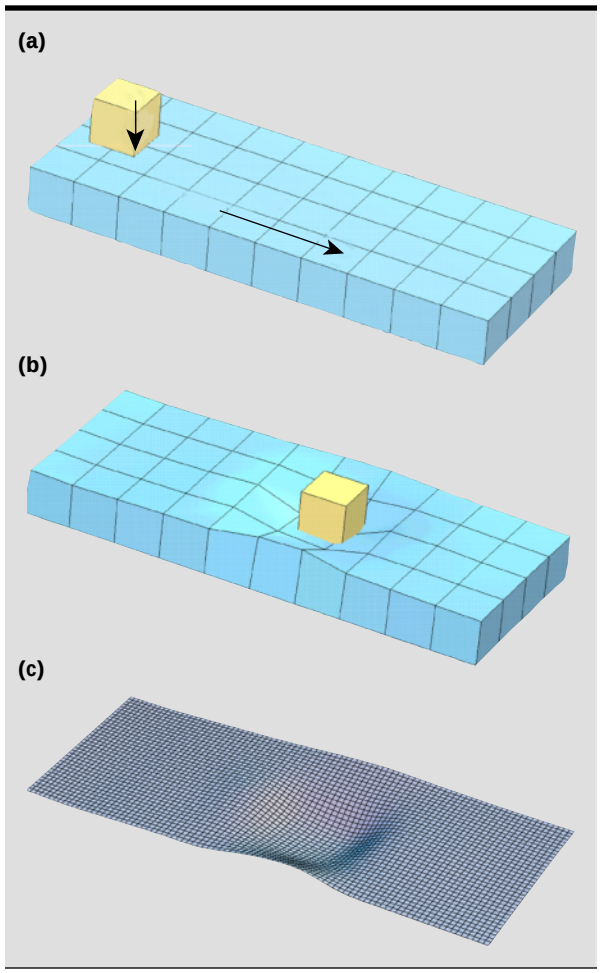

Figure 4. (a) Block loaded vertically and subsequently dragged along surface. (b) Final configuration. (c) Smoothed representation of surface.

Table 2. Energy norm results for block.

Iteration #	New method	Old method
1	2.0144×10^{1}	2.1177×10^{1}
2	4.5219×10^{-3}	-4.2748×10^{1}
3	5.4617×10^{-7}	-3.2830×10^{1}
4	1.3365×10^{-14}	5.1037×10^{3}
5	1.0987×10^{-28}	2.1842×10^{2}
6		1.3931×10^{2}
7		1.0540×10^{2}
8		8.4054×10^{1}
9		8.5236
10		3.3749×10^{1} (diverged)

displacements are bounded and stability is ensured. In our work we generalize the energy conservation method to include coupled rigid/flexible body systems and contact with friction.

Ultimately, materials with plasticity will be included. With these effects, the new algorithmic balance is given by

$$\boldsymbol{v}_{n+1}\, \boldsymbol{M}\boldsymbol{v}_{n+1} + \boldsymbol{w}_{n+1}\, \boldsymbol{I}\boldsymbol{w}_{n+1} + U(\boldsymbol{u}_{n+1})$$

$$- \boldsymbol{v}_n\, \boldsymbol{M}\boldsymbol{v}_n - \boldsymbol{w}_n\, \boldsymbol{I}\boldsymbol{w}_n - U(\boldsymbol{u}_n) = -D \leq 0 \qquad (2)$$

where $\boldsymbol{I}$ is the rotational inertia of a rigid part, $\boldsymbol{w}$ is the rigid body's rotational velocity and D is a positive amount of dissipation due to friction. We call this the algorithmic energy-consistent method. This new method is an extension of previous work.[4–5]

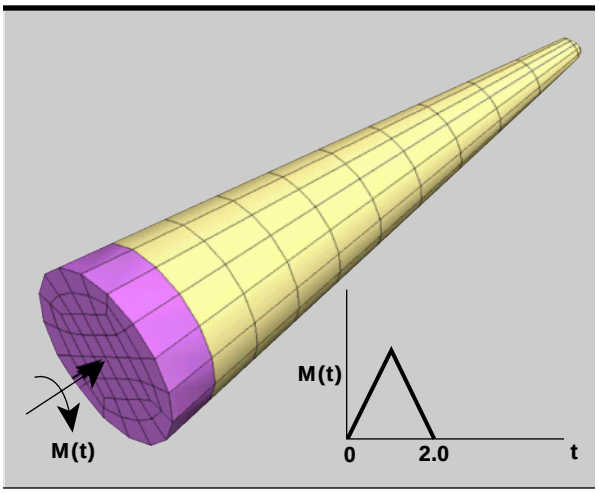

Figure 5. A pulse moment applied to a top with a rigid base and flexible cone.

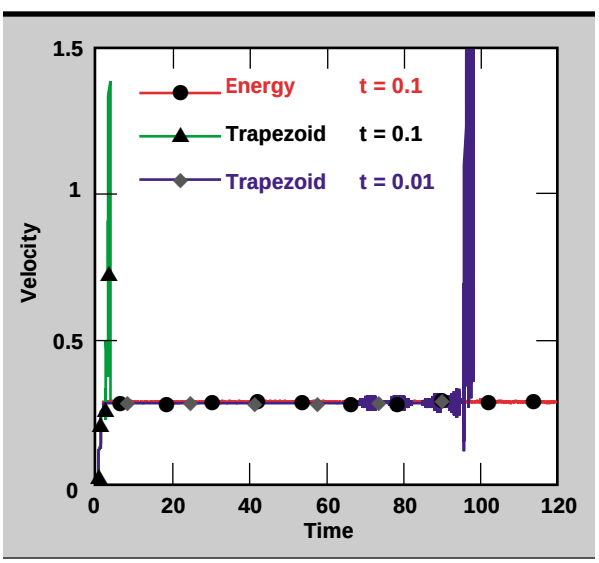

Figure 6. Velocity magnitude of a point near the tip of the top.

In the first example (**Fig. 5**), a pulse moment is applied at the base of rigid/flexible top. The base is a rigid material and the cone is flexible. The top is simulated using the new energy-consistent method and the classical trapezoid method. The resulting nodal velocity of a point near the top's tip is shown in **Fig. 6**. From **Fig. 6**, the trapezoid method is seen to become unstable for both the large ($\Delta t = 0.1$) and small ($\Delta t = 0.01$) time steps. The new energy method remains stable (independent of time step) as guaranteed by **Eqs. 1** and **2**.

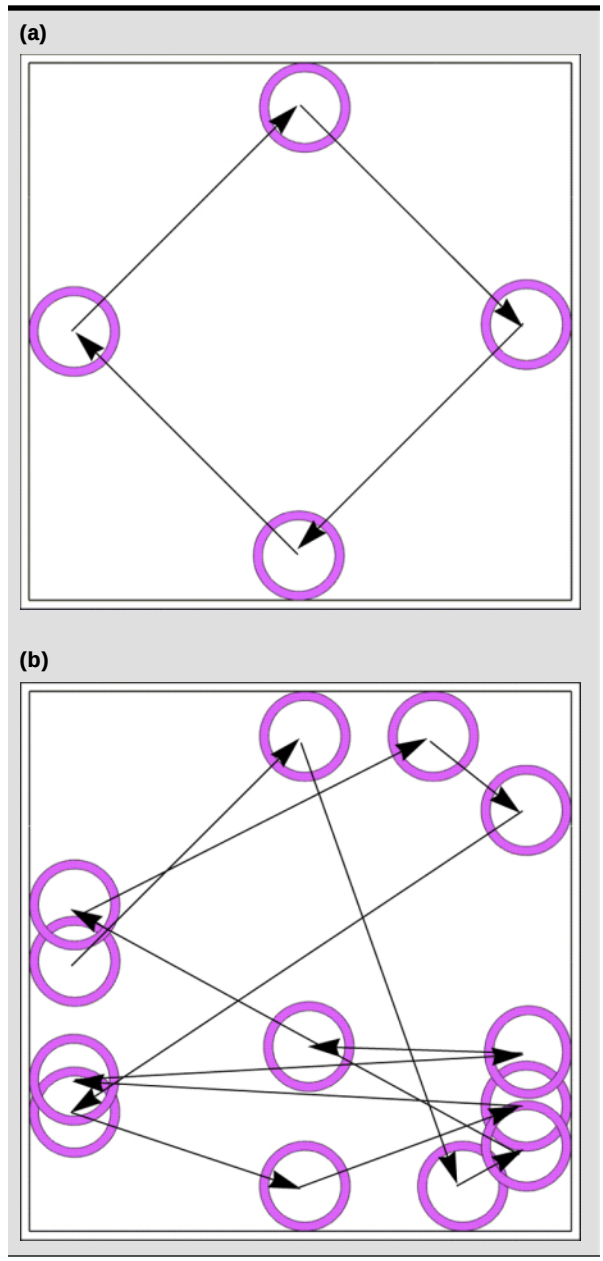

Figure 7. Flexible ring within a fixed rigid box. The ring is initially against the left wall and is given an initial velocity at 45° from the vertical. (a) The displacement pattern resulting from the new energy method. (b) The pattern resulting from the old trapezoid method.

In the next example (**Fig. 7**), a stiff flexible ring placed within a fixed rigid box is given an initial velocity at a 45° angle from the rigid wall. With the energy-consistent method, the ring bounces within the box in the expected way, returning almost exactly back to its original position in a given cycle (**Fig 7a**). With Newmark's trapezoid rule, the ring picks up energy at the boundary and eventually becomes unstable (**Fig. 7b**). The algorithmic energy is plotted versus time in **Fig. 8** for the ring in box.

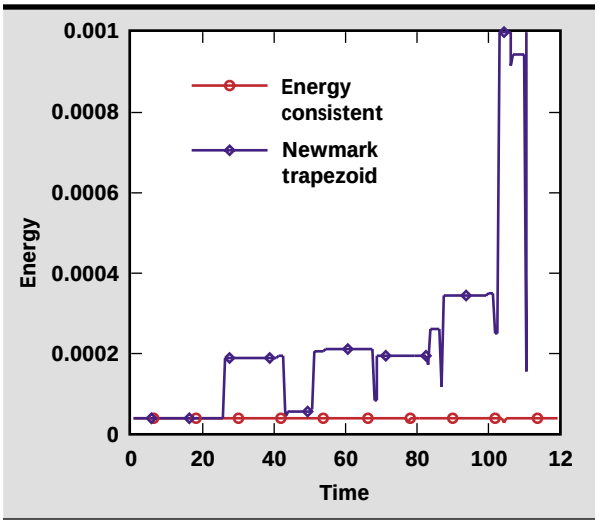

Figure 8. Algorithmic energy vs. time for the ring in box.

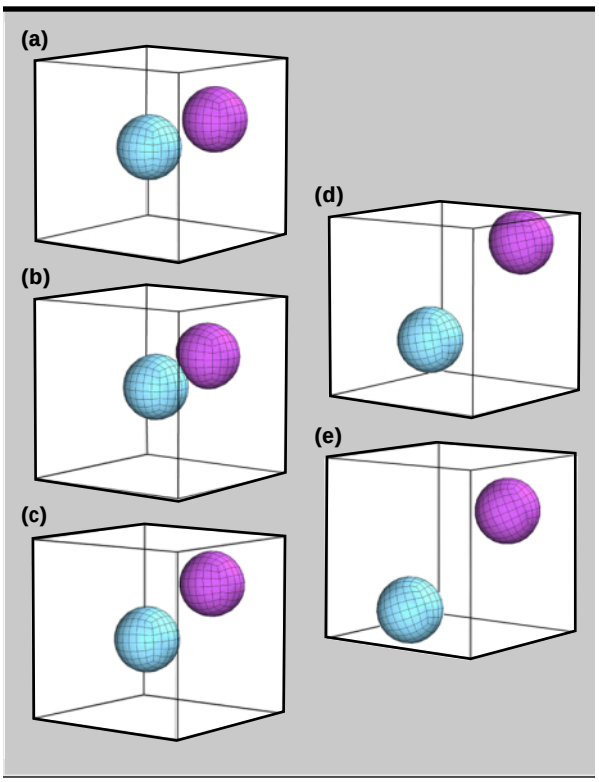

Figure 9. Sequence of configurations of flexible balls bouncing within a rigid box.

In the final example, the effects of frictional dissipation are demonstrated. In **Fig. 9**, two flexible balls are given an initial velocity within a rigid (unfixed) box. The balls then bounce around within the rigid box as shown in the sequence in **Fig. 9**. Since friction is included the new energy-consistent method dissipates algorithmic energy as shown in **Fig. 10**. The trapezoid rule gains energy despite the friction.

Future Work

We have demonstrated the results of significantly more robust implicit finite element algorithms. Consequently, we are able to solve many new problems that were previously intractable.

Currently we are in the process of adding friction to the contact smoothing algorithm and adding the logic for determining locations in a mesh where smoothing is to be neglected. Furthermore, we are developing a complementary solver for computing the Lagrange multiplier contact forces more efficiently than the current augmented Lagrange method used in NIKE3D.

For implicit dynamics, we anticipate adding the dissipation effects of plasticity. We would also like to look at alternative conserving (or nearly conserving) algorithms that are simpler to implement.

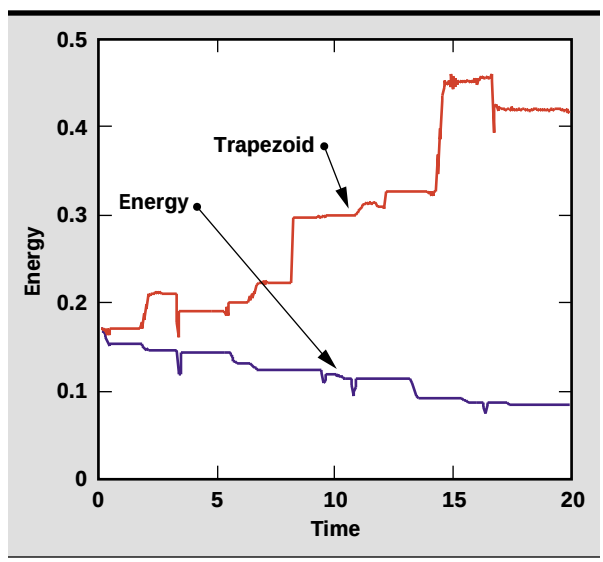

Figure 10. Algorithmic energy vs. time for the balls in box with friction.

References

1. M. Puso (to appear), "A highly efficient enhanced assumed strain hexahedral element," *IJNME*.

2. S. Wolfram (1993), "Mathematica: a system for doing mathematics by computer," Addison-Wesley Publishing Company Inc., Reading, Massachusetts.

3. J. Simo and N. Tarnow (1992), "The discrete energy-momentum method. Conserving algorithms for nonlinear elastodynamics," *ZAMP*, **43**.

4. M. Puso and E. Zywicz (1998), "Energy conserving rigid body contact methods," *ICES98 Proc.*

5. E. Zywicz and M. Puso (1999), "A general conjugate-gradient based predictor-corrector solver for explicit finite element contact," *Int. J. Numer. Meth. Engng.* **44**.

Post-Processing and Data Management Software Development for Computational Mechanics

Douglas E. Speck
Computer Applications Sciences and Engineering
Computation Organization

The introduction of the Mili I/O library to Lawrence Livermore National Laboratory (LLNL)'s Methods Development Group code suite, and an increased workforce, have spurred the release of a new GRIZ post-processor. These and other developments mean significant increases in capability and flexibility for users. New tools have been introduced to formalize and improve our software development process.

Introduction

In FY-99 we made considerable progress in the post-processing and data management areas of computational mechanics at LLNL. The unifying theme of our accomplishments in these areas is greatly improved flexibility. This leap forward was enabled and driven by the introduction of Mili (Mesh I/O Library), a library for reading and writing self-defining simulation databases. With our finite element post-processor, GRIZ, we completed a major redevelopment effort to accommodate the flexible data content permitted in Mili file families.

As a first step in integrating Mili into the analysis codes, code developers implemented modules in DYNA3D/ParaDyn and NIKE3D to write out the current collection of state variables to a Mili file family. Enhanced flexibility for post-processing extended to the parallel computing domain with the implementation of a prototype parallel rendering of GRIZ.

A second theme is improvement and formalization of our software development process. Building on an existing practice of maintaining source code in a repository accessed only by version control software, we added a web-based application for submission and management of software change requests and trouble reports. Additionally, a regression test suite was developed for GRIZ to automate the laborious process of validation testing new releases.

Progress

Mili Version 1.0

Version 1.0 of the Mili library was released to developers simultaneously with GRIZ 4.0, the new version of GRIZ that reads the Mili database. Mili accomplishes its primary goal of creating self-defining simulation databases by letting applications define formats that document the contents of state records to be written during a simulation. An application that reads the simulation database first reads the format descriptions to learn how to interpret the state data in the database.

Mili uses a conceptual model of an unstructured finite-element mesh as a collection of mesh objects (such as nodes or elements) for which simulation state data exists that an application may need to save to disk. Mesh objects with like topological and physical characteristics are grouped together in mesh object classes, each of which is identified by a unique class name. For example, hexahedral elements in a mesh might belong to a class called "brick." The application creates as many mesh object classes as necessary to fully define the mesh for data output.

As like objects make up a class, so can multiple classes be derived from the same superclass. Mili defines a set of superclasses that provide the basic semantics for each class created by the application.

Put another way, a class is a named instance of a superclass, and one of the parameters specified by the application when a class is created is its superclass. **Table 1** identifies the superclasses currently defined by Mili.

The reason for this superclass>class>object hierarchy is flexibility. From the superclass, an application knows very basic information about the class and therefore how to operate on it generally. For example, both **m_quad** and **m_tet** imply element mesh objects with four nodal connectivities, but a **m_tet** element is inherently 3-D and has obvious computational or rendering requirements associated with it, whereas a **m_quad** element can be either 2- or 3-D and has different associated requirements. With superclasses, Mili provides a logical shorthand for communicating basic information about groups of objects.

By permitting (demanding) applications to create classes, Mili allows specialization within a superclass. The superclass conveys common characteristics and the class confers some amount of uniqueness. This is useful when objects that might be identical at the superclass level are in fact modeled differently and mean something different to the analyst. For example, DYNA3D supports both thick shell elements and hexahedral volume elements, both with eight nodal connectivities. For writing data to the old TAURUS plot database, DYNA3D must combine both types of elements into that database's single collection of eight-noded elements. In post-processing, any original distinguishing information is lost and the analyst must know *a priori* which "bricks" are really bricks and which were thick shells in the analysis. Under Mili, DYNA3D can create separate classes, each derived from superclass **m_hex** but having different class names, to allow each type of element to be explicitly identified in the output and subsequent post-processing.

Table 1. Mili object superclasses.

Class name	Node quantity	Object type
m_unit	N/A	Arbitrary
m_node	1	Node
m_truss	2	Truss
m_beam	3	Oriented beam
m_tri	3	Triangle
m_quad	4	Quadrilateral or shell
m_tet	4	Tetrahedron
m_pyramid	5	Pyramid
m_wedge	6	Wedge or prism
m_hex	8	Hexahedron or brick
m_mat	N/A	Material
m_mesh	N/A	Mesh

Additional flexibility is available through Mili because the objects of a particular class can be subdivided on output for customizing the set of state variables being written. The most natural example of this would be a division of the elements within a class along material lines, since differing material models in the analysis would confer different sets of state variables for the participating subsets of elements. Finally, Mili also permits applications to define multiple state record formats in a single database. This opens the door to varying the amount of data being written dependent upon activity in the simulation.

GRIZ Version 4.0

The flexibility permitted in a Mili database represents a great change from the previous TAURUS plot database, and large parts of GRIZ were re-written (or invented) to accommodate the new features. GRIZ version 4.0 (GRIZ4) is the outcome of this redevelopment effort. The goal in producing GRIZ4 was to have GRIZ change outwardly as little as possible while accommodating the potential variability in a Mili database. Most of the command-set changes were made to accommodate the variable nature of database contents under Mili. For instance, commands that formerly required a parameter such as "node," "brick," or "shell" to indicate the object type of a numeric identifier now require a class name instead.

Visually, there are few changes in GRIZ4. Most apparent is the replacement of the previous "Result" pulldown menu with two new menus, "Derived" and "Primal." The Derived menu essentially holds the contents of the old Result menu, but the menu contents adapt to display only results that can be derived from the contents of the current database. The Primal menu allows access to all results written into the current database, without any derivation or transformation applied.

Through the Primal menu, GRIZ4 offers access to global mesh results and material results in both Mili and TAURUS databases. These data have been written to the TAURUS database for some time but were not previously accessed by GRIZ.

GRIZ4 does not support data from all Mili superclasses equally. There is no support for **m_wedge** or **m_pyramid** elements in 3-D rendering. Also, Mili's **m_unit** superclass, which by design has no semantics

associated with it, cannot be related by GRIZ4 to the mesh in any way that is guaranteed to be generally useful for rendering. However, data from every class in a database, regardless of its superclass, can be read by GRIZ4 and plotted as a time history curve, so GRIZ4 has some utility even for object types it doesn't fully support.

Aside from the new adaptive menus, the only other visual change in GRIZ4's graphical user interface is on the Utility Panel. There, users now have the option of assigning any node or element class to any mouse button for picking operations, instead of the previous option to assign the middle mouse button to pick either shells or beams.

GRIZ's time history plotting capability was completely reworked for GRIZ4. Although the old "timhis" command is still supported, the new "plot" command provides users with much more capability and flexibility. Patterned after the THUG time history plotter's "plot" command, GRIZ4's "plot" accepts the specification of multiple results and/or mesh objects, generating a curve for every result/object pair supported by the database. GRIZ4's "plot" command syntax also permits parametric plotting of one result versus another result from the same mesh object (multiple objects allowed) with time as an implicit parameter. Additional development is planned, as the old legend is inadequate to describe the complexity now possible in time series plots.

Although GRIZ4 was developed primarily with the goal of integrating Mili into it, we knew from the outset that GRIZ4 would need to read both Mili and TAURUS databases, and considering developments under ASCI there was potentially a strong need to support additional I/O library interfaces as well. To accommodate multiple I/O interfaces, the GRIZ I/O (GIO) layer was implemented to abstract details of any particular I/O library and provide a common high-level internal interface to I/O functions. To interface to a given I/O library, a "driver" is written which provides the correct function interfaces for GIO but calls the desired I/O library internally. GRIZ4 has drivers for Mili and the TAURUS plot databases built in; other drivers can be added as dynamically-linked shared objects.

GRIZ4 Parallel Rendering Prototype

Pre- and post-processing are the two major bottlenecks facing code users in the parallel domain. This year we took a significant step to ease the post-processing bottleneck by developing a prototype parallel renderer in GRIZ4. We implemented a master/slave approach in which the master processor manages the user interface and the slaves perform the parallel rendering. In the rendering algorithm, each processor renders its local mesh partition (determined by the domain decomposition from the analysis phase) followed by a global reduction of pixel red/green/blue values from all processors' images based on pixel Z (depth) values. In the final composited image, each pixel's color is taken from that initial image for which the depth value of the pixel was smallest (the pixel closest to the view eyepoint).

The parallel implementation was not intended as a production-ready solution but as a first step and baseline for experimentation and further development. Indeed, in using the domain decomposition from the analysis phase, we are almost assured of poor load balancing for rendering because only those local domains that have visible elements facing the view eyepoint can contribute pixels to the final image—the rendering effort on all other processors is wasted. Nevertheless, this was an attractive approach because of its simplicity and the fact that it offered the opportunity for parallel speedup while using the same serial rendering library (OpenGL) GRIZ already relies upon.

The parallel implementation must use offscreen rendering to memory, since the compute nodes of a parallel computer lack displays to render to. This has a beneficial by-product since it opens the door to "batch-mode" offscreen serial rendering as well, a long-sought capability for GRIZ.

Parallel-rendering GRIZ4 is still very much in the experimental stage. One of our priorities for the new fiscal year is to evaluate and profile the performance of this initial approach across an array of mesh sizes and processor quantities, then set the direction for a follow-on implementation leading to a production solution.

Combiner/Splitter Utility

An identified requirement associated with parallel processing is the need to remap the parallel outputs from an analysis run onto a different quantity of processors for subsequent post-processing or an analysis restart. In a similar vein, ParaDyn analysts need to combine **n** parallel Mili databases into one for serial post-processing. We met these needs by developing a combiner/splitter utility. Developed as a callable library with a driver program to provide the command-line interface, this utility will read multiple parallel Mili or TAURUS databases, plus the analysis partition file, and combine them (with translation, in the case of TAURUS) into a single Mili

database. The splitter code reads a second partition file for the target distribution of data and splits a single Mili database into the required number of parallel databases.

Web-Based Change-Request Tracking

In the past year, several factors combined to elevate the visibility of our software development process and the need for formalization. Fueled by ASCI funding, the growth in the number of code developers participating in graphics and data management software development highlighted the need for standardized conventions in our process and the use of software engineering tools. The *de facto* process arising from the old "one code, one code developer" environment is inadequate for a team of developers.

Taking advantage of LLNL's Computation Directorate's Software Technology Center, we requested a SCRTrack server to provide web-based management of software change requests (SCRs) and trouble reports. SCRTrack provides "cradle-to-grave" maintenance of SCRs on a product-by-product basis with support for a comprehensive set of user roles and SCR status conditions, plus automatic email notification of SCR state transitions. GRIZ4, Mili, and the GRIZ User Manual have been entered as products into the server, with plans for other codes to follow.

Regression Testing

Another aspect of the software process is quality assurance. One requirement associated with the release of GRIZ4 was the need to validate results against those from GRIZ version 2 (GRIZ2). This requirement manifests itself two ways. First, GRIZ4 must produce the same results as GRIZ2 when reading the same TAURUS database. Second, GRIZ4 reading a Mili database must produce the same results as GRIZ2 (or GRIZ4) reading results from the same analysis written out in a TAURUS database.

We developed a test script, written in the Python scripting language, that uses a standard set of DYNA and NIKE test problems and a collection of associated GRIZ command scripts to provide a basic validation of GRIZ4 with a comprehensive set of mesh configurations. The testing is not exhaustive in exercising all possible GRIZ capabilities, but it does thoroughly exercise data access and result computations and provides a baseline upon which to build additional testing capabilities. This addition to the GRIZ development process is valuable since it offers a great productivity boost for releasing GRIZ updates.

GRIZ4 ExodusII Driver

During the year, collaborators at Los Alamos National Laboratory (LANL) requested GRIZ modifications to read the Exodus II databases generated by Sandia's Pronto analysis code. With GIO developed for such a purpose, GRIZ4 is ideally suited for this effort. By year's end, GRIZ4 supported ExodusII, and it is currently in use by Engineering Services at LANL.

ASCI DMF Integration

Another I/O library compatibility requirement arises out of the ASCI program and its Data Models and Formats Application Programming Interface (DMFAPI), currently in active development. One of our goals under ASCI is to support DMFAPI in our "ASCI" analysis codes and in the GRIZ post-processor. GRIZ4's GIO layer again offers a natural entry point for integrating the DMFAPI, but ParaDyn has no equivalent abstraction layer in its output code. Our chosen approach for ParaDyn, which follows a pattern established at Sandia and at LLNL, is to layer our current API (Mili) on top of the DMFAPI. This allows us to write out ASCI format databases with few if any source changes in ParaDyn. Essentially, only a re-link is required, replacing the Mili library with a new one that consists of the DMF library and a set of wrapper functions that conform to the Mili API.

The DMFAPI uses a very general data model with a strong, abstract mathematical foundation. It represents a significant departure from other I/O library APIs. We have layered Mili's output calls over DMFAPI to enable ParaDyn to write out a DMFAPI database. The DMFAPI is still evolving, and with continued effort, its capabilities will be supported in other codes.

Future Work

Mili enables many changes, so it emerges as a natural focal point for additional development. Mili's design is such that supporting additional superclasses is straightforward, and one such superclass already identified for inclusion is a "surface" or "face list" superclass. A surface object would be an arbitrary set of 3-D element faces, quad elements, or triangular elements that have special significance in the generating application. For example, a surface might be defined where a boundary condition is being applied in a simulation, or it might be a contact surface for which information exists in the simulation not found on all elements in general.

Another necessary capability that code developers have identified is restart management of the database; specifically, the ability to overwrite state records at an arbitrary point in the simulation. Our analysis codes implement slightly different approaches to this, so a generalized approach is needed.

The planned restart support will be impacted by a more recent requirement for Mili. An inter-code "link" file capability developed for the analysis codes is now scheduled to be re-expressed under Mili. This file was originally developed to convey state information between NIKE3D and DYNA3D. It is also now being used as a "lightweight" DYNA3D restart file. Implementing a Mili version of the link/stress-restart file imparts greater flexibility in its use (for instance, building on GRIZ4's Mili compatibility, it opens the door to visualizing the link file) and provides an organized framework for ongoing extension of the file's contents.

As mentioned above, GRIZ4's prototype parallel rendering capability is scheduled to receive attention in FY-01. First we will characterize the prototype's performance over an array of problem sizes and processor quantities. This is expected to be followed by profiling to identify where bottlenecks lie in the current approach. These efforts will support a subsequent re-design of GRIZ4's parallel rendering software.

Our software process improvement activities will continue into the new fiscal year. We have two priorities in this domain. First, we will expand use of SCRTrack to include other codes and user manuals. Second, we plan to develop software scripts which will interact with our source repository during release builds and automate versioning of application binaries (specifically GRIZ, but the motivation applies to all our codes).

Acknowledgments

The author acknowledges the work of Y. Lee, E. Pierce, V. Castillo, O. Simek, and M. Miller.

Linear Equation Solvers for Parallel Computational Mechanics

Robert M. Ferencz
Defense Technologies Engineering Division
Mechanical Engineering

Chandrika Kamath
Center for Applied Scientific Computing
Computation Organization

Linear equation solvers present key performance issues for simulation codes using implicit time integration. This article summarizes our efforts to characterize solver methodologies suitable for inclusion in a new parallel implicit finite-element code.

Introduction

The Accelerated Strategic Computing Initiative (ASCI) program at Lawrence Livermore National Laboratory (LLNL) is tasking LLNL's Methods Development Group with the creation of a parallel implicit mechanics code. This effort builds upon our longstanding expertise in serial implicit finite-element codes for stress analysis (NIKE) and thermal analysis (TOPAZ), and will complement its ongoing development of the parallel *explicit* capability of the PARADYN code.

For present purposes, the fundamental difference between implicit and explicit simulation codes is that implicit codes use much larger step sizes for time integration. This makes implicit techniques suitable for modeling steady-state and low-frequency response, but this ability requires the solution of a set of linear equations at least once per time step. For the nonlinear materials and large-deformation phenomena typically modeled with NIKE, multiple linear solves are required at each time step. Hence, solving linear equations almost always represents the single largest share—at least 50%—of the overall computational cost in 3-D implicit simulations.

Linear equation solvers are typically divided into two classes: direct and iterative. Direct methods are known for their robustness and predictable number of operations. However, they require a global data structure that grows rapidly with problem size. Further, the algorithms used in direct solvers present challenges for large-scale parallelism. Iterative methods typically use a much smaller data structure that can be readily distributed for large-scale parallelism. Yet they often perform poorly on problems exhibiting characteristics quite common in our simulations: material softening and damage, material anisotropy, mesh refinement to capture local effects, combined bending and membrane response of shells, and near-singularities as buckling behavior is approached. In addition to their memory and/or time cost, linear equation solvers can add significant complexity to the software architecture needed to support large-scale parallel computers. So, in designing the new parallel implicit code we not only need to incorporate the experience of PARADYN's development, but we must also extend it to address these added issues. In preparation for that design phase we have been performing studies of two linear solvers.

Progress

PSPASES Sparse Direct Solver

This solver was developed in the research group of Profs. V. Kumar and G. Karypis at the University of Minnesota.[1] We have previously interacted with this academic team that created the graph partitioning utility METIS used by PARADYN as part of its overall domain decomposition preprocessing. (The METIS package is also used by many other parallel applications developed throughout the world.) This same partitioning technology has now been applied to the

issue of equation reordering for efficient sparse direct equation solving on distributed memory machines. The PSPASES package solves symmetric, positive-definite systems of equations and must use a collection of 2^N processors, where N is an integer.

We are evaluating this solver technology and monitoring its evolution. Last year we created a simple prototype of a "master/slave" architecture. The first processor is essentially running the serial NIKE code: it performs all I/O, computes the finite-element matrices and assembles the global system of linear equations. At that time, the remaining 2^N-1 processors are sent portions of the global equation system, and then all processors execute PSPASES to reorder and solve the system. This solution is then consolidated on the first processor where the remainder of NIKE's serial algorithms continue execution.

Obviously such a prototype is not a long-term approach to creating a production capability. But it has allowed us to exercise PSPASES within the context of a nonlinear finite-element code and provide feedback to its developers. For example, we identified and documented an anomaly in total memory use that occurred when multiple pairs of matrix reordering and factorization were requested in sequence. This is a fundamental requirement for nonlinear finite-element codes, but one not tested by the typical "test driver" that simply reads in a pre-computed matrix and does a single set of reordering/factorization/backsolve operations. With these data the developers were able to locate and correct the programming error, and memory usage has been verified to be essentially constant under the circumstances described. A growth in factorization CPU time has been documented for some situations and that information has also been passed to the developers.

Figure 1 shows a mesh used for some of the performance benchmarking. It is a subset of an overall model created by P. Raboin and S. Creighton for the Modal Analysis Correlation Experiment being undertaken jointly by LLNL, Sandia National Laboratories and the United Kingdom's AWE. This particular mesh leads to a linear system having 250,007 degrees of freedom. The factorized form of the matrix contains 180×10^6 nonzero entries and requires 330×10^9 floating-point operations to compute.

Figure 2 shows timing data for this problem from runs on the ASCI "Blue Pacific" IBM SP system. The $\log_2$ of wall time for matrix factorization is plotted versus $\log_2$ of the number of processors used. The dashed line represents perfect scaling: the timing of each doubling of processors exactly halved the execution wall time. The PSPASES data show good scalability from 16 to 256 processors: each doubling of processors results in a 40% reduction in wall time. (Stated differently, each doubling of processors provides a 67% speed-up.) That the scalability suffers when pushed to 512 processors is not surprising, since that represents only 500 equations per processor and thus not many floating-point operations to amortize the increasing communication.

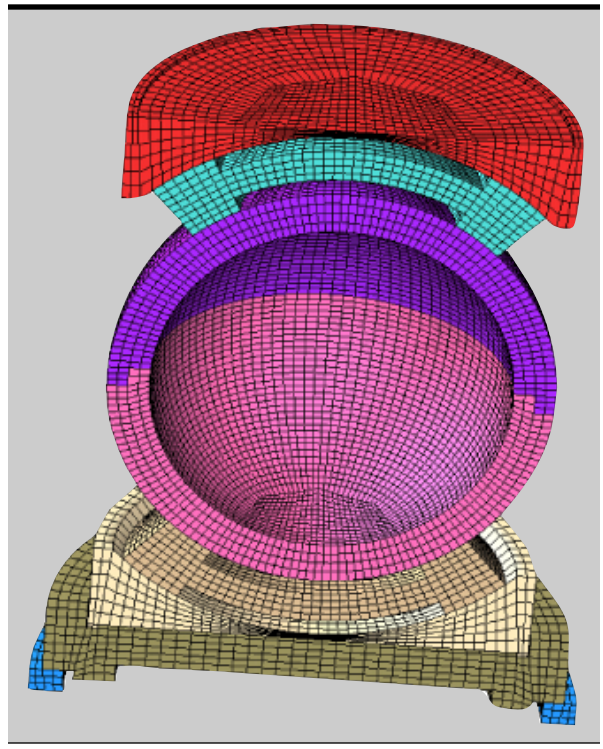

Figure 1. Mesh for a sub-assembly of the Modal Analysis Correlation Experiment (MACE). This mesh generates a system of 250,007 linear equations for stress analysis.

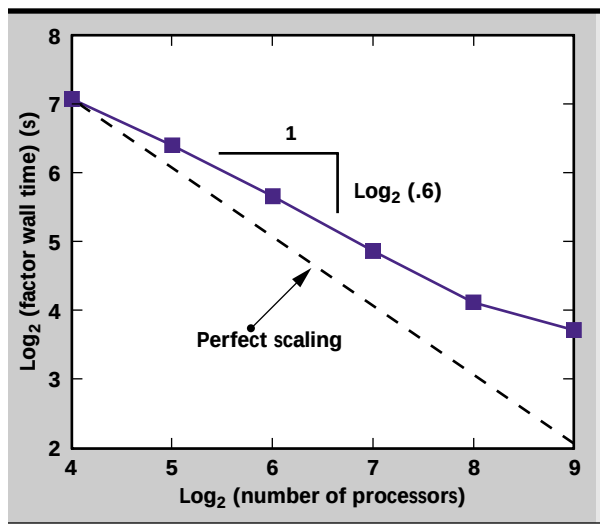

Figure 2. Timing data for the MACE benchmark run on the ASCI "Blue Pacific" IBM SP system.

This work demonstrates that a distributed sparse direct equation solver can remain a viable methodology for implicit mechanics on at least hundreds of processors. This point had been in doubt–it is not uncommon to hear opinions that "direct solvers cannot scale beyond 8 or 16 processors." While hundreds of processors represent only a fraction of an ASCI platform, it already would provide more than an order of magnitude increase in the size of implicit simulation we can perform in support of our engineering missions. The scalability of a direct solver on *thousands* of processors will be a longer-term issue, and motivates our examination of hybrid methods that combine iterative and direct equation solving technologies.

FETI

The Finite-Element Tearing and Interconnecting (FETI) method is a Lagrange-multiplier-based domain decomposition method. As a hybrid method, it has the potential of combining the best of both worlds, namely, the robustness of direct solvers and the scalability of iterative solvers as the number of processors is increased. Our work in this area has focused on developing a serial prototype of the FETI level 1 method,[2] with the aim of understanding the behavior of these methods on problems of interest to LLNL.

In the FETI method, the computational domain, Ω, is partitioned into N_s non-overlapping subdomains, $\Omega^{(s)}$. Lagrange multipliers, λ, are introduced at the subdomain interfaces to enforce the compatibility of the subdomain generalized displacements, $u^{(s)}$. As a result, the original linear system over Ω,

$$Ku = f \tag{1}$$

where K, u, and f are the stiffness matrix, the displacement vector and the force vector, respectively, is reduced to the equivalent set of equations:

$$K^{(s)}u^{(s)} = f^{(s)} - B^{(s)^T}\lambda \quad \text{for s = 1,…, N}_s \tag{2a}$$

$$\sum_{s=1}^{N_s} B^{(s)}u^{(s)} = 0 \tag{2b}$$

where, for each subdomain $\Omega^{(s)}$, the variables $K^{(s)}$, $u^{(s)}$, and $f^{(s)}$, denote the generalized stiffness matrix, the generalized displacements, and the generalized force vectors for that subdomain, respectively. The matrices $B^{(s)}$ are signed Boolean matrices that extract from a subdomain vector its signed contribution to the interface boundary of the problem.

If each of the subdomain stiffness matrices are non-singular, then we can solve for the subdomain displacements by first substituting $u^{(s)}$ from **Eq. 2a** into **Eq. 2b** and solving for λ, and then using **Eq. 2a** to solve for $u^{(s)}$. However, in practice, the domain decomposition process often generates one or more floating subdomains which do not have enough prescribed displacements to eliminate the local rigid body modes, resulting in a singular system in **Eq. 2a** for the corresponding subdomain. If this system is consistent, then the displacement $u^{(s)}$ for the floating subdomain $\Omega^{(s)}$ can be written in terms of λ as follows:

$$u^{(s)} = K^{(s)^+}(f^{(s)} + B^{(s)^T}\lambda) + R^{(s)}\alpha^{(s)} \tag{3}$$

where $K^{(s)^+}$ is the pseudo-inverse of $K^{(s)}$, $R^{(s)}$ is the matrix of rigid body modes of $\Omega^{(s)}$, and $\alpha^{(s)}$ is a vector of unknowns that determines the contributions of each of the rigid body modes. By the definition of rigid body modes, the columns of $R^{(s)}$ form the basis of the null space of $K^{(s)}$. The introduction of the new unknowns $\alpha^{(s)}$ requires additional equations which can be obtained from the observation that for the singular equation to admit a solution, the right hand side must have no component in the null space of $K^{(s)}$, that is

$$R^{(s)^T}(f^{(s)} + B^{(s)^T}\lambda) = 0 \tag{4}$$

Combining **Eqs. 2a**, **2b**, **3**, and **4** for all the domains in the problem, the FETI interface problem becomes

$$\begin{bmatrix} F_I & -G_I \\ -G_I^T & 0 \end{bmatrix}\begin{bmatrix} \lambda \\ \alpha \end{bmatrix} = \begin{bmatrix} d \\ -e \end{bmatrix} \tag{5}$$

where

$$F_1 = \sum_{s=1}^{N_s} B^{(s)}K^{(s)^+}B^{(s)^T}$$

$$G_1 = \left[B^{(1)}R^{(1)}\ B^{(2)}R^{(2)}\ \ldots\ B^{(N_f)}R^{(N_f)}\right],$$

$$d = \sum_{s=1}^{N_s} B^{(s)}K^{(s)^+}f^{(s)},$$

$$\alpha = \left[\alpha_1^T\ \alpha_2^T\ \ldots\ \alpha_{N_f}^T\right]^T,$$

$$e^{(s)} = \left[f^{(s)}R^{(s)}\right]^T, \quad s = 1, \ldots N_f$$

where N_f is the number of floating subdomains in the problem. The matrix $K^{(s)^+}$ reduces to $K^{(s)^{-1}}$ for non-singular systems.

While the matrix F_I is symmetric positive-definite, the system matrix in **Eq. 5** is indefinite, and we cannot directly apply the conjugate gradient method to solve for the Lagrange multipliers. However, we

observe that **Eq. 5** is equivalent to solving the equality constraint problem

$$\underset{\lambda}{Minimize}\ \Phi(\lambda) = \frac{1}{2}\lambda^T F_I \lambda - \lambda^T (G_I \alpha + d)$$

$$\text{Subject to } G_I^T \lambda = e$$

This implies that we can use the conjugate gradient method with projected gradient to solve **Eq. 5**, with F_I as the system matrix, d as the right hand side and λ as the unknowns. The conjugate gradient with projected gradient technique is identical to the conjugate gradient algorithm, but, in addition, it ensures that the constraint is satisfied at each iteration. If we choose the initial λ to satisfy the constraint, that is,

$$\lambda_0 = G_I (G_I^T G_I)^{-1} e$$

then the constraint is satisfied at each iteration if

$$G_I^T \lambda_k = 0$$

which can be ensured by projecting the direction vectors in the conjugate gradient method onto the null space of G_I^T, using the projector

$$I - G_I \left(G_I^T G_I\right)^{-1} G_I^T \ .$$

As with the standard conjugate gradient method, the performance of the basic conjugate gradient with projected gradient method can be improved through the use of preconditioning. Farhat and Roux[3] suggest the following two preconditioners:

$$\textit{Lumped}:\quad F_I^{-1} = \sum_{s=1}^{N_s} B^{(s)} \begin{bmatrix} 0 & 0 \\ 0 & K_{bb}^{(s)} \end{bmatrix} B^{(s)^T}$$

Dirichlet:

$$F_I^{-1} = \sum_{s=1}^{N_s} B^{(s)} \begin{bmatrix} 0 & 0 \\ 0 & K_{bb}^{(s)} - K_{ib}^{(s)^T} K_{ii}^{(s)^{-1}} K_{ib}^{(s)} \end{bmatrix} B^{(s)^T}$$

where the matrix $K^{(s)}$ is partitioned as

$$K^{(s)} = \begin{bmatrix} K_{ii}^{(s)} & K_{ib}^{(s)} \\ K_{ib}^{(s)^T} & K_{bb}^{(s)} \end{bmatrix}$$

where the subscripts i and b indicate interior and boundary variables, respectively. Note that the Dirichlet preconditioner is a better approximation to the inverse of F_1, albeit a more expensive one.

We have implemented a serial version of the FETI level 1 method in Fortran 77. The current version of the code can handle cross-points in the decomposition as well as heterogeneous domains.[4] The subdomain problems that arise in the application of the conjugate gradient with projected gradient technique are solved using a skyline solver. While this is not the most efficient direct solver, it does enable easy calculation of the pseudo-inverses and rigid body modes.[2]

To understand the behavior of the FETI method, we experimented with the problem in **Fig. 3**, which solves the equations of static equilibrium for a simple 2-D bar extension problem using quadrilateral elements. The problem has four subdomains, with a single cross-point where the four subdomains meet. Subdomains 2 and 3 are floating subdomains with a single rigid body mode each, while subdomain 4 has three rigid body modes. The iterations of the preconditioned conjugate gradient with projected gradient method are stopped when the two norm of the preconditioned projected residual is less than 10^{-8}. Further details on the implementation of the method are given elsewhere.[5]

Table 1 lists the iterations for the FETI method for our simple test problem as the properties of the subdomain are varied to represent problems of interest to LLNL. We observe that the number of iterations required for convergence, especially with the Dirichlet preconditioning, remains constant as the problem is made more ill-conditioned. Note that these are the iterations required to solve the interface problem using the preconditioned conjugate gradient with

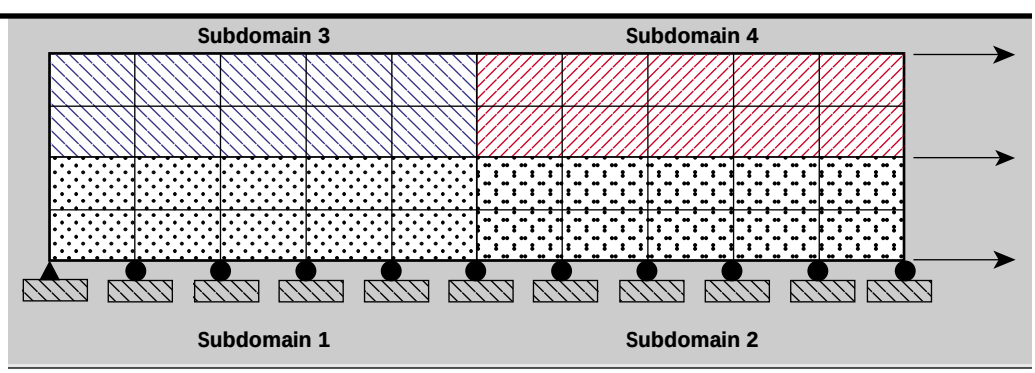

Figure 3. Test problem for FETI level 1.The global problem has 94 equations, while the interface problems has 38 equations.

projected gradient method. Finally, to compare the performance of the FETI method with standard iterative schemes, we present in **Table 2** the results of solving the global system using the iterative solvers from Compaq's DXML™ solver library.[6] This data shows that while standard iterative solvers may work in some problems, they are not always scalable as the problem becomes more ill-conditioned.

These early results demonstrate that the FETI technique shows promise of being a viable method for solving ill-conditioned problems when the source of ill-conditioning arises from commonly occurring situations in LLNL simulations. The scalability of the FETI method on problems of a size of interest to ASCI has already been demonstrated[7] on the ASCI option Red supercomputer. However, as outlined below, several additional experiments are necessary before we can say that the FETI method can solve difficult problems of interest in an efficient and effective way on massively parallel machines.

Table 1. Iteration counts for the FETI method on the test problem in Fig. 3. The iterations are for the solution of the interface problem using preconditioned conjugate gradient with projected gradient technique.

	No preconditioning	Lumped preconditioning	Dirichlet preconditioning
Problem 4 Homogeneous stiffness	22	13	10
Problem 4a Subdomain 4: 10× stiffer	25	13	10
Problem 4b Subdomain 4: 1000× stiffer	24	13	9
Problem 4c SD1: 100×, SD2: 10×, SD3: 1×, SD4: 1000×	34	17	10
Problem 4d Homogeneous, nearly incompressible elasticity	22	34	15
Problem 4d With re-orthogonalization	20	27	12

Table 2. Iteration counts for standard conjugate gradient techniques with various preconditioners applied to the global system obtained from the problem in Fig. 3.

	No preconditioning	Diagonal preconditioning	Polynomial preconditioning	ILU preconditioning
Problem 4a	94 (close to the solution)	67	48	25
Problem 4b	94 (not close to the solution)	86	62	34
Problem 4c	94	75	55	28
Problem 4d	No convergence	No convergence	No convergence	Preconditioned matrix not positive-definite

Tolerance: 10^{-8}
Maximum iterations permitted: 94
Order of polynomial preconditioner: 2

Future Work

Our work with PSPASES will now be folded into the on-going design effort for LLNL's new parallel implicit mechanics code. By considering from the outset the requirements of both direct and iterative/hybrid equation solvers, the code will incorporate methodologies suitable for a broad range of simulations. The numerical robustness of the sparse direct solver will also be useful during the development of the code, as it will permit us to focus on other aspects of the code's overall behavior and performance.

Our work on the FETI level 1 method has so far focused on simple 2-D problems, where the subdomains are homogeneous, though the material properties may be different across subdomains. To ensure that this method is indeed a versatile one, we need to repeat our experiments on simple 3-D problems, and study the effects of heterogeneity when it occurs within a subdomain. We also plan to study the effects of changing the aspect ratio of the subdomains. The subdomain aspect ratio is an important factor in determining the convergence of the FETI method.[3] If we use a mesh partitioning software such as METIS, it is not clear if it will provide subdomains with near-unity aspect ratios, or if additional work will be required, especially as the simulation evolves over time and the partitioning changes.[8, 9]

References

1. M. Joshi, G. Karypis, V. Kumar, A. Gupta and F. Gustavson (1999), "PSPASES: An efficient and scalable parallel sparse direct solver," in *Proc. Int. Workshop on Frontiers of Parallel Numerical Computations and Applications*, Annapolis, Maryland, February.

2. C. Farhat and F. X. Roux (1991), "A method of finite element tearing and interconnecting and its parallel solution algorithm," *Int. J. Numer. Meth. Eng.*, Vol. **32**, pp. 1205–1227.

3. C. Farhat and F. X. Roux (1994), "Implicit parallel processing in structural mechanics," *Comp. Mech. Adv.*, Vol. **2**, No. 1, pp. 1–124, June.

4. D. Rixen and C. Farhat (1999), "A simple and efficient extension of a class of substructure based preconditioners to heterogeneous structural mechanics problems," *Int. J. Numer. Meth. Eng.*, Vol. **44**, pp. 489–516.

5. C. Kamath, "The FETI level 1 method: theory and implementation," LLNL Technical report, in preparation.

6. C. Kamath, R. Ho, and D. Manley (1994), "DXML: A high performance scientific subroutine library," *Digital Technical Journal*, Vol. **6**, No. 3, Summer.

7. M. Bharadwaj, D. Day, C. Farhat, M. Lesoinne, K. Pierson, and D. Rixen (1999), "Applications of the FETI method to ASCI problems: scalability results on one thousand processors and discussion of highly heterogeneous problems," Sandia Report, SAND99-0937, April.

8. C. Farhat, N. Maman, and G. Brown (1995), "Mesh partitioning for implicit computations via iterative domain decomposition: Impact and optimization of the sub-domain aspect ratio," *Int. J. Numer. Meth. Eng.*, Vol. **38**, pp. 989–1000.

9. D. Vanderstraeten, C. Farhat, P.S. Chen, R. Keunings, and O. Ozone (1996), "A retrofit based methodology for the fast generation and optimization of large-scale mesh partition: beyond the minimum interface size criterion," *Comp. Meth. Appl. Mech. and Eng.*, Vol. **133**, pp. 25–45.

EIGER Preprocessor and User Interface

Robert M. Sharpe, Nathan J. Champagne, and Andrew J. Poggio
Defense Sciences Engineering Division
Electronics Engineering

Our goal is to facilitate the use of advanced computational electromagnetics (CEM) tools by application designers and analysts. Specifically, this entails developing an advanced preprocessor and graphical user interface (GUI) for frequency-domain electromagnetics codes (for example, EIGER). The preprocessor reads and interprets the mesh files that are output from commercial mesh generation packages, and assists with the decisions and assignments that are needed to perform the requisite CEM analysis. The complexity of the geometry often requires automated diagnostics to ensure proper connectivity and discretization of the problem. In addition, the wide variety of analysis options available in the new generation of CEM tools necessitates an interface that assists users with the decision process and problem setup so that designers may concentrate on their specific analysis rather than on the CEM issues.

Introduction

Modern software engineering methods enable analysis tools development with an unprecedented degree of flexibility in incorporating different formulations for advanced physics, and numerical methods for a single self-consistent solution. This in turn yields general-purpose tools, such as the EIGER[1–4] software suite, with an unparalleled range of applicability.

Current applications include advanced microelectromechanical machines (MEMMs), microwave components (RF isolators and splitters), radar cross-section (RCS) analysis, broad-band antenna design, frequency-selective surface design, Navy ship topside design, and phased array analysis and design. This wide variety of applications on one hand and the extensive set of features and options in the computational tools on the other hand yield a technology gap that must be bridged to successfully transition this technology to the various user communities both within and outside Lawrence Livermore National Laboratory (LLNL).

Progress

The graphical user-oriented interface (EIGER Build) is a principal part of the EIGER framework (**Fig. 1**) for frequency-domain electromagnetics analysis. It assists

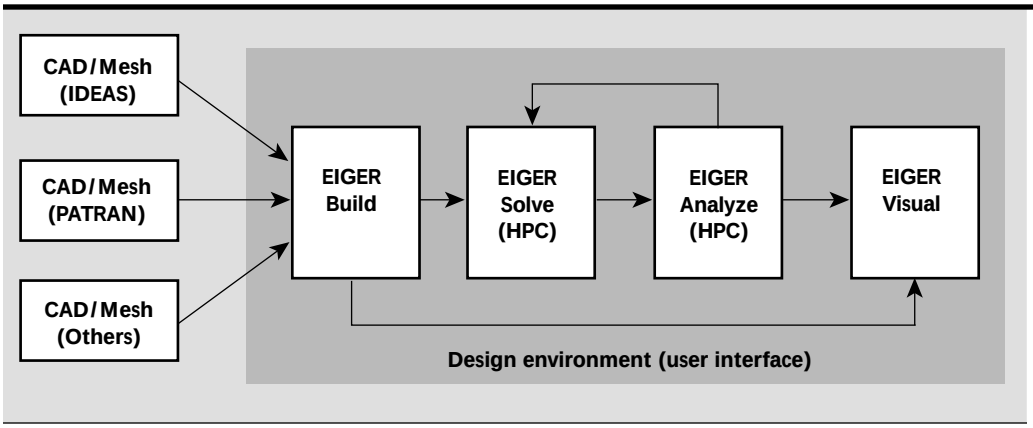

Figure 1. The four components of the EIGER Framework. EIGER Build is the graphical preprocessor; EIGER Solve is the physics engine; EIGER Analyze is the physics post-processor; and EIGER Visual is the graphical post-processor.

designers in the most time-consuming and error-prone portions of a CEM simulation—the problem setup and definition phase. Simulation files are created in EIGER Build based on a project concept.

The project contains all of the components needed for a CEM model, such as the geometry, the boundary conditions, and the excitations. The meshed geometry is created by a CAD/mesh program, such as PATRAN or I-DEAS, and then read into EIGER Build. The discretized geometry is visually inspected in EIGER Build for errors. If the mesh is satisfactory, CEM-specific information to the geometry is interactively applied to complete the simulation model. By storing the simulation model in a project file, any minor updates made in the CAD program will not adversely affect the project. This allows, for example, geometrical parameter studies to be done with minimal effort.

An EIGER Build project is composed of a set of databases. The entries in each are associated, by EIGER Build, with parts of the geometry or the model as a whole. The databases include:

1. visuals, for controlling the appearance of the geometry;
2. boundary conditions, for specifying the presence of electric and magnetic currents;
3. integral equations, for enforcing the selected boundary conditions;
4. materials, for augmenting the geometry information with electromagnetic properties;
5. plane waves and voltage sources, for exciting the model;
6. lumped loads, for representing ports;
7. spectral information, for picking the desired frequencies and modes;
8. far-field sampling points, for describing grids of angles at which far-field calculations are desired; and
9. near-field sampling points, for describing grids of points at which total field calculations are desired.

A sample input database form for a plane wave excitation is shown in **Fig. 2**.

There are several analyses that are performed to assist in geometry validation. The analyses are done automatically after a mesh is read into EIGER Build. However, these analyses can be redone via menu selections that produce visual results. The different analyses available are as follows:

Boundary edges. The surface elements in a mesh are analyzed for open boundaries. These are edges of any surface element that do not connect to another surface element. This collection of element edges can be thought of as the apertures. This analysis is used to look for unintended (or missing) apertures in a model.

Joint edges. The surface elements in a mesh are analyzed for multiply connected boundaries. These

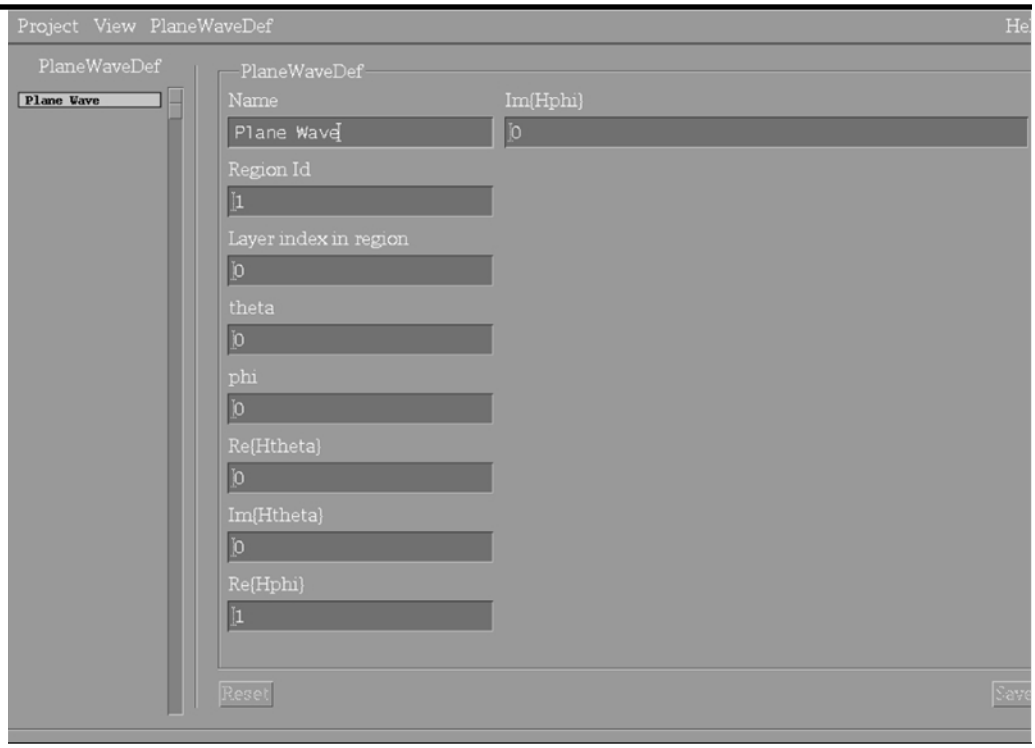

Figure 2. Database input screen for a plane wave excitation.

are edges of any surface element that connect to more than one other surface element. This analysis is used to look for unintended (or missing) contact sites.

Surface edges. The surface elements in a mesh are analyzed for singly connected edges. These are edges of any surface element that connect to exactly one other surface element. This collection of element edges can be thought of as the ordinary edges of the mesh. As such, its information is limited, but it does provide the complement of the other surface element analyses. This analysis is used as an eyeball aid while viewing other analyses.

Wires. The wire elements in a mesh are collected into a single group. This collection provides a simple way to view all the wires at once. The collection even includes wire elements that were not put into groups. This analysis is used to verify that all of the wires are present.

Free wire ends. The ends of wire elements in a mesh are analyzed for unattached ends. These are ends of any wire element that do not connect to another wire or surface element. This analysis is used to verify that all of the wires are properly attached to the geometry.

Junction wire ends. The ends of wire elements in a mesh are analyzed for ends touching surfaces. These are ends of any wire element that connect to at least one surface element. This analysis is used to verify that all of the appropriate wires are properly attached to the surface geometry.

An example of an analysis result in EIGER Build is shown in **Fig. 3**. The meshed structure is a Navy patrol craft modeled with surface and wire elements. The particular analysis shown is "free wire ends," which is used to determine if all the wires are attached properly. This is visually shown by crosses at the wire ends. A close up of a collection of wires near the bow is shown in **Fig. 4**. Upon closer inspection, it is determined that a wire that should be attached to the surface is not attached after all. If an electromagnetic simulation were run with this error, the results would not be correct, especially in the area surrounding this collection of wires.

Future Work

During the next phase of this project, we will incorporate volume finite elements into the EIGER software suite. This is a necessary step to treat geometries with a hybrid finite element/boundary element formulation. Additionally, higher-order interpolatory functions and elements will be addressed to further enhance the capabilities of the EIGER suite by increasing the accuracy and efficiency for more complicated models.

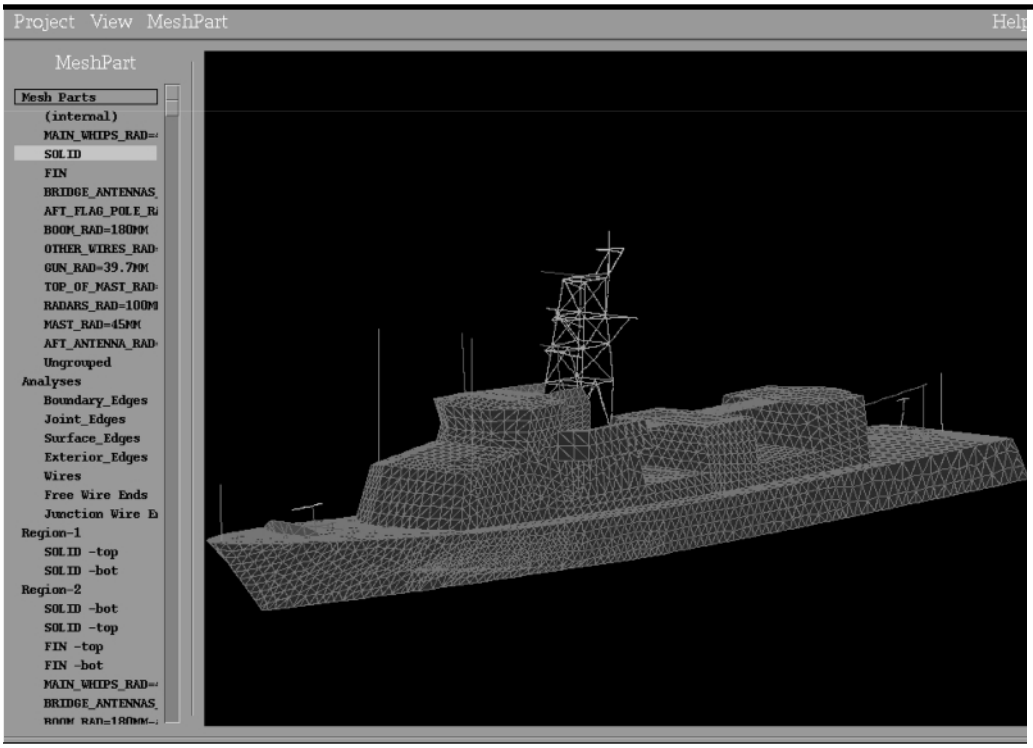

Figure 3. Screen shot of EIGER Build. The geometry is a Navy patrol craft. The crosses at the wire ends indicate that they are unattached.

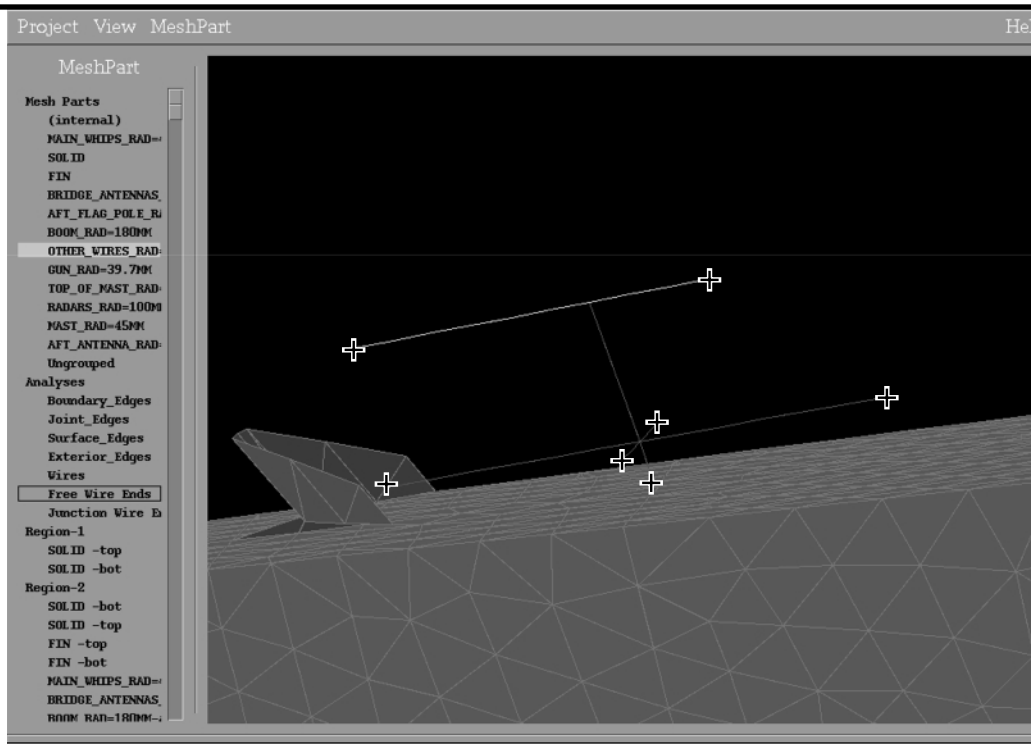

Figure 4. Close-up of a collection of wires near the bow of the craft shown in Fig. 3. The crosses indicate that the wires are not attached to the craft surface.

References

1. R. M. Sharpe, J. B. Grant, N. J. Champagne, W. A. Johnson, R. E. Jorgenson, D. R. Wilton, W. J. Brown, and J. W. Rockway (1997), "EIGER: Electromagnetic Interactions GEneRalized," *IEEE AP-S International Symposium and North American URSI Radio Science Meeting*, Montreal, Canada, July.

2. R. M. Sharpe, J. B. Grant, N. J. Champagne, W. A. Johnson, R. E. Jorgenson, D. R. Wilton, D. R. Jackson, J. W. Rockway, and C. W. Manry (1998), "Electromagnetic Interactions GEneRalized (EIGER): Algorithm abstraction and HPC implementation," *Twenty-Ninth Plasmadynamics and Lasers Conference*, Albuquerque, New Mexico, June.

3. W. A. Johnson, R. E. Jorgenson, L. K. Warne, J. D. Kotulski, J. B. Grant, R. M. Sharpe, N. J. Champagne, D. R. Wilton, and D. R. Jackson (1998), "Our experiences with object oriented design, Fortran 90, and massively parallel computations," *IEEE AP-S International Symposium and North American URSI Radio Science Meeting*, Atlanta, Georgia, June.

4. W. A. Johnson, R. E. Jorgenson, L. K. Warne, J. D. Kotulski, J. B. Grant, R. M. Sharpe, D. R. Wilton, and D. R. Jackson (1999), "Our experiences with object oriented design, FORTRAN90, and massively parallel computations," *Progress In Electromagnetics Research Symposium Proceedings*, March 22–26, **1**, Taipei, Taiwan, p. 164.

Strength and Reliability of Brittle Materials

Robert A. Riddle
Defense Technologies Engineering Division
Mechanical Engineering

Chol K. Syn and Michael J. O'Brien
Manufacturing and Materials Engineering Division
Mechanical Engineering

Steve Duffy, Joe Palko, and Eric Baker
Connecticut Reserve Technologies

We have tested the strength and reliability of brittle materials using statistical fracture mechanics incorporating Weibull parameters into finite-element methods. Results are given for four-point bend bar tests on beryllium oxide.

Introduction

Components fabricated from brittle materials find wide use in numerous programs at Lawrence Livermore National Laboratory (LLNL). Examples include structural ceramics, windows and synchrometers in particle accelerator technology, and optical components for lasers. The use of components of such materials in these applications requires knowledge of appropriate stress levels through a wide variety of loading scenarios.

Traditional methods of safety assessment work less well for brittle materials because of the larger scatter in strength values as determined by materials testing, and because the amount of data scatter increases as the component increases in size. Use of statistical fracture mechanics incorporating Weibull parameters will allow a rational, state-of-the-art, and probabilistic prediction of failure. Used in conjunction with finite-element methods, safe stress levels may be chosen based on the required reliability.

An important part of this effort is the incorporation of the state of the art in the design and application of advanced ceramic materials. The CARES (Ceramic Analysis and Reliability Evaluation for Structures) program from NASA Lewis represents a successful effort.[1] The CARES program takes a description of the state of stress from brittle material and derives a probability of failure based on Weibull strength test parameters and estimates of the effects of the biaxiality of the stress state. Our effort incorporates the CARES type failure prediction within constitutive models for brittle materials within the LLNL finite-element codes.

Progress

Weibull Statistical Method for Failure Prediction

The Weibull method for statistical failure prediction is based on the concept of a distribution of flaws both in terms of size and orientation within the microstructure of a brittle material. Weibull described this method as a 'weakest link' description for the size effect on failures in solids.[2] Then, following the derivation of Robinson,[3] for small volume elements where the stress can be assumed to be uniform, the probability of failure per unit volume is P_o. The probability of survival, S, of a volume, V, of the material is given by

$$S = (1 - P_o)^V \qquad (1)$$

for the simultaneous survival of small volume elements.

Taking the logarithm of each side of **Eq. 1** gives

$\ln S = -V\ln(1 - P_o)$.

The risk of rupture is defined as $R = -\ln S$, which in terms of an infinitesimal element gives

$dR = -\ln(1 - P_o)dV$.

The term $-\ln(1 - P_o)$ is assumed to be a positive function depending on only the tensile stress $n(\sigma)$. Then

$dR = n(\sigma)dV$

and

$R = \int_V n(\sigma)dV$

where R is the risk of rupture integral. From the definition of R we get the probability of failure as

$P_f = 1 - \exp[-\int_V n(\sigma)dV]$.

For the three parameter Weibull distribution

$$n(\sigma) = \left(\frac{\sigma - \sigma_u}{\sigma_0}\right)^m,$$

known as the general Weibull distribution function. In this distribution the quantity 'm' is unitless and is termed the shape factor or Weibull modulus. It is a measure of the variability of the material strength distribution. The quantity σ_o is the Weibull scale parameter and has units of stress volume$^{(1/m)}$. For a material component of unit volume, σ_o is the expected value of strength at the 63.2% probability level. The quantity σ_u is the Weibull threshold parameter, and is the stress value below which no failures are expected to occur. For conservatism and mathematical convenience, the threshold stress is normally considered to be zero, and a simpler two-parameter Weibull model is used.

Weibull Prediction of Size Effect and Stress Distribution

Consider two similar components of the same material but of different volumes, V_1 and V_2. If the stress state is uniform tension, the size effect in the predicted strength for a two-parameter Weibull failure model is:[3]

$$\frac{\sigma_1}{\sigma_2} = \left(\frac{v_2}{v_1}\right)^{\left(\frac{1}{m}\right)}$$

As an example of the size effect, consider the case where the volume ratio of the two components is 10, and the Weibull modulus of the material is 10, as would be typical for the high strength ceramic. Then the strength ratio is

$$\frac{\sigma_1}{\sigma_2} = \left(\frac{10}{1}\right)^{\left(\frac{1}{10}\right)} = 1.26.$$

The large component would be only 80% as strong as the small component.

A similar effect may be shown for size effect,[3] where a component in tension would be predicted to have 73.5% of the strength of a component under pure bending.

These are the size and stress distribution effects in the simplest of circumstances. When 3-D combined stress states, and both volumetrically and surface distributed flaws are considered, as would be the case in most real applications, effects of size and stress distribution take a more complex form.[4] It has been shown that some brittle materials show a definite size effect (glass cylinders under compressive loads), while others do not (cement paste cylinders). The appropriate use of a Weibull distribution to model a material's failure behavior depends on the details of the observed failure data.

Correlation of Fracture Toughness and Weibull Parameters

The fracture mechanics approach to failure prediction is deterministic, with failure predictions based on known flaw sizes and the material's resistance to crack growth, called the fracture toughness. Based on a given flaw geometry, and the far-field load application, the applied stress intensity factor may be calculated at the crack tip. When the applied stress intensity factor equals the critical stress intensity factor, or fracture toughness, crack propagation occurs.

By contrast, Weibull statistics predicts failure based on unknown flaw distributions and far-field stress fields. The results are predicted probabilities of crack propagation. It is possible that there are connections between the two methods.

One attempt to categorize the scatter for fracture toughness measurements[5] could correlate the two methods. Fracture is treated as a weakest link phenomenon, while failure is treated in a probabilistic fashion. The fundamental expression for the probability of failure is given by

$$P_f = 1 - \exp\left[-_v \rho dV\right].$$

Here V is a specified volume, and ρ is a failure function per unit volume.

It would seem that to use the preceding equation the function ρ must be defined, or its characteristics must be inferred. This function must be dependent upon stress. As noted above, Anderson[5] cites earlier work by Ritchie, Knott and Rice[6] where a model was postulated that predicted cleavage failure when the stress ahead of a crack exceeds the failure stress of the material (σ_f) over a characteristic length. Later work by Curry and Knott[7] used statistical arguments to show that a finite volume of material must be subjected to a stress field severe enough to fail, with a defect large enough to initiate cleavage.

Thus the volume stipulated in the preceding equation must be a region surrounding the crack tip. The size of the region is defined by the severity of the crack tip stress field and the inert strength of the material. The inert strength of a material is defined by ρ and because of this a specific form for ρ is never needed. The material tested will dictate what this function is. In a sense the material is the function. Test loads and boundary conditions serve as input and test data serves as output from the function. However, the crack tip stress field must be specified to derive the cumulative distribution functions (cdf) for K_{IC} (fracture toughness) and J_C (critical energy release rate). Since cleavage fracture is the assumed failure mechanism, stress fields associated with small scale yielding (SSY) must be used.

The function ρ is a function of the stress field near a crack tip. Using the work of Hutchinson[7] the stress field can be shown to take the form

$$\sigma = f\left(\frac{J}{r}, \theta\right).$$

Anderson[5] invokes the relationship between the J-Integral and the stress intensity factor K to obtain the expression

$$P_f = 1 - \exp\left\{-\left(\frac{K_{IC}}{\theta_K}\right)^4\right\}.$$

One implication of this relationship is that when a single large flaw under tensile loading is the dominant failure mode in a material, the Weibull modulus would be measured as 4.0. Other effects such as loading mode mixity, crack propagation effects, and flaw interactions tend to change the value of the Weibull modulus. Indeed, Stienstra[8] has calculated that certain crack propagation effects tend to increase the value of the measured Weibull modulus.

The idea that certain aspects of the microstructural failure modes may be inferred from the value of the Weibull modulus is demonstrated to a preliminary level of certainty. That further aspects of microstructural failure modes could be inferred from the Weibull failure parameters through material microstructural failure simulation and observation is of great interest in terms of fabrication process improvement and understanding of failure strengths in brittle materials.

Experimental Data Reduction for Weibull Parameters

Four-point bend bar tests were conducted on specimens fabricated from beryllium oxide (BeO) components to measure the effect of specimen surface finishing. One set of specimens had a machine ground surface, while the second set were polished to a mirror finish. The specimens were all nominally size A according to the ASTM specification C-1161.[9] Both sets of specimens were fabricated and tested in accordance with this specification, and the data reduction followed the guidelines of ASTM C-1239.[10] The size A specimens are nominally 2.0 mm wide, 1.5 mm deep, and 25 mm long. In the four-point bend test apparatus the inner span is 10 mm, with the outer span twice that. A good discussion of the issues of accuracy and reliability in the testing aspects for ceramic materials is found elsewhere.[11]

A third set of specimens is referred to in the results as the BeO annealing study. Annealing temperatures were applied to the material to see if there could be positive results from pore closure, crack healing, and residual stress relief due to material flow at elevated temperatures. If there were such effects, they are subtle, and these data points are included for comparison purposes.

Figure 1 shows the four-point bend tests results with failure stress in pounds per square inch as a function of probability of failure. There was an

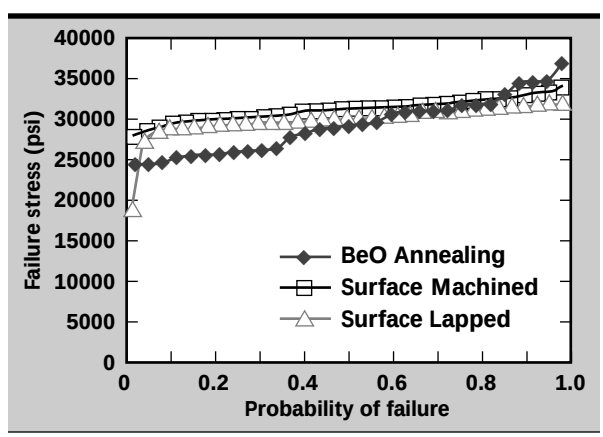

Figure 1. BeO four-point bend specimen failure comparisons.

additional surface-machined specimen which broke in fabrication, with the remaining 30 points plotted. The CARES program[1] and the 'WeibPar' program from CRT associates[12] were used for the data reduction. The two programs agree to within numerical error.

The BeO failure data for the polished or lapped samples, along with the plots of the curve fit parameter from the WeibPar program are shown in **Fig. 2**. Using the maximum likelihood estimators as the curve fit technique, the Weibull modulus, m, is calculated to be 25.83, with the Weibull scale parameter 22,070 psi*$(in^3)^{(1/25.83)}$. The single low data point is an obvious 'outlier' from the distribution. It lies far from the other data points and from the curve fit parameters. When a linear regression curve fit is used to better capture this outlying point, m is calculated to be 10.77 while the scale parameter is 15,770 psi*$(in^3)^{(1/25.83)}$.

The large change in material parameters with the change in curve fit techniques is understandable, but also somewhat disturbing. It is understandable in that the linear regression curve fit technique biases the curve fit to the low-level points. It is disturbing in that it reduces the confidence level that the curve fit parameters represent real material properties.

From the curve fits, and the persistence in each case of low stress level failures, it appears that there is a second type or distribution of flaws which is less prevalent but whose consequence on failure is much more severe. The existence of this second type of flaw distribution must be confirmed by additional tests on larger samples to bolster predictions of its effects. This represents a real difficulty in applying Weibull statistics to ceramic materials. It also offers the hope that if the larger defects could be eliminated through better material processing, very significant improvements could be made in raising the expected design stress of BeO components.

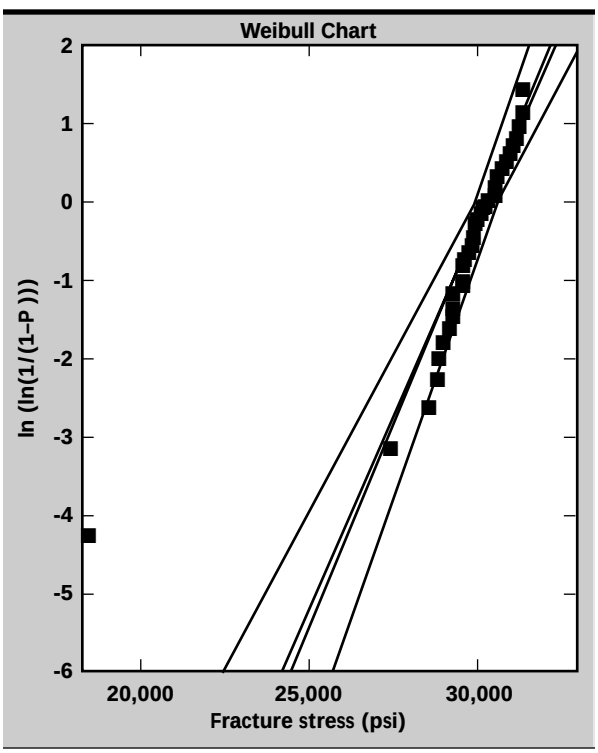

Figure 2. Weibull Chart for lapped BeO specimens.

Fractography of the Failed BeO Specimens

Fractography of the failed samples is required to verify the assumption that the flaws that caused failure were distributed throughout the volume of the material, and not just present on the surface. The Military Handbook 790[13] provides useful guidelines and information regarding the characterization of failed ceramic surfaces.

The surface of the as-machined BeO specimen is seen in **Fig. 3** as a micrograph from a scanning electron microscope. The areas marked (a), (b), and (c) show the features of machining striations, a machining induced crack, and machining debris on the surface.

The as-lapped specimens show polished smooth surfaces mixed with voids. The voids are of various sizes and shapes as shown in **Fig. 4a** and their internal structures reveal the individual grains or clusters of grains as shown in **Fig. 4b**. **Figure 4b** is the enlarged view of the rectangular area marked in **Fig. 4a**. Evidences of unbonded boundaries between two neighboring grains are shown by arrows in **Fig. 4a** and unbonded three-grain junctions are shown in **Fig. 4b**.

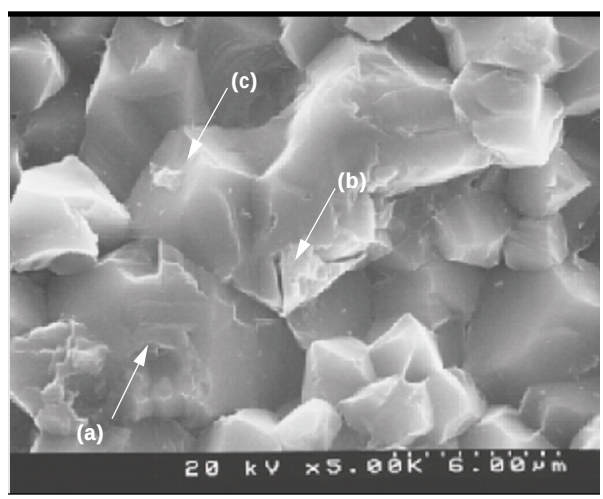

Figure 3. Surface of the as-machined BeO samples. Areas marked (a), (b), and (c) show features of machining mark, machining-induced crack, and machining debris, respectively, on the machined surface.

From **Figs. 3** and **4**, the average grain size of the present material was determined by a simple line intercept method to about 3 µm. It is not clear whether the microstructure shown in **Fig. 4a** represents the true bulk microstructure or near-surface microstructure where the machining damage is still visible. If the voids seen on the surface in **Fig. 4a** are a part of the true bulk structure, then the material must contain a fairly high content of voids. If the voids are due to the machining damage and left in place by insufficient lapping, a further lapping is necessary to remove the machining-induced damage and reach the true bulk microstructure. The volume fraction of the voids in **Fig. 4a** is calculated to be 14% by the line intercept method.

For purposes of the data reduction it is assumed that the specimen critical flaws are volumetrically distributed.

Figure 5 shows the fracture path in the as-lapped sample. The arrows indicate the propagation of a secondary crack as revealed on the "tensile" surface of the four-point bend test specimen. The fracture path is seen to follow the grain boundaries and connect the voids. From the micrographs of the failure surface it seems apparent that the failure of the ceramic material on the microstructural level is strongly influenced by the fracture toughness of the grain boundaries, as compared to the matrix of the crystalline materials, and that voids play a large role in both crack initiation and crack propagation.

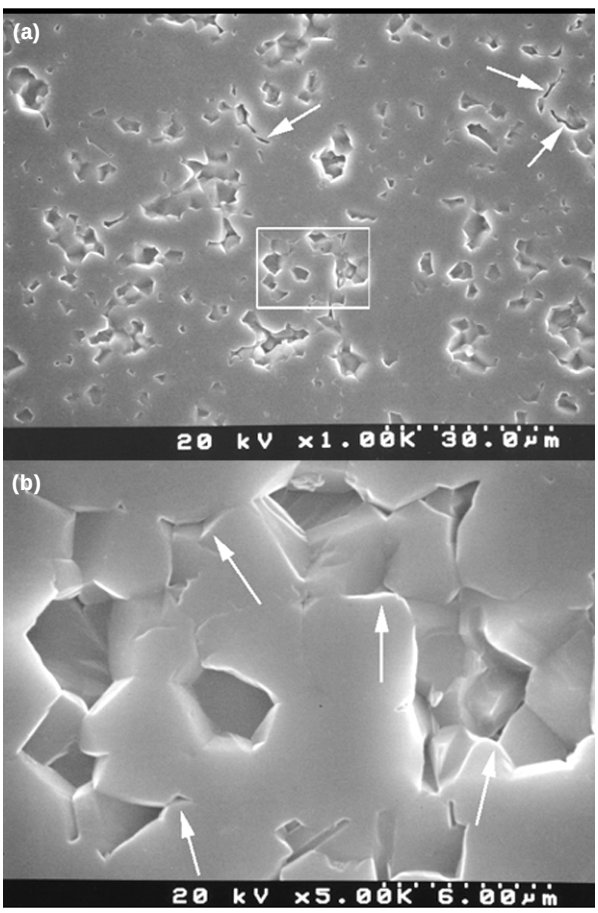

Figure 4. (a) Microstructure of the as-lapped surface. Arrows indicate sharp crack-like unbonded boundaries between two neighboring grains, where a fracture can be initiated.
(b) Enlarged view of the area marked by a rectangle in Fig. 4a. Arrows indicate where three or more grains meet and form an unbonded junction, which can act as a fracture initiation point.

Implementation of the Weibull Failure Predictions in NIKE2D

The implementation of the Weibull distribution for uniaxial stress is quite straightforward for the two-parameter failure model. For arbitrary 3-D stresses an equivalent uniaxial stress is calculated, and the analysis becomes complicated by additional choices. Two methods for arriving at an equivalent uniaxial stress, given a 3-D stress field, were examined in depth and implemented in NIKE2D. These methods are termed the principle of independent action, and the Weibull averaged normal tensile stress.

For the principle of independent action, if the principal stresses are tensile, this approach gives a probability of failure as

$$P_{fv} = 1 - exp\left[-k_{wv}\int_v \left(\sigma_1^m + \sigma_2^m + \sigma_3^m\right)dV\right]$$

where m is the Weibull modulus and k_{wv} is $(\sigma_{oV})^{-m}$.

The Weibull normal stress method gives more conservative estimates of the probability of failure.[1] The risk of fracture at any point in the specimen is a function of the tensile normal stress distribution, σ_n,

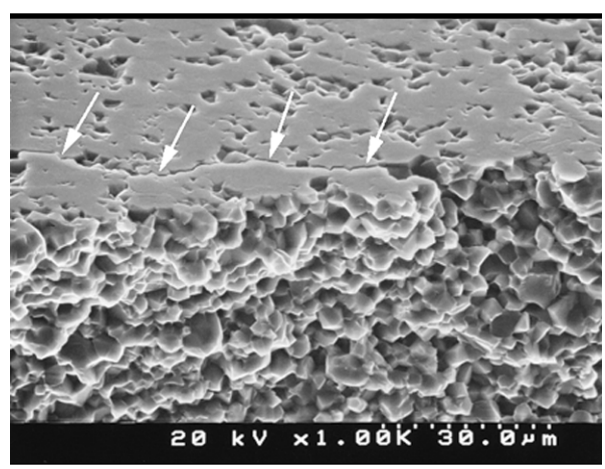

Figure 5. Fracture path in the as-lapped sample. Arrows indicate the propagation of a secondary crack as revealed on the "tensile" surface of the four-point bend test sample. The fracture path is seen to follow the grain boundaries and connect the voids.

on all planes passing through the point.[14] All the planes passing through the point can be represented, in turn, as normal vectors of unit length, which terminate on a sphere of unit radius in principal stress space. For an arbitrary multiaxial load on an element of material volume, the principal stresses acting on the element must be projected onto those portions of the unit sphere for which the averaged stress is tensile, under the assumption that an average compressive stress is not harmful to the material.

This projected average quantity, σ_n, is equal to:

$$\sigma_n = (\cos\phi)^2 [\sigma_1(\cos\psi)^2 + \sigma_2 (\sin\psi)^2] + \sigma_3 (\sin\phi)^2$$

where σ_1, σ_2, and σ_3 are the principal stresses, ϕ is the azimuthal angle, and ψ the polar angle for the unit sphere, as seen in **Fig. 6**. The equivalent uniaxial stress is then given by

$$\overline{\sigma_n^m} = \frac{\int_A \sigma_n^m dA}{\int_A dA}$$

where dA is an elemental area on the reference sphere of unit radius.

The failure probability, P_F, is then given by:

$$P_{fV} = 1 - exp\left[-\int_V k_{wpV}\, \overline{\sigma_n^m} dV\right]$$

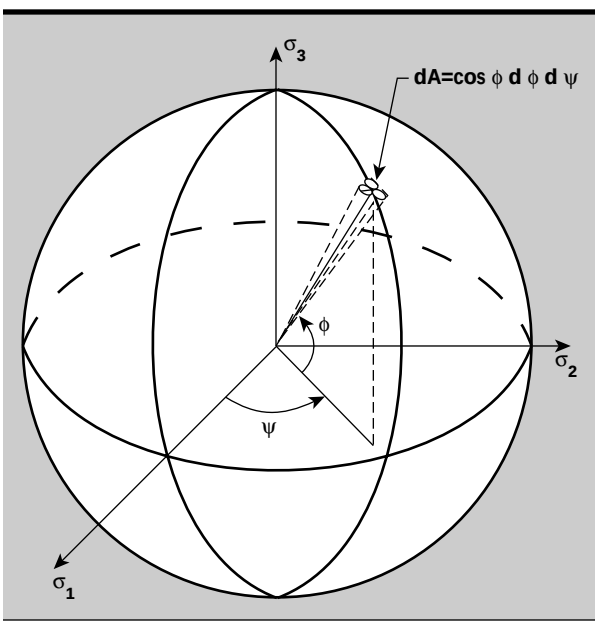

Figure 6. Angle definition for calculation of the Weibull averaged normal stress.

where dV is a differential volume in the specimen over which the principal stresses are approximately constant. In the preceding equation, m is the Weibull modulus as before, and k_{wpV} is the polyaxial Weibull crack density coefficient. The relationship between k_{wV} and k_{wpV} is found by equating the failure probability for uniaxial loading to that obtained for the polyaxial stress state when the latter is reduced to a uniaxial condition.[1] The result is

$$k_{wpV} = (2m+1)\, k_{wV}.$$

These integral equations can be replaced with a discrete expression suitable for implementation in a numerical algorithm on a computer:

$$\int_0 \int_{-\pi/2} (\sigma_n)^m \cos\phi \, d\phi \, d\psi = \sum \sum (\sigma_n)^m \cos\phi \, \Delta\phi \, \Delta\psi$$

where the functions $\cos\phi$ and σ_n are evaluated at $\phi = -\pi/2 + (j-1)\Delta\phi$ and $\psi = (i-1)\Delta\psi$.

These expressions have been incorporated into a version of NIKE2D. The results of these efforts are currently being verified.

References

1. N. N. Nemeth, J. M. Mandersheid, and J. P. Gyekenyesi (1990), "Ceramic analysis and reliability evaluation of structures (CARES) users and programmers manual," NASA TP-2916, National Aeronautics and Space Administration.

2. W. Weibull (1951), "A statistical distribution function of wide applicability," *ASME J. of Appl. Mech.*, September, pp. 293–297.

3. E. Y. Robinson (1964), "Some theoretical and experimental aspects of design with brittle material," Lawrence Livermore National Laboratory, Livermore, California (UCRL-7729), August 3.

4. P. Kittl and G. Diaz (1988), "Weibull's fracture statistics, or probabilistic strength of materials: state of the art," *Res Mechanica* **24**, pp. 99–207.

5. T. L. Anderson (1995), "Fracture mechanics: fundamentals and applications," 2nd Edition, CRC Press, p. 292.

6. R. O, Ritchie, J. F. Knott, and J. R. Rice (1973), "On the relationship between critical tensile stress and fracture toughness in mild steel," *J. of the Mechanics and Physics of Solids*, Vol. **21**, pp. 395–410.

7. J. W. Hutchinson (1968), "Singular behavior at the end of a tensile crack tip in a hardening material," *J. of the Mechanics and Physics of Solids*, Vol. **16**, p. 13.

8. Auen-Stienstra, D. I. (1990), "Stochastic micromechanical modeling of cleavage fracture in the ductile-brittle transition region," Texas A&M Dissertation, August, p. 99.

9. American Society for Testing and Materials, "ASTM C-1161-94, Standard Test Method for Flexural Strength of Advanced Ceramics at Ambient Temperature," 1994, Philadelphia, Pennsylvania.

10. American Society for Testing and Materials, "ASTM C-1239-94a, Standard Practice for Reporting Uniaxial Strength Data and Estimating Weibull Distribution Parameters for Advanced Ceramics," 1994, Philadelphia, Pennsylvania.

11. D. C. Cranmer and D. W. Richerson (1998), "Mechanical testing methodology for ceramic design and reliability," Marcel Dekker, New York, New York.

12. S. D. Duffy and E. H. Baker (1997), "Weibull parameter estimation: theory and background information," CRT Technologies, November.

13. Military Handbook, MIL-HDBK-790, March 1993, Information Handling Services, DODSTD Issue DW9805.

14. O. Vardar and I. Finnie (1975), "An analysis of the Brazilian disk fracture test using the Weibull probabilistic treatment of brittle strength," *Int. J. of Fracture*, Vol. **11**, No. 3, June, pp. 495–508.

Lattice Boltzmann Modeling of Spherical Solutes in Confined Domains

David S. Clague
Electronics Engineering Technologies Division
Electronics Engineering

The primary aim of this effort is to develop a unique lattice Boltzmann (LB) simulation capability to understand the dynamic behavior of macromolecules, cells, and spores in bounded flow domains. The proposed effort for FY-99 included benchmark studies with spherical solutes to verify the utility and accuracy of the LB method. These studies include calculating the hydrodynamic force and torque acting on a stationary, spherical particle in bounded flows and calculation of the hydrodynamic force acting on a mobile particle in the presence of a stationary wall. This year's results show that the LB accurately solves these non-trivial flow problems. Selected results for stationary and mobile macroparticles are presented. An additional milestone that was achieved ahead of schedule is that the 2- and 3-D LB codes with macroparticles are now parallel.

Introduction

Many fluid-based processes used, for example, in the chemical and pharmaceutical industries, involve the transport of nanometer-to-micron sized particles in confined flow domains. To augment the design process and to better understand the fundamental behavior of particles in such systems, one needs to be able to model and simulate the flow field, the mechanisms for transport phenomena associated with charged, polar particles in the presence of electric fields, and the other relevant force interactions. In the work presented here, the LB method was chosen to solve these complex problems.

As opposed to more traditional continuum methods, such as Boundary Element and Finite Element methods, the LB method is a mesoscopic approach. Specifically, when using this approach, one keeps track of the single-particle velocity distribution function on a regular mesh of lattice sites. This approach derives from the Boltzmann transport equation, which is the conservation equation found in the kinetic theory of gases.[1] Under the appropriate flow conditions, for example, small Mach and Knudsen number flows, the LB method accurately captures the hydrodynamic behavior of viscous fluids.[2,3] Additionally, because the approach is discrete, it can easily handle bounding walls, mobile particles, external fields, and finite Reynolds numbers.

Another convenient feature of the LB method is that fluid velocity disturbances are transmitted locally from lattice site to lattice site. As a consequence, the *fluid phase* is easily parallelizable relative to the conventional methods such as finite element methods.

Progress

The selected results presented here include calculating the hydrodynamic force acting on an infinite medium of equispaced stationary spheres, a stationary sphere in a bi-periodic simulation cell with bounding walls at the top and bottom of the flow cell, and a single sphere translating in direct approach toward a stationary planar surface. The results presented were calculated using a parallel LB code developed during FY-99. The parallelization includes both the fluid phase and the particulate phase. All simulations were performed on multiprocessor machines using MPI. Simulations were conducted on local Dec Alpha clusters and on an IBM SP2 machine with multiple processors.

The benchmark studies on stationary or captured macroparticles produced interesting results. Specifically, when passing a flow through an infinite medium of stationary periodic spheres, the force on the test sphere increases with increasing solids fraction. **Fig. 1** shows the unit cell that gets replicated throughout space forming an infinite medium of equally spaced spheres.

As shown, the hydrodynamic drag force calculated using the LB method is nearly identical with the well-accepted result of Zick and Homesy.[4] Also, it is important to note that the drag force increases with increasing solids fraction. In contrast, when placing the sphere in a flow channel bounded at the top and bottom with parallel walls, the drag force decreases as the solids fraction is increased. **Figure 2** shows a sphere of radius a bounded by parallel walls separated by distance H. Also shown are the upstream and downstream periodic images of the central sphere.

The result shown in **Fig. 2** shows the opposite trend in drag force as was seen in **Fig. 1**. For example, the hydrodynamic drag force decreases as the spheres are brought closer together, or for increasing solids fraction. As shown, it is necessary to separate the periodic spheres by a minimum of 30 sphere radii to ensure that the central sphere is hydrodynamically de-coupled from its neighbors. The flow system depicted in **Fig. 2** is very much like particle capture apparatus used in many flow systems that contain particulates; hence, the result presented here can be used to calculate the hydrodynamic force acting on capture macroparticles in an actual flow cell.

Essentially, the observed difference between the drag force shown in **Figs. 1** and **2** has two explanations. First, for the flow configuration in **Fig. 1**, the fluid flux area between periodic spheres decreases with increasing solids fraction which in turn increases the drag force for a constant pressure gradient. In contrast, the fluid flux area for the flow configuration in **Fig. 2** is constant for all solids fractions; hence, there is no change in the bulk fluid velocity with change in solids fraction. The second reason that the drag force in **Fig. 2** decreases with increasing solids fraction is a form of "drafting." More specifically, the fluid velocity disturbance caused by the upstream sphere does not recover to the bulk fluid velocity before it encounters the next neighboring downstream sphere. Others have observed this same "drafting-like" phenomenon in sedimentation problems at low Reynolds numbers.

The final result presented here is for a sphere translated at constant velocity in direct approach to a stationary wall (**Fig. 3**).

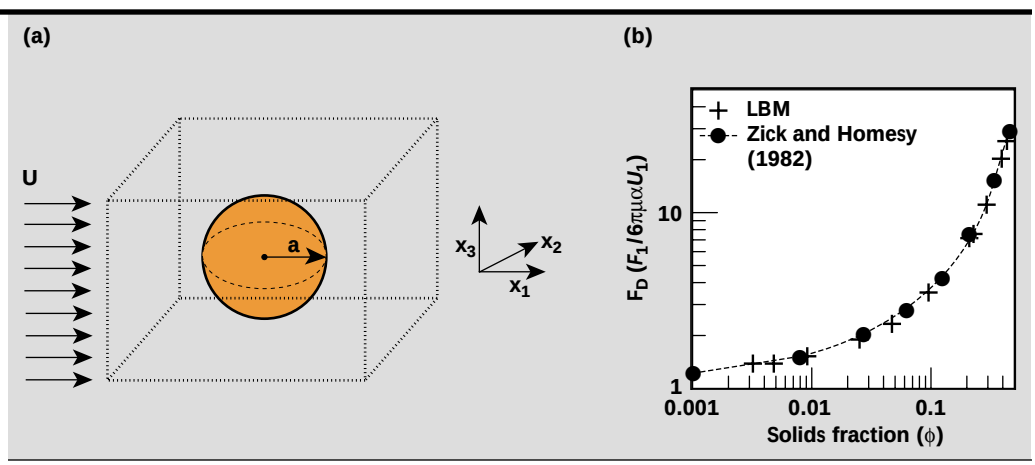

Figure 1. Hydrodynamic drag force acting on a periodic array of spheres. (a) Flow configuration. (b) Comparison of drag force calculated using the LB method with the well-accepted result of Zick and Homesy.

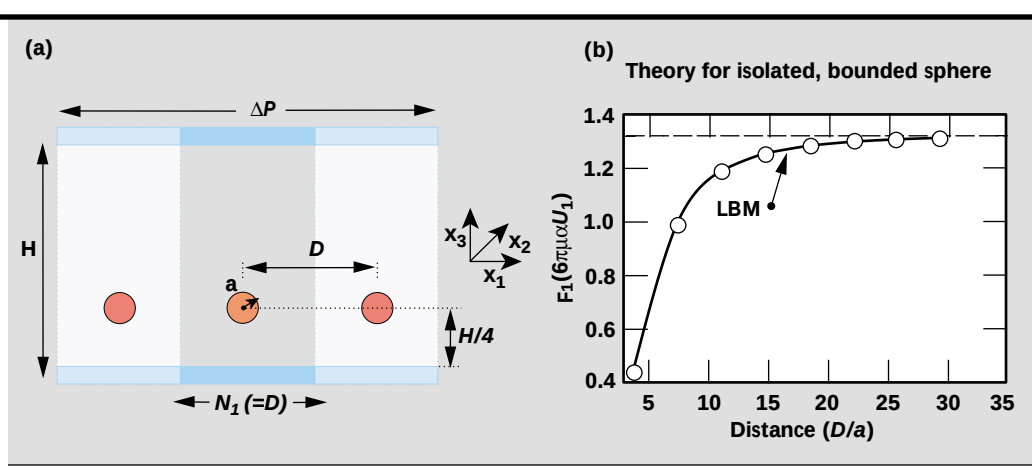

Figure 2. (a) Hydrodynamic force acting on a stationary spherical body in Poiseuille flow. (b) Hydrodynamic drag force acting on the central sphere as a function of the number of sphere radii between the central sphere and the nearest periodic neighbor.

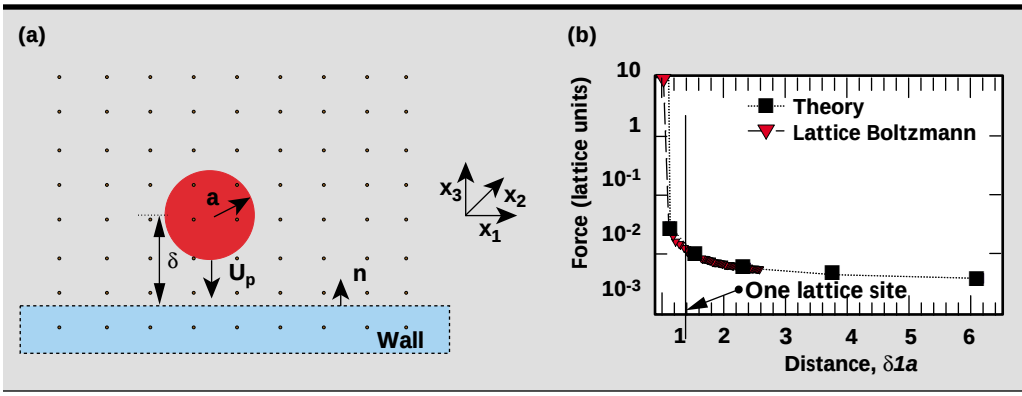

Figure 3. (a) Sphere of radius a at a sphere-wall separation of δ approaching the wall with constant velocity, U_p, in an otherwise quiescent fluid. (b) The LB results are in agreement with theory over the entire range of sphere-wall separations considered.

The LB results are in excellent agreement with theory even at infinitesimal sphere-wall separations. This demonstrates that the LB approach accurately captures hydrodynamic interactions for mobile macroparticles.

In addition to the selected results presented above, the LB simulation capability has also been used successfully to study fluid behavior for flow through conduits with irregular cross-sectional geometry. Furthermore, simulations are in progress to study the behavior of a single macroparticle in Poiseuille flow in bounded conduits. Work is also in progress to include external fields such as gravitational and electromagnetic fields in the parallel LB codes.

Future Work

The LB simulation capability has developed into a useful predictive tool. The work for this coming year will include validation of the LB method with experimental results and inclusion of new physics relevant to laboratory needs. The validation studies will include the study of suspension behavior in rectangular conduits and particle capture due to external fields.

In FY-00, intermolecular force will be included in the LB simulation capability and the resulting suspension behavior will be studied.

References

1. Landau and Lifshitz (1989), "A course of theoretical physics, Volume 10," Pergamon Press.

2. D. S. Clague, *et al*. "On the hydraulic permeability of (un) bounded fibrous media using the lattice Boltzmann method," submitted to *Phys. Rev. E.*

3. D. S. Clague (1998), "Lattice Boltzmann simulation of complex fluids," *Engineering Research, Development and Technology*, Lawrence Livermore National Laboratory, Livermore, California (UCRL-53868-98).

4. A. A. Zick and G. M. Homesy (1982), "Stokes flow through periodic arrays of spheres," *J. Fluid Mech.* **115**, 13.

Modeling of Anisotropic Inelastic Behavior

Daniel J. Nikkel, Jr. and Deepak S. Nath
New Technologies Engineering Division
Mechanical Engineering

Arthur A. Brown and James Casey
University of California at Berkeley
Berkeley, California

An experimental capability, developed at Lawrence Livermore National Laboratory (LLNL), is being used to study the yield behavior of elastic-plastic materials. The objective of our research is to develop better constitutive equations for polycrystalline metals. We are experimentally determining the multidimensional yield surface of the material, both in its initial state and as it evolves during large inelastic deformations. These experiments provide a more complete picture of material behavior than can be obtained from traditional uniaxial tests. Experimental results show that actual material response can differ significantly from that predicted by simple idealized models. These results are being used to develop improved constitutive models of anisotropic plasticity for use in continuum computer codes.

Introduction

At a microstructural level, polycrystalline metals are composed of aggregates of individual crystals, each of which has its own orientation and properties. When subjected to loading, metals initially exhibit reversible deformation, due to the stretching of the lattice. When the loads become sufficiently large, permanent deformations can occur through a number of mechanisms, such as dislocation motion, twinning, or grain boundary sliding. As a consequence of having randomly distributed grain orientations, annealed polycrystalline metals typically exhibit isotropic behavior with respect to a reference configuration; that is, at a given point in the material, the material response of a specimen in any direction is the same. This includes the elastic behavior and the initial yield behavior. However, significant processing of materials, or even moderate plastic deformations, can cause grains which were initially randomly oriented to become aligned, resulting in behavior which is anisotropic, where material response in different directions is quite different.

The ability of numerical simulations to predict the behavior of systems involving materials undergoing large deformations is contingent upon having a realistic model of the material behavior. Such models must be accurate in the full range of possible loading conditions to which the materials may be subjected. Use of overly simplified models in regimes where they are not well suited can seriously compromise the validity of a simulation. Many problems of engineering interest involve metals undergoing large deformation under multiaxial states of stress and the need for reliable models for these applications can hardly be overemphasized. Experimental data demonstrate that simple models for plasticity commonly used in numerical codes do not accurately predict material behavior under these conditions.

Engineering models of polycrystalline metals generally omit microstructural details and describe the effective macroscopic behavior in terms of a phenomenological continuum model. Viewed from the macroscopic perspective, the initial material response is path-independent and there is a one-to-one correspondence between stress and strain. However, if the deformation or loads become sufficiently large, the material begins to exhibit plastic behavior. There is no longer a one-to-one correspondence between stress and strain, the response is dependent on the loading path taken to reach a given state of deformation, and permanent deformation

remains after external loads are removed. This gives rise to the theoretical idealization of an elastic-plastic material, and in particular, to the notion of a yield function[1] denoted by

$$f(s_{kl}, e^p_{kl}, \kappa, ...) = g(e_{kl}, e^p_{kl}, \kappa, ...) \ . \qquad (1)$$

Here, s_{kl} denotes the components of the stress tensor; e_{kl} denotes the components of the strain tensor; e^p_{kl} denotes the components of the plastic strain tensor; κ is a scalar measure of work hardening; and the ellipses represent other inelastic state variables which may be present, depending on the complexity of the chosen constitutive theory.

The yield function is a key ingredient of the constitutive theory of elastic-plastic materials. The condition $f = 0$ (or $g = 0$) describes the boundary between stresses (or strains) that result in only elastic behavior, and those which result in inelastic behavior. For fixed values of the inelastic variables, the yield condition can be interpreted geometrically from the point of view of stress space (or strain space), as a surface which bounds the region in which only elastic behavior occurs (the elastic region). When the loading path intersects the yield surface and tries to cross it, inelastic behavior occurs and plastic deformation results. The current state never moves outside the yield surface, but instead the surface is carried along with it. Typically, the yield surface changes both in shape and size as the inelastic deformation increases. Measured yield surfaces for three of the states along the complex stress path depicted in **Fig. 1a** are shown in **Fig. 1b**.

In addition to the yield function, the constitutive theory includes evolution equations for the inelastic variables during loading ($g = 0, \hat{g} > 0$). Thus, for the plastic strain, we have

$$\dot{e}^p_{kl} = \rho_{kl}(e_{mn}, e^p_{mn}, \kappa, ...)\hat{g} \ , \quad \hat{g} \equiv \frac{\partial g}{\partial e_{mn}} \dot{e}_{mn} \ . \qquad (2)$$

Here ρ_{kl} is a constitutive response function that is independent of the rates of stress or strain. For a broad class of materials, under a physically reasonable assumption regarding work in closed cycles in strain space, ρ_{kl} can be replaced with the product of a scalar function and the normal to the yield surface in stress space, thus requiring the specification of only one additional scalar response function.[1] For special classes of materials, this scalar function is determined from the yield function and hardening and does not require an independent specification.

Most plasticity models implemented into numerical codes for metals use a yield criterion which corresponds to a fixed shape of the yield surface (for example, elliptical in the case of the Mises yield criterion). What distinguishes different models is how the yield surface evolves (for example, it may translate rigidly, or alternatively change its size while maintaining its shape, or follow some combination of these simple hardening laws). Many simulations are run with a model that assumes an elliptic yield surface of fixed aspect ratio that only changes in size due to hardening. While the initial yield surface of isotropic materials may be represented reasonably well by an ellipse, subsequent to even moderate plastic deformation, the shape of the yield surface in real materials can change significantly (**Fig. 1b**). For this reason, simple representations of the yield function will be satisfactory only under very restrictive loading conditions (such as monotonic or uniaxial), and are inadequate for general multiaxial loading conditions, especially

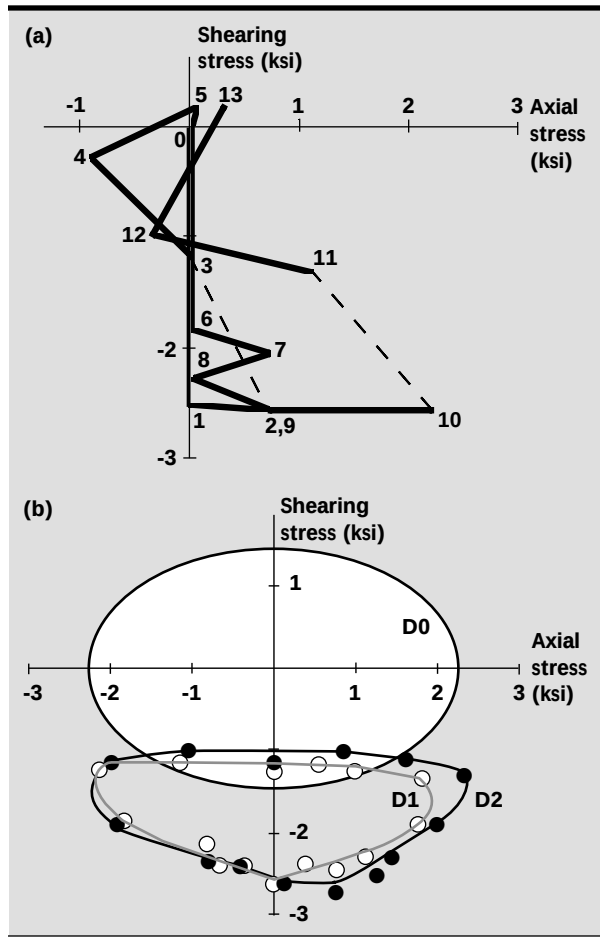

Figure 1. (a) Imposed sequence of loading states for yield surface measurement on a single specimen, identified as "D" in Table 1. (b) Measured points on yield surfaces in 2-D stress space from a single 1100 aluminum specimen subjected to the loading states in Fig. 1a. For clarity, only the surfaces measured at load states 0, 1, and 2 in Fig. 1a have been shown. The subsequent yield surfaces show significant deviation from an idealized ellipse even though the strains involved are moderately small.

when loads can reverse and change direction during the history of loading.

In view of these considerations, and motivated by the fact that the vast majority of available experimental data on polycrystalline metals are for uniaxial (and generally monotonic) loading, our group developed an experimental capability to map out the yield surface at various fixed states of large inelastic deformation under multiaxial loading. By determining the yield surfaces on a single specimen at multiple fixed states, the evolution of the yield surface during plastic deformation can be observed. These data provide the basis for developing improved constitutive equations for phenomenological descriptions of polycrystalline metals.

Progress

This project is a combination of a program of novel experiments characterizing inelastic material behavior together with an effort to develop better material models for implementation into numerical analysis codes. The primary approach has been to obtain improved experimental data for the macroscopic response as a guide to the development of better phenomenological models. During FY-99, we have further refined the experimental procedures developed in previous years, and have obtained some important new data.

In addition to this direct macroscopic approach, we have begun to examine the alternative strategy of incorporating information from lower length scales where explicit consideration is taken of material microstructure, and we have also begun to explore how this mesoscale description can be homogenized to obtain improved macroscopic models.

Further, work on general issues related to numerical implementation of anisotropic plasticity models has been pursued, in the context of both purely Lagrangian and arbitrary Lagrangian-Eulerian (ALE) formulations.

Experiments

The experimental portion of this project involves determination of the yield surface under multiaxial states of loading, using thin-walled tension-torsion specimens with a 2-in. inside diameter. The experimental determination of the yield surface of the material is carried out by loading a specimen under multiaxial conditions and probing until the point of yield is reached, then backing off and probing in a different direction in stress space (and in strain space) until the next yield point is found. This process is repeated until the entire surface is mapped out. The sensitive nature of the measurements being made requires careful attention to the issues of specimen design and preparation, experimental methodology, and interpretation of the data. The general description of the experiments and the difficulty in carrying out these measurements have been discussed previously,[2,3] and this year a comprehensive description of the experimental procedure has been compiled.[4]

Ideally, a measured yield surface represents the boundary between elastic and inelastic behavior at a given elastic-plastic state. As a practical matter, the identification of the yield point requires loading somewhat beyond the elastic region so that the inelastic behavior becomes evident. The procedure which has been developed can detect yield without producing a plastic strain much greater than 5×10^{-6} (5 μ-strain), and yield surfaces can be obtained for multiple elastic-plastic states from a single specimen. It is clear from the data that the yield surfaces determined from multiaxial loading tests are strongly dependent on the method used to identify the yield point. Many different definitions of the yield point are possible; these vary in both experimental complexity and in the amount of plastic deformation that is induced during the determination of yield at a given point. The measured yield surfaces can vary from appearing roughly isotropic when a coarse large off-set or back-extrapolation method is used, to clearly exhibiting material anisotropy when a small off-set definition of yield is used (**Fig. 1b**). The definition of yield point is related to the idealized way in which the theoretical model represents real material behavior. These issues are discussed more fully elsewhere.[4] After investigating various alternatives, we adopted a 5 μ-strain offset definition of yield as the most meaningful for our current interests.

In addition to generating data from the measurement of yield surfaces, we are also exploring the fundamental question as to the proper definition of plastic strain in the context of large inelastic deformations.[5,6] When yield surfaces have moved so that they no longer enclose the origin in stress space (for example, yield surfaces D1 and D2 in **Fig. 1b**), the material cannot be unloaded to zero stress without causing new plastic deformations.

The traditional way of defining plastic strain is to identify it with the residual strain remaining when the load is removed. This definition arose intuitively from consideration of uniaxial tests with small deformation, but it is clearly inadequate in the situation of more general states of loading where the yield surface no longer encloses the origin in stress space. Plastic strain is not among the set of kinematic

variables that come from classical continuum mechanics. Since it is a primitive variable in the constitutive theory, one must be able to identify it unambiguously for the theory to be meaningfully predictive and not simply a sophisticated curve-fit.

Previously, an experimental methodology was proposed for verifying the validity of our prescription for identifying plastic strain, in cases where the origin lies outside the stress space yield surface. It is defined as the point in strain space corresponding to the point on the yield surface in stress space closest to the origin.[5,6] This method exploited the property from **Eq. 2** that the direction of the increment in plastic strain is independent of the size and direction of an applied increment in stress or strain. By comparing the directions of the plastic strain increment for two different loading directions originating from the same state, the prescription can be verified. The high precision necessary to be able to make the measurements required for this verification was a driving force governing the refinement of experimental procedures. Three different verifications (requiring the determination of six distinct yield surfaces) have been completed which do in fact validate this prescription for identifying plastic strain.

Characterization of Experimental Results

One consistent observation in the experimental data with a 5 μ-strain off-set definition of yield (such as in **Fig. 1b**) is a distortion of the shape of the yield surface after moderate plastic deformation when loading away from the origin. The initial yield surface is close to elliptical in shape. For subsequent yield surfaces, the side away from the loading point (and closest to the origin) tends to flatten, while it tends to elongate near the loading point, resulting in a D-shaped surface. There are classical closed curves, such as the folium, the piriform, and the pear-shaped quadric, that are somewhat D-shaped.[7] However, after some effort it was found not possible to use these functions to represent the data in a robust manner. An alternative approach to using a single analytical function to represent the yield surface in two dimensions is to approximate it with a collection of smooth intersecting segments. As a curve-fitting scheme this approach is capable of matching a given set of data with any desired degree of accuracy, but such a representation provides little physical insight towards the development of improved models. Moreover, describing yield surface evolution in a general way becomes problematic, and it also presents difficulties in terms of numerical implementation.

To characterize the data, and to give some direction to the development of improved models, "best fits" to the data were performed with polynomial functions representing closed curves. Even for quadratic polynomials this is a nontrivial exercise. In the usual routine task of fitting a function to discrete *x-y* data, an error function is defined and the unknown coefficients are determined by minimizing the error. The resulting system of equations is linear and a unique solution is guaranteed.

For the problem at hand, however, the data pairs (x_i, y_i) cannot be approximated by an explicit function of the form $y = f(x)$; rather they must be represented by implicit functions of the form $f(x,y) = 0$. To fit an implicit function to the data, an error function is defined as usual, but the system of equations that must be solved to determine the unknown coefficients is highly nonlinear and there is no guarantee of uniqueness as in the linear case. Solving the system of nonlinear equations numerically is a complex undertaking requiring sophisticated solution techniques.

Quadratic fits to all the data sets were obtained by using a package for orthogonal distance regression, ODRPACK, which is publicly available from NIST[8] **(Fig. 2)**. The program finds the parameters that minimize the sum of the squared weighted orthogonal distances from a set of observations to the curve or surface determined by the parameters. This procedure provided a method of characterizing the data in terms of change in position, size, and orientation of subsequent yield surfaces. Results of the data reduction for various measured yield surfaces are shown in **Table 1**. A second-order polynomial is sufficient for gauging the size, location, and some sense of the "orientation" of the yield surface, but it cannot adequately represent features such as relative elongation and flattening of the yield surface. Higher order

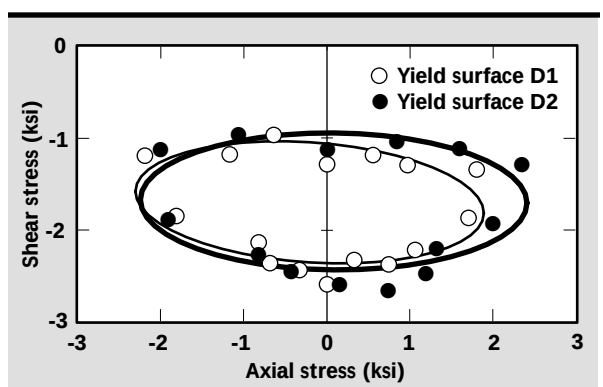

Figure 2. Second-order polynomial fits to yield surface data. Quadratic functions can capture the trends in size, location and some sense of orientation, but provide no characterization of the distortion into the observed D-shapes.

function fits could likely provide better representations of the D-shaped data curves, but ODRPACK was unable to give reliable fits in a unique, robust manner.

Numerical Modeling

The Mises yield condition, which is a quadratic polynomial in the deviatoric stress components, is known to agree well with experimental data on annealed (isotropic) polycrystalline metals, and it also has a physically appealing interpretation in terms of distortion energy. For anisotropic materials, the most general quadratic yield function representing a smooth initial yield surface which reduces to the Mises yield function in the special case of isotropic materials is of the form[9]

$$f = B_{klmn} s_{kl} s_{mn} - \kappa^2 , \tag{3}$$

where due to symmetries the coefficients B_{klmn}, have 21 independent components. If, as is commonly done, the further assumption is made that the yield behavior is independent of the mean stress (pressure), then the stress tensor in **Eq. 3** can be replaced by its deviatoric part and the coefficient tensor can be replaced by a reduced tensor which has 15 independent coefficients. As mentioned previously, a quadratic representation of the yield surface can reasonably capture its location, size, and a sense of the orientation observed in real materials, but it does not capture the distortion of the yield surface from elliptical to D-shaped. Nevertheless, **Eq. 3** is much more general than the Mises yield function, and it contains as special cases other anisotropic yield models which have been implemented into LLNL codes.

An anisotropic plasticity model with the yield function in **Eq. 3** was implemented into the parallel version of the code ALE3D. **Figure 3** shows a Lagrangian numerical simulation of a Taylor impact test using an anisotropic tantalum cylindrical projectile. The predicted ovaling of the impact footprint is in agreement with experimental data.[10]

Since a basic feature of anisotropic behavior is that the response depends on the material direction, it is necessary to track material directions during deformation. While this is a straightforward issue within a Lagrangian formulation, implementation of anisotropic plasticity models in the context of an ALE formulation is complicated by the fact that nodes of a mesh are not material points, and the element edges are not material curves. An alternative approach must be used to keep track of material directions. Material direction vectors m_i can be stored as element-based variables, and can then be updated during the Lagrangian step according to

$$\dot{m}_i = (L_{ij} - (L_{kl} m_k m_l)\delta_{ij}) m_j , \tag{4}$$

where L_{ij} are the components of the velocity gradient tensor. These element-based quantities can then be updated as other history variables during the advection step. There are increased memory storage costs associated with modeling anisotropic plasticity. Along with storing the material direction vectors and any additional constitutive variables, properly invariant formulations of anisotropic

Table 1. Characteristics of yield surface data obtained from quadratic fits. The yield surface designation comes from a specimen identification letter and a state number.

Yield surface	Offset Def. (μ-strain	e^p_{11} (μ-strain)	e^p_{12} (μ-strain)	Center (psi)	Orientation angle (°)	Subaxis 1 (psi)	Subaxis 2 (psi)	Aspect ratio
A1	15	300	0	(857, –57)	29.8	1250	1460	0.86
A2	15	8690	7128	(871, 947)	–16.3	3000	1380	2.17
B0	1	0	0	(–87, 94)	3.91	1770	1060	1.67
B1	1	1	–17	(–11, –263)	2.23	1840	890	2.07
B2	1	92	–2055	(37, –1809)	–1.12	1550	370	4.19
C1	1	–4578	102	(–3425, 114)	24.7	770	1170	0.66
C2	1	–5008	234	(–3713, 82.4)	40.4	640	1050	0.61
D1	5	5	–2020	(–209, –1698)	–7.2	2230	650	3.43
D2	5	30	–2100	(80, –1698)	–0.9	2330	750	3.11
D4	5	30	–2010	(84, –1230)	–3.3	2610	770	3.39
D10	5	1030	–3660	(1250, –1918)	14.0	2380	670	3.55
D12	5	990	–3560	(1145, –1459)	26.0	2570	1070	2.40

models also require storing additional kinematical quantities such as the rotation and stretch tensors.

Alternative Approaches Using Mesoscale Homogenization

The approach described earlier seeks to develop a macroscopic phenomenological model directly from measurements of the macroscopic inelastic behavior. An alternative strategy is to examine the governing processes in terms of microphysical behavior at lower length scales, and then to deduce a model for the effective macroscopic behavior through an appropriate averaging, or homogenization, procedure.

Working toward a theoretical approach to homogenization, using a variational principle, and in the context of strain gradient crystal plasticity, we developed a new upper bound for the effective yield surface of a polycrystal.[11] This procedure uses one- and two-point correlation functions of the orientation distribution. This bound demonstrates a grain size effect via its dependence on the polycrystal's spatial and orientation distribution statistics. It can be shown that this bound almost always improves upon the Taylor model bound.

It is also possible to approach the homogenization from the point of view of numerical simulations using a so-called *virtual test sample*. A representative volume element of material can be modeled in which individual grains are explicitly resolved, and represented by a single-crystal plasticity model. Such a numerical test sample can be used to simulate the macroscopic behavior under a wide variety of loading conditions, guiding the development of a macroscopic phenomenological model. In preparation for this approach, detailed orientation imaging microscope (OIM) scans have been made at regular depths through a carefully prepared tantalum specimen, mapping out the orientation of individual grains (**Fig. 4**). From this detailed database a 3-D numerical model can be generated which accurately represents the real microstructure of the material. This numerical model can then be subjected to a variety of loading conditions, and the effective macroscopic behavior predicted. The yield surface data that has been generated can be used as a validation check for both theoretical and numerical homogenization methodologies.

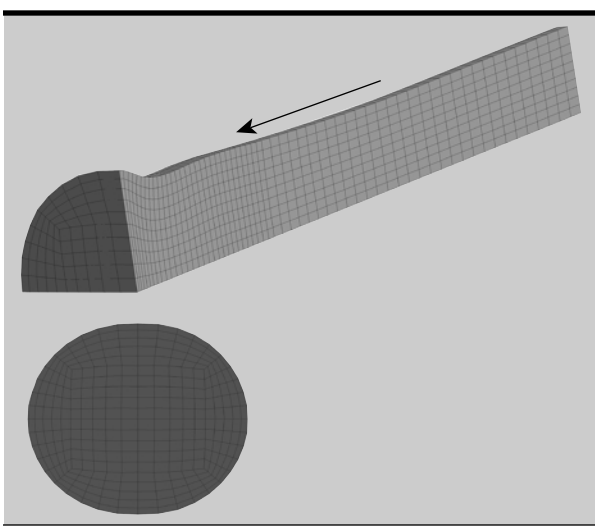

Figure 3. Numerical simulation of a Taylor impact test of an anisotropic tantalum circular cylinder exhibiting ovaling of the impact footprint. For isotropic material properties, the cylinder would expand axisymmetrically at the impacting end. The calculation agrees with experimental results.

Future Work

This project has produced an experimental capability that provides multiaxial data, which can be used to develop and validate advanced constitutive models. We have also established a solid framework from which to pursue numerical developments of anisotropic plasticity. From this foundation, further developments will continue, focusing on the development of improved material models for ASCI codes.

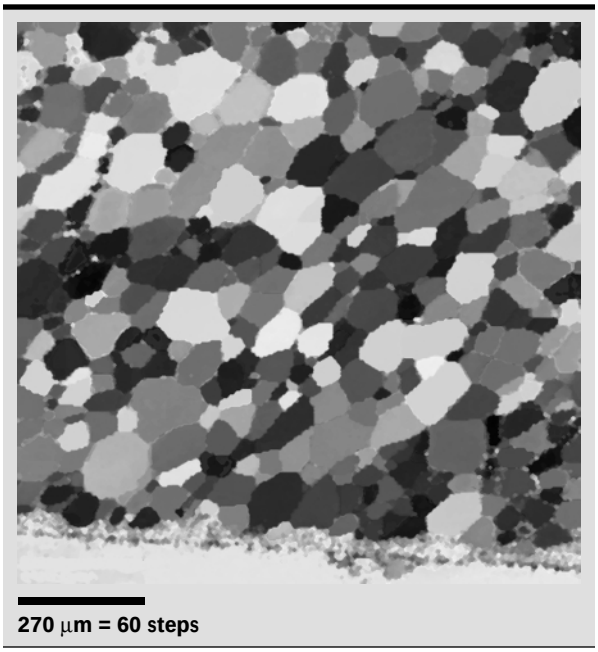

Figure 4. Orientation Imaging Microscope scan of one plane of a well-characterized tantalum polycrystal. The shading indicates particular crystal orientation. Similar scans, at a sampling resolution of 4.5 μm, have been made at 47 planes through the sample. From these data a 3-D numerical model can be constructed representing the microstructure.

Acknowledgments

Contributions to this project by J. Casey result from work supported by a grant from the Solid Mechanics Program of the National Science Foundation. Part of the support for A. Brown's work, and material used during the development of the experimental procedure, were also provided through this grant.

References

1. P. M. Naghdi (1990), "A critical review of the state of finite plasticity," *J. Appl. Math. Phys. (ZAMP)*, **41**, pp. 315–394.

2. D. J. Nikkel, A. A. Brown, and J. Casey (1998), "Evolution of anisotropic yield behavior," *Engineering Research, Development and Technology*, Lawrence Livermore National Laboratory, Livermore, California (UCRL53868-97), pp. 5-1–5-5.

3. D. J. Nikkel, A. A. Brown, and J. Casey (1999), "Modeling of anisotropic inelastic behavior," *Engineering Research, Development and Technology*, Lawrence Livermore National Laboratory, Livermore, California (UCRL 53868-98), pp. 6-1–6-6.

4. A. A. Brown, and D. J. Nikkel (1999), "Experimental methodology for yield surface measurement under biaxial states of stress," Lawrence Livermore National Laboratory, Livermore, California, in preparation.

5. J. Casey and P. M. Naghdi (1992), "A prescription for the identification of finite plastic strain," *Int. J. Engng. Sci.*, **30**, pp. 1257–78.

6. J. Casey, and P. M. Naghdi (1992), "On the identification of plastic strain at finite deformation," in *Defects and Anelasticity in the Characterization of Crystalline Solids*, L. M. Brock, ed., ASME AMD Vol. **148**, pp. 11–33.

7. J. D. Lawrence (1972), *A Catalog of Special Plane Curves*, Dover, New York.

8. P. T. Boggs, R. H. Byrd, J. E. Rogers, and R. B. Schnabel (1992), "User's reference guide for ODRPACK version 2.01: software for weighted orthogonal distance regression," U. S. Department of Commerce, (NISTIR 92-4834).

9. A. E. Green and P. M. Naghdi (1965), "A general theory of an elastic-plastic continuum," *Arch. Rat. Mech. Anal.*, **18**, pp. 251–281.

10. P. J. Maudlin, J. F. Bingert, J. W. House, and S. R. Chen (1999), "On the modeling of the Taylor cylinder impact test for orthotropic textured materials: experiments and simulations," *Int. J. Plasticity*, **15**, pp. 139–166.

11. D. D. Sam and V. P. Smyshlyaev (1999), "Grain size effect for the polycrystal's yield surface in strain gradient plasticity," in preparation.

Development of Laser-Driven Photocathode Injector and Femtosecond-Scale Laser Electron Synchronization for Next Generation Light Sources

Gregory P. Le Sage
Defense Sciences Engineering Division
Electronics Engineering

Thomas E. Cowan
Physics and Space Technology

Todd R. Ditmire
Laser Science and Technology
Laser Programs

J. Rosenzweig
University of California at Los Angeles
Los Angeles, California

A high brightness photoinjector has been developed at Lawrence Livermore National Laboratory (LLNL). This injector, combined with the 100-TW FALCON laser, and the existing LLNL 100-MeV S-Band RF linac will enable development of a high brightness, femtosecond-scale, tunable, hard x-ray probe for time-resolved material measurements. A low emittance electron beam synchronized with femtosecond accuracy to an intense laser will revolutionize x-ray dynamics studies of materials. This project will lead development of ultrafast x-ray dynamics research on problems important in physics, chemistry, biology, and materials science. Precise diagnostics for measurement of relativistic electron beams have also been developed.

Introduction

Short pulse x-rays enable time-resolved characterization of shock dynamics, and examination of materials under extremes of pressure and temperature. Examples include equation-of-state characterization on high-density materials, crystal disorganization and re-growth in shocked and heated materials, and measurement of short time scale phase transition phenomena. Single shot evaluation, requiring high peak flux, is important for complex experiments such as probing of laser-shocked actinides.

Our photoinjector project enables the development of a high brightness, femtosecond-scale, tunable, hard x-ray probe for time-resolved material measurements.

The x-ray pulse intensity will be five orders of magnitude higher than previous demonstration experiments, extending the range of applicability beyond repetitive solid-state applications. Success of this project will place LLNL at the forefront of ultrafast x-ray dynamics and establish a world class electron beam dynamics research program.

The key goals of the photoinjector include development of a photoinjector integrated with the LLNL RF linac, and implementation of techniques to synchronize the photoinjector with an RF linac and the high power FALCON laser system. New techniques have been proposed to meet the synchronization requirements of the system in its final configuration.[1] Characterization of the beam parameters and optimization of the laser-electron interaction will be accomplished using new diagnostic techniques developed at LLNL.[2,3]

Progress

Despite the highly ambitious goals and schedule, all milestones have so far been met or exceeded. A summary of first year accomplishments follows: (1) high-power RF system commissioned with 18 MW delivered to the photoinjector lab; (2) photoinjector cavity designed, cold tested, brazed, and installed with all specifications met or exceeded; (3) LLNL innovations, including HIP copper, diamond-turned cathode, and improved vacuum; (4) photoinjector test beamline designed and implemented, complete with optics and diagnostics; (5) UV laser system nearing completion; and (6) RF linac synchronized with the FALCON laser system.

Future Work

The first goals for FY-00 include synchronization of the photoinjector and FALCON laser, and continuing detailed characterization of the photoinjector beam. The low energy (4 to 5 MeV) electron beam and the FALCON laser will be used in the early part of FY-00 for Thomson scattering using the photoinjector independent of the RF linac. Photoinjector integration with the linac will follow these initial experiments. Additional experiments relating directly to high gradient accelerator science and technology, as well as advanced diagnostics will be performed with time permitting, and should lead to important publications.

The final product of this proposal enables an operational short pulse x-ray test-bed. Development of the photoinjector and integration with the linac also leads to a world class electron beam research program. The project will evolve into an ongoing program on shocked materials.

References

1. J. P. Rosenzweig and G. P. Le Sage (1998), "Synchronization of sub-picosecond electron and laser pulses," *AIP Conf. Proc.*, No. 472, 795–810.

2. G. P. Le Sage, T. E. Cowan, R. B. Fiorito, and D. W. Rule (1999), "Transverse phase space mapping of relativistic electron beams using optical transition radiation," submitted to *Phys. Rev., Special Topics, Accelerators and Beams*, September.

3. G. P. Le Sage and T. E. Cowan (1999), "A device for transverse mapping of divergence and energy for charged particle beams with arbitrary spatial profiles," Lawrence Livermore National Laboratory, Record of Invention 10561, July 5.

A Segment-to-Segment Sliding Interface Algorithm for DYNA3D

Jerry I. Lin
Defense Technologies Engineering Division
Mechanical Engineering

This report describes an interface algorithm focusing on the detection of interference among segments, instead of the traditional approach of nodes against segments. It is designed to treat the edge-to-edge contact between structures, but versatile enough to handle general contact/impact problems. This algorithm can be implemented to complement the existing sliding interface algorithms in DYNA3D or as a stand-alone sliding interface option.

Introduction

There are several sliding interface options available in the explicit finite-element code DYNA3D.[1] They are designed to address different contact/impact scenarios and are based on the detection of interference between a node and a segment. A segment in sliding interface terms usually means a shell/plate element or a facet of a volume element. Even for the contact options with both sides of the sliding interface defined by segment lists, DYNA3D internally sorts out the nodes associated with one segment list and checks against the other segment list. The node-to-segment approach hinges on the detection of the interference between a node trajectory within a certain period of time, usually a time step, and a given segment. The trajectory of a node within a integration time step can be properly represented by its velocity vector. This method has been the backbone of the DYNA3D sliding interfaces and has performed very well over time, but it fails to detect the interference for certain cases.

One of these cases is the so-called edge-to-edge contact that is depicted in **Fig. 1** in an extreme way. The arrow in the figure indicates the motion of one shell element; the other is stationary. The two shell elements clearly interpenetrated each other, but will not be detected because the trajectories of the nodes associated with one element never interfere with the other element.

Experienced finite-element analysts have used modeling techniques to overcome this shortcoming in simulating edge-to-edge contact. One of the methods used is to add rigid shell elements perpendicular to the shell structure edges to aid the contact detection. However, modeling techniques of this nature require knowing the penetrating entities *a priori* and often lead to falsely identified interference.

For analyses involving unpredictable structural damage, such as the damage assessment of bomb-blasted buildings or the integrity assessment of underground structures, these modeling techniques appear impractical since the disintegration of structures is unknown to the analyst until the event takes place.

The failure of the nodes-to-segments sliding interface algorithms can be attributed to the loss of sight of segment connectivity on the side that is represented by a simple list of nodes. To remedy this problem, a segment-to-segment algorithm, which considers the nodal connectivity of both interfering entities, is a logical alternative. Because of the complicated mathematical representation for a polygon in 3-D space, a definitive identification of segment interference can be costly. To make methods of this class feasible in a production finite-element code like DYNA3D, robust and effective procedures in checking the interference must be

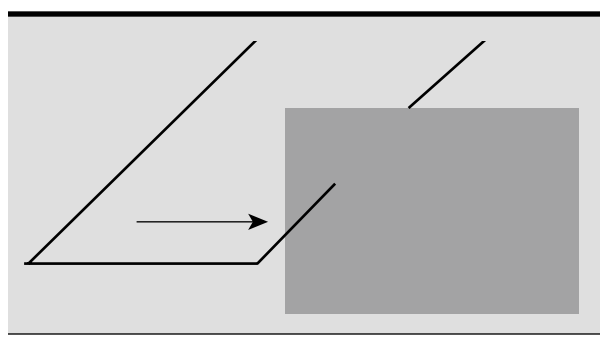

Figure 1. Segment edge-to-edge contact.

made available. A proposed detection algorithm that does not require solving nonlinear equations is outlined in the following section. With the help of the existing sorting[2] and preliminary screening[3] techniques, this segment-to-segment detection method represents a robust and complementary alternative to the node-to-segment approaches. Once the interference between a pair of segments is identified, it can be resolved by applying the separation forces to either the segment or the individual nodes.

Progress

The Segment-to-Segment Detection Procedure

Because of the significant cost associated with the contact detection calculation, all sliding interface algorithms, including node-to-segment and segment-to-segment, prefer to deal with as few interfering candidates as possible. Two preliminary screening techniques, namely the bucket sort[2] and the pinball search,[3] are frequently used in reducing the candidate list. Both of these methods are implemented in the existing DYNA3D sliding interface options and over the years have proven to be highly effective. They will again be used in the proposed detection scheme to sort out the possible interfering pairs. The segment-to-segment detection procedure is described in its execution sequence as follows:

1. The Bucket Sort. An imaginary rectangular parallelepiped large enough to cover the entire contact domain is imposed on the sliding interface. This box is then broken into contiguous cubes, originally called *cells*[3] but more commonly referred to as *buckets*. The size of these buckets is determined by the code. All relevant segments are sorted into these buckets according to the locations of their centroids. When detecting the interference for a specific segment, only segments located in the same or adjacent buckets will be checked against it in the subsequent steps.
2. The Pinball Search. A sphere, hence the name *pinball*, is assigned to each segment on the sliding interface. The pinball is centered at the centroid of the segment and is large enough to enclose its associated segment. A preliminary screening of identifying overlapping pinballs is conducted next. Only pairs of segments with overlapping pinballs will be further examined in the subsequent steps.
3. The Segment Interference Check. Segments *A* and *B* in **Fig. 2**, defined by nodes *1-2-3-4* and *5-6-7-8* respectively, represent a generic pair being checked for possible interference. $\mathbf{n}_A$ and $\mathbf{n}_B$ are their unit normal vectors, and $\mathbf{x}_A$ and $\mathbf{x}_B$ are the locations of their centroids. (Bold face characters denote vector quantities in the rest of our discussion.) Side *5-6* of segment *B* is first checked against segment *A*. Let us denote the plane passing through $\mathbf{x}_A$ and having $\mathbf{n}_A$ as its unit normal vector plane *A*. The following parametric equation of *p* represents the point at which the ray *5-6* intersects plane *A*.

$$[\mathbf{x}_5+p(\mathbf{x}_6-\mathbf{x}_5)-x_A] \bullet \mathbf{n}_A=0 \tag{1}$$

Solving for *p* yields

$$p=\frac{(\mathbf{x}_A-\mathbf{x}_5)\bullet\mathbf{n}_A}{(\mathbf{x}_6-\mathbf{x}_5)\bullet\mathbf{n}_A} \tag{2}$$

If $0\le p\le 1$, which means nodes *5* and *6* are on opposite sides of plane *A*, the intersection point *P* can be expressed as

$$\mathbf{x}_p=\mathbf{x}_5+p(\mathbf{x}_6-\mathbf{x}_5) \tag{3}$$

Otherwise side *5-6* of segment *B* does not intersect segment *A*, and no further action is needed for side *5-6*. For the case $0\le p\le 1$, we must determine whether $\mathbf{x}_P$ falls within segment *A*. If

$$(\mathbf{x}_P-\mathbf{x}_3)\bullet[(\mathbf{x}_2-\mathbf{x}_3)\times\mathbf{n}_A]\ge 0, \tag{4}$$

$\mathbf{x}_P$ is on the same side of line *2-3* as the segment centroid $\mathbf{x}_A$. If the inequality (**Eq. 4**)

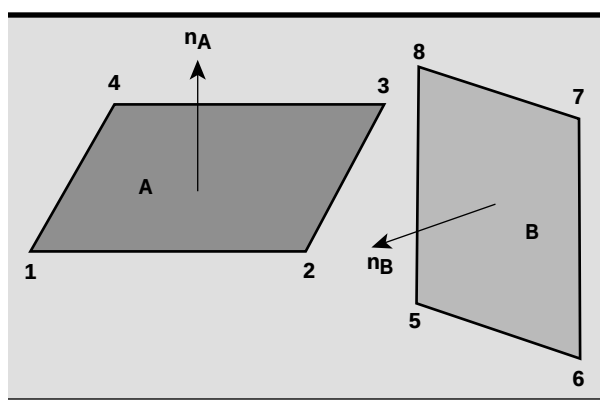

Figure 2. A pair of segments under interference check.

holds true, the same check must be applied to the remaining three sides of segment *A*. If any of the four sides of segment *A* do not satisfy **Eq. 4**, side *5-6* of segment *B* does not intersect segment *A*, and we should proceed to check the remaining sides of segment *B*. Only if $\mathbf{x}_P$ is on the same side as segment centroid $\mathbf{x}_A$ for all four sides of segment *A*, can the interference be declared. Once interference with segment *A* is identified for any one side of segment *B*, the unchecked side(s) of segment *B* can be skipped.

4. The Centroid Position Check. One scenario of interference, as shown in **Fig. 3**, can still go undetected by the procedures outlined in step 3. In this case, the two segments under consideration are perfectly parallel and the subsequent motion does not change this situation. Even when the two segments pass through each other, the sides of a segment do not intersect its counterpart. However this situation can be quickly identified by

$$(\mathbf{x}_B - \mathbf{x}_A) \cdot \mathbf{n}_A \leq 0, \tag{5}$$

which indicates $\mathbf{x}_B$, the centroid of segment *B*, has dipped under segment *A*.

Interference Resolution

After the interference between two segments is detected, a set of forces must be applied to resolve the interference. These forces can be decided either by examining the relative position and motion between individual nodes and the opposing segment or by examining the relative position and motion of two segment centroids.

The former is essentially going back to a localized node-to-segment approach. It allows forces of different magnitudes and directions to be imposed on individual nodes according to their respective position and motion. Its shortcomings are higher cost, increased possibility of erroneous nodal motion, and the need for double-path processing to maintain possible symmetry.

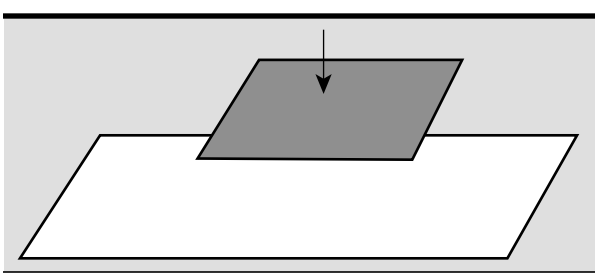

Figure 3. Two parallel segments: the top one passes through the bottom one.

The latter approach treats the segments as collective entities and calculates the separation forces as functions of relative position and motion. Nodes are not examined individually, and forces are applied uniformly to the nodes of a segment. This approach may not be adequate for cases requiring accurate node repositioning. However it will be more cost-effective, stable, and inherently maintains possible symmetry.

Future Work

It is very difficult, if not impossible, to design a sliding interface algorithm that covers all contact conditions. The proposed detection scheme complements the existing sliding interface options in DYNA3D and makes analyzing problems with arbitrary structure disintegration feasible. This new algorithm does not incur great expense since no iterations or solving systems of equations is required. There should be little doubt that extreme scenarios can be drawn up to foil the algorithm, but it should be able to simulate most of the contact situations in our application.

Further studies and experiments are needed for the separation force calculation. This is especially true if a node-to-segment approach is to be adopted and individual node trajectories do not intersect the opposing segment. Past research in this area[3] should provide a good guideline for future work.

The implementation of this algorithm into DYNA3D is to be carried out in the next fiscal year, and the new feature should be ready by the latter half of 2000.

References

1. R. G. Whirley and B. E. Engelmann (1993), "DYNA3D: a nonlinear, explicit, three-dimensional finite element code for solid and structural mechanics—user manual," Lawrence Livermore National Laboratory, Livermore, California (UCRL-MA-107254).

2. T. Belytschko and J. Lin (1987), "A three-dimensional impact-penetration algorithm with erosion," *Computers and Structures*, Vol. **25**, pp. 95–104.

3. T. Belytschko and M. O. Neal (1991), "Contact-impact by the pinball algorithm with penalty, projection and Lagrangian methods," *Int. J. for Numer. Methods in Eng.*, Vol. **31**, pp. 547–572.

Usability Enhancements for TIGER

David J. Steich, Gerald J. Burke, and Jeffery S. Kallman
Defense Sciences Engineering Division
Electronics Engineering

S Terry Brugger
Computer Applications Sciences and Engineering
Computation Organization

Daniel A. White
Center for Applied Scientific Computing
Computation Organization

This report discusses our progress with the Time-Domain Generalized Excitation and Response (TIGER) code. Our activities this year focused on building usability enhancements for TIGER and modeling a septum structure.

Introduction

Last year we extended our prototype version of the TIGER code to model realistic accelerator kicker structures being built for the Experimental Test Accelerator (ETA-II) at Lawrence Livermore National Laboratory (LLNL). We also added high-order wake field capabilities for the kicker structures and explored time-domain thin-wire algorithms.

This year we began by modeling a septum to better understand the wake fields caused by having the high-current electron beam pass by this structure. The modeling of the septum, shown in **Fig. 1**, presented many new challenges. Although the septum has many similarities with kicker structures, there are also significant physics differences.

This is the last year we will build on the prototype version of TIGER. The prototype version allowed us to test many of our object-oriented abstractions in TIGER while solving some near-term problems of interest to LLNL's accelerator programs. It is our intent to move the prototype version's capabilities into a more production level code. The work involved in building a production level, time-domain, full-wave physics electromagnetics code for structured/unstructured, serial/parallel situations involves two main efforts.

The first effort is the management of the complexity and the bookkeeping involved in hybrid meshes, massively parallel environments, and multiple algorithms with disparate overheads. The second effort is the research into the generalization of algorithms so they work in hybrid situations. Both of these efforts are non-trivial. It is our hope that the object-oriented framework that we have been building will insulate the programmer from the complexities of hybridization involved in the first task. At the same time, we hope the platform provides a programming environment that facilitates quick testing and implementation of the new physics that must be developed for the hybridizations/generalizations of the second task.

The object-oriented framework is several months behind schedule, but is proceeding rapidly. A first beta version of a series of three libraries, which represent the core of TIGER's object-oriented bookkeeping abstractions, is intended to be finished in early 2000. Earlier versions of TIGER have, to varying degrees, tested major portions of the abstractions. The latest version ties everything together.

Progress

This year's efforts were directed at TIGER usability enhancements and the modeling of a septum structure. Specifically, we built a simple Graphical User Interface (GUI) and mesh generator, developed and implemented a general field sensor capability

for unstructured finite volume meshes, developed and implemented a current sourcing procedure for unstructured grids, and ran several septum applications requiring these features.

These usability enhancements were required to help transition TIGER's research technologies into a more production level environment. The development of sourcing and sensing capabilities for unstructured meshes, described in this report, were unresolved research topics that needed to be addressed to increase TIGER's overall applicability.

Meshing and GUI

The GUI we built is at present very limited, but does allow us to query the mesh about detailed topological questions. The mesh generator is simplistic and was built solely to circumvent difficulties encountered using the I-DEAS mesh generation package. Our mesh generator builds an all-hexahedral mapped mesh.

Although the mesh generator is very crude and not user friendly, it allows us to build septum geometries in a few hours to a few days depending on the complexity of the geometry. We were still not quite finished building the septum shown in **Fig. 1** after spending roughly two months of effort using the I-DEAS software package. The knife edge seam where the waveguide section splits into two rectangular pipes, as well as the curved depression areas in the waveguide, caused considerable difficulties in I-DEAS. **Figure 2** shows part of the outer surface mesh of the septum built with our mesh generator and displayed using the GUI.

3-D Vector Field Interpolation

The finite-difference time-domain (FDTD) algorithm is a simple but elegant algorithm for modeling Maxwell's equations. The algorithm has matured since its inception at LLNL in 1966. FDTD is a very powerful computational method and is still by far the most popular method used today. FDTD does have a severe limitation in that the modeled geometry must be built out of rectangularly shaped brick elements.

Finite-volume time-domain (FVTD) techniques such as the discrete surface integral (DSI)[1] method remove this limitation by allowing the mesh to conform to the geometry. However, FVTD techniques are much newer, more complex, more research-oriented, and are less mature, with only dozens of papers published to date as compared to thousands for FDTD.

One open research area for FVTD techniques is the implementation of sources and sensors when the mesh is non-orthogonal. In a FDTD method, the mesh is always orthogonal and so each of the vector field components is de-coupled from the others.

This allows one to interpolate/extrapolate various field components independently.

In a finite-element method (FEM), basis functions are used which uniquely determine the fields at any point within the element. In a FVTD method however, the vector field components are coupled when the mesh is non-orthogonal, and in general, no basis function has been assumed to determine fields at an arbitrary point.

When modeling accelerator components it is often desirable to compute wake potentials by integrating

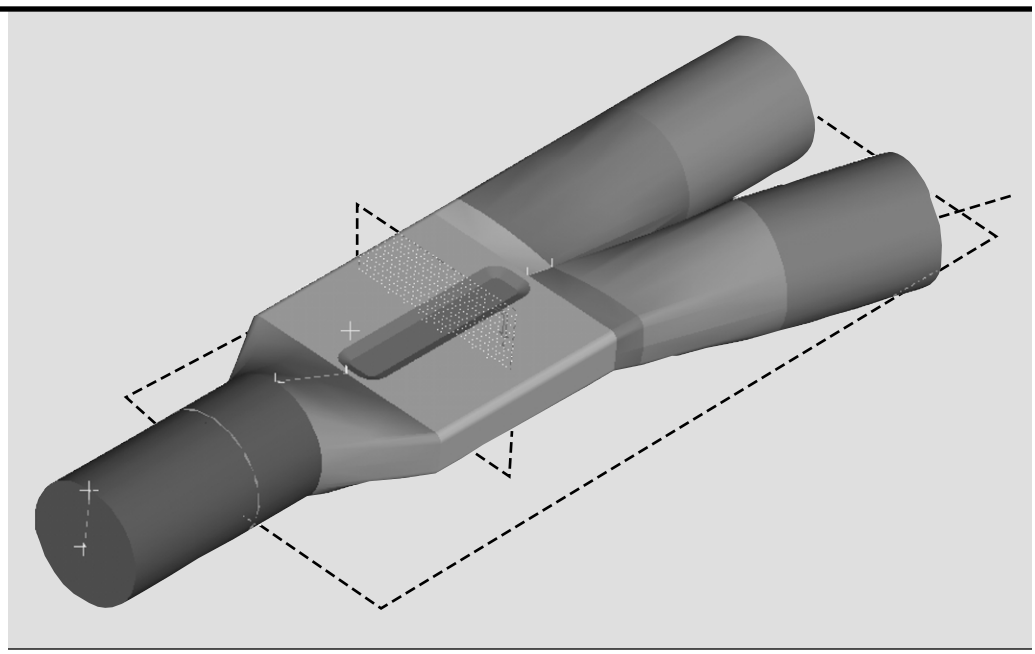

Figure 1. Septum structure modeled to determine wake potentials.

fields over an arbitrary cylindrical surface that does not conform to the mesh.

Usually this surface is determined by the physics, and cannot conform to the mesh. Since the edges in the unstructured mesh do not conform to the cylindrical surface, and in general are not aligned with the coordinate axes, the fields must be interpolated to the required points. Linear interpolation was used on the vector fields in three dimensions. The vector interpolation function for point (x, y, z) is

$$\mathbf{F}(x, y, z) = F_x(x,y,z)\mathbf{x} + F_y(x,y,z)\mathbf{y} + F_z(x,y,z)\mathbf{z}$$

with

$$F_x(x,y,z) = C_1 + C_2x' + C_3y' + C_4z' + C_5x'y' + C_6x'z' + C_7y'z' + C_8x'y'z' \quad (1)$$

$$F_y(x,y,z) = C_9 + C_{10}x' + C_{11}y' + C_{12}z' + C_{13}x'y' + C_{14}x'z' + C_{15}y'z' + C_{16}x'y'z' \quad (2)$$

$$F_z(x,y,z) = C_{17} + C_{18}x' + C_{19}y' + C_{20}z' + C_{21}x'y' + C_{22}x'z' + C_{23}y'z' + C_{24}x'y'z' \quad (3)$$

and $x' = x - x_0$, $y' = y - y_0$, $z' = z - z_0$ for a reference point (x_0, y_0, z_0). To determine the constants C_j a set of 24 edges is chosen in the vicinity of (x_0, y_0, z_0) and the dot products of $\mathbf{F}(x,y,z)$ with the edge directions are matched to the edge fields from the DSI solution. If d_{ix}, d_{iy} and d_{iz} are the direction cosines of edge i, and E_i is the edge field at (x_i, y_i, z_i), the set of 24 equations is

$$E_i = \mathbf{F}(x_i, y_i, z_i)\bullet\mathbf{d}_I = (C_1 + C_2x'_i + C_3y'_i + C_4z'_i + C_5x'_iy'_i + C_6x'_iz'_i + C_7y'_iz'_i + C_8x'_iy'_iz'_i)d_{ix} + (C_9 + C_{10}x'_i + C_{11}y'_i + C_{12}z'_i + C_{13}x'_iy'_i + C_{14}x'_iz'_i + C_{15}y'_iz'_i + C_{16}x'_iy'_iz'_i)d_{iy} + (C_{17} + C_{18}x'_i + C_{19}y'_i + C_{20}z'_i + C_{21}x'_iy'_i + C_{22}x'_iz'_i + C_{23}y'_iz'_i + C_{24}x'_iy'_iz'_i)d_{iz} \quad (4)$$

for $i = 1,\ldots 24$. This set of equations is solved for the coefficients C_j to determine the interpolation function. If are the elements of the inverse of the matrix of coefficients of the C_j in **Eq. 4**, then

$$C_i = \sum_{j=1}^{24} A_{ij}^{-1} E_i$$

for $i = 1, 24$.

In evaluating the wake potentials we interpolated the fields to points with spacing on the order of the mesh cell dimensions and approximated the integrals as sums of pulses. In this case, each interpolation function and corresponding set of edges is used for only one evaluation point. By choosing the reference point at the evaluation point x', y' and z' become zero, and the interpolation function simplifies to

$$\mathbf{F}(x_0, y_0, z_0) = \sum_{j=1}^{24} (A_{1,j}^{-1}\mathbf{x} + A_{9,j}^{-1}\mathbf{y} + A_{17,j}^{-1}\mathbf{z})E_j$$

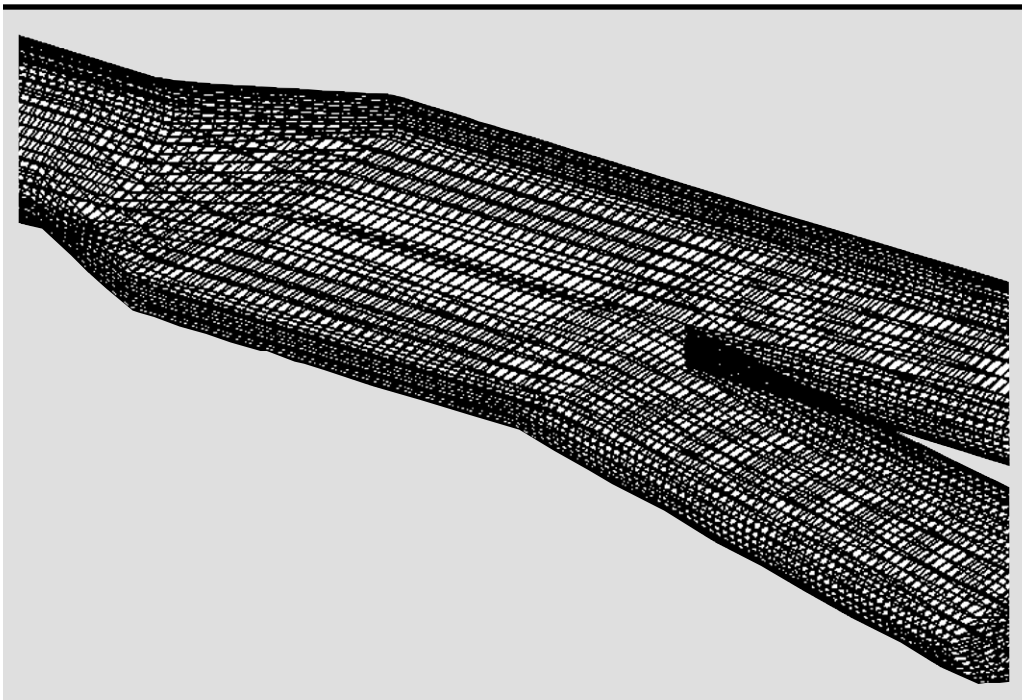

Figure 2. Mesh developed for the septum model.

Thus only 3×24 coefficients must be stored for each point for use with the E_j from each time step.

The choice of edges for fitting the interpolation function was found to require care, since a bad choice could result in a singular or ill-conditioned matrix. For each interpolation point all edges within a radius of several times the maximum cell dimension were selected. These were separated into edges predominately in the *x*, *y*, and *z* directions and sorted by distance from the interpolation point. Then for each vector direction the nearest edges were chosen, to obtain eight edges surrounding the point in the *x*, *y*, and *z* directions. When an edge in a given octant of space about the point could not be found, the next nearest edge in another octant was used, but this sometimes resulted in an ill-conditioned matrix. This process worked smoothly once the division between *x*-, *y*-, and *z*-directed edges had been optimized for the meshes being used, although fancier logic could make the process more robust.

Non-Orthogonal Current Source Modeling

The 3-D vector interpolation works for sensing the fields at arbitrary points in a non-orthogonal mesh. The scheme works perfectly, neglecting finite precision errors, for fields that have a linear variation. One must be more careful when dealing with sources. A rigid electron beam with known trajectory can be modeled as a current source in a FVTD scheme. However, the current source must be introduced so that it is charge conserving and causal.

Using FDTD or FVTD on orthogonal grids for current sources moving along straight grid edges is trivial. The implementation of current sources on orthogonal grids is still straightforward even if the current sources change direction, as long as the above mentioned constraints are enforced and the current sources remain tied to grid edges. The left side of **Fig. 3** depicts typical DC fields left behind if one models current jumping from one edge to

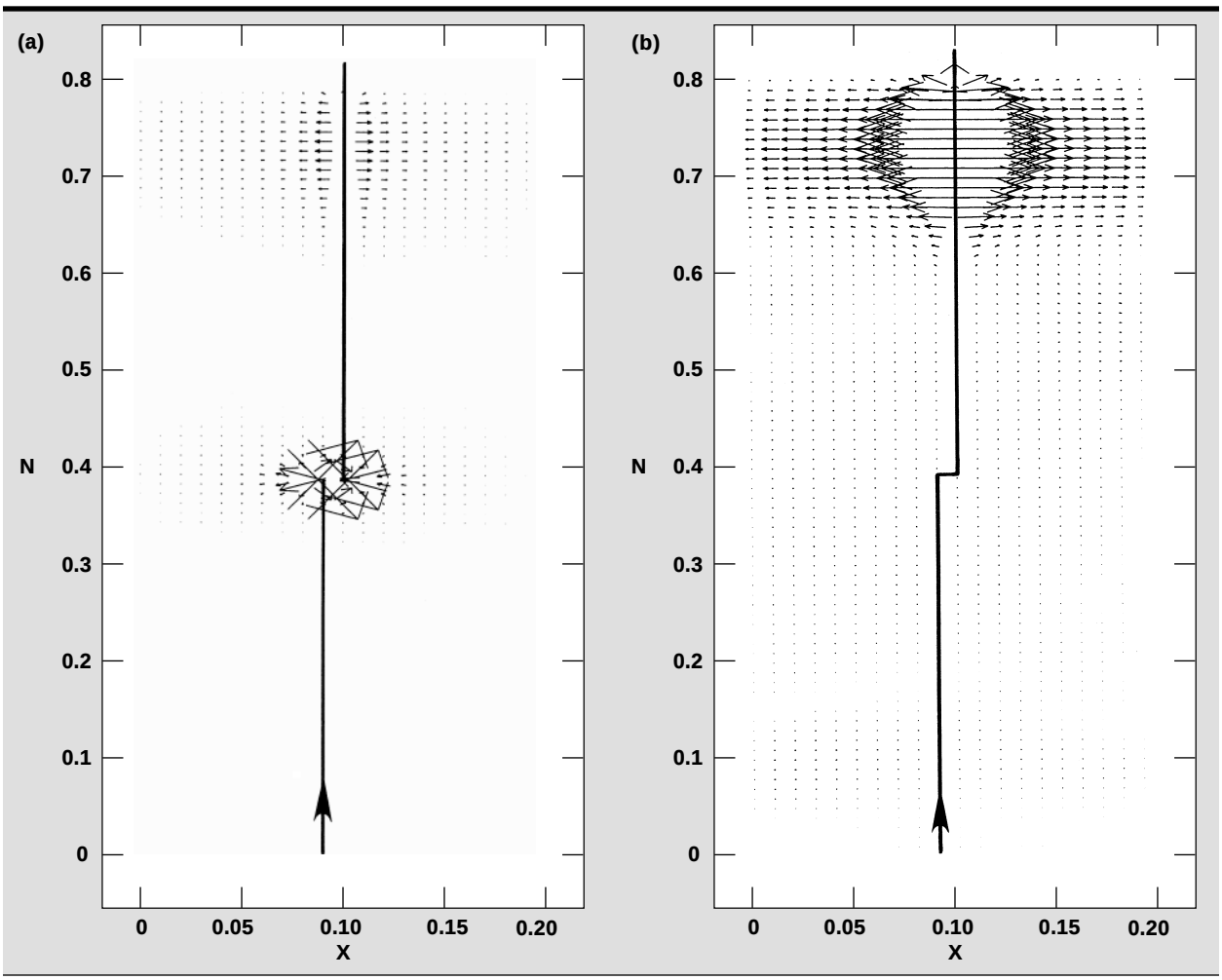

Figure 3. Fields produced by a current source moving at the velocity of light, showing the DC fields that result when continuity and causality are not correctly enforced (a) and the correct result (b).

another instantaneously without changing direction on a continuous path. The right side of **Fig. 3** depicts the correct way of modeling sources in a FDTD method. The current path is continuous around the stair-steps and causality is enforced by appropriate edge-to-edge delays in the incident current. The large DC field left behind when continuity or causality are not enforced correctly can often produce late time instabilities in a FDTD or FVTD method.

Now consider how to model a current source that was traveling just a few degrees tilted with respect to one of the grid axes so that it cannot conform to the grid edges. One could model the current source as a superposition of current sources along surrounding grid edges, weighted based on the local source position. This approach causes the beam cross-section to increase significantly.

One could model the current source as in the right side of **Fig. 3** where the current source trajectory is a series of edges that are the closest fit to the true path. This approach works well unless high-frequency phase information is critical. One could surrender and use a full-blown Particle In Cell (PIC) approach at the expense of dramatically increasing memory and CPU overheads. Or lastly, one could modify the mesh to conform to the source trajectory. In general, this will force the mesh surrounding the sourced edge to be non-orthogonal where the field components are coupled. This latter approach is the one we have taken. The modification of the DSI algorithm to introduce a current source through the cells is outlined below.

Consider updating a current edge as shown in **Fig. 4**. Using the DSI method for the unstructured mesh, the change in the electric flux density at the corner of faces a, b_i, c_i, is

$$\frac{\partial D_i}{\partial t} = \frac{b_i \times c_i \sum_a + c_1 \times a \sum_{b_i} + a \times b_i \sum_{c_i}}{a \bullet b_i \times c_i}$$

where for each face a, b_i, c_i we define

$$\oint_{Face} \overrightarrow{H^k} \bullet \vec{dl} \equiv \sum_{Face}$$

and a, b_i, c_i are vector area normals for the faces depicted in **Fig. 4**. Assuming we are one or more cells away from any exterior boundaries, the full electric flux density is the summation of the partial electric flux densities traversing the corners of face a for the upper and lower cells. The total electric flux density can then be written as

$$\frac{\partial D_{total}}{\partial t} = \sum_{cell}^{upper+lower} \sum_i W_i \frac{\partial D_i}{\partial t}$$

where w_i is a weighting term.

The electric field dotted along a given edge can then be easily written using the above equation. However, correction terms must also be added to every electric field update that uses face a in its update stencil. In simple terms, every $\sum_a$ should be replaced with $\sum_a + I_a$. The electric field for a given edge including all potential current sources can be written

$$E^k \bullet \vec{dl} = E^{k-1} \bullet dl + \frac{\Delta t}{\varepsilon} \left(\sum_{cell}^{upper+lower} \frac{\sum_i W_i \left(b_i \times c_i (\sum_a + I) + c_i \times a (\sum_{b_i} + I_{bi}) + a \times b_i (\sum_{c_i} + I_{ci}) \right)}{\sum_i a \bullet b_i \times c_i} \right) \bullet \vec{dl} \quad (5)$$

where I_{bi}, and I_{ci} are current sources through faces b_i and c_i respectively. In general, there will be eight correction terms for each sourced edge on a hexahedral grid.

The first term on the right hand side of **Eq. 5** can be thought of as the orthogonal portion while the remaining terms on the right hand side can be thought of as correction terms due to the non-orthogonal mesh. These non-orthogonal corrections are required to preserve current continuity. Non-physical DC fields and instabilities can arise when these correction terms are missing. In a fully Cartesian mesh **Eq. 5** reduces to the usual update equation including current.

Equation 5 leaves no DC fields behind. It is noteworthy to mention that even if the correction terms are very small, say ~10^{-4} of the orthogonal contribution, their contribution can dramatically affect the

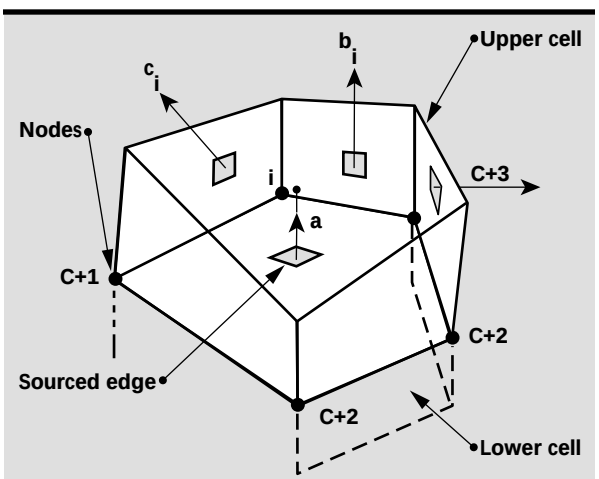

Figure 4. Mesh faces used in updating a field component in the DSI algorithm.

overall solution. Even changing the contributions in the sixth or seventh decimal place can have a significant impact on the overall solution accumulated over time. Research into why these terms are overly sensitive to numerical precision is ongoing.

Septum Modeling

Figure 5 shows the outer surface of the septum built for the ETA-II accelerator. **Figures 1** and **2** show the actual septum we modeled. The purpose was to get a better understanding of the wake fields caused by such a structure. A high-current electron beam is "kicked" upstream. The beam comes into the septum waveguide structure displaced +/- ~3 cm off the center axis of the septum. The beam has a tilt of roughly 0.86° entering the waveguide section.

In computing and processing the wake fields we started with the septum model and later looked at simpler situations such as a "T" junction in the pipe. The septum presented a number of new problems that made the wakefield processing more difficult than in previous cases such as the kicker. With the kicker, or any straight pipe that does not have protrusions into the pipe volume, the beam source can be replaced by equivalent source fields along the pipe walls. The equivalent source fields exist only over cavities or apertures in the pipe walls, so errors due to launching the wave from the problem-space boundary are avoided, and the source does not accumulate dispersion error over the length of the pipe. Early modeling of wake fields with TSAR did not use equivalent sources, but the solution for the field of the beam in a clean pipe was subtracted from the solution for the pipe with cavity or kicker. While errors were introduced in launching the source field and through dispersion, the subtraction was very effective in canceling these errors. Neither an equivalent source nor subtraction could be used with the septum, since there is no straight pipe path through the structure. Hence we had to work with the raw fields from the solution for the septum model.

Since the septum was modeled with the DSI algorithm, a continuous string of edges could be chosen to follow the beam path. The source was introduced as a Gaussian pulse of current traveling at the velocity of light, $v = c$, along the source edges. Fields were set up over the boundary where the pulse entered the problem space as if the pulse had come from infinity. The fields set up on the entry surface and also the absorbing boundary introduce errors into the solution, but these errors are confined to near the boundaries and were excluded in computing wake fields.

As each model was run, the electric and magnetic fields were saved for all edges and all time steps. Then in post-processing the fields were selected along the beam path or on a cylinder about the path. The fields on the cylinder were evaluated for 32 azimuthal angles about the beam using linear vector interpolation. Wake potentials were computed from the fields using the standard definitions

$$W_z(r,s) = \frac{1}{Q}\int_{z=-\infty}^{\infty} E_z(r,z,t)\Big|_{t=(z+s)/v} dz$$

$$W_t(r,s) = \frac{1}{Q}\int_{z=-\infty}^{\infty} \left(E_r(r,z,t) - vH_\phi(r,z,t)\right)\Big|_{t=(z+s)/v} dz$$

The wake potentials were then Fourier-transformed to obtain coupling impedances. When the wake potentials had significant ringing at the end of the solution record they were extrapolated using

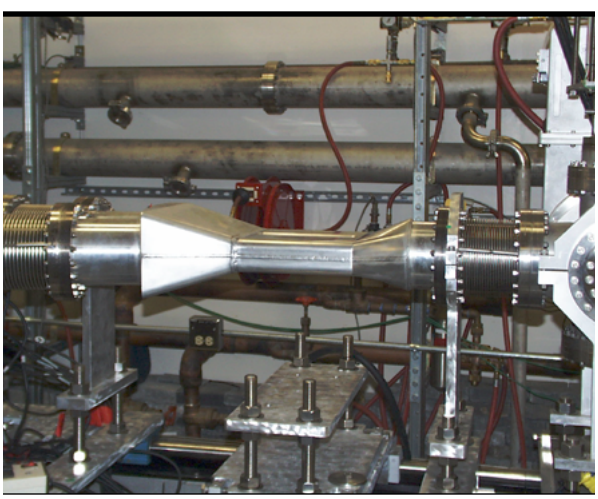

Figure 5. Outer surface of the ETA-II septum.

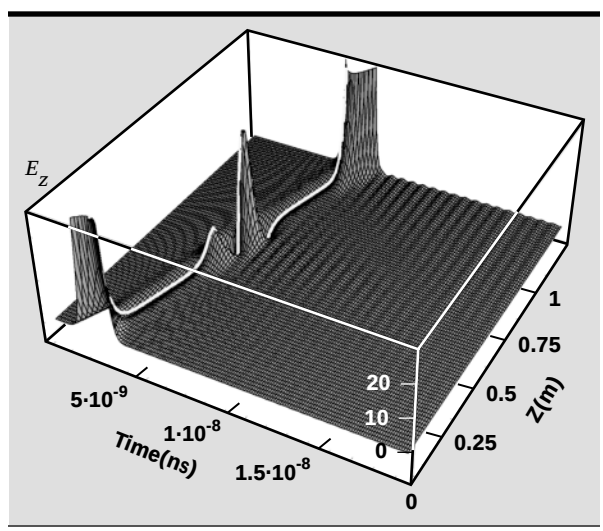

Figure 6. Longitudinal field along the beam path through a "T" junction. The velocity of light line representing the source pulse is shown as a white line.

decaying exponentials obtained with the Generalized Pencil of Functions method.[2]

Before computing the wake potentials we examined the longitudinal $E_r(r, z, t)$ fields and transverse field $E_r(r,z,t) - vH_\phi(r,z,t)$ on 3-D plots versus z and t. A typical plot is shown in **Fig. 6** for a simple "T" pipe junction. The wake potential $W(s)$ is the integral of the field along a line $t = (z+s)/v$, where $s = 0$ corresponds to the beam line shown in white in **Fig. 6**. Plots such as **Fig. 6** show the sources of the wake fields and can also reveal errors that would go unnoticed in the final wake potential. A number of problems were corrected in this way before getting the final wake potential results. The large fields near the ends of the beam line are errors due to launching and absorbing the pulse and were excluded from the fields used in the wake potential evaluation. The crease following the beam line is due to inherent solution and processing errors. It can be removed when a solution for a clean pipe can be subtracted. Otherwise it must be considered as a source of error in the wake potential, since it has low amplitude but long duration.

A plot of the field E_z along a line in the z, t space of **Fig. 6** is shown in **Fig. 7** for the $m = 0$ mode of the septum. The dotted line is the field $E_z(0,z,z/v)$ normalized to fit on the plot, and the solid line is the integral of this field. Thus the final value of the solid line represents the wake potential $W_z(0)$. This plot shows the scattered field due to the split in the septum where the waveguide contracts in height and expands in width before splitting. The field, and hence the kick imparted to the particle, has both positive and negative components that partially cancel in the integral.

The wake field in the input pipe has a small value, but makes a significant contribution to the integral due to its long duration. This field may be partly due to inherent errors in the solution and processing and partly due to the real effect of the beam traveling on a tilted path with respect to the pipe axis. One method considered to reduce the processing errors was to start the beam parallel to the axis and then bend it to the correct path. The field at a point where the beam is parallel to the axis can then be used to remove some solution and processing errors over the rest of the beam path. While not as effective as subtracting a full clean-pipe solution, this method reduces the errors somewhat. The standard evaluation of wake potential, with integration to infinity, would require that the beam start and end parallel to the pipe axis, but that raises questions of how to treat the fields produced where the beam changes directions without a self-consistent PIC solution. In our modeling we considered only a tilted beam truncated about 0.6 m before and after the split in the septum. While the result obtained will depend on the truncation distances, our modeling showed the wake potential of the septum to be much smaller than that of the kicker, and on the order of that for the "T" junction discussed below. Experimental results appear to verify this assessment.

To get a better understanding of the wake fields in a structure having some of the properties of the septum we modeled several structures such as the

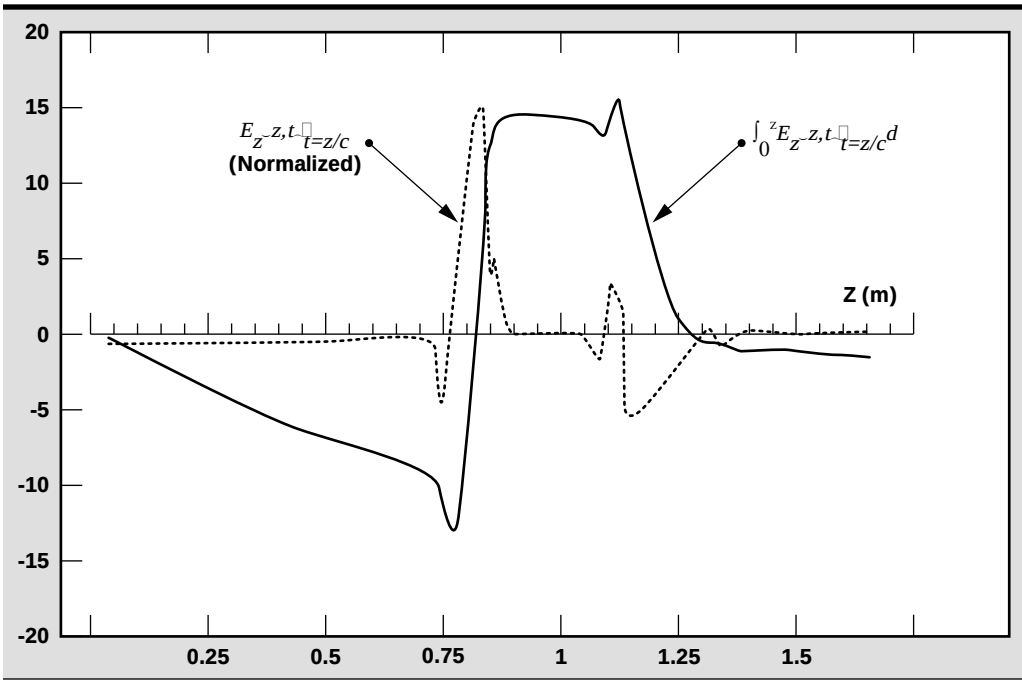

Figure 7. Longitudinal wake field and the integral for the wake potential W(s) at s = 0 for the septum. The scale applies for the wake potential integral, while the wake field has been normalized.

"T" junction shown in **Fig. 8**. The notch in the beam pipe in **Fig. 8** is a result of the side pipe having straight edges on its end. We also modeled smooth pipe junctions. The "T" junction is similar to the DHART septum, but with the branch normal to the beam pipe rather than tilted. Since this model had a straight pipe, the clean-pipe solution could be subtracted to reduce errors. The longitudinal wake impedance for the "T" is shown in **Fig. 9** for m =0, 1 and 2, and transverse impedances for m = 1 and 2 are shown in **Fig. 10**. It should be noted that m indicates the azimuthal variation of the wake impedance, but an m = 0 source is always assumed here.

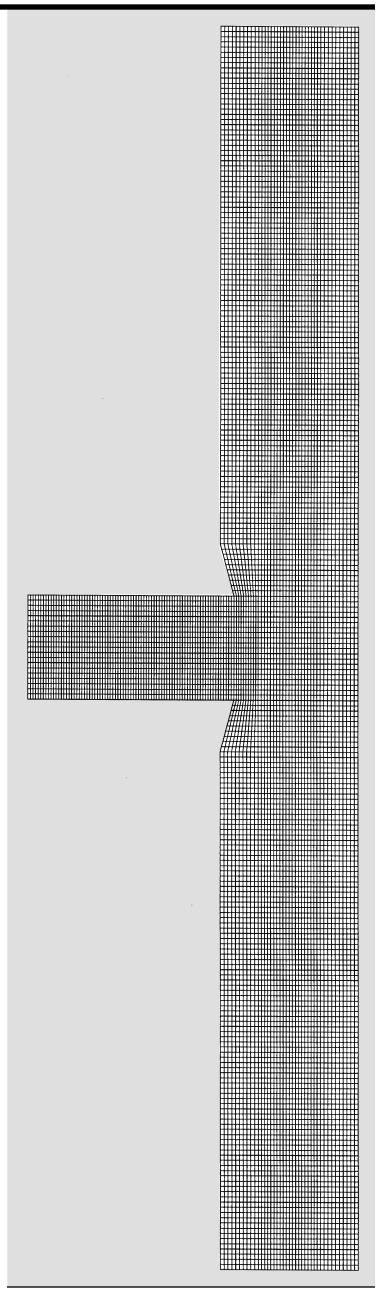

Figure 8. Section through the mesh for a "T" junction with the side pipe ending in straight edges.

The coupling impedances for the "T" pipe were compared with approximations based on scattering by a small hole in a pipe published by Gluckstern.[3] Gluckstern derived the m = 0 longitudinal impedance due to a m = 0 source and the m = 1 transverse impedance due to a m = 1 source. Since we considered only m = 0 sources here, we followed Gluckstern's small-hole analysis to get the longitudinal impedance approximations for m = 0, 1 and 2:

$$Z_{z0}(k) = \frac{ja^3 k\eta_0}{6b^2\pi^2}$$

$$Z_{z1}(k) = \frac{ja^3 kr\eta_0}{3b^3\pi^2}$$

$$Z_{z2}(k) = \frac{ja^3 kr^2\eta_0}{3b^4\pi^2}$$

and transverse impedance approximations

$$Z_{x1}(k) = \frac{ja^3\eta_0 \cos(\theta)}{3b^3\pi^2}$$

$$Z_{x2}(k) = \frac{2ja^3 r\eta_0 \cos(2\theta)}{3b^4\pi^2}$$

for pipe radius a, hole radius b and test particle at r. Gluckstern's analysis assumes a hole small compared to the pipe diameter and wavelength and a thin pipe wall. For an infinitely thick pipe wall, corresponding to our case, he suggests a correction factor of 56% of the above values. For **Figs. 9** and **10**, the hole in the beam pipe had width 8 cm and length 10 cm, so we used $b = \sqrt{lw/\pi}$ = 0.05 m, while a = 0.0667 m. With the 56% correction these approximations yield 2.16 Ω, 0.64 Ω and 0.097 Ω for longitudinal impedance at 1 GHz for m = 0, 1 and 2, respectively, and 3.09 Ω and 0.93 Ω for transverse impedance for m = 1 and 2. Considering the large

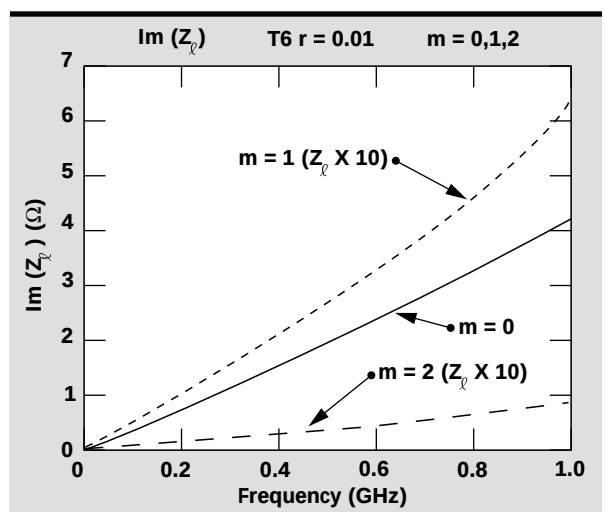

Figure 9. Longitudinal wake impedance for a "T" junction in a beam pipe, showing the m = 0, 1, and 2 response to a m = 0 beam excitation.

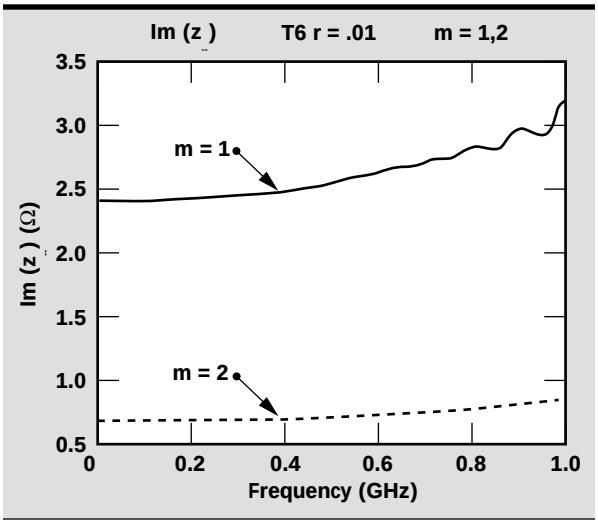

Figure 10. Transverse wake impedance for a "T" junction in a beam pipe, showing the m = 1 and 2 response to a m = 0 beam excitation.

diameter side pipe in our model violates some of Gluckstern's assumptions, these values are in reasonable agreement with the results in **Figs. 9** and **10**, with the largest error occurring for $m = 0$ longitudinal. It appears that the wake fields of this "T" structure are on the order of those of the septum.

We also modeled a "T" junction where the hole in the beam pipe was a slot 2 cm wide by 20 cm long. The longitudinal $m = 0$ impedance at 1 GHz was 0.8 Ω, in agreement with Gluckstern's assertion that slots have lower impedance than circular holes of similar area. A "T" model with a smooth beam pipe junction showed a somewhat smaller wake potential than the model of **Fig. 8**. We also ran 2-D cases involving a pipe with a step in, step out, cavity or collimator. We compared the results to analytic solutions and performed symmetry checks (a dual "T") and convergence checks to gain confidence.

In summary, we can obtain accurate wake fields for situations where we can subtract a solution for a clean pipe, or any reference solution for zero wake potential. If wake fields are very small (10^{-4} to 10^{-5} down from the source fields) then numerical errors can become a dominant error source. When the beam is tilted in the pipe, modified definitions for wake potentials must be developed before more meaningful results can be obtained.

Future Work

We plan on incorporating the new physics and usability enhancements developed here into a more production level code. All of these enhancements, along with the developments of previous efforts are vital as we transition TIGER's technologies out of a research environment and into a user environment.

As always, there are many things on our wish list to incorporate into this new code. However, at the top of the list, is the need to more accurately model highly distorted non-orthogonal cells near boundaries. Currently, when we have distorted cells next to metal surfaces we can have a small charge buildup. This charge buildup can lead to errors and instabilities. We have seen this charge buildup near the knife edge seam of the septum, especially when the cells are highly distorted.

References

1. N. K. Madsen and R. W. Ziolkowski (1988), "Numerical solution of Maxwell's equations in the time domain using irregular nonorthogonal grids," *Wave Motion*, Vol. **10**, pp. 583–596.

2. T. K. Sarkar and O. Pereria (1995), "Using the matrix pencil method to estimate the parameters of a sum of complex exponentials," *IEEE Antennas and Propagation Magazine*, Vol. **37**, No. 1, February.

3. R. L. Gluckstern (1992), "Coupling impedance of a single hole in a thick-wall beam pipe," *Phys. Rev. A*, Vol. **46**, No. 2, July 15.

Enhanced Fluid Dynamics Capability and Multidisciplinary Coupling in ALE3D

Rose C. McCallen, Timothy A. Dunn, and John S. Dolaghan
New Technologies Engineering Division
Mechanical Engineering

Richard G. Couch
New Technologies Engineering Division
Defense and Nuclear Technology
Mechanical Engineering

An incompressible flow model has been successfully implemented in the multi-physics code ALE3D. This model will provide a simulation capability for low Mach number flows where compressibility effects can be neglected. We have also completed several code enhancements to the compressible flow model as part of our investigation of applications in hemodynamics, microfluidics, and aerodynamics.

Introduction

The need for robust multidisciplinary modeling tools is increasing. ALE3D provides many of the physics options required, but not all. The area in which the deficiency is the greatest is in the treatment of low Mach number flows where a compressible flow model with explicit time integration is inefficient. The objective of this project at Lawrence Livermore National Laboratory (LLNL) is to provide an improved modeling capability for the low Mach number area by incorporating an incompressible flow module in ALE3D. With this capability, many programmatic problems of immediate and future concern can be solved. Examples include modeling of vehicle aerodynamics and underhood thermal transport for reducing energy consumption, modeling near-field biological or chemical dispersion for counterproliferation and missile defense projects, modeling of arterial hemodynamics for medical applications, microfluidics modeling, and thermal convection in storage facilities for the defense programs.

Additional improvements in ALE3D algorithms allow the code to better support modeling needs in microfluidics and medical fields. LLNL's Medical Technology Program has identified a need for detailed modeling of arterial flow as a means of understanding the mechanisms that control the formation of aneurysms. The use of arterial inserts, or stents, to affect arterial structure or evolution is now becoming common. The interaction of these artificial structures on flow dynamics is not well understood and is currently not adequately characterized in the design process.

The term hemodynamics has been used to describe this general technical area. Such modeling is best performed with the incompressible model and will require close coupling to the dynamics of the arterial response. Models to describe the viscous flow properties of blood as well as the arterial response will have to be developed. The existing explicit, compressible algorithms in ALE3D are being used to address modeling issues and determine the applicability of the modeling approach while the incompressible capability is under development.

The microfluidics work, particularly with respect to the representation of fluid properties, has considerable synergism with modeling activities in the arterial flow arena. An initial ALE3D calculation of a piezoelectric crystal-driven fluid indicated potential utility for LLNL's Acoustically-Driven Microfluidic System Project.[1] The initial microfluidic investigations were also performed with the explicit, compressible algorithms in ALE3D.

Much of the computational fluid dynamics (CFD) parallelization and the numerical solution methods are new in this work, as well as the multi-physics coupling of the thermal/fluid models and

structural/fluid models. (The flow, diffusion, and structural phenomena have different stability and accuracy criteria which direct the numerical solution approach, grid resolution, and time step.) The ALE3D code is at the forefront of multi-physics modeling and its capabilities and demonstrated applications in massively parallel computing are unmatched by currently available commercial and non-commercial software. The addition of an incompressible flow model coupled to its structural, heat transfer, and chemistry models pushes us into previously unattainable areas of computational modeling.

Progress

Incompressible Flow Model

An Eulerian formulation of the time-dependent incompressible Navier-Stokes equations is solved using a finite-element approach. The finite-element method (FEM) used is similar to that developed by Gresho *et al.*[2] Unlike their original investigations our algorithms allow for the use of unstructured meshes with one-point integration, hour-glass stabilization, and balancing tensor diffusivity (BTD) for explicit time integration.

Using Galerkin FEM, the discretized continuity and momentum equations can be written in matrix form as

$$\mathbf{C}^{\mathbf{T}}\mathbf{u}=0 \tag{1}$$

$$\boldsymbol{M}\dot{\boldsymbol{u}}+\left(\boldsymbol{K}+\boldsymbol{N}\left(u\right)\right)\boldsymbol{u}+\boldsymbol{C}\boldsymbol{p}=\boldsymbol{F} \tag{2}$$

where **u** is the nodal velocity vector, **p** is the pressure vector, **M** is the mass matrix, **K** is the diffusivity, **N**(u) is the advection operator, **C** is the gradient operator, and **F** is the user supplied natural boundary condition.

In the current implementation, a lumped mass matrix is used and the coefficient matrices are generated using one-point Gaussian quadrature. The Q1P0 element formulation is used, which provides trilinear velocity support with piecewise constant pressure in three dimensions. The equation solution method was chosen for compatibility with the solver finite element interface[3] developed by Sandia National Laboratories (SNL) in collaboration with LLNL. The continuity and momentum equations are solved together for the velocity difference and pressure with an explicit forward Euler time integration

$$\begin{bmatrix} \boldsymbol{M} & \boldsymbol{C} \\ \boldsymbol{C}^{\boldsymbol{T}} & \boldsymbol{0} \end{bmatrix}\begin{bmatrix} \boldsymbol{v} \\ \boldsymbol{p} \end{bmatrix}=\begin{bmatrix} \boldsymbol{f} \\ \boldsymbol{0} \end{bmatrix} \tag{3}$$

where

$$\mathbf{f}=\mathbf{F}-(\mathbf{K}+\mathbf{N}(\mathrm{u})),\ \text{and} \tag{4}$$

$$\boldsymbol{v}=\frac{\boldsymbol{u}^{\boldsymbol{n+1}}+\boldsymbol{u}^{\boldsymbol{n}}}{\Delta \boldsymbol{t}} \tag{5}$$

where **n** is the time step level.

An additive correction (diffusivity) to the diffusion matrix balances the negative diffusion induced by the explicit Euler time integration (that is, BTD, Gresho *et al.*[2]). Also an hour-glass correction is added to the one-point quadrature diffusion matrix to damp any zero energy modes that may be present because of the reduced integration scheme (Goudreau and Hallquist[4] and Gresho *et al.*[2]). To reduce the computational effort in the evaluation of the advection term, we use a "centroid advection velocity" simplification as was done by Gresho *et al.*[2]

For turbulent flow modeling a large-eddy simulation (LES) capability is available. In an LES of turbulent flows, the large-scale motion is calculated

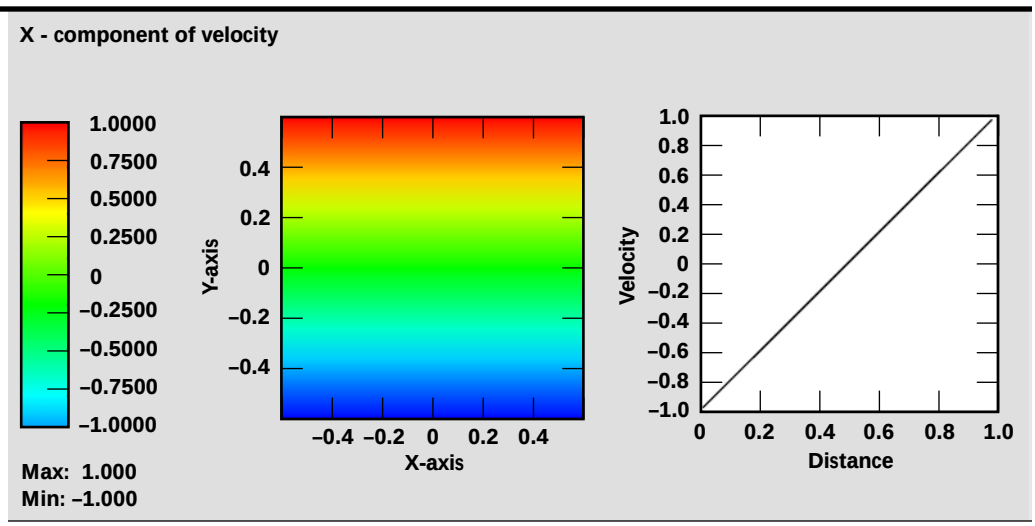

Figure 1. Incompressible flow simulation of shear-driven flow.

explicitly (that is, resolved) and the small-scale motion is modeled (that is, approximated with semi-empirical relations). For more details on the model see McCallen *et al.*[5]

Figures 1 and **2** are example simulations for a shear-driven flow and a lid-driven cavity, respectively. The shear driven flow was one case used for model verification.

Compressible Flow Model

Several compressible flow model enhancements were completed for application to flow around a circular cylinder, a hemodynamics application of pulsating flow in an artery with a stent, shock impact on a droplet, and two microfluidics applications of supersonic flow in a micro-nozzle and acoustically driven micro-channel flow.

Verification: Flow around a Circular Cylinder. The simulation of laminar flow around a circular cylinder at Reynolds number, Re, of 1200 and Mach number, Ma, of 0.3 is shown in **Fig. 3**. (The Reynolds number is a measure of inertial forces to viscous forces: Re = UD/υ, where U is the freestream velocity, D is the cylinder diameter and υ is the fluid kinematic viscosity.) The calculated drag coefficient, C_D, and Strouhal number, St, for our 2-D and 3-D calculations agree with those of Cox *et al.*[6] (The drag coefficient, C_D, is a dimensionless drag force defined as the drag force/(dynamic pressure x projected area). The Strouhal number is defined as the oscillation frequency over the mean speed and is a measure of the vortex shedding frequency.) In 2-D, the calculated C_D = 1.6 and St = 0.23. In 3-D, C_D = 1.4 and St = 0.20.

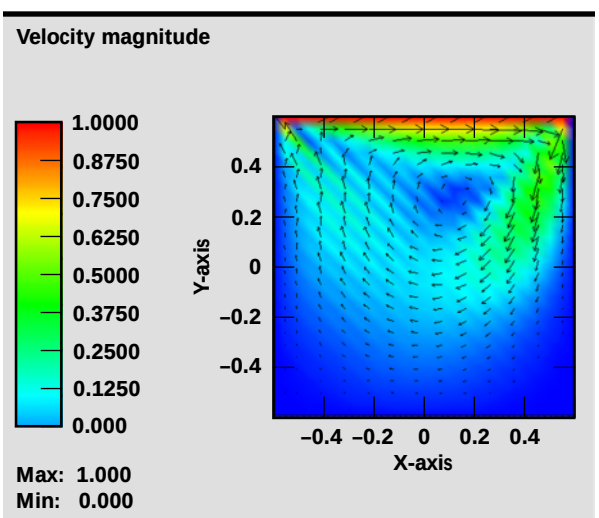

Figure 2. Incompressible flow simulation of "non-leaky" lid-driven cavity (that is, slip at top boundary with no-slip at top corners).

Hemodynamics: Pulsating Flow through an Arterial Stent. Modeling the effects of a stent in an artery requires the coupling of a pulsing blood flow and the response of the artery wall. **Figure 4** is an example calculation of pulsating flow through an arterial stent. In this first attempt, the stent is modeled with a simple material change. The region of the artery with the stent is a stiff material compared to the more flexible artery wall region.

Microfluidics: Supersonic Flow in a Micro-Nozzle and Acoustically-Driven Micro-Chamber Flow. ALE3D's capability as a microfluidics analysis tool was evaluated by application to two sample problems. The first case is a supersonic micro-nozzle flow that was developed and investigated by Massachusetts Institute of Technology for use by the spacecraft industry to drive low-thrust propulsion systems.[7] **Figure 5** shows the calculated Mach number distribution for Re = 2805. The

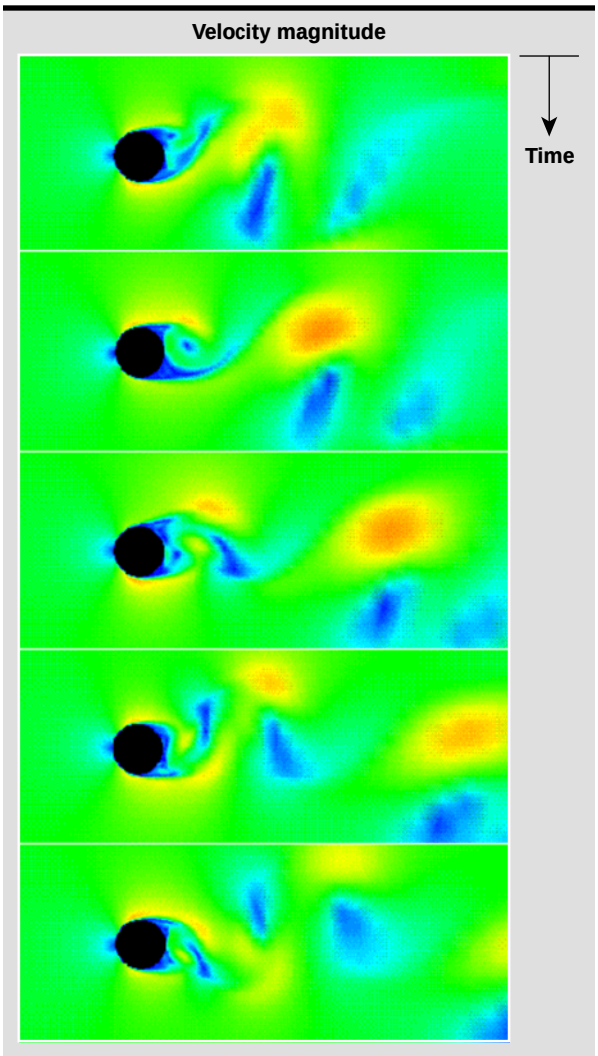

Figure 3. Simulation of turbulent vortex shedding behind a circular cylinder.

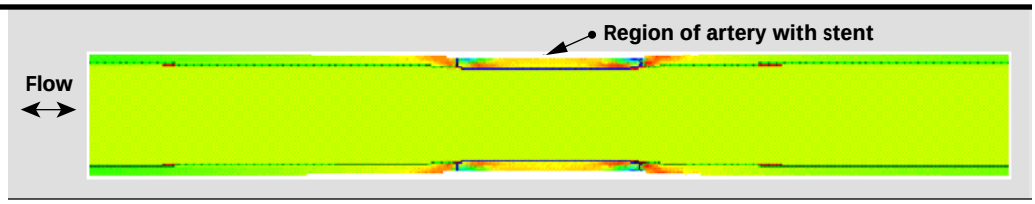

Figure 4. Simulation of an artery and stent with pulsating flow and the calculated relative stress.

challenge for this nozzle simulation is to capture the reduction in mass flow due to viscous effects at the wall (that is, flow blockage due to a substantial boundary layer or velocity gradient at the nozzle wall).

The second case is an acoustic micro-chamber. The modeled chamber is being developed by A. Wang at LLNL in the Center for Microtechnology. **Figure 6** shows the modeled geometry. The acoustic energy collects the macromolecules in the system. Important issues are the coupling of the driving mechanism to the chamber and the delivery and distribution of the acoustic energy.

Source Characterization: Shock Impact on a Droplet. Source characterization of the explosion and dispersion of biological or chemical substances is important to LLNL's counterproliferation and missile defense projects. One phenomenon of importance is the shock impact on a droplet and subsequent fluid breakup. **Figure 7** shows calculated droplet deformation due to shock impact.

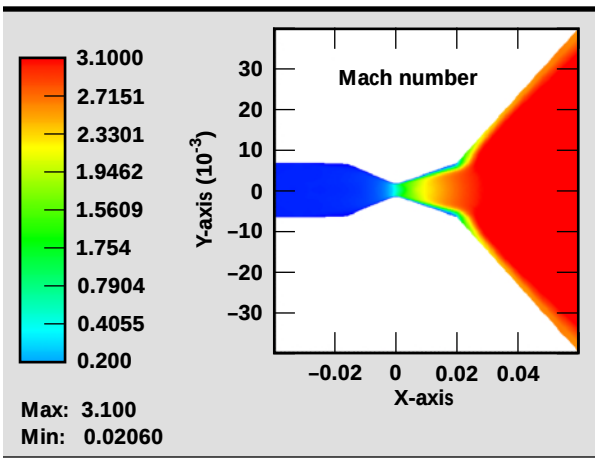

Figure 5. Simulation of flow through a supersonic micro-nozzle used for positioning of spacecraft.

Future Work

The first priority for the coming year is to complete a verification and validation study of the incompressible flow model. It is also important to investigate the code performance for parallel computing to verify that expected speed-ups are achieved.

Coupling of the incompressible flow model to the diffusion model in the ALE3D code is necessary for simulating thermal-advection problems as with applications involving the heating of an air filled room by machinery or other heat sources. For thermal-advection modeling, the addition of a buoyancy term to the flow model is required.

Capturing the expansion and contraction of an artery wall due to the pulsing blood flow will require the coupling of the incompressible flow and structural modules in the code. Plans are to use simple grid re-mapping techniques for the fluid/structure interface.

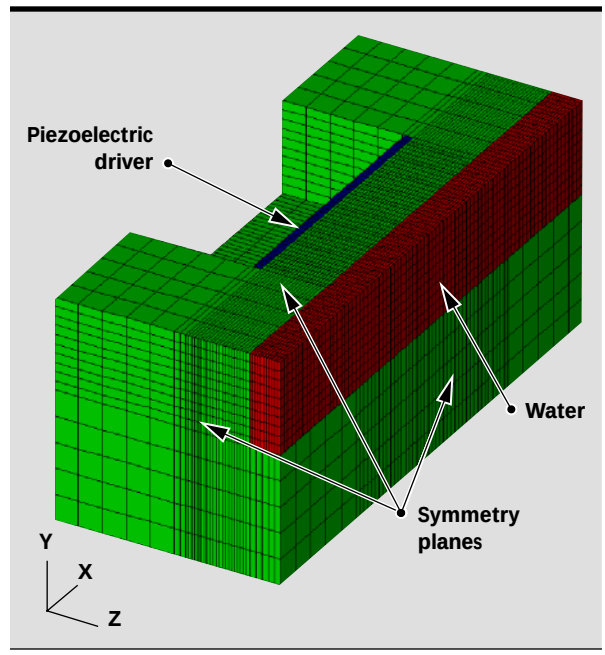

Figure 6. Model of acoustic microchamber.

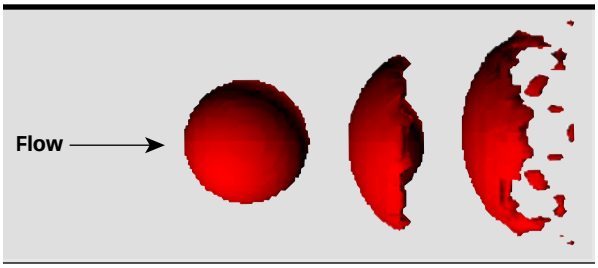

Figure 7. Simulation of shock impact on a droplet.

Acknowledgments

We gratefully acknowledge the support of C. Aro and K. Mish of LLNL and A. Williams of SNL in the implementation of the solver finite element interface. We are also grateful to P. Gresho of LLNL for his review of the project and guidance in flow modeling aspects and fluid-structure interaction modeling.

References

1. A. Wang (1999), "Acoustically-driven microfluidic system," to be published in the LLNL Annual FY99 Engineering Research, Technology, and Development Report.

2. P. M. Gresho, S. T. Chan, R. L. Lee, and C. D. Upson (1984), "A modified finite element method for solving the time-dependent, incompressible Navier-Stokes equations, Part 1: Theory," *Int. J. for Numerical Methods in Fluids*, Vol. **4**, pp. 557–598.

3. R. L. Clay, K. D. Mish, I. J. Otero, L. M. Taylor, and A. B. Williams (1999), "An annotated reference guide to the finite-element interface (FEI) specification," Version 1.0, Sandia Report SAND99-8229, January.

4. G. L. Goudreau and J. O. Hallquist (1982), "Recent developments in large-scale finite element Lagrangian hydrocode technology," *Comput. Methods in Appl. Mechanics and Eng.*, Vol. **33**, p. 725.

5. R. C. McCallen, B. T. Kornblum, and W. Kollmann (1997), "Large-eddy simulation in complex domains using the finite element method," ASME Fluids Eng. Division Summer Meeting, June 22–26, FEDSM97-3496.DOC.

6. J. S. Cox, K. S. Brentner, and C. L. Rumsey, "Computation of vortex shedding and radiated sound for a circular cylinder: subcritical to transcritical Reynolds numbers," *Theoret. Comput. Fluid Dynamics*, Vol. **12**, pp. 233–253.

7. R. L. Bayt and K. S. Breuer (1998), "Viscous effects in supersonic MEMS-fabricated micronozzles," *Proc. 3rd ASME Microfluids Symp.*, Anaheim, California, November.

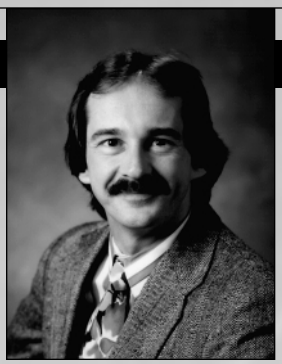

Harry E. Martz, Jr., Center Director

The Center for Nondestructive Characterization (CNDC) envisions significantly advancing research and development of nondestructive characterization science to enable successful Lawrence Livermore National Laboratory (LLNL) and Department of Energy (DOE) programs, and to be a national science and technology resource.

The CNDC near-term strategic mission objectives will advance core competencies and technologies in two areas: 1) quantitative NDC and 2) fast 3-D nanoscale imaging.

Quantitative NDC includes quantitative multidimensional nondestructive measurements to determine physical properties such as geometry, density, elemental and molecular composition; thermal, structural, and mechanical properties; stress state; and radioactive assay, in three dimensions and as a function of time.

Fast nanoscale imaging provides many programs with quantitative multidimensional (>3-D) imaging down to nanometer-scale lengths.

Our long-term strategic mission objectives include extension of near-term missions, plus embedded-in-design, multi-spectral imaging, and miniaturization for portability. The embedded-in-design objective will unite currently diverse and non-coupled technologies such as design, modeling, materials properties with characterization, testing, process monitoring and control, reverse engineering, and refurbishment and reuse into a global package to impact the engineering process. Multi-spectral imaging will expand the spectral range of CNDC imaging technologies and increase the synergism between different methodologies. The portability objective is to reduce current and new CNDC systems to the size of a small suitcase.

The CNDC FY-99 mission objectives are advancing core competencies and technologies, including the following programs:

Weapon system performance—this includes 3-D measurements over a large extent with high spatial resolution and advanced diagnostics. Examples include the Advanced Radiography Campaign and materials properties;

Science-based stockpile stewardship—specifically, durability and life prediction;

Extraordinary laser systems—this includes advanced diagnostics, for example, for fusion targets and automated *in situ* optics damage inspection;

Nonproliferation, arms control, and international security—related to reducing the threat from weapons of mass destruction.

CNDC supports a multidisciplinary team, consisting of mechanical and electronics engineers, physicists, materials and computer scientists, chemists, technicians, and radiographers, from LLNL, academia, and industry, within the U.S. and abroad. This collaboration brings together disciplines to provide the key scientific and technological advancements required to address LLNL programmatic and industrial nondestructive characterization challenges.

CNDC provides materials characterization, aid in process design and development, and encompasses process monitoring and control sensors and the monitoring of in-service damage. CNDC is also being applied at the end of a part's life for proper reuse or safe and proper disposal. Therefore, CNDC is becoming a front-line and end-of-line technology that strongly impacts issues of certification, life prediction, life extension, reuse, and disposal.

This year CNDC collaborated with Defense and Nuclear Technologies, Enhanced Surveillance Program, Nonproliferation, Arms Control and International Security, Lasers, the Microtechnology Center and Johns Hopkins University. Such collaborations enable CNDC to stay at the leading edge of CNDC technology, research, and development.

The primary contributions of the CNDC this year are described in the nine reports that follow: 1) The Optically Parallel Ultrasound Sensor (OPUS); 2) Speckle Reduction for LIDAR Using Optical Phase Conjugation; 3) Evaluation of an Amorphous-Silicon Array for Industrial X-Ray Imaging; 4) High-Frequency Laser-Based Ultrasound for NDC Applications; 5) New Developments in RECON; 6) Component Gap Detection by Infrared Imaging; 7) Quantitative Tomography Simulations and Reconstruction Algorithms; 8) Ultra-Wideband Phased Array; and 9) Photonic Velocimetry System Optimization.

Center for Nondestructive Characterization

5

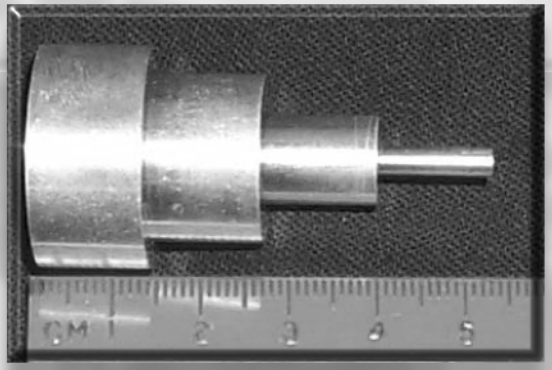

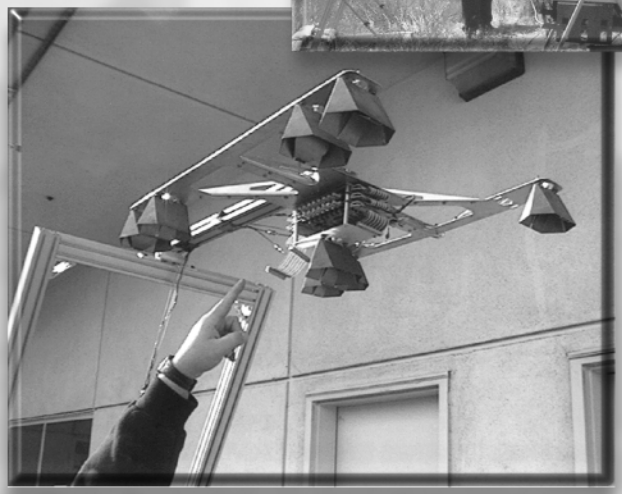

5. Center for Nondestructive Characterization

Overview
Harry E. Martz, Jr., Center Director

The Optically Parallel Ultrasound Sensor (OPUS)
Jeffrey S. Kallman, A. Elaine Ashby, Graham H. Thomas, and Dino R. Ciarlo 5-1

Speckle Reduction for LIDAR Using Optical Phase Conjugation
Mark W. Bowers 5-5

Evaluation of an Amorphous-Silicon Array for Industrial X-Ray Imaging
Kenneth W. Dolan, Clinton M. Logan, Jerry J. Haskins, R. Derrill Rikard, and Daniel J. Schneberk 5-11

High-Frequency Laser-Based Ultrasound for NDC Applications
Robert D. Huber, Graham H. Thomas, Howard Lee, Christopher Richardson, and Professor James Spicer . . 5-25

New Developments in RECON
Jessie A. Jackson 5-31

Component Gap Detection by Infrared Imaging
Charles S. Landram, Richard W. Martin, Nancy K. Delgrande, and Philip F. Durbin 5-37

Quantitative Tomography Simulations and Reconstruction Algorithms
Harry E. Martz, Jr., Dennis M. Goodman, Jessie A. Jackson, Clinton M. Logan,
Maurice B. Aufderheide, III, Alexis Schach von Wittenau, James M. Hall, and Dale M. Sloan 5-47

Ultra-Wideband Phased Array
Rexford M. Morey 5-71

Photonic Velocimetry System Optimization
Paul D. Sargis, Nicole E. Molau, Jeffrey B. Cooke, Oliver T. Strand, and Mark E. Lowry. 5-77

The Optically Parallel Ultrasound Sensor (OPUS)

Jeffrey S. Kallman
Defense Sciences Engineering Division
Electronics Engineering

A. Elaine Ashby and Graham H. Thomas
Manufacturing and Materials Engineering Division
Mechanical Engineering

Dino R. Ciarlo
Engineering Research Division
Electronics Engineering

In FY-99 we extended the FY-98 proof-of-principle work on the Optically Parallel Ultrasound Sensor (OPUS) and produced working acoustic field sensors. We used these sensors to acquire transmission ultrasound data over a planar region. These sensors will be useful in transmission ultrasound imaging as well as ultrasonic tomography.

Introduction

Nondestructive Characterization (NDC) is important for evaluating materials and processes without causing damage. At Lawrence Livermore National Laboratory (LLNL) we have a variety of means of doing nondestructive inspections. The main imaging technologies involve either x rays or ultrasound. X-ray imaging is very useful, but sometimes a subject is either difficult to penetrate, has low x-ray contrast, or might be damaged by radiation. Ultrasonic inspection is sometimes used in these situations. Ultrasound has different penetration and contrast characteristics than x rays, as well as eliminating the subject's exposure to ionizing radiation.

Among the ultrasound modalities in use at LLNL is transmission ultrasound imaging. This modality is best suited to imaging subjects that are lossy (such as ceramics). In this modality the subject is placed in an ultrasound medium bath, insonified by an acoustic source, and the resultant output acoustic field is mechanically scanned with an ultrasound sensor (see **Fig. 1**). This imaging modality, although useful, is very time-consuming (taking approximately 20 min to collect the data from small objects).

Transmission ultrasound imaging yields the phase and amplitude of the acoustic field transmitted by the object of interest. These data are the information needed to perform volumetric imaging of the object of interest. Unfortunately, many views of the object are required before the volume can be reconstructed, and the time required to collect the necessary views means that this imaging modality is so expensive that only the most important objects can be imaged in this manner.

In an effort to speed the acquisition of transmission ultrasound data (and make feasible the routine use of volumetric ultrasound imaging), we have developed the Optically Parallel Ultrasound Sensor (OPUS). This sensor uses the phenomenon of frustrated total internal reflection (FTIR)[1] to make the acoustic field modulate an optical beam. The OPUS allows the acquisition of an entire plane

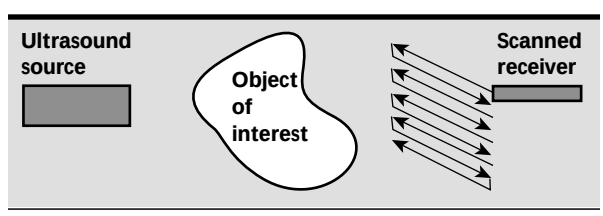

Figure 1. Transmission ultrasound imaging, currently performed using a mechanically scanned point or line sensor.

of acoustic field data at once. The OPUS has the potential to reduce the time of data acquisition by up to four orders of magnitude (see **Fig. 2**).

In FY-98 we carried out proof-of-principle research into making an OPUS. Funding was granted in FY-99 to design and fabricate the system.

The OPUS exploits FTIR: when light is incident at angle θ_1 on the interface between a slow medium (refractive index n_1) and a fast one (index n_2), light is refracted at an angle θ_2 in accordance with Snell's law[2], $n_1 \sin\theta_1 = n_2 \sin\theta_2$ (**Fig. 3a**). When $(n_1 \sin\theta_1)/n_2 \geq 1$, total internal reflection (TIR) occurs (**Fig. 3b**).

In TIR, 100% of the light that hits the interface is reflected. There is, however, a small evanescent wave that exists outside the high index medium. This evanescent wave falls off exponentially with distance and is almost nonexistent one wavelength beyond the interface. If another piece of high index medium intercepts this evanescent wave (**Fig. 3c**), the light is transmitted across the gap, and the TIR is frustrated (because it is no longer 100% total). The amount of light that is transmitted (and consequently the amount reflected) is very sensitively dependent on the size of the gap. By changing the gap, we can modulate the reflection of light off the TIR interface.

The heart of the OPUS is a thin silicon nitride membrane mated to an optical TIR interface by short gold walls. The membrane and walls maintain an air gap between an acoustic medium (water) and the optical interface (see **Fig. 4**). When there is no ultrasound, the membrane is still and light that hits the interface is partially reflected and partially transmitted. When exposed to ultrasound, the membrane vibrates, changing the air gap and modulating the reflected light. The gold walls divide the membrane into small acoustic pixels (60 mm on a side) that are staggered to minimize cross-talk.

Given a continuous light source we could use a photodiode to monitor the modulation of the reflected beam, but we'd need a photodiode per acoustic pixel and multiplexed electronics. An alternative is to use a strobed light source and a digital camera to take a sequence of images that allow us to extract the phase and amplitude of the vibration of the entire set of acoustic pixels. Just as a strobe light can be used to watch the vibration of a drum head, we're using a strobed source to watch the relative phases and amplitudes of tens of thousands of tiny drum heads, all at once. Given a sequence of images (ten over the course of the acoustic cycle (see **Fig. 5**)) and calibration data, we can extract the phase and amplitude of the vibration, and thus extract the pressure phase and amplitude.

The system we built to acquire these images consists of the sensor (mounted to the side of a water tank), an acoustic source, a synchronized optical source, and a digital camera (see **Fig. 6**). The main timing signal for both the acoustic and optical sources comes from the oscillator. The oscillator output is split among an amplifier, an oscilloscope, and the optical pulse generator. The output from the amplifier is fed to a power meter and then to the acoustic source transducer. The output from the pulse generator is fed to both the

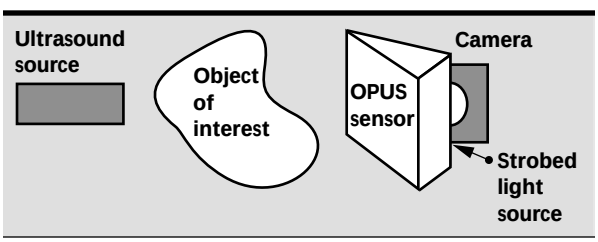

Figure 2. Illustration of the OPUS. Imaging is accelerated by acquiring the data from an entire plane of the acoustic field at once.

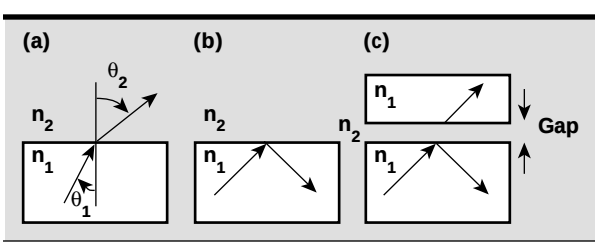

Figure 3. (a) Snell's law refraction of light from region of index n_1 to region of index n_2; (b) total internal reflection; (c) frustrated total internal reflection.

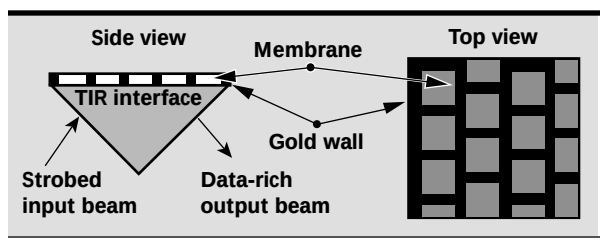

Figure 4. Structure of the OPUS, built from a silicon nitride membrane that stands over a TIR interface on short gold walls. The gold walls form staggered acoustic pixels.

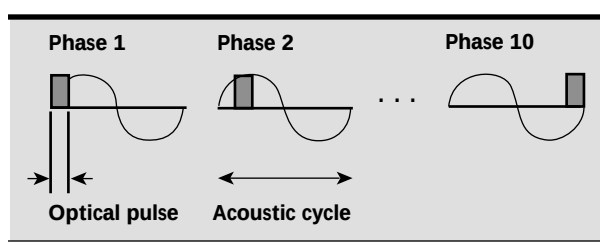

Figure 5. Sequence of images taken at ten different phases of the acoustic cycle.

LED and the oscilloscope. The light from the LED is homogenized, polarized, and collimated. It impinges on the sensor where it is modulated and then picked up by the digital camera. The digital camera data is acquired by the computer.

In a typical data acquisition session, both a calibration set (without the subject) and a data set (with the subject) are acquired. To acquire data the operator sets the oscillator frequency (nominally 1 MHz) and the amplifier gain, reads the power meter, sets the data set name into the computer, sets the phase on the pulse generator, and has the computer acquire an image. To take the next image in the sequence the user adjusts the pulse generator to put the optical pulse at the correct acoustic phase, changes the data file name on the computer, and has the computer acquire an image. This happens a minimum of ten times per image sequence. We are pursuing the automation of this process.

Progress

Working from the proof-of-principle system and data collected in FY-98 we constructed the OPUS data acquisition system shown in **Fig. 6** and used the facilities and personnel of the microfabrication group to build several sensors. Over the course of the year we experimented with the sensors, collecting data and making refinements to the sensor designs (both microstructure and macrostructure). We discovered that the membranes must be very carefully cleaned prior to sensor assembly, as any contamination larger than 0.2 μm was large enough to cause the membrane to deform around it, concentrating stress, and eventually breaking the membrane under the hydrostatic load of being immersed into the operating fluid.

We also found that the nonplanarity of the silicon wafers on which the membranes are grown can accentuate the membrane fragility. We have discovered ways to mitigate these effects. Another aspect of our work this year was the start of automating the acquisition of data. Eventually this will require the purchasing of a computer-controlled signal generator, amplifier, power meter, and pulse generator. We began the modifications to the computer program that acquires the data to minimize the human interactions during sequence acquisition.

The sensor we have been working with most recently has a 0.7 cm^2 sensing region. The image in **Fig. 7** is the result of using this sensor to look at the acoustic fields transmitted through a candle placed 2.5 cm in front of the sensor. Two sequences of data were taken, one without the candle in the acoustic path (**Fig. 7a**) and one with the candle (**Fig. 7b**). Each pixel of both sequences of data was examined to extract the amplitude of the sinusoidal variation in brightness through the sequence. The ratio of these amplitudes to their respective backgrounds gives an indication of the relative pressure at every pixel. Dark pixels occur when there is a lower relative pressure; bright pixels occur where the relative pressure is higher. The acoustic wavelength at which the data that went into this image was acquired is 1.75 mm. We expect the two images to differ in the following ways: **Fig. 7a** should show no structure, while **Fig. 7b** should show similar structure in every horizontal row (the candle was suspended vertically in front of the sensor, so we expect to see relatively constant vertical columns in the data). Of course, there are reasons to expect nonuniformity as well: nonuniformity of the source and nonuniformity of the candle (the presence of a wick) being among these.

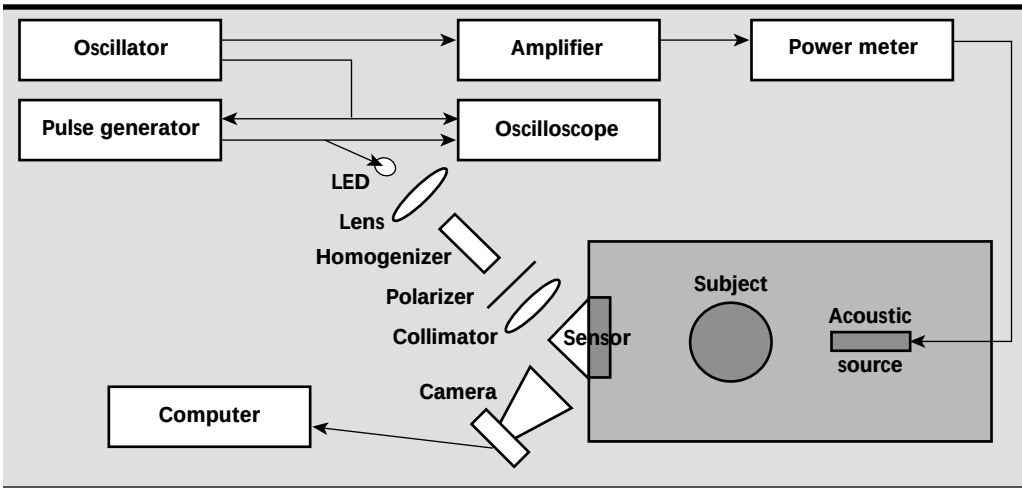

Figure 6. Schematic view of the OPUS data acquisition system.

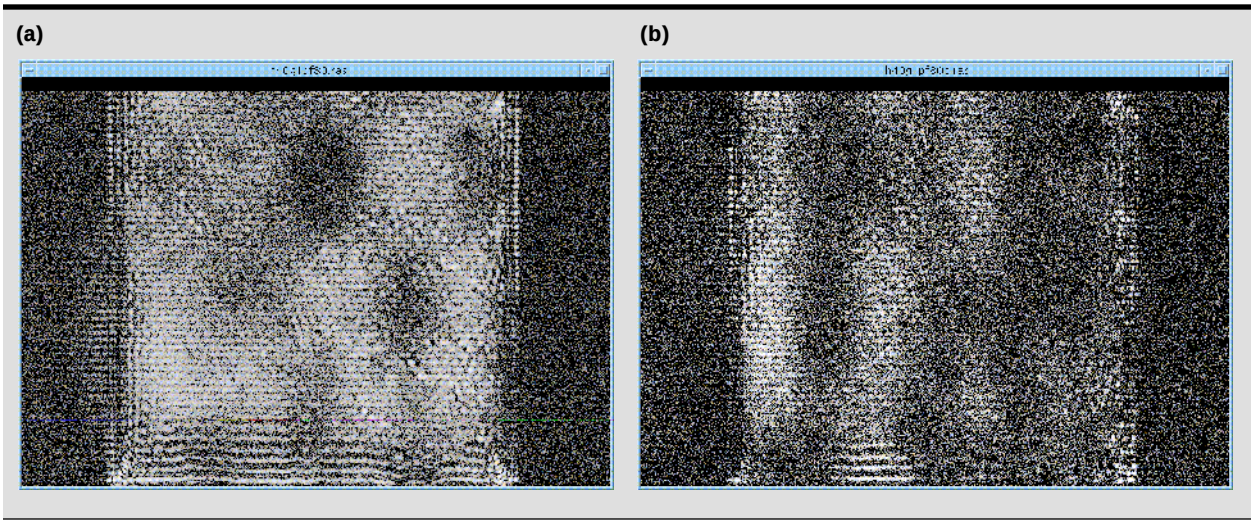

Figure 7. Relative acoustic pressure data extracted from two sequences of data images: (a) without a candle and (b) with a candle. Note that image (b) has bright vertical columns while image (a) does not.

Future Work

There has been great progress on this project in the last year, but there remain a number of challenges to make this device useful: the sensor aperture must be expanded to several times the current size, the sensor must be made more sensitive, time for data acquisition must be reduced, and the data acquisition must be automated.

We are currently looking at ways of expanding the aperture, including making mosaics of the current membranes and working with membranes set up like paned windows. To make the membranes more sensitive we are examining new membrane materials. To reduce the data acquisition time, we are examining the possibility of changing our light source and using a nonlinear optical temporal novelty filter[3] to increase our signal to noise level to the point that we can use video-rate cameras. The automation of the data acquisition is perhaps the simplest problem to solve, requiring only the purchase of the computer-controlled hardware and the time to program it.

Another aspect of this work is the use of the pressure phase and amplitude information to do acoustic tomography. This is the great promise of the technology: that hitherto infeasible acoustic inspections will become commonplace. At this point much work needs to be done on the algorithms to do these reconstructions.

FTIR has been harnessed to allow acoustic pressure to modulate optical beams. These beams are acquired one plane at a time. Optically-strobed sequences of images acquired in this manner allow the extraction of relative pressure phase and amplitude. This technology promises to revolutionize transmission acoustic imaging, allowing near real-time imaging of 2-D projections, and fast data acquisition for volumetric image processing.

References

1. J. Strong (1958), “Concepts of Classical Optics,” W. H. Freeman and Company, Inc., New York, New York, p. 124.

2. F. A. Jenkins and H. E. White (1950), “Fundamentals of Optics,” McGraw-Hill Book Company, Inc., New York, New York, p. 5.

3. G. F. Albrecht, H. F. Robey, and T. R. Moore, “An optical technique for the measurement of turbulent spectra using the photorefractive properties of $BaTiO_3$,” Lawrence Livermore National Laboratory, Livermore, California (UCRL-102551).

Speckle Reduction for LIDAR Using Optical Phase Conjugation

Mark W. Bowers
Defense Systems Engineering Division
Electronics Engineering

We are developing a novel method for increasing the accuracy and expediency of remote detection LIDAR (light detection and ranging) systems. Laboratory and numerical studies have shown that it is possible to increase the signal-to-noise (S/N) ratio for LIDAR systems under certain conditions using optical phase conjugation. This increase in S/N results in more accurate detection of chemical effluents while simultaneously reducing the time necessary to acquire this information. Research has shown that it is possible to expand this work into the near- and mid-infrared regime, two regimes that are commonly used for remote detection by LIDAR. Bulk phase conjugate systems as well as liquid and solid waveguides have been studied for their viability in this application.

Introduction

Remote detection systems can be used to monitor dangerous chemical spills as well as environmental conditions around the world. It is imperative that these detection systems work reliably and accurately while being as distant from the source as possible. It would be advantageous if, in addition, the remote detection systems were compact and consumed little power so that they could be carried in smaller vehicles, planes, or spacecraft. LIDAR (light detection and ranging) is well suited for these applications. A LIDAR system is one in which a laser beam is transmitted out towards an area to be probed. The return scatter from the aerosol itself or the topographic background is detected and measured.

LIDAR systems can measure chemical effluents accurately by using a detection technique known as differential absorption LIDAR (DIAL). In the DIAL technique two or more laser pulses of different frequencies are transmitted sequentially towards a target area. The differences in return signal power for each of these frequencies are measured. Since it is assumed that the returned power would be identical for all frequencies in the absence of absorption, this differencing technique can determine the relative absorption at the transmitted frequencies.

In practical, field operational systems, the simplistic view given above is complicated by noise sources, such as speckle. Speckle, as shown in **Fig. 1a**, results from the light scattering off a diffuse surface. The light returning to any one point in the detector aperture will originate from multiple points on the diffuse surface. Each of these individual light rays will add constructively or destructively with its own phase. The random phases of each light ray will result in a random, but deterministic, light irradiance at each point in the detector aperture. If viewed with a camera, this pattern will appear as bright and dark spots (**Fig. 1b**).

The exact number of bright and dark spots in the detector aperture is a random number, although the mean value and variance can be calculated for a given situation. Thus, the total irradiance measured by the detector is random, resulting in an unknown deviation from the expected signal return. The atmosphere will complicate even this picture by adding turbulence that can change the speckle return over time, usually over a few milliseconds time period.

In current field operating systems, the noise contribution by speckle and atmospheric turbulence can be reduced significantly, but at a cost. The mean and the variance of the signal are deterministic, and thus can be reduced by averaging. Averaging can improve the S/N by an amount proportional to the square root of the number of pulses averaged. Since each pulse must wait at least long enough for the speckle field to change, the time between pulses will be on the order of milliseconds. In order to get adequate results, averaging times of seconds or minutes may be necessary. The maximum averaging

time is also limited by slow system drifts and will limit the accuracy of the resultant measurements to something well below that which is necessary to complete the desired mission.

Optical phase conjugation is a nonlinear optical method of removing the phase differences of the diffuse rays of light described above. By removing the phase differences the light can be made to add constructively over the entire detector aperture, thus removing the presence of a speckle pattern and the associated noise. For optical phase conjugation to completely compensate for the speckle noise, all of the light over 2π steradians must be collected and conjugated. This is not possible for LIDAR systems due to the large distances between the LIDAR source and the topographic background.

Previously it was generally accepted that capturing only a portion of the scattered light would reduce or completely null out the effects of optical phase conjugation. This belief was based on the premise that microscopic scattering dominates the phase-front of the optical beam propagation. Unpublished numerical studies have shown that the macroscopic scattering properties of a surface can be just as important in the wavefront evolution. Microscopic and macroscopic here refer to feature sizes smaller than or larger than the diffraction limited optical spot sizes, respectively. This project is intended to show that it is possible, under most normal LIDAR operating conditions, to use optical phase conjugation to mitigate the effects of speckle.

Progress

Stimulated Brillouin Scattering (SBS) was chosen as the nonlinear process to achieve the optical phase conjugation for a variety of reasons. The properties of SBS have been studied extensively,

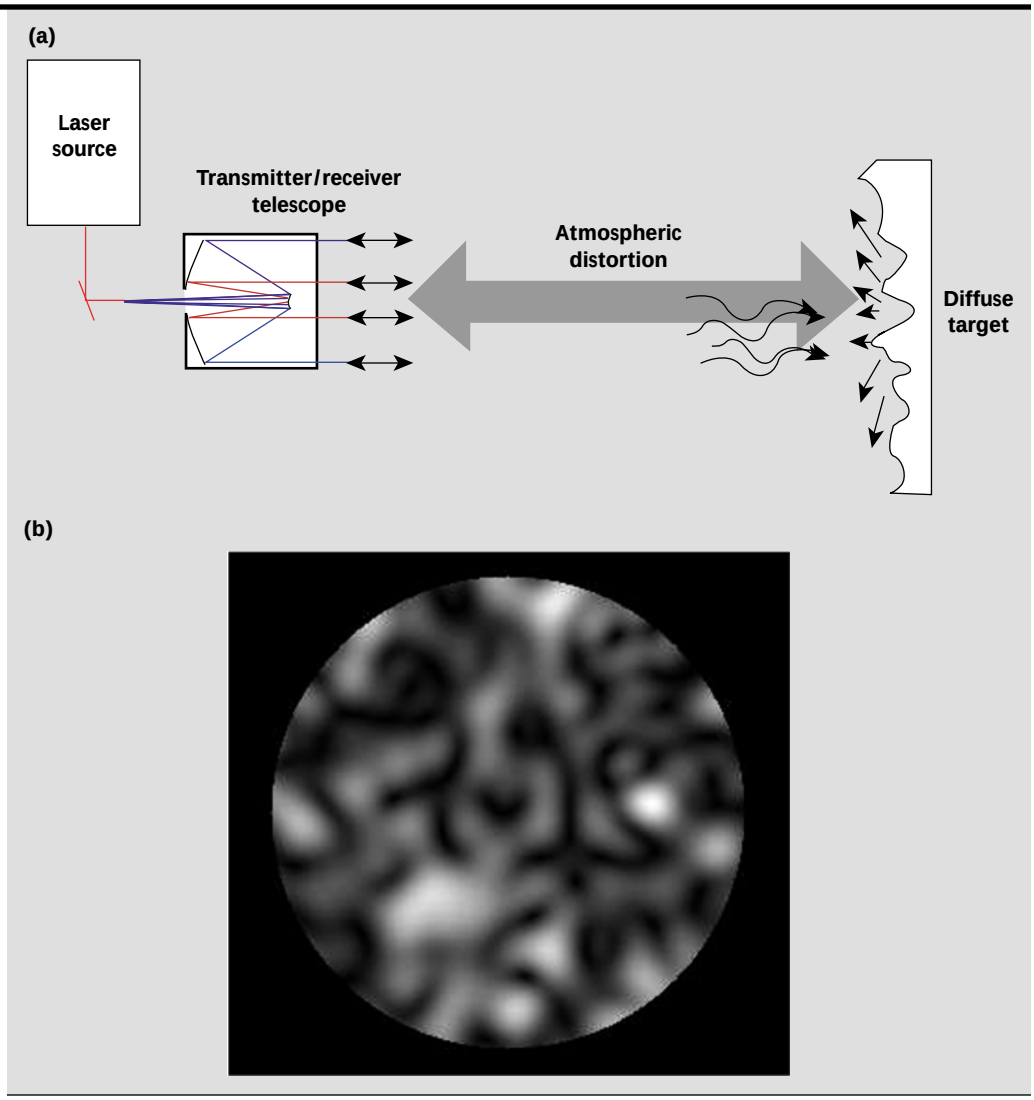

Figure 1. Speckle. (a) Laser light reflecting off a diffuse surface. The received image of the laser spot on the diffuse surface is as shown in (b), not a single spot as would be expected with incoherent light.

resulting in a wide information base on which to build. Two notable works are by Bruesselbach *et al.*[1] for atmospheric turbulence compensation and Delaye *et al.*[2] where SBS is used for optical phase conjugation of a diffuse optical field. Other advantages of SBS include conjugator response times faster than that of atmospheric turbulence, high gains (single stage gains of >80 dB have been demonstrated[3]) that can overcome the losses in propagating over large distances. Another important fact about SBS is that it has been widely used with the LIDAR laser systems, thus making retrofitting existing LIDAR systems simpler and less costly.

The main goal in this first year of the project was to demonstrate the technical feasibility of using optical phase conjugation to reduce the undesirable effects of speckle. The first step toward this goal was to perform a numerical study to show what regimes, both in fieldable systems and in laboratory experiments, would benefit from this new technology. The optical fields were modeled using the analytical software package "MatLab" in a manner consistent with current LIDAR simulation programs. Representative results from this numerical study are shown in **Fig. 2** for a field LIDAR system. The 10-km distance to the topographic background and the 1-m-aperture detector resulted in a loss of 70 dB in the return signal information and power, not normally a regime in which optical phase conjugation is considered practical. From this numerical study it was determined that the quality of the phase conjugation process is directly dependent upon the number of speckle bright spots, called speckle cells, in the detection aperture.

A laboratory experiment was planned that would closely approximate an outdoor field LIDAR system. A numerical study was performed using MatLab to ensure that the detection aperture would have adequate phase conjugation quality, determined mainly by the number of speckle cells in the collection aperture. Usually more than 20 will suffice. The number of speckle cells is a controllable parameter determined only by the characteristics of the LIDAR itself, not by the properties of the target used.

The experiment was planned using a Nd:YAG laser system and a CS_2-filled cell as the nonlinear SBS material. The results of this initial experiment, **Figs. 3a** and **3b**, showed that the SBS process significantly improved the quality of the scattered light. The single pulse S/N improvement for this system was 100:1 and the multiple pulse S/N improvement with averaging was 9.3:1. The SBS gain was 10 dB, lower than estimated above due to the bulk focusing optics used, but adequate for the laboratory testing used here. Although good, the results were less than expected from the numerical studies performed earlier. The problem was found to be in the geometry of the SBS phase conjugator.

Although the geometry is the one most commonly used for SBS phase conjugation, it was not appropriate for fields with a large number of speckle cells. The geometry prevented light rays that were entering at extreme angles from participating in the phase conjugation process. Thus, some of the information was lost and incomplete phase conjugation resulted. We were able to reproduce this effect numerically, as shown in **Figs. 3c** and **3d**.

Waveguides, which can capture the light rays that enter at extreme angles, were the solution to this problem. The waveguides are cylindrical pipes or fibers that are filled with an SBS active material. Liquid and solid filled waveguides were tested. The liquid filled waveguides did have good phase conjugation properties. These waveguides, however, suffered from heat buildup near the entrance that created bubbles after several minutes of operation.

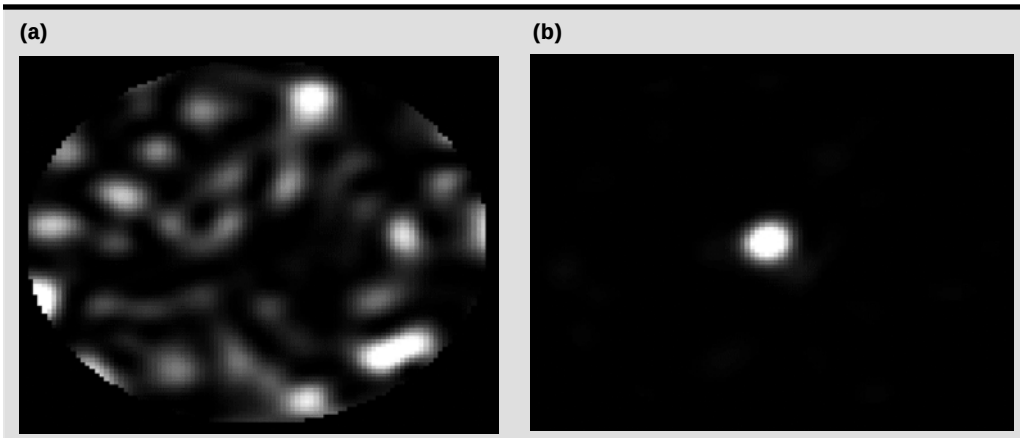

Figure 2. Numerical simulations of a LIDAR return signal with speckle noise (a) and after correction using optical phase conjugation (b). Results are for a 10-km range and a 1-m aperture. The single bright spot in (b) is the desired signal for a LIDAR receiver. The peak intensities have been normalized.

The bubbles would be drawn into the waveguide, stopping the SBS process. This problem can be corrected by flowing the liquid continuously through the waveguide, removing bubbles whenever they form.

The solid waveguides are essentially optical fibers that are specially shaped to enhance the SBS process. These waveguides have similar phase conjugation properties to those of the liquid filled counterparts, but do not suffer from the bubble formation. For the incorporation of the waveguide SBS generators into a LIDAR system it is essential that they reach SBS threshold well below the power levels available. Since the power available is approximately 600 μJ for the oscillator/generator, the threshold should be below 100 μJ to achieve adequate conjugate intensity. Low thresholds for SBS initiation, as low as 70 μJ, were demonstrated as part of this project thus far. This is an enhancement over the original bulk CS_2 cells that had a threshold of more than 2 mJ.

The maximum power permissible in the fibers tested is limited to twice the threshold value, too low to yield sufficient energy for the speckle correction testing. New fibers that have an improved geometry for SBS enhancement have been ordered. The threshold for these new fibers has been calculated to be better than 10 μJ with a maximum of power of several millijoules.

A collaborative effort, funded through this project, was undertaken with the nonlinear optics group at the University of Rochester, to search for appropriate materials for the SBS process in wavelength regions of interest to most commercial DIAL systems. The most desirable wavelength region is that from 2 to 4 μm. A table of more than 100 suitable materials was found and narrowed down to the best candidates. From this list it was evident that commercially available infrared (IR) fibers would be suitable candidates due to their availability in a waveguide form. IR sapphire fibers can be commercially manufactured to our desired geometry while maintaining a high damage threshold. Tests were performed at the University of Rochester on the SBS process in sapphire fibers to determine the optimum geometry. More tests are needed on these fibers to determine if they can work with the short pulses delivered by the LIDAR system.

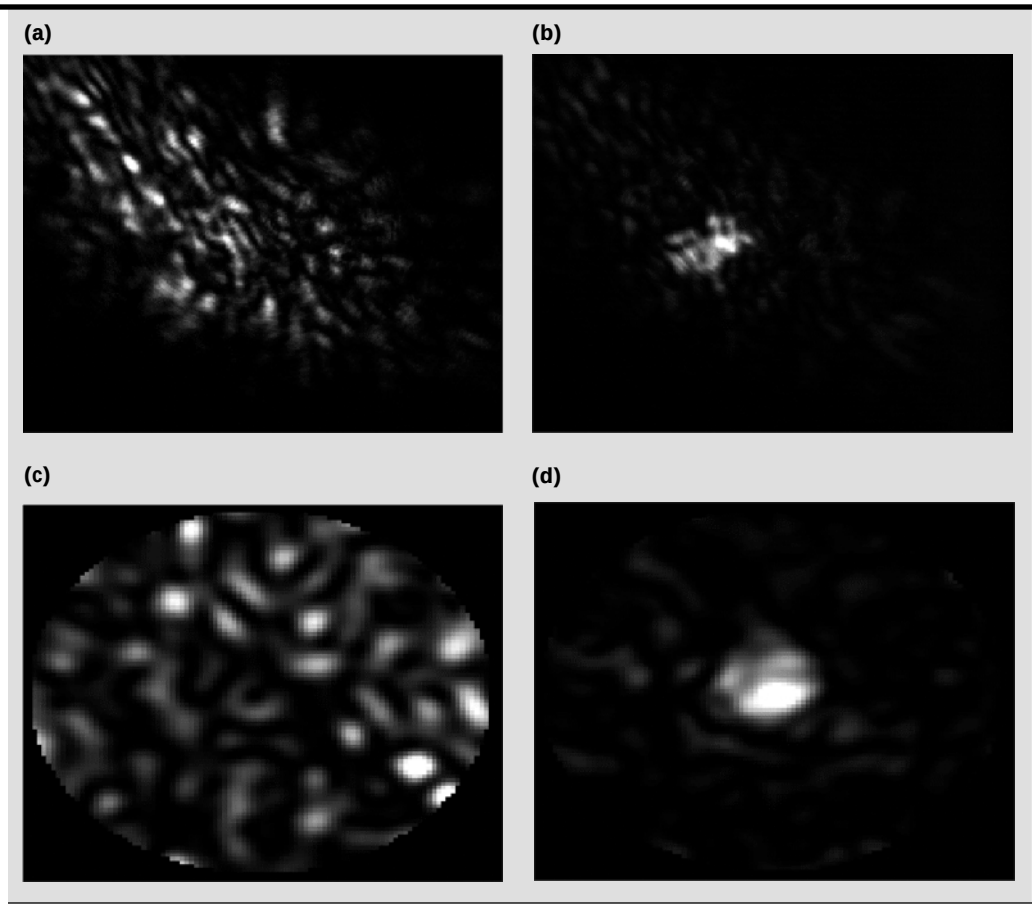

Figure 3. Experimental results for our laboratory prototype system, showing speckle noise (a) for a LIDAR return signal, and significantly better signal quality (b) after the incorporation of the optical phase conjugation. Images (c) and (d) are the numerical simulations of (a) and (b), respectively. In image (d) the effect of losing the extreme rays is taken into account. The peak intensities in (b) and (d) have been attenuated by 30 dB for display purposes.

Summary

Although previously thought impractical, numerical and experimental evidence in this project suggest that optical phase conjugation can significantly improve the S/N for LIDAR systems. Numerical simulations show that ideal phase conjugation can lead to improvements in the S/N for real world LIDAR applications. The laboratory experiments have also demonstrated large improvements in the S/N, although less than ideal due to extreme optical rays. This data is supported with numerical simulations attenuating the extreme rays. New fiber designs and materials are being studied that will significantly improve the properties of the system.

Future Work

In the second year of this project the useful energy range of the SBS fiber phase conjugators will need to be expanded. Fibers are on order that should have the energy range and wavelength range desired for the laboratory experiments. The initial testing of these fibers will be done with the Nd:YAG laser.

Finally, a field demonstration of a DIAL that will be retrofitted with the SBS optical phase conjugation system is planned. We plan to do minimal alterations to the existing LIDAR system, thus choosing the correct SBS material for the phase conjugator is paramount. This particular LIDAR has 5-ns optical pulses at a wavelength of 1.5 μm. The material chosen must have a phonon decay time of <5 ns and be transparent at that optical wavelength. The phonon decay time of sapphire is currently unknown and will need to be measured using the laser system in the LIDAR itself. If the sapphire fiber proves to be too slow, a liquid with a fast phonon decay time, such as freon-113 in a waveguide geometry, may be used or the pulse length of the laser will need to be lengthened.

The field demonstration will show the increase in the S/N of a DIAL system in a real environment. The first field demonstration will take place using a specular target at a distance of 700 m. This test will be used to work out the bugs in the system and demonstrate the quality of the optical phase conjugation as incorporated into the DIAL system. The next test will use a diffuse target in place of the specular target at the same range. An increase in the S/N of just three in this test will prove to be an order of magnitude reduction in the averaging time needed for this DIAL to perform its intended functions.

References

1. H. Bruesselbach, D. C. Jones, D. A. Rockwell, R. C. Lind, and G. Vogel (1995), "Real-time atmospheric compensation by stimulated Brillouin-scattering phase conjugation," *J. Opt. Soc. Am. B.*, Vol. **12**, pp. 1434–1447.

2. P. Delaye, A. Blouin, D. Drolet, and J. Monchalin (1995), "Heterodyne detection of ultrasound from rough surfaces using a double phase conjugate mirror," *Appl. Phys. Lett.*, Vol. **67**, pp. 3251–3253.

3. A. M. Scott and K. D. Ridley (1989), "A review of Brillouin-enhanced four-wave mixing," *IEEE JQE*, Vol. **25**, pp. 438–459.

Evaluation of an Amorphous-Silicon Array for Industrial X-Ray Imaging

Kenneth W. Dolan, Clinton M. Logan, Jerry J. Haskins, and R. Derrill Rikard
Manufacturing and Materials Engineering Division
Mechanical Engineering

Daniel J. Schneberk
Computer Applications Science and Engineering Division
Computation Organization

We are evaluating flat panel imagers, both amorphous silicon and amorphous selenium, for use as imaging elements in digital radiography and computed tomography (CT) systems. Digital radiography systems are being developed for applications where the digital image format and fast image acquisition provide an advantage over film, and where image quality and dynamic range requirements can be satisfied. CT systems based on the flat panel technologies are being developed as a means of improving the speed of image acquisition and image quality when the field of view is greater than 5 or 6 in. on a side. Results of evaluations and applications of amorphous-silicon flat panel imagers are reported here.

Introduction

The results of the amorphous-selenium (a-Se) work were reported by us last year[1] and appear elsewhere.[2–26]

The Flashscan 20, a large flat panel amorphous-silicon (a-Si) x-ray imaging array made by dpiχ, Incorporated, Palo Alto, California, was used in the present digital radiography and computed tomography (CT) application evaluations. The sensitive area of the array is 195 mm × 244 mm (7.7 in. × 9.6 in.), pixel dimensions are 127 µm × 127 µm (0.005 in. × 0.005 in.) with 1536 data lines by 1920 gate lines, resulting in 2.95×10^6 pixels.[27] The array incorporates charge sensitive amplifiers and 12-bit A/D converters, but the useful dynamic range is approximately 11 bits.

The a-Si array converts light images into electrical charge, pixel by pixel. The light images are produced by x-ray interactions in a scintillating screen placed in intimate contact with the a-Si array. The construction of the array (**Fig. 1**) consists of a thin film a-Si over a large area glass substrate. Photodiodes (n-i-p) made from the a-Si thin film layer convert light energy into electrical energy, and thin film transistors serve as pixel switches. The scintillating screen can be selected to provide an optimal configuration for image acquisition speed, contrast sensitivity, spatial resolution, and source energy.

The a-Si flat panel arrays are suitable for radiographic imaging applications because the photodiodes have good light sensitivity (for example, quantum efficiency at the visible wavelengths is approximately 70%), and low dark current. Fill factors for the sensitive area can be made sufficiently high (57% with the present panel), and photocurrent decay times are sufficiently long to allow readout without loss of signal. In the readout operation, the gate lines are switched on sequentially, and the charge stored in the associated row of photodiodes is transferred to parallel data lines for readout by a bank of amplifiers. The amplifiers read the charge signals in parallel, and then output them sequentially as analog voltage signals to A/D converters. The digital image is typically corrected for offset and gain variations, and interpolations are performed for defective pixels.

With this protocol the x-ray source can be operated in the continuous exposure mode for image acquisition. In this mode the array is acquiring data *during* the readout cycle. Readout time is 1.6 s. Exposure is added to this in 0.1- or 0.2-s increments to provide up to 4.8 s exposure per frame, as shown in **Table 1**.

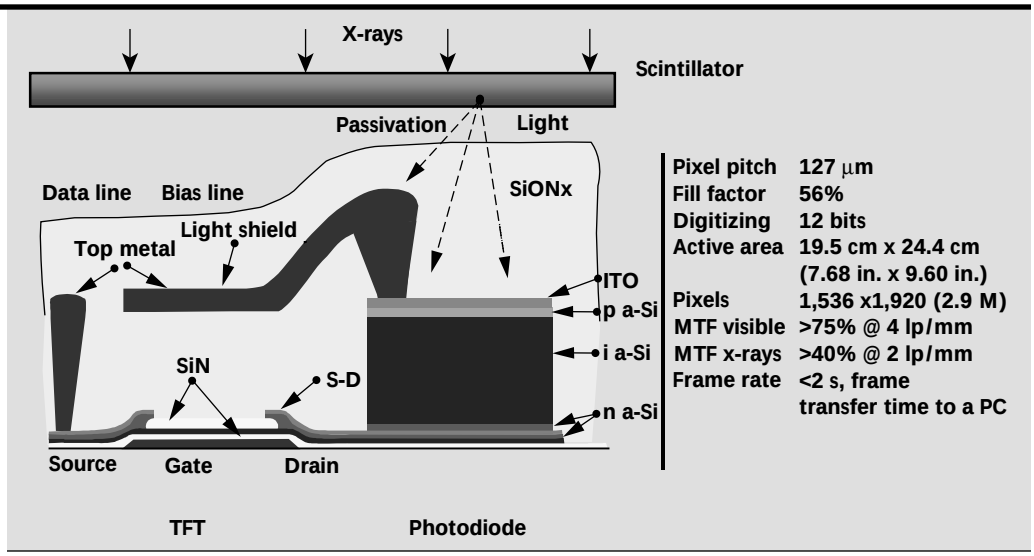

Figure 1. Schematic of dpiχ a-Si array.

The disadvantage of this is that variations in source intensity during the readout cycle will affect the data. For this reason source stability checks must be made before and after each image, using at least two unattenuated beam (I_0) regions in the image.

Progress

Calculated X-Ray Spectra

X-ray exposures were obtained with a conventional x-ray tube with maximum operating potential 450 kV, beryllium tube window, and focal spot of 1.0 mm. Filtered and unfiltered source spectra for this tube were calculated using Tubdet[28]. Results of these calculations are shown in **Figs. 2** through **4**. The calculated unfiltered spectra are shown in **Fig. 2** for x-ray tube operating potentials 120, 250 and 450 kV-peak (kVp). The characteristic Kα - and Kβ -fluorescence lines from the tungsten anode are apparent at 58.8 kV and 67.6 kV, but are clipped in these figures to allow display of the continuum spectrum. Unfiltered spectra are commonly used at lower operating potentials for radiography of thinner, lower atomic number materials to obtain the highest contrast sensitivity where latitude (that is, ability to image a range of thicknesses in a test object) is not an important consideration.

Table 1. Integration time options for dpiχ array.

Switch setting	Delay (s)	Readout (s)	Total
0	0.1	1.6	1.7
1	0.2	1.6	1.8
2	0.4	1.6	2
3	0.6	1.6	2.2
4	0.8	1.6	2.4
5	1	1.6	2.6
6	1.2	1.6	2.8
7	1.4	1.6	3
8	1.6	1.6	3.2
9	1.8	1.6	3.4
10	2	1.6	3.6
11	2.2	1.6	3.8
12	2.4	1.6	4
13	2.6	1.6	4.2
14	2.8	1.6	4.4
15	3	1.6	4.6
16	3.2	1.6	4.8

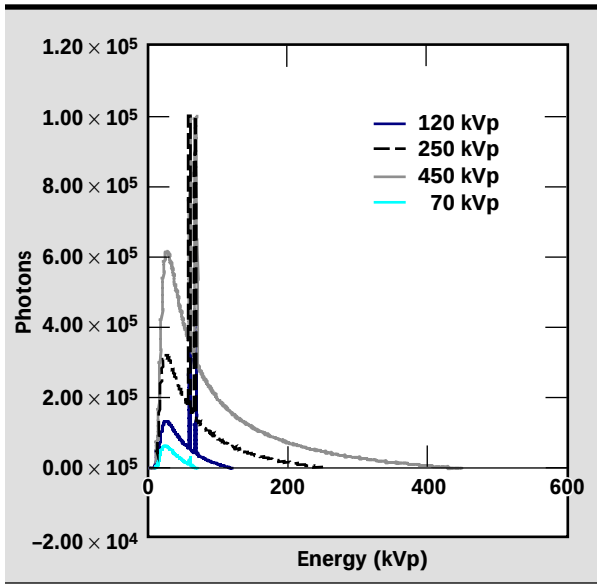

Figure 2. Calculated x-ray source spectra, unfiltered, at operating potentials of 70, 120, 250 and 450 kVp.

The calculated output spectra as filtered by 0.076 mm (0.003 in.) tungsten at 120 kVp, 3.2 mm (0.125 in.) copper at 250 kVp, and 6.5 mm (0.25 in.) copper at 450 kVp are shown in **Fig. 3**. Filtered spectra are commonly used at higher operating potentials for radiography of thicker, higher atomic number, or higher density materials to increase latitude and reduce scatter. A comparison of the filtered and unfiltered spectra at 120 kVp is shown in **Fig. 4** to indicate the reduced intensity in the low energy portion of the spectrum, and the reduced overall relative intensity. A step intensity change in the spectrum associated with the K-absorption edge of the tungsten filter at 69.5 kV is also apparent in **Fig. 4**.

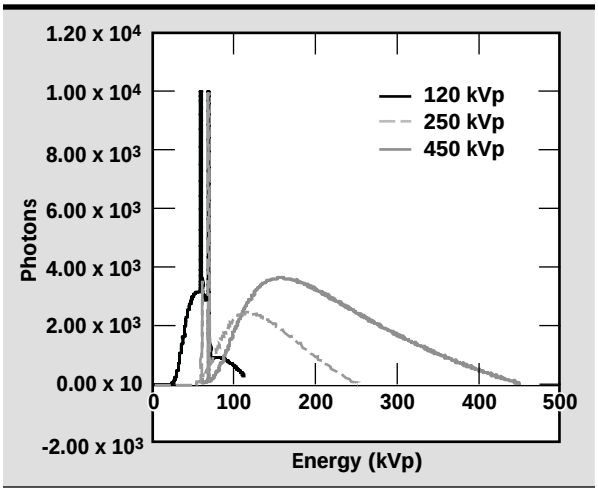

Figure 3. Calculated x-ray source spectra filtered by 0.076 mm W at 120 kVp, 3.2 mm Cu at 250 kVp, and 6.5 mm Cu at 450 kVp.

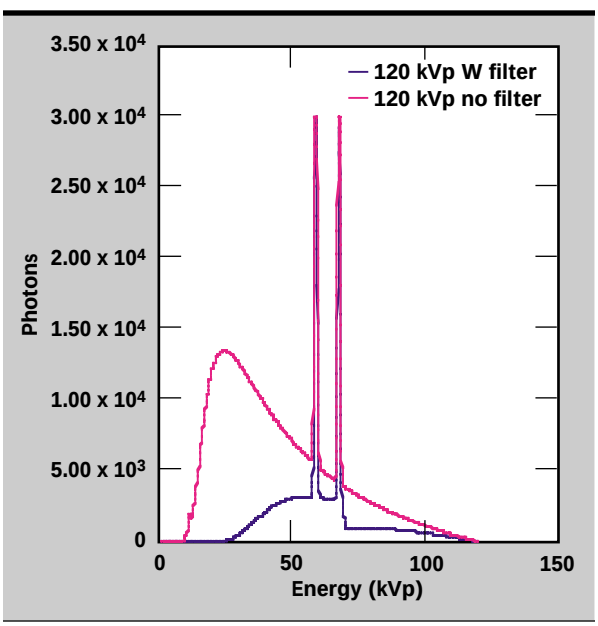

Figure 4. Comparison of calculated filtered and unfiltered x-ray source spectra at operating potential 120 kVp showing difference in low energy content.

Shielding

The a-Si array itself is not easily damaged by radiation exposure,[22] but electronic read-out components adjacent to the array within the panel enclosure are susceptible to radiation damage. The threshold for damage of these components is not known, and it was not the purpose of these tests to determine the threshold and thereby disable the panel. A short exposure x-ray image of the panel was taken to determine the location of sensitive components, and lead shielding was positioned to protect these components. The damage threshold for many electronic components is 1 krad of exposure, so lead shielding was sized to reduce accumulated exposures to below this level. This consisted of 6 to 12 mm of lead with the 450-kVp conventional x-ray tube source, and up to 50 mm of lead for the 9-MV linear accelerator. In addition, 150 mm of tungsten collimation limited the x-ray beam to the area of the panel for the 9-MV images.

Geometric Unsharpness

Unsharpness in the radiographic image that results from the geometric arrangement of x-ray tube, test object, and imager is always a concern when attempting to obtain best resolution. Geometric unsharpness (U), is given by the relationship U = F*T/D where F is the x-ray source focal spot diameter, T is the object-to-imager plane distance, and D is source-to-object distance.

In the present case, the a-Si array is separated from the front cover surface of the flat panel assembly by no more than approximately 6 mm (0.25 in.). This gives a U of 0.006 mm with the conventional x-ray tube using 1.0 mm focal spot, source-to-object distance 1 m, and object positioned directly against the front surface of the panel. This is only a small fraction of a pixel size, 0.127 mm, and is therefore not a contributor to degraded resolution for thin or small diameter objects. Geometric unsharpness that would contribute to degraded resolution comes from values of U that are a significant fraction of a pixel size, such as more than one-half pixel dimension or 0.06 mm. This condition would occur for an object-to-imager separation, or object cord length of more than 50 mm, given 1.0 mm focal spot and 1 m source-to-object distance. Acceptably small U for larger diameter objects, or larger object-to-imager separations, are obtained by increasing source-to-object distance with considerations of reduced x-ray intensity at the imager due to the larger source-to-imager distance.

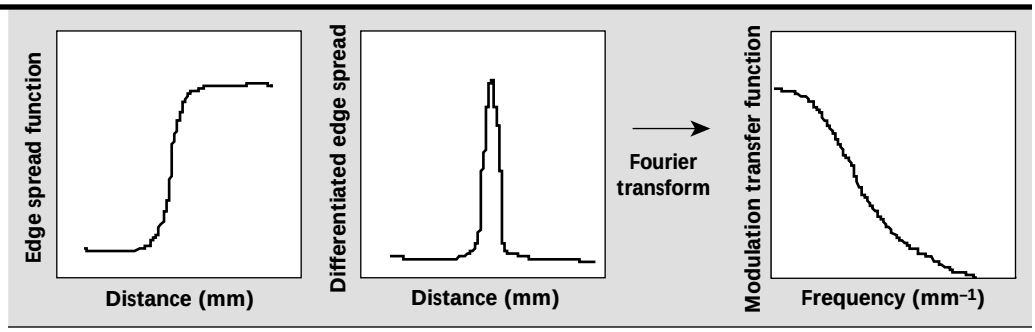

Figure 5. Principle of the edge-spread function in determining the modulation transfer function.

Modulation Transfer Function

The modulation transfer function (MTF) describes contrast transmission as a function of feature size. It is a function that is sensitive to all the elements of an imaging system that contribute to image unsharpness, and provides a practical measure of the capability of an imaging system to distinguish features of various sizes. One method for obtaining an MTF is to determine the edge spread function. This is done by obtaining the image of a totally absorbing object that has a sharp edge, such as a thin parallelopiped block, where the edge surface is positioned parallel to the centerline of the x-ray beam. In our case, a thin right parallelopiped tantalum block was positioned against the front panel of the a-Si imager on the centerline of the x-ray beam. A line trace of the image intensity across the edge is obtained, and then the differential of this trace is determined (see **Fig. 5**). The differential trace can be fit to a Gaussian or multiple Gaussian functions to model the peaks and tails to eliminate noise variations. The MTF is then obtained as the normalized magnitude of the Fourier transform of the differentiated edge spread function (see **Fig. 5**), and has units of spatial frequency, such as mm^{-1} or line pair/mm (lp/mm).

Calibrating the dpiχ Array

To use the output of the Flashscan 20 flat panel array for quantitative digital radiography and CT we have calibrated raw panel output to a scale that is roughly linear with x-ray intensity. The procedure we have developed differs somewhat from the approach put forth by dpiχ, but is similar in concept. Both procedures derive from the intrinsic properties of the panel as it responds to radiation.

The raw image from the Flashscan 20 flat panel array contains many features characteristic of the construction of the array, and the way in which the a-Si responds to scintillation light. **Figure 6** is an image of a "dark-field," the image of the panel with no x rays impinging on the detector. Unlike a CCD-based imager, or an image intensifier, dpiχ has chosen a convention such that pixels in the detector start at the maximum value, somewhere between 3700 and 4000. Notice the differences in digital values for the horizontal bands across the image.

The Flashscan 20 array is put together in 128 pixel row elements, which are then combined to make the full panel. There are small gain and offset variations between the bands as observed in **Fig. 6** where the gray scale lookup table has been set to emphasize these variations. There is a slight banding in the other direction. In addition, there is a small additive bias across the panel. While not as visible in the reduced image in the figure (resampling was required to get the image onto the page), a number of bad pixels (pixels which have a poor or unusual impulse response) are also a part of the panel.

Figure 7 is an image of the "light-field" of the panel acquired at 9 MV at a source-to-imager distance of 6 m. The acquired image appears darker with increases in scintillation light. The features related to the bands are present for increased intensity, although the relative response of each band is a bit different. One band may be close to saturation (very dark), while an adjacent band is up to 500 counts lighter. Consequently, the dynamic range of each bank is different.

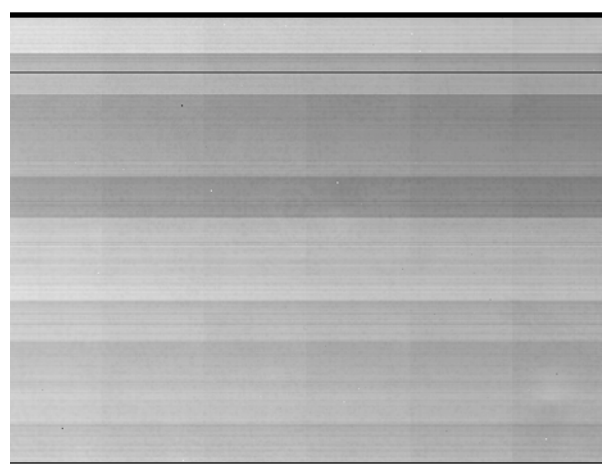

Figure 6. The "dark field" image of the 8-x-10 Flashscan 20 array.

In evaluating individual pixels, it was clear that the response is not linear over the number of possible digital levels. The pixels respond to the scintillation light by losing digital counts, and it is this change which is the digital record of the x-ray image. To evaluate the change in intensity per pixel we have re-normalized the digital levels to be dark field minus signal. **Figure 8** plots the re-normalized digital readout for 3 pixels in the same bank, and **Fig. 9** shows similar data for 4 pixels in a different bank.

Notice the small but significant nonlinearity in the response of the pixels as the panel detects more scintillation light. This effect gets more pronounced for normalized counts greater than 3400. There is a transition in the linearity of the scale for this array, which takes place at about 2000 to 2200 normalized counts (mid-field signal). Another transition takes place at 3300 to 3400 normalized counts (dark-field signal). Dpiχ does not recommend attempting to calibrate using intensity values greater than 3400. In addition the values in the unnormalized light-field should not be lower than 500 for the lowest valued bank.

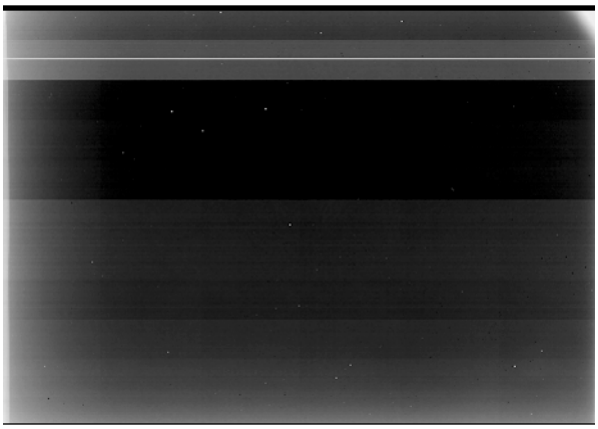

Figure 7. The "light-field" image of the 8-×-10 Flashscan 20 array. The light outer boundary on the left side and at the upper right of this image is collimator cutoff.

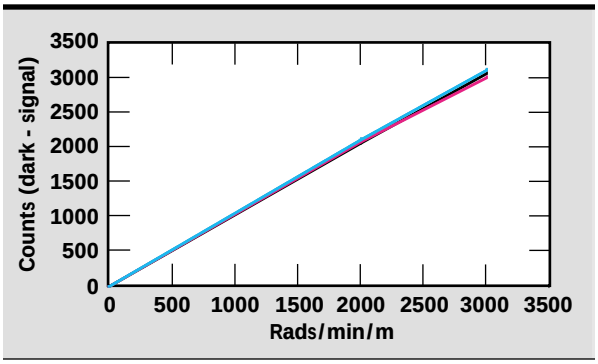

Figure 8. Flashscan 20 panel counts vs radiation intensity for 3 pixels in the same bank.

To produce images that equilibrate the effects of banding, account for the small bias, and correct for the other effects in the raw panel images, dpiχ has developed a "two-gain-factor" approach for the a-Si array. First they acquire a light-field image with no bank lower than 500 counts. Then they acquire a mid-field image at somewhere between 2200 and 1200 (50 to 80% change in digital counts from the light field). Finally they acquire a dark-field image. From the three images they calculate two gain coefficients (one from dark and mid, one from mid and light). The gain coefficients are applied per pixel as the raw pixel signal value falls into the dark-mid or mid-light range.

For compatibility with current medical inspection practice, the method chosen by dpiχ results in digital images calibrated to look like film (low digital values where there is high intensity, and high digital values for low radiation intensity). Values at high and low ends of the digital scale are clipped to enable the best viewing of the object. For CT applications, we prefer the raw images be calibrated to a scale that is the reverse of film (high digital values where there is high intensity, and low digital values where there is low intensity). An additional requirement for CT is that the digital values not be clipped to some value at either the high or low end of the digital scale. Consequently, we developed a calibration technique that uses the basic scheme of the dpiχ approach, but by using the re-normalized data puts the data on a positive scale.

For both approaches bad pixels are handled in a similar fashion. Once a pixel is determined to be bad it is replaced by the average or median value of adjacent good pixels. The dpiχ software finds bad pixels with the dark-field image, identifying those locations that have values below a certain level. We are just as concerned about pixels that read too high, as about those that read too low. Consequently, we use the mid-field image and identify bad pixels as those that are different from

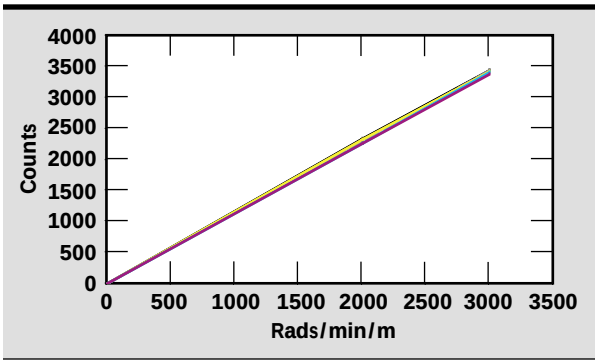

Figure 9. Flashscan 20 panel counts vs radiation intensity for 4 pixels in the same bank.

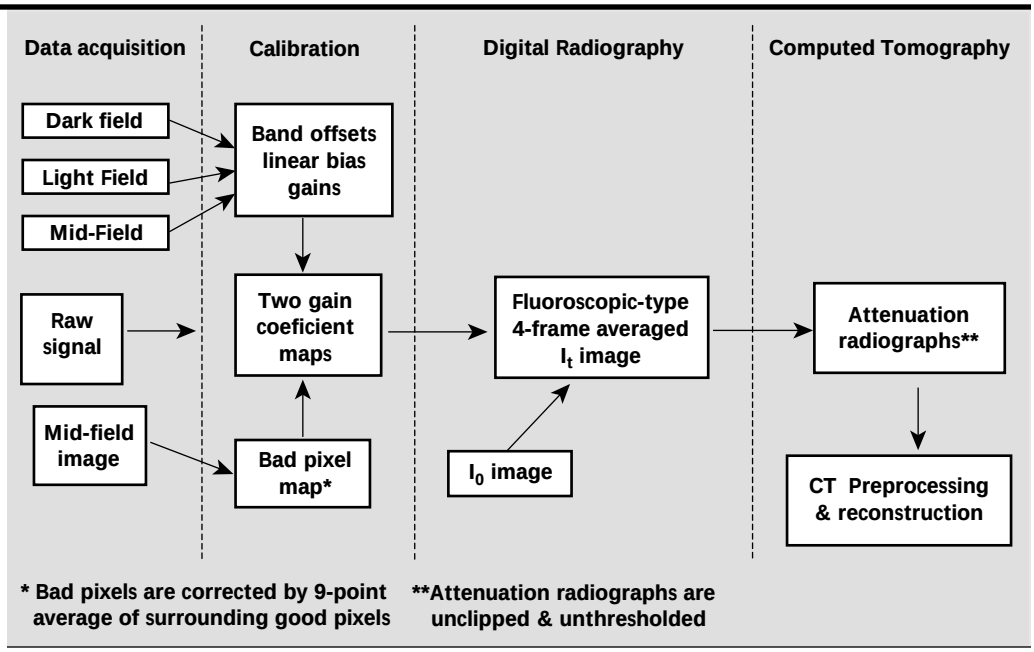

Figure 10. Block flow diagram of the data processing protocol for digital radiography and CT with the dpiχ flat panel imager.

a median of the neighborhood by certain value. We use the median of the good adjacent pixels as the best estimate of the bad pixel replacement values. The use of the median value is part of our attempt to do better at bank boundaries. We also routinely acquire an I_0 image that is the detected level of the radiation without the part in the field of view, and use this image to further process out small offsets in the images. The I_0 image is also important for calculating attenuation radiographs, a necessary step for subsequent CT pre-processing and reconstruction. The processing protocol we use is shown in **Fig. 10**.

Our calibration produces images in counts, which are larger with higher x-ray intensity, and smaller with lower intensity. **Figure 11** (by permission of Ford Motor Company, Dearborn, Michigan) is a calibrated image of a Ford prototype clutch retainer acquired at 4 MV with the dpiχ panel. **Figure 12** contains a CT slice from the 3-D CT volume using the calibrated data and rotation-only scanning. The CT slice shows the inner detail of a 150-µm slice of the laser weld joint. A small cupping artifact is present in the data, which is a result of beam hardening. Otherwise, the data is an accurate representation of the internals of this object. The artifact content in CT reconstructed images grows with the proportion of nonlinear effects in the input digital imagery. These CT data and other scans attest to the roughly linear character of the calibration scheme we have developed.

Evaluation Process

Our evaluation process included a study of scintillation screens, plain glass, and bare metals to determine their potential as image forming elements, producing either visible light or secondary electron emission. We determined the MTF by the absorptive edge method at a number of different x-ray energies, including both unfiltered and filtered spectra at 120, 250, and 450 kV, and 4 and 9 MV. Spatial resolution for the unfiltered spectra at 120, 250, and 450 kV was also determined using a diverging line pair gauge. Contrast sensitivity and

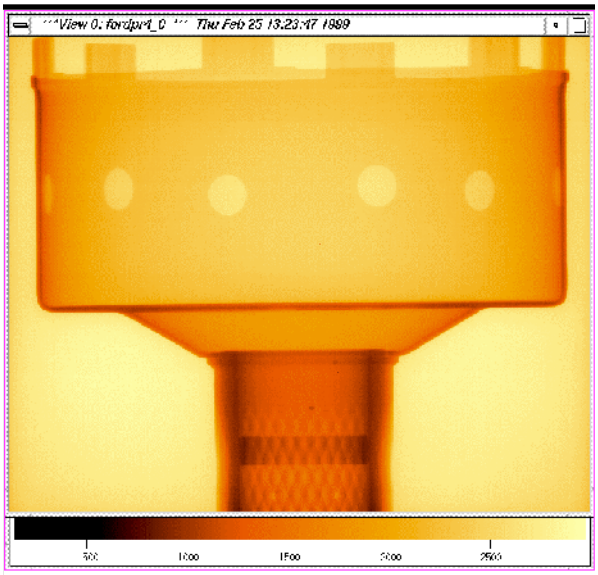

Figure 11. Calibrated image of Ford prototype clutch retainer housing (by permission of Ford Motor Company, Dearborn, Michigan).

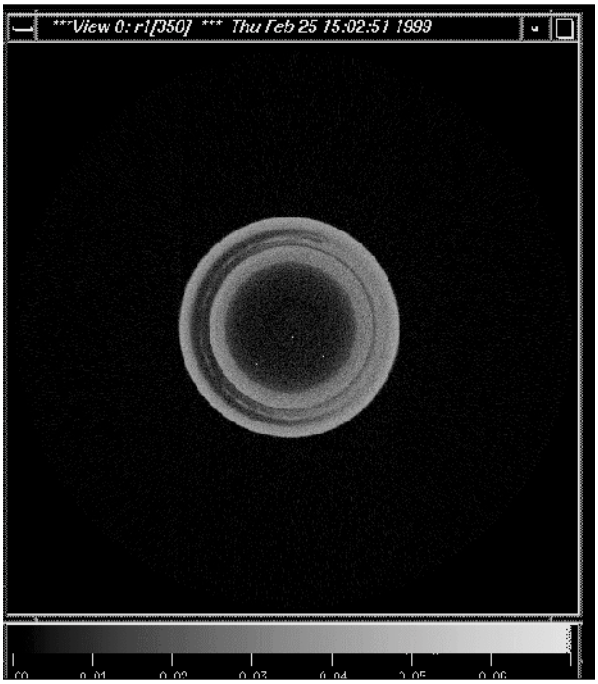

Figure 12. CT slice at laser weld joint of Ford prototype clutch retainer housing (by permission of Ford Motor Company, Dearborn, Michigan).

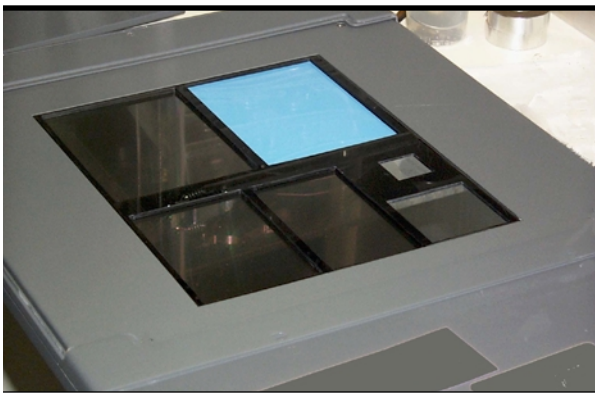

Figure 13. Photograph of test setup. The metal plates are not visible.

latitude were determined with step wedges of various materials. Dark current, image reproducibility, dynamic range, image acquisition speed, throughput, potential for latent image formation, and corrective measures for source instability were also addressed.

Results

A number of different materials—gadolinium-oxysulfide (GdO_2S_2) particulate scintillator screens, high-Z metal sheets, two scintillator glass plates, and a scintillator glass fiber optic plate—were configured with the Flashscan 20. The particulate screens are commercial products composed of GdO_2S_2 powders of different sizes, binder, dyes, and coatings on a plastic substrate. The two scintillating glass plates are commercial, terbium-doped clear glass. One plate had no surface coating and the other had a mirror coating on one side and an anti-reflective coating on the other. The fiber optic screen is made up of the same glass material drawn into 6-µm fibers.

The screens, sheets, and plates were positioned inside the light-tight enclosure of the a-Si imager in direct contact with the imager elements, held in contact by compressive force with a sponge rubber mat. A mosaic array of these materials was configured to obtain relative efficiencies for converting x-ray exposure to image signal. A photograph of the setup is shown in **Fig. 13**. Metal foils were also placed directly against the a-Si diode array to determine sensitivity to electron emission directly from the foils when irradiated by a 9-MV Bremsstrahlung spectrum.

A digital image of the test matrix and horizontal lineouts is shown in **Fig. 14**. Because of wrap-around problems and calibration constraints, no quantitative assessment can be made of relative speeds of the screens.

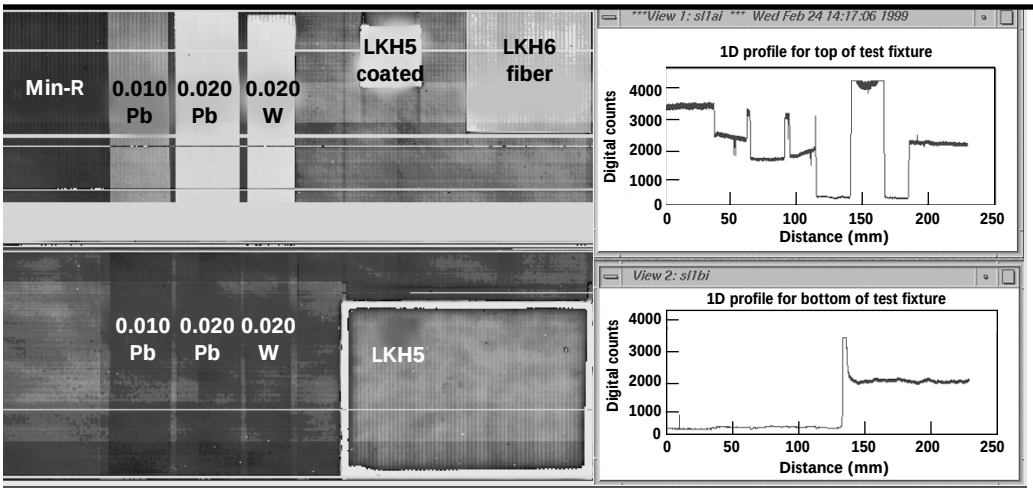

Figure 14. Digital image and horizontal lineouts of image.

The conversion mosaic array was tested first at 9 MV with the intention of taking the most promising results and applying them at the lower energies, such as 120 to 450 kV. Results of the conversion efficiency measurements at 9 MV are given in **Table 2**.

We do not observe the Flashscan 20 to be sensitive to electrons emitted by the bare metal, but a metal sheet in combination with scintillating screens does have a small enhancement effect over the screen alone, as expected. The scintillator glass plates, mirror coated and uncoated, and glass fiber plate scintillator are all more effective in producing image signal than the particulate (Min-R) screen but the resolution is not as good as the particulate screen. From the plain glass results we can conclude that there is no measurable effect from Cerenkov light.

Because the Flashscan 20 proved to be an efficient x-ray imager with the slower but higher resolution GdO_2S_2 particulate screens, a mosaic array of GdO_2S_2 screens only was tested at 120, 250, and 450 kVp, using both filtered and unfiltered x-ray spectra. The screens in this array were Kodak Lanex-Fine, Lanex-Regular, Lanex-Fast, and Min-R. We later discovered, and our studies confirm, that Lanex-Fast and Lanex-Regular are the same material, and that Lanex-Fine and Min-R are the same material with slightly different thickness and backing.

Table 2. Relative efficiency and spatial resolution of different combinations of materials used in the a-Si panel assembly for conversion of x-ray exposure to image signal.

Screen/Material	Supplier	Sheet/Plate thickness (mm)	Relative sensitivity rank order*	Relative resolution rank order*
Min-R screen only	Kodak	N/A	7	1
Min-R Screen + 0.508-in. W sheet	Kodak	0.50	5	2
Min-R screen + 0.508-mm Pb sheet	Kodak	0.50	5	2
Min-R screen + 0.254-mm Pb sheet	Kodak	0.25	4	2
LKH5 glass plate scintillator (2 mm thick)	IQI	2.0	2	Negligible
LKH6 glass fiber scintillator (12 µm dia. fiber, 1.6 mm thick)	IQI	1.6	2	5
LKH5 glass plate scintillator, mirror coated (2 mm thick)	IQI	2.0	1	Negligible
Pb sheet only	N/A	0.50	Negligible	N/A
W sheet only	N/A	0.50	Negligible	N/A
Glass sheet only	N/A	2.0	Negligible	N/A

* Rank order no. 1 indicates best performance.

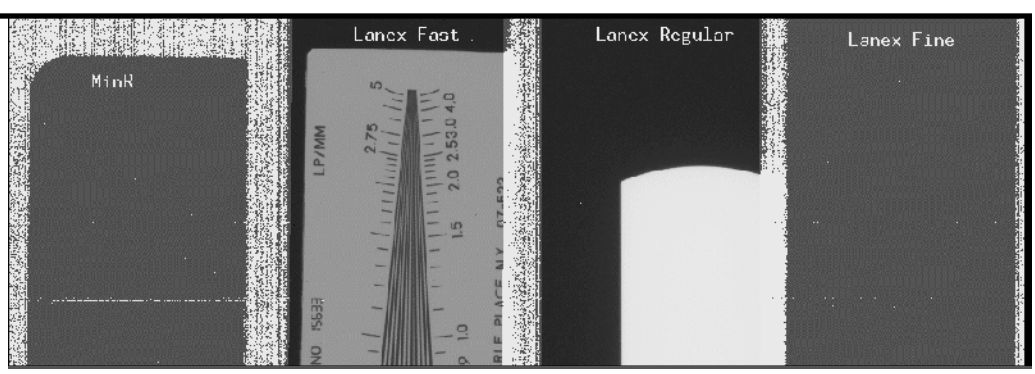

Figure 15. Image of screen array including Min-R, Lanex-Fast, Lanex-Regular, and Lanex-Fine as obtained with Flashscan 20. Diverging line pair gauge is positioned to image with Lanex-Fine. Tantalum block is positioned to image with Lanex-Regular.

A diverging line-pair gauge, tungsten block and tantalum cylinder were imaged with the array of screens as shown in **Fig. 15** (tantalum cylinder not shown).

A digital image of a line pair gauge taken at 120 kVp is shown in **Fig. 16a**. Lineouts at 2, 3, and 4 lp/mm are shown in **Fig. 16b**. Note that aliasing begins between 3 and 4 lp/mm which is consistent with the pixel pitch and the MTF data presented below.

Images of the tantalum pieces were used to determine the MTF by the edge-spread method. The tungsten pieces provide total absorption, or near total absorption, at all x-ray spectra at operating tube voltages 120 kV to 450 kV. The MTFs for the four screens at 120, 250 and 450 kVp, respectively, are shown in **Figs. 17**, **18**, and **19**. Note that the Lanex-Fine and Min-R curves are very similar as are the Lanex-Regular and Lanex-Fast.

The MTF results for unfiltered and filtered spectra are shown in **Figs. 20** and **21**, respectively. The MTF for the unfiltered spectra show essentially no energy dependence, and provide useful modulation, for example, greater than 5%, up to 3.5 lp/mm. This indicates that the limiting factor in resolution for these tests is the pixel size of the a-Si array (4 lp/mm). The MTF for the filtered 250 and 450 kV spectra are nearly the same, while the MTF for the filtered 120 kV spectrum is considerably lower.

An important measure for practical use of the a Si imager is the maximum exposure that can be applied to the imager without saturating the electronic storage capacity of the array. The useful range of the imager in our case corresponded to a pixel value of 3400 with no exposure (for example,

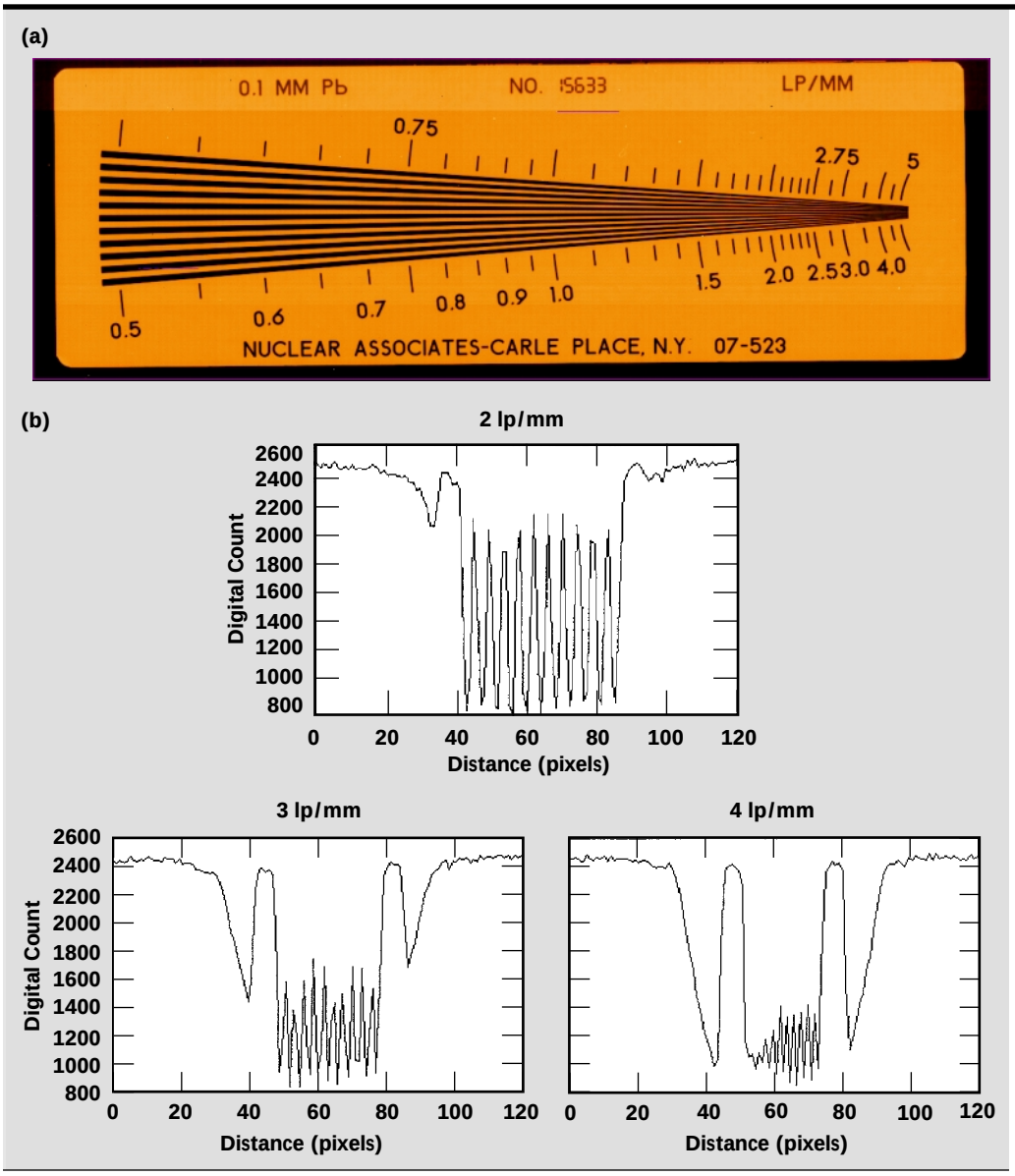

Figure 16. Digital image of (a) line pair gauge and (b) lineouts at 2, 3, and 4 lp/mm.

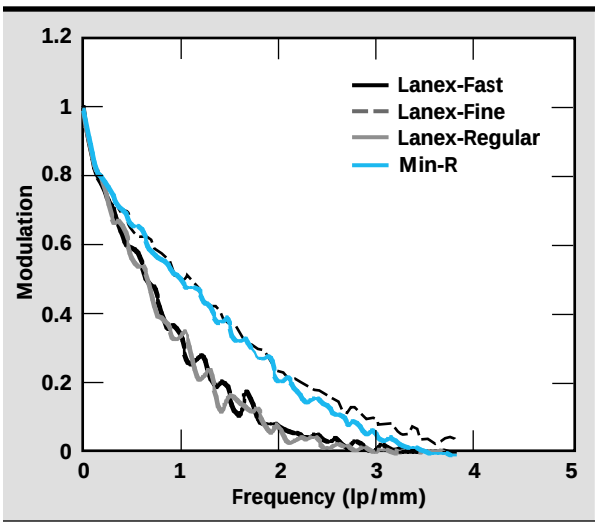

Figure 17. Modulation transfer function of a-Si imager with four different screens at x-ray source energy 120 kVp.

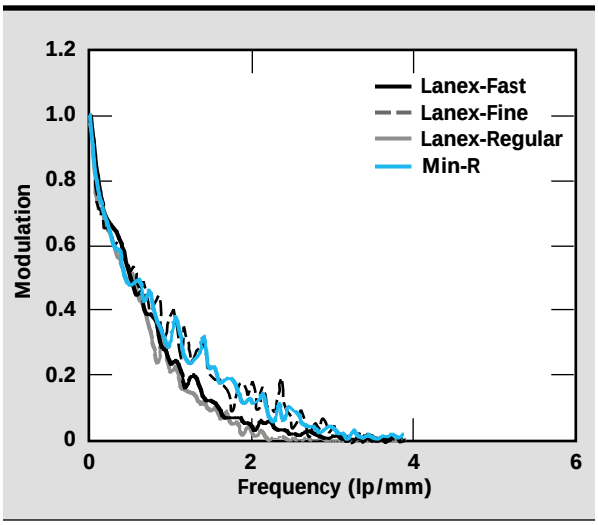

Figure 18. Modulation transfer function of a-Si imager with four different screens at x-ray source energy 250 kVp.

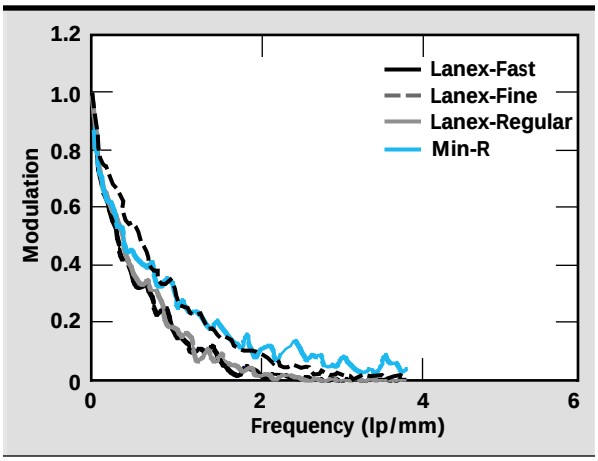

Figure 19. Modulation transfer function of a-Si imager with four different screens at x-ray source energy 450 kVp.

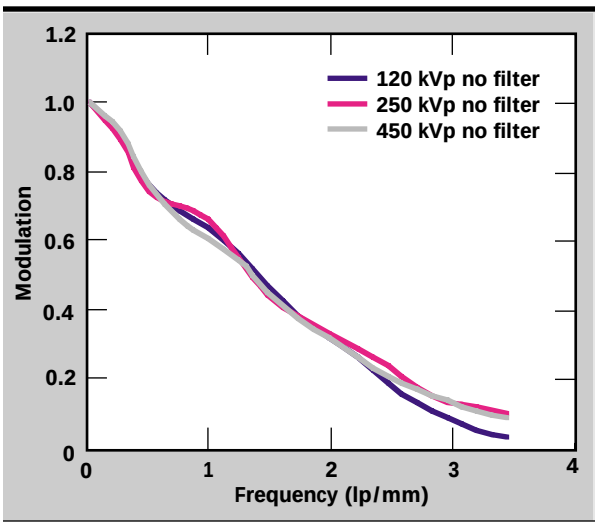

Figure 20. Modulation transfer function of a-Si imager with Min-R screen for unfiltered spectra at 120 kVp, 250 kVp, and 450 kVp.

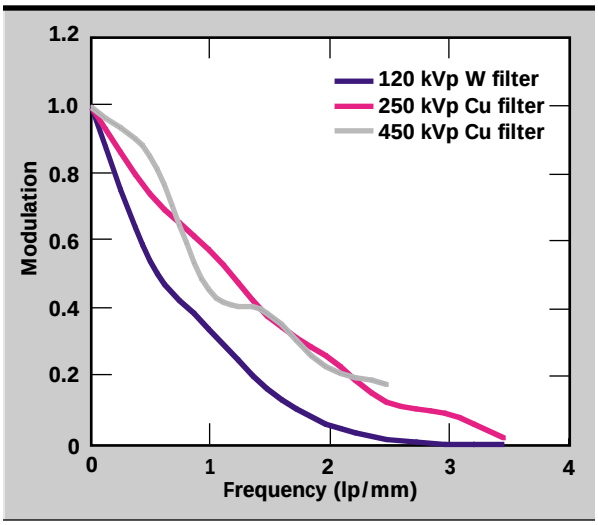

Figure 21. Modulation transfer function of a-Si imager with Min-R screen for filtered spectra at 120 kVp, 250 kVp, and 450 kVp.

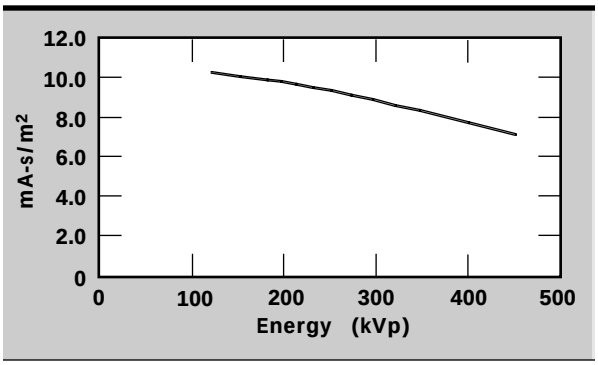

Figure 22. Exposure parameters required to produce light-field image, for example, maximized image without saturation, in terms of x-ray machine settings and source-to-imager distance in units of mA-s/m^2.

dark-field image as previously described in the calibration section) to a value of 500 with maximum exposure (for example, light-field image previously described in the calibration section). This provides a useful dynamic range of nearly 3000, which is less than the 12-bit (4096) digital capability of the panel, but greater than 11 bits (2048). The exposure required to produce the light-field image in terms of x-ray machine settings and source-to-imager distance in units of milliampere-seconds/square meter (mA-s/m^2) is shown in **Fig. 22** for unfiltered source spectra.

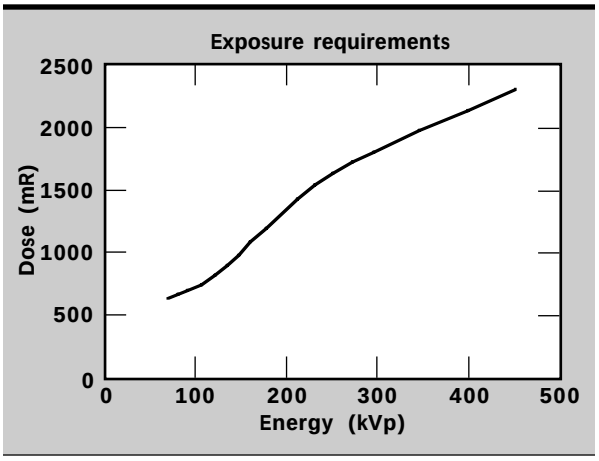

Figure 23. Exposure requirement for unfiltered x-ray spectra to produce light-field image, for example, maximized image without saturation, in terms of accumulated dose (milliroentgen).

The exposure requirements to produce the light-field image in terms of accumulated exposure at the imager is shown in **Fig. 23** for unfiltered source spectra.

Applications

The dpiχ a-Si flat panel imager provides a quality large area digital image for a variety of applications. We have used the present 8-in.-×-10-in. flat panel imager, and additional 12-in.-×-16-in. imagers for programmatic test objects, automotive components, castings, and structural components.

A 76-mm-diameter steel bridge pin was inspected at 9 MV, using both digital radiography and CT.[29] Known defects were detected and measured. A digital radiograph of a bridge pin is shown in **Fig. 24** along with two horizontal slices. Vertical slices are shown in **Fig. 25**. A digital radiograph and a CT slice of a prototype clutch retainer are shown in **Fig. 26**.

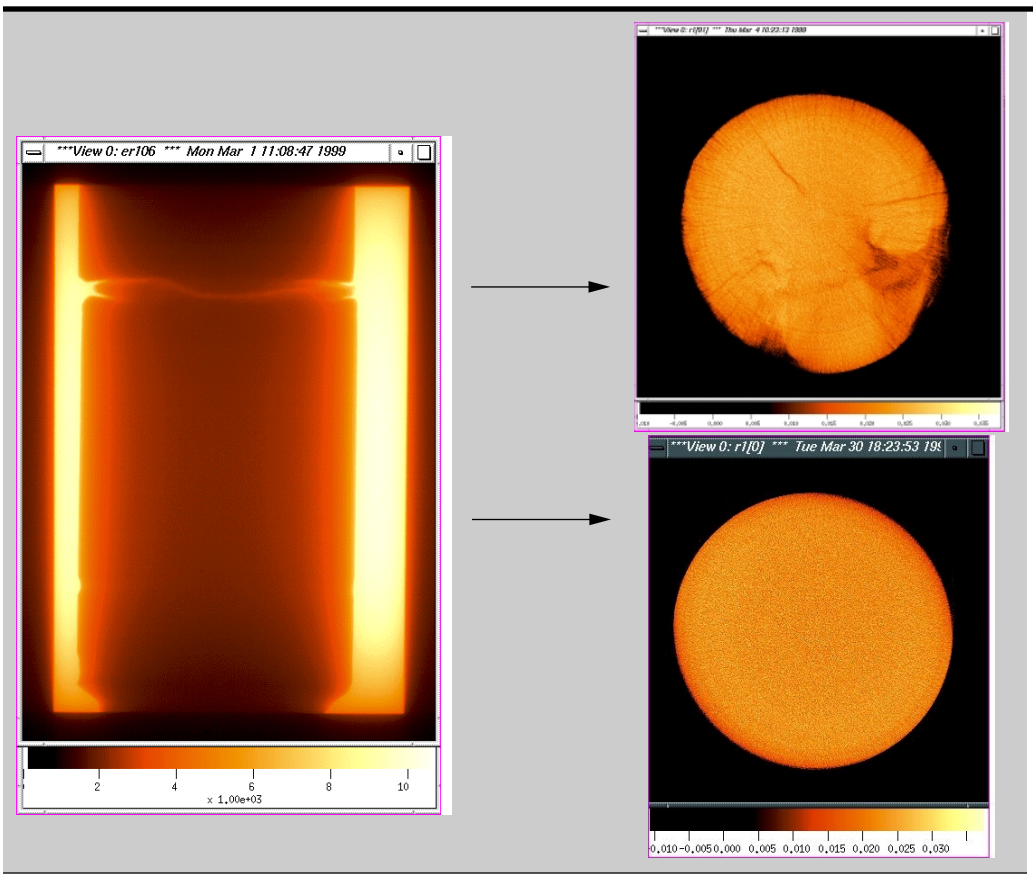

Figure 24. Digital radiograph (left) and CT slices (right) of a bridge pin with a-Si flat panel imager at 9 MV.

Conclusions

The dpiχ a-Si flat panel has been shown to be extremely useful for digital radiography and CT. The image acquisition time, image quality, and field of view (image area) makes possible fast turnaround radiographic evaluation of components, quantitative evaluation of the digital images based on existing image analysis codes, on-line inspection for production applications, and data acquisition for large CT data sets (many angular views). The useful energy range spans all the energies attempted here, 120 kV to 9 MV. The spatial resolution is limited by the pixel size of the imager to approximately 3.5 lp/mm and the dynamic range is approximately 3000. Image areas are available up to 300 mm × 400 mm, and a mosaic arrangement of 4 panels will give 1200 mm × 1600 mm image area. Radiation damage is a concern, but we believe recent developments have moved sensitive components sufficiently away from the image area that they can be adequately shielded.

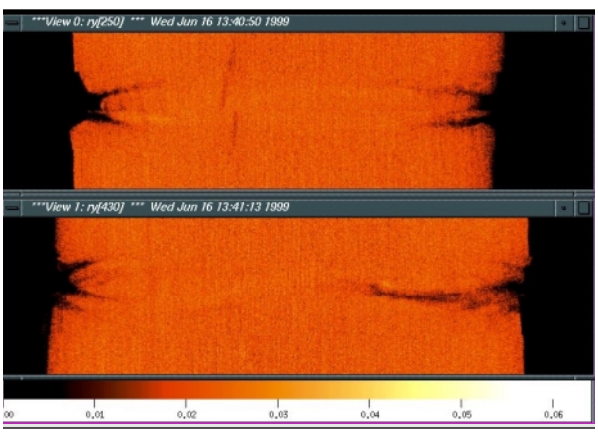

Figure 25. Vertical CT slices from bridge pin data.

Acknowledgments

We would like to acknowledge the contributions of E. Updike, K. Morales, and A. Guerrero for data acquisition and test setup configurations, and A. Waters for bridge pin CT reconstructions.

References

1. C. M. Logan *et al*, "MTF results: dpiχ Flashscan 20 imaging array in a 9-MV linac spectrum and comparison to IQI glass/CCD," in press.

2. R. A. Street, S. Nelson, L. Antonuk, and V. Perez-Mendez (1990), "Amorphous silicon sensor arrays for radiation imaging," *Materials Research Society Symposium Proceedings*, Vol. **192**, pp. 441–452.

3. L. E. Antonuk, J. Yorkston, W, Huang, J. Boudry, E. J. Morton, and R. A. Street (1993), "Large-area flat-panel a-Si:H arrays for x-ray imaging," *SPIE Proceedings*, Vol. **1896**, pp. 18–29.

4. R. A. Street and L. E. Antonuk (1993), "Amorphous silicon arrays develop a medical image," *IEEE Circuits and Devices*, pp. 38–42.

5. P. K. Gallagher (1995), "Amorphous silicon arrays promise large-area imagers," *Laser Focus World*, May.

6. W. Que and J. A. Rowlands (1995), "X-ray imaging using amorphous selenium inherent spatial resolution," *Med. Phys.*, Vol. **22**, No. 4, pp. 365–374, April.

7. J. A. Rowlands and D. M. Hunter (1995), "X-ray imaging using amorphous selenium: photoinduced discharge (PID) readout for digital general radiography," *Med. Phys.*, Vol. **22**, No. 12, pp. 1983–1996, December.

8. R. E. Colbeth, M. J. Allen, D. J. Day, D. L. Gilblom, M. E. Klausmeier-Brown, J. Pavkovich, E. J. Seppi,

Figure 26. Digital radiograph (a) and CT slice (b) of Ford prototype clutch retainer housing (by permission of Ford Motor Company, Dearborn, Michigan) with a-Si flat panel imager at 4 MV.

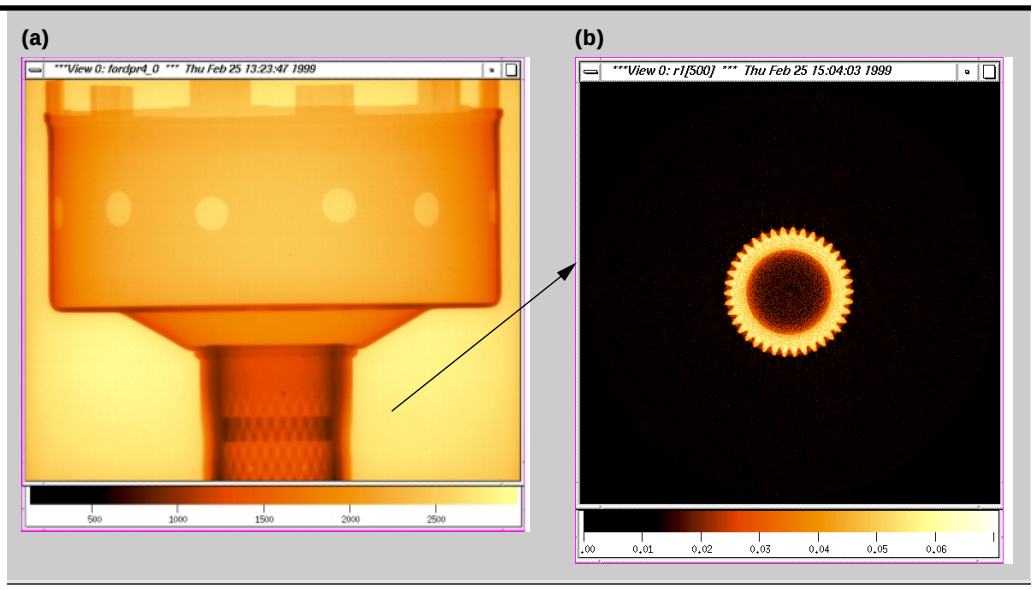

and E. G. Shapiro (1997), "Characterization of an amorphous silicon fluoroscopic imager," *Proc. of SPIE Conference on Medical Imaging, Physics of Medical Imaging, SPIE,* Vol. **3032**, February 22–28.

9. D. L. Gilblom (1997), "From amorphous silicon: large-area electronic imagers for x-ray and more," *Advanced Imaging*, pp. 44–48, September.

10. P. K. Solatani, D. Wysnewski, and K. Swartz (1999), "Amorphous selenium direct radiography for industrial imaging," *Proc. of Computerized Tomography for Industrial Applications and Image Processing in Radiology*, Berlin, Germany, March 15–17.

11. M. J. Yaffe and J. A. Rowland (1997), "X-ray detectors for digital radiography," *Physics in Medicine and Biology*, Vol. **42**, pp. 1–39.

12. W. Zhao and J. A. Rowlands (1997), "Digital radiology using active matrix readout of amorphous selenium: theoretical analysis of detective quantum efficiency," *Med. Phys.*, Vol. **24**, No. 12, pp. 1819–1833, December.

13. L E. Antonuk, Y. El-Mohri, A. Hall, K-W Jee, M. Maolinbay, S. C. Nassif, X. Rong, J. H. Siewerdsen, Q. Zhao, and R. L. Weisfield (1998), "A large-area, 97 µm pitch, indirect-detection, active matrix, flat-panel imager (AMFPI)," *Proc. of SPIE Conference on Medical Imaging, Physics of Medical Imaging, SPIE,* Vol. **3336**, pp. 2–13, February 22–24.

14. C. Bueno and G. A. Mohr (1998), "Advanced digital x-ray radiographic systems," *Proc. of ASNT Fall Conference and Quality Testing Show*, pp. 121–123, October 19–23.

15. R. E. Colbeth, M. J. Allen, D. J. Day, D. L. Gilblon, R. A. Harris, I. D. Job, M. E. Klausmeier-Brown, J. M. Pavkovich, E. J. Seppi, E. G. Shapiro, M. D. Wright, and J. M. Yu (1998), "Flat-panel imaging system for fluoroscopy applications," *Proc. of SPIE Conference on Medical Imaging, Physics of Medical Imaging, SPIE,* Vol. **3336**, pp. 376–387, February 22–24.

16. M. E. Klausmeier-Brown, M. J. Allen, S. J. Boyce, R. E. Colbeth, D. L. Gilblom, I. D. Job, M. Koenig, J. M. Pavkovich, M. Wright, and J. M. Yu (1998), "Real-time image processing in a flat-panel, solid-state, medical fluoroscopic imaging system," *Proc. of SPIE Conference on Real-Time Imaging III, SPIE,* Vol. **3303**, January 26.

17. C. M. Logan, J. J. Haskins, K. E. Morales, E. O. Updike, J. M. Fugina, A. D. Lavietes, D. J. Schneberk, G. J. Schmid, K. Springer, P. Soltani, and K. Swartz (1998), "Evaluation of an amorphous selenium array for industrial imaging," Lawrence Livermore National Laboratory, Livermore, California (UCRL-ID-132315).

18. D. Mah, J. A. Rowlands, and J. A. Rawlinson (1998), "Sensitivity of amorphous selenium to x-rays from 40 kVp to 18 MV: measurements and implications for portal imaging," *Med. Phys.*, Vol. **25**, No. 4, pp. 444–456, April.

19. G. Pang, W. Zhao and J. A. Rowlands (1998), "Digital radiology using active matrix readout of amorphous selenium: geometrical and effective fill factors," *Med. Phys.*, Vol. **25**, No. 9, pp. 1636–1646, September.

20. E. Samei, M. J. Flynn, and D. A. Reiman (1998), "A method for measuring the presampled MTF of digital radiographic systems using an edge test device," *Med. Phys.*, Vol. **25**, No. 1, pp. 102–112, January.

21. J. H. Siewerdsen, L. E. Antonuk, Y. El-Mohri, J. Yorkston, and W. Huang (1998), "Signal, noise power spectrum, and detective quantum efficiency of indirect-detection flat-panel imagers for diagnostic radiology," *Med. Phys.*, Vol. **25**, No. 5, pp. 614–628, May.

22. J. H. Siewerdsen and D. A. Jaffray (1999), "A ghost story: spatio-temporal response characteristics of an indirect-detection flat-panel imager," *Med. Phys.*, Vol. **26**, No. 8, August.

23. R. E. Colbeth, V. N. Cooper III, D. L. Giblom, R. Harris, I. D. Job, M. E. Klasumeier-Brown, M. Marc, J. Pavkovich, E. J. Seppi, E. G. Shapiro, M. D. Wright, and J. M. Yu (1999), "Characterization of a third generation, multi-mode sensor panel," *Proc. of SPIE Conference on Medical Imaging, Physics of Medical Imaging*, Vol. **3659**, pp. 491–500, February.

24. K. M. Gibbs, H. Berger, T. Jones, J. Haskins, D. Schneberk, and J. Brenizer (1999), "Flat panel imaging of thermal neutrons," *Proc. of ASNT Fall Conference and Quality Testing Show*, pp. 140–142, October 11–15.

25. T. S. Jones (1999), "Evaluation of digital x-ray imaging systems for US Air Force applications," *Proc. of ASNT Fall Conference and Quality Testing Show*, pp. 137–139, October 11–15.

26. C. M. Logan and A. E. Scach von Wittenau, "Back shield albedo effects on imagery with a dpiχ Flashscan 20 using a 9 MV Bremsstrahlung spectrum," Lawrence Livermore National Laboratory, Livermore, California, in press.

27. R. L. Weisfield, M. A. Hartney, R. A. Street, and R. B. Apte (1998), "New amorphous-silicon image sensor for x-ray diagnostic medical imaging applications," *Proc. of SPIE Conference on Medical Imaging, Physics of Medical Imaging*, Vol. **3366**, pp. 444–452, February 22–24.

28. D. E. Perkins, R. R. Ryon, J. J. Haskins, and K. W. Dolan (1991), "Calculation of x-ray tube spectra on the Macintosh," *Proc. of ASNT Spring Conference*, March.

29. A. M. Waters, H. E. Martz, C. M. Logan, E. Updike, and R. E. Green, Jr. (1999), "High energy x-ray radiography and computed tomography of bridge pins," Lawrence Livermore National Laboratory, Livermore, California (UCRL-JC-132822), May.

High-Frequency Laser-Based Ultrasound for NDC Applications

Robert D. Huber and Graham H. Thomas
Manufacturing and Materials Engineering Division
Mechanical Engineering

Howard Lee
Defense and Nuclear Technology

Christopher Richardson and Professor James Spicer
The Johns Hopkins University
Baltimore, Maryland

We have demonstrated the feasibility of using a pump-probe system to generate and detect very high-frequency ultrasound. We have investigated materials such as Mo/Si multilayers. Frequencies as high as 892 GHz were detected, and the effects of 100-nm-diameter defects were observed. High-frequency laser-based ultrasound has proven useful for nondestructive characterization applications.

Introduction

Many new high-technology materials and structures have critical dimensions that can be quite small, down to the nanometer level, and therefore the critical size for defects of such materials and structures is also quite small. To ensure the integrity of these materials, nondestructive characterization techniques with extreme resolution are desired. Extremely high-frequency ultrasound is one possibility for characterizing these nanoscale materials, which may include thin films for optical coatings, multilayer materials for fast electronics and mask blanks for the Extreme Ultraviolet Lithography (EUVL) program at Lawrence Livermore National Laboratory (LLNL). However, traditional contact ultrasound above 100 MHz can be quite difficult because of various limitations. Ultrafast laser-based ultrasound offers a way to generate and detect ultrasound of very high frequencies (>100 GHz), and therefore has the resolution required to characterize nanoscale materials.

A major difficulty in using very high-frequency ultrasound, regardless of how it is generated, deals with the increase in attenuation as the frequency of the ultrasound increases. Ultrasound at frequencies above 100 GHz will propagate only extremely short distances. The use of transducers becomes increasingly difficult as the frequency is increased since the energy must be coupled from the transducer into the material. Impedance mismatches between transducers and materials become critical, and couplant layers of any thickness can attenuate the wave to a useless level before it enters the material to be investigated.

By using a pulsed laser to generate the ultrasound, the ultrasound is generated directly in the material, avoiding the problems associated with coupling the ultrasound into the material. And, by using a laser-based system to detect the ultrasound, there is no loading of the surface by transducers, which can greatly affect the ultrasound. There is also no need to couple the ultrasound into a detector, thus avoiding the coupling problems on the detection side as well.

The current state of the art for ultrafast laser-based ultrasound uses a pump-probe technique[1,2] in which a short duration laser pulse is split to provide both a pump beam to generate the ultrasound, and a probe beam to detect the ultrasound. **Figure 1** shows the basic set-up for a pump-probe system. Unlike traditional ultrasonic testing which can gather amplitude versus time data in a single shot, the pump-probe technique gathers data for single points in time with respect to time zero (pumping of the sample). Information from different points in time are gathered, and then the information is assembled to form an amplitude versus time plot for the ultrasonic displacement of the material. The

pump-probe technique uses a variable optical delay that consists of a retro-reflector mounted on a linear translation stage. For our tests, the optical delay can be used to gather data up to 300 ps after the pumping of the sample.

For this technique, the pump and probe beams are focused to very small spot sizes (micrometers). However, this dimension is quite large compared to the thickness of the samples that are usually investigated using this technique. The depth of absorption is quite shallow compared to the focused size of the laser beam, and so the interaction volume is disk-shaped. The pump and probe beams are co-located on the sample, and many aspects of the testing can be considered to be one-dimensional. For a material consisting of a thin layer on a substrate, if the pump laser pulse is absorbed entirely in the layer, the ultrasound generated in the sample propagates normally into the material and then reflects off the layer-substrate interface. The ultrasound can then be detected when it reaches the free surface of the layer. If the ultrasonic velocity of the material is known, the thickness can be calculated very accurately from the time-of-flight information gathered from the pump-probe run. The pump-probe technique has been used to measure layer thicknesses from as small as 0.5 nm to a few hundreds of nm.[1–7]

Because the pump-probe technique cannot gather data in a single shot, it is impractical to use this technique to scan very large areas. With improvements to lasers and other hardware, the time to gather data from a single point on a material has been reduced, but further reduction is required to make scanning large areas practical. Also, LLNL programs such as EUVL need to scan large numbers of samples, and therefore rapid scan times are required. We have proposed a novel white light detection scheme whereby an entire amplitude versus time trace can be gathered from a single laser pulse. This technique takes the single frequency probe pulse, and converts it to a white light pulse that is then directed towards the sample. The various spectral components of the white light pulse are delayed and reach the sample at different times over the continuum of frequencies of which the light is composed. The white light pulse is then sent to a spectrometer, which outputs an amplitude versus time trace based on the amplitude and arrivals of the components of the white light pulse. We hope to obtain funding to investigate this novel technique, and believe that this work will be a major contribution in the field of ultrafast laser-based techniques.

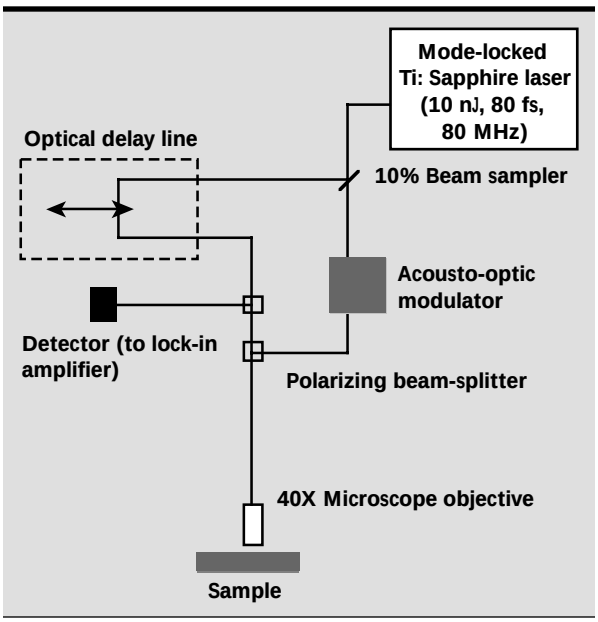

Figure 1. Pump-probe system.

Basically, the pump-probe technique measures the change in reflectivity of the sample as a function of time. Energy from the pump pulse is absorbed by the material, and this energy is converted to heat. This localized change in temperature of the material can lead to a localized change in stress which can propagate through the material as an ultrasonic wave. There can also be a thermal pulse which propagates through the material as a function of the thermal properties of the material. Changes in temperature and pressure of materials can lead to changes in reflectivity. Since the pump-probe technique measures only the change in reflectivity, the change due to temperature must be separated from the change due to the passage of an ultrasonic wave. For the detection of ultrasound, the pump-probe technique depends on materials showing a strong piezoreflectivity effect. For materials that show weak piezoreflectivity, an interferometer must be used as the detection mechanism. This would involve a change to the set-up shown in **Fig. 1**.

We have been working with members of the EUVL project at LLNL to discuss material characterization concerns of that program. EUVL is a promising contender for next generation lithography technologies. Unlike traditional lithography, EUVL operates in the extreme ultraviolet regime, ~10 to 14 nm in wavelength. One critical problem in the program is producing defect-free mask blanks. Currently, the mask blank is composed of 41 layer pairs of Mo/Si deposited on Si wafers, the total thickness of the multilayer being about 280 nm. The program is interested in finding defects in these multilayer structures, both on the substrate, within the multilayer, and on the surface. Currently, commercially available optical scattering inspection tools are used

for full mask blank inspection and atomic force microscopy (AFM), scanning electron microscopy (SEM), and EUV scatter are used to look at specific defects. The critical defect size predicted by modeling is around 50 nm. Ultrafast laser-based ultrasound is capable of generating and detecting frequencies high enough to provide the resolution for these dimensions. Ultrafast laser-based ultrasound has the possibility of becoming a process-monitoring technique during the growth of these multilayers if it can meet the characterization requirements for these multilayer materials.

However, there is much work to do to get to that point. Large increases in the rate of data acquisition are required since the current wafers are 6 in. in diameter, and the goal is to move to 8-in. diameter wafers. The probe beam in the pump-probe system is focused to about 1 μm. Scanning a large area the size of a multilayer wafer with such a small footprint is quite a challenge, and the only way that this may become practical is for the data to be acquired in a single-shot mode such as with the white light detection scheme. The white light detection could reduce the data acquisition time for one location from the few minutes that are required for the pump-probe technique to less than one second. The EUVL program has a goal of scanning 1 wafer/min, but presently would accept a rate of 5 to 10 wafers/h.

Progress

The initial goal of this project was to investigate ultrafast laser-based ultrasound to see how it may benefit various LLNL programs. In collaboration with The John Hopkins University, we set up a pump-probe system, and used it to investigate materials of importance to LLNL, such as Mo/Si multilayers.

One goal of the team is to take this technique beyond its current research role. To make this technique more practical for use outside of the laboratory, it is necessary to reduce the time required to gather data. This would allow the technique to move toward the scanning of objects, since images of entire objects are usually desired for the display of information. The idea of using a white light continuum for detection of the ultrasound was developed. Once a white light detection system is set up, data gathered using the more traditional pump-probe technique which uses a single frequency of laser light in the detection pulse would be compared to the data gathered using the white light technique. The equipment to conduct the white light detection has been assembled, and we plan to implement this technology in the Fall of 1999.

During the summer of 1999, the pump-probe system was set up, and data was successfully gathered on several materials of interest to the EUVL program. We exceeded our initial goal and set up a pump-probe system which was state-of-the-art. At the present time, the system is still set up, and could be used to gather data on various materials. We would like to run more tests on EUVL mask blanks, as well as materials of interest to other LLNL programs using also the more traditional pump-probe set up.

Experimental Results

The two main materials used to investigate the pump-probe technique this summer were Si wafers and Mo/Si multilayers. Silicon wafers are used to provide a good substrate for multilayer materials. These wafers are generally too thick for ultrasound generated by the pump-probe technique to propagate through the thickness and then be detected at the surface after reflection from the back side because of the attenuation of these very high-frequency ultrasonic waves. However, these substrates work quite well to help in the initial set-up of the system since one can monitor the change in reflectivity of the sample due to heating by the probe beam.

The Mo/Si multilayered wafers are interesting materials to work with for the laser-based generation of ultrasound. The bilayers of Si and Mo are on the order of 7 nm in thickness, with the Mo being approximately 3 nm and the Si being approximately 4 nm. Almost all of the optical energy is absorbed by the Mo, with very little absorption occurring in the Si. The absorption of the optical energy by the Mo takes place over several layers, not just in the first layer. Because the laser pulse is absorbed primarily in the Mo layers, they begin to increase in temperature directly after the laser pulse strikes the materials, while there is little increase in temperature in the Si layers. This sets up a temperature gradient between the layers and thermal diffusion then takes place to even out the temperature distribution through the layers near the surface. Because of the differential energy absorption, the ultrasound generated is greatly affected by the layer thicknesses in that ultrasound of frequencies with wavelengths corresponding to the Mo/Si bilayer thickness can be generated. Lower frequencies will also be generated. The highest frequencies will be attenuated very rapidly.

Figure 2 shows a long time trace (~300 ps) of the change in reflectivity of a Mo/Si multilayer, as gathered using the pump-probe system. The figure plots the change in reflectivity with respect to the

reflectivity of the sample versus time. This figure shows that there is a rapid increase in the reflectivity of the sample directly after heating by the pump beam. This initial change in reflectivity results from the increase in temperature of the material. On this long time scale, there is no ultrasound visible. However, a higher resolution scan (shorter time scale) was then run. One variable in the data acquisition using this technique is the number of averages taken at each location. Increasing the number of averages increases the signal-to-noise ratio, but increases the time required to obtain the data. The

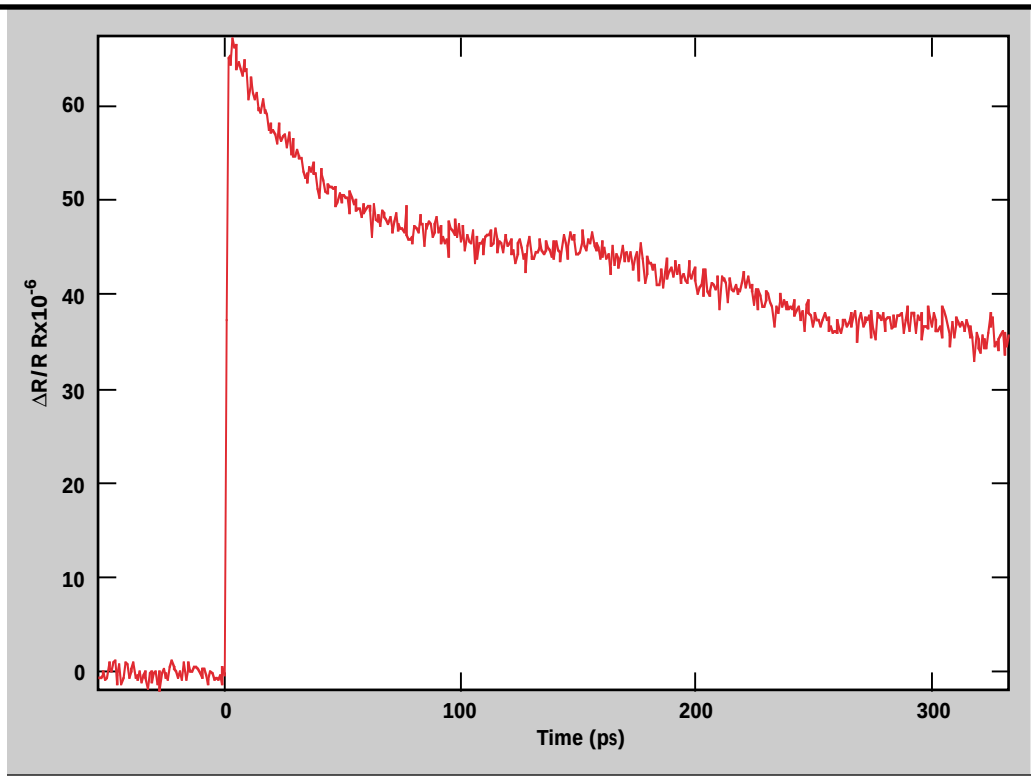

Figure 2. Pump-probe trace of Mo/Si multilayer.

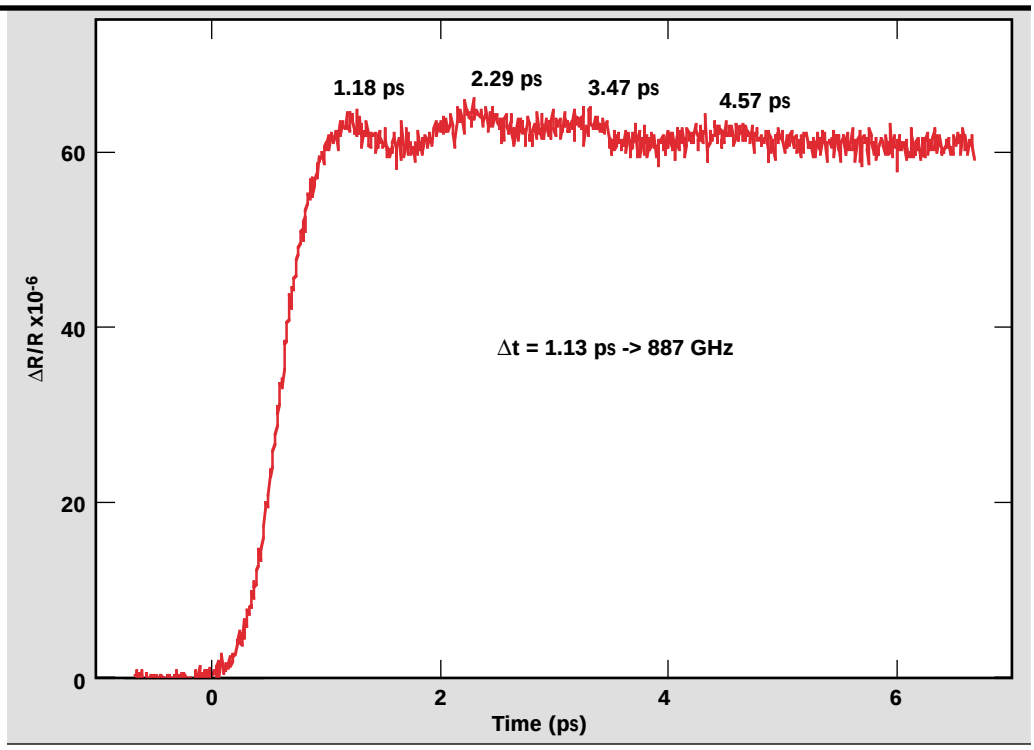

Figure 3. High resolution (short time) trace of Mo/Si multilayer.

delay increment is also variable, and the size of the increment will affect the resolution.

The results of the higher resolution scan are shown in **Fig. 3**. The ripples seen in the data on this time scale correspond to ultrasound. The arrival times of the ultrasound in picoseconds are shown on the figure. The ultrasound occurs directly after the heating pulse. A fast Fourier transform (FFT) was then run on the data to determine the frequency composition of the ultrasound. The FFT is shown in **Fig. 4**. This figure shows significant energy at frequencies as high as 892 GHz. This frequency is around five orders of magnitude higher than that found in typical ultrasonic characterization of materials. It is believed that these high frequencies result from the differential absorption of the pump beam by the Mo and Si layers, and that varying the thicknesses of these layers would lead to a change in the detected frequencies.

A test was then run on a Mo/Si multilayer wafer that had 100 nm gold spheres embedded at the substrate-multilayer interface to simulate defects. This and the other samples used in this study were all fabricated at LLNL. Currently, all of the EUVL wafers are grown on top of Si substrates. The gold sphere inclusion samples provide wafers with known defects.

Figure 5 shows pump-probe traces from three different spots on the wafer. Two traces are nearly identical, with the third showing a considerably different behavior. The two similar traces are quite different from the typical response shown by the Mo/Si multilayer while the third trace appears quite similar to the response of the multilayer without the gold sphere inclusions (**Fig. 2**). This could be indicative of the effects of a conductor, in this case the gold spheres, on the thermal behavior of the wafers which thereby affects the change in reflectivity of the material at those locations. The traces believed to show the effects of the gold spheres are labeled "defect spot" in the figure. The trace showing the typical multilayer response is labeled "multilayer." This shows the potential of using this technique to find defects located at the substrate-multilayer interface.

Conclusions

We successfully constructed a pump-probe system to investigate the feasibility of generating and detecting very high-frequency ultrasound in materials important to LLNL programs. Frequencies as high as 892 GHz were detected. The effects of 100-nm-diameter buried "defects" on received signals were seen. We believe that we will be able to decrease greatly the time required for data acquisition through the implementation of a white light detection technique which we hope to implement soon. High-frequency laser-based ultrasound is clearly a useful technique for NDC applications, and will only increase as technology and new materials are developed.

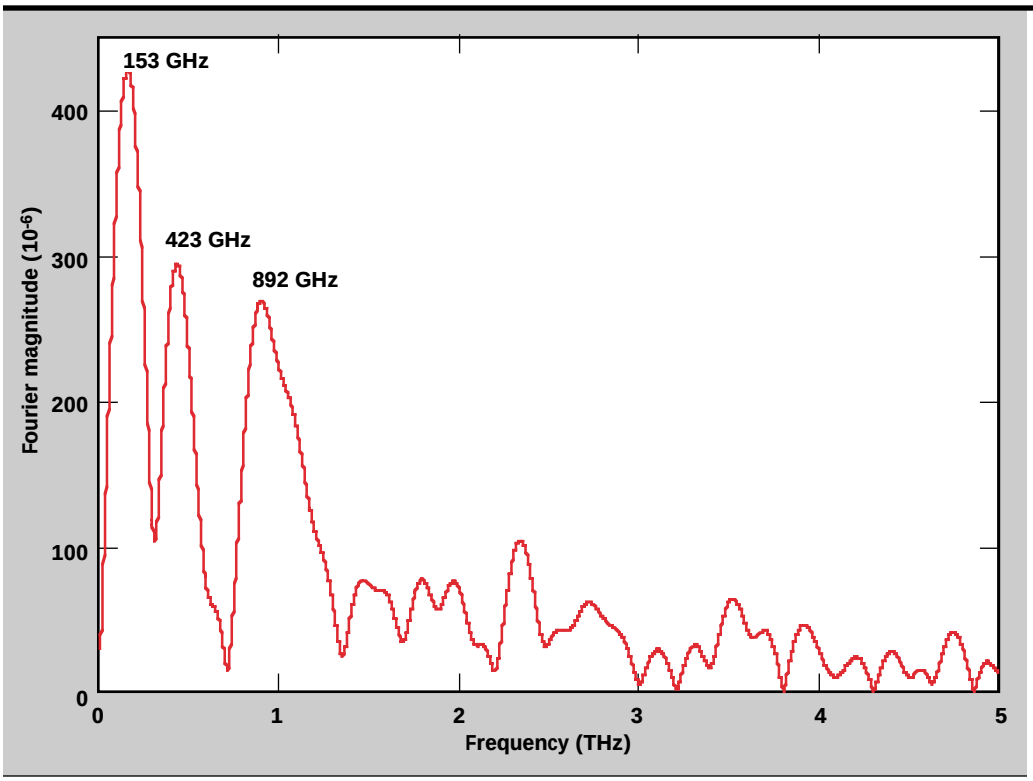

Figure 4. FFT of data shown in Fig. 3.

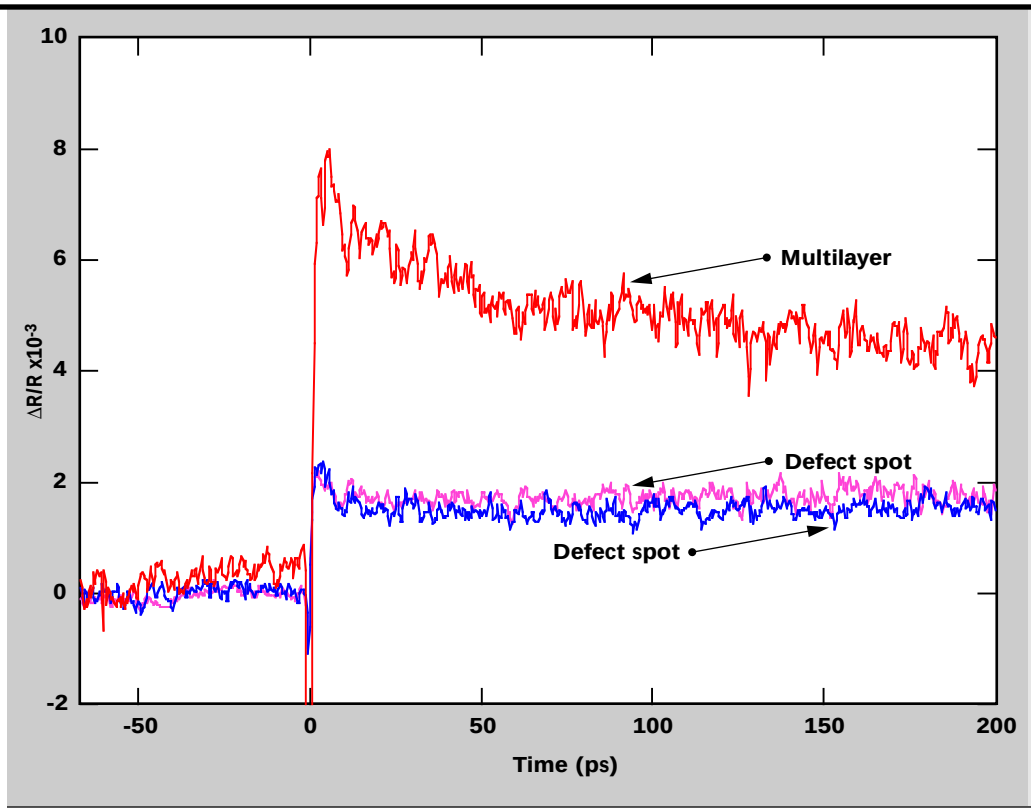

Figure 5. Data from multilayer material with 100-nm gold sphere inclusions, demonstrating successful detection of simulated defects using the pump-probe technique.

Future Work

Because of the success we achieved on this project, we will seek funding to continue, developing a dedicated ultrafast laser-based ultrasonic characterization system which will allow us to look at various materials of importance to LLNL and to the country.

Future work will focus on the white light detection scheme which holds the promise of greatly increasing the rate of data acquisition, thus making scanning practical. Successful implementation of this detection scheme would be a major contribution to the ultrafast phenomena field.

Acknowledgments

The authors would like to thank members of the EUVL Mask Project of the Information Science and Technology Program at LLNL for providing samples for this work.

References

1. K. Fiedler (1996), "The interferometric detection of ultrafast pulses of laser generated ultrasound," Ph. D. Thesis, The Johns Hopkins University, Baltimore, Maryland.

2. C. Richardson (1998), "Theoretical and experimental ultrafast laser ultrasonic inspection of extended interfaces," Master's Essay, The Johns Hopkins University, Baltimore, Maryland.

3. H. T. Grahn, H. J. Maris, J. Tauc, and K. S. Hatton (1988), *Appl. Phys. Lett.*, Vol. **53**, p. 2281.

4. H. T. Grahn, D. A. Young, H. J. Maris, J. Tauc, J. M. Hong, and T. P. Smith, III (1988), *Appl. Phys. Lett.*, Vol. **53**, p. 2023.

5. H. N. Lin, R. J. Stoner, H. J. Maris, and J. Tauc (1991), *J. Appl. Phys.*, Vol. **69**, p. 3816.

6. C. A. Paddock and G. L. Easley (1986), *J. Appl. Phys.*, Vol. **60**, p. 285.

7. G. Tas, R. J. Stoner, H. J. Maris, G. W. Rubloff, G. S. Oehrlein, and J. M. Halbout (1992), *Appl. Phys. Lett.*, Vol. **61**, p. 1787.

New Developments in RECON

Jessie A. Jackson
Laser Engineering Division
Electronics Engineering

Over ten years ago Lawrence Livermore National Laboratory (LLNL) began research and development in computed tomography (CT). One product of this work is a package of reconstruction and simulation codes called RECON. RECON has been successfully used for nondestructive characterization, but is in need of revision to keep up with advances in CT and user-friendly interfaces. Some reconstruction codes need to be modified and new ones need to be added. However certain code-wide upgrades must be completed before this can happen. The user interface has been redesigned and a new cone-beam reconstruction code has been implemented with this new user interface.

Introduction

Computed Tomography (CT) is a nondestructive imaging technique for determining a 3-D characterization of an object from a series of 2-D radiographs. For over ten years the Nondestructive Evaluation (NDE) Section at LLNL has used CT for the inspection of industrial materials, objects and assemblies.[1,2] During this time NDE personnel built an extensive CT system, including a suite of CT reconstruction and simulation codes called RECON.

RECON is available as copyrighted software from the Technology Transfer Office at LLNL.[3] The RECON codes have been used extensively for processing and reconstructing radiographic projection data.[4] However, the code has suffered from a lack of maintenance, documentation and reliability. Also, since the time when RECON was designed computer systems have changed, some of the original design criteria are no longer applicable, and there are many new display and imaging tools available. An effort has begun to upgrade, modernize, and further document RECON.

NDE CT System

There are three major functional parts to the current NDE CT system: the acquisition or simulation of 2-D radiographic data, the reconstruction of a 3-D object from the 2-D data, and the ability to display and examine both 2-D and 3-D data.

The system accomplishes these functions using both hardware and software. The hardware in the system consists of scanners and computers. The scanners include radiographic sources, stages, and digital detectors used for the manipulation of the object and the acquisition of 2-D radiographs. The computers are used for acquiring, processing, analyzing and displaying data. The software includes codes to control the scanners for acquisition of data and the creation of information and data files, the RECON codes for simulating radiographs and reconstructing images, and a software package called VIEW[5] for displaying and analyzing digitized images. From the beginning a set of operating conventions, nomenclature, and software standards was adapted which all scanners, simulators and reconstruction codes follow.[6]

The CT scanners each produce their own format of raw data files, which are initially processed by dedicated programs to eventually produce a standard CT parameter file and data files. **Figure 1** shows the interconnection between the scanners, RECON, VIEW and the data files.

The CT parameter file is saved in an ASCII file, referred to as an SCT file. This file contains all necessary information from a scan regarding the configuration of the acquisition system, such as geometric information, dimensions, energies, number of rotations, position of the object, and size of pixels. A new SCT file is created at each processing step with information about the processing just performed as well as all the past processing. This allows a record of processing to be maintained for each data file. An SCT file is also created by RECON when the simulation codes are used to create radiographic data.

The data files are stored in VIEW format using two files for each set of data. The data itself is saved in a binary file called an SDT file. Each data file is accompanied by an ASCII file called an SPR file, containing the dimensional information of the binary file, the type of data, real or integer, how many dimensions, the size of each dimension, the pixel size and the origin of the data. As seen in **Fig. 1**, VIEW can also be used to create object data files to be used as input to the RECON simulation codes. In this case the user must manually create an SCT file. It is important to note that even though RECON is being upgraded the output data produced by the scanners is not changing, so the input to RECON will continue to be in the SCT/SPR/SDT format.

Status of RECON

RECON consists of a number of interconnected codes. There are a variety of reconstruction codes for such applications as filtered back-projection (FBP), convolution back-projection (CBP), constrained-conjugate-gradient parallel and fan beam, and active and passive CT (A&PCT). The simulation codes create simulated radiographs from object descriptions or pixelized images. The bulk of this code is written in the C programming language, while some algorithms are written in FORTRAN. RECON was built to operate on UNIX workstations and VAX computers. The code currently has UNIX system calls in it, so RECON must be run on UNIX platforms. The RECON codes were designed for compatibility with the VIEW signal and image processing software, though VIEW software is not required to use the RECON codes.

Currently each application is compiled into separate executable programs. There is a manager program that allows the user to select and start an application. This process is UNIX-dependent. Each application can also be started independently of the manager program. In either case, at start-up RECON reads in a user-specified SCT file. A user interface is provided to allow the user to modify CT parameter values interactively before starting the application process. The user interface is time-consuming and some new options do not work consistently or correctly. RECON currently reads and writes data in VIEW format. Each application has to read and write the CT parameters and data. At present there are a number of input/output (I/O) codes and although the codes are used in all the applications they are scattered throughout each application.

The current structure of the RECON code is complex and highly interconnected, and since there is little documentation it is difficult to learn.

The above problems have made RECON less useful than is acceptable.

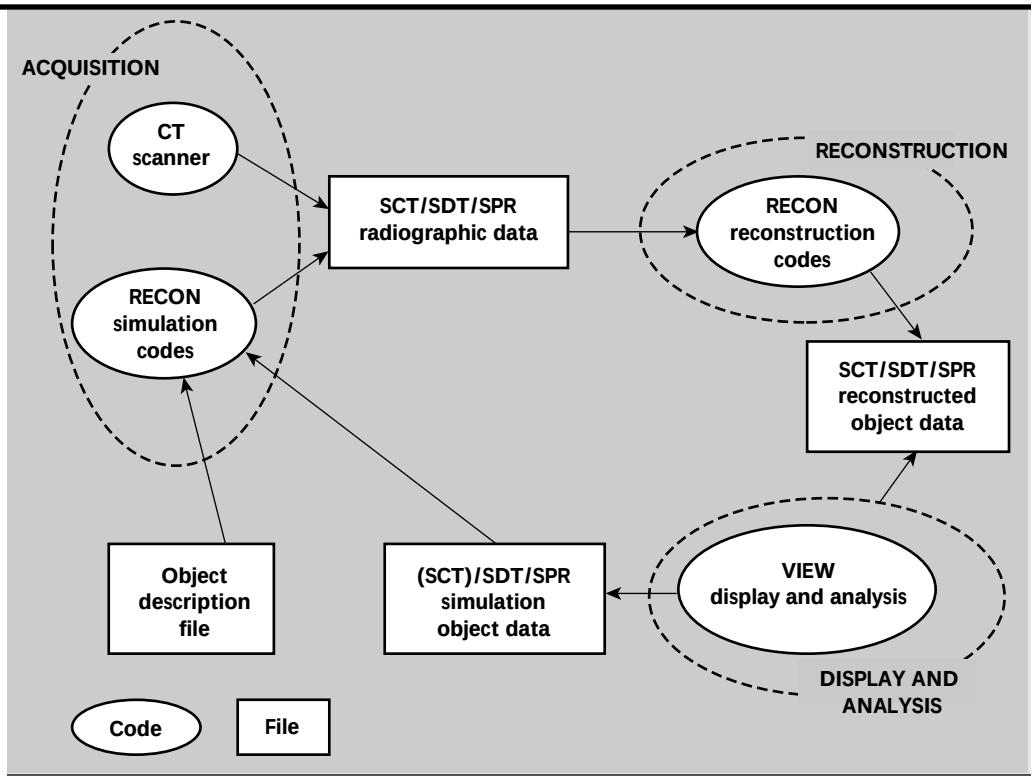

Figure 1: CT System showing interconnects among components.

Progress

In addition to fixing problems and adding new reconstruction techniques there are a number of improvements that need be included to make RECON state-of-the-art. These improvements involve the portability and modularity of the code.

To assure compatibility with a wide variety of users, RECON must be portable to computers other than UNIX platforms, such as Macs and PCs. This can be accomplished by building a version of RECON that can be used on any platform that runs C-language executables. There are also a number of software packages available that provide elegant user interfaces and data I/O. However, since often these packages have to be purchased it can not be assumed that every machine that would use RECON would have them available. To satisfy as many users as possible it would be desirable to be able to create versions of RECON to run on machines with different capabilities.

The first step in upgrading RECON is to develop a plan that will accommodate the desired functionality.

RECON Redesign

The structure for the upgraded RECON is shown in **Fig. 2.** The interfaces among the functions are clear and concise. As in the original design each CT application would be compiled into its own executable. The user interface and the CT parameter and data I/O codes would then be common to all the applications. There are two obvious advantages to this design.

One advantage is that any module for data or parameter I/O can be exchanged for one with different capabilities without affecting the application processing. For example, for a user with a UNIX machine with no special display software, a line-input user interface could be replaced with an X-Window interface. For a Mac without X-Windows, a system could be built with a line-input user interface.

Another example involves the package of codes called Interactive Data Language (IDL). IDL could be used to create a window interface for the CT parameters, and windows for displaying the data, as well as providing data I/O for data of many types of formats. A limitation of IDL is that it is a commercial product that not all RECON users may have. An IDL program will run without modifications on UNIX machines, Macs and PCs. A RECON code constructed as shown in **Fig. 2**, would easily allow the building of a version of RECON with the CT parameter, user interface, and data I/O sections of the code replaced with an IDL interface, as shown in **Fig. 3**.

Another advantage to this design is that the upgrade work can take place in two stages. The first stage would be the implementation of the user interface and

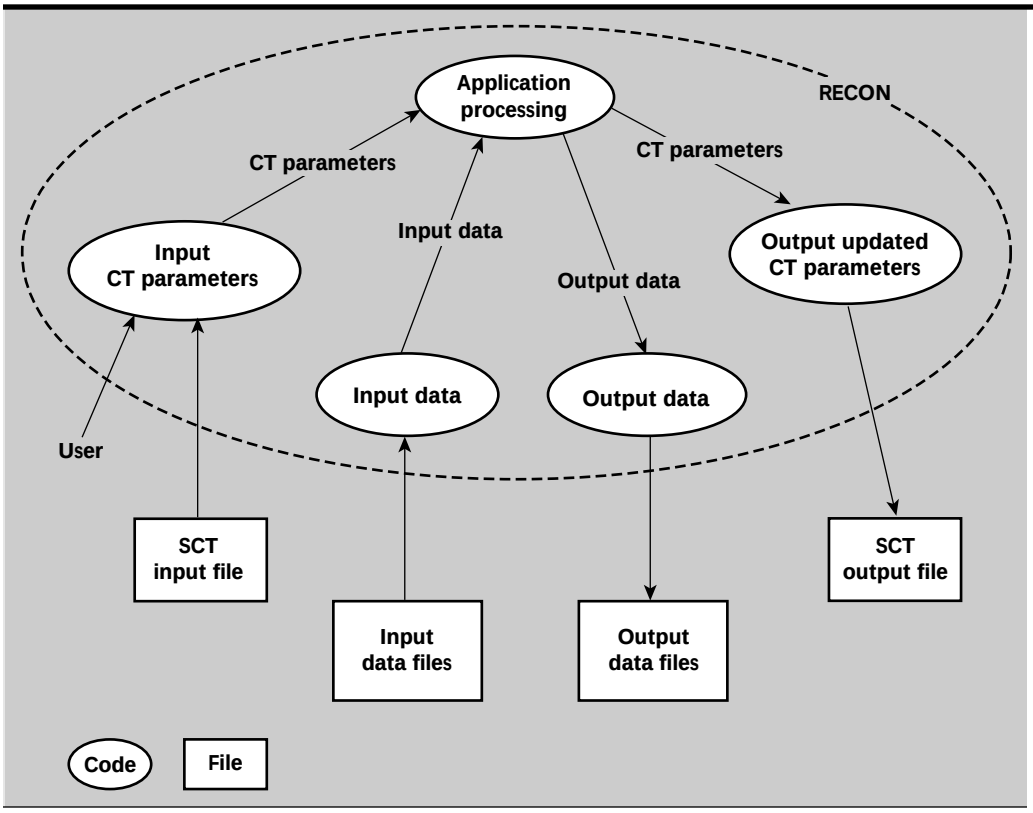

Figure 2: Upgraded RECON Data Flow Diagram.

Figure 3: IDL/Upgraded RECON Data Flow Diagram.

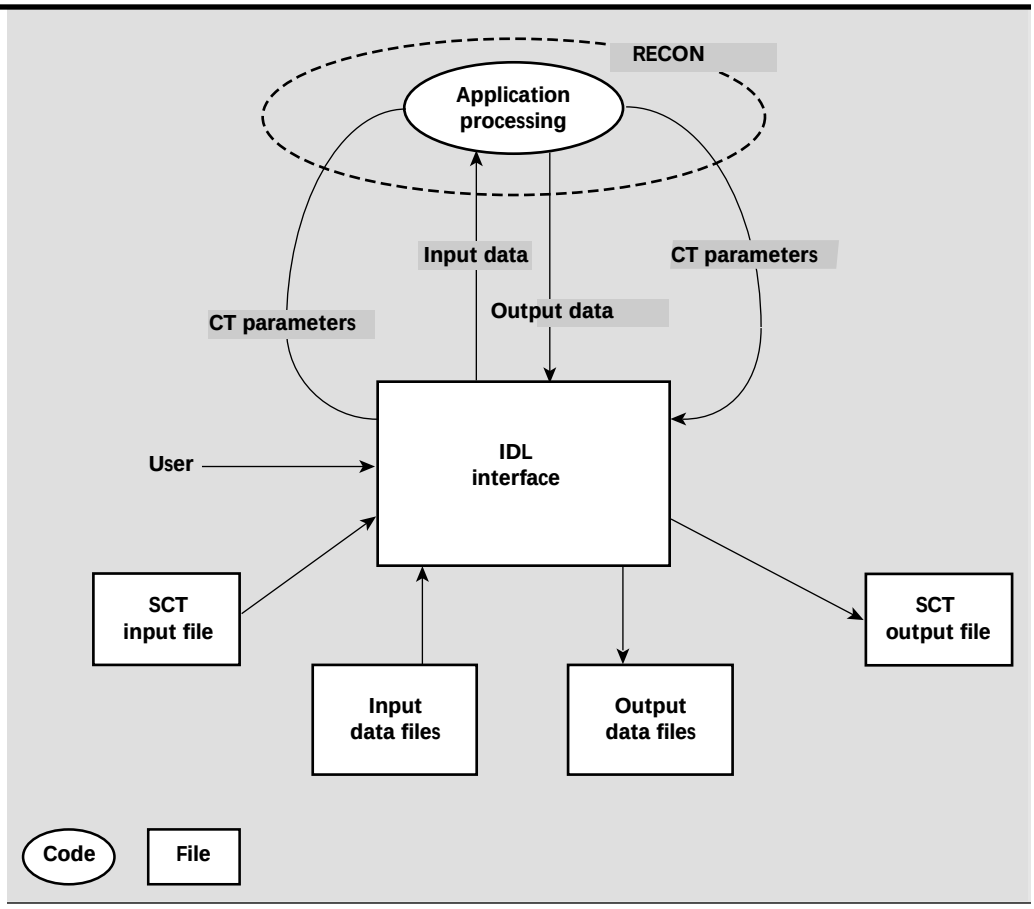

CT parameter and data I/O. Then each application can be modified. This will allow the users access to completed applications before the entire process is complete.

RECON Development Plan

In planning the development of the RECON upgrade the following assumptions and design goals have been established.

Assumptions: (1) RECON will continue to use SCT file formats to input CT parameter information; (2) data I/O will still need to be available in VIEW formats and others to be determined; (3) no major changes will be made to the existing algorithms.

Design goals: (1) clean up and simplify the codes by making the codes more object-oriented and making the data and CT parameter I/O modular; (2) make the code C-language only so that it can be easily ported to Macs and PCs by removing all UNIX system calls and minimizing the use of FORTRAN; (3) improve the user interface, both the reliability and ease of use; (4) document the software; (5) document the CT algorithms; (6) restructure the codes to make future maintenance easier; (7) develop a modular method of building versions for different hardware platforms; (8) develop an IDL interface for RECON; (9) possibly develop an X-window interface for the UNIX machines, and (10) write modules for data I/O in formats other than VIEW.

RECON Implementation Status

A new line-input C-language-only user interface is complete. Many of the data I/O routines for VIEW data files have upgraded. A new constrained-conjugate-gradient cone beam (JCONE-CCG) algorithm has been implemented with the new user interface and data I/O.

Future Work

The next phase of this project will be to finish the work of modularizing the interfaces to the applications. Then the data I/O routines for VIEW data files will be completed. The JCONE-CCG code will be ported to a Mac and a PC to test the compatibility of RECON on a non-UNIX platform. An IDL interface for JCONE-CCG will also be developed to test the usefulness of IDL as an interface for RECON. The user interface and data I/O will be documented.

Then the process of converting each application will begin. The user interface for each code will be designed. The new application module will be created and the algorithm and the code will be documented. This process will continue application by application.

Acknowledgments

The author would like to thank R. Roberts, J. Haskins, H. Martz and P. Roberson for their knowledge, support and encouragement in this effort. The author also appreciates the support given by LLNL's NDE Section, Materials and Manufacturing Engineering Division, Mechanical Engineering Department and the Center for NDC.

References

1. S. G. Azevedo, H. E. Martz, J. M. Brase, and K. E. Waltjen (1988), "Computed tomography," *Engineering Research, Development, and Technology*, Lawrence Livermore National Laboratory, Livermore, California (UCRL-53868-88), June.

2. J. M. Brase, K. E. Waltjen, and H. E. Martz (1988), "Research in computed tomography," *Engineering Research, Development, and Technology*, Lawrence Livermore National Laboratory, Livermore, California (UCRL-53868-87).

3. S. G. Azevedo (1991), "Model-based computed tomography for nondestructive evaluation," Ph.D. thesis, University of California at Davis, (also Lawrence Livermore National Laboratory (UCRL-LR-106884), March 1991).

4. S. G. Azevedo, H. E. Martz, and G. P. Roberson (1990), "Computerized tomography reconstruction technologies," November/December, *Energy and Technology Review*, Lawrence Livermore National Laboratory, Livermore, California (UCRL-52000-90-11·12).

5. "The VIEW signal and image processing system," J. M. Brase, V. J. Miller, and M. G. Weiting (1988), Lawrence Livermore National Laboratory, Livermore, California (UCID-21368), March.

6. S. G. Azevedo, H. E. Martz, M. F. Skeate, D. J. Schneberk, and G. P. Roberson (1990), "Computed tomography software and standards," Lawrence Livermore National Laboratory, Livermore, California (UCRL-ID-105132), February.

Component Gap Detection by Infrared Imaging

Charles S. Landram and Richard W. Martin
New Technologies Engineering Division
Mechanical Engineering

Nancy K. Delgrande and Philip F. Durbin
Manufacturing and Materials Engineering Division
Mechanical Engineering

The depth of gaps located below a lamp-heated surface can be determined from infrared (IR) surface temperature images following a single pulse of heat. The gaps are assumed to reside at a fixed depth in a plane parallel to the surface. The magnitude of the image spatial contrast (in temperature) and the time at which it is the sharpest (brightest) provide two unique quantities whose measurements can be used to determine gap depth. This determination requires (direct) numerical solution to the unsteady, multidimensional heat conduction equation based on a tentative buried gap shape similar to that observed at the surface. The procedure is illustrated for a cylindrical gap buried 3/8 in. from the surface of a 3-in. slab of stainless steel. Also considered are detection of gaps interfacing cylindrical shells and cracks perpendicular to the surfaces of thin shells.

Introduction

Methods for detecting subsurface cavities from outer surface IR images have been developed for internally heated (or cooled) cavities or the volumetrically heated containing solid.[1–4] For the heated cavity, its fluid temperature and heat transfer coefficient must be specified as a means of providing a known steady-state heating rate. Experimental implementation is difficult owing to the need to provide intrusive cavity heating and instrumentation for determining imposed heat cavity, heat flux, or power density within the solid.

When the cavities are defects, such as delamination gaps between composite material layers that should otherwise be well bonded, the gaps are thin and lie at a subsurface depth in a plane parallel to the outer surface. These kinds of defects have been experimentally revealed by flash heating the outer surface followed by observation of resulting delayed IR images.[5] In this nonintrusive transient method, the surface images are observed long after the impulsive heating occurs to avoid irradiance of the camera from sources other than sample emission.

The purpose of this work is to determine the gap depths that can be resolved, quantifying these in terms of their size parallel to the surface, the thermal properties of the solid, the energy flux imposed, and the heat losses from the heated surface. This determination requires numerical solution to the unsteady heat conduction equation applied to the solid, and validation with experimental data.

Progress

Figure 1 illustrates the presence of a thin, subsurface defect at depth L, and residing in a plane parallel to the surface. The defect has a contour of

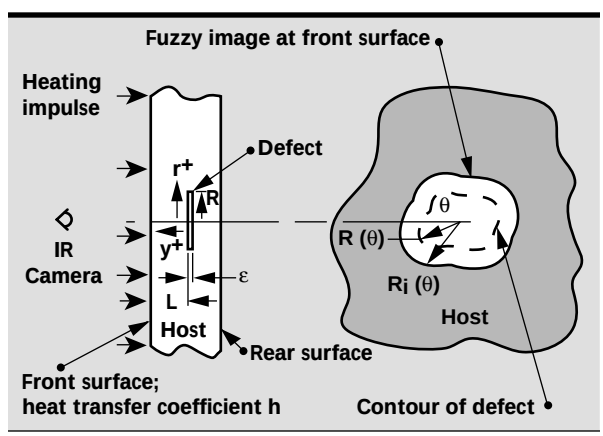

Figure 1. Model and coordinate system for subsurface defect.

R(θ) as shown. The defect is considered an adiabatic void since the contained gas (air) has less than three orders of magnitude smaller thermal conductivity than that of the solid (host). When the surface is impulsively heated, a thermal diffusion front is propagated axially from the surface towards the defect in the $-y^+$ direction. As the front approaches the defect, the conductive heat flux changes direction and transfers radially along the face of the defect, $y^+ = 0$, in the r^+ direction. Near the outer edge of the defect, $r^+ = R$, the radial heat flux merges with the axial heat flux in $r^+ > R$, and the combined flux flows around the backside of the defect and toward the inner regions of the solid.

This transport distributes a temperature along the front face of the defect. The temperature is greatest at $y^+ = r^+ = 0$ and decreases along $y^+ = 0$ monotonically with increasing r^+ in $0 < r^+ < R$. This local rise in temperature near the defect is propagated back to the front surface at $y^+ = L$ as an attenuated and broadened surface temperature spatial perturbation, which is represented by the observed image.

In addition to the spatial transport, temporal events are also important. The impulsive surface heating causes elevated solid temperatures in early times during which the remainder of the solid including the defect remain near the initial (ambient) temperature. In very late times the entire system equilibrates to the ambient temperature. It will be shown that the images can only be captured in intermediate times and that particular times occur when the images are brightest.

Formulation

The unsteady, multi-directional heat conduction equation applied to the solid regions of **Fig. 1** and written in dimensionless coordinates is given by

$$\frac{\partial v}{\partial t} = \frac{\partial^2 v}{\partial y^2} + \frac{1}{r}\frac{\partial}{\partial r}\left(r\frac{\partial v}{\partial r}\right) + \frac{1}{r^2}\frac{\partial^2 v}{\partial \theta^2} \tag{1}$$

where the dimensionless temperature field is v = v (y, r(θ), t). The internal boundary conditions on the faces of the defect require the normal temperature gradients to vanish there. Initially, v (y, r(θ), 0) = 0. The external boundary conditions are given as follows:

$$\frac{\partial v}{\partial y} + Biv = \begin{Bmatrix} -1/t_0, 0 < t < t_0 \\ 0, \quad t > t_0 \end{Bmatrix} \text{ on } y = 1 \tag{2}$$

where Bi is the front surface Biot number, and t_0 is the dimensionless time over which the impulse occurs. The back side of the solid was taken as semi-infinite; that is, $v \to 0$ as $-y \to \infty$. This condition was appropriate for the plate thickness considered and tested. At radial positions far from the defect, that is, for r >> R/L, the following exact solution holds if $t >> t_0$:

$$v = \frac{1}{\sqrt{\pi t}} exp\left[-\left(1-y\right)^2 / \left(4t\right)\right]. \tag{3}$$

Had two different materials comprised the slab of **Fig. 1**, well-bonded along y = 0, but possessing the same defect, it would be necessary to apply appropriately scaled versions of **Eq. 1** to both materials and couple their solutions at the contacting surface by continuity of temperature and normal heat flux.

Implementation

In general, R(θ) and L are sought from surface images observed at y = 1. As illustrated in **Fig. 1**, the surface image contour $R_i(\theta)$ is slightly enlarged relative to the actual defect contour R(θ), but the two will have similar shapes. Their mean circumferential values are respectively denoted $\overline{R_i}$ and $\overline{R}$. From the observed image, the function g(θ) is defined by

$$g(\theta) = \frac{R_i(\theta)}{\overline{R_i}} \tag{4}$$

subject to the image area constraint

$$\frac{1}{2\pi}\int_0^{2\pi} g^2(\theta)d\theta = 1. \tag{5}$$

Therefore by similarity,

$$R(\theta) = g(\theta)\overline{R}. \tag{6}$$

Henceforth g(θ) is considered known from **Eqs. 4** and **5**, but $\overline{R}$ is taken as unknown. For time scales much greater than that for impulsive heating, solutions to **Eqs. 1** and **3** depend on just two parameters, $\overline{R}$/L and Bi, the former having been introduced by enforcement of the adiabatic condition on the faces of the thin defect and the latter by **Eq. 2**. Since Bi depends on the unknown depth L, it is tentatively set to zero; then once L is found with this restriction, Bi is updated, and the process (to be presented) is repeated until convergence is obtained by the method of successive approximations. Therefore, for fixed values of Bi, and chosen values of $\overline{R}$/L, direct solution to **Eqs. 1** and **3** can be obtained numerically for the dimensionless temperature field in the solid, v (y, r(θ), t).

The important result from the solution is the surface image contrast factor defined as u (t):

$$u(t) = v_{s1}(t) - v_{s2}(t) \tag{7}$$

where

$$v_{s1}(t) = v(1, 0, t)$$

and

$$v_{s2}(t) = v(1, \infty, t).$$

On physical grounds, as discussed previously, it is evident for impulsive heating that $u(0) = u(\infty) = 0$ and that at intermediate times u achieves a maximum, $u_{max} = u(t_{max})$ at which time

$$du/dt = 0 \text{ when } t = t_{max}. \tag{8}$$

The surface contrast factor is obtained for an array of $\bar{R}$/L values. Curve fits f_1 and f_2 are respectively determined for u_{max} and t_{max} in terms of polynomial curve fits in $\bar{R}$/L for fixed Bi. Returning to the dimensional definitions for temperature T and time τ, these curve fits can be written as:

$$u_{\max} \equiv \frac{(T1 - T2)_{\max}}{q_s \tau_0 / \rho c L} = f_1\left(\bar{R} / L\right) \tag{9}$$

and

$$t_{\max} \equiv \tau_{\max} \alpha / L^2 = f_2\left(\bar{R} / L\right). \tag{10}$$

The surface energy flux $q_s\ \tau_0$ is obtained by separate calibration to be discussed, and $(T1 - T2)_{max}$ and τ_{max} are the measured contrast temperature at the time it is the brightest. Since f_1 and f_2 are known, simultaneous solution of **Eqs. 9** and **10** provide unique values for the two unknowns $\bar{R}$ and L at the tentatively selected value of Bi = 0. With this value of L, the Biot number can be evaluated and the process repeated until convergence is achieved. In the following application, the converged value of Bi = 0.014 was rapid and required only a single iteration.

Application to Plates

The method is demonstrated for the case of a defect in the shape of a disk so that all dependence on the circumferential direction θ is removed in **Eq. 1**, and the function g in **Eqs. 4** and **5** is identically unity.

Computational Methods. The finite element code TOPAZ2D[6] was used to numerically resolve the axisymmetric, 2-D temperature field, v (y, r, t), centered at the origin of the disk. Two different meshes were used. The first was for an infinitesimally thin disk ($\varepsilon = 0$) having finite R and L in the solid, whose outer solid regions for the radial, r, and axial directions, –y, could be considered infinite. The second mesh more faithfully modelled the actual experimental case which was a 0.32-cm-thick gap, having an outer radius boundary of 5 R in a slab of thickness 7.62 cm with adiabatic boundary conditions at radial and axial extremities. Results obtained from these two different meshes did not differ significantly, so neither defect thickness nor outer boundary placement were deemed to be very important within the range of values considered. In the case tested, upon which discussion is deferred, the solid was 304 stainless steel, with a disk gap of radius 2.54 cm at a depth of 0.9525 cm.

In the case of the mesh whose radial and axial dimensions were semi-infinite, the mesh was spatially truncated in r where the numerical solution agreed to within 1% of the exact solution there (**Eq. 3**) and in –y to within the same accuracy with v = 0 there. Mesh size was also varied, especially near the defect, to find the required size for adequately resolving the temperature distribution. The steepest temperature gradients were found near y = 0, on the front side of the defect, along about $0.7 < r^+ /R < 1$ where the mesh was made relatively small. As many as 101 total front-face defect nodes were used, and as many as 7011 total nodes were used within the entire solid.

A fixed dimensionless time step of between 0.5 and 1 was used, and numerical output was found to be insensitive to the value. In the experimental case, these time steps correspond to between about 0.05 to 0.1 s. Some care was required to accurately capture the effects of the impulsive heating (see **Eq. 2**). To avoid having a very small time step initially, the problem was started at t = 0.05. Prior to this time **Eq. 3** gives the starting solution since in this early time the diffusion front is far from the defect. Also, front surface heat losses can be ignored during this early time.

Numerical Results. For this application, the numerical results for u (t) are shown in **Fig. 2** for several values of R/L at Bi = 0. For each R/L the time t_{max} at which u has the maximum, u_{max}, is clearly evident. Values of t_{max} and u_{max} are monotonically increasing functions of R/L as demonstrated by the points shown in **Figs. 3** and **4**. In the range 0.5 < R/L < 4, curve fits for f_1 and f_2 in **Eqs. 9** and **10** were found to be:

$$u_{\max} = f_1(R/L) = \sum_{n=0}^{4} a_n (R/L)^n \qquad (11)$$

and

$$t_{\max} = f_2(R/L) = \sum_{n=0}^{2} b_n (R/L)^n \qquad (12a)$$

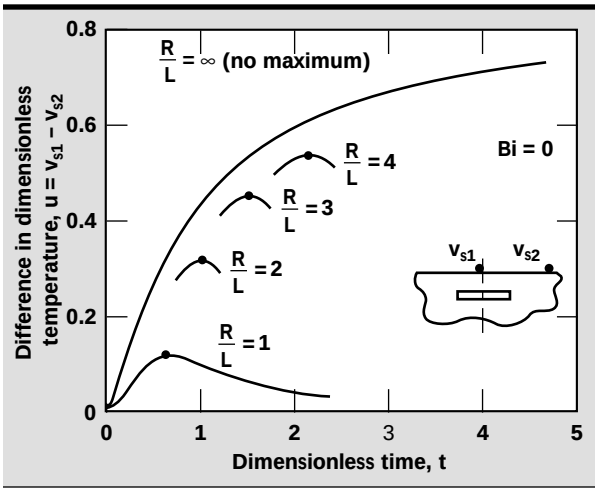

Figure 2. Locus of image contrast maxima.

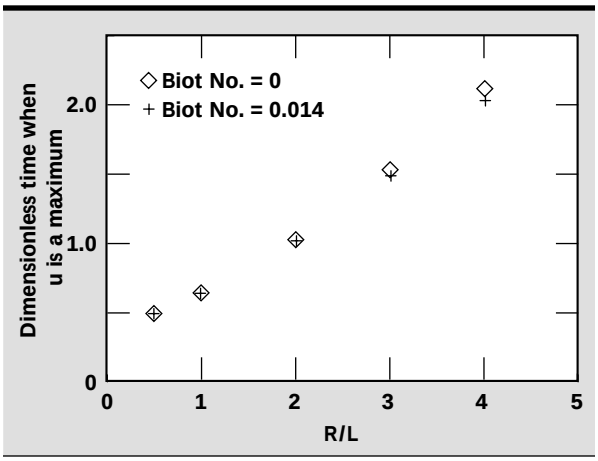

Figure 3. Time for optimal image.

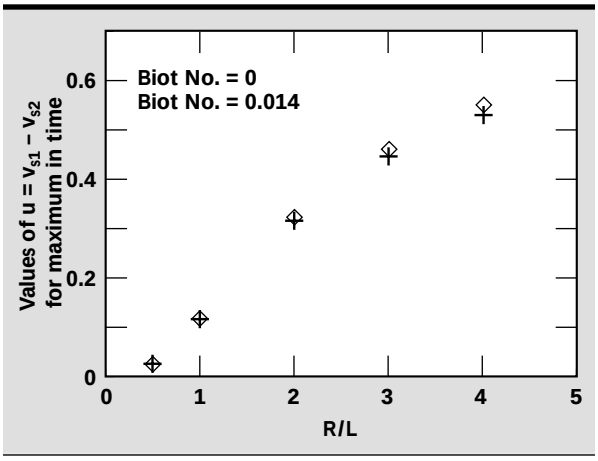

Figure 4. Optimum image contrast.

where the coefficients are given in **Table 1** for Bi = 0. The inverse of **Eq. 12a** is obtained as

$$R/L = \frac{-b_1}{2b_2} + \sqrt{\left(\frac{b_1}{2b_2}\right)^2 + \left(\frac{\alpha\tau_{\max}}{L^2} - b_0\right)} / b_2 \,. \qquad (12b)$$

Application to Curved Surfaces

We also applied the methods to solids other than the flat plate. A cylindrical shell composite was tested and simulated numerically using TOPAZ2D.[6] The cylinder had a 4-in. nominal diameter and was composed of an outer shell of one material and an inner shell of another. The shell thicknesses are shown in **Fig. 5a**. The two shells had a 0.003-in. interference fit producing a 450-psi pressure where they contacted. There were two parallel circumferential gaps, each about 0.75 in. wide, intentionally made by machining the inner shell, as illustrated in **Fig. 5a**. To be discussed subsequently are the images observed in **Fig. 5a**, which are revealed only along the cylinder's centerline, and their corresponding contrast plotted in **Fig. 5b**. The analytical curve shown in **Fig. 5b** was obtained by ignoring temperature drops across each of the thin shells separating the gap and using Laplace transform methods to solve the resulting differential equations describing unsteady axial conduction within each shell. The methods in obtaining the numerical results curve in **Fig. 5b** were similar to those previously discussed for the flat plate except that an insulated boundary at the inner surface of the inner shell was used for the thin shells and different thermal properties were considered for each shell.

In **Fig. 6** results are shown for calculations performed that simulate a spherical shell composite having a gap between two shells at the apex viewed by the camera. The shell materials and thicknesses were similar to those shown in **Fig. 5a** for the cylinder. The purpose of these calculations was to determine the importance of lamp orientation in sensing gaps for curved parts.

Table 1. Coefficients of Eqs. 11–12a for Bi = 0.

N	a_n	b_n
0	–0.000398	0.36
1	–0.02622	0.24
2	0.20242	0.05
3	–0.06958	
4	0.007283	

Application to Cracks

When a crack develops in a material perpendicular to its surface, impulsive lamp heating is an ineffective means of crack detection. For these cases, we evaluated the benefits of steady-state heating and cooling of the material's edges that roughly parallel the length of the crack. The computational model that precedes future experiments is illustrated in **Fig. 7**. Shown is a segment of a disk of the material under consideration having a circumferential crack whose length runs 10% of its radial location. The center is heated 30 °C higher than the outer periphery is cooled. The hot and cold heat sources may be as simple as heated or chilled rubber water bottles that could be reoriented 90° to

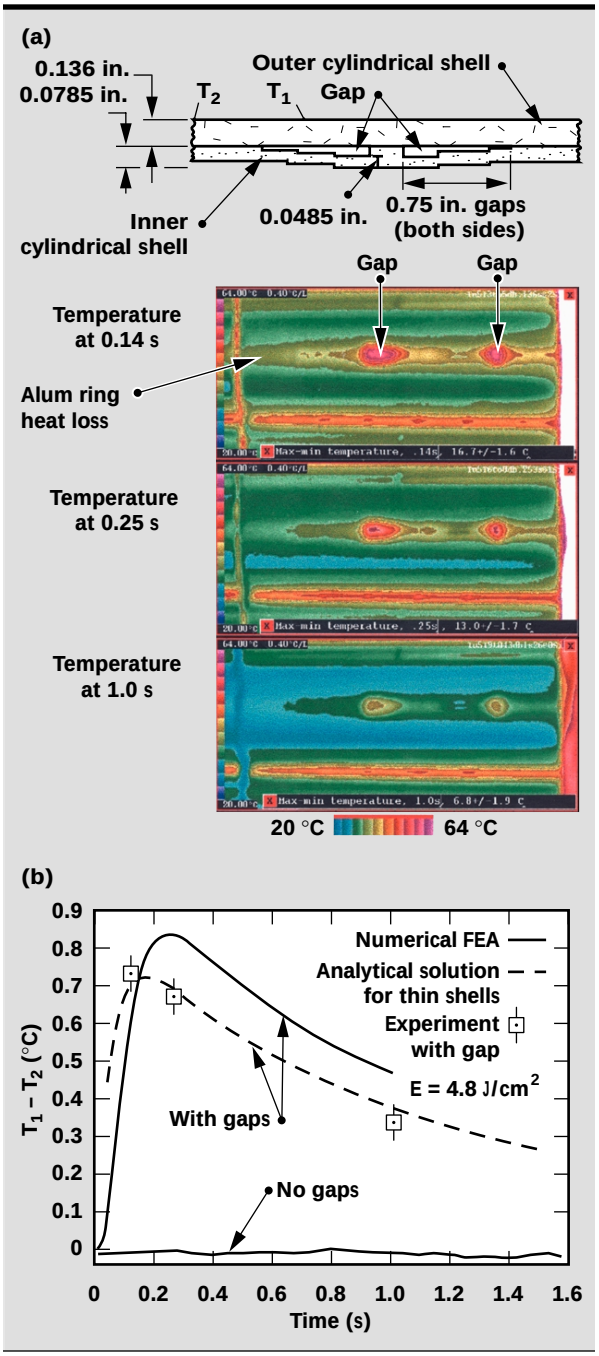

Figure 5. Application to cylindrical shells. (a) Section of composite shell thickness with gaps and images seen by camera; (b) calculated and measured contrast of gap images at top dead center.

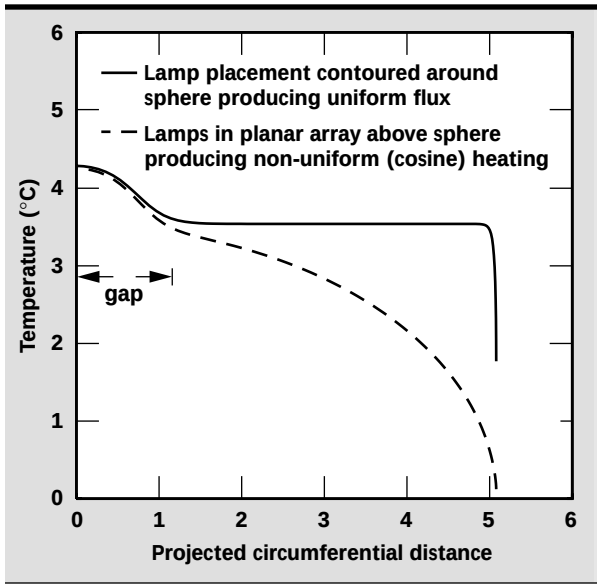

Figure 6. Impact of lamp orientation on gap detection for the sphere.

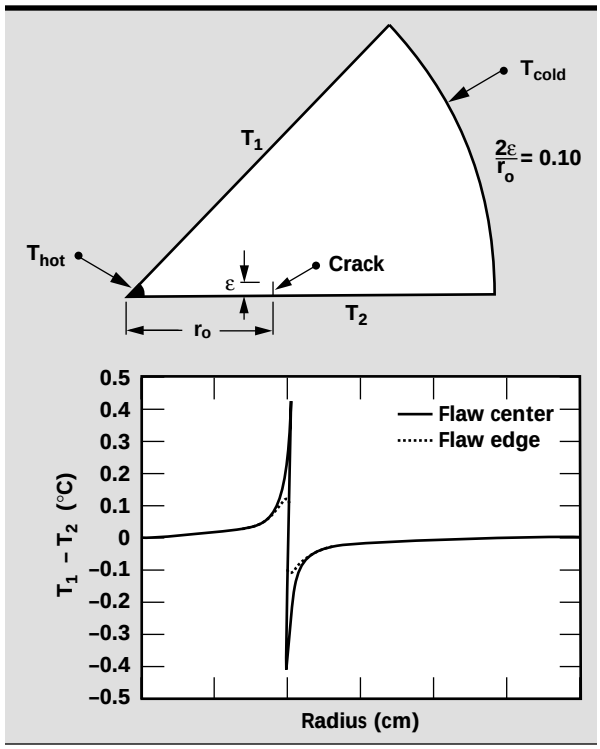

Figure 7. Sensing cracks perpendicular to shell surfaces.

also reveal radially running cracks. The camera would see a simulated contrast as shown in **Fig. 7**, which is within the limits of the measurements.

Experiment

Plate with Defect. The dual-band (centered at about 5 and 10 μm) infrared system,[7] obtained from Bales Scientific, Inc., has a shrouded, four-lamp array in a square pattern in a plane above and parallel to the surface of the test specimen which was a 12.7-cm-radius stainless disk of thickness 7.62 cm. The stainless steel test specimen containing the circular gap defect was fabricated by back-drilling from the rear face of the 7.62-cm-thick specimen and partially filling with a 2.54-cm-radius stainless slug having a slight interference fit around the periphery. The resulting gap thickness of 0.32 cm was small compared to the gap radius of 2.54 cm. The resulting gap depth was 0.9525 cm. The energy flux imposed on the specimen was 4.84 J/cm^2, and the lamps were on for about 4 ms. To experimentally resolve the curves shown in **Fig. 2**, their peak values should be no smaller than about 0.6 °C since relative temperature differences of about 0.1 °C can just be resolved. The gap dimensions illustrated here produced results approaching this measurement limit. Results obtained for smaller depths or larger gap radii than those considered here are more easily obtained.

For this system, a high emittance (emissivity) coating is desired to mitigate test surface reflected irradiance originating from the heated shroud and from the lamps which are cooling. In the interest of nondestructive evaluation, we require that the coating be easily removed without damaging the surface finish. For this reason, a water-based, black poster paint was brushed on as the coating material. Both the surface of the test specimen as well as that of the calibration plate, a 0.9-cm-thick 6061 aluminum slab, were covered by the same coating. The calibration plate was used to determine the energy flux, which was needed for the analysis in obtaining the product $q_s\tau_0$ which is used to compare experimental and computational results and in the depth determinations.

Cylindrical Shell Composite. The aforementioned cylindrical composite was also tested with the same lamp array used for the plate. Because of the planar lamp array, the cylindrical surfaces were not uniformly heated. The uppermost portion of the cylinder facing the lamp was heated more than lower portions having a less favorable view of the lamps. Discussion is deferred on the consequences of this non-uniform heating.

For reasons also to be discussed subsequently, tests on the cylindrical composite were performed both with and without the black poster paint external coating.

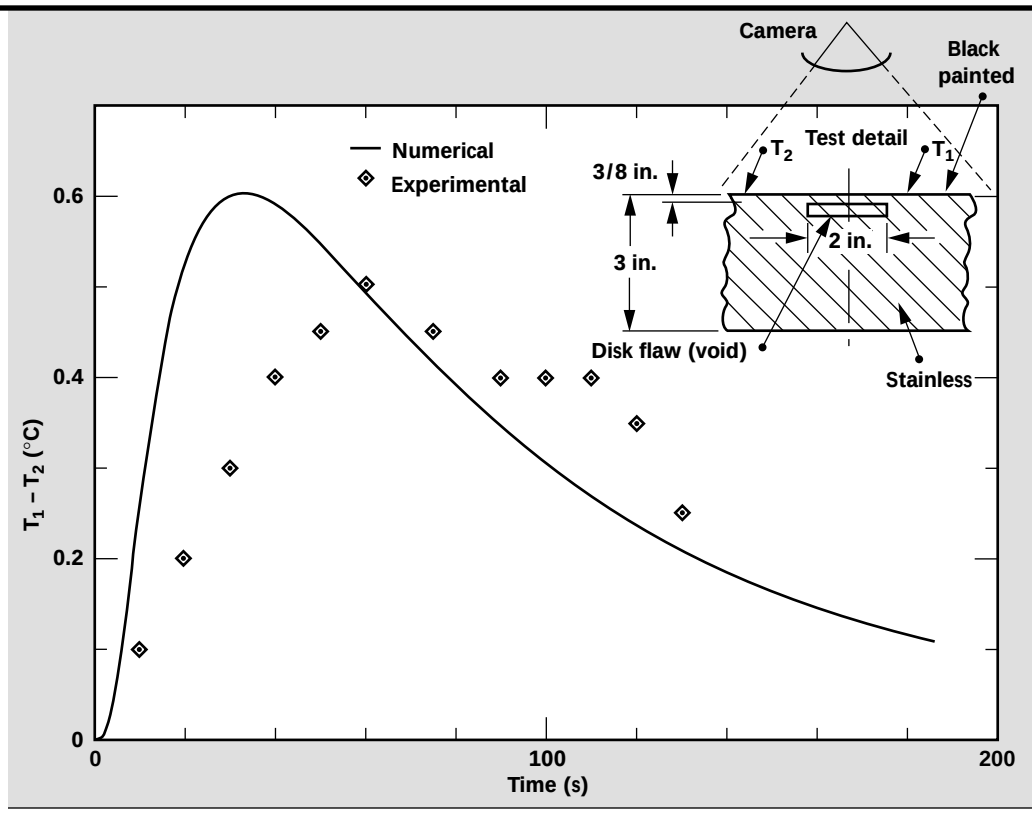

Figure 8. Comparison between numerical solution and experimental results for the plate.

Results

Plate. The calculated and measured transient image temperature contrast, T1 – T2, is compared in **Fig. 8** for the applicable Biot number of 0.014. The corresponding surface images are shown in **Fig. 9** at times before, during, and after the times when the experimental contrast is near its peak. The comparison in **Fig. 8** reveals that the experimental data lag the calculated results in times prior to about 60 s, which has the effect of increasing the experimental value of τ_{max} and decreasing the experimental value of $(T1 - T2)_{max}$ relative to their calculated values, as shown in **Table 2**.

The calculated results in **Fig. 8** do not include the presence of the surface coating in retarding the surface images which are produced by conducting subsurface information through the coating. Separate calculations have shown this is an important effect that depends on coating thickness and thermal conductivity and is responsible for the early-time mismatch between experimental and computational results. Use of a more suitable removable coating having good optical as well as thermal properties is therefore desirable.

Depth Detection. As a consistency check on the method for depth detection, the computed results from **Table 2** were first used to obtain depth L and gap radius R from simultaneous solution of **Eqs. 11** and **12b**. The results for R and L were within 1.8 and 1.9% of their respective actual values, these errors reflecting minor curve-fitting errors associated with **Eqs. 9** and **10**. This same evaluation was repeated using the measured values of **Table 2**, and the results are shown in **Table 3** (second row). Because of the previously discussed coating conductive losses, the depth and gap radius detected using the experimental data are greater than their actual values.

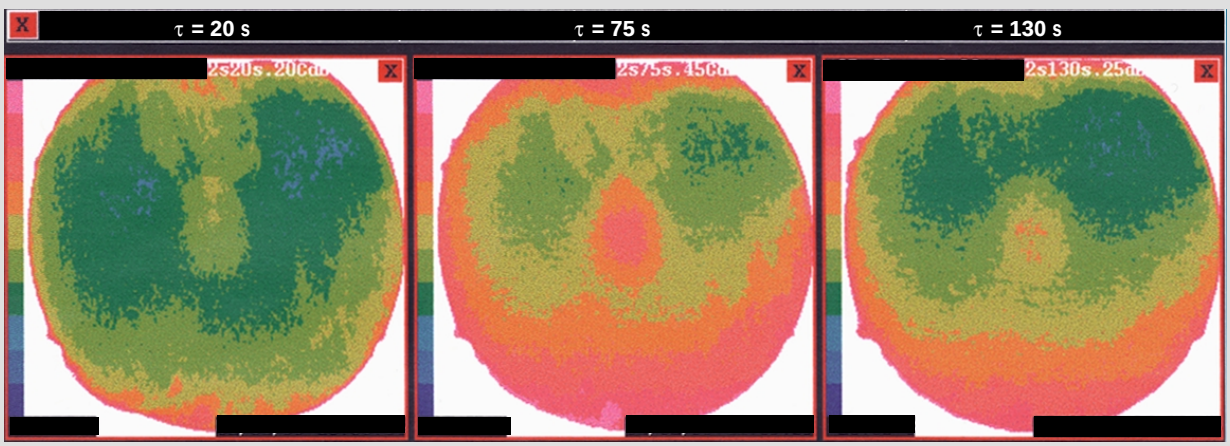

Figure 9. Images before, during, and after peak contrasts.

Table 2. Peak image contrast and time for Bi = 0.014, energy flux= 4.84 J/cm², R = 2.54 cm, L = 0.9525 cm in stainless steel.

	Peak contrast, $(T1 - T2)_{max}$ (°C)	Time at peak contrast, τ_{max}(s)
Computed, no conductive coating, temperature drop	0.60	29
Measured, with coating	0.50	60

Table 3. Depth detection; image radius observed, R^i = 2.65 + 0.1 cm.

Method	Depth, L (cm)	Radius, R (cm)
Actual	0.9525	2.54
Simultaneous solution to Eqs. 11–12b	1.24	3.86
Find L from Eq. 11 using Ri = 2.65 cm	1.06	2.65

An alternative depth estimate based on the experimental data was also made and is reported in the third row of **Table 3**. Here only **Eq. 11** is enforced, and, instead of using **Eq. 12b**, the observed image radius of approximately 2.65 cm is used to obtain the depth L. The error made in this surface image size observation is estimated to be ±0.1 cm. This produces a much closer depth prediction of 1.06 cm, about 11% higher than the actual depth.

Detection Limits. Equation 11 was evaluated for L = L(R) and the results were plotted in **Fig. 10**. In this portrayal, a fixed value of $(T1 - T2)_{max} = 0.87$ °C was used as a measure of a contrast that could easily be seen when the system is used in a routine inspection mode. The product of density and specific heat capacity for most metals above room temperature is about 3.5 J/cc/°C, which was also used in constructing **Fig. 10**. At a particular energy flux, depths above the curve are not detectable; those below the curve provide surface images that can be seen. These curves represent the detection limits for metals.

Curved Surfaces. The apparent gaps revealed by the images in **Fig. 5a** appear as spots rather than expected circumferential rings. One possible explanation for the spots is that the lamps, which are arrayed as a planar heating source above the cylinder, produce circumferential temperature gradients that cause the gaps to be undetected except at the centerline where these gradients are small. This effect is demonstrated for the sphere in **Fig. 6**.

Figure 5b demonstrates that predicted and measured contrast factors are in good agreement both with respect to magnitude and time. (The better agreement for the analytical solution is fortuitous because the numerical solution more faithfully represents the thermal problem than does the analytical solution whose approximations were previously described.) The time scales of **Fig. 5b** are less than about 1 s owing to the thin shells having a small thermal capacitance. These times are much smaller (on the order of minutes) than those for the thicker flat plate (see **Fig. 8**).

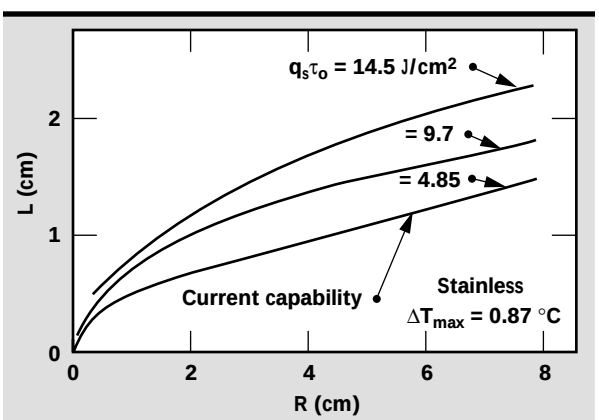

Figure 10. Detection limits for metals at 0.87 °C peak contrast (depths L above the curves are not detectable).

It is important to mention that the experimental results for the cylinder were obtained for an unpainted, bare outer surface. The painted cylindrical surface produced such weak images that they could not be seen, this caused by the aforementioned coating insulating effect which is significantly exacerbated in the short time scales of 1 s. Even though the measured contrast factor (ordinate of **Fig. 5b**) agreed well with predicted results, we as yet cannot rule out that some or much of the images seen may be artificial and due to reflected irradiance originating from the cooling, unshuttered lamps.

Conclusions

The following conclusions are drawn relating to impulsive surface heating and image observation:

1. Surface images are created by the multidimensional heat flow around the subsurface flaw (gap).
2. An optimum, opportune time, dependent on host thermal diffusivity among other parameters, occurs when the brightest image appears.
3. Subsurface depths are over-predicted, this caused by an insulating effect of the coating used.
4. Detection limits are governed by instrument sensitivity, flaw geometry (depth and transverse size), host density and specific heat capacity and energy flux imposed; the limits are independent of host thermal conductivity.
5. With all other parameters fixed, an increase in energy flux does not return a proportionate increase in detection depth.
6. Curvature effects need to be accommodated by arraying the lamps to conform to the body shape.
7. Low thermal conductivity coatings applied to thin, metallic shells seriously retard the images.
8. If a suitable coating cannot be found for thin shells, it will be necessary to a) blacken (and possibly water-cool) the shroud surrounding the test section and b) shutter the lamps. A shutter must operate within about 100 ms.

Future Work

We have two major challenges: (1) lamps should be arrayed to conform to component shapes, thereby achieving a more uniform heating; and (2) an optical coating needs to be identified that possesses good heat conduction properties yet is removable without surface damage. In absence of such a coating, the lamps will require shuttering and the shroud will need to be water-cooled.

References

1. C. K. Hsieh and K. C. Su (1980), *ASME Trans., J. Heat Trans.*, Vol. **102**, p. 324.

2. C. K. Hsieh and K. C. Su (1981), *ASME Trans., J. Heat Trans.*, Vol. **103**, p. 42.

3. C. K. Hsieh and A. J. Kassab (1986), *Int. J. Heat Mass Trans.*, Vol. **29**, p. 47.

4. C. K. Hsieh, C-Y. Choi and K. M. Liu (1989), *J. Nondestr. Eval.*, Vol. **8**(3), p. 195.

5. D. J. Roth, J. R. Bodis and C. Bishop (1997), *Res. Nondestr. Eval.*, Vol. **9**, p. 147.

6. A. B. Shapiro (1986), Lawrence Livermore National Laboratory, Livermore, California (UCID-20824).

7. L. A. LeSchack and N. K. Del Grande (1976), *Geophys.*, Vol. **41**(6), p. 1318.

Quantitative Tomography Simulations and Reconstruction Algorithms

Harry E. Martz, Jr.
Center for Nondestructive Characterization

Dennis M. Goodman and Jessie A. Jackson
Laser Engineering Division
Electronics Engineering

Clinton M. Logan
Manufacturing and Materials Engineering Division
Mechanical Engineering

Maurice B. Aufderheide, III and Alexis Schach von Wittenau
Defense and Nuclear Technology

James M. Hall
Physics

Dale M. Sloan
Computation

We are researching, developing, and implementing quantitative imaging tools (radiographic simulations and image reconstruction algorithms) with three main goals in mind. First, they will allow optimization studies to be made for tomography equipment to optimize geometry, source, and detector choices. Second, the simulation tools will allow more accurate corrections to be made to experimental radiographs resulting in very accurate tomographic image reconstructions. Third, these tools will be integrated with existing reconstruction routines to build state-of-the-art forward-modeling tomographic image reconstruction codes. These codes will use a constrained-conjugate-gradient (CCG) algorithm to perform reconstructions with complete and limited numbers or portions of views. By merging the simulation capability with the CCG reconstruction technique, we will have a physics-based, forward-model image reconstruction code.

Introduction

Transmission radiography and tomography are important diagnostic tools at the heart of Lawrence Livermore National Laboratory (LLNL)'s effort to meet the DOE DP-10 Advanced Radiography Campaign goals. This campaign seeks to improve radiographic simulation and analysis so that radiography can be a useful quantitative diagnostic tool for stockpile stewardship.

This project will advance tomographic imaging capabilities in LLNL programs. Current radiographic accuracy does not allow us to satisfactorily separate experimental effects from features of the radiographic or tomographic reconstructed object image. This can lead to difficult and sometimes incorrect interpretation of radiographic and tomographic image results.[1–3] By improving our ability to simulate the whole radiographic and tomographic system, it will be possible to examine the contribution of system components to various experimental effects, with the goal of removing or reducing them. By merging this simulation capability with a maximum likelihood constrained-conjugate-gradient (CCG) reconstruction technique, we will have a physics-based, forward-model image reconstruction code.

Forward-modeling techniques are being explored in a variety of places. This project is unique in its physics simulation approach, in its use of CCG to reconstruct 2-D and 3-D meshes, and in the breadth of data to which it will be applied and tested. This includes x-ray, neutron[4-6] and proton radiographic data. The ability to make quantitative attenuation-image reconstructions will be attractive to many applications leading to new collaborations in earth science, plant science, medicine, material development, manufacturing, and defense.

Current computed tomography (CT) image reconstruction back-projection methods make strong assumptions about the radiographic projection data. These assumptions include energy-independent photon attenuation cross-sections, no detector or source-spot blur, no scattering, no noise or artifacts. None of these assumptions is strictly correct. Radiation attenuation cross-sections depend strongly on energy and material composition; detector and source-spot blur is usually significant; scattering is present; noise and artifacts are common.

Some of these assumptions can be treated in the forward model of a reconstruction algorithm. In this project, we seek to improve the accuracy of CT from transmission radiographs by studying what physics is needed in the forward model.

Presently, accuracy in attenuation estimates of roughly a few percent is possible, over a volume whose length is on the order of 1/1000 the object characteristic length. A simple example of a magnesium (Mg) phantom is shown in **Fig. 1**. The tomography projection data was acquired using KCAT, a CT scanner that consists of a 160-kV microfocus x-ray source and a scintillator lens coupled to a CCD camera detector system. The source-to-detector distance for the Mg phantom study was 92 mm, with the object 15 mm in front of the detector. The source was set to 75 kV and 0.12 mA and was filtered with 76 µm of Al. The total data acquisition time was ~5 h for 360 projections over 360°. The data was reconstructed using a convolution back-projection (CBP) algorithm. The CT image shown in **Fig. 1** to first order appears to be a uniform x-ray attenuating disk as expected. The CT image also shows a nice sharp

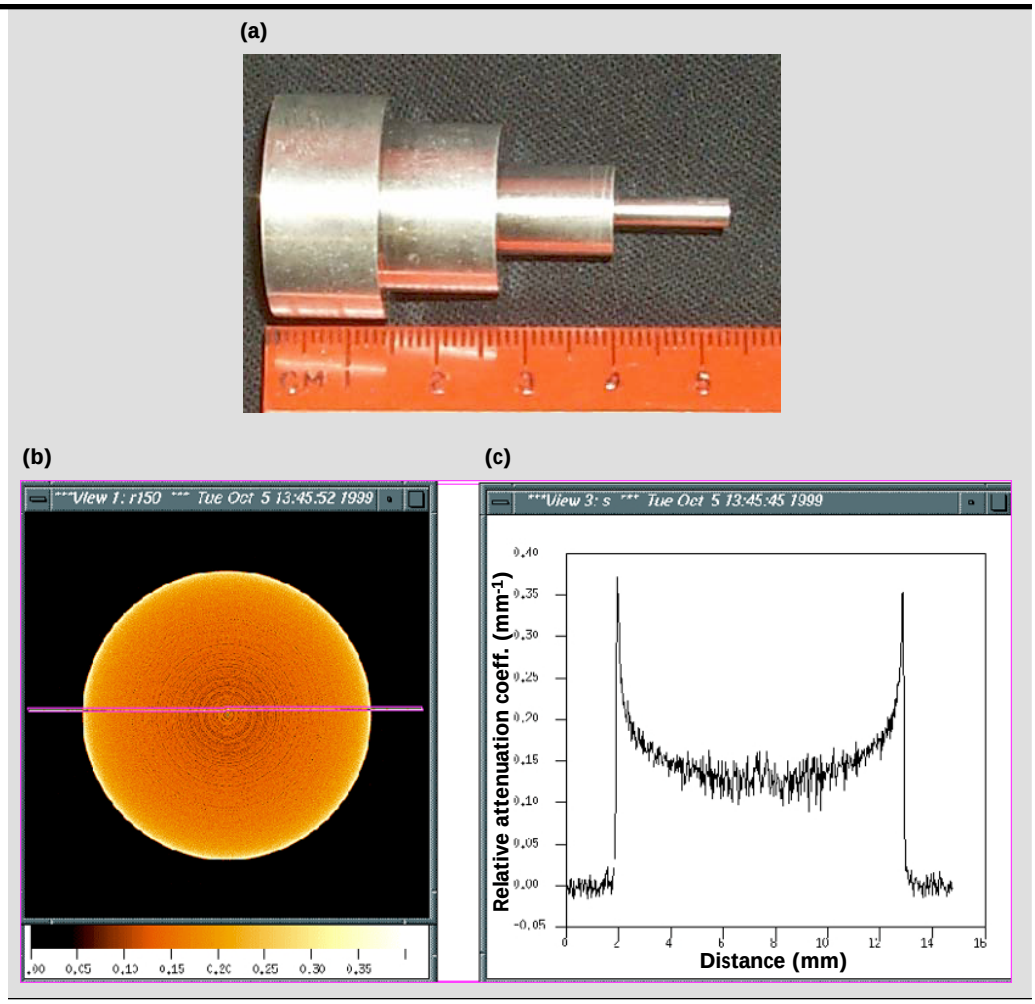

Figure 1.
(a) Photograph of a Mg phantom for the Mg tensile bar CT study. The phantom is made of 99.9% pure Mg of density 1.74 g/cm^3. From left to right the outer diameter of the rod is 25.28, 19.05, 10.16, and 3.31 mm.
(b) CBP reconstructed image for the Mg phantom. (c) The 1-D profile for the line shown in the CT image.

edge. However, closer analysis of the image and the profile reveals that there are ring and cupping artifacts. The ring artifacts are reduced by processing the sinogram[7] before image reconstruction. The ring-removed CT image is shown in **Fig. 2a**.

The cupping artifact results in relative linear attenuation coefficient values that are greater than 100% (near the edges) of the mean, 0.14±0.02 mm^{-1}. (The means and standard deviations in this report were determined from a 374 × 337 extracted rectangle from within the CT slice plane.) This profile should be flat since the phantom is 99.9% Mg with uniform density.

This so-called cupping artifact is due to x-ray beam-hardening and scattering. Most of this can be accounted for by applying a beam-hardening correction[1] as shown in **Fig. 2c**. Even when this data is corrected for rings and beam hardening the standard deviation within the uniform part of the CT image (see central portion of the profile in **Fig. 2d**) is on the order of 17%, 0.29±0.5 mm^{-1}. We are developing and applying better simulation and reconstruction tools to make a more complete characterization of the system and its components, and are striving to achieve accuracies to better than 1%. It is possible to attempt this goal now because radiographic simulation, CT, and computers have matured sufficiently.

Technical Approach

Radiography Modeling. This project has two main aspects. First, we are accurately modeling the process of x-ray transmission radiography, enabling us to accurately assess and mitigate experimental effects that compromise CT image reconstruction from radiographs. This modeling effort uses three

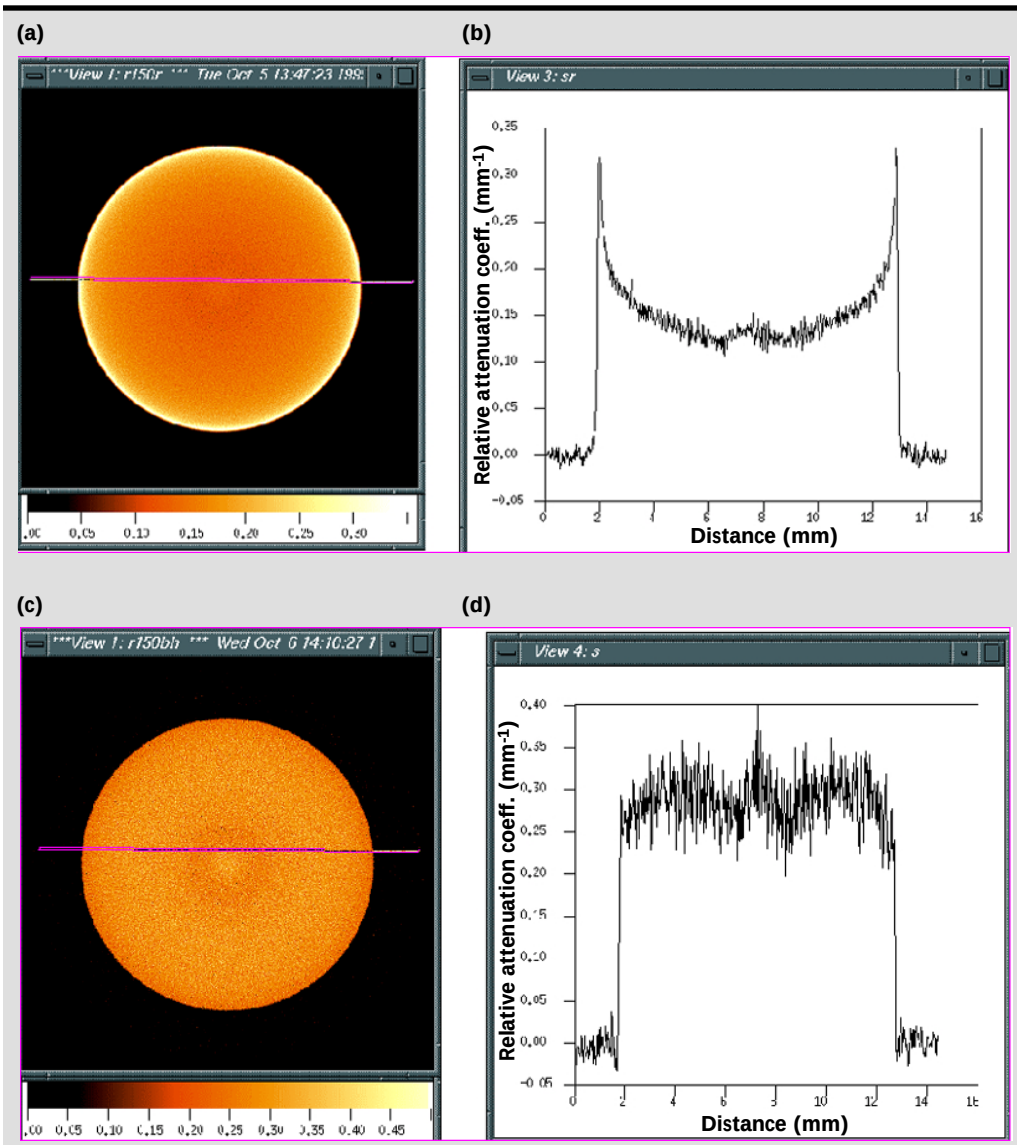

Figure 2. (a) CBP reconstructed image after ring removal applied to the sinogram for the Mg phantom. (b) The 1-D profile for the line shown in the CT image. (c) CBP reconstructed slice after ring removal and beam hardening was applied to the sinogram for the Mg phantom. (d) The 1-D profile for the line shown in the CT image.

simulation codes, HADES,[8] COG,[9] and MCNP.[10] Our suite of experimental digital radiography (DR)/CT systems and image reconstruction algorithms are being used to study how experimental effects produce reconstruction artifacts. Radiographic simulation tools have been used to a limited extent[8,11–14] for assessing experimental effects and have been helpful in analyzing experimental CT images. In this project we will extend our simulation capabilities.

HADES is a radiographic simulation code that uses ray-tracing techniques to compute radiographs through a mesh.[8] The full geometry of cone beams is treated exactly. A variety of meshes, including 3-D Cartesian meshes, can be ray-traced by the code. In addition, objects such as spheres, cones, cylinders, and plates can be added to the problem as defined by the user. Blur from detectors and finite-spot-size sources is included in the simulation by convolution. Sources of any arbitrary input spectrum can be specified and the spectrally dependent transmission is computed using energy groups.

Using exposure conversion curves, HADES is able to compute, for a given input photon fluence and spectrum, the energy deposited at the detector plane, adding the appropriate statistical fluctuations, if requested. HADES also can simulate GeV-proton radiography and will soon have a low-energy neutron simulation capability. Because HADES uses ray-tracing techniques, it can simulate radiographs very quickly. Hence it is useful as an iterative tool.

Some aspects of x-ray physics are not adequately included in HADES, particularly scattering, secondary Bremsstrahlung, and detailed detector response. A Monte Carlo approach, such as COG, is needed to better understand how scattering and secondary Bremsstrahlung may be incorporated into HADES.

COG is a detailed Monte Carlo neutron, photon and electron transport code capable of providing accurate answers to complex deep-penetration (or shielding) problems.[9] Unlike many of its predecessors, COG is free of the physics compromises and approximations traditionally used in radiation-transport codes. The COG code is fully 3-D, uses point-wise-correct cross-sections and exact angular scattering functions and provides the user with a full range of statistical biasing options to speed up problem solving. Problem geometries can be set up manually using simple but powerful constructs (more than 30 complex pseudo-surfaces such as boxes, spheres, cylinders, and cones are included in COG's geometry package as elementary types) or developed using CAD tools and then transformed automatically into the proper input format. Geometrical elements in a problem can be visualized in both cross-sectional and perspective views to ensure fidelity, and complex geometries can be debugged on a standard desktop computer. COG allows users to score the results of a simulation using a number of built-in detector types (for example, boundary crossing detectors, reaction detectors, point flux estimators, or pulse detectors) or specialized, user-written detector packages linked in at run time (for example, radiographic imaging detectors).

The ultimate accuracy of a COG simulation is limited only by the accuracy of the data contained in its reference libraries. COG's accuracy and reliability have been verified by extensive benchmarking on radiation shielding and nuclear criticality problems relevant to LLNL programs.

In this project, we are extending the existing radiographic imaging capability of COG to handle a wider range of object thicknesses (for example, optically thick objects, greater than 3 to 4 mean free paths). Accurate Monte Carlo imaging requires a very large number of simulation particle histories. For example, on the order of 10^{10} histories are required to simulate a 1-k-×-1-k detector with 1% statistics. This will require Accelerated Strategic Computing Initiative (ASCI) level computational resources.

We are simulating radiographs of phantoms using COG, MCNP and HADES. COG and MCNP are being used to determine what experimental factors have the largest effect on the blur and scattering profiles. The source and detector blur and aspects of the problem that do not have a large effect on scattering can be iterated many times with HADES, while still including COG's or MCNP's blur and scattering profiles. This required developing a data link between the Monte Carlo codes and HADES so that the Monte Carlo estimates of scattering can be incorporated into HADES simulations. In addition, the Monte Carlo codes are used to calibrate any approximate blur and scattering treatments implemented by HADES. The Monte Carlo and HADES simulated radiographs are validated by comparison with DR using phantoms.

Phantoms. Key parts of this work are the DR and CT phantoms or test objects, helpful in understanding and validating the simulation codes. The phantoms were designed to meet several criteria: ability to be simulated by COG, MCNP and HADES; ease of fabrication; adaptability to different types of problems; and presentation of a challenging imaging situation.

CT Algorithms. The second aspect of this project involves merging the improved version of HADES with a recently developed CT method based on our CCG optimization algorithm.[15] This approach expresses the image reconstruction problem as a large matrix equation relating a model for the object being reconstructed to its projections (radiographs).

The CCG algorithm is used to seek a maximum likelihood solution. The search continues until the match between the measured projections and the calculated projections is satisfactory. A flow diagram of the tomographic image reconstruction process to recover an object function from radiographic projections is shown in **Fig. 3**.

CT reconstruction involves solving an inverse problem that yields an image or recovered object, which is in some sense a best match to the observed data. The goal is to obtain a good estimate of the true object **o**. The problem of reconstructing an object from the observed data can be described as follows: given the observed data vector **p**, reconstruct an estimate of the object, represented by the vector $\hat{\mathbf{o}}$, that produced this data. The statistical relationship between $\hat{\mathbf{o}}$ and **p** can be written as $L(\mathbf{p},\hat{\mathbf{o}})$, where $L(\cdot,\cdot)$ is a negative log-likelihood function.[16] The function $L(\cdot,\cdot)$ is determined by the physics of the property being measured, the geometry of the measurement system, and the statistics of the noise corrupting the data. The maximum likelihood solution for estimating **o** from **p** is

$$\hat{\boldsymbol{o}} = \underset{\tilde{\boldsymbol{o}}}{Arg\min}\left\{L(\boldsymbol{p},\tilde{\boldsymbol{o}})\right\}, \qquad (1)$$

where the vector $\hat{\mathbf{o}}$ yielded by the Argmin operator is the value of $\tilde{\mathbf{o}}$ that minimizes $L(\mathbf{p},\tilde{\mathbf{o}})$.

The difficulty with this estimate of **o** is that most inverse problems are ill-posed in the sense that small changes in **p** may produce large changes in $\hat{\mathbf{o}}$. This is especially true of limited data CT reconstructions. Consequently, $\hat{\mathbf{o}}$ typically is too large and very noisy. A common method for obtaining better estimates is the regularization or penalized likelihood approach that adds Euclidean norm and/or absolute value norm terms to $L(\mathbf{p},\hat{\mathbf{o}})$. These terms penalize large $\hat{\mathbf{o}}$. Frequently regularization is not sufficient to yield a high quality reconstruction, so any additional prior information about the unknown must be included. Many properties such as energy, absorption, and reflection are inherently non-negative, and adding this constraint often greatly enhances reconstruction quality. Furthermore, there often are physical reasons for placing upper bounds on the estimate. The result is upper and lower bounds for each component of the object vector $\hat{\mathbf{o}}$. If we denote the set of **o** vectors that obey the bound constraints by S, then our modified maximum likelihood problem is

$$\hat{\boldsymbol{o}} = \underset{\tilde{\boldsymbol{o}} \in S}{Arg\min}\left\{L(\boldsymbol{p},\tilde{\boldsymbol{o}}) + \eta\left\|\tilde{\boldsymbol{o}}\right\|_1 + \lambda\left\|\tilde{\boldsymbol{o}}\right\|_2\right\}, \qquad (2)$$

where η and λ are Lagrange multipliers that control, respectively, the degree of absolute value norm and Euclidean norm regularization.

A second problem is the dimensionality of **Eqs. 1** or **2**. The discretized object usually contains 10^5 to 10^7 pixels (voxels) resulting in an **o** vector of the same length. Conventional nonlinear minimization algorithms use Newton or quasi-Newton techniques that require storing an approximation to the inverse of the matrix of second partials of $L(\mathbf{p},\hat{\mathbf{o}})$ with respect to $\hat{\mathbf{o}}$. Because even a $10^5 \times 10^5$ matrix is too large to store in memory, these techniques are not appropriate for the inverse problems we are considering.

In the case of an unconstrained problem, such as **Eq. 1**, either the conjugate gradient algorithm, which in effect builds up second derivative information without directly storing it, or limited-memory quasi-Newton algorithms, which store a low rank approximation to the inverse matrix of second partials, are the methods of choice when the dimensionality is too large for conventional quasi-Newton methods.

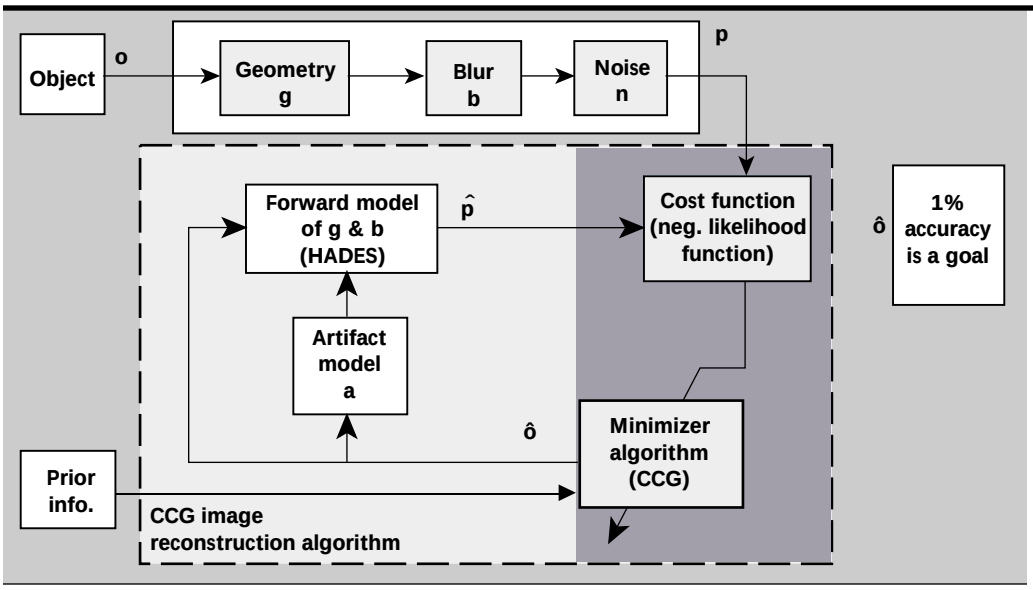

Figure 3. Flow diagram of the process for recovering an object function from radiographic projection data using the CCG image reconstruction algorithm. Details of this diagram are provided in the text. The circumflex (ˆ) appearing over some parameters indicates they are estimated quantities.

For constrained problems, such as **Eq. 2**, conventional optimization techniques usually allow only one variable per iteration to attain a bound, so for very large bounded inverse problems these techniques are very slow since they spend too much effort finding bounds. Consequently, standard approaches to inverse problems use the projection onto convex sets (POCS) algorithm,[17] the expectation-maximization (EM) algorithm,[18] or variants of the algebraic reconstruction technique (ART).[17] These methods can attain multiple bounds in an iteration, but they essentially use a steepest descent strategy and converge very slowly, sometimes not at all.

We have developed an extension of the conjugate gradient algorithm that incorporates bound constraints on the variables.[15] It is unique in that it incorporates a bending line search, which allows multiple variables per iteration to attain bounds. Given the dimensionality of our problems of interest, this is a major advantage over the conventional techniques. Our algorithm has been applied with great success to a variety of practical problems.[15,19]

We have also developed a limited memory quasi-Newton algorithm that uses the same bending line search as our CCG algorithm, using matrix updates.[20] The choice of algorithm is problem dependent. Our conjugate gradient algorithm requires an accurate line search to ensure fast convergence. Fortunately, it is possible to take advantage of the special structure of most tomography problems to greatly reduce the effort required by the line search.[21] On the other hand, when symmetries or complicated prior information are applied to the reconstruction problem, or when blurring occurs in the projection data, the special structure may no longer apply, and our quasi-Newton algorithm is usually a better choice.

CT Imaging Artifacts. Our work on improving the accuracy of tomographic reconstructions is highly dependent on improved reconstruction algorithms. This year we have concentrated on three issues: reducing artifacts, mitigating the effects of beam hardening, and compensating for blur. These issues are highly complex, and we will continue our work on them in FY-00.

The problems our techniques have been designed to handle can be described as follows. First there is a deterministic model of the relationship between the unknown object and the projection data:

$$\hat{\boldsymbol{p}} = h(\hat{\boldsymbol{o}}) \tag{3}$$

where the vector $\hat{\mathbf{o}}$ represents an estimate of the unknown object we wish to reconstruct, and h is a function that represents such effects as geometry, g, and absorption that lead to the expected data $\hat{\boldsymbol{p}}$ that would result if $\hat{\mathbf{o}}$ were the true object. The actual observed data is $\mathbf{p}$, and the estimate of the true object is obtained by using an optimization algorithm to adjust $\hat{\mathbf{o}}$ so that $\hat{\boldsymbol{p}}$ is a best fit to the actual data according to some criterion function, say

$$f(\boldsymbol{p}, \hat{\boldsymbol{p}}). \tag{4}$$

where the choice of the criterion function depends on the statistics of $\mathbf{p}$. Consequently, our reconstruction problem involves minimizing with respect to a function of the form

$$L(\boldsymbol{p}, \hat{\boldsymbol{o}}) = f(\boldsymbol{p}, h(\hat{\boldsymbol{o}})). \tag{5}$$

If $L(\mathbf{p},\hat{\mathbf{o}})$ is the negative log-likelihood function, the recovered object is the maximum likelihood estimate of the unknown.

Artifacts in a reconstructed object are frequently caused by outliers in the observed projection data $\mathbf{p}$. These outliers can result from mismodeling the imaging system, bad detectors, and "hits" from extraneous radiation. The maximum likelihood method is generally highly sensitive to outliers. Robust statistical methods[22] involve modifying $f(\boldsymbol{p}, \hat{\boldsymbol{p}})$ to make the resulting estimator much less sensitive to outliers, yet have it perform almost as well as maximum likelihood in the absence of outliers. For tomography systems that are photon rich, the typical assumption is that noise on the observed projection data $\mathbf{p}$ is, in the absence of outliers, Gaussian with constant variance. The maximum likelihood principle leads to applying a least-squares fit between the observed data $\mathbf{p}$ and the modeled data $\hat{\boldsymbol{p}}$. The squared error function is

$$f(\boldsymbol{p}, \hat{\boldsymbol{p}}) = \sum_{i=1}^{N} r_i^2 = \boldsymbol{r}'\boldsymbol{r}\ , \tag{6}$$

where the *residual* vector $\mathbf{r} = \mathbf{p} - \hat{\mathbf{p}}$ is one indication of mismatch between the observed data and the model of the data. Unfortunately, this criterion function is very sensitive to outliers. For example, suppose N=10,000 in **Eq. 6**, and the magnitude of a typical component of the residual is 1.0, except for one component r_k whose value is 100.0. Then r_k contributes roughly as much to the squared error as do all the other components combined, and the minimization algorithm will try very hard to match the outlier at the expense of all the other data points.

The most common robust criterion is

$$f(\boldsymbol{p}, \hat{\boldsymbol{p}}) = \sum_{i=1}^{N} g(r_i)\ , \tag{7a}$$

where

$$g(r) = \begin{matrix} r^2 & if & |r| \le c \\ 2c|r| - c^2 & if & |r| > c \end{matrix}\ . \tag{7b}$$

The function $g(r)$ transitions smoothly from a squared penalty to a linear penalty, thereby reducing the influence of large residuals. The choice of c is data dependent.[22] We have demonstrated both that CCG is very effective in minimizing **Eq. 5** when **Eq. 7** is the criterion function and that this approach greatly improves reconstruction quality in the face of outliers. The effectiveness of CCG has permitted—to our knowledge—the first successful application of robust statistical techniques to tomographic inverse problems.

Adding a saturation region to **Eq. 7b** for very large data mismatches results in the criterion function:

$$g(r) = \begin{cases} r^2 & if \quad |r| \le c \\ 2c|r| - c^2 & if \quad c < |r| \le d \\ 2c|d| - c^2 & if \quad |r| > c \end{cases} . \tag{8}$$

This function is even more robust in the face of very large outliers than is **Eq. 7b**. Unfortunately, using **Eq. 8** makes L**(p,ô)** a nonconvex function of **ô**; consequently, it has local minima. Typically, using $g(r)$ as in **Eq. 8** and starting with **ô**=**0** results in convergence to a local minimum and a meaningless reconstruction.

One solution is first to solve the problem using **Eq. 7b**; then use the resulting **ô** as a starting point for the problem defined by using **Eq. 8**. We have found this approach to be satisfactory, although there is no guarantee of convergence to the exact global minimum.

This year we have demonstrated that robust techniques show great promise for artifact reduction in tomography, but much work remains to be done. We intend to study other robust criteria. For example, changing the saturation region in **Eq. 8** to a zero response region would force the reconstruction algorithm to pay no attention whatever to very large residuals, but local minima would be an even more serious problem. In the cases of photon-starved x-ray tomography, neutron and proton tomography, and emission tomography, the appropriate noise model is Poisson, not Gaussian. The residuals do not appear directly in the Poisson likelihood function, so the functions in **Eqs. 7b** and **8** are not immediately useful. In particular **Eq. 7a** must be replaced by

$$f(\boldsymbol{p}, \hat{\boldsymbol{p}}) = \sum_{i=1}^{N} p_i \log \hat{p}_i - \hat{p}_i , \tag{9}$$

to obtain the maximum likelihood estimate.[23] There is no clear best approach to making the Poisson likelihood function robust though several possibilities exist.[22,23]

Beam Hardening. Another cause of artifacts in reconstructions is due not to data errors but to mismodeling. The model for the intensity or energy, I_1, deposited on a detector for a polychromatic x-ray source for a single ray projection is given by

$$I_1 = I_0 \int T(E) \exp\left\{ -\int_L a(l,E) dl \right\} dE , \tag{10}$$

where I_0 is the incident intensity or energy on the object, $a(l,E)$ is an attenuation function that depends both on the position l along the ray and the spectral frequency or energy E, and $T(E)$ is the spectral energy distribution function of the x-ray source.[24] The value of $a(l,E)$ at each point l along the ray depends on the densities and absorption characteristics at spectral frequency E of each material present at location l. Most reconstruction algorithms neglect the effects of a polychromatic source and use the simplified model

$$I_1 = I_0 \exp\left\{ -\int_L a(l) dl \right\}. \tag{11}$$

Unfortunately, the absorption of most materials is a strong function of x-ray spectral frequency with absorption generally being higher at lower spectral energies. Consequently the spectral distribution at the detector is different from that at the source. This phenomenon is called beam hardening or spectral hardening, and use of **Eq. 11** rather than **Eq. 10** can lead to severe artifacts (see **Fig. 1**). If we let the data vector be the logarithm of the detector data described by **Eq. 11**, then the discretized version of **Eq. 11** leads to the following simple linear model for **Eq. 3**:

$$\hat{\boldsymbol{p}} = \boldsymbol{B}\hat{\boldsymbol{o}} , \tag{12}$$

where the matrix **B** represents the geometric relationship between object voxel and detector position. The usual approach to reducing the effects of beam hardening artifacts is to solve the problem defined by **Eq. 12**, correct for beam hardening in the logarithmic data vector, and then solve the problem once again by fitting the corrected data vector (see **Fig. 2c** and **d**).

In the first half of this year we developed a much better approach to avoiding beam hardening artifacts using the original detector data (we took no logarithm) and a discretized version of **Eq. 10** for **Eq. 3**. For the single material case, the model was

$$\hat{p}_i = \sum_{k=1}^{Nfreq} I_k \exp\left\{ -\mu_k \boldsymbol{b}_i \hat{\boldsymbol{o}} \right\}. \tag{13}$$

In **Eq. 13** we divided the x-ray frequency spectrum into $Nfreq$ bins so that I_k was the incident energy in the kth bin and μ_k is the mass absorption coefficient for the kth bin. The row vector $\mathbf{b}_i$ is the ith row of the geometry matrix **B**, and **ô** is the unknown vector of material densities.

We have implemented this model, and we have demonstrated that it is a superior method for mitigating the effects of beam hardening on reconstructions of simulated data. We achieved this success because both our CCG and our limited-data quasi-Newton algorithms were able to deal with this highly nonlinear model, whereas the usual steepest descent approaches typically failed.

We also considered the multiple material case in which **o** becomes:

$$\boldsymbol{o} = \begin{bmatrix} \boldsymbol{o}^1 \\ \cdot \\ \cdot \\ \boldsymbol{o}^{Nmat} \end{bmatrix}, \tag{14}$$

where there are *Nmat* materials, and o_j^m is the density of the mth material in the jth voxel.
This leads to the model

$$\hat{p}_i = \sum_{k=1}^{Nfreq} I_k \exp\left\{ \sum_{m=1}^{Nmat} \mu_k^m \boldsymbol{b}_i \hat{\boldsymbol{o}}^m \right\}, \tag{15}$$

where μ_k^m is the absorption of the mth material in the kth spectral bin. Unfortunately, the multiple material problem is highly ill-posed and our algorithms converged slowly to poor reconstructions. This is not surprising: by assuming *Nmat* materials we increase the number of unknowns by a factor of *Nmat* over the single material case, but the amount of data stays the same.

In the case where the region of each material in the object is known, our bound constraints can be used to make the problem better behaved. If these regions are not known, spectrally selective detectors can be used to increase the amount of data at each detector location. We successfully used spectrally selective detectors to solve an important waste drum tomography problem.[25–27] This work is currently being commercialized. Not only will this approach mitigate beam hardening, it also has the possibility of localizing or detecting materials in an unknown object. We will continue this work in FY-00.

Blur reduction. For many tomography problems blurring of the projection data is a serious issue. This blurring can be induced by finite beam spot size and other phenomena in the imaging system. This year for the blurring problem we neglected beam hardening issues and focused solely on the linear model described by **Eq. 12**. Blurring may be removed with a deconvolution algorithm prior to applying a reconstruction algorithm; however, an approach that is both more computationally efficient and more appropriate statistically is to fold both the blur model and the projection model into the deterministic model of the relationship of the object and the data shown in **Eq. 3**. Let the noise-free and blur-free projection model be given by

$$\boldsymbol{u} = \boldsymbol{B}\hat{\boldsymbol{o}} \tag{16}$$

where **B** is the geometry matrix defined earlier. Now let the blurring model be given by:

$$\hat{\boldsymbol{p}} = \boldsymbol{C}\boldsymbol{u}, \tag{17}$$

where $\hat{\boldsymbol{p}}$ is the modeled blurred projection data and

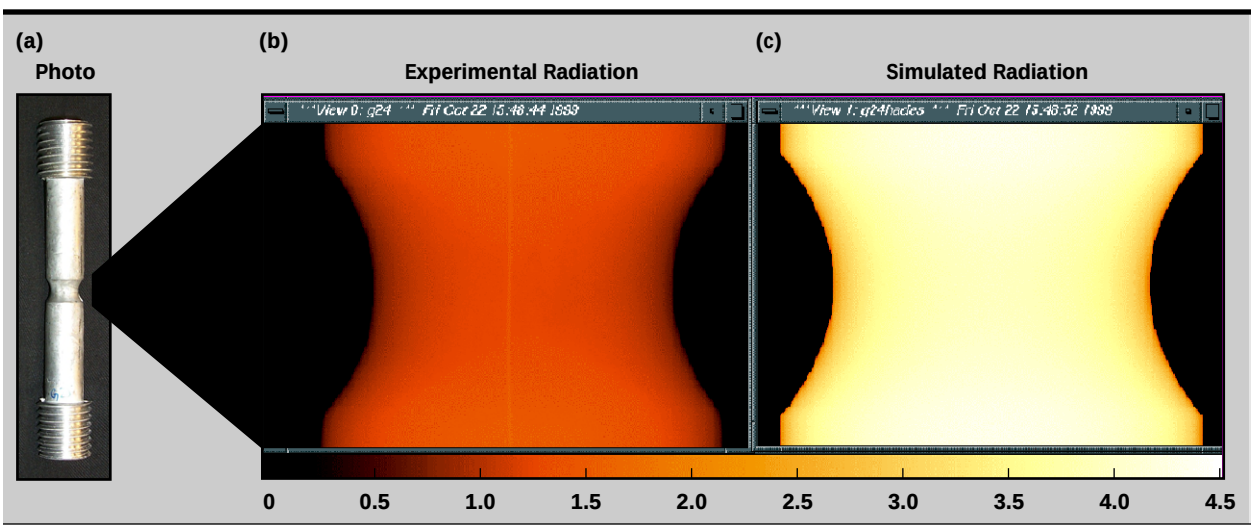

Figure 4. (a) Photograph of a cast Mg-alloy tensile bar. The bar is 11.5-cm long with a maximum diameter of 1.8 cm. (b) An experimental radiograph of a Mg tensile bar obtained by KCAT with a 75-kV source and a 0.08-mm Al filter. (c) A HADES simulated radiograph of the Mg-alloy tensile bar obtained with a 75-kV source and 0.08-mm Al filter.

C is a matrix representing the point spread function (PSF) that caused the blur. **Equation 3** now becomes

$$\hat{\boldsymbol{p}} = \boldsymbol{A}\hat{\boldsymbol{o}} \ , \qquad (18)$$

where **A=CB**. Because **Eq. 18** must be computed many times in either of our two optimization algorithms, computational efficiency is a serious issue. **Equation 16** represents a collection of line integrals, so **B** usually is very sparse. Furthermore, if the blurring function is shift invariant, which is usually the case for x rays and some times the case for neutrons but not the case for protons, then **Eq. 17** can be calculated using FFTs. Therefore, calculating **Eq. 16** and then **Eq. 17** may be more efficient than implementing **Eq. 18** directly.

This year we have developed a FFT-based implementation of **Eq. 17** and its adjoint (which our algorithms also require) and we have used this implementation to develop a highly effective deconvolution algorithm that permits use of all the possible criterion functions that we have described above. We have successfully applied this algorithm to astronomical data. In the future we intend to merge our blurring model with the beam hardening models described above.

First Year Accomplishments

Implementation of HADES. HADES has been ported to computers to be used for radiographic and tomographic simulation studies. The first project for which the code has been used is to model a Mg alloy (AM60, ~6% Al) tensile bar. Cast light metals, Al and Mg, are being used in an ever-increasing number of applications to reduce automobile weight for improved gas mileage and lower emissions. The tensile bars are used for material strength testing. Notched Mg tensile bars are being characterized by radiographic and tomographic imaging before and after mechanical testing. [28] The damage in these bar specimens will first be determined using CT and subsequently by metallography analysis intended to benchmark the CT technique.

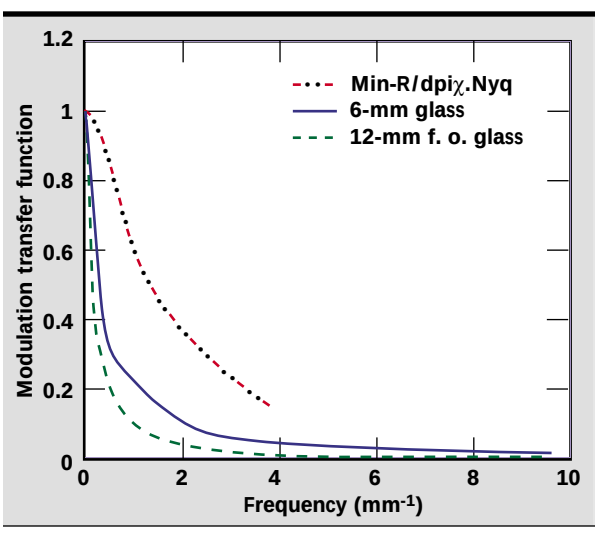

Figure 5. Experimentally determined MTF of a radiographic 3.175-mm-thick depleted-U edge for the Min-R/dpiχ detector system and two scintillator/lens/CCD detector systems at LLNL.

Low-energy radiographs have been taken of the bars for tomographic image reconstruction as shown in **Fig. 4b**. HADES is being used to generate synthetic radiographs of notched Mg bars with defects, to determine the smallest defects that can be characterized by CT. This will help understand the CT performance, and segmentation methods of CT data and conversion to finite-element analysis (FEA) meshes.

We simulated a radiograph of a pure Mg tensile specimen using the actual object and scanner (512 × 768 pixels, 0.0218-mm pixel size, 77-mm source-to-object distance and 92-mm source-to-detector distance (sdd)) geometries. The source was modeled at 75 kV with 0.08-mm Al filter. The detector efficiency was determined and included into the HADES simulation. The PSF of the detector was not determined and thus was not included into the HADES simulation. The resultant simulated radiograph is shown in **Fig. 4c**. We are currently incorporating the actual CT spectrum and detector response.

Experimental Set-Up. For our experimental work we have focused on using LLNL's 9-MV LINAC.

Recently, commercial detector arrays have become available that are based on fabrication methods developed for flat-panel displays. Early this fiscal year we began evaluation of an amorphous-Si (a-Si) array made by *dpiχ*[29] for use with the 9-MV Bremsstrahlung spectrum. These preliminary results are so exciting (see **Fig. 5**) that we have decided to use the *dpiχ* "Flashscan 20" detector for our experimental work.

The Flashscan 20 is a flat-panel array of light-sensitive photodiodes using thin film transistors. The Si is amorphous, resulting in good radiation resistance. The active area of the 12-bit a-Si array is 19.5 cm × 24.4 cm, with 1536 × 1920 pixels of size 127 × 127 µm. This array must be used with a scintillator to convert x-ray radiation energy to visible light. We have selected a commercial mammography "screen", Min-R, as having the best spatial resolution and sensitivity for this application.[30]

Phantoms. We selected the following test objects:

Cu-step wedge—We designed and fabricated a

step wedge with Pro-E software, fabricated from certified CDA 110 Cu, inspected and density verified. The wedge is 101.7 mm wide and 175.0 mm long. A solid model with as-inspected thickness for each step is shown in **Fig. 6**. A full inspection report with perpendicularity and parallelism is available by request to logan2@llnl.gov.

Ta edge—An edge is a widely used configuration with which to evaluate the frequency response of an imaging system. The edge-spread function (ESF) and the modulation transfer function (MTF) are derived from the image of an edge. Ideally one desires the edge to be very highly attenuating for the incident x rays and to be of zero thickness to eliminate alignment errors. We chose Ta with 8-mm thickness as an attainable compromise. Because 9-MV radiation is so penetrating and because nearly every primary interaction results in secondary photons and particles that can reach the detector, an MTF derived from an edge image contains many effects not present at lower energy. This measure of 9-MV imaging performance cannot be compared to similar measurements at lower energy or even 9-MV measurements done with a different object.

Ta slug—We have an existing Ta cylinder that is 24.7 mm in diameter and 20.6 mm long. For imagers at 450-kV tube potential and below, the length of this object is sufficient for it to be effectively opaque (attenuation $>10^5$). This object is present in some images at 9 MV, but we do not consider it opaque at this energy.

Nail CT Phantom—This is a CT phantom of steel nails, and steel and Al bolts arranged for easy interpretation of CT artifacts if alignment errors exist.

D-38 CT Test Object—Its main interest to this project is the larger features and the fact that it is made of dense material.

BTO—This is a high-opacity, axially-symmetric, British-made test object (BTO). Its main interest to this project is the simplicity of the geometry, high opacity (100 g/cm^2) and the fact that many labs in the US and UK are imaging this object.

W shell—This object is widely used in imaging applications.

Opaque Rod—This object is important to provide a means of estimating room return and detector scatter. For this purpose, it is placed between the source and detector so as to block direct primary radiation from the detector. As with many other aspects of x-ray imaging, this can be difficult when using a 9-MV spectrum. The rod is W in the form of a right circular cylinder with ~150-mm length. By making the diameter large, ~50 mm, we ensured that the region near the center of the rod x-ray shadow is nearly free from object scatter as well.

Experimental Results. We acquired a series of radiographic images with 6-m sdd and two different object-to-detector distances (odd), 1 and 0.5 m. Photographs of the experimental DR and CT set-up are shown in **Fig. 7**. For the Cu-step wedge, we also acquired data at 0-m (on the detector) and 0.2-m odds. The Cu-step wedge was positioned with the flat surface of the wedge towards the detector. For the Ta edge we acquired data at 0- and 1-m odds. Two data sets with the Ta edge in the vertical and horizontal directions were obtained for each distance to determine any difference in the detector response. The opaque rod, and Ta edge and slug radiographs were

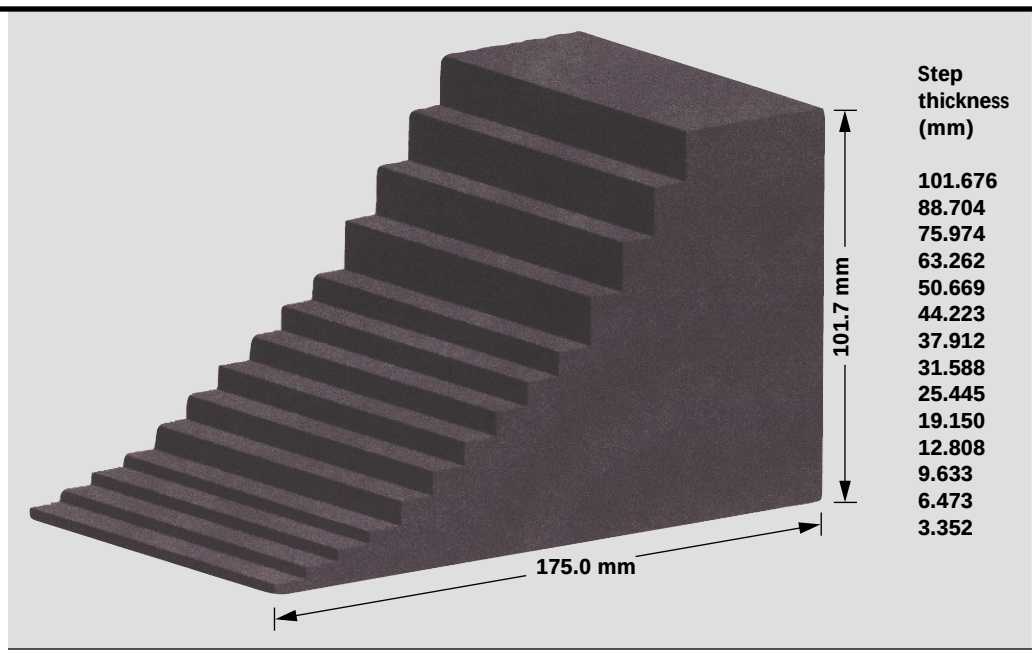

Figure 6. CAD drawing of the Cu-step wedge with as-built dimensions overall and for each step. An L-bracket was also fabricated of Al to support the Cu-step wedge and to minimize x-ray scatter (not shown).

(a)

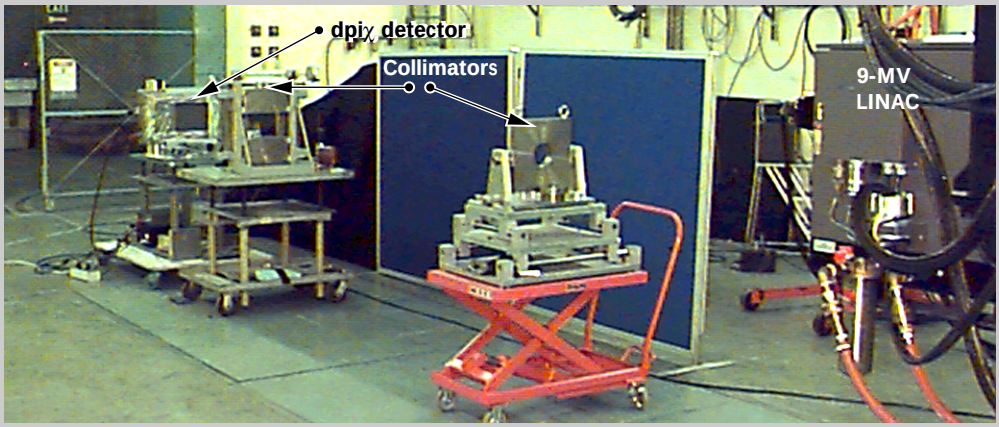

(b)

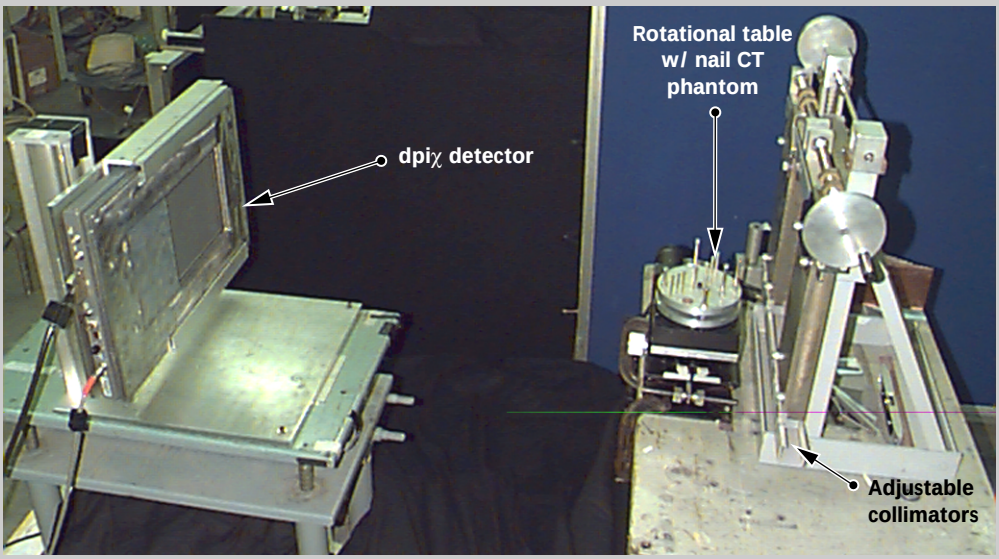

Figure 7.
(a) Photograph of the 9 MV LINAC and Min-R/dpiχ experimental set-up. Overall view of the setup. (b) Close up of the detector and rotational table with nail CT phantom.

(a) (b)

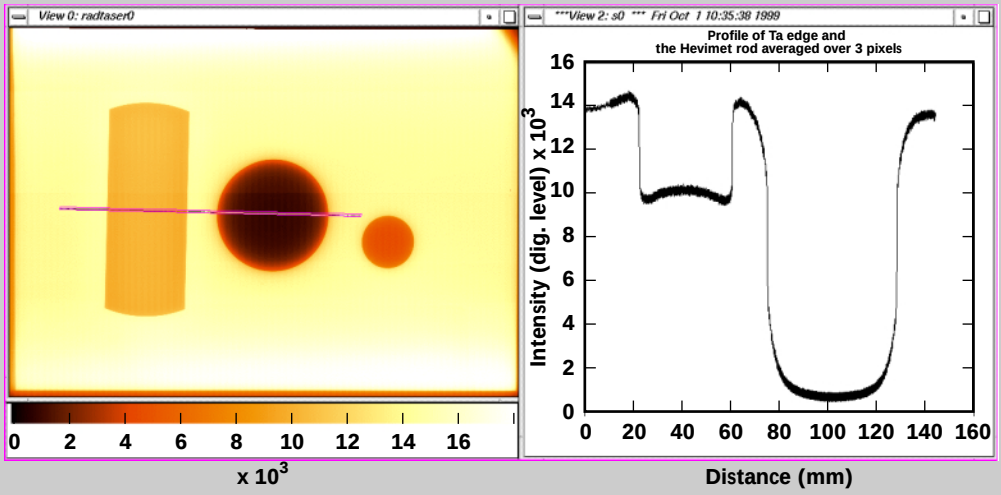

Figure 8.
(a) Representative experimental 9-MV radiograph of the Ta edge (left) and slug (right), and opaque rod (middle). These phantoms were located on the detector front surface supported by foam for an object-to-detector distance of 0 m.
(b) Profile of the Ta edge and opaque rod.

acquired at 0-m (see **Fig. 8**) and 1-m odd. We also acquired CT data of the nail CT phantom. For this data the center-axis-of-rotation of the CT system was located at a 1-m odd.

We used the opaque rod to understand scatter in the detector and to measure back shield albedo influence on the *dpiχ* imager. An important finding of this work[31] is that the observed signal in the shadow of the opaque rod is 8% of the unattenuated signal, even with no back shield albedo contribution. This work also establishes design guidance for shield design and placement.

Simulation and Experimental Results. Models of the test object's structure have been generated for the HADES ray-tracing simulation code. To validate these models a monoenergetic (4 MV) photon source and perfect detector were used to generate most of the simulated radiographs. Simulated and experimental radiographs for the nail CT phantom are shown in **Figs. 9** and **10**, respectively. **Figure 10** also shows representative experimental results at 9 MV of a convolution back-projection reconstructed image of the nail phantom. Simulated radiographs for different assemblies of the D38 CT test object are shown in **Fig. 11**. Simulated and experimental radiographs of the BTO are shown in **Figs. 12** and **13**, respectively. Some of the simulated radiographs were reconstructed into tomograms such as the BTO as shown in **Fig. 12**. HADES, COG, and experimental radiographs for the Cu-step wedge are shown in **Fig. 14**.

The simulated radiographic and tomographic images were compared with the original mechanical drawings for each of the test objects. This validates the complete simulation process of going from mechanical drawings through simulated radiographs to reconstructed tomograms. Now that we have agreed upon the experimental source (9 MV) and detector (Min-R/*dpiχ*) for the radiographic system more realistic calculations are being performed. Other effects, such as energy distribution of the source, finite source spot size, detector response, and scattered radiation, are being treated as well.

The energy distribution of the radiation source used by HADES can be read from a user-specified input file corresponding to the radiation source of interest. Radiation distributions corresponding to any particular accelerator are obtained from full-physics Monte Carlo simulations, using machine drawings and materials specifications supplied by the manufacturers (**Fig. 15**). The source spot is assumed to be Gaussian, and its effect is included either by blurring the simulated image or, as of this year, by directly tracing multiple rays from the

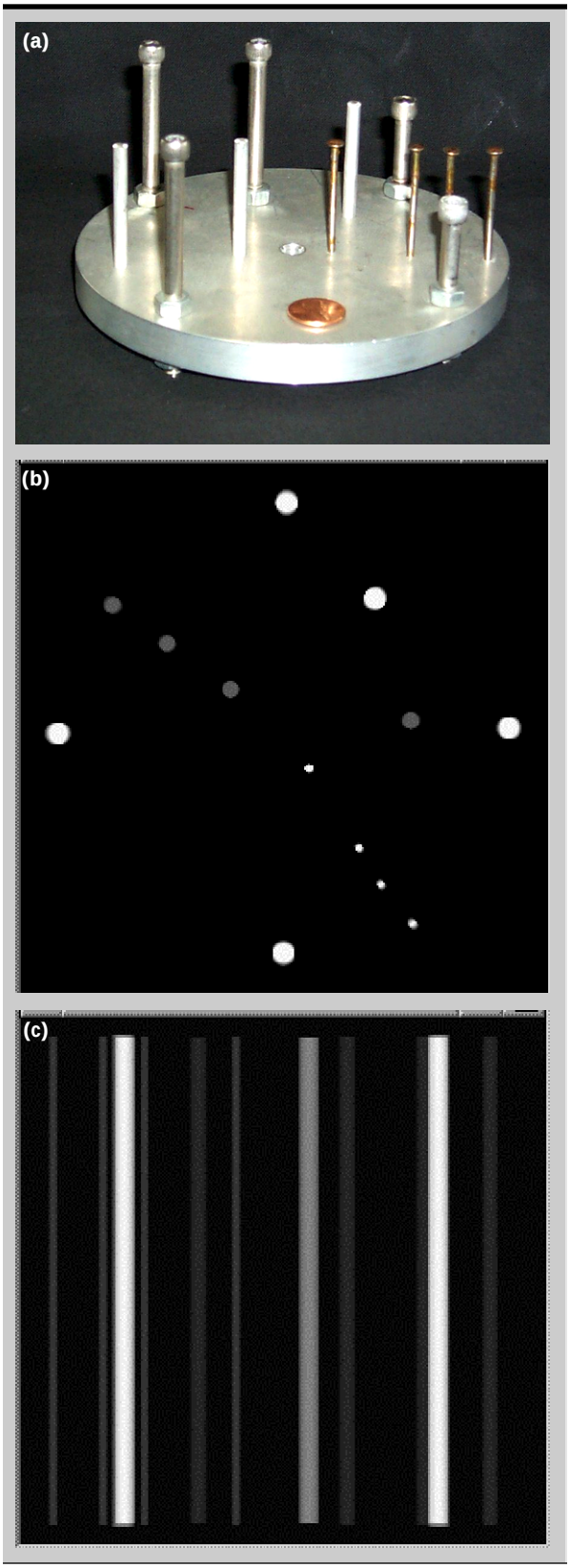

Figure 9. (a) Photograph of the nail CT phantom. Two HADES simulated monoenergetic 4-MV radiographic images [(b) top view and (c) side view] of the nail CT phantom.

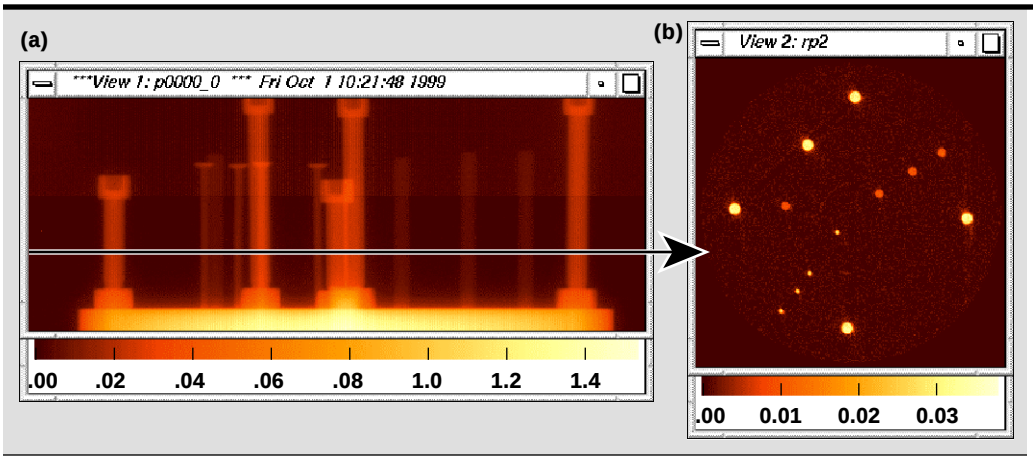

Figure 10. (a) Experimental 9 MV and Min-R/dpiχ radiographic image (units are ln Io/I) of the nail CT phantom. (b) CBP reconstructed experimental CT image of the phantom (units cm^{-1}).

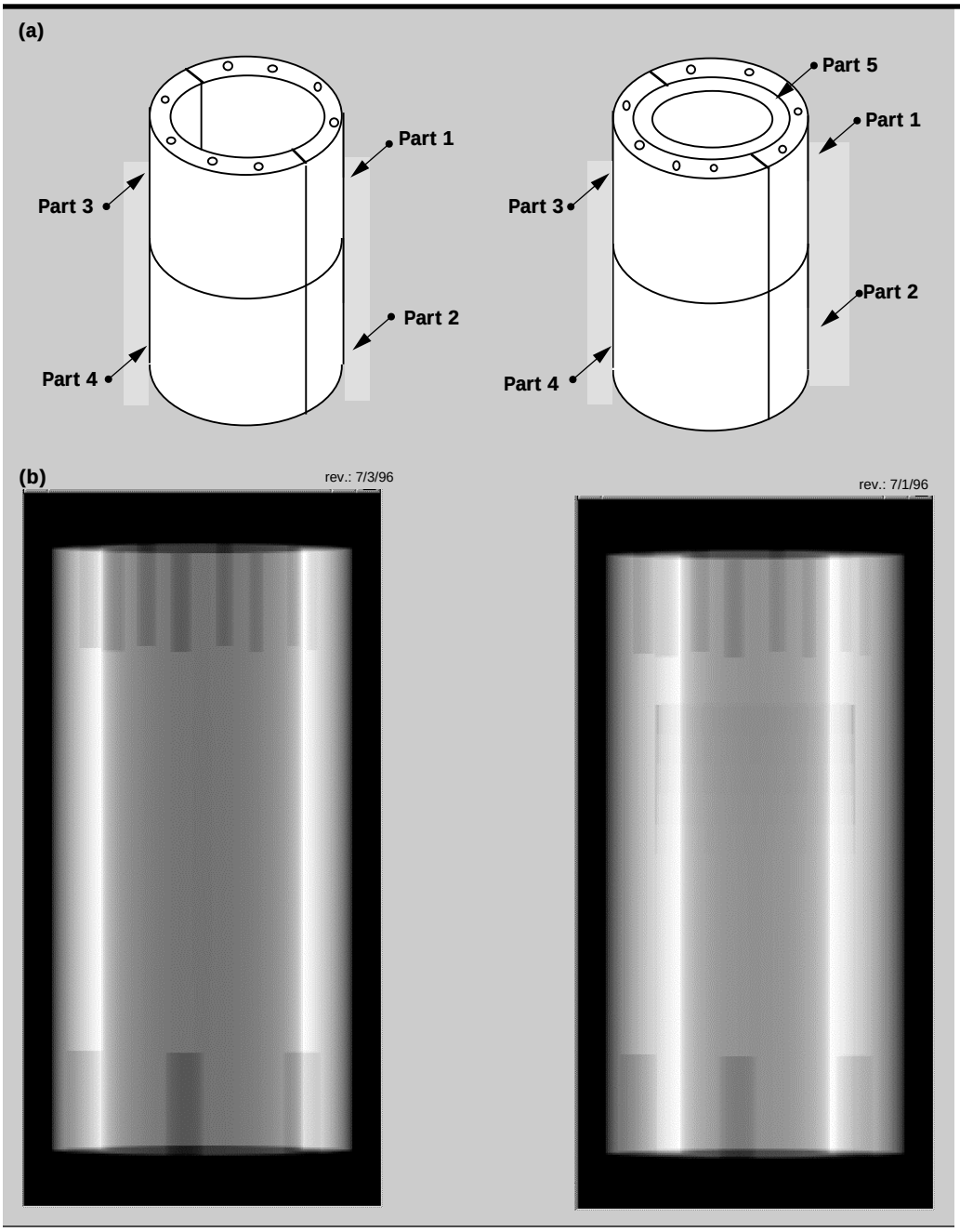

Figure 11. (a) Two assembly drawings of the D38 test object. (b) HADES simulated monoenergetic 4-MV radiographic image of its respective above drawing.

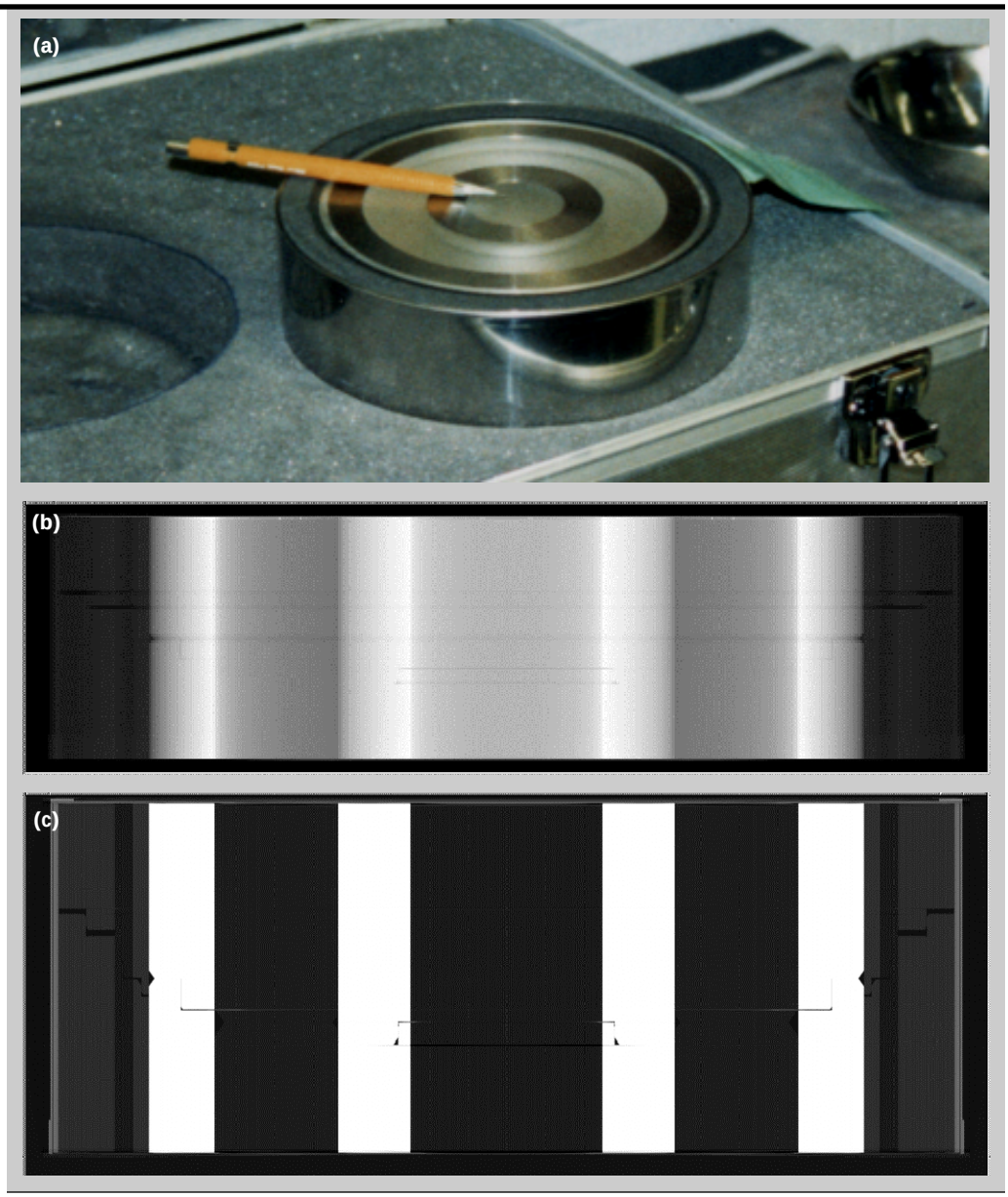

Figure 12.
(a) Photograph of the BTO. (b) HADES simulated monoenergetic 4-MV radiograph. (c) A representative reconstructed tomogram at the central vertical plane of the BTO.

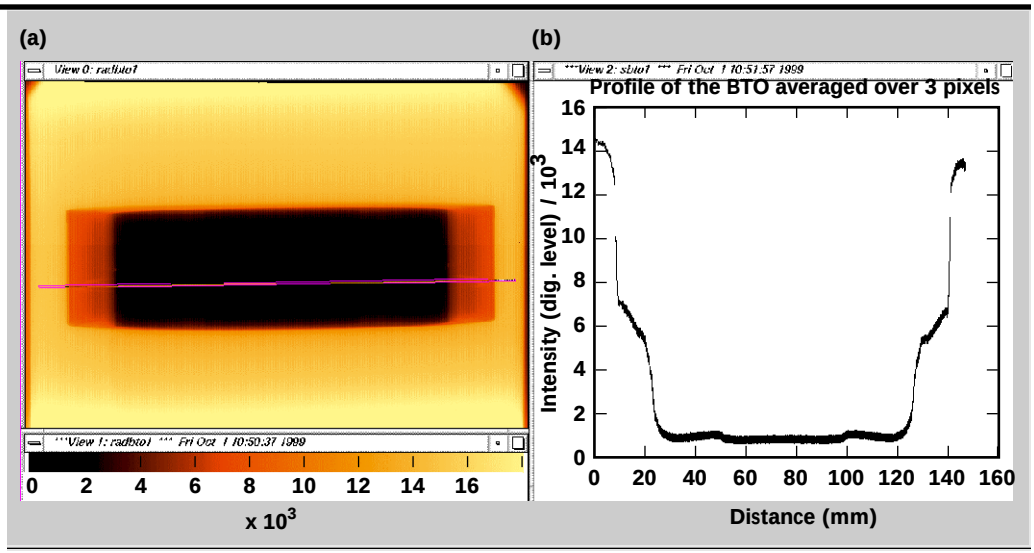

Figure 13.
(a) Representative 9 MV and Min-R/dpiχ experimental radiographic image (in digital detector level units) of the BTO. The grey scale was adjusted to enhance the outer portion of the BTO. (b) Profile from the line in the radiograph that reveals some of the internal details within the BTO.

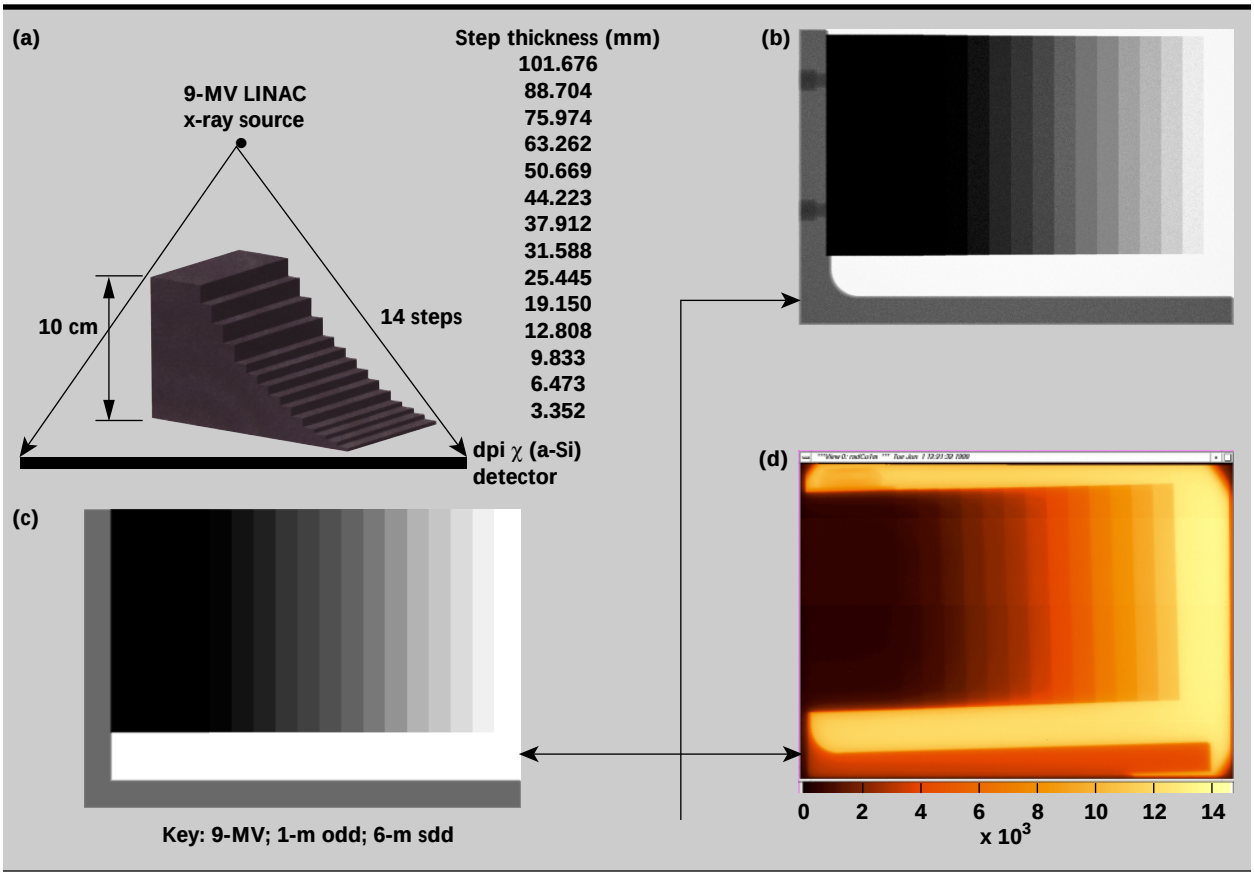

Figure 14. (a) Schematic showing the source, detector and Cu-step wedge geometry (not to scale). (b) Resultant COG Monte Carlo simulated radiographic image. (c) HADES simulated radiographic image. (d) Experimental radiographic image at 9 MV.

source distribution to the detector(s). The detector response, which previously was described as a Gaussian blur, has been enhanced to include energy-dependent blur as a user option.

A schematic of the Monte Carlo detector model is shown in **Fig. 16**. The point-spread function (PSF) of this detector model was obtained as a function of energy. These results have been added to the detector library of HADES.

In FY-99, we have been studying by simulation the scattered radiation component (or background) of several radiographically thick objects. Our experience in using full-physics Monte Carlo methods to radiographically model these objects, has led us to conclude that the scattered radiation in many cases, is slowly varying (see **Fig. 17**). We have modified HADES to read, if desired, user-specified data files describing radial variation of the scattered radiation level, as well as the average user-specified energy spectrum of the scattered radiation. The scattered radiation level does not have to be flat and the energy spectrum of the scattered radiation is not a scaled version of the input spectrum.

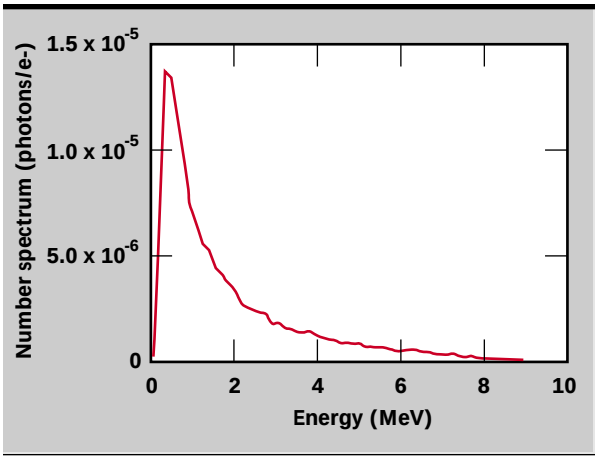

Figure 15. MCNP computed simulation of the Bremsstrahlung spectrum of the B239 VARIAN 3000 9-MV LINAC. This simulation was for the target and target holder. It did not include the mirror or other components.

Some aspects of the overall tomography problem are independent of the object being studied, for example, incident source distribution and detector response, may be pre-calculated with full-physics Monte Carlo codes and stored as user-specifiable

input files. Aspects of the overall tomography problem that depend on the object being studied (for example, the scattered radiation level), but do not depend strongly on the fine details of the object's structure, may also be included via user-specifiable files. These files may or may not be updated during the course of a reconstruction. Thus the experimental effects being added to HADES improve its overall realism and its radiographic simulation capability without compromising HADES speed.

We have used the Monte Carlo code COG to model the 9-MV electron-bremsstrahlung x-ray source and, thus far, three of the six test objects. Our initial approach has been to use a relatively simplistic (though still fairly accurate) Monte Carlo source model and a "boundary-crossing" imaging detector model (already incorporated into COG). These simulations are currently being run on the ASCI Blue-Pacific machine using between 80 and 160 CPUs per run. We are also writing a new imaging module for COG that will allow us to model the detailed response of the Min-R/*dpiχ* detector array (for example, electron energy deposition in the GdO_2S_2CH scintillation layer). This should lead to improved agreement with experimental radiographs and Ta-edge spatial resolution measurements (see **Fig. 18**).

Comparisons between Experiments and Simulations. The Ta-edge radiographs were used to determine the MTF for the Min-R/*dpiχ* detector array. This was determined by the edge-spread function method. This method requires a profile across the edge, the differential of this edge and then the Fourier transform is taken of the differentiated edge. The transform results are normalized to unity and only the positive frequencies are plotted. This is a convenient experimental procedure for characterizing the spatial response of an imaging system.

To be a pure measurement of the imager, the edge should be positioned close to the imager to effectively eliminate source size contributions. It should also be opaque to radiation and not be a source of scattered radiation. It must also be thin to facilitate alignment. While convenient, this method is prone to error and uncertainty regarding the low-frequency portion of the response. This information is carried in the subtle roll-off in signal at large distance from the edge. It is difficult to measure in the presence of noise and effects from non-uniform radiation field. In addition, when this type of measurement is done using 9-MV radiation, the edge is neither opaque nor non-scattering. When deriving an MTF in this manner, it is imperative that the line-out and its derivative extend over sufficient distance to capture the low frequency effects. The results will depend on the extent of the data. If the data do not sufficiently capture the low frequency content, then all the derived MTF for higher frequencies is incorrect.

We present MTFs derived from the Ta edge in **Fig. 18**. Note that for our work we orient the *dpiχ* detector with the long dimension of the panel horizontal. Much of what is indicated by these MTFs is understandable and reassuring.

First, the MTF is reduced when the Ta edge is 1 m from the panel (odd = 1 m). We expect this because the source penumbra projected onto the panel is about 400-μm full width at half maximum

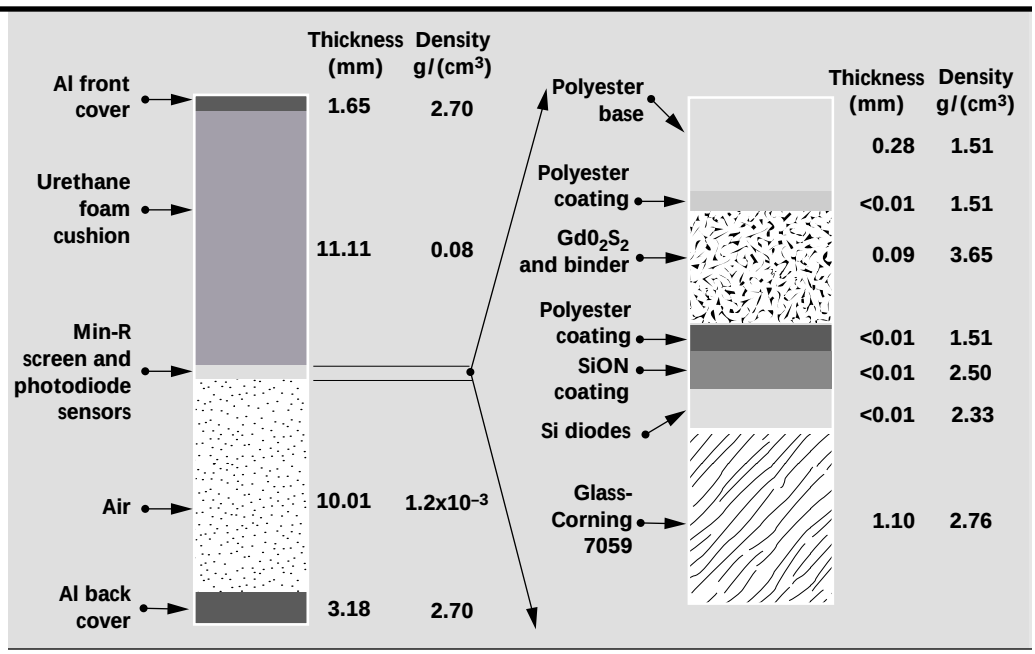

Figure 16. A schematic of the Min-R/dpiχ detector model used in our Monte Carlo calculations of the detector response function as a function of energy.

and this should cause the MTF to approach zero around 2 lp/mm.

Second, the MTF is slightly smoother but little different when we average more pixels. This is also as expected.

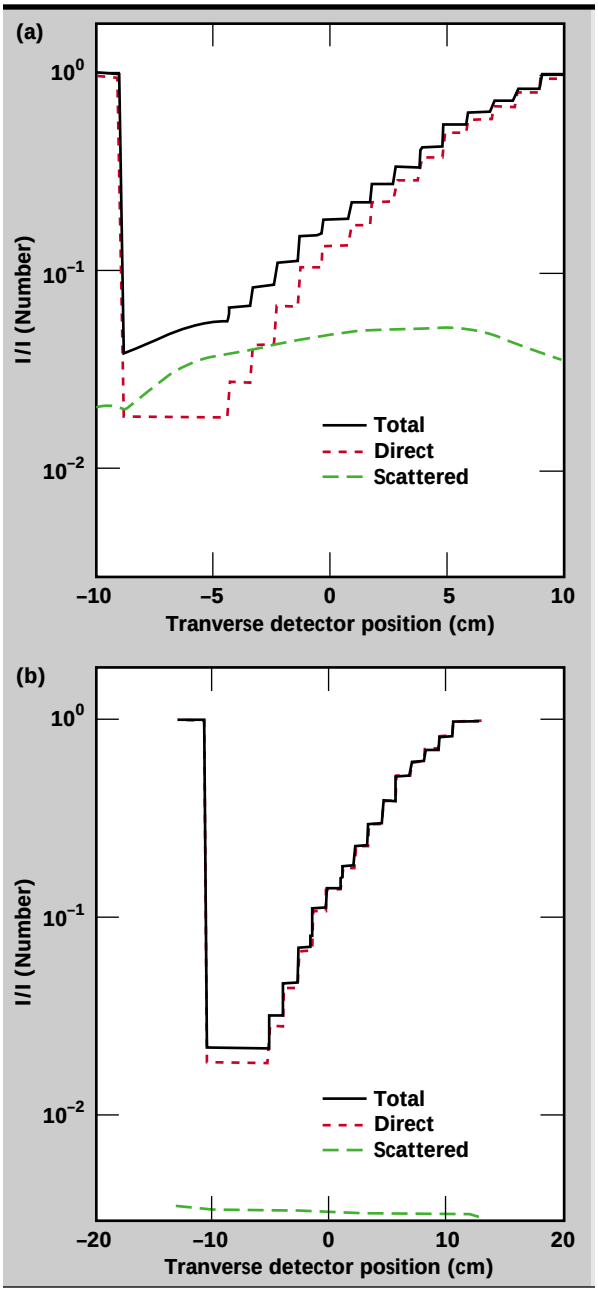

Figure 17. Line outs of a full-physics Monte Carlo simulated radiographic image of the Cu-step wedge. A 9-MV Bremsstrahlung source was used to generate the radiograph. (a) Cu-step wedge 20-cm from the detector. (b) Cu-step wedge positioned 1 m from the detector. This shows that we can estimate scatter from simulations of different experimental geometries. Note that the scattered radiation is slowly varying as compared to the object. Thus we believe that the scatter within HADES needs only to be updated periodically.

Third, no significant change is seen when comparing the intensity image (I) to the normalized image (I/I_o). This is the case, because we have attempted to

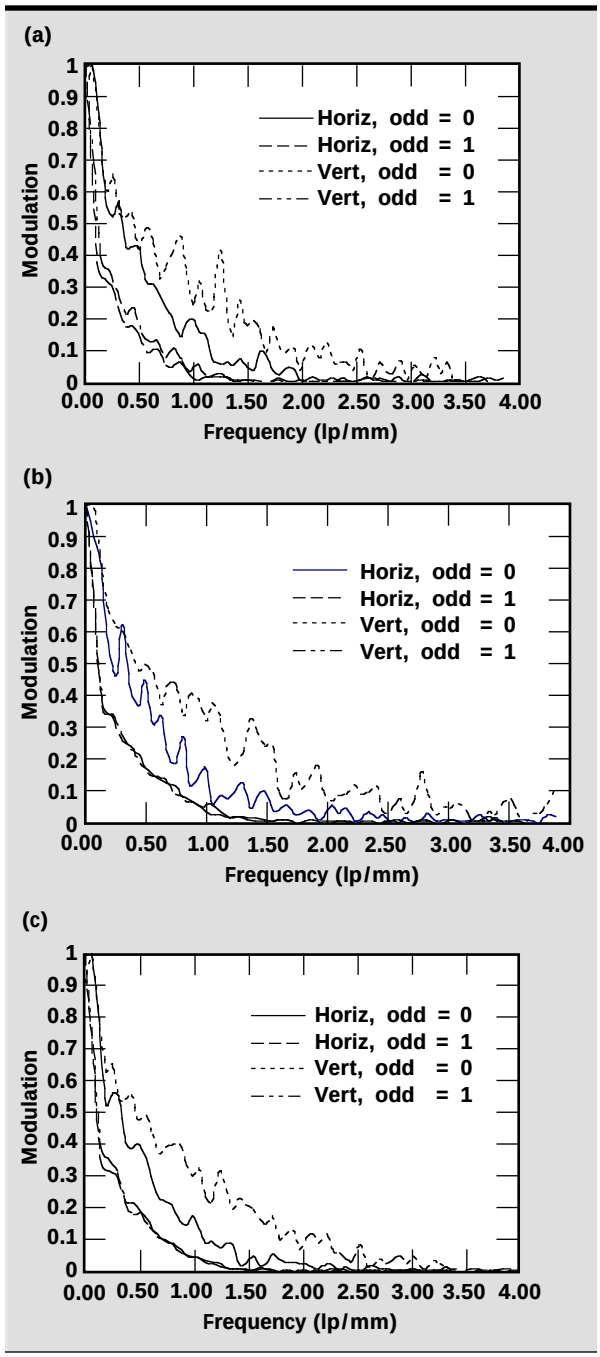

Figure 18. Experimentally determined MTF data of the Min-R/dpiχ detector at 9 MV determined from the Ta-edge radiographs. (a) MTF for the intensity, I, radiograph. The edge extracted was averaged over five pixels in width to reduce noise. (b) MTF for the I/Io radiograph. The edge was averaged over five pixels. (c) MTF for the intensity radiograph. The edge was averaged over ten pixels. The horizontal and vertical label refers to the orientation of the Ta edge. A profile was extracted normal to this edge to calculate the MTF.

linearize the detector response by calibration, and we do not expect large field-flatness effects.

However, there is one unexpected result depicted in **Fig. 18**. The MTF in the *dpiχ* detector is different in the two directions for odd = 0 m. This is probably not attributable to source asymmetry since it persists with the Ta edge in contact with the detector. It must be a property of our *dpiχ* detector when these data were acquired. We were experiencing poor detector performance in that we were getting high line-to-line noise in one direction in the detector. More work is required to understand these results.

Figures 17 through **21** show examples of our codes' abilities to predict artifacts that occur for a specific combination of photon source, experimental object, experimental configuration, and detector system. **Figure 17** shows MCNP-based estimates of the level of scattered radiation that is expected at the detector plane, as the odd is changed from 0.20 to 1.0 m. The calculations suggest that there should be a measurable decrease in the background level as the object approaches the source. This prediction is confirmed by the experimental results shown in **Fig. 19**. The data in **Fig. 19** have not been re-scaled to be distance at the object. It is encouraging that the experimental radiographic data of the Cu-step wedge also reveal that several steps are not observed when the wedge is placed on the detector, which is consistent with the simulation results given in **Fig. 17**.

A more quantitative comparison between simulation and experimental results is shown in **Fig. 20**. Our first HADES simulation results **(Fig. 20a)** do not match the experimental results. In this case the HADES simulation did not account for all of the blur due to the detector. Note that the simulated results show a sharp step function while the experimental data are more blurred. We modeled only the detector's physical pixel size of $127 \times 127\ \mu m^2$. As mentioned earlier we modeled and studied the Min - R/*dpiχ* detector PSF as a function of energy. Incorporation of the PSF into HADES simulations of the step wedge **(Fig. 20b)**begins to account for much of the distortion caused by the detection

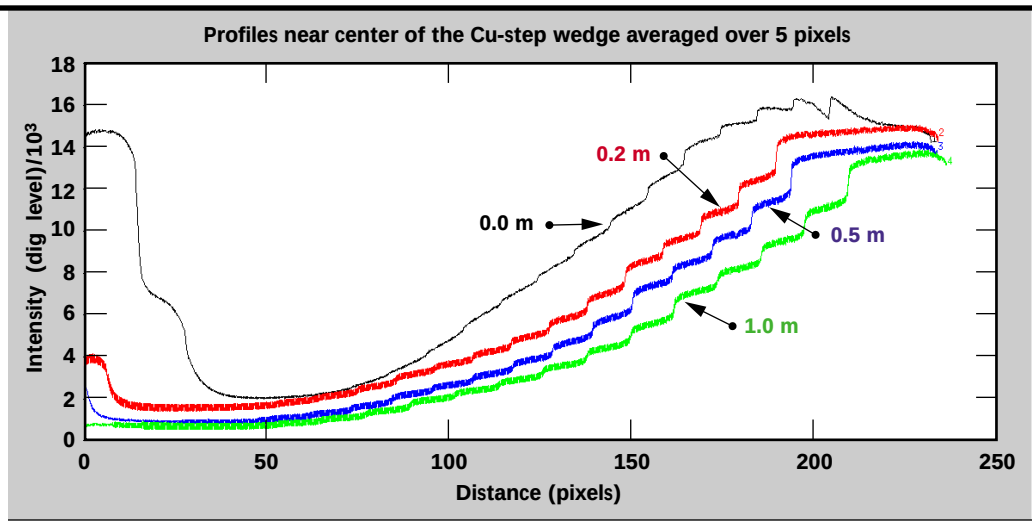

Figure 19. A horizontal attenuation profile from each of the Cu-step wedge experimental radiographs obtained at several distances from the detector, as labeled. It should be noted that the magnification of the object is increasing as the object gets closer to the x-ray source. This was not corrected for in the data shown.

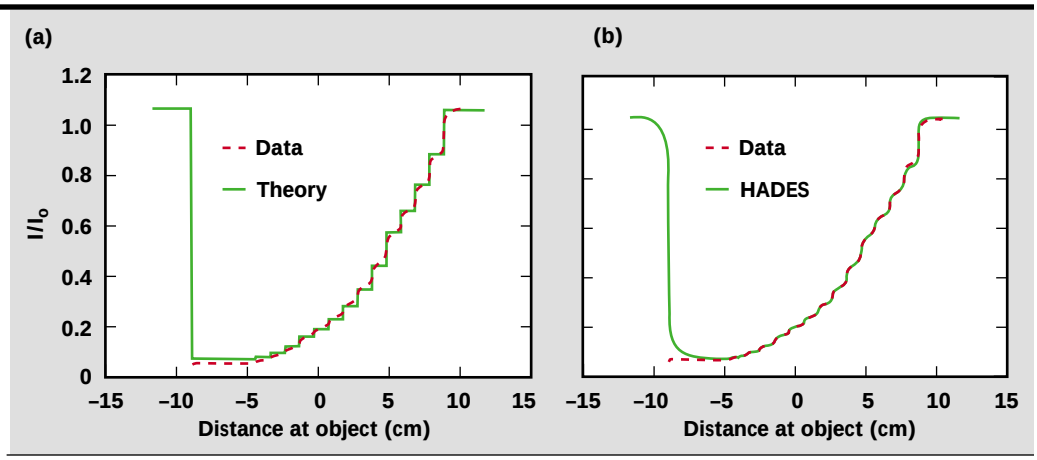

Figure 20. Comparison between HADES simulated results and experimental results for the Cu-step wedge 1 m from the detector. (a) HADES results with a 9-MV Bremsstrahlung source and a perfect detector. (b) HADES results with a 9-MV Bremsstrahlung source and a Monte Carlo determined detector response function.

system: the rounding of the steps is due to the long "tail" in the experimentally measured ESF of this detector. Note that the HADES simulated results in this case provide a much better match with the experimental data.

The ratio of the measured intensity to our HADES calculated intensity is shown in **Fig. 21**.

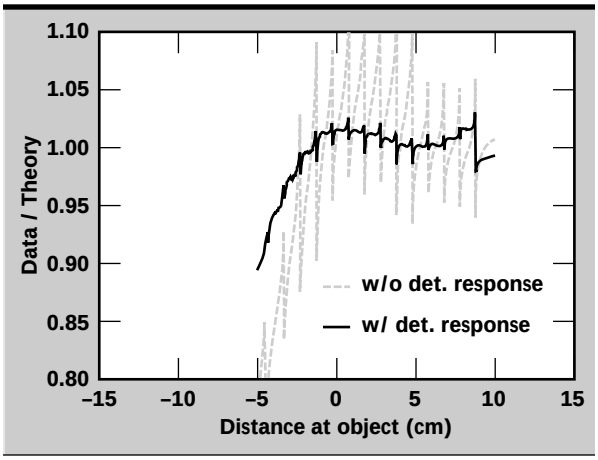

Figure 21. The ratio of the experimental data to HADES simulated data from Fig. 20 reveals that there are still some discrepancies that need to be further investigated.

There is a low-frequency error of a few percent, suggesting possibility of improving the assumed energy distribution of the photon source and/or the energy-dependent sensitivity of the detector model. There is also a high-frequency component, suggesting the need for an improved understanding of the blurring processes.

Image Reconstruction Algorithms. The reconstruction process associated with CCG can be described as follows. First an initial value for the desired image of the object is chosen. Then a forward projector model calculates the radiographs associated with this image. CCG then compares these calculated radiographs with the actual projections or radiographs and determines a better set of values for the image. The process is repeated until a satisfactory stopping point is reached. The ultimate goal of this part of the project is to create HADES-CCG, where HADES supplies the projectors and CCG performs the image reconstruction (see **Fig. 3**).

CCG has a number of stopping criteria built into the code. At this time these criteria do not seem to work with the cone-beam forward projection geometry. JCONE-CCG is being used to study how to determine when to stop the search during cone-beam

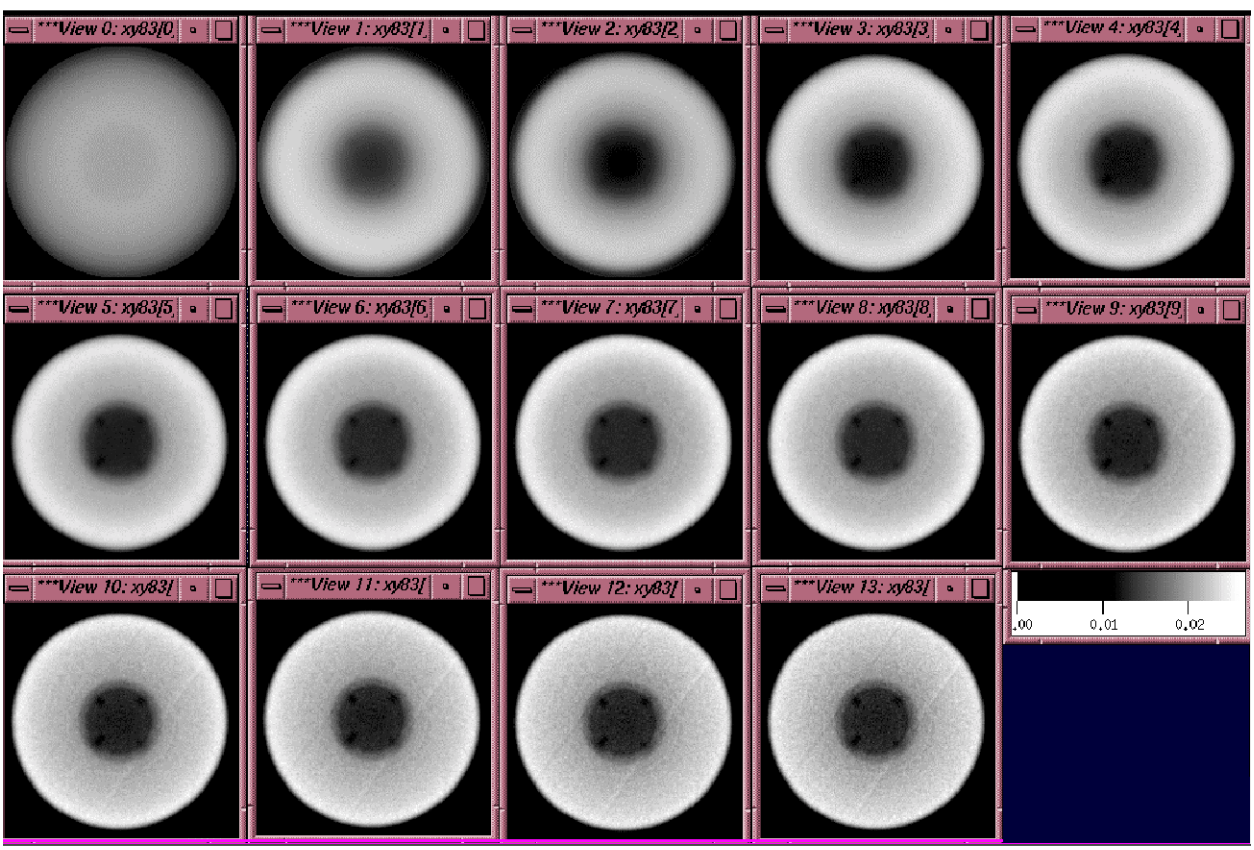

Figure 22. Successive iterations (from left to right, top to bottom) of JCONE-CCG for reconstruction of a single slice from high-energy neutron data of a test object consisting of nested cylinders of different materials (W/brass/polyethylene). The later iterations show interior details machined into the inner polyethylene cylinder.

image reconstruction. One effective stopping criterion involves plotting the norm of the residuals versus the norm of the solution.[32] The residual is the difference between the calculated and measured radiographs, $||\mathbf{B}\hat{\mathbf{o}} - \mathbf{p}||$. This method was used to analyze experimental high-energy neutron data of a test object consisting of nested cylinders of different materials (W/brass/polyethylene). The inner cylinder (polyethylene) featured a set of slots of different depths. **Figure 22** shows the same cross-sectional slice of the object for each iteration obtained by JCONE-CCG. Note that the slots in the polyethylene are clearly visible in the later iterations.

The plot of the norm of the residual versus the norm of the solution for each iteration is shown in **Fig. 23**. The norm of the residual decreases as the solution approaches the correct value. The norm of the solution provides a measure of the change of the solution from one iteration to the next. As seen in **Fig. 23**, the curve shows an initial steep drop as the image rapidly approaches the best solution. After a point the curve begins to level off, at this time the search begins to work on noise. This can lead to undesirable results. With respect to **Fig. 22**, it can be seen that before iteration 5 (View 4) some of the object features do not appear as clearly as after iteration 5. After iteration 8 it appears that the object becomes noisier and eventually two parallel lines appear across the object beginning around iteration 9 (View 8).

These lines are not a real effect within this data as we have observed that these two lines also show up in the iterations of other data sets. Analysis of **Fig. 23** reveals that the norm of the residuals begins to level off around iteration 5 and there are only small changes after iteration 8. We are studying how to use this and other methods to determine the optimum number of iterations to produce the best results automatically.

RECON/CCG and HADES are both large complicated codes, created and maintained by separate organizations. Since the interactions between the two codes is limited and clearly defined, it has been decided to run the codes separately and exchange information between them using shared memory.

This year we concentrated on three issues: reducing artifacts, mitigating the effects of beam hardening, and blur removal. We present an example of artifact removal. Streak and ring artifacts are very common in tomographic reconstructions. Streak artifacts result when a detector has been corrupted in a single projection: the usual cause is a hit by extraneous radiation. Ring artifacts result when a detector has been uniformly corrupted over all projections: typical causes are gain misadjustments and electronics problems in which the detector is either "cold" (zero) or "hot" (saturated).

We present a simulated example. The true unknown is shown in **Fig. 24a**, and the corrupted projection data in the form of a sinogram is given in **Fig. 24b**. A sinogram is a 2-D image created by displaying all the detector outputs at one projection angle along a horizontal line and stacking these lines according to projection angle. Radiation hits were simulated by Gaussian mixture noise with probability 0.99 that the noise at a detector is Gaussian with standard deviation σ, and with probability 0.01 that it is Gaussian with standard deviation 100 σ. Consequently, there is a hit 1% of the time. These outliers are obvious as speckles in **Fig. 24b**. The projection data were further corrupted by setting one detector output to zero for all projections, the result is the vertical line in the sinogram. The maximum likelihood estimation method with the usual assumption that the noise on the observed data is Gaussian with constant variance leads to the usual least-squares fit between observed data and modeled data generated from the current estimate of the unknown image. Least-squares is the method commonly used in iterative tomography algorithms.

Unfortunately, the squared error function is highly sensitive to outliers. This is demonstrated in the image reconstructed using least squares shown in **Fig. 24c**. Radiation hits caused the streak artifacts in **Fig. 24c**, and the cold detector produced the ring artifact. We used robust statistical methods to mitigate the effects of the outliers.

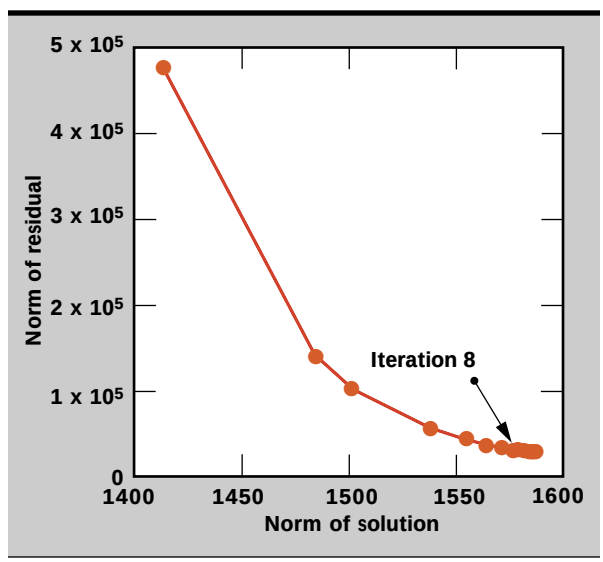

Figure 23. Plot of the norm of the residual versus the norm of the solution as a function of iteration for the neutron data shown in Fig. 22. This curve is used to determine the iteration that contains the best recovery of the object with the least noise.

First, as described by **Eq. 7**, we modified the squared error function so that it transitioned from a squared penalty for small mismatches between observed data and modeled data to a linear penalty for large mismatches, thereby making the fitting function much less sensitive to outliers. The result is shown in **Fig. 24d**: the streak artifacts have disappeared, but an attenuated ring artifact remains. To improve the reconstruction further, we added another transition from the linear penalty for large mismatches to a saturated penalty for very large mismatches. This error function is shown in **Eq. 8**. The result of using **Eq. 8** is shown in **Fig. 24e** where the ring artifact has almost completely disappeared. To our knowledge this has been the first application of robust statistical techniques to tomography. This was made possible by the effectiveness of CCG in minimizing the modified cost functions. The results for our simulated example were dramatic.

There are many real problems at LLNL and elsewhere that are replete with streak and ring artifacts. Our initial investigation into using this method to reduce these artifacts was only partially successful. Work continues in this area.

Other work on artifacts due to outliers, beam hardening, scatter and blurring will continue for the rest of the year and through FY-00. We are currently extending our robust algorithms to Poisson data problems that occur in photon-starved x-ray tomography, neutron and proton tomography, and emission tomography.

In addition, we have developed algorithms that model selective attenuation at different spectral energies. These algorithms model beam hardening directly in the reconstruction process, rather than using a polynomial correction for this in the sinogram before image reconstruction. These algorithms apply to both the single material and the multiple material problems.

Finally, we have developed an efficient deconvolution algorithm to deal with the blurring problem, and we are in the process of incorporating it into our tomography algorithms.

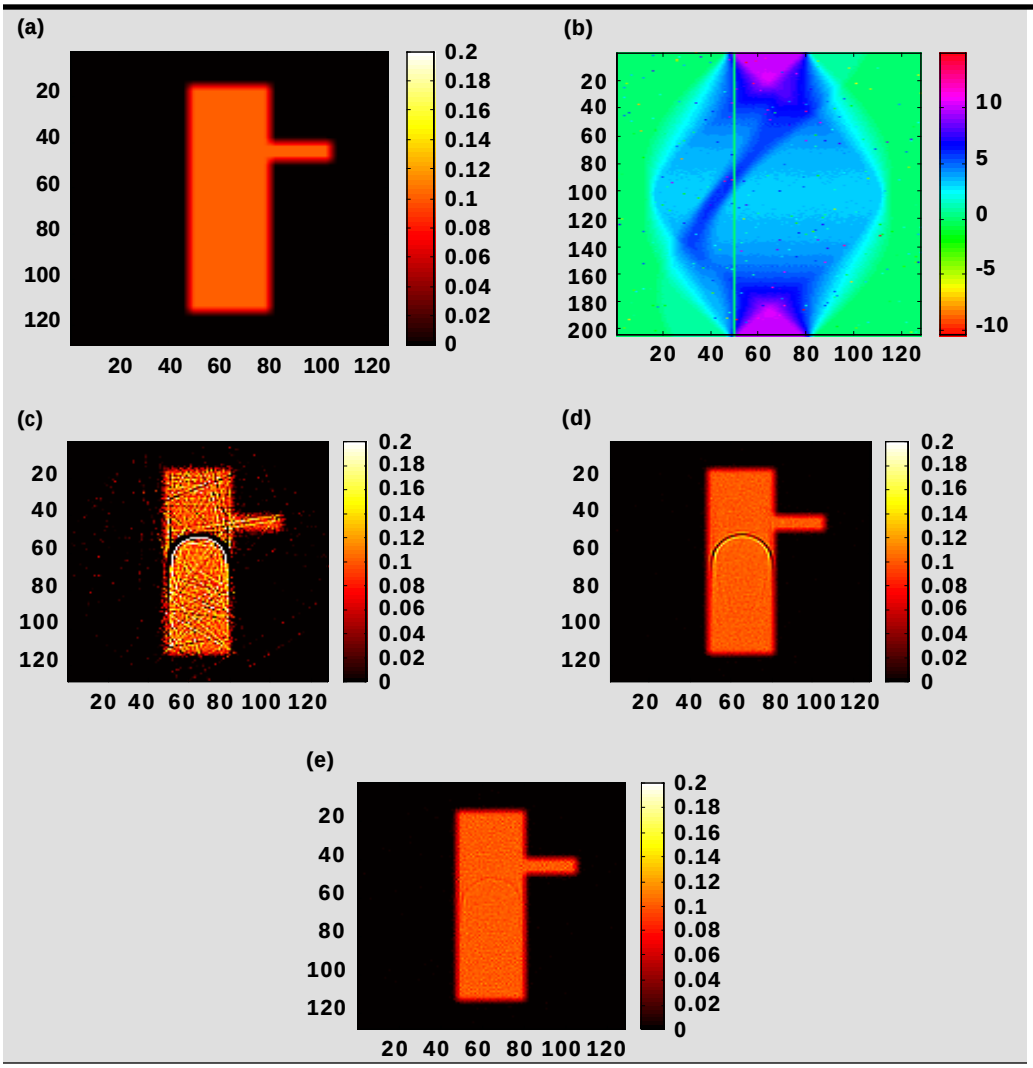

Figure 24. Simulation results for CT artifact reduction. (a) Original true image. (b) Sinogram with outliers—bad single pixels and a bad detector that creates the column of bad pixels. Reconstructed image with (c) least squares penalty—a typical CT method, (d) squared to linear penalty, and (e) squared to linear to a saturated penalty statistical method.

Summary

Preliminary scattering models have been incorporated into HADES and this code has been transferred to LLNL programs. HADES is being used to simulate a Mg tensile bar specimen.

We are using an a-Si array with a Min-R scintillator at 9 MV for radiographic and tomographic imaging. The spatial response for this system has been measured. Monte Carlo simulations were used to determine the energy spectrum for the source and detector spatial response as a function of energy.

We have acquired experimental radiographs and HADES simulations for all test objects, and detailed COG simulations for some of them. We have begun validation of the radiation models by comparison with experimental radiographs.

Incorporation of both the source spectral information and detector PSF were required to improve HADES simulated radiographs to within 5% of the measured radiographs. These results are encouraging however, we need better agreement than this to get tomographic image reconstructions with 1% accuracy.

We have determined a method to merge the CCG and HADES codes into a new image reconstruction code.

Future Work

We will demonstrate accurate and fast radiographic simulation tools by further investigation and refinement of our Monte Carlo and HADES models to improve the agreement with the measured radiographic results. We will complete the designs and fabrication of phantoms such as an opaque test object. Experimental radiographs of the test objects will be acquired as well as more emphasis placed on CT projection data. The merging of CCG and HADES will be completed and several performance tests with simulated and experimental CT data will be studied.

We need to demonstrate that our methods to reduce CT artifacts in simulated data work as well with experimental data. New methods will be developed to reconstruct images of objects with high-Z/high-density (opaque) components, which compromise traditional CT algorithms.

Acknowledgments

The authors would like to thank D. Rikard, E. Updike, K. Morales, A. Guerrero and D. Schneberk for acquiring and processing the DR data; R. Perry for helping process the Ta-edge DRs to generate edge response and MTFs; A. Waters for providing the Mg radiographic and tomographic data; and D. Schneberk for processing and reconstructing the nail phantom data.

References

1. A. C. Kak and M. Slaney (1987), "Principles of computerized tomographic imaging," IEEE Press, New York, New York.

2. C. J. Leliveld, J. G. Maas, V. R. Bom, and C. W. E. van Eijk (1994), "The effects of detected scattered radiation and beam hardening in x-ray computerized tomographic imaging of industrial objects," *Proc. of the Int. Symp. on Computerized Tomography for Industrial Applications*, Berlin, Germany, June 8–10.

3. D. J. Schneberk, S. G. Azevedo, H. E. Martz, and M. F. Skeate (1990), "Sources of error in industrial tomographic reconstructions," *Mat. Eval.*, Vol. **48**, No. 609.

4. F. Dietrich and J. Hall (1996), "Detector concept for neutron tomography in the 10–15 MeV energy range," Lawrence Livermore National Laboratory, Livermore, California (UCRL-ID-123490).

5. F. Dietrich, J. Hall, and C. Logan (1997), "Conceptual design for a neutron imaging system for thick target analysis operating in the 10–15 MeV energy range," J. Duggan and I. Morgan (eds.), *Application of Accelerators in Research and Industry* (AIP CP392), AIP Press, New York, New York, pp. 837–840.

6. J. Hall, F. Dietrich, C. Logan, and G. Schmid (1999), "Development of high-energy neutron imaging for use in NDE applications," to be published in *Proc. of SPIE Conference*, Denver, Colorado, July.

7. G. Kowalski (1978), "Suppression of ring artifacts in CT fan-beam scanners," *IEEE Trans. Nucl. Sci.*, Vol. **NS25**, No. 5, pp. 1111–1116.

8. M. B. Aufderheide, D. Slone, and A. Schach von Wittenau (1999), "HADES: A code for radiographic simulation," Lawrence Livermore National Laboratory, Livermore, California (UCRL-CODE-99035).

9. T. Wilcox and E. Lent (1993), "COG - a particle transport code designed to solve the Boltzman equation for deep-penetration (shielding) problems," Vol. **1** Users Manual, Lawrence Livermore National Laboratory, Livermore, California (M-221-1); see also R. Buck and E. Lent (1993), "COG: a new, high-resolution code for modeling radiation transport," LLNL Energy and Technology Review (June); additional information on COG may be obtained via the Web at URL http://www-phys.llnl.gov/N_Div/COG/.

10. J.F. Briesmeister (1997), "MCNP—a general Monte Carlo N-particle transport code," Technical Report LA-12625-M, Los Alamos National Laboratory, Los Alamos, New Mexico.

11. G. P. Roberson, D. J. Schneberk, J. J. Haskins, C. M. Logan, H. E. Martz, D. E. Perkins, and D. R. Rikard (1998), "Improving computed tomography design and operation using simulation tools," Lawrence Livermore National Laboratory, Livermore, California, *Engineering Research, Development and Technology* (UCRL-53868-97), January.

12. D. L. Weirup, H. E. Martz, and D. J. Schneberk (1993), "New production reactor target particle characterization by computer simulation of computed tomography systems," Lawrence Livermore National Laboratory, Livermore, California (UCRL-UR-114836), August.

13. J. Hall (1996), "Monte Carlo modeling of neutron and gamma-ray imaging systems," *Neutrons in Research and Industry, SPIE*, Vol. **2867**, No. 465, Lawrence Livermore National Laboratory, Livermore, California (UCRL-JC-122830).

14. R. Buck and J. Hall (1999), "Applications of the COG multiparticle Monte Carlo transport code to simulated imaging of complex objects," to be published in *Proc. of SPIE Conference*, Denver, Colorado, July.

15. D. M. Goodman, E. M. Johansson, and T. W. Lawrence (1993), "On applying the conjugate gradient algorithm to image processing problems," Ch. 11 in *Multivariate Analysis: Future Directions*, C. R. Rao, ed., Elsevier Science Publishers.

16. H. W. VanTrees (1968), "Detection estimation and modulation theory," John C. Wiley and Sons, New York, New York.

17. H. Stark (1987), "Image recovery: theory and application," Orlando Academic Press.

18. L. Kaufman (1993), "Maximum likelihood, least squares and penalized least squares for PET," *IEEE Trans. Med. Imaging*, Vol. **12**, No. 2.

19. D. M. Goodman, T. W. Lawrence, E. M. Johansson, and J. P. Fitch (1993), "Bispectral speckle interferometry to reconstruct extended objects from turbulence-degraded telescope images," Ch. 13 in *Handbook of Statistics, Vol. 10: Signal Processing and its Applications*, N. K. Bose and C. R. Rao, eds., North Holland.

20. R. H. Byrd, J. Nocedal, and R. B. Schnabel (1994), "Representations of quasi-Newton matrices and their use in limited memory methods," *Math. Prog.*, Vol. **63**, No. 2, January.

21. D. M. Goodman (1997), "Maximum likelihood estimation with Poisson (counting) statistics for waste drum inspection," Lawrence Livermore National Laboratory, Livermore, California (UCRL-ID-127361), May.

22. P. J. Huber (1981), "Robust Statistics," John C. Wiley and Sons, New York, New York.

23. P. McCullagh and J. A. Nelder (1989), "Generalized Linear Models," 2nd Ed., Chapman and Hall, London.

24. F. Natterer (1986), "The Mathematics of Computerized Tomography," John C. Wiley and Sons, New York, New York.

25. H. E. Martz, G. P. Roberson, D. C. Camp, D. J. Decman, and J. A. Jackson (1998), "Active and passive computed tomography mixed waste focus area final report," Lawrence Livermore National Laboratory, Livermore, California (UCRL-ID-131695), November.

26. R. T. Bernardi (1997), "Field test results for radioactive waste drum characterization with waste inspection tomography (WIT)," presented at the *5th Nondestructive Assay and Nondestructive Examination Waste Characterization Conference*, Salt Lake City, Utah, January 14–16, INEL CONF-970126, pp. 107–115.

27. R. T. Bernardi and H. E. Martz, Jr. (1995), "Nuclear waste drum characterization with 2 MeV x-ray and gamma-ray tomography," *Proc. of the SPIE's 1995 International Symposium on Optical Science, Engineering, and Instrumentation*, Vol. **2519**, San Diego, California, July 13–14.

28. A. M. Waters, H. Martz, K. Dolan, M. Horstemeyer, D. Rikard, and R. Green (1999), "Characterization of damage evolution in an AM60 magnesium alloy by computed tomography," R. E. Green, Jr., ed., *Proc. of Nondestructive Characterization of Materials™*, Sydney, Australia, June 28–July 2; pp. 616–621.

29. R. L. Weisfield, M. A. Hartney, R.A. Street, and R. B. Apte (1998), "New amorphous-silicon image sensor for x-ray diagnostic medical imaging applications,"*SPIE Medical Imaging, Physics of Medical Imaging*, Vol. **3336**, pp. 444–452.

30. K. Dolan, C. Logan, J. Haskins, D. Rikard, and D. Schneberk (1999), "Evaluation of an amorphous silicon array for industrial x-ray imaging," *Engineering Research Development and Technology* (UCRL-53868-99), Lawrence Livermore National Laboratory, Livermore, California, January.

31. C. M. Logan and A. E. Schach von Wittenau (1999), "Effects of back shield albedo on imagery with a dpiχ Flashscan 20 using a 9-MV Bremsstrahlung spectrum: measurements and Monte Carlo simulations," submitted to *Materials Evaluation*, Lawrence Livermore National Laboratory, Livermore, California (UCRL-JC-136055).

32. C. L. Lawson and R. J. Hanson (1974), "Solving Least Squares Problems," Prentice-Hall, Inc., Englewood Cliffs, New Jersey.

Ultra-Wideband Phased Array

Rexford M. Morey
Laser Engineering Division
Electronics Engineering

We have explored the unique characteristics of ultra-wideband phased arrays. We performed proof-of-principle experiments and calculated radiation patterns as a function of number of elements and element spacing for a linear and a planar array.

Introduction

The Micropower Impulse Radar (MIR) program at Lawrence Livermore National Laboratory (LLNL) has led to many successful demonstrations of ultra-wideband (UWB) radar, such as concrete bridge deck inspection (HERMES) and plastic mine detection (LandMark). These applications use a single transmit/receive unit or an array of transmit/receive units, which essentially operate independently of each other and not in a phased array configuration. With the low power available from MIR transmitters, signal-to-noise ratios limit the useful radar range of single-channel MIR implementations. Target detectability is a function of power on the target. To increase power on the target, an array of MIR transmitter/antenna units can be time-triggered to transmit as a time-domain UWB phased array.

UWB phased arrays have several unique characteristics that are not achievable with narrow-band phased arrays. We have explored several of these unique characteristics. In contrast to narrow-band phased arrays, UWB phased array elements can be sparse and randomly spaced. Also beam-width and side lobe level can be independently controlled. Therefore, there are several significant reasons to investigate UWB time-domain phased arrays, including extended radar range, deeper penetration into solid materials, side lobe level versus radiated beam-width, and beam steering.

Important applications of UWB phased arrays include characterizing deep underground structures, monitoring fluids and fluid flow in the earth for environmental restoration, detailed imaging of distress in concrete infrastructures, and vehicle control in subway systems (such as the San Francisco transit system, BART) and the Automated Highway System (for example, intelligent cruise control).

This report presents the initial steps of a new program to develop a core technology in high-power arrays for 3-D image formation and visualization in dense media such as the subsurface of the earth. The program is built on the extensive body of work at LLNL in geophysics,[1–4] MIR technology,[5] ground-penetrating radar (GPR) imaging,[6–8] and laboratory measurements of electromagnetic (EM) properties of materials.[9]

To determine the utility of high-power UWB arrays, proof-of-principle experiments and array modeling were performed. These experiments required assembling a time-domain phased array using MIR technology. The proof-of-principle experiments included assembling and testing a two-element, a four-element, and an eight-element transmitting array. The model studies included calculating the radiation patterns of arrays of UWB transmitters as a function of number of elements and element spacing for a linear array and a planar array. Also radiation patterns were calculated when beam steering is invoked.

Applications of high-power arrays include characterizing underground facilities (UGFs), battle-damage assessment of targeted UGFs, detection and mapping of unexploded ordnance (UXO), and geophysical surveys, such as earthquake assessment and monitoring fluid flow. The deployment of a sparse multi-element UWB array, which includes multiple time-synchronized transmitters, has not been done before.

Past UWB and GPR research has included development of single-channel radar systems and data processing methods for locating hazardous waste, profiling lake bottoms, determining characteristics of geological interfaces, and evaluating civil structures and materials such as concrete.[10–13] The multi-element UWB system signal-to-noise (SNR) will

increase over a single-channel UWB system by using an array of time-synchronized UWB transmitters to put more energy on a subsurface volume element (voxel).

Progress

Recent advances in diffraction tomography,[14] in seismic exploration,[15] and in acoustical diagnostic imaging[16] have come from using multiple transmitting and/or receiving elements which look at the same voxel from a variety of angles. In the future we propose using multiple transmitters and multiple receivers in large time-domain phased arrays. Simultaneous triggering of the multiple transmitters increases radar range by putting more power on the target, while the multiple receivers collect more of the reflected energy.

Modeling

A typical UWB signal can be characterized as single cycle of a sine wave called a monocycle. A Mathcad program was developed to calculate the radiation pattern from various array configurations transmitting UWB monocycle signals.

Figure 1 is an example of the time-space radiation pattern for a nine-element linear array. If the monocycle pulse-width is 1 ns, then the element spacing is about 1 ft and the array length is 8 ft. The radiation pattern is created from the superposition of the nine transmitter pulses synchronized to arrive on boresight (0°) at the same time. If the observer is at +90°, then the signal from the nearest transmitter arrives first, followed by a sequence of pulses from each of the other transmitters, forming the "side lobes" of the array radiation pattern.

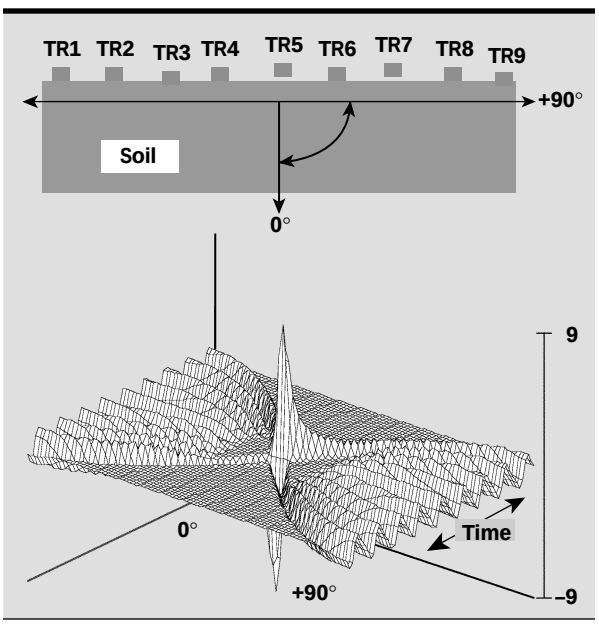

Figure 1. Time-space space beam pattern of a linear array of nine elements with element spacing equal to one pulse width.

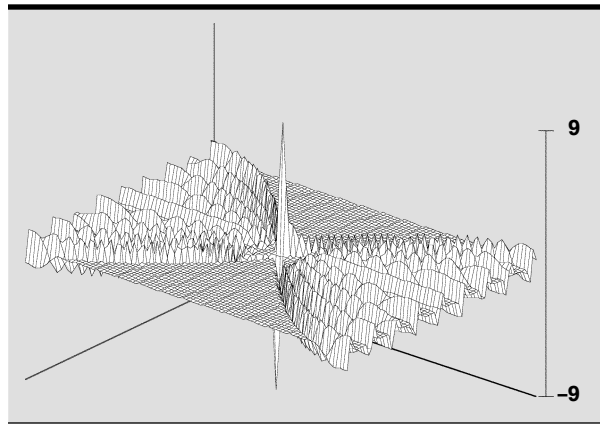

Figure 2. Time-space radiation pattern of a nine-element linear UWB array with element spacing equal to two pulse widths.

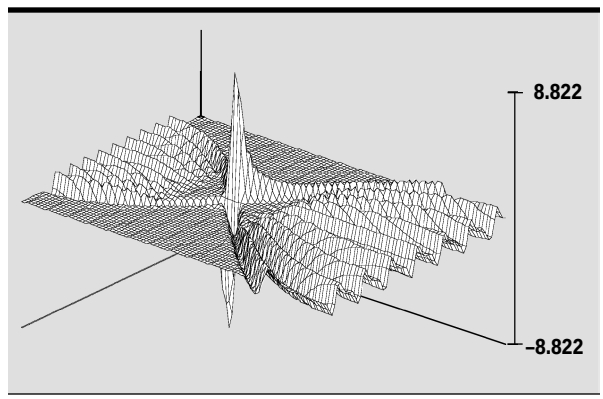

Figure 3. Time-space radiation pattern with the main beam steered off boresight by 20°.

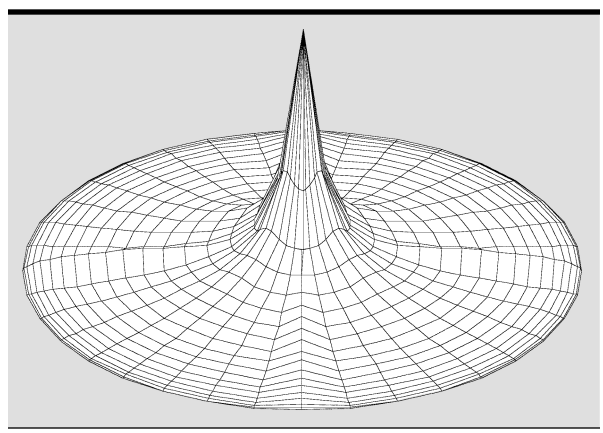

Figure 4. Time-space radiation pattern for a 9-×-9-element planar array with a one-pulse-width element spacing.

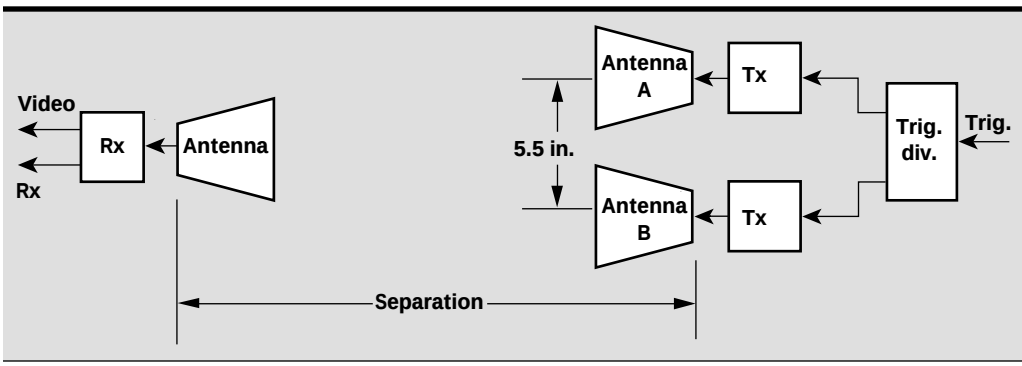

Figure 5. Diagram of two-transmitter measurement setup.

Figure 2 represents the calculated radiation pattern when the element spacing is two pulse-widths, doubling the array length and thus narrowing the 3-dB width of the main beam. The side-lobe level is the same as in **Fig. 1**, thus we have independent control of main-beam characteristics and side-lobe level, a property of UWB arrays that is not available with conventional narrow-band arrays.

An example of beam steering is shown in **Fig. 3** for the same nine-element linear array. The width of the main beam increases as the beam is steered off boresight by 20°.

Modeling was also done for planar arrays as shown in **Fig. 4**.

Patterns for a planar array are calculated using a unicycle pulse (half of a monocycle) for simplicity of display. The plots are in spherical coordinates (ρ, θ, and ϕ) showing the envelope of the beam pattern.

Simple Array Measurements

The first experiment was conducted to determine the result of transmitting from two MIR transmitters simultaneously. The purpose is to see if the voltage wavelets radiated from two transmitters added at the receiver.

Figure 5 is a diagram of the test setup showing two closely spaced MIR transmitter/antenna units, A and B. The transmitters are triggered simultaneously so that the two transmitted signals arrive at the receiving antenna at the same time.

Measurements were made at two 'separations': 26 in. and 105 in. The measurement procedure consisted of first pointing Antenna B away from the receiving antenna and recording the received voltage-versus-time signal transmitted by Antenna A only. Then the measurement was repeated for recording Antenna B signal only. Finally antennas A and B were pointed at the receiving antenna to record the combined transmitted signal.

Figure 6 shows plots of the received signal for the 26-in. separation for Antenna A and Antenna B. The individual signals are nearly identical. The "Antennas A and B" plot, **Fig. 7**, is the received signal when both transmitting antennas are pointed at the receiver. The individual A and B signals were mathematically added in a computer and are plotted in **Fig. 8**, "Antennas A plus B." Note that the results are nearly identical. Similar results were obtained when the separation was increased to 105 in.

In conclusion, when two identical transmitting antennas are directed at a receiving antenna the voltage signals are added, thus doubling the received voltage.

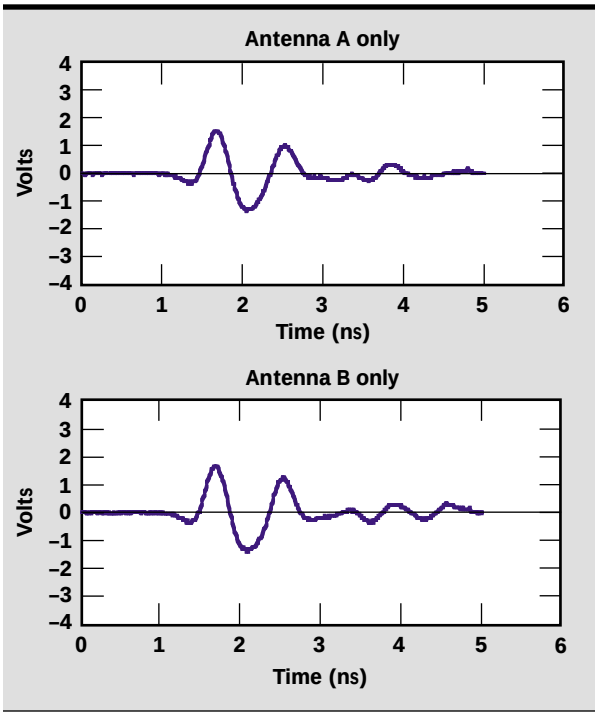

Figure 6. Signals transmitted from Antennas A and B.

Multi-Element Array Measurements

A five-element MIR array was assembled and tested as illustrated in **Fig. 9**, with four transmitters on the outside of the square and one MIR receiver in the center. The transmitters were synchronized electronically to focus the multi-element beam about 10 ft in front of the array. **Figures 10** and **11** show the results of the reflected signal as each transmitter is turned on in sequence.

The signal reflected from the ground increases in amplitude as more transmitters are turned on without a noticeable increase in clutter and noise. Therefore, the signal-to-noise is improved as more transmitters are used, obviously increasing the radar range and performance.

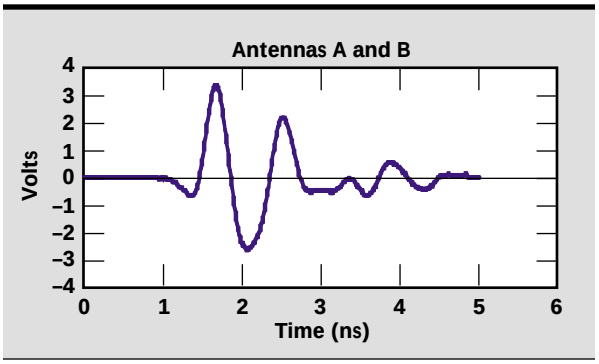

Figure 7. Signal transmitted from both antennas simultaneously.

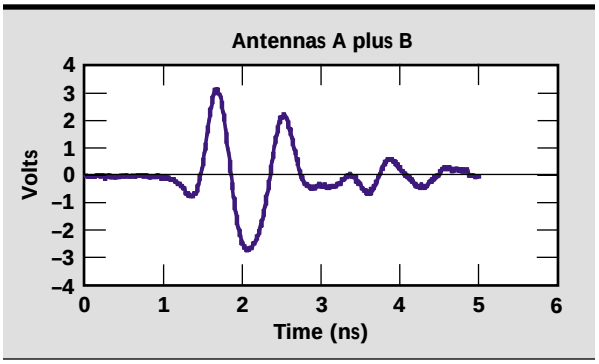

Figure 8. Result of mathematically adding signals from Antennas A and B.

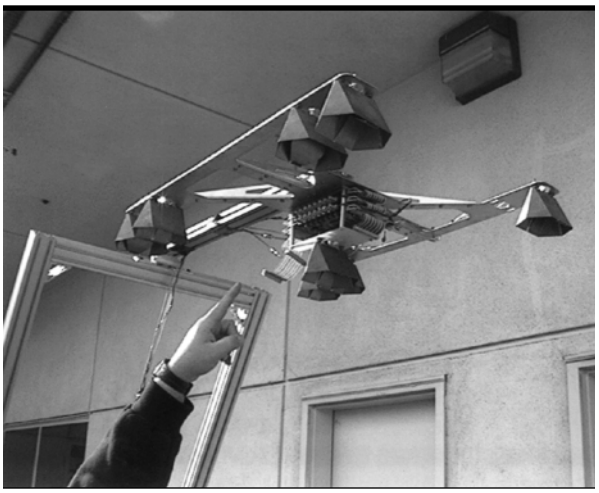

Figure 9. UWB array setup using four transmitters and one receiver.

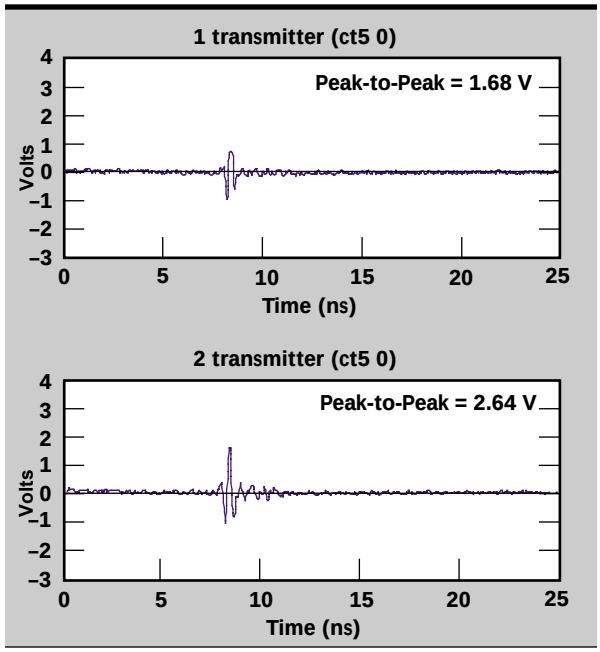

Figure 10. Reflected signal when one and then two transmitters are turned on.

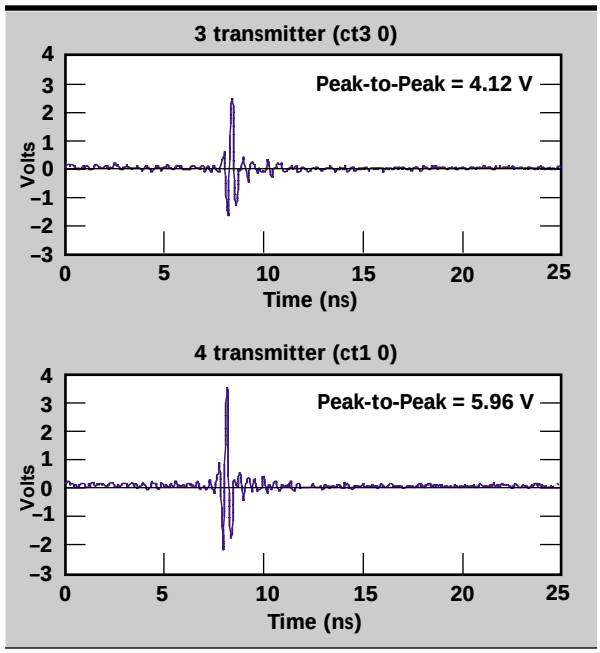

Figure 11. Reflected signal when three and then four transmitters are turned on.

Figure 12. Linear array of eight transmitters and one receiver.

A nine-element linear array was also assembled and tested as seen in **Fig. 12**. The single receiving unit is at the center of the array with four transmitters on either side. The transmitter synchronization test results are the same as for the five-element array, except that the reflected signal is the superposition of eight transmitters.

Future Work

Other groups both inside and outside LLNL are showing interest in multi-element UWB arrays. As an example, a presentation was made to DARPA on using UWB arrays for UGF characterization. Present day GPR will not reliably detect deep UGF. Model studies indicate that a large GPR array will increase radar range to a level that will interest DARPA and also DTRA. These programs and others will be pursued.

References

1. R. J. Lytle, E. F. Laine, D. L. Lager, and D. T. Davis (1979), "Cross-borehole electromagnetic probing to locate high-contrast anomalies," *Geophys.*, Vol. **44**, No. 10, October.

2. W. Daily, A. Ramirez, D. LaBrecque, and J. Nitao (1992), "Electrical resistivity tomography of vadose water movement," *Water Resource Research*, Vol. **28**, pp. 1429–1442.

3. S. D. Nelson and E. Johansson (1995), "Single pass surface-to-borehole reconstruction," *Engineering Research, Development and Technology*, Lawrence Livermore National Laboratory, Livermore, California (UCRL-53868-95).

4. A. Ramirez, W. Daily, M. Butner, and D. LaBrecque (1997), "Electrical resistivity monitoring of the thermomechanical heater teat in Yucca Mountain," *Proc. of the Symp. on the Application of Geophysics to Engineering and Environmental Problems*, Reno, Nevada, Vol. **1**, pp. 11–20.

5. J. Mast, S. Azevedo, W. Haddad, L. Ng, and G. Burnett, "Micropower impulse radar technology and applications," Lawrence Livermore National Laboratory, Livermore, California (UCRL-ID-130474).

6. S. D. Nelson (1994), "Electromagnetic modeling for ground penetrating radar using fine difference time domain modeling codes," *Proc. on Advanced Microwave and Millimeter Wave Detectors, SPIE Proceedings*, Vol. **2275**, July.

7. J. E. Mast and E. M. Johansson (1994), "Three-dimensional ground penetrating radar imaging using multi-frequency diffraction tomography," *SPIE*, Vol. **2275**, July.

8. E. M. Johansson *et al.* (1994), "Three-dimensional ground penetrating radar imaging using synthetic aperture time domain focusing," *Proc. on Advanced Microwave and Millimeter Wave Detectors, SPIE Proceedings*, Vol. **2275**, July.

9. J. J. Roberts, E. Carlberg, and W. Lin, "Electrical properties of tuff from the ESF as a function of water saturation and temperature," Lawrence Livermore National Laboratory, Livermore, California (UCRL-ID-129594).

10. N. Osumi and K. Ueno (1988), "Detection of buried plant," *IEE Proc. on Communication, Radar, and Signal Processing*, Vol. **135**, Pt. F, pp. 330–342, August.

11. G. Junkin and A. P. Anderson (1988), "Limitations in microwave holographic synthetic aperture imaging over a lossy half-space," *IEE Proc. on Communication, Radar, and Signal Processing*, Vol. **135**, Pt. F, pp. 321–329, August.

12. Y. Michiguchi, K. Hiramoto, M. Nishi, T. Ootaka, and M. Okada (1988), "Advanced subsurface radar system for imaging buried pipes," *IEEE Trans. on Geoscience and Remote Sensing*, Vol. **GE-26**, pp. 733–740, November.

13. C. Liu and L. C. Shen (1991), "Numerical simulation of subsurface radar for detecting buried pipes," *IEEE Trans. on Geoscience and Remote Sensing*, Vol. **GE-29**, pp. 795–798, September.

14. A. J. Devaney (1982), "A filtered back propagation algorithm for diffraction tomography," *Ultrasonic Imaging*, Vol. **4**, pp. 336–350, April.

15. E. A. Robinson and S. Treitel (1980), *Geophysical Signal Analysis*, Prentice-Hall, Englewood Cliffs, New Jersey.

16. H. Lee (1984), "Formation of the generalized backward projection method for acoustical imaging," *IEEE Trans. on Sonics and Ultrasonics*, Vol. **31**, pp. 157–161, May.

Photonic Velocimetry System Optimization

Paul D. Sargis, Nicole E. Molau, and Jeffrey B. Cooke
Defense Sciences Engineering Division
Electronics Engineering

Oliver T. Strand
Defense and Nuclear Technology

Mark E. Lowry
Information Science and Technology Program

We have developed an optimized photonic Doppler velocimeter with improved stability and stronger signal levels compared to our FY-98 prototype as a diagnostic for high explosives tests.

Introduction

Surface velocity measurements are of great interest to the high-explosives physics community. Currently, physicists at Lawrence Livermore National Laboratory (LLNL) perform these measurements using a technique called Fabry-Perot Velocimetry (FPV). Although FPV yields excellent data, the total number of data channels will always be less than optimum due to the high procurement cost of custom hardware, the high manpower costs, and the large volume occupied by FPV.

Photonic Doppler velocimetry (PDV) is intended to supplement the FPV diagnostic with many additional low-cost data channels. Our hardware consists of commercial off-the-shelf telecommunications components that fit together in a small chassis. Data is recorded on a transient digitizing oscilloscope.

Figure 1 illustrates the basic PDV system. Infrared light from a laser passes through a multi-mode fiber-optic coupler and is focused onto a moving surface by means of a probe lens. The reflected light is Doppler-shifted and is heterodyned with a fraction of the laser output in a "square law" optical detector. Under the appropriate polarization and modal conditions, the detector generates an electrical current proportional to the square of the optical fields. For the Doppler-shifted light, this corresponds to a beat frequency proportional to the instantaneous velocity of the target. Multi-mode fiber is used to maximize the amount of light collected from the target.

We carried out a successful R&D demonstration of this technique in FY-98. When operated in parallel with the FPV diagnostic, our data showed excellent agreement. At the end of that year, however, it became clear that another year of development would be necessary to optimize the signal-to-noise ratio and improve the stability of the system.

Progress

Our efforts in FY-99 have focused on identifying the causes of system instability and weak signal levels. Since we demonstrated consistency of results with the FPV system during explosives testing last year, we confined our experiments to the photonics laboratory this year.

Last year, our actual system configuration was a bit more complicated than the diagram shown in **Fig. 1**. We used commercial off-the-shelf probes that

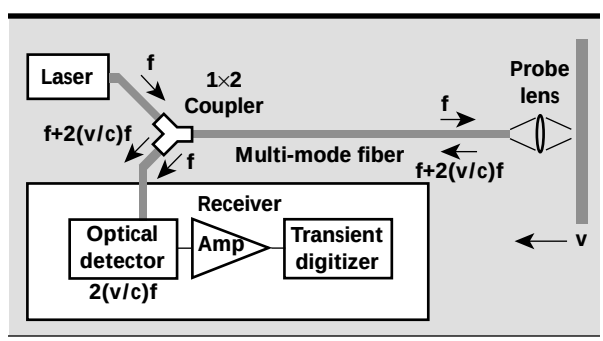

Figure 1. Basic block diagram of the photonic Doppler velocimeter system.

had been designed to reduce optical back-reflections from the surface of the lens to a level of 0.01%. This is generally a desirable specification in the fiber-optics industry, but in our case, it required us to inject a fraction of the laser source power back into the detector to permit heterodyning with the Doppler-shifted light. We accomplished this by using a 2-×-2 fiber-optic coupler as shown in **Fig. 2**.

Early in the year, we came to the conclusion that a major source of our heterodyne inefficiency was due to this practice of having the Doppler-shifted light and the unshifted laser light traverse different optical paths on the way to the optical detector. The Doppler-shifted light was filling different modes and undergoing different polarization changes than the unshifted laser light, due to the extra segment of multi-mode fiber between the probe and the coupler. The most likely causes of the unstable heterodyne signal are the spatial overlap of the speckle patterns and the polarization state overlap of the two signals.

Upon recognition of this problem, we began using probes having an optical back-reflection of 3%. This is approximately equal to the level of reflection from the diffuse moving surface whose velocity we are measuring. In this new configuration, both wavelengths follow the same fiber-optic path, as illustrated in **Fig. 1**.

We also addressed the problem of polarization instability. The laser generates polarized light, but multi-mode fiber does not depolarize it. Instead, the polarization wanders in a random fashion as the light passes through the fiber. This causes the heterodyne signal to vary in amplitude. In addition, repositioning or creating bends in the fiber induces changes in the polarization state at the detector. In fact, we have been able to demonstrate almost total extinction of the heterodyne signal by moving the fiber into just the right position.

Since the development of a depolarized laser source was beyond the scope of this project, we built a polarization diversity receiver, as illustrated in **Fig. 3**, to address the polarization instability issue. The polarization diversity receiver takes the place of the receiver block in **Fig. 1**. The incoming light is collimated into a miniature polarization beam-splitting cube. The orthogonal polarization states are each collimated into a short multi-mode fiber, followed by an optical detector. Ideally, when one polarization state is at a null, the orthogonal state is at a maximum. However, due to the poor collimation inherent with a multi-mode source, the actual extinction ratio is only five to one.

We tested the polarization-diversity receiver on a low-velocity experiment involving a shock-driven niobium foil target. The niobium foil has a diffuse surface and is identical to the material we use for surface ejecta measurements. Transient digitizer data from the S and P polarization states is shown in **Fig. 4**. Some of the amplitude variation can be attributed to motion of the target. However, the drastic amplitude change at 7 μs would suggest that the polarization wanders on a microsecond time scale. It is therefore advisable to record both polarization states so that a high signal-to-noise ratio can be obtained from one channel or the other.

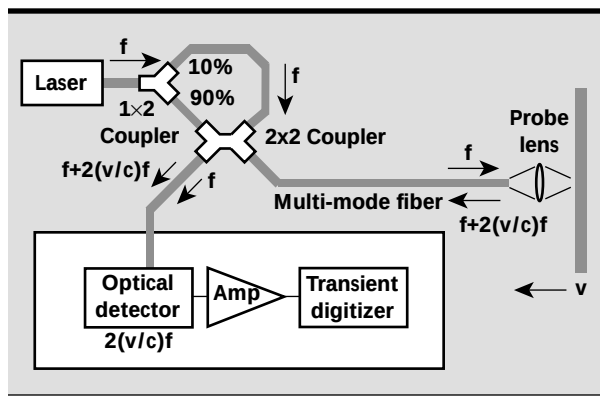

Figure 2. Detailed block diagram of FY-98 photonic Doppler velocimeter system.

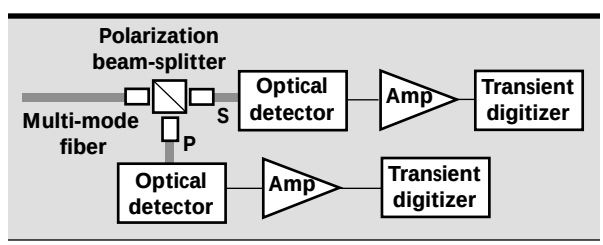

Figure 3. Polarization diversity receiver diagram.

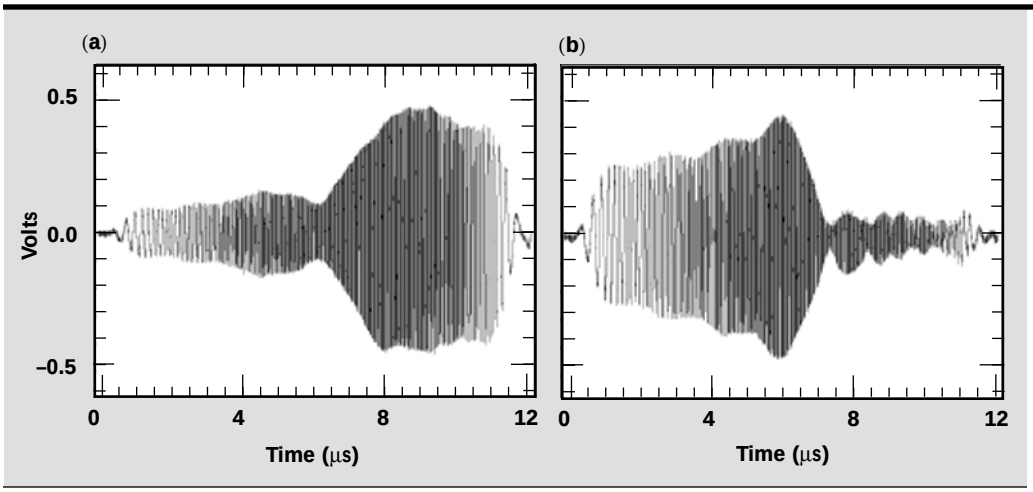

Figure 4. Raw data from niobium foil experiment: (a) S polarization, (b) P polarization.

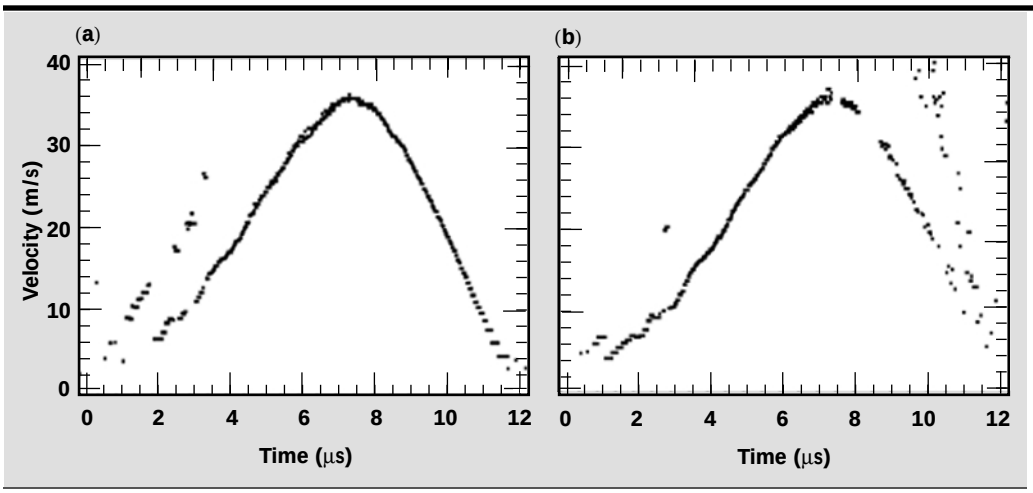

Figure 5. Processed data from niobium foil experiment: (a) S polarization, (b) P polarization.

The Doppler beat frequency signal from each channel was converted to instantaneous frequency versus time, and then to velocity versus time, as shown in **Fig. 5**. No filtering or smoothing was used to obtain these results. The instantaneous frequency was obtained by calculating the time between zero crossings. A more sophisticated technique such as a sliding power spectral density calculation yields smoother results, but this simple processing method emphasizes the value of recording both polarization states.

Future Work

We plan to develop a versatile field-hardened version of the PDV that can be used for a wide variety of high-explosives applications at LLNL. Before we release the hardware for general use, we will verify the reliability on a series of dedicated shots at the High Explosives Applications Facility (HEAF). We will also refine our data processing techniques so that experimenters will have quick post-shot access to velocity data.

Selected Engineering Publications

Selected Engineering Publications

Aceves, S. M. and G. Berry (1998), "Analysis of hydrogen vehicles with cryogenic high pressure storage," *Hydrogen Energy Progress XII*, J. C. Bolcich and T. N. Veziroglu, eds., Vol. **2**, June, pp. 943–952.

Aceves, S. M. and G. Berry (1998), "Analytical and experimental evaluation of pressure vessels for cryogenic hydrogen storage," *216th Am. Chem. Soc. National Meeting, Division of Fuel Chemistry*, Vol. **43**, No. 3, August, pp. 570–574.

Aceves, S. M. and J. Martinez (1999), "Effects of evaporator frosting on the performance of air-to-air heat pump," *ASME J. of Energy Resources Technology*, Vol. **121**, No. 1, pp. 60–65.

Aceves, S. M. and J. R. Smith (1998), "A desiccant dehumidifier for electric vehicle heating," *ASME J. of Energy Resources Technology*, Vol. **120**, No. 2, pp. 131–136.

Aceves, S. M. and J. R. Smith (1998), "Hybrid and conventional hydrogen engines that meet EZEV emissions," *SAE Transactions, J. of Passenger Vehicles*.

Aceves, S. M. and G. Berry (1998), "Thermodynamics of insulated pressure vessels for vehicular hydrogen storage," *ASME J. of Energy Resources Technology*, Vol. **120**, No. 2, pp. 137–142.

Aceves, S. M., G. D. Berry, and G. D. Rambach (1998), "Insulated pressure vessels for hydrogen storage on vehicles," *Int. J. of Hydrogen Energy*, Vol. **23**, No. 7, pp. 583–591.

Aceves, S. M., J. R. Smith, C. Westbrook, and W. Pitz (1998), "Compression ratio effect on methane HCCI combustion," *Proc. of the 1998 ASME Internal Combustion Engine Fall Technical Conf.*, ICE—Vol. **31-3**, pp. 49–57.

Ackler, H. (1998), "Healing of lithographically introduced cracks in glass and glass containing ceramics," *J. Am. Ceram. Soc.*, Vol. **81**, No. 12, pp. 3093–3103.

Ackler, H., P. Krulevitch, R. Miles, W. Benett, S. Swierkowski, V. Malba, P. R. C. Gascoyne, X. Wang, and G. deGasperis (1998), "Microfluidic systems for electrochemical and biological studies," *Sym. Y1 Proc., Microstructures and Microfabricated Systems IV*, pp. 54–61, *194th Meeting of the Electrochemical Soc.*, Boston, Massachusetts, November 1–6.

Albert, K. J., M. L. Myrick, S. B. Brown, F. P. Milanovich, and D. R. Walt (1999), "High-speed fluorescence detection of explosives vapor," *13th Int. Sym. on Aerospace/Defense Sensing, Simulation, and Controls*, April 5–9.

Albrecht, G. F., S. B. Sutton, E. V. George, W. R. Sooy, and W. F. Krupke (1998), "Solid state heat capacity disk laser," *Laser and Particle Beams*, Vol. **16**, No. 4, pp. 605–625.

Alford, O. J., P. D. Barnes, Jr., A. K. Chargin, W. D. Dekin, E. P. Hartouni, J. N. Hockman, A. S. Ladran, M. A. Libkind, T. L. Moore, J. W. Pastrnak, R. E. Pico, R. J. Souza, J. M. Stoner, J. H. Wilson, A. G. Ruggiero, and S. Ohnuma (1999), "The scrounge-atron: a phased approach to the advanced hydrotest facility utilizing proton radiography," *1999 Particle Accelerator Conf.*, New York, New York, March 29–April 3.

Belgrader, P., W. Benett, D. Hadley, G. Long, R. Mariella, Jr., F. Milanovich, S. Nasarabadi, W. Nelson, J. Richards, and P. Stratton (1998), "Rapid pathogen detection using a microchip PCR array instrument," *Clinical Chemistry*, Vol. **44**, pp. 2191–2194.

Belgrader, P., W. Benett, D. Hadley, J. Richards, R. Mariella, Jr., and F. Milanovich (1999), "PCR detection of bacteria in seven minutes," *Science*, April 16, Vol. **284**, pp. 459–450.

Belgrader, P., W. Benett, R. Frattaroli, D. Hadley, R. Langlois, S. Lehew, R. Mariella, Jr., F. Milanovich, S. Nasarabadi, M. A. Northrup, J. Richards, P. Stratton, and K. S. Venkateswaran (1998), "Multi-chamber, real-time DNA analysis in the field using microfabricated silicon chambers," *Proc. of the Sym. on Microelectromechanical Systems, 1998 ASME Int. Mechanical Engineering Congress and Exposition*, Anaheim, California, November 15–20.

Belian, A. P., J. F. Latkowski, and E. C. Morse (1998), "Experimental studies of concrete activation at the National Ignition Facility using the rotating target neutron source," *Fusion Technology*, Vol. **34**, No. 3, Pt. 2, November, pp. 1028–1032.

Benett, W. and P. Krulevitch (1998), "Interconnects for micro-fluidic systems," *Conf. on Micro Total Analysis Systems '98*, Banff, Canada, October 13–16.

Benett, W. and P. Krulevitch (1999), "A flexible packaging and interconnect scheme for microfluidic systems," *SPIE conference on Micro- and Nanofabricated Structures and Devices for Biomedical Environmental Applications*, San Jose, California, January 25–26.

Benford, J., D. Price, and W. DeHope (1998), "Lowered plasma velocity with cesium iodide/carbon fiber cathodes at high electric fields," *Int. Conf. On Plasma Science*, Raleigh, North Carolina, June 1–4.

Benford, J., D. Price, and W. DeHope (1998), "Lowered plasma velocity with cesium iodide/carbon fiber cathodes at high electric fields," *12th Int. Conf. on High-Power Beams*, Haifa, Israel, June 7–12.

Bennett, C. V. and B. H. Kolner (1998), "Up-conversion time microscope demonstrates 103x magnification of ultrafast waveforms with 300 fs resolution," *Proc. LEOS '98*, Dec. 1–4.

Bennett, C. V. and B. H. Kolner (1999), "Principles, performance and demonstration of an up-conversion time microscope," *Proc. Ultrafast Electronics and Optoelectronics '99*, Aspen, Colorado, April 12–16.

Benton, J., J. Glaser, J. Bicha, W. Dougherty, D. Demenko, and V. Yemelyanov (1998), "U.S. transparency monitoring of HEU weapons components conversion at two Russian oxidation plants," *39th Ann. Meeting Int. Nuclear Material Management*, Naples, Florida, July 26–30.

Bertolini, L. R., O. J. Alford, A. C. Paul, C. C. Shang, and G. A. Westenskow (1999), "The mechanical design for the second axis beam transport line for the DARHT facility," *1999 Particle Accelerator Conf.*, New York, New York, March 29–April 3.

Bland, M. (1999), "HPM effects infrastructure and missiles," *17th Ann. Hardened Electronics and Radiation Technology Conf.*, March 9–12.

Bliss, E., S. Boege, R. Boyd, D. Davis, R. Demaret, M. Feldman, A. Gates, F. Holdener, C. Knopp, R. Kyker, C. Lauman, T. McCarville, J. Miller, V. Miller-Kamm, W. Rivera, T. Salmon, J. Severyn, S. Sheem, S. Thomas, C. Thompson, M. Yeoman, R. Zacharias, C. Chocol, J. Hollis, D. Whitaker, J. Bruckner, L. Bronisz, and T. Sheridan (1998), "Design process for National Ignition Facility laser alignment and beam diagnostics," *Solid State Lasers for Application to Inertial Confinement Fusion*, Monterey, California, June 7–12.

Bond, S. W., S. Jung, O. Vendier, M. Brooke, N. M. Jokerst, S. Chai, A. Lopez-Laguanas, D. S. Wills, G. Dagnall, and A. Brown (1998), "3D stacked Si CMOS VLSI smart pixels using through-Si optoelectronic interconnections," *Technical Digest, IEEE LEOS Summer Topical Meeting*, Monterey, California, July.

Botkin, M. E., N. L. Johnson, E. Zywicz, and S. Simunovic (1998), "Crashworthiness simulations of composite automotive structures," *Proc. of the 13th Ann. Eng. Soc. of Detroit Advanced Composites Technology Conf. and Exposition*, Detroit, Michigan, September 28–29.

Braun, D. G., T. M. Anklam, L. V. Berzins, D. T. Blackfield, M. A. McClelland, T. C. Meier, K. W. Westerberg, I. Boyd, and J. Balakrishnan (1998), "Simulation of an EBPVD titanium vapor plume and comparison to experiment," *Electron Beam Melting and Refining State of the Art*, R. Bakish, ed., pp. 177–194, Bakish Materials Corp., Englewood, New Jersey.

Brereton, S. and T. Altenbach (1998), "Risk ranking methodology for chemical release events," *Proc. of the Int. Topical Meeting on Probabilistic Safety And Management PSAM4*, A. Mosleh and R. A. Bari, eds., Vol. **3**, pp. 1743–1748, Springer-Verlag, New York, New York, September.

Brereton, S. J., C. A. Taylor, and J. M. Yatabe (1998), "The safety and environmental process for the design and construction of the National Ignition Facility," *Proc. of the ANS 13th Topical Meeting on the Technology of Fusion Power*, Nashville, Tennessee, June, published in *Fusion Technology*, Vol. **34**, Pt. 2, November, pp. 760–766.

Brereton, S. J., D. R. Becker, G. P. Brumburgh, J. A. Pryatel, C. R. Wolfe, and J. M. Yatabe (1998), "Assuring safety in the National Ignition Facility," *Proc. of the EFCOG 8th Ann. Safety Analysis Working Group Conf.*, Park City, Utah, June.

Brereton, S. J., H. P. Alesso, T. J. Altenbach, C. T. Bennett, and C. Ma (1998), "AVLIS criticality risk assessment," *Proc. of the EFCOG 8th Ann. Safety Analysis Working Group Workshop*, Park City, Utah, June.

Brereton, S., J. Latkowski, M. Singh, M. Tobin, and J. Yatabe (1998), "Decontamination and decommissioning the National Ignition Facility," *Proc. of the ANS 13th Topical Meeting on the Technology of Fusion Power*, Nashville, Tennessee, June, published in *Fusion Technology*, Vol. **34**, Pt. 2, November, pp. 1041–1046.

Brereton, S., M. Lane, C. Smith, and J. Yatabe (1998), "Risk management plan for the National Ignition Facility," *Proc. of the Int. Topical Meeting on Safety and Management PSAM4*, A. Mosleh and R. A. Bari, eds., Vol. **4**, pp. 2807–2812, Springer-Verlag, New York, New York, September.

Breunig, T. M., G. W. Marshall, J. H. Kinney, D. L. Haupt, and S. J. Marshall (1999), "Transparent dentin associated with natural carious lesions," *J. of Dental Research*, Vol. **78**, p. 411.

Burgess, E. L., J. D. Comins, W. M. Fawley, D. V. Munson, M. Nyman, L. T. Jackson, C. Peters, L. Reginato, H. L. Rutkowski, M. C. Vella, W. Waldron, S. S. Yu, Y. Chen, T. Houck, R. Briggs, D. L. Birx (1999), "A long pulse linac for the second phase of DARHT," *1999 Particle Accelerator Conf.*, New York, New York, March 29–April 3.

Burnett, G. C. and R. J. Leonard (1999), "Use of Kodak EktaPro high-speed digital cameras in laryngoscopy," *Phonoscope*, Vol. **2**, No. 1, March, pp. 33–40.

Campbell, G. H., S. M. Foiles, H. Huang, D. A. Hughes, W. E. King, D. H. Lassila, D. J. Nikkel, T. Diaz de la Rubia, J. Y. Shu, and V. P. Smyshlayaev (1998), "Multi-scale modeling of polycrystal plasticity: a workshop report," *Materials Science and Engineering A*, Vol. **251**, pp. 1–22.

Canaan, R. E. and D. E. Klein (1998), "A numerical investigation of natural convection heat transfer within horizontal spent-fuel assemblies," *Nuclear Technology*, Vol. **123**, August, pp. 193–208.

Candy, J. (1998), "Dynamic surface imaging for the space shuttle experiment," *Int. J. of Imaging Systems and Technology*.

Candy, J. (1999), "Processing of RV signatures from radar tracking data," *SET Conf. On High Resolution Imaging* (Classified), Granada, Spain.

Candy, J. and D. Chambers (1999), "Model-based dispersive wave processing: a recursive Bayesian approach," *J. Acoust. Soc. Am.*, Vol. **103**.

Candy, J., R. Huber, D. Chambers, and G. Thomas (1999), "Matched-field imaging of laser ultrasound using a correlation canceling approach," *109th Meeting of Acoust. Soc. Am.*, Berlin, Germany.

Carter, P. H., D. J. Pines, and L. vE. Rudd (1998), "Approximate performance of periodic hypersonic cruise trajectories for global reach," *8th AIAA Int. Spaceplanes and Hypersonics Systems and Technologies Conf.*, Norfolk, Virginia, April 27–30.

Carter, P. H., D. J. Pines, and L. vE. Rudd (1998), "Approximate performance of periodic hypersonic cruise trajectories for global reach," *AIAA J. of Aircraft*, Vol. **35**, No. 6, November–December.

Carter, P. H., F. Mitlitsky, A. H. Weisberg, J. C. Whitehead, and R. W. Humble (1998), "Design trade space for a Mars ascent vehicle for a Mars sample return mission," *3rd IAA Int. Conf. on Low-Cost Planetary Missions*, Pasadena, California, April 27–May 1.

Cartland, H. E., J. W. Hunter, A. S. Driesman, H. E. Gilreath, W. M. Kroshl, and M. E. White (1999), "Light gas gun launch to space," *2nd Int. Conf. on Integrated Micro/Nanotechnology for Space Applications*, Pasadena, California, April 14.

Chen, Y., T. L. Houck, and W. M. Fawley (1998), "Study of the transverse beam motion in the DARHT phase II accelerator," *Proc. of the 19th Int. Linac Conf.*, Chicago, Illinois, August 23–28.

Clauson, T. (1998), "Performance comparison of dual and single flow thrust vector nozzles," High-Angle-of-Attach technology: accomplishments, lessons learned, future directions, NASA/CP-1998-207676/PT2, June, pp. 1033–1050.

Crane, J. K., D. Browning, C. B. Dane, M. Henesian, M. Martinez, B. Moran, F. Penko, J. E. Rothenberg, and R. B. Wilcox (1998), "Integrated optical pulse generation system for the National Ignition Facility," *Proc. Conf. on Lasers and ElectroOptics*, May.

Crane, J. K., R. B. Wilcox, B. D. Moran, N. Hopps, D. Browning, C. B. Dane, M. Henesian, M. Martinez, F. Penko, J. E. Rothenberg, L. A. Hackel, K. Skulina, C. Laumann, L. Kot, R. A. Jones, F. Deadrick, and G. Dreifuerst (1998), "Optical pulse generation system for the National Ignition Facility," *Proc. from the 13th Embedded Topical Meeting of Fusion Energy*, June 7–11.

Crane, J. K., R. B. Wilcox, N. Hopps, D. Browning, M. Henesian, M. Martinez, B. D. Moran, F. Penko, J. E. Rothenberg, C. B. Dane, and L. A. Hackel (1998), "Integrated operation of the National Ignition Facility pulse generation system," *Solid State Lasers for Application to Inertial Confinement Fusion*, Monterey, California, June 7–12.

Dardenne, Y. X., T. F. Wang, A. D. Lavietes, G. J. Mauger, W. D. Ruhter, and S. A. Kreek (1999), "Cadmium zinc telluride spectral modeling," *Nuclear Instruments and Methods in Physics Research, Radiation Measurements and Applications*, Vol. **A422**, Section A, pp. 159–163.

Dehghani, M. and H. Hamidzadeh (1998), "Stability analysis of flexible cam follower systems," *ASME Int. Congress and Exposition*, Anaheim, California, November 15–20.

Dehghani, M. and H. Hamidzadeh (1998), "Transverse vibration of thin rotating disks non-linear model analysis," *ASME Int. Congress and Exposition*, Anaheim, California, November 15–20.

Dehghani, M. and H. Hamidzadeh (1998), "Evaluation of dynamic properties for an elastic half-space medium," *ASME Eng. System Design and Analysis Conf.*, Berlin, Germany, July 6–9.

Dimonte, G., D. Nelson, S. Weaver, and M. Schneider (1998), "Comparative study of viscoelastic properties using virgin yogurt," *J. of Rheology*, Vol. **42**, No. 4, July–August.

Dunn, T. A. and E. Loth (1999), "Effects of simulated-spanwise ice shapes on airfoils: computational investigation," *AIAA-99-0093*, January.

Dyer, J. S., T. A. Edmunds, J. C. Butler, and J. Jia (1998), "A multiattribute utility analysis of alternatives for the disposition of surplus weapons-grade plutonium," *J. of Operations Research*, Vol. **46**, No. 6, December, pp. 749–762.

Fawley, W. M., Y. Chen, and T. L. Houck (1999), "Beam breakup calculations for the second axis of DARHT," *1999 Particle Accelerator Conf.*, New York, New York, March 29–April 3.

Feit, M. D., C. Widmayer, W. H. Williams, R. R. Sacks, P. A. Renard, and M. A. Henesian (1998), "The National Ignition Facility's assessment of the optical damage threat for flat-in-time pulses," National Ignition Facility Performance Ratings, *Supplement to Proc. of SPIE*, Vol. **3492**, pp. 39-48, *Solid State Lasers for Application to Inertial Confinement Fusion*, Monterey, California, June 7–12.

Feit, M. D., C. Widmayer, W. H. Williams, R. R. Sacks, P. A. Renard, and M. A. Henesian (1998), "The National Ignition Facility's assessment of the optical damage threat for shaped ICF pulses," *Supplement to Proc. of SPIE*, Vol. **3492**, pp. 61–64, *Solid State Lasers for Application to Inertial Confinement Fusion*, Monterey, California, June 7–12.

Fitch J. P., J. W. Balch, M. S. Bass, L. R. Brewer, A. C. Copeland, J. C. Davidson, L. M. Kegelmeyer, J. R. Kimbrough, R. S. Madabhushi, P. M. McCready, D. O. Nelson, R. L. Pastrone, P. M. Richardson, S. P. Swierkowski, L. A. Tarte, M. Vainer, and T. E. Warth (1999), "A microchannel electrophoresis DNA sequencing system," *1999 Conf. on Information Sciences and Systems*, Baltimore, Maryland, March 17–19.

Franks, M., J. N. Corlett, R. Rimmer, P. Corredoura, M. Minty, T. O. Raubenheimer, M. C. Ross, H. Schwarz, and R. C. Tighee (1999), "The next linear collider damping ring RF system," *1999 Particle Accelerator Conf.*, New York, New York, March 29–April 3.

Franks, M., K. Hernandez, D. Otting, D. Plate, T. Henderson, and R. Rimmer (1999), "Mechanical design and fabrication processes for the ALS third harmonic cavities," *1999 Particle Accelerator Conf.*, New York, New York, March 29–April 3.

Garcia, M. (1998), IEEE Conf. Record—Abstracts, *1998 IEEE Int. Conf. on Plasma Science*, p. 211, Raleigh, North Carolina, June 1–4.

Garcia, M. (1999), "Integro-differential equations," *Wiley Encyclopedia of Electrical and Electronics Engineering*, Vol. **10**, pp. 436–445, John Wiley and Sons, Inc., New York, New York.

Gilreath, H. E., A. S. Driesman, W. M. Kroshl, M. E. White, H. E. Cartland, and J. W. Hunter (1998), "The feasibility of launching small satellites with a light gas gun," *12th AIAA/USU Conf. on Small Satellites*, Logan, Utah, Aug. 31.

Groot, W. A., L. A. Arrington, J. F. McElroy, F. Mitlitsky, A. H. Weisberg, P. H. Carter, II, B. Myers, B. D. Reed, and R. W. Humble (1998), "Unitized electrolysis propulsion and fuel cell power for selected satellite missions," *33rd Intersociety Engineering Conf. on Energy Conversion*, Colorado Springs, Colorado, August 2–6.

Hage, M. and S. Couture (1999), "Evolutionary software for autonomous path planning," *Proc. of the Am. Nuclear Soc., 8th Int. Topical Meeting on Robotics and Remote Systems*, Pittsburgh, Pennsylvania, April 25–29.

Haley, T. A., R. Karimi, P. G. Prassinos, and K. Jimali (1998), "Progression and advancement of aircraft crash hazard analysis models," *PSAM4*, New York, New York, September 13–18.

Hall, T. B. (1999), "Development of a safety interlock system for the National Ignition Facility optical line replaceable unit transport and handling systems," *Proc. of the Am. Nuclear Soc., 8th Int. Topical Meeting on Robotics and Remote Systems*, Pittsburgh, Pennsylvania, April 25–29.

Hartemann, F. V., G. P. Le Sage, C. V. Bennett, E. C. Landahl, and N. C. Luhmann, Jr. (1998), "Photoelectron production in an X-band RF gun for free electron laser and nonlinear electron-photon scattering experiments," *Proc. IEEE Int. Conf. on Plasma Science*, Raleigh, North Carolina, June 1–4, p. 238.

Haupt, D. L. and J. H. Kinney (1999), "Shear punch instrument for measuring shear properties in dentin," Poster presentation, *77th General Session of the Int. Association of Dental Research* in conjunction with *The 28th Ann. Meeting of the Am. Association of Dental Research* and *The 23rd Ann. Meeting of the Canadian Association of Dental Research*, Vancouver, B.C., March.

Haupt, D. L. and J. H. Kinney (1999), Shear punch instrument for measuring shear properties in dentin, *J. of Dental Research*, Vol. **78**, p. 252.

Heller, A. and P. J. Van Arsdall (1998), "Controlling the world's most powerful laser," *Science & Technology Review*, November, pp. 4–11.

Henesian, M. A., J. K. Crane, C. B. Dane, J. Davin, L. Kot, C. Laumann, J. Lawson, M. Martinez, B. Moran, J. Miller, R. Sacks, K. Skulina, and W. Williams (1998), "Diffraction modeling of the National Ignition Facility optical pulse generation system and integration into the end-to-end system model," *Solid State Lasers for Application to Inertial Confinement Fusion*, Monterey, California, June 7–12.

Hildum, J. S., S. Brereton, R. Hickman, B. Odell, D. Price, and A. Williams (1998), "Hazard classification process at LLNL," *Proc. of the EFCOG 8th Ann. Safety Analysis Working Group Workshop*, Park City, Utah, June.

Holzrichter, J. F., G. C. Burnett, T. J. Gable, and L. C. Ng (1998), "Micro-power electro-magnetic sensors for speech characterization: recognition, verification, and other applications," *5th Int. Conf. on Spoken Language Processing*, Sidney, Australia, November 30–December 4.

Hoover, C. G., A. J. De Groot, and R. J. Sherwood (1998), "Parallel contact algorithms for explicit finite element analysis," *Int. Conf. on Eng. Science*, Atlanta, Georgia, October, and published in *Modeling and Simulation Based Engineering*, S. N. Atluri and P. E. O'Donoghue, eds., Tech Science-Press, Palmdale, California.

Hopps, N. W., R. B. Wilcox, M. R. Hermann, M. D. Martinez, E. H. Padilla, and J. K. Crane (1998), "Optimization of the alignment and energy stability of the National Ignition Facility regenerative amplifier," *Solid State Lasers for Application to Inertial Confinement Fusion*, Monterey, California, June 7–12.

Hossain, Q. A. (1998), "Probabilistic determination of missile characteristics for aircraft impact analysis," *Proc. of the Am. Soc. of Mech. Eng., Pressure Vessel and Piping Conf.*, July.

Houck, T. L., G. A. Westenskow, D. E. Anderson, S. Eylon, E. Henestroza, S. M. Lidia, D. L. Vanecek, and S. S. Yu (1998), "Diagnostics for a 1.2-kA, 1-MeV electron induction injector," *Proc. of the 8th Beam Instrumentation Workshop*, Stanford Linear Accelerator Center, Palo Alto, California, May 4–7.

Houck, T. L., M. Garcia, and S. Sampayan (1998), "Faraday cup measurements of the plasma plume produced at an x-ray converter," *Proc. of the 19th Int. Linac Conf.*, Chicago, Illinois, August 23–28.

Houck, T. L., Y. Chen, C. C. Shang, L. L. Reginato and S. S. Yu (1998), "Physics design of the DARHT 2nd axis accelerator cell," *Proc. of the 19th Int. Linac Conf.*, Chicago, Illinois, August 23–28.

Huber, R. and G. Thomas (1998), "Process control monitoring of laser cutting," *Review of Progress in Quantitative Nondestructive Evaluation*, Vol. **18b**, Plenum Press, New York, pp. 2273–2277.

Hurst, P., M. Simmons, and H. Wong (1999), "Precision assembly and alignment of large optic modules for the National Ignition Facility," *Eng. Design and Automation Conf.*

Hyde, R. A., L. Seppala, I. Barton, and S. Dixit (1999), "EYEGLASS: a large aperture diffractive telescope," *Ultra Lightweight Space Optics Challenge Workshop*, Napa, California, March 24–25.

Isherwood, W. and S. Aceves (1998), "Energy storage for hybrid remote power systems," *Proc. of the Polartech 98 Conf.*, Nuuk, Greenland.

Jackson, J. A., D. M. Goodman, G. P. Roberson, and H. E. Martz (1998), "An active and passive tomography algorithm with a constrained conjugate gradient solution," *Proc. of the 6th Nondestructive Assay Waste Characterization Conf.*, Salt Lake City, Utah, November 17–19.

Jones, O. S., D. R. Speck, W. H. Williams, P. A. Renard, and J. K. Lawson (1998), "The National Ignition Facility's power and energy ratings for ICF-shaped temporal pulses," National Ignition Facility Performance Ratings, *Supplement to Proc. of SPIE*, Vol. **3492**, pp. 49–54, *Solid State Lasers for Application to Inertial Confinement Fusion*, Monterey, California, June 7–12.

Jorgensen, B. R., T. Woehrle, M. Eli, and C. T. Chow (1999), "Modal response of interior mass based upon external measurements," *Int. Modal Analysis Conf.*, Kissimmee, Florida, February 8–11, pp. 2038–2041.

Jorgensen, B., J. Goudreau, T. Woehrle, M. Eli, and T. S. Chow (1999), "Study of interior masses modal responses based on measurements on exterior parts," *Int. Modal Analysis Conf.*, Kissimmee, Florida, February 8–11.

Kimura, C. Y. and G. P. Brumburgh (1998), "Aircraft crash hit analysis of the decontamination and waste treatment facility (DWTF) at the Lawrence Livermore National Laboratory," *4th Int. Conf. on Probabilistic Safety Assessment and Management*, New York, New York, Vol. **3**, September 13–18, pp. 1818–1825.

Kinney, J. H., J. T. Ryaby, D. L. Haupt, and N. E. Lane (1998), "Three-dimensional *in vivo* morphometry of trabecular bone in the OVX rat model of osteoporosis," *Technology and Health Care*, Vol. **6**, pp. 339–350.

Kinney, J. H., M. Balooch, D. L. Haupt, G. W. Marshall, and S. J. Marshall (1999), "Elastic properties of dentin are not affected by tubule orientation," *J. of Dental Research*, Vol. **78**, p. 539.

Kirbie, H., B. Hickman, B. Lee, C. Ollis, C. Brooksby, and R. Saethre (1998), "An all solid state pulse power source for high PRF induction accelerators," *Proc. of the 23rd Int. Power Modulator Sym.*, Rancho Mirage, California, June 22–25, p. 6.

Kirbie, H., B. Hickman, B. Lee, M. Bland, C. Brooksby, and R. Saethre (1998), "High PRF pulsed power from a solid state induction voltage adder," *High Voltage Workshop*, Daytona Beach, Florida, October 19–22.

Kirbie, H., G. Caporaso, R. Hanks, B. Hickman, B. Lee, C. Brooksby, and R. Saethre (1999), "MHz repetition rate solid-state driver for high current induction accelerators," *1999 Particle Accelerator Conf.*, New York, New York, March 29–April 3.

Ladd, A. J. C., J. H. Kinney, D. L. Haupt, and S. A. Goldstein (1998), "Finite-element modeling of trabecular bone: comparison with mechanical testing and determination of tissue modulus," *J. of Orthopaedic Research*, September, Vol. **16**, No. 5, pp. 622–628.

LaFiandra, C., P. Mehta, G. Goldstein, R. Zacharias, and S. Winters (1998), "National Ignition Facility deformable mirror, solid state lasers for application to inertial confinement fusion," *Solid State Lasers for Application to Inertial Confinement Fusion*, Monterey, California, June 7–12.

Landahl, E. C., F. V. Hartemann, G. P. Le Sage, W. E. White, H. A. Baldis, C. V. Bennett, J. P. Heritage, N. C. Luhmann, Jr., and C. H. Ho (1998), "Phase noise reduction and photoelectron acceleration in a high-Q RF gun," *IEEE Trans. on Plasma Science*, Vol. **26**, No. 3, *IEEE*, June, pp. 814–824.

Lane, N. E., D. Haupt, D. B. Kimmel, G. Modin, and J. H. Kinney (1999), "Early estrogen replacement therapy reverses the rapid loss of trabecular bone volume and prevents further deterioration of connectivity in the rat," *J. of Bone and Mineral Research*, February, Vol. **14**, No. 2, pp. 206–214.

Lane, N. E., J. M. Thompson, D. Haupt, D. B. Kimmel, G. Modin, and J. H. Kinney (1998), "Acute changes in trabecular bone connectivity and osteoclast activity in the ovariectomized rat *in vivo*," *J. of Bone and Mineral Research*, Vol. **13**, pp. 229–236.

Latkowski, J. F. (1998), "Neutron activation of the National Ignition Facility final optics assemblies and their effect upon occupational doses," *Fusion Technology*, Vol. **34**, No. 3, Pt. 2, November, pp. 767–771.

Latkowski, J. F. and J. L. Vujic (1998), "Inertial fusion energy: a clearer view of the safety and environmental aspects," *Fusion Technology*, Vol. **33**, No. 3, May, pp. 298–340.

Latkowski, J. F., J. J. Sanchez, and L. C. Pittenger (1999), "Neutronics and activation analysis for the National Ignition Facility cryogenic target positioner," *Fusion Technology*, Vol. **35**, No. 2, March, pp. 255–259.

Lavietes, A. D., G. J. Mauger, and E. H. Anderson (1999), "Electromechanically-cooled germanium radiation detection system," *Nuclear Instruments and Methods in Physics Research, Radiation Measurements and Applications*, Vol. **A422**, Section A, pp. 252–256.

Le Sage, G. P., C. V. Bennett, W. E. White, E. C. Landahl, L. L. Laurent, N. C. Luhmann Jr., F. V. Hartemann, C. H. Ho, W. K. Lau, and T. T. Yang (1998), "A high brightness, X-band photoinjector for the production of coherent synchrotron radiation," *Physics of Plasmas*, Vol. **5**, No. 5, *AIP*, May, pp. 2048–54.

Leach, D., D. Thomas, D. Decman, J. Glaser, K. Lewis, J. Benton, and A. Demenko (1998), "U.S. transparency monitoring of HEU oxide and blending of LEU hexaflouride at three Russian blending plants," *39th Ann. Meeting Int. Nuclear Material Management*, Naples, Florida, July 26–30.

Ledebuhr, A. G., J. F. Kordas, L. C. Ng, M. Jones, R. Gaughn, E. Breitfeller, and M. Dittman (1998), "Autonomous, agile, micro-satellites and supporting technologies for use in low-earth orbit missions," *12th Ann. AIAA/Utah State University Conf. on Small Satellites*, November 30.

Ledebuhr, A. G., J. F. Kordas, L. C. Ng, M. S. Jones, O. Edwards, J. C. Whitehead, R. J. Gaughan, and M. D. Dittman (1998), "Autonomous, agile, micro-satellites and supporting technologies for use in low-earth orbit missions," *12th Ann. AIAA/Utah State University Conf. on Small Satellites*, August 31–September 3.

Lee, C. L. (1998), "Limit cycle measurements from a cantilever beam attached to a rotating body," *AIAA J.*, Vol. **36**, No. 8, August.

Lesuer, D. R., C. K. Syn, and O. D. Sherby (1998), "Superplasticity in laminated metal composites," *Sym. on Superplasticity and Superplastic Forming*, pp. 40–42.

Lesuer, D. R., C. K. Syn, O. D. Sherby, and J. Wadsworth (1998), "Laminated metal composites—fracture and ballistic impact behavior," *Advanced Materials and Processing*, pp. 407–416.

Lesuer, D. R., R. Glaser, and C. K. Syn (1998), "The evolution of grain size distribution during deformation of superplastic materials," *Sym. on Superplasticity and Superplastic Forming*, pp. 40–42.

Lesuer, D., C. Syn, W. Whittenberger, and O. Sherby (1999), "Microstructure-property relations in as-extruded UHCS," *Metallurgical and Materials Transactions*, Vol. **30A**, pp. 1559–1568.

Lewis, K. (1998), "Angle-frequency spectra for broadband pulses," *136th Meeting Acoustical Soc. of Am.*, Norfolk, October 12–16.

Lewis, K. (1998), "Localized wave pulse generation from a standard underwater array," *4th European Conf. on Underwater Acoustics*, Rome, September 21–25.

Lewis, K. (1998), "Localized wave pulses in the Keyport experiment," *Joint ICA/ASA Conf. on Acoustics*, Seattle, Washington, June 20–26.

Lewis, K. (1998), "Localized wave pulses in the NUWC Keyport experiment," *IEEE Ocean Engineering Soc. Meeting*, Nice, September 28–October 1.

Lewis, K. (1998), "Time-frequency analysis of low diffraction beam pulses," *136th Meeting Acoustical Soc. of Am.*, Norfolk, Virginia, October 12–16.

Libkind, M., P. Duffy, R. Carr, J. Skaritka, and G. Rakowsky (1999), "LSAFEL—001 mechanical design of the VISA undulator," *1999 Particle Accelerator Conf.*, New York, New York, March 29–April 3.

Lidia, S. M., S. Eylon, E. Henestroza, D. L. Vanecek, S. S. Yu, T. L. Houck, G. A. Westenskow, and D. E. Anderson (1999), "Initial commissioning results of the RTA injector," *1999 Particle Accelerator Conf.*, New York, New York, March 29–April 3.

Luck, J. P., C. Q. Little, and R. S. Roberts (1998), "A human supervisory approach to modeling industrial scenes using geometric primitives," *Proc. of the 1998 IEEE Int. Conf. on Robotics and Automation*, Leuven, Belgium, May 16–20.

Luo, G., J. H. Kinney, J. J. Kaufman, D. Haupt, A. Chiabrera, and R. S. Siffert (1999), "Relationship between plain radiographic patterns and three-dimensional trabecular architecture in the human calcaneus," *Osteoporosis Int.*, April, Vol. **9**, pp. 339–345.

Majumdar, K. and T. Altenbach (1998), "A graded approach for initiating event selection in a facility hazard analysis," *Int. Conf. on Probabilistic Safety Assessment and Management*, New York, New York, September.

Martinez, M. D., K. M. Skulina, F. J. Deadrick, J. K. Crane, B. Moran, J. Braucht, B. Jones, S. Hawkins, R. Tilley, J. Crawford, D. Browning, and F. Penko (1999), "Performance results of the high gain, Nd:glass, engineering prototype preamplifier module (PAM) for the National Ignition Facility (NIF)," *SPIE Proc. on Laser Resonators II*, San Jose, California, January, Vol. **3611**, pp. 169–180.

Martinez, M., J. K. Crane, L. A. Hackel, F. Penko, and D. Browning (1998), "Optimized diode-pumped regenerative amplifier for the National Ignition Facility," *Solid State Lasers for Application to Inertial Confinement Fusion*, Monterey, California, June 7–12.

Mascio, L. N., B. K. Yuen, W. P. Kegelmeyer, Jr., K. Matsumoto, J. Briner, and A. J. Wyrobek (1998), "Advances in the automated detection of metaphase chromosomes labeled with fluorescence dyes," *Cytometry 33*, Vol. **10**, October 18.

Mastel, E., J. Staggs, J. Benton, and J. Glaser (1998), "Implementation of transparency monitoring under the U.S./Russian HEU purchase agreement (July 1998)," *39th Ann. Meeting Int. Nuclear Material Management*, Naples, Florida, July 26–30.

McCallen, R., R. Couch, J. Hsu, F. Brow, and M. Hammache, A. Leonard, M. Brady, K. Salari, W. Rutledge, J. Ross, B. Storms, J. T. Heineck, D. Driver, J. Bell, and G. Zilliac (1999), "Progress in reducing aerodynamic drag for higher efficiency of heavy-duty trucks (Class 7–8)," *Soc. of Automotive Engineers, Government Industry Conf. Proc.*, Washington, DC, April 26–28.

McCarrick, J. and T. Houck (1999), "The effect of trapped backstreaming ions on beam focus and emittance in radiographic accelerators," *1999 Particle Accelerator Conf.*, New York, New York, March 29–April 3.

McCarrick, J., Y. J. Chen, T. L. Houck, and B. R. Poole (1998), "Trapping backstreaming ions from an x-ray converter using an inductive cell," *Proc. of the 19th Int. Linac Conf.*, Chicago, Illinois, August 23–28.

McKoon R. H. (1998), "Decarburization of uranium via electron beam processing, *Proc. of the Conf. on Electron Beam Melting and Refining State of the Art 1998*, Vol. **12**, No. 11, *Meeting of ASME*, pp. 170–176, Anaheim, California, November.

Milner, T. E., S. A. Telenkov, B. S. Tanenbaum, J. S. Nelson, and D. M. Goodman (1998), "Non-invasive evaluation of biological materials using pulsed photothermal tomography," *Proc. The Winter Ann. Meeting of ASME*, pp. 170–176, Anaheim, California, November.

Mishima, J., A. Wooten, D. Pinkston, S. Brereton, J. Cohen, T. Foppe, D. Gordon, H. Jordan, G. Kaiser, R. Marusich, C. Mueller, L. Restrepo, C. Steele, and W. Williams (1998), "Airborne release fractions at non-reactor nuclear facilities," *Am. Nuclear Soc. and Am. National Standards Institute*, May.

Mok, G. C., L. E. Fischer, S. S. Murty, and M. C. Witte (1998), "Shipping container response to three severe railway accident scenarios," *Am. Soc. of Mechanical Engineers Joint Pressure Vessels and Piping Conf.*, San Diego, California, July 26–31.

Ng, L. C., J. F. Holzrichter, G. C. Burnett, and T. J. Gable (1998), "Acoustic and EM waves for speech processing," *136th Meeting Acoustical Soc. of Am.*, Norfolk, Virginia, October 13.

Ng, L.C., E. Breitfeller, A. G. Ledebuhr, and F. A. Handler (1999), "Air-bearing guided intercept and line-of-sight experiments," *1st Biennial AIAA National Forum on Weapon System Effectiveness*, Ft. Walton Beach, Florida, April 6–8.

Nieh, T. G., R. O. Kaibyshev, and D. R. Lesuer (1998), "Superplasticity in a conventional coarse-grained 6061 Al and the liquid phase effect," *Sym. on Superplasticity and Superplastic Forming*, pp. 137–144.

O'Connell, W. J., W. L. Bourcier, J. Gansemer, and T. S. Ueng (1998), "Performance assessment modeling for Savannah River glass HLW disposal in a potential repository at Yucca Mountain," *Science and Technology for Disposal of Radioactive Tank Wastes*, Plenum Press, New York, New York, pp. 403–412.

O'Connor, T. G., S. Shen, P. Fabbricatore, S. Farinon, R. Musenich, C. Priano, R. A. Bell, M. Berndt, W. Burgess, W. Craddock, L. Keller, O. Dormicchi, P. Moreschi, R. Penco, P. Valente, and N. Valle (1998), "Design and testing of the 1.5 T superconducting solenoid for the BaBar detector at PEP-II in SLAC," *Applied Superconductivity Conf.*, Palm Springs, California, September.

Orth, C., R. Beach, C. Bibeau, E. Honea, K. Jancaitis, J. Lawson, C. Marshall, R. Sacks, K. Schaffers, J. Skidmore, and S. Sutton (1998), "Design modeling of the 100-J diode-pumped solid-state laser for Project Mercury," *Proc. of the SPIE*, Vol. **3265**, pp. 114–129.

Pao, H. and A. J. Poggio (1999), "Design of a TEM waveguide for ultra-wideband applications," *1999 IEEE AP-S Int. Sym. and USNC/URSI National Radio Science Meeting.*

Perry, M. D., D. Pennington, B. C. Stuart, G. Tietbohl, J. A. Britten, C. Brown, S. Herman, B. Golick, M. Kartz, J. Miller, H. T. Powell, M. Vergino, and V. Yanovsky (1999), "Petawatt laser pulses," *Optics Letters*, Vol. **24**, No. 4, February 1.

Poole, B. R., G. J. Caporaso, Y. J. Chen, and L. Wang (1998), "Analysis and modeling of a stripline beam kicker and septum," *Proc. of the 19th Int. Linac Conf.*, Chicago, Illinois, August 23–28.

Poole, B. R., G. J. Caporaso, Y. J. Chen, S. D. Nelson (1999), "Beam coupling impedance of fast stripline beam kickers," *1999 Particle Accelerator Conf.*, New York, New York, March 29–April 3.

Prassinos, P. G. and C. Y. Kimura (1998), "Aircraft crash assessment of U.S. nuclear power plants sites using the NRC methodology," *ASME/JSME/SFEN Int. Conf. on Nuclear Engineering*, San Diego, California, May 10–14.

Puso, M. A. and E. Zywicz (1998), "Energy and momentum conserving algorithms for rigid body contact," *Proc. of the Int. Conf. on Computational Engineering Science*, Atlanta, Georgia, October 22.

Richardson, R. A. and T. L. Houck (1998), "Physics design of the DARHT 2nd axis accelerator cell," *Proc. of the 19th Int. Linac Conf.*, Chicago, Illinois, August 23–28.

Riddle, R. A. (1998), "The radioactive materials packaging handbook, ORNL/M-5003, L. B. Shappert, ed., Ch. 6, "Materials," published for U.S. Department of Energy.

Roberson, G. P., H. E. Martz, D. E. Decman, J. A. Jackson, R. T. Bernardi, and D. C. Camp (1998), "Nondestruction assay using active and passive computed tomography," *39th Ann. Meeting Int. Nuclear Material Management*, Naples, Florida, July 26–30.

Roberson, G.P., H. E. Martz, D. E. Decman, J. A. Jackson, D. Clark, R. T. Bernardi, and D. C. Camp (1998), "Active and passive computed tomography for nondestructive assay," *Proc. of the 6th Nondestructive Assay Waste Characterization*, Salt Lake City, Utah, November 17–19.

Roberts, R. S., W. D. Aimonetti, and J. V. Bixler (1998), "Material characterization using a hyperspectral infrared imaging spectrometer," *Proc. of the 32nd Ann. Asilomar Conf. on Signals, Systems, and Computers*, Pacific Grove, California, November 1–4.

Rothenberg, J. E., J. M. Auerbach, S. N. Dixit, S. W. Haan, S. M. Pollaine, and W. H. Williams (1998), "Focal spot conditioning for indirect drive on National Ignition Facility," *Proc. of SPIE*, Vol. **3492**, pp. 65–77, *Solid State Lasers for Application to Inertial Confinement Fusion*, Monterey, California, June 7–12.

Rudd, L. vE., D. J. Pines, and P. H. Carter (1999), "Sub-optimal periodic cruise trajectories for hypersonic flight," *AIAA J. of Aircraft*, Vol. **36**, No. 2, March–April.

Runkel, M. (1998), "Monte Carlo simulation of the R/1 automated damage test," *Sym. on Laser Induced Damage in Optical Materials, SPIE Proc.*, Vol. **3578**.

Runkel, M., R. Jennings, J. DeYoreo, W. Sell, D. Milam, N. Zaitseva, L. Carmen, and W. Williams (1998), "An overview of recent KDP damage experiments and implications for National Ignition Facility tripler performance," *Solid State Lasers for Application to Inertial Confinement Fusion*, Monterey, California, June 7–12.

Runkel, M., W. W. Williams, and J. J. De Yoreo (1998), "Predicting bulk damage in National Ignition Facility triple harmonic generators," *Proc. SPIE*, Vol. **3578**, pp. 322–335; "Laser-induced damage in optical materials," G. J. Exarhos, A. H. Guenther, M. R. Kozlowski, K. L. Lewis, and M. J. Soileau, eds., September 28–October 1.

Sacks, R., J. Auerbach, E. Bliss, M. Henesian, J. Lawson, K. Manes, P. Renard, T. Salmon, J. Trenholme, W. Williams, S. Winters, and R. Zacharias (1998), "Application of adaptive optics for controlling the National Ignition Facility laser performance and spot size, solid state lasers for application to inertial confinement fusion," *Solid State Lasers for Application to Inertial Confinement Fusion*, Monterey, California, June 7–12.

Sampayan, S. (1998), "Mixed electron emission from lead zirconate-titanate ceramics," *J. of App. Physics*.

Sampayan, S., G. Caporaso, Y. Chen, M. Garcia, T. Houck, R. Richardson, J. Weir, G. Westenskow, C. Crist, and M. Krogh (1998), "Experimental investigation of beam optics issues at the Bremsstrahlung converters for radiographic applications," *Proc. of the 19th Int. Linac Conf.*, Chicago, Illinois, August 23–28.

Sampayan, S., R. Buckles, G. Caporaso, Y. Chen, C. Crist, S. Falabella, T. Houck, J. McCarrick, R. Richardson, D. Sanders, J. Weir, G. Westenskow, C. Crist, and M. Krogh (1999), "Beam-target interaction experiments for Bremsstrahlung converters applications," *1999 Particle Accelerator Conf.*, New York, New York, March 29–April 3.

Sandquist, G. M., D. M. Slaughter, C. Y. Kimura, and D. L. Sanzo (1998), "Risk assessment of high altitude free flight commercial aircraft operations," *4th Int. Conf. on Probabilistic Safety Assessment and Management*, New York, New York, Vol. **3**, September 13–18, pp. 1970–1975.

Sangster, T. C., J. J. Barnard, T. V. Cianciolo, G. D. Craig, A. Friedman, D. P. Grote, E. Halaxa, R. L. Hanks, G. Kamin, H. C. Kirbie, B. G. Logan, S. M. Lund, G. Mant, A. W. Molvik, W. M. Sharp, S. Eylon, D. Berners, T. J. Fessenden, D. L. Judd, L. Reginato, H. S. Hopkins, A. Debeling, W. Fritz, and J. Meredith (1998), "Status of experiments leading to a small recirculator," *Nuclear Instruments and Methods in Physics Research*, **A 415**, pp. 310–314.

Santangelo, P. J., D. L. Flowers, and I. M. Kennedy (1998), "Demonstration of droplet size and vaporization rate measurements in the near field of a two-phase jet with droplet lasing spectroscopy," *Appl. Optics*, Aug. 20, Vol. **37**, No. 24, pp. 5573–5578.

Seppala, L. G. (1998), "The IODC98 optical design problem: method of progressing from an achromatic to an apochromatic design," *Proc. of the Int. Optical Design Conf.*, Kona, Hawaii, June.

Sheaffer, M. K., G. R. Thomas, R. K. Dann, and E. W. Russell (1998), "Engineering drawings for 10 CFR Part 71 package approvals," U.S. Nuclear Regulatory Commission (NUREG/CR-5502), May.

Sheaffer, M. K., L. E. Fischer, and M. E. Wangler (1998), "Considerations for neglecting water leakage in the criticality analysis of individual packages," *Proc. of the 12th Int. Conf. on the Packaging and Transportation of Radioactive Materials*, Paris, France, May, Vol. **1**, pp. 245–250.

Shen, S., K. Kishiyama, D. Behne, J. Berg, J. Bowman, T. DaCosta, M. Harper, F. Spinos, R. Valdiviez, and D. Schrage (1999), "Testing of vacuum system for APT/LEDA RFQ," *1999 Particle Accelerator Conf.*, New York, New York, March 29–April 3.

Shoaff, P. V., G. Hansen, K. Kishiyama, and S. Shen (1999), "Design and development of the vacuum systems for the accelerator production of tritium project ED&D cryomodule," *1999 Particle Accelerator Conf.*, New York, New York, March 29–April 3.

Shoari, S., N. Bagherzadeh, D. Goodman, T. E. Milner, D. J. Smithies, and J. S. Nelson (1998), "A parallel algorithm for pulsed laser infrared tomography," *Pattern Recognition Letters*, Vol. **19**, No. 5–6, April, pp. 521–526.

Shu, J. Y. and C. Y. Barlow (1999), "Strain gradient effects on microscopic strain field in a metal-matrix composite," *Proc. of 7th Int. Sym. on Plasticity and Its Current Applications*, January, pp. 523–526.

Shu, J. Y. (1998), "Scale-dependent deformation of porous single crystals," *Int. J. of Plasticity*, Vol. **14**, Nos. 10–11, pp. 1085–1107.

Shu, J. Y. and N. A. Fleck (1999), "Strain gradient crystal plasticity: the size-dependent deformation of bicrystals," *J. of the Mechanics and Physics of Solids*, Vol. **47**, February, pp. 297–324.

Shu, J. Y., W. E. King, and N. A. Fleck (1999), "Finite elements for materials with strain gradient effects," *Int. J. for Numerical Methods in Eng.*, Vol. **44**, January, pp. 373–391.

Simon, J., S. Saffer, F. Sherman, and C. J. Kim (1998), "Lateral polysilicon microrelays with a mercury microdrop contact," *IEEE Transactions on Industrial Electronics*, Vol. **45**, No. 6, December, pp. 854–60.

Smithies, D. J., T. E. Milner, B. S. Tanenbaum, D. M. Goodman, and J. S. Nelson (1998), "Accuracy of subsurface temperature distributions from pulsed photothermal radiometry," *Physics in Medicine and Biology*, September.

Sommer, S. (1998), "National Ignition Facility laser system performance ratings," *Supplement to Proc. of SPIE*, Vol. **3492**, *3rd Ann. Int. Conf. on Solid State Lasers for Application to Inertial Confinement Fusion*, Bellingham, Washington.

Sommer, S. C. (1998), "National Ignition Facility laser system performance ratings," *Solid State Lasers for Application to Inertial Confinement Fusion*, Monterey, California, June 7–12.

Sommer, S. C. and E. S. Bliss (1998), "Beam position error budget developed for National Ignition Facility," *Solid State Lasers for Application to Inertial Confinement Fusion*, Monterey, California, June 7–12.

Sommer, S. C. and P. B. MacCalden (1998), "The development and implementation of seismic design and evaluation criteria for National Ignition Facility," *1998 ASME/JSME Joint Pressure Vessels and Piping Conf.*, San Diego, California, July 26–30.

Sommer, S. C., J.A. Caird *et al.* (1998), "The Z-Backlighter, a laser x-ray diagnostic for high energy density physics in matter," *Solid State Lasers for Application to Inertial Confinement Fusion*, Monterey, California, June 7–12.

Stitzer, K., K. Albert, D. Walt, T. Swager, F. Milanovich, S. B. Brown, and M. L. Myrick (1999), "Interference filters designed specifically for optical sensing with the nile red TNT polymer sensors," *PITTCON®'99*, Orlando, Florida, March 7–12.

Stolz, C. J., L. M. Sheehan, S. M. Maricle, S. Schwartz, and J. Hue (1998), "Laser conditioning methods in hafnia silica multilayer mirrors," *High-Power Lasers*, S. Basu, ed., *Proc. SPIE, No.* 3264, pp. 105–112.

Stolz, C. J., L. M. Sheehan, S. M. Maricle, S. Schwartz, and J. Hue (1999), "Laser conditioning methods of hafnia silica multilayer mirrors," *Laser-Induced Damage in Optical Materials: 1998*, G. J. Exarhos, A. H. Guenther, M. R. Kozlowski, K. L. Lewis, and M. J. Soileau, eds., *Proc. SPIE, Vol.* **3578**, pp. 144–152.

Sunwoo, A. J., T. S. Chow, and C. J. Long (1998), "Effect of physical vapor deposition on microstructure and properties of U-6wt%NB alloy," *J. of Nuclear Materials*, May.

Sunwoo, A., R. N. Accardo, and W. H. Gourdin (1998), "Effects of heat treatment on grain refinement in cast U-0.25wt%V alloy," *J. of Nuclear Materials*, July.

Sutton, S., A. Erlandson, R. London, K. Manes, C. Marshall, C. Petty, R. Pierce, L. Smith, L. Zapata, J. Beullier, and B. Bicrel (1998), "Thermal recovery of the National Ignition Facility amplifiers," *Solid State Lasers for Application to Inertial Confinement Fusion*, Monterey, California, June 7–12, *SPIE*, July.

Syn, C. K., D. R. Lesuer, T. G. Nieh, H. S. Yang, K. R. Brown, R. O. Kaibyshev, and E. N. Petrov (1998), "Roll forming technology for manufacturing axisymmetric automotive components," *Automotive Alloys II*, pp. 173–183.

Tabatabaie, M., S. Sommer, and P. MacCalden (1998), "Analysis of soil-structure interaction due to ambient vibration," *1998 ASME/JSME Joint Pressure Vessels and Piping Conf.*, San Diego, California, July 26–30.

Taleff, E., G. Henshall, T. Nieh, D. Lesuer, and J. Wadsworth (1998), "Warm-temperature ductility in Al-Mg alloys," *Metallurgical and Materials Transactions A*, Vol. **29A**, pp. 1081–1091.

Telenkov, S. A., D. J. Smithies, D. M. Goodman, B. S. Tanenbaum, J. S. Nelson, and T. E. Milner (1998), "Infrared imaging of *in vivo* microvasculature following pulsed laser irradiation," *J. Biomedical Optics*, October.

Telenkov, S. A., D. M. Goodman, B. S. Tanenbaum, J. S. Nelson, and T. E. Milner (1998), "Infrared imaging of laser-heated port wine stains," *Ann. Meeting of the Optical Soc. of America*, Baltimore, Maryland, October.

Thomas, G., J. Candy, D. Perkins, R. Huber, and M. Axelrod (1998), "Acoustic characterization of prosthetic heart valves," *Review of Progress in Quantitative Nondestructive Evaluation*, **18b**, Plenum Press, New York, New York, pp. 1587–1592.

Tiszauer, D., S. Yakuma, and D. McMahon (1999), "A six-degree of freedom end effector places 8000 lb. robotic canisters in the National Ignition Facility," *8th Int. Topical Meeting on Robotics and Remote Systems*, Pittsburgh, Pennsylvania, April 26.

Tiszauer, D., S. Yakuma, and D. McMahon (1999), "Development of an automated guided vehicle system for large scale materials handling of optics in the National Ignition Facility," *8th Int. Topical Meeting on Robotics and Remote Systems*, Pittsburgh, Pennsylvania, April 26.

Trummer, D. J., R. J. Foley, and G. S. Shaw (1998), "Stability of optical elements in the National Ignition Facility target area building," *Solid State Lasers for Application to Inertial Confinement Fusion*, Monterey, California, June 7–12.

Tung, L. S. and S. Shen (1999), "Vacuum simulation of RF cavities to optimize pump configurations," *1999 Particle Accelerator Conf.*, New York, New York, March 29–April 3.

Van Arsdall, P. J., R. C. Bettenhausen, F. W. Holloway, R. A. Saroyan, and J. P. Woodruff (1998), "National Ignition Facility integrated computer control system," *Solid State Lasers for Application to Inertial Confinement Fusion*, Monterey, California, June 7–12.

Vogt, D. K., D. Thomas, J. Millacci, V. N. Archangelskiy, and J. B. Benton (1999), "Status and performance of the HEU purchase contract between the U. S. enrichment corporation and Techsnabexport Co.," *Institute of Nuclear Materials Management, 40th Ann. Meeting*, July 25–29.

Walsh, B., J. Miller, and T. G. O'Connor (1998), "High current tests of the full size BaBar superconductor," *Applied Superconductivity Conf.*, Palm Springs, California, September.

Walters, D., J. Wondra, S. Nunan, and M. Bland (1999), "Graphical interface for the physics-based generation of inputs to 3D MEEC SGEMP and SREMP simulations," *GOMAC Digest of Papers 17th Ann. Hardened Electronics and Radiation Technology Conf.*, March 9–12.

Wang, L., S. M. Lund, G. J. Caporaso, Y. J. Chen, and B. R. Poole (1999), "A prototype dipole septum magnet for a fast high current kicker," *1999 Particle Accelerator Conf.*, New York, New York, March 29–April 3.

Weakley, S. C., C. J. Stolz, Z. L. Wu, R. P. Bevis, and M. K. von Gunten (1999), "Role of starting material composition in interfacial damage morphology of hafnia silica multilayer coatings," *Laser-Induced Damage in Optical Materials: 1998*, G. J. Exarhos, A. H. Guenther, M. R. Kozlowski, K. L. Lewis, and M. J. Soileau, eds., *Proc. SPIE*, Vol. **3578**, pp. 137–143.

Westenskow, G. A., T. L . Houck, D. E. Anderson, S. Eylon, E. Henestroza, S. M. Lidia, D. L. Vanecek, and S. S. Yu (1998), "RTA gun performance," *Proc. of the 19th Int. Linac Conf.*, Chicago, Illinois, August 23–28.

Westenskow, G. A., T. L. Houck, D. E. Anderson, S. Eylon, E. Henestroza, S. M. Lidia, D. L. Vanecek, and S. S. Yu (1998), "Progress on the relativistic klystron two-beam accelerator prototype," *Proc. of the 8th Advanced Accelerator Workshop*, Baltimore, Maryland, June.

Williams, W. H. (1998), "Simulations of a phase corrector plate for the National Ignition Facility," *Proc. of SPIE*, Vol. **3492**, *Solid State Lasers for Application to Inertial Confinement Fusion*, Monterey, California, June 7–12.

Williams, W. H., J. M. Auerbach, M. A. Henesian, J. K. Lawson, and R. A. Sacks (1998), "The National Ignition Facility's basic focal spot for ICF temporally shaped pulses," National Ignition Facility Performance Ratings, Supplement to *Proc. of SPIE*, Vol. **3492**, pp. 55–60, *Solid State Lasers for Application to Inertial Confinement Fusion*, Monterey, California, June 7–12.

Williams, W. H., J. M. Auerbach, M. A. Henesian, J. K. Lawson, P. A. Renard, and R. A. Sacks (1998), "The National Ignition Facility's power and energy ratings for flat-in-time pulses," National Ignition Facility Performance Ratings, *Supplement to Proc. of SPIE*, Vol. **3492**, pp. 11–20, *Solid State Lasers for Application to Inertial Confinement Fusion*, Monterey, California, June 7–12.

Williams, W. H., J. M. Auerbach, M. A. Henesian, J. K. Lawson, P. A. Renard, and R. A. Sacks (1998), "The National Ignition Facility's basic focal spot for temporally flat pulses," National Ignition Facility Performance Ratings, Supplement to *Proc. of SPIE*, Vol. **3492**, pp. 22–38, *Solid State Lasers for Application to Inertial Confinement Fusion*, Monterey, California, June 7–12.

Winters, S. E., T. Arnold, E. S. Bliss, J. Bergum, M. A. Kartz, J. T., Salmon, C. J. Stolz, B. M. Van Wonterghen, P. J. Wegner, C. Weinzapfel, W. Whistler, and R. A. Zacharias (1998), "Design overview of a prototype large aperture deformable mirror for the National Ignition Facility," *Proc. 13th Ann. Am. Soc. of Precision Engineering Conf.*, Monterey, California, October.

Winters, S., T. Arnold, E. Bliss, J. Bergum, M. Kartz, T. Salmon, C. Stolz, B. Van Wonterghem, P. Wegner, C. Weinzapfel, W. Whistler, and R. Zacharias (1998), "Design overview of a prototype large aperture deformable mirror for the National Ignition Facility," *Proc. 13th Ann. Am. Soc. of Precision Engineering Conf.*, Monterey, California, October.

Witte, M. C., J. Hovingh, G. C. Mok, S. S. Murty, T. F. Chen, L. E. Fischer, and D. T. Ta (1998), "Summary and evaluation of steel billet testing," *Am. Soc. of Mechanical Engineers Joint Pressure Vessels and Piping Conf.*," San Diego, California, July 26–31.

Woodruff, J. P. and P. J. Van Arsdall (1998), "A large distributed control system using ADA in fusion research," *Int. SIGAda Conf. Proc.*, *Association for Computing Machinery*, November 8, pp. 121–131.

Yakuma, S. and E. Grasz (1998), "Getting one-ton, phone-booth-sized optic modules into the world's largest laser," *2nd Int. Conf. on Engineering Design and Automation*, Maui, Hawaii, August 9–12.

Yakuma, S., E. Grasz, S. Bahowick, A. Rowe, J. Sander, D. Swan and D. Tiszauer (1998), "Getting one-ton, phone-booth-sized optic modules into the world's largest laser," *Solid State Lasers for Application to Inertial Confinement Fusion*, Monterey, California, June 7–12.

Yakuma, S., S. Bahowick, A. Rowe, and D. McMahon (1999), "Installation of line replaceable units into the National Ignition Facility," *8th Int. Topical Meeting on Robotics and Remote Systems*, Pittsburgh, Pennsylvania, April 26.

Zacharias, R., E. Bliss, M. Feldman, A. Grey, M. Henesian, J. Koch, R. Sacks, T. Salmon, J. Toeppen, L. Van Atta, P. Wegner, W. Williams, S. Winters, C. LaFiandra, and D. Bruns (1998), "The National Ignition Facility (NIF) wavefront control system, solid state lasers for application to inertial confinement fusion," *Solid State Lasers for Application to Inertial Confinement Fusion*, Monterey, California, June 7–12.

Zaitseva, N., J. Atherton, R. Rozsa, L. Carmen, I. Smolsky, M. Runkel, R. Ryon, and L. James (1998), "Design and benefits of continuous filtration in rapid growth of large KDP and DKDP crystals," *J. of Crystal Growth*, Vol. **197**, June 10, pp. 911–920.

Zywicz, E. and M. A. Puso (1999), "A general conjugate—gradient based predictor-corrector solver for explicit finite-element contact," *Int. J. for Numerical Methods in Engineering*, Vol. **44**, pp. 439–459.

Author Index

Author Index

Ackler, H. D. 2–1, 2–11
Allen, D. 2–31
Amendt, P. 2–41
Ashby, A. E. 5–1
Astaneh-Asl, A. 1–1, 1–25
Aufderheide, III, M. B. 5–47

Baker, E. 4–27
Baldwin, J. M. 3–25
Balooch, M. 2–3
Benett, W. J. 2–1, 2–63
Blaedel, K. L. 3–29
Bond, S. W. 2–49
Born, D. K. 3–21
Bowers, M. W. 5–5
Brewer, L. R. 2–19
Brown, A. A. 4–39
Brown, S. B. 2–41
Brugger, S T. 4–53
Buettner, M. H. 1–51
Burke, G. J. 4–53
Burnett, G. C. 1–33

Carlisle, K. 3–11
Carr, J. W. 3–1
Casey, J. 4–39
Champagne, N. J. 4–23
Chapline, G. F. 2–45
Chien, C. 2–57
Ciarlo, D. R. 1–41, 2–3, 2–7, 2–31, 5–1
Clague, D. S. 4–35
Clark, G. A. 1–33
Clayton, K. 2–31
Colston, Jr., B. W. 2–41
Cooke, J. B. 5–77
Cooper, G. A. 2–15
Couch, R. G. 2–63, 4–63
Cowan, T. E. 4–47
Cowan, W. D. 2–11
Cunningham, B. J. 2–31

Da Silva, L. 2–41
Daily, W. D. 1–51
Delgrande, N. K. 5–37
DeTeresa, S. J. 2–31
Ditmire, T. R. 4–47
Dolaghan, J. S. 4–63
Dolan, K. W. 5–11
Duffy, S. 4–27
Dunn, T. A. 4–63
Durbin, P. F. 5–37

Edson, S. L. 3–11
Emanuel, M. A. 2–49
Everett, M. J. 2–41

Ferencz, R. M. 4–17
Folta, J. A. 2–11
Fu, C. Y. 2–45
Fuller, C. D. 2–63

Goodman, D. M. 5–47
Graff, R. T. 2–27
Groves, S. E. 2–3, 2–31

Hagans, K. G. 2–15
Hall, J. M. 5–47
Hamilton, J. 2–1
Harren, M. 1–41
Haskins, J. J. 5–11
Hilken, D. L. 2–7
Hoehler, M. S. 1–43
Huber, R. D. 5–25

Jackson, J. A. 5–31, 5–47
James, D. L. 2–41
Jankowski. A. F. 2–23
Jones, L. M. 2–27

Kallman, J. S. 4–53, 5–1
Kamath, C. 4–17
Krulevitch, P. 2–11, 2–19

Landram, C. S. 5–37
Larsen, S. C. 1–25
Larson, M. C. 2–49
Le Sage, G. P. 4–47
Lee, A. P. 2–7, 2–21, 2–41
Lee, H. 5–25
Lewis, J. P. 1–43
Lin, J. I. 4–49
Logan, C. M. 5–11, 5–47
London, R. A. 2–41
Lowry, M. E. 2–49, 5–77

Martin, R. W. 5–37
Martz, Jr., H. E. 5–47
McCallen, D. B. 1–1, 1–25, 1–33, 1–43

McCallen, R. C. 4–63
McConaghy, C. F. 2–57, 2–59
Molau, N. E. 5–77
Morey, R. M. 1–51, 5–71
Morse, J. D. 2–15, 2–23, 2–27

Nath, D. S. 4–39
Nikkel, Jr., D. J. 4–39
Noble, C. R. 1–33, 1–43

O'Brien, M. J. 4–27
Olivier, S. S. 2–11, 2–45
Orme, M. 4–1

Palko, J. 4–27
Petrich, L. I. 2–45
Piscotty, M. A. 3–17
Pocha, M. D. 2–49
Poggio, A. J. 4–23
Puso, M. A. 4–5

Richardson, C. 5–25
Riddle, R. A. 4–27
Rikard, R. D. 5–11
Rosenzweig, J. 4–47
Sargis, P. D. 5–77
Schach von Wittenau, A. 5–47
Schneberk, D. J. 5–11
Schumann, D. L. 2–41
Seward, K. P. 2–3, 2–21
Shapiro, A. B. 4–1
Sharpe, R. M. 4–23
Shell, T. E. 2–1
Simon, J. 1–41, 2–9
Sloan, D. M. 5–47
Speck, D. E. 4–11
Spicer, J. 5–25
Steich, D. J. 4–53
Strand, O. T. 5–77
Swift, D. W. 3–29
Syn, C. K. 4–27

Thomas, G. H. 5–1, 5–25
Trevino, J. C. 2–7

Wang, A. W. 2–21, 2–41, 2–63
White, D. A. 4–53

Yoon, C. 2–31
Yu, J. 2–11

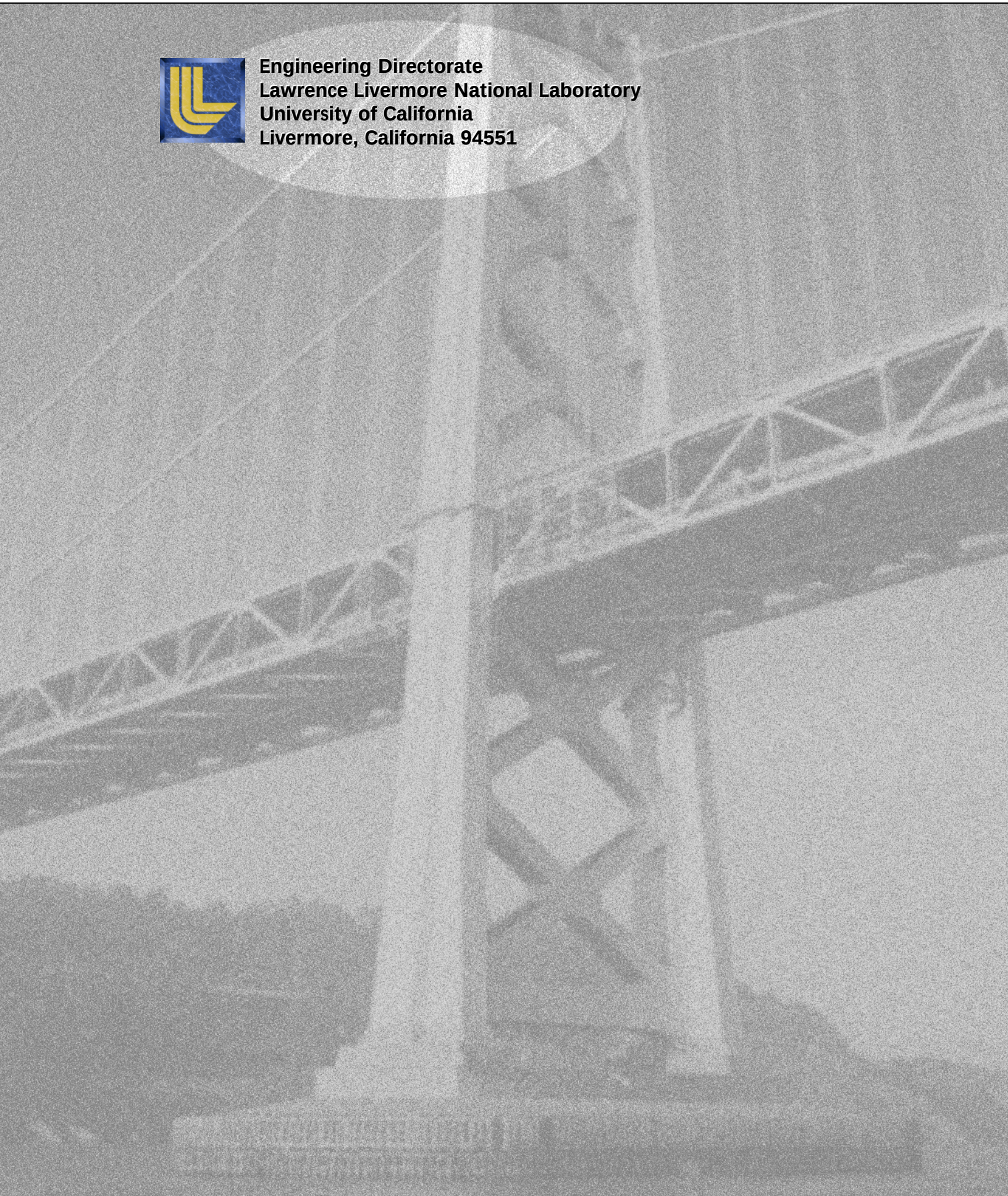

Engineering Directorate
Lawrence Livermore National Laboratory
University of California
Livermore, California 94551